



universität
wien

DISSERTATION / DOCTORAL THESIS

Titel der Dissertation / Title of the Doctoral Thesis

Drivers of Mesozoic Paleoclimate Change across Time Scales – Supercontinent Breakup, Orbital Cycles and Volcanic Disruptions

verfasst von / submitted by

Jan Philip Landwehrs

angestrebter akademischer Grad / in partial fulfillment of the requirements for the
degree of

Doktor der Naturwissenschaften (Dr. rer. nat.)

Wien, 2022 / Vienna 2022

Studienkennzahl lt. Studienblatt /
degree programme code as it appears on
the student record sheet:

UA 796 605 426

Dissertationsgebiet lt. Studienblatt /
field of study as it appears on
the student record sheet:

Erdwissenschaften

Betreut von / Supervisor:

Univ.-Prof. Dr. Michael Wagreich

Betreut von / Supervisor:

PD Dr. Georg Feulner

Abstract

The natural world that we live in today is the result of the Earth’s evolution since its formation ~ 4.6 billion years ago. Unraveling its eventful history thus helps us to comprehend where we are coming from, which mechanisms govern the Earth system and how this is framing the future. The Mesozoic era (~ 252 – 66 million years ago) was a crucial period of transition from the last supercontinent Pangea towards the modern fragmented continental configuration with its familiar climatic patterns, as well as from “ancient” Paleozoic to “modern” Cenozoic forms of life, including the evolution of mammals. This thesis aims to contribute to a deeper understanding of paleoclimate change and its drivers during this geologic era. To accomplish this, coupled Earth system models (ESM) are used here to simulate the dynamics of climate under conditions and forcing factors that characterize the Mesozoic. Manifold environmental changes and their respective drivers acted throughout Earth history. For this thesis, three layers with different time scales and forcing mechanisms are considered: (I) the long-term climate evolution throughout the whole Mesozoic, shaped by >1 Myr tectonic-scale processes, (II) climatic oscillations paced by orbital cycles with periodicities on ~ 10 – 100 kyr scales, (III) disruptive events on 1 yr to 100 kyr time scales caused by large scale volcanism. Each of these regimes is addressed in one of the three publications forming this dissertation, with a focus on certain aspects or time periods.

For the first part, the Mesozoic long-term climate evolution and its drivers are assessed with an ensemble of equilibrium climate simulations for 40 equally spaced geologic time slices. More than 200 simulations are carried out with the CLIMBER-3 α ESM and systematically varied boundary conditions, including the paleogeography, atmospheric CO₂ concentrations, orbital parameters and solar luminosity. These simulations identify a baseline warming trend through the Mesozoic, driven by increasing continental flooding and insolation. Relatively high reconstructed p CO₂ levels support especially warm greenhouse conditions during the Triassic and mid-Cretaceous, while lower levels contribute to cooler temperatures in the Jurassic and latest Cretaceous. Continental fragmentation and flooding are found to drive a trend towards more humid, less seasonal and more zonal climates from the Late Triassic towards the mid-Cretaceous. This synthesis of various model and proxy data provides a new integrated perspective of secular climate trends through the Mesozoic. It also serves to contextualize the following two parts of this thesis which focus on shorter-term processes with representative examples from certain stages of the Mesozoic.

One of these examples is represented by the Late Triassic cyclic lake sediment record of the Newark-Hartford basins (NHB) of the eastern United States. This geologic archive reveals the profound modulation of climate by orbital cycles on $\sim 10^4$ – 10^5 yr time scales in the tropics of Pangea during a global greenhouse climate phase without evidence of major glaciations. The second part of this dissertation analyzes an ensemble of orbitally-driven transient climate simulations with the CLIMBER-X ESM for nine geologic time slices from 230 to 190 Ma. The simulations are carried out with two different paleogeographic reconstructions, three p CO₂ values and a simplified orbital forcing composed of three eccentricity, precession and obliquity periodicities (20, 40 and 100 kyr). This provides novel opportunities for the climatic interpretation of the NHB lake level trends and fluctuations. Pangea’s northward drift is found to cause a shift from tropical humid conditions in the NHB region towards more seasonal and ultimately semi-arid climates. In agreement with the record, the maximum orbital modulation of the precipitation–evaporation balance is simulated during the 220–200 Ma interval, whereas it is limited by reduced seasonality before and enhanced aridity afterwards. Low p CO₂ levels cause drier conditions and a

mutated orbital signal during the Rhaetian (~ 208 – 201 Ma), whereas higher levels linked to volcanic carbon emissions contribute to wetter conditions and stronger humidity cycles at the Triassic–Jurassic boundary (~ 201 Ma). The simulations suggest that signals of obliquity in the NHB region could derive from higher-latitude effects on the seasonal shift of the tropical rainfall belt. This work presents the first framework of transient orbitally-driven coupled climate model simulations under long-term paleogeographic changes developed for any Mesozoic time period. The approach bears great potential for the interpretation and correlation of other cyclostratigraphic archives.

Of the major rapid environmental disruptions of the Mesozoic many have been linked to Large Igneous Province (LIP) volcanic episodes. The third part of this thesis studies effects of volcanogenic gas emissions from the Central Atlantic Magmatic Province (CAMP) and their role in the end-Triassic mass extinction event. An ensemble of climate–biogeochemistry simulations with the CLIMBER-3 α +C ESM is carried out for a Late Triassic paleogeography and initial equilibrium states at different $p\text{CO}_2$ values. The initial states are perturbed by brief (~ 1 – 6 kyr) volcanic emission pulses during which 2500–7500 GtC are released to the atmosphere and 0–500 GtS form stratospheric aerosols. The simulations show that these simultaneous forcings can cause a sequence of short and variable global cooling followed by long-term warming by the added greenhouse gases ($+1.8$ to $+4.4$ °C). The annual to millennial scale cooling is caused by the radiative forcing of the sulfur aerosols and exceeds -4 °C in many of the tested scenarios. The latter are synthesized from available constraints on the style, amounts and timing of volcanogenic emissions of the CAMP. As their reconstruction from geologic records is extremely challenging, the modeling describes possible consequences in a range of scenarios. The results suggest that the modeled cooling–warming sequences would have pushed coral reef habitats to sub-optimal temperatures, with amplified thermal stress due to the alternating temperature trends. Ocean acidification and deoxygenation are observed as well. These mechanisms are universally discussed as the LIP-related drivers of the prominent geological events of the Mesozoic. Together with the representation of this entire era (Part I), the developed modeling approach could pave the way to a unified assessment of environmental perturbations during Mesozoic LIP episodes.

Altogether, the presented research provides a comprehensive perspective on Mesozoic paleoclimates and general mechanisms of climate change across annual to multi-million year time scales. The three parts yield new insights into the tectonic-scale long-term climate evolution, the modulation of climate by orbital cycles and the disruption of the Mesozoic Earth system by LIP volcanism. Each part establishes novel modeling approaches making use of fast Earth System Models of Intermediate Complexity (EMIC). In addition to computationally more demanding Atmosphere–Ocean General Circulation Models, these flexible tools are particularly useful in deep time paleoclimate research because they allow for large ensembles and relatively long simulations. This enabled incorporating other relevant empirical and modeled evidence into the scientific approach, both for constraining and driving the ESMs as well as for linking the model results to proxy data.

Keywords

Mesozoic, Paleoclimate, Climate Modeling, Orbital Cycles, Large Igneous Provinces, Triassic, Jurassic, Cretaceous

Zusammenfassung

Die natürliche Umwelt unserer Gegenwart ist aus der Entwicklung der Erde seit ihrer Entstehung vor rund 4,6 Milliarden Jahren hervorgegangen. Das Entschlüsseln dieser ereignisreiche Geschichte hilft uns daher zu erfassen, woher wir kommen, welche Mechanismen das Erdsystem bestimmen und wie mögliche zukünftige Entwicklungen einzuordnen sind. Das Mesozoikum (~ 252 –66 Millionen Jahre vor heute) war eine entscheidende Phase des Übergangs vom letzten Superkontinent Pangäa hin zur gegenwärtigen, fragmentierten Kontinentalverteilung mit ihren bekannten Klimazonen, sowie von alten paläozoischen zu moderneren känozoischen Lebensformen, einschließlich der Evolution der Säugetiere. Diese Dissertation hat das Ziel, zu einem tieferen Verständnis von paläoklimatischen Veränderungen dieser geologischen Ära beizutragen. Um die Dynamik des Klimas unter den Rahmenbedingungen und Antriebskräften des Mesozoikums zu charakterisieren, werden dabei gekoppelte Erdsystemmodelle (ESM) verwendet. Eine Vielzahl von Umweltveränderungen und ihrer jeweiligen Treiber haben im Laufe der Erdgeschichte gewirkt. Für die vorgelegte Arbeit werden drei Ebenen mit jeweils unterschiedlichen Zeitskalen und Antriebsmechanismen betrachtet: (I) die langfristige Klimaentwicklung über das gesamte Mesozoikum, die von Prozessen auf tektonische Zeitskalen (>1 Myr) angetrieben wurde, (II) Klimaoszillationen, die durch Orbitalzyklen mit Periodendauern von ~ 10 –100 kyr angetrieben wurden, (III) Umweltstörungen auf Zeitskalen von 1 yr bis 100 kyr, die durch großskaligen Vulkanismus hervorgerufen wurden. Jedes dieser drei Regime wird in einer von drei Publikationen dieser Dissertation behandelt, wobei der Fokus jeweils auf bestimmte Aspekte oder Zeiträume liegt.

Im ersten Teil der Arbeit wird die langfristige Klimaentwicklung des Mesozoikums mithilfe eines Ensembles von Gleichgewichtsklimasimulationen für 40 geologische Zeitscheiben untersucht. Dafür wurden mehr als 200 Simulationen mit dem CLIMBER-3 α ESM bei systematisch variierten Randbedingungen, einschließlich der Paläogeographie, der atmosphärischen CO₂-Konzentrationen, der Orbitalparameter und der Sonnenleuchtkraft durchgeführt. Diese Simulationen zeigen einen grundlegenden Erwärmungstrend während des Mesozoikums an, der durch eine zunehmende Überflutung der Kontinente und die wachsende Sonnenleuchtkraft angetrieben wurde. Relativ hohe rekonstruierte p CO₂-Werte legen besonders warme Treibhausbedingungen während der Trias und der Mittelkreide nahe, wohingegen niedrigere p CO₂-Werte zu niedrigeren Temperaturen im Jura und am Ende der Kreidezeit beitragen. Die Fragmentierung und Überflutung verursachte einen Trend hin zu feuchteren, weniger saisonalen und stärker zonalen Klimaten. Die präsentierte Zusammenführung von verschiedenen Modell- und Proxy-Daten bietet einen vertieften Einblick in die großen klimatischen Trends des Mesozoikums. Dies dient auch dazu, die folgenden zwei Teile dieser Arbeit in einen langfristigen Rahmen einzuordnen, da sie sich mit kurzfristigeren Prozessen anhand repräsentativer Beispiele aus bestimmten Stufen des Mesozoikums befassen.

Eines dieser Beispiele stellen die zyklischen Abfolgen von Seesedimenten der späten Trias dar, welche aus den Newark-Hartford Becken (NHB) im Osten der USA stammen. Dieses geologische Archiv offenbart die starke Modulation des Klimas durch Orbitalzyklen auf Zeitskalen von $\sim 10^4$ – 10^5 Jahren in den Tropen Pangäas in einem Treibhausklimazustand. Der zweite Teil dieser Arbeit analysiert ein Ensemble von orbital angetriebenen transienten Klimasimulationen mit dem CLIMBER-X ESM für neun geologische Zeitscheiben von 230 bis 190 Ma. Die Simulationen werden mit zwei verschiedenen paläogeographischen Rekonstruktionen und für drei p CO₂-Werte durchgeführt. Angetrieben werden sie durch ein idealisiertes Orbitalforcing, das sich aus periodischen Änderungen der Exzentrizität, Präzession und Obliquität zusammensetzt (20, 40 und 100 kyr). Dies bietet neuartige Möglichkeiten,

die Trends und Fluktuationen der Seewassertiefen in den NHB klimatisch zu interpretieren. Die Bewegung Pangäas nach Norden verursacht in den Simulationen einen Übergang von einem tropisch feuchtem Klima in der NHB-Region hin zu stärker saisonalen und schließlich semi-ariden Klimaten. In Übereinstimmung mit den Sedimentbefunden ist die orbitale Modulation der Niederschlags-Verdunstungsbilanz während des Zeitraums von 220 bis 200 Ma am stärksten ausgeprägt. Für frühere Zeitscheiben ist sie durch eine geringe Saisonalität limitiert, für spätere Zeitscheiben durch die ausgeprägtere Trockenheit. Niedrige $p\text{CO}_2$ -Werte verursachen trockenere Bedingungen und ein gedämpftes Orbitalsignal im Rhaetium (~ 208 – 201 Ma). Höhere Werte als Resultat von vulkanischen Kohlenstoffemissionen tragen hingegen zu humideren Bedingungen und stärkeren Feuchtigkeitszyklen an der Trias-Jura-Grenze (~ 201 Ma) bei. Die Simulationen legen außerdem nahe, dass Obliquitätssignale in der NHB Region daher stammen, dass sich Effekte aus höheren Breiten auf die saisonale Verschiebung des tropischen Niederschlagsgürtels auswirken. Diese Arbeit stellt den ersten Rahmen von transienten, orbitalgetriebenen, gekoppelten Klimamodellsimulationen unter Einbeziehung langfristiger paläogeographischer Veränderungen dar, der für eine Zeitperiode des Mesozoikums entwickelt wurde. Dieser Ansatz birgt großes Potential für die Interpretation und Korrelation weiterer zyκλοstratigraphischer Archive.

Von den ausgeprägtesten und schnellsten Umweltstörungen des Mesozoikums wird ein Großteil mit vulkanischen Episoden, den magmatischen Großprovinzen (LIPs), in Verbindung gebracht. Der dritte Teil dieser Arbeit untersucht Auswirkungen von vulkanischen Gasemissionen der Zentralatlantischen Großprovinz (CAMP) und ihre mögliche Rolle für das Massenaussterbeereignis am Ende der Trias. Ein Ensemble von Klima-Biogeochemie-Simulationen mit dem CLIMBER-3 α +C ESM wurde hierfür unter Verwendung einer Paläogeographie für die späte Trias und von Ausgangszuständen bei drei $p\text{CO}_2$ -Werten durchgeführt. Diese Ausgangszustände wurden dann durch kurze (~ 1 – 6 kyr) vulkanische Emissionspulse gestört, im Zuge derer 2500–7500 GtC in die Atmosphäre emittiert werden und 0–500 GtS stratosphärische Aerosole bilden. Die Simulationen zeigen, dass diese gleichzeitigen Antriebe eine Abfolge von kurzer, variabler Abkühlung und nachfolgend langanhaltender, globaler Erwärmung ($+1.8$ bis $+4.4$ °C) verursachen können. Die Abkühlung über Zeiträume von Jahren bis Jahrtausenden wird dabei durch den Strahlungsantrieb der Schwefelaerosole verursacht und überschreitet -4 °C in vielen der getesteten Szenarien. Letztere sind auf Grundlage verfügbarer Abschätzungen über die Art, Menge und zeitliche Verteilung der vulkanischen Emissionen der CAMP gestaltet worden. Da deren Rekonstruktion anhand geologischer Befunde jedoch eine große Herausforderung darstellt, dient die Modellierung auch dazu, mögliche Auswirkungen einer Reihe verschiedener Szenarien zu beschreiben. Die Ergebnisse zeigen, dass die modellierten Abkühlungs- und Erwärmungssequenzen zu suboptimalen Temperaturen in Korallenhabitaten und durch die abwechselnden Trends erhöhten Temperaturstress geführt haben könnten. Eine Versauerung und zunehmende Sauerstoffarmut sind ebenfalls zu beobachten. Diese Mechanismen werden allgemein als die durch LIPs hervorgerufenen Treiber der markanten geologischen Ereignisse des Mesozoikums diskutiert. Zusammen mit der Abbildung dieses Gesamtzeitraums (Teil I), können die hier entwickelten Modellierungsansätze den Weg für eine zusammenführende Untersuchung der Umweltstörungen im Zuge der LIP-Episoden des Mesozoikums ebnen.

In Summe bietet diese Forschungsarbeit einen umfassenden Blick auf das Paläoklima des Mesozoikums und im Allgemeinen auf natürliche Klimaveränderungen auf Zeitskalen von Jahren bis zu vielen Jahrillionen. Die drei Teile der Arbeit gewähren neue Erkenntnisse über die langfristige Klimaentwicklung auf tektonischen Zeitskalen, die Klimamodulation durch Orbitalzyklen sowie Störungen des Erdsystems während des Mesozoikums durch LIP-Vulkanismus. Jeder der drei Teile entwickelt neuartige Modellierungsansätze unter

der Verwendung von Erdsystemmodellen mittlerer Komplexität (EMICs). Im Ergänzung zu ressourcenintensiveren AOGCMs (Atmosphere-Ocean General Circulation Model) sind dies wertvolle Werkzeuge zur Erforschung der fernen Erdvergangenheit, da sie große Ensembles und relativ lange Simulationen erlauben. Dadurch können relevante empirische und modellierte Erkenntnisse in den Modellierungsansatz einbezogen werden, einerseits um Randbedingungen und Antriebsfaktoren der Modelle zu definieren und andererseits um die Modellierungsergebnisse mit Proxydaten zu verknüpfen.

Schlagwörter

Mesozoikum, Paläoklima, Klimamodellierung, Orbitalzyklen, Magmatische Großprovinzen, Trias, Jura, Kreidezeit

Contents

List of Publications	xi
1 Preamble	1
1.1 Introduction	1
1.1.1 Earth System Evolution on Tectonic Time Scales	4
1.1.2 Orbital Climate and Sedimentary Cycles	9
1.1.3 Volcanic Environmental Disruptions	14
1.1.4 Modeling Paleoclimate across Time Scales	20
1.2 Synopsis of the Publications	28
2 Publications	33
P.I Investigating Mesozoic Climate Trends and Sensitivities with a Large Ensemble of Climate Model Simulations	33
P.II Modes of Pangean Lake-Level Cyclicity Driven by Astronomical Pacing Modulated by Continental Position and $p\text{CO}_2$	53
P.III Climatic Fluctuations Modeled for Carbon and Sulfur Emissions from end-Triassic Volcanism	69
3 Concluding Discussion	81
Bibliography	99
Appendix	123
A.I Supplementary Information to P.I	123
A.II Supplementary Information to P.II	159
A.III Supplementary Information to P.III	183
A.IV Supplementary Figures	205

List of Publications

This thesis is based on the following manuscripts and publications:

Publication I:

Landwehrs, J., Feulner, G., Petri, S., Sames, B. and Wagemann, M. (2021), “Investigating Mesozoic Climate Trends and Sensitivities With a Large Ensemble of Climate Model Simulations”, doi:10.1029/2020PA004134, *Paleoceanography and Paleoclimatology* 36(6), e2020PA004134.

Publication II:

Landwehrs, J., Feulner, G., Willeit, M., Petri, S., Sames, B., Wagemann, M., Whiteside, J.H. and Olsen, P.E. (2022), “Modes of Pangean Lake-Level Cyclicity Driven by Astronomical Pacing Modulated by Continental Position and $p\text{CO}_2$ ”, (in review).

Publication III:

Landwehrs, J., Feulner, G., Hofmann, M. and Petri, S. (2020), “Climatic Fluctuations Modeled for Carbon and Sulfur Emissions from end-Triassic Volcanism”, doi:10.1016/j.epsl.2020.116174, *Earth and Planetary Science Letters* 537, 116174.

1. Preamble

1.1 Introduction

Since Earth’s formation about 4.6 billion years ago, the Earth system has undergone profound transformations (e.g., Catling and Zahnle 2020, Torsvik and Cocks 2016), leading to the world that we find ourselves in today. Studying the complex interplay of geologic, climatic and biogeochemical processes throughout our planets eventful history provides deep insights into the fundamental mechanisms governing this system. Understanding these natural experiments also helps to contextualize present global changes and to anticipate future trajectories (Tierney et al. 2020).

This work focuses on climate and its changes during the Mesozoic era, which is the geologic interval encompassing the middle part of the Phanerozoic Eon from 252 to 66 million years ago (Ma)¹. The start of the Phanerozoic at 541 Ma is marked by the diversification of complex life on Earth. In many ways, the Mesozoic represents a crucial phase of transition between the “ancient” Paleozoic and the “modern” Cenozoic world. After the end-Permian extinction (Dal Corso et al. 2022) as the start of the Mesozoic, the “modern” mollusc-dominated Mesozoic–Cenozoic evolutionary marine invertebrate fauna ascended to dominance, while the brachiopod-dominated Paleozoic fauna declined (Sepkoski 1981; 1984, Bush and Bambach 2011, Bush and Payne 2021). Scleractinian corals evolved and established as the dominant reef builders they are today (Kiessling et al. 2002, Martindale et al. 2019). With the “Mesozoic marine revolution”, important planktonic calcifiers (e.g. coccolithophorids and dinoflagellates) diversified and colonized the open ocean (Hüneke and Henrich 2011, Knoll and Follows 2016, Suchéras-Marx et al. 2019). This is thought to have introduced a pelagic carbonate pool that has since then stabilized the global carbon cycle against perturbations (Ridgwell 2005, Goddérís et al. 2008, Aloisi 2018). On land, the Triassic vegetation was dominated by ferns, conifers and cycads but in the course of the Mesozoic, the flowering plants (angiosperms) evolved, diversified and expanded (Chaboureau et al. 2014, Li et al. 2019b, Condamine et al. 2020, van der Kooi and Ollerton 2020). Although it is also the time that the first mammals appeared, the Mesozoic is most famously known as the age of the dinosaurs, during which both land and sea were populated by a diverse and dominant reptile fauna (Wicander and Monore 2010, Stanley and Luczaj 2015).

The Mesozoic furthermore represents a paleogeographic transition towards the modern world in that it is characterized by the plate tectonic breakup of the supercontinent Pangea and the establishment of the fragmented continental configuration familiar to us today (Torsvik et al. 2021, see also Fig. 1.1). The evolution of life and its paleobiogeographic patterns through the Mesozoic were closely coupled to global tectonic and/or climate changes (e.g. Reddin et al. 2018, Dunne et al. 2021, Bush and Payne 2021, Chiarenza et al. 2022). For example, the expansion of angiosperms has been linked to the breakup

¹all geologic ages are reported according to the International Chronostratigraphic Chart v2021/10 (Cohen et al. 2013, updated).

of Pangea and subsequently more humid terrestrial climates (Chaboureaud et al. 2014). In addition to such long-term developments, the Mesozoic is marked by several prominent environmental perturbations during which climatic changes contributed to ecologic turnover. These events include mass extinctions (Bambach 2006, Lowery et al. 2020), Ocean Anoxic Events (OAE, Takashima et al. 2006, Sageman 2009, Jenkyns 2010, Monteiro et al. 2012) and Large Igneous Provinces volcanism (LIP; Ernst and Youbi 2017, also see Sec. 1.1.3), which were in several cases linked to each other (Fig. 1.6; Clapham and Renne 2019, Percival et al. 2020, Joo et al. 2020, Torsvik et al. 2021b). For example, the end-Permian and end-Triassic mass extinctions respectively provided the opportunity for the diversification of modern marine invertebrate fauna (Bush and Bambach 2011) and dinosaurs (Brusatte et al. 2010, Benson 2018) during the early Mesozoic.

Different approaches allow gaining knowledge about the climatic and environmental conditions under which this evolution of life and the Earth system took place throughout the Mesozoic. The primary source of information are geologic structures, like fossils or sedimentary rocks. To name a few examples, the geographic distribution of certain indicators of humid (e.g. coals), dry (evaporites), warm (crocodile and palm tree fossils) and cold (glacial deposits) climates have been used to outline major climate zones (Boucot et al. 2013) and rainfall patterns (Chandra et al. 2021). This suggests widespread low- to mid-latitude aridity during the Triassic and Jurassic and temperate climates up to the poles during most of the Mesozoic (Boucot et al. 2013). The oxygen isotope composition ($\delta^{18}\text{O}$) of marine fossils can be used to estimate global temperatures, yielding warm anomalies during the Triassic and the mid-Cretaceous (Veizer and Prokoph 2015). Regarding the climate modulation by orbital cycles, changes in the lacustrine sediment deposition in a Late Triassic tropical rift basin can, for example, be linked especially to a changing balance of rainfall and evaporation (Olsen and Kent 1996, see also Sec. 1.1.2). In the context of the end-Triassic extinction event, greenhouse gas emissions from the Central Atlantic Magmatic Province can be estimated from the magmatic rock volume and linked to paleosol-based $p\text{CO}_2$ estimates (Schaller et al. 2011; 2012) to constrain the amount of global warming (see Sec. 1.1.3). This variety of proxies contains a huge amount of information but achieving a satisfactory spatial coverage, temporal resolution and unambiguous interpretation for the respective scientific problem is often challenging.

It is therefore useful to complement these empirical approaches with the application of numerical or statistical models. This work specifically employs coupled Earth system models (ESM) to simulate climate conditions and their changes through the Mesozoic. This class of numerical models combines submodels for the major components of the Earth system, including the ocean, atmosphere, cryosphere, land surface and vegetation (see Sec. 1.1.4). The models are based on equations describing the fluxes of energy, water and air inside and between these subsystems. For this, they solve, i.a. the physical equations of motion and energy balance to simulate the atmospheric and oceanic circulation in three dimensions on a rotating sphere representing the Earth. In a deep time paleoclimate context like the Mesozoic, an ESM has to be supplied with some information that characterizes the respective time in Earth history and potential drivers of the phenomenon of interest. The boundary conditions most importantly include a paleogeographic reconstruction that accounts for plate tectonic movement as well as atmospheric greenhouse gas concentrations, and orbital parameters that characterize the Earth's movement in the solar system. Model experiments can then be carried out either through equilibrium or transient climate simulations. While the first mode yields equilibrium climatologies for fixed boundary conditions, the second mode deals with the dynamic response to an external forcing, for example changes in the incoming solar radiation. Both modes allow to systematically assess drivers of paleoclimatic changes to explain features of the geologic record. Earth

system modeling approaches have been applied to the Mesozoic in a number of studies before (e.g., Kutzbach 1994, Huynh and Poulsen 2005, Sellwood and Valdes 2006, Donnadieu et al. 2006a, Chaboureaud et al. 2014, Farnsworth et al. 2019a), but all manuscripts forming this thesis elucidate important new aspects with comprehensive and innovative methodologies.

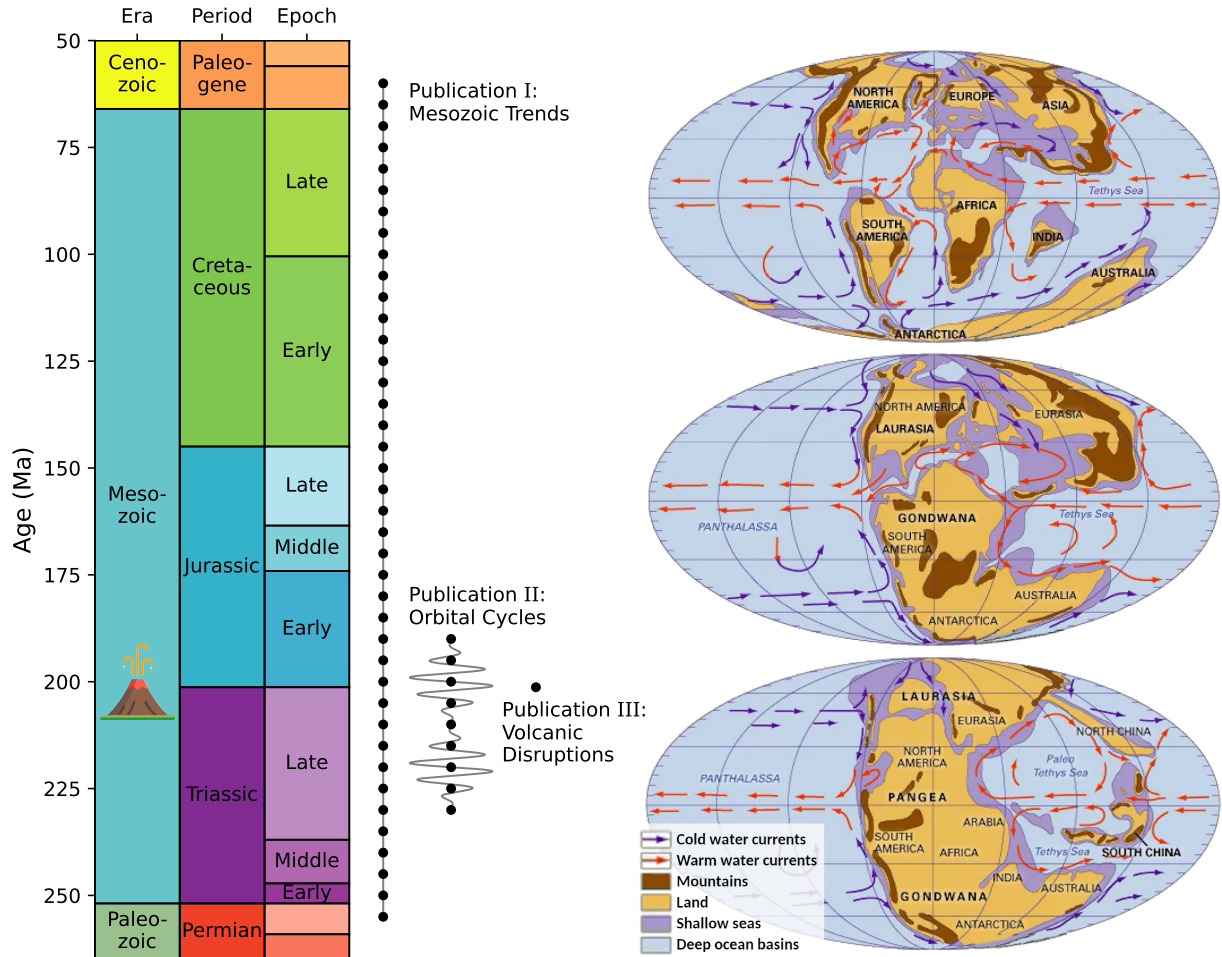


Figure 1.1: Overview of the Mesozoic era and research in this thesis. Dots indicate the geologic time slices studied in P.I, P.II and P.III (Landwehrs et al. 2020; 2021; 2022) through climate model simulations. The maps show the changing global paleogeographic setting for the Early Triassic, Late Jurassic and Late Cretaceous (modified from C.R. Scotese, as published in Tang 2022).

The goal of this thesis is to identify and study major factors that shaped Mesozoic climates on millennial to multi-million year time scales. This is addressed by three studies, focusing on tectonic-scale trends (P.I), orbital cycles (P.II) and volcanic disruptions (P.III), respectively. A summary of the time slices studied in this work is provided by Fig. 1.1. Publication I (Landwehrs et al. 2021) assesses global climate conditions and the tectonically-driven long-term climate evolution through the whole Mesozoic. With an ensemble of more than 200 equilibrium climate simulations for 40 geologic time slices, it provides the currently most extensive paleoclimate model framework for the Mesozoic. It addresses specifically the respective contributions of paleogeography, sea level, $p\text{CO}_2$, solar luminosity to global mean temperature changes as well as the consequences of the supercontinent breakup on global climate patterns. Publication II (Landwehrs et al. 2022) is dedicated to climatic effects of orbital cycles on 10–100 kyr time scales. It tests the hypothesis that the modulation of the precipitation–evaporation balance by an orbital forcing,

continental drift and $p\text{CO}_2$ changes can explain major features of the exceptional lacustrine record of the mainly Late Triassic Newark-Hartford basins (Olsen and Kent 1996, Olsen et al. 2019). This is done with an ensemble of transient orbitally-driven climate simulations for 9 geologic time slices from 230 to 190 Ma. This set of simulations is the first of its kind for Mesozoic times. Dealing with the most rapid phenomena, Publication III (Landwehrs et al. 2021) investigates climatic and biogeochemical effects of millennial scale carbon and sulfur emission pulses from LIP volcanism. Specifically, it assesses the combined effects of carbon-driven greenhouse warming and sulfur aerosol cooling in the context of the end-Triassic extinction event, considering current knowledge about the eruption history of the Central Atlantic Magmatic Province. While P.I provides the big picture of the whole Mesozoic, P.II and P.III focus on specific periods with exceptional geologic records to study orbital and volcanic climate forcing. The latter do not nearly cover the multitude of equally important records and events that the Mesozoic represents. However, the principles and methodologies developed here can be easily extended to other geologic settings.

In the following, Sections 1.1.1–1.1.3 provide an introduction to the tectonic, orbital and volcanic climate effects during the Mesozoic that are studied in the three manuscripts forming this thesis. Section 1.1.4 includes a brief description of the CLIMBER-3 α and CLIMBER-X Earth system models and how they are used in this work.

1.1.1 Earth System Evolution on Tectonic Time Scales

Climate change on geological time scales is tightly linked to plate tectonics via its effects on paleogeography, atmospheric and ocean circulation, global sea level and atmospheric greenhouse gas concentrations (Barron et al. 1980, Crowley 2000, Donnadieu et al. 2009, Farnsworth et al. 2019a, Mills et al. 2021). Other factors include the increasing luminosity of the sun (Gough 1981, Feulner 2012) and changes in biogeochemical cycling related, for example, to biological evolution (Kasting 1993, Boyce and Lee 2017, Catling and Zahnle 2020). The first part of this thesis (P.I, see Fig. 1.1) evaluates the contribution of some of these factors to long-term Mesozoic climate patterns and changes.

The Mesozoic era is characterized by the breakup of Pangea and the establishment of a fragmented continental configuration already similar to the present (Fig. 1.1). Pangea reached its maximum size during latest Paleozoic and early Mesozoic times after collision of Gondwana and Laurussia during the late Carboniferous (~ 320 Ma; Torsvik et al. 2021). In the Triassic, Pangea was still largely intact with vast continuous land masses almost stretching from pole to pole. They were surrounded on three sides by the giant Panthalassa ocean with the tropical-subtropical Tethys Sea projecting into eastern Pangea (Fig. 1.1; Torsvik et al. 2021, Marcilly et al. 2021). These large land masses must have experienced strongly continental, seasonal climates (Hallam et al. 1993, Parrish 1993) and geologic climate indicators like evaporite deposits suggest that western Pangea was largely arid in the low to middle latitudes (Hallam 1985). This has also been attributed to a weakening of the ITCZ and the tropical rain belt over western Pangea as the trade winds crossed the large continent (Hallam 1984; 1985, Frakes et al. 1992). Pronounced summer heating and continental low pressure cells drove moisture from the warm Tethys to eastern Pangea, causing monsoonal rainfall. This unique situation has been described as the Pangean “megamonsoon” which was further amplified by the symmetric arrangement of the continents around the Tethys (Kutzbach and Gallimore 1989, Parrish 1993, Wang et al. 2014).

At the end of the Triassic (~ 201 Ma), the emplacement of the Central Atlantic Magmatic

Province (CAMP, see Sec. 1.1.3; Marzoli et al. 2018) heralded the breakup of the supercontinent. It was linked to the rifting between Laurussia and Gondwana and the opening of a narrow central Atlantic ocean in the Jurassic (~ 195 Ma; Torsvik et al. 2021, Marcilly et al. 2021). At around 170 Ma, Gondwana also began to disintegrate with rifting between south-eastern Africa, Antarctica and India, again preceded by LIP volcanism (Karoo-Ferrar LIP, ~ 183 Ma; Torsvik et al. 2021). The continents collectively migrated northwards until the Early Jurassic (P.I Fig. 3c; Torsvik et al. 2021, Marcilly et al. 2021). The average latitude of continental area then remained relatively constant but its latitudinal spread continued to increase (see A.I Fig. S13b; Torsvik et al. 2021). Despite these changes, Jurassic global climate patterns remained similar to the Triassic (Hallam et al. 1993).

Continental fragmentation continued through the Cretaceous, including spreading between South America and Africa from ~ 130 Ma on (Gernon et al. 2021, Torsvik et al. 2021). This opening of the South Atlantic is associated to the Paraná-Etendeka LIP (~ 134 Ma), of which magmatic rocks can now be found in Brazil and Namibia (Torsvik et al. 2021). At the same time, Eurasia and East Asia were assembling. Global sea levels in the Triassic and Early Jurassic had been among the lowest of Phanerozoic times and similar to today. Towards the Late Cretaceous (~ 100 – 90 Ma) they rose by up to 200 m to their Phanerozoic peak (Haq et al. 1987, Wright et al. 2020, Torsvik et al. 2021, Young et al. 2022). This led to substantial flooding of more than a third of the global continental area (Hallam 1985, Price 2009, Marcilly et al. 2021), in marked contrast to earlier Mesozoic periods (Marcilly et al. 2021, Scotese 2021). The volume of mid-ocean ridges is a major control of eustatic sea level so that high seafloor spreading rates during the Pangea breakup contributed to this sea level rise (Seton et al. 2009, Conrad 2013, Karlsen et al. 2019; 2020, Wright et al. 2020, Marcilly et al. 2021). Together with continental fragmentation and formation of new seaways, this inundation contributed to a larger maritime influence in many places that dampened climatic seasonality and contributed to more humid and moderate climates (Hallam 1984; 1985, Scotese et al. 2021). This is evidenced by the replacement of abundant Triassic–Jurassic evaporites by coal and ironstone deposits indicating more humid equatorial conditions in the Late Cretaceous (Hallam 1984; 1985). Towards the end of the Cretaceous and the Mesozoic, sea level and flooded land area began to drop to their present-day states (Marcilly et al. 2021).

The described Mesozoic changes are derived from paleogeographic reconstructions which also provide crucial boundary conditions for climate model simulations. The work presented here makes extensive use of the reconstructions of Scotese (2014), Scotese and Wright (2018), Cao et al. (2017; 2018) and Marcilly et al. (2021). These are constructed from a variety of data, starting with a plate tectonic model that consistently describes the motion of the different tectonic plates through time (e.g. Matthews et al. 2016, Torsvik and Cocks 2017). In such a model, continents are positioned for example using paleomagnetic poles preserved in rocks or by linking volcanic units to stationary hotspots or plume generation zones in the Earth’s mantle (Torsvik and Cocks 2016; 2017). Ancient coastlines as well as topographic features are then defined by occurrences of lithofacies and fossils that characterize the depositional environment (Torsvik and Cocks 2017, Cao et al. 2017, Kocsis and Scotese 2021, Scotese 2021, Marcilly et al. 2021).

Atmospheric carbon dioxide concentrations are an important determinant of global temperatures (Royer et al. 2004) and proxy reconstructions suggest that $p\text{CO}_2$ has fluctuated through the Phanerozoic, contributing to its history of cold and warm periods (Foster et al. 2017). On geologic time scales, $p\text{CO}_2$ is closely coupled to the balance of time-dependent carbon sources, especially plate tectonic degassing, and carbon sinks like continental sil-

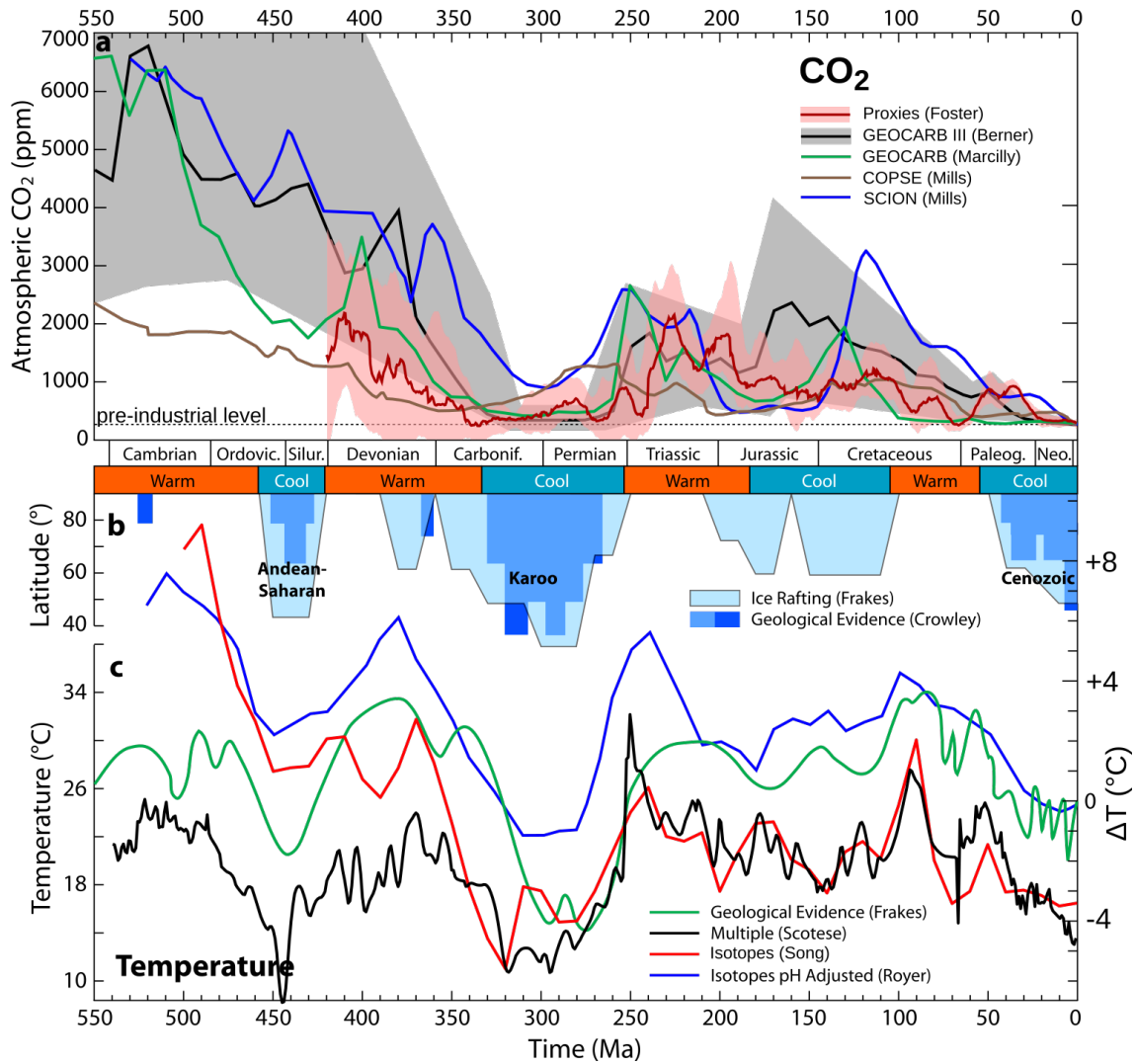


Figure 1.2: Phanerozoic $p\text{CO}_2$ (a), glaciation (b) and temperature (c) from various reconstructions. (a): Proxy $p\text{CO}_2$ (fitted mean $p\text{CO}_2$ with 95% confidence interval indicated by red line and shading, Foster et al. 2017). Modeled $p\text{CO}_2$ from GEOCARB III (Berner and Kothavala 2001), GEOCARBSULFvolc M12 (Marcilly et al. 2021), COPSE (Mills et al. 2019) and SCION (Mills et al. 2021). (b): Warm and cool climate modes after Frakes et al. (1992). Paleolatitudes of ice-rafted deposits (Frakes and Francis 1988). Glaciological geologic evidence for continental scale glaciation (Crowley 1998). (c): Conceptual relative global temperature curve from various geological evidence (right scale, but with arbitrary units; Frakes et al. 1992). Low-latitude sea surface temperature from $\delta^{18}\text{O}$ proxies (Song et al. 2019). Global average temperature estimated from these isotope values, combined with geological indicators of climate zonation (Scotese et al. 2021). Relative temperature changes from $\delta^{18}\text{O}$ proxies (right scale; Royer et al. 2004). Adapted from Vinós (2019), but with several updated data.

icate weathering (Marcilly et al. 2021). The latter consumes atmospheric CO_2 that is eventually buried again in marine sediments. Silicate weathering is promoted by warm and humid climate, high continental runoff and physical erosion (Marcilly et al. 2021). It can be therefore be enhanced by plate tectonics through mountain building, positioning of continents in tropical and temperate humid belts as well as high CO_2 degassing rates leading to warmer climates (Marcilly et al. 2021). Plate tectonic degassing is the major source of CO_2 and occurs especially at continental arcs and rifts as well as mid-ocean ridges (Brune et al. 2017, Marcilly et al. 2021). Models of the long-term carbon cycle like GEOCARBSULF (Berner 2006, Royer et al. 2014, Marcilly et al. 2021), COPSE (Lenton

et al. 2018, Mills et al. 2019), GEOCLIM (Donnadieu et al. 2006a; 2009, Godd ris et al. 2014, Godd ris and Donnadieu 2019) or SCION (Mills et al. 2021) represent these sources and sinks to reconstruct past $p\text{CO}_2$ changes and understand their causes (Marcilly et al. 2021).

Pathways of $p\text{CO}_2$ obtained from these models and the proxy record can serve as input to climate models to assess associated climatic changes, as in P.I for the Mesozoic. During the mid-Carboniferous to Permian interval, $p\text{CO}_2$ fell to present-day levels but increased significantly again in the Triassic, expressing the transition from the Late Paleozoic ice age (330 to ~ 275 Ma; Monta nez and Poulsen 2013) to the Mesozoic Greenhouse (Fig. 1.2b; Foster et al. 2017, Torsvik et al. 2021, Marcilly et al. 2021). On aggregated continents like Pangea, inland rainfall and runoff are reduced, so that aridity limits CO_2 drawdown by silicate weathering (Marcilly et al. 2021). This contributed to high atmospheric CO_2 concentrations during the early Mesozoic (Fig. 1.2a; Donnadieu et al. 2006a, Marcilly et al. 2021, Zhang and Torsvik 2022). The global subduction flux, indicating tectonic activity and degassing, had declined over the Pangea phase to a Early Jurassic minimum with rates comparable to present-day. It subsequently rose to a peak with a doubled flux in the Early Cretaceous, before declining until today (Marcilly et al. 2021). This enhanced subduction of ocean sediments and remobilization of carbon during the Pangea breakup contributed to elevated $p\text{CO}_2$ and the exceptionally warm mid-Cretaceous greenhouse climate (Fig. 1.2; Donnadieu et al. 2006a, Marcilly et al. 2021, Zahirovic et al. 2022).

Along with proxy- and model-based $p\text{CO}_2$ reconstructions, long-term global temperature changes through the Mesozoic are indicated by oxygen isotope paleothermometry, especially using $\delta^{18}\text{O}$ signatures in marine fossil shells (Veizer and Prokoph 2015, Song et al. 2019). Low-latitude sea surface temperatures (SST) around 22°C have been reconstructed for the Mesozoic–Early Cenozoic warm period, with warm anomalies on the order of $5\text{--}10^\circ\text{C}$ in the Early Triassic, the Toarcian and the Late Cretaceous (Fig. 1.2c; Song et al. 2019). Global climate changes during this time were additionally inferred from distribution patterns of climate sensitive deposits that outline climatic zonation, together with fossil flora and fauna (Ziegler et al. 2003, Rees et al. 2004, Markwick 2007, Hay and Fl gel 2012, Boucot et al. 2013, Cao et al. 2018, Chandra et al. 2021). As mentioned above, coal, kaolinite and bauxite depositions are generally indicative of humid conditions, while evaporites, calcretes, red beds or aeolian sandstones tend to be associated to arid or semi-arid conditions (Hallam 1984, Sellwood et al. 1993). Scotese et al. (2021) combined a paleoclimate zonation and equator-to-pole temperature gradients derived from these criteria (Boucot et al. 2013) with $\delta^{18}\text{O}$ -based tropical temperature changes (Song et al. 2019) into a Phanerozoic global temperature curve (Fig. 1.2c). Similar to Frakes et al. (1992), they describe the Mesozoic as the succession of a Triassic Hothouse (Trotter et al. 2015), a Jurassic–Early Cretaceous cool interval and a mid-Cretaceous–Paleogene Hothouse. After the Cenomanian–Turonian thermal maximum (~ 94 Ma; O’Brien et al. 2017), temperatures gradually cooled towards the Maastrichtian and the Cretaceous–Paleogene boundary (Scotese et al. 2021).

The Mesozoic has been overall considered the most prolonged Phanerozoic greenhouse climate period, without formation of major continental ice sheets. This is contrasting the preceding Late Paleozoic Ice Age (330 to ~ 275 Ma; Monta nez and Poulsen 2013) and the current Late Cenozoic Ice Age (since 34 Ma; Fig. 1.2b; Marcilly et al. 2021, Scotese et al. 2021). Nevertheless, there is undeniable evidence for the presence of ice, especially during the Jurassic–Early Cretaceous cool phase (Price 1999, Royer et al. 2004, Cather et al. 2009, Mills et al. 2019; 2021, Scotese et al. 2021). This includes glacier-abraded rock surfaces, tillites, dropstones and glendonites (Price 1999) to a degree that indicates high-

latitude freezing conditions but no large-scale glaciation (Fig. 1.2b; Boucot et al. 2013, Scotese et al. 2021). The extent and climatic significance of glaciations in the Mesozoic will continue to be a matter of research (Flögel et al. 2011, Ladant and Donnadieu 2016, Vickers et al. 2019, Alley et al. 2020, Ruebsam and Schwark 2021, Nordt et al. 2022). Fossil flora and fauna suggests that warm temperatures supported temperate vegetation (ferns, gymnosperms) and warmth-loving fauna (dinosaurs, crocodiles, coral reefs) in unusually high latitude regions of both hemispheres throughout the Mesozoic, even during cooler climate phases (Hallam 1985, Hallam et al. 1993, Sellwood and Valdes 2006, Klages et al. 2020, Spicer et al. 2020, Scotese et al. 2021).

Earth system models have been employed in a considerable number of studies to investigate climatic conditions during certain Triassic (Huynh and Poulsen 2005, Winguth et al. 2015, Dunne et al. 2021), Jurassic (Chandler et al. 1992, Valdes and Sellwood 1992, Sellwood et al. 2000, Sellwood and Valdes 2008, Robinson et al. 2017), and especially Cretaceous (Donnadieu et al. 2006b; 2016, Fluteau et al. 2007, Flögel and Wagner 2006, Flögel et al. 2011, Zhou et al. 2012, Craggs et al. 2012, Hunter et al. 2013, Poulsen et al. 2007, Poulsen and Zhou 2013, Upchurch et al. 2015, Tabor et al. 2016, Niezgodzki et al. 2017, Ladant et al. 2020, Laugié et al. 2020, Steinig et al. 2020, Tabor et al. 2020, Brugger et al. 2017; 2021) time periods.

However, the goal of the first part of this thesis (P.I) is to assess climate patterns and contributions of different drivers to long-term changes through the whole Mesozoic in a continuous and consistent framework of climate model simulations. This blends with important previous work, that differed in its scope and extent, however. With a focus on coupling climate and biogeochemical cycles in the GEOCLIM model, Donnadieu et al. (2006a) and Donnadieu et al. (2009) assessed seven Mesozoic time slices. This approach simulates the equilibrium $p\text{CO}_2$ for each paleogeographic configuration and the authors find a strong $p\text{CO}_2$ decline and cooling in response to the Pangea breakup, related to enhanced humidity and continental weathering. Chaboureau et al. (2014) adopt similar climate model components to five Mesozoic time slices, but use a comparison with coal/evaporite distributions and seawater temperature proxies to find the best model-proxy fit for a set of fixed $p\text{CO}_2$ values. The authors then link the modeled shrinking of arid climate belts to the expansion of angiosperm plants in the Cretaceous. Another series of studies is based on different variants of the HadCM climate model. Sellwood and Valdes (2006) performed coupled atmosphere and sea ice model simulations for one Triassic, Jurassic and Late Cretaceous time slice, respectively, and discussed the obtained climatic patterns regarding various geologic indicators and their distribution. Lunt et al. (2016) and Farnsworth et al. (2019a) carried out an ensemble of coupled climate simulations for each Cretaceous to Eocene stage ($\sim 145\text{--}34$ Ma). Although it only covers a part of the Mesozoic, their approach is particularly relevant for this work because it allowed to identify the contribution of paleogeography, solar luminosity and $p\text{CO}_2$ to temperature changes. Valdes et al. (2021) extended their HadCM3 simulations to 109 geological stages of the whole Phanerozoic, using the Scotese and Wright (2018) paleogeographies and testing two $p\text{CO}_2$ pathways based on Foster et al. (2017). However, the primary goal of this publication was to assess the correlation of surface and deep ocean temperatures through the Phanerozoic, especially with respect to the interpretation of benthic $\delta^{18}\text{O}$ records.

In comparison to the described studies, Landwehrs et al. (2021) dedicate the so far most extensive climate model assessment to the Mesozoic (P.I). The model ensemble covers 40 equally spaced geologic time slices from 255 to 60 Ma, for which more than 200 simulations with systematically varied $p\text{CO}_2$, vegetation patterns, sea level and solar luminosity are performed (see Sec. 1.1.4). The evolving continental configurations and sensitivity exper-

iments allow to assess the role of these drivers of long-term climate change through the Mesozoic. The study investigates both spatial climate patterns and global mean climate conditions from Triassic Pangea to the mid-Cretaceous greenhouse. The systematic parameter variations within the model ensemble are also useful in disclosing uncertainty ranges that result from uncertain boundary conditions like $p\text{CO}_2$ as well as model limitations. This thesis thus contributes to an integrated picture of the climate system and its drivers during the Mesozoic, the important time of transition from “ancient” biota and continents into the modern world. With the breakup of Pangea and pronounced plate-tectonic effects on sea level and $p\text{CO}_2$ this elucidates general mechanisms of climate system evolution on tectonic time scales.

1.1.2 Orbital Climate and Sedimentary Cycles

Plate tectonics shaped Mesozoic climate conditions over multi-million year time scales, as outlined in the previous section. Superposed on such long-term trends, astronomical cycles introduce periodic changes with characteristic time scales of mostly 10^4 to 10^5 years. These cycles result from variations in the Earth’s orbit around the sun and the orientation of its rotation axis due to the gravitational interaction of the bodies in the solar system (Lourens 2016, Hinnov 2018). The astronomical modulation of the seasonal and spatial distribution of incoming solar radiation (insolation) and thus climate on Earth is well known as the Milankovitch theory and has been established as the pacemaker of Pleistocene glacial–interglacial dynamics (Milankovitch 1941, Hays et al. 1976, Loutre 2003, Berger and Yin 2012).

The three climatically most important astronomical parameters of the orbital insolation forcing are eccentricity, precession and obliquity (e , ω and ε ; Loutre 2003, Lappler and Lohmann 2009, Huang 2018). The orbital eccentricity (e) describes the departure of Earth’s elliptic orbit from a circular shape and varies between ≈ 0 and 0.067 (Lourens 2016). Major periodicities are found at ~ 100 and ~ 405 kyr (Fig. 1.4a), but reach up to 2.4 Myr (Hinnov and Cozzi 2021). Eccentricity is the only of the three orbital parameters that affects the total amount of solar energy received by the Earth over one year $W = S_0/4 \cdot (1 - e^2)^{-0.5}$ (Laskar et al. 1993, Berger and Yin 2012, Lourens 2016). Here, S_0 is the solar constant which has a value of $\sim 1361 \text{ W/m}^2$ today. High eccentricity thus contributes to slightly elevated global mean temperatures, but the global insolation changes remain small ($< 0.5\%$; Loutre et al. 2004, Berger and Yin 2012).

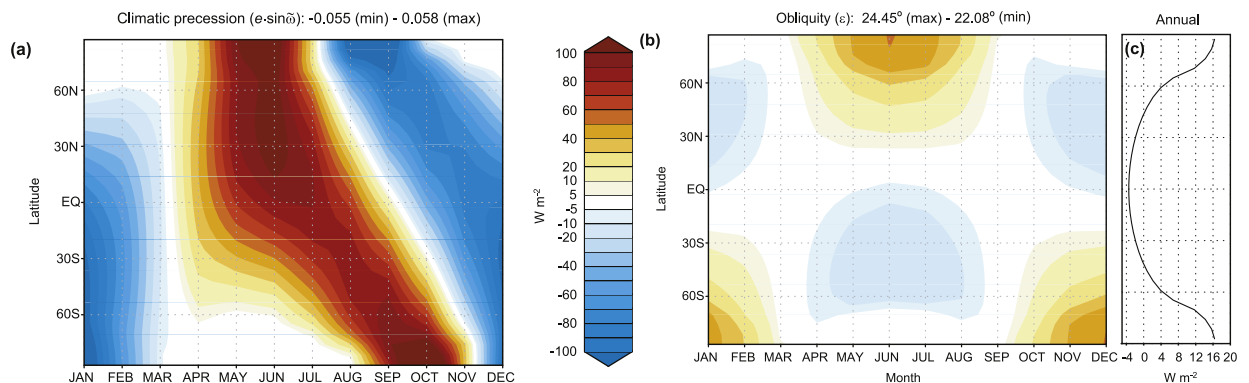


Figure 1.3: Orbital insolation forcing of precession (a) and obliquity (b,c). Monthly averaged zonal insolation difference between a climatic precession minimum and maximum (a) and an obliquity maximum and minimum (b). The annual mean of (b) is shown in (c). From Lourens (2016).

The more important climatic effect of eccentricity cycles is that they modulate the seasonal difference of the Earth–Sun distance and thus the amplitude of precessional insolation cycles (Läpple and Lohmann 2009). Precession results from the changing orientation of Earth’s rotation axis due to the tidal forces of the sun and moon (axial precession, clockwise, ~ 25.8 kyr period) as well as Earth’s revolving orbital ellipse (apsidal precession, anticlockwise, ~ 100 kyr period) (Crucifix et al. 2007). The combined effect shifts the time of year at which Earth reaches the perihelion and aphelion, respectively. Figure 1.3a shows that Northern hemisphere (NH) insolation is enhanced by more than 100 W/m^2 when boreal summer occurs in perihelion, while the winter insolation is reduced accordingly. Precession therefore mainly affects the strength of the seasonal cycle which is amplified at precession minima in the NH and reduced in the SH (Lourens 2016). Its effect is thus opposite between the hemispheres and causes a seasonal redistribution of insolation while the annual mean effect is zero at every latitude (Loutre 2003, Läpple and Lohmann 2009). Figure 1.3a also illustrates the effect of a shortened NH summer (SH winter) at minimum precession, because Earth moves faster through the perihelion. Precession cycles exhibit periods of ~ 19 to 23 kyr which combine to a mean ~ 21 kyr quasi-period. Precession is often described through the eccentricity-modulated climatic precession index $e \cdot \sin \omega$ which is the main factor determining the daily insolation (Fig. 1.4a; Loutre 2009b, Lourens 2016). Earth’s position on its orbit is expressed in many cases by the angle ω between perihelion and vernal point (longitude of vernal/spring equinox $+ 180^\circ$). Climatic precession is then at a minimum when the NH summer solstice is in perihelion, corresponding to $\omega = 270^\circ$ (Lourens 2016).

Obliquity cycles relate to the tilt (ϵ) of Earth’s rotation axis which varies between ~ 22 and 24.5° with a main period of ~ 41 kyr. From minimum to maximum obliquity, the high latitudes receive up to $\sim 50 \text{ W/m}^2$ additional summer insolation, while winter insolation is reduced by $\sim 15 \text{ W/m}^2$ (Fig. 1.3b; Lourens 2016). In contrast to precession, obliquity changes the seasonality simultaneously in both hemispheres and also influences the annual mean insolation at each latitude. At higher obliquity, the annual mean insolation increases at high latitudes ($>43^\circ$), balanced by a reduction at lower latitudes (Fig. 1.3c). The obliquity forcing is therefore symmetric between the hemispheres, but antisymmetric between the tropics and high latitudes (Fig. 1.3b,c; Loutre 2003; 2009a, Loutre et al. 2004, Crucifix et al. 2007, Läpple and Lohmann 2009, Lourens 2016). Altogether, the insolation changes linked to the three orbital parameters generally cause temperature variations in which eccentricity and semi-precession (9.5 – 11.5 kyr; Crowley et al. 1992, Berger and Loutre 1997, Berger et al. 2006, Ashkenazy and Gildor 2008, Whiteside et al. 2011a) frequencies are best expressed in the tropics, while the precession band dominates the subtropics and mid-latitudes. Obliquity band variability is most important in the high latitudes and has a secondary maximum in the tropics (Läpple and Lohmann 2009).

The orbital forcing persisted in this general form through the Mesozoic, although some of the frequencies continuously decreased over geological time and the chaotic planetary movement prevents accurate astronomical solutions before ~ 50 Ma (Berger and Loutre 1994, Laskar et al. 2004, Olsen and Whiteside 2009, Laskar et al. 2011, Hinnov 2018). However, the response of the Earth system in the Mesozoic is expected to differ because of the overall warmer background climate state with a lesser role of major ice sheets as well as the different distribution of landmasses. Astronomical signals of climate change can be preserved in cyclic sedimentary sequences, superimposed on longer-term trends of sediment deposition (Hinnov 2013, Huang 2018). Cyclostratigraphic records have been recovered for the Triassic (Vollmer et al. 2008, Sha et al. 2015, Li et al. 2018; 2019, Ikeda et al. 2020, Ikeda and Tada 2014; 2020, Chu et al. 2020, Bahr et al. 2020, Hinnov and Cozzi 2021, Liu et al. 2021, Wang et al. 2022), Jurassic (Martinez and Dera 2015, Ruhl

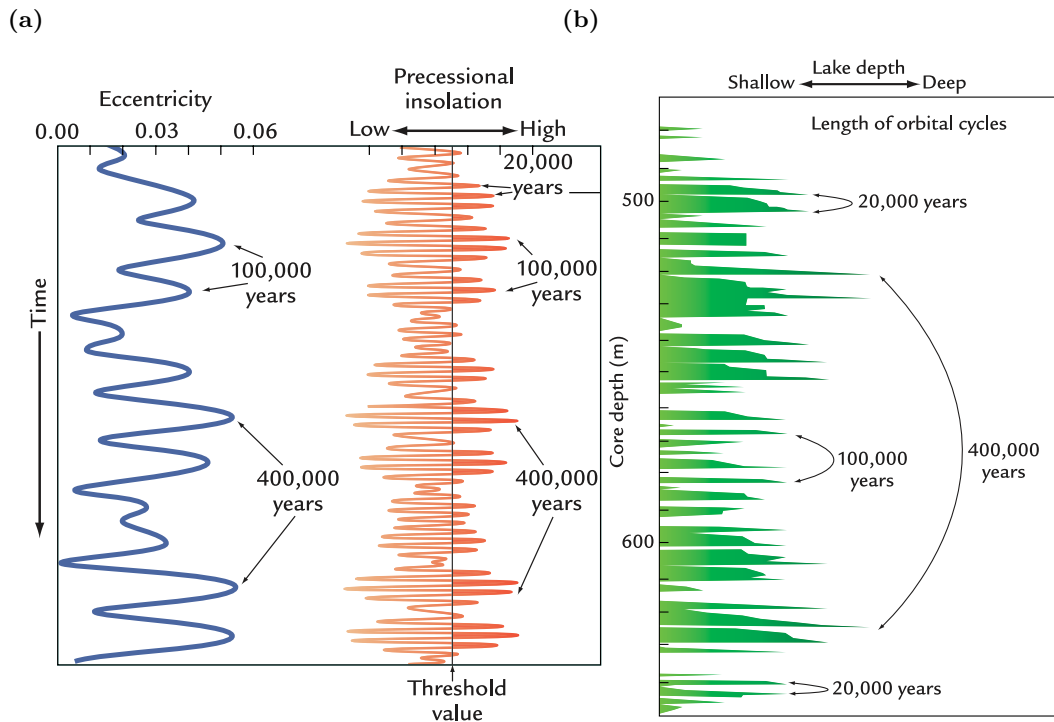


Figure 1.4: Orbital forcing (a) and lake depth sedimentary cycles in the Newark Basin record (b). (a) shows the periodic variations of eccentricity e (left) and their modulation of climatic precession and the resulting summer insolation (right), for example at the Newark-Hartford basin (NHB) paleo-location. The figure also illustrates the concept of a threshold behavior in the NHB lake sediment deposition which only records the truncated orbital signal when maximum insolation exceeds a certain level. (b) shows a part of the NHB lake level record (Olsen and Kent 1996) with the ~ 20 kyr Van Houten precession cycles and their modulation at the ~ 100 and ~ 400 kyr eccentricity periods. From Ruddiman (2014).

et al. 2010; 2016, Boulila et al. 2022) and Cretaceous (Batenburg et al. 2016, Thibault and Husson 2016, Charbonnier et al. 2018, Martinez et al. 2020, Liu et al. 2020, Laurin et al. 2021, Huang et al. 2021). Their facies, geochemistry, mineralogy, magnetism and color have been studied with respect to orbital climate and carbon cycle dynamics as well as the construction a Astronomical Time Scale (ATS) for precise geological dating (Hinnov 2013, Huang 2018).

One superb deep time record of orbital climate oscillations comes from the Newark-Hartford basins (NHB) of the eastern United States (Olsen and Kent 1996, Olsen et al. 1996b; 2019). These basins belong to the tropical rift system between North America and Africa produced during the initial breakup of Pangea. They host thousands of meters thick successions of continental strata deposited during the Late Triassic to Early Jurassic (233–199 Ma, Norian to Hettangian; Olsen et al. 1996b, Olsen and Kent 1996, Olsen 1997; 2010, Kent et al. 2017, Hinnov 2018). The NHB had been occupied by large playa to perennial lakes and accumulated largely lacustrine and fluvial sediments (Olsen et al. 1996b, Kent et al. 2017). A precisely dated composite sediment sequence of 6770 m thickness has been obtained from several overlapping drilling cores (Olsen and Kent 1990, Olsen et al. 1996b, Kent and Olsen 1999, Kent et al. 2017). The sedimentary record reveals depositional cycles comprising repeated sequences of lithofacies sensitive to lake water depth which have been classified into lake “depth rank” time series (P.II Fig. 3c; Olsen 1986, Olsen and Kent 1996). Quantitative assessments of the depth rank and sediment color time series revealed a hierarchy of lake level cycles with the most obvious

at outcrop scale being the “Van Houten” cycles that correspond to a ~ 20 kyr precession periodicity (Smoot 1991, Smoot and Olsen 1994, Olsen 1986, Olsen and Kent 1996, Olsen et al. 2019). These cycles are typically 3–6 m thick and include one phase of lake level high stand (e.g. >80 m depth; Olsen and Kent 1996), often characterized by well bedded, dark, organic-rich and partly varved mudstones as well as the occurrence of fossil fish (Fig. 1.5). These are over- and underlain by playa or vegetated dry lake sediments, often expressed by lighter colored (red, purple, gray), mudcracked and rooted sedimentary fabrics with occurrences of evaporites and reptile footprints that indicate lake regression or even sub-aerial exposure (Olsen et al. 1996b, Olsen and Kent 1996, Olsen 1997; 2010, Kent et al. 2017). These lake deepening–shallowing sequences are interpreted as orbitally-paced shifts in the precipitation–evaporation balance and thus between relatively dry and wet climate conditions (Olsen and Kent 1996, Ruddiman 2014). The Van Houten cycles periodically vary in their expression, which is described as the “short” and “intermediate” modulating cycles, corresponding to the ~ 100 kyr and ~ 405 kyr periods of eccentricity that modulate climatic precession (Fig. 1.4a,b; Olsen and Kent 1996, Ruddiman 2014). Because the latter is consistently well expressed and its period is particularly stable through geologic time, it is also used as a metronome for the astrochronostratigraphic time scale of the NHB record (Kent et al. 2017, Huang 2018, Olsen et al. 2019). Signals of obliquity and its modulation by orbital inclination had long remained undetected (Olsen and Kent 1996, Kent et al. 2017) but were recently revealed (Margulis-Ohnuma et al. 2021, Whiteside et al. 2021). As the direct insolation forcing of obliquity in the low paleolatitudes of the NHB is small, possible linkages to higher latitude climate now have to be evaluated (P.II). The exceptionally long, continuous and well-resolved NHB record provides detailed evidence for profound orbital climate pacing, especially in the tropics of Pangea and during greenhouse climate states.

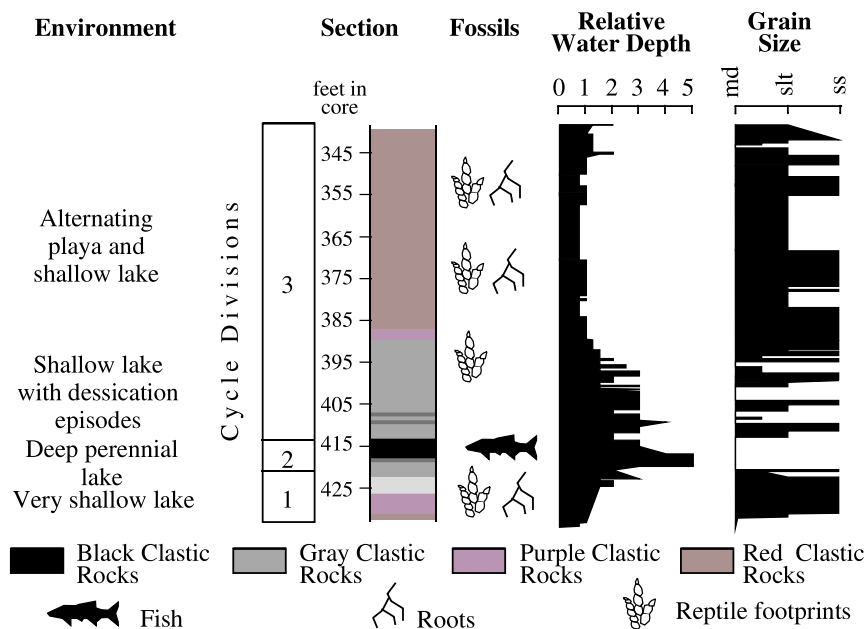


Figure 1.5: A “Van Houten” cycle in Newark Basin lacustrine sediments. This illustrates one example of a typical Van Houten precession cycle from the Nursery no.1 drilling core. From Kent et al. (2017), based on Olsen et al. (1996b).

As outlined above, the periodic lake level fluctuations are climatically interpreted as the result of an astronomical modulation of the basin hydrology (Olsen and Kent 1996). One possible cause is that high summer insolation in the climatic precession cycle led to am-

plified monsoonal precipitation and filling of the basin lake. In contrast, lower summer insolation would have been associated with weaker monsoons and thus drier conditions and lake regression (Olsen and Kent 1996, Ruddiman 2014). Specifically, it has been proposed that the NHB sediments recorded a truncated or clipped monsoon response when insolation and humidity above a certain threshold promoted basin lakes of fluctuating size and depth (Fig. 1.4; Crowley et al. 1992, Ruddiman 2014). During intervening drier phases, the lakes retreated and sedimentation became less sensitive to orbital changes. Van Houten cycles with the best expression of deep water facies are associated with times of maximum precessional variability at eccentricity peaks, whereas they are less expressed and lack dark mudstones in intervals corresponding to eccentricity minima (Kent et al. 2017).

This concept extends the theory of an orbital control on monsoon strength (“orbital monsoon hypothesis”; Kutzbach 1981, Ruddiman 2014) to the early Mesozoic climate regime and lacustrine sediment record. This theory was originally developed for Quaternary times to explain deeper East African lake levels and other evidence of humidification (e.g. Rossignol-Strick 1985) by a strengthened African monsoon at climatic precession phases with elevated northern hemisphere insolation (Kutzbach 1981, Kutzbach and Otto-Bliesner 1982, Kutzbach and Street-Perrott 1985, Kutzbach and Webb III 1991, Ruddiman 2014, Braconnot et al. 2008, Lourens 2016). It also shows that orbitally-induced climate change is not limited to glacial–interglacial variability, but equally affects mid- and low-latitude climate by regulating its major mode of seasonality (Kutzbach et al. 1996; 2008; 2020, Weber and Tuenter 2011, Bosmans et al. 2015a;b, de Boer et al. 2021, Ding et al. 2021). Higher NH summer insolation leads to intensified low pressure cells over northern Africa and Eurasia, stronger landward winds, enhanced moisture convergence and thus strengthened monsoons (Braconnot et al. 2008, Weber and Tuenter 2011, Bosmans et al. 2012; 2015a;b, Lourens 2016). Climate simulations for the mid-Holocene (6 ka) suggest, for example, that the 5 % higher NH summer insolation caused an up to 46 % higher simulated monsoon precipitation in North Africa (Bosmans et al. 2012; 2015a, Hilgen et al. 2015, Marzocchi et al. 2015). An enhanced cloud cover over the monsoon regions additionally contributes to a 5 °C surface cooling and therefore greater humidity despite the enhanced insolation (Bosmans et al. 2015a).

Orbital paleoclimate effects have been assessed with climate models for the Mesozoic and earlier geologic periods before, but most of such work has obviously focused on much more recent phenomena like the North African monsoon. Transient orbitally-forced Earth System Model simulations over 10^4 – 10^6 yr time scales have mostly been targeted at Neogene and Quaternary climate cycles (Kutzbach et al. 2008; 2020, Tigchelaar et al. 2018; 2019), including a number of studies using the CLIMBER models (Weber and Tuenter 2011, Ganopolski and Brovkin 2017, Willeit et al. 2019, de Boer et al. 2021). Other studies have analyzed ensembles of equilibrium climate simulations for sets of fixed orbital parameters (“snapshots”, e.g. Bosmans et al. 2015a;b, Marzocchi et al. 2015). This has also been the common approach in the Mesozoic paleoclimate context (Park and Oglesby 1991, Crowley et al. 1992b, Kutzbach 1994, Valdes et al. 1995, Valdes and Glover 1999, Flögel et al. 2005, Flögel and Wagner 2006, Flögel et al. 2008, Winguth and Winguth 2013, Zhang et al. 2019), or even more ancient periods (Horton et al. 2010; 2012, Feulner 2017, Brugger et al. 2019). While this snapshot approach has its virtues, it is limited in representing the dynamic Earth system response to an orbital forcing, particularly regarding carbon cycle, ice-sheet, bedrock and deep ocean responses and feedbacks. Earth system models of intermediate complexity (EMICs) like CLIMBER-2 and CLIMBER-X are useful tools to capture these complex dynamics while still being computationally lightweight enough to allow for transient simulations that cover several orbital cycles (Loutre 2003). This type of

modeling more readily enables to implement different continuous orbital-scale forcings and integrate their simulated effects with time series of proxy data, for example over multiple glacial cycles, or even the whole Quaternary (Ganopolski and Brovkin 2017, Willeit et al. 2019).

Modeling the orbital climate response specifically for Late Triassic to Early Jurassic Earth system configurations and paleoclimate records is the subject of P.II. This work constitutes the first framework of transient orbital climate simulations developed for any Mesozoic period and focuses on the Newark-Hartford Basin record in particular. By elaborating on the climatic interpretation of this exceptional geological archive, this work contributes to our understanding of the orbital pacing of Earth’s climate system, especially in warm greenhouse climate states that prevailed for the majority of Phanerozoic times (Scotese et al. 2021) but remain much less studied than the Quaternary ice age. For this purpose, Landwehrs et al. (2022) study the climatic expression of an idealized orbital forcing in the NHB region and how it is modulated by reconstructed plate tectonic shifts and $p\text{CO}_2$ changes. Transient CLIMBER-X climate model simulations for nine geologic time slices from 230 to 190 Ma with two paleogeographic reconstructions (Cao et al. 2017; 2018, Marcilly et al. 2021) enable an assessment of effects of the northward drift from ~ 5 to 21°N of the NHB (Kent and Tauxe 2005, Whiteside et al. 2011a, Olsen et al. 2019) on the regional climate trends and orbital signals. Variations of $p\text{CO}_2$ reconstructed from proxies in the same strata (Schaller et al. 2011; 2012; 2015) also have relevant climatic effects as shown by simulations for low, medium and high $p\text{CO}_2$ cases (750, 1500, 3000 ppm). Ultimately, the study evaluates the simulated clipped wet season net precipitation against trends and orbital signals in the NHB record, following the orbital monsoon theory introduced above. Furthermore, the expression of the orbital forcing is also discussed with respect to contemporaneous cyclostratigraphic records from the Germanic Basin, the Junggar Basin and the Colorado Plateau in their respective paleogeographic setting (Bahr et al. 2020, Sha et al. 2015, Lepre and Olsen 2021, Lepre et al. 2021). This is a step towards a consistent climatic framework for the integration and correlation of evidence from different regions on the global orbital response of Pangean climates. In addition to the long record of climate cycles, the Newark supergroup rift basins host magmatic rocks and other evidence of the end-Triassic volcanism and extinction event (Olsen et al. 1996, Whiteside et al. 2007; 2011b, Schaller et al. 2015), which are investigated in P.III, as described in the next section.

1.1.3 Volcanic Environmental Disruptions

In addition to the tectonic long-term trends (Sec.1.1.1) and regular orbital cycling (Sec. 1.1.2), the Earth system experienced dramatic disruptions by several phases of Large Igneous Province (LIP) volcanism during the Mesozoic (Clapham and Renne 2019, Torsvik et al. 2021b). These represent Earth’s largest volcanic episodes during which magma volumes typically on the order of $\sim 10^6 \text{ km}^3$ cover areas of $\sim 10^6 \text{ km}^2$ within $\sim 1 \text{ Myr}$ or less (Ernst and Youbi 2017, Clapham and Renne 2019, Black et al. 2021, Kasbohm et al. 2021). Much of the Mesozoic LIP volcanism has been associated to the tectonic breakup of Pangea (Peace et al. 2020, Torsvik et al. 2021b, also see Sec. 1.1.1).

At least two LIPs have been linked to major mass extinction events identified from the fossil record (Fig. 1.6; Kidder and Worsley 2010, Bond and Wignall 2014, Rampino and Self 2015, van de Schootbrugge and Wignall 2015, Bond and Grasby 2017, Clapham and Renne 2019, Kasbohm et al. 2021): The Siberian Traps marking the transition from the Paleozoic into the Mesozoic (Sun et al. 2012, Dal Corso et al. 2022) and the Central Atlantic Magmatic

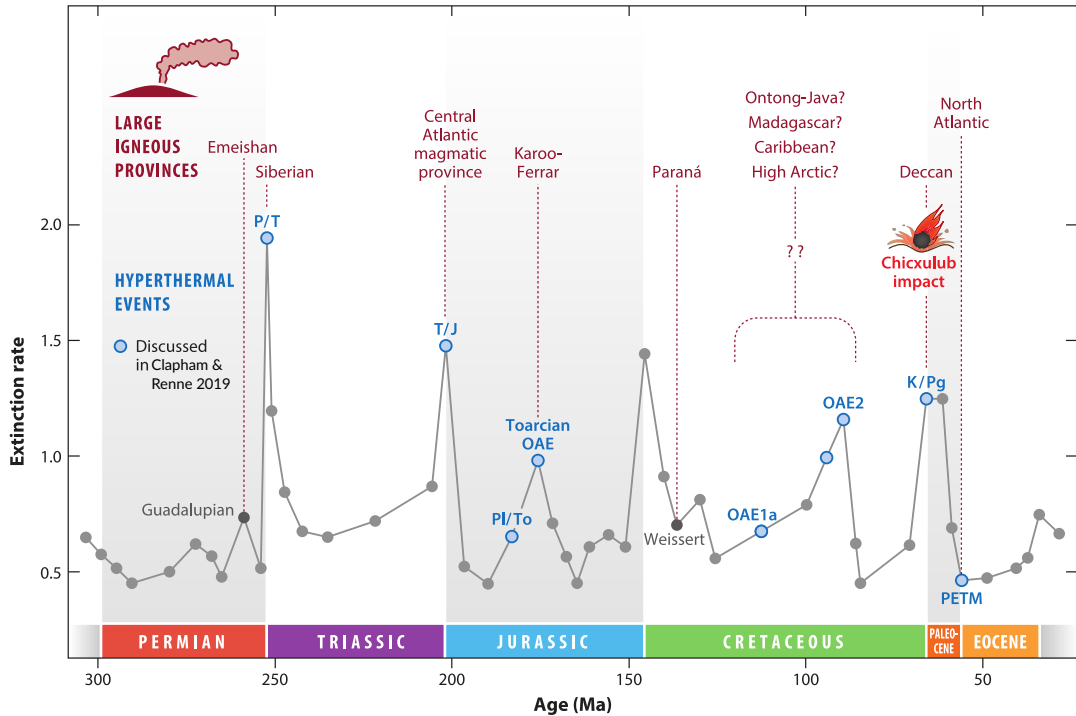


Figure 1.6: Mesozoic extinction events, Large Igneous Provinces and OAEs. The grey line shows relative marine invertebrate extinction rates based on fossil occurrences in the Paleobiology Database. Blue dots indicate major hyperthermal events discussed in Clapham and Renne (2019) and associated LIPs are indicated in red. From Clapham and Renne (2019).

Province (CAMP) at the Triassic–Jurassic boundary (TJB, ~201.36 Ma; Lindström et al. 2021). Massive volcanic outgassing of greenhouse gases and other volatiles is generally considered as the main cause of the biotic crises leading to the end-Permian and end-Triassic mass extinctions (Lindström et al. 2021). Although Deccan Traps volcanism did not actually cause the end-Cretaceous extinction (Schulte et al. 2010), its role is still being discussed (Tobin et al. 2017, Hull et al. 2020). LIP volcanism has furthermore been linked to several OAEs (Clapham and Renne 2019, Torsvik et al. 2021b) like the Toarcian OAE (~183 Ma, Karoo-Ferrar LIP; Percival et al. 2015, Heimdal et al. 2021), OAE 1a (~123 Ma, Ontong-Java Plateau LIP; Erba et al. 2015, Percival et al. 2021), OAE 2 (~94 Ma, Caribbean LIP; Monteiro et al. 2012, Joo et al. 2020, Percival et al. 2018; 2020) as well as the the Carnian Pluvial Episode (~234–232 Ma, Wrangellia LIP; Dal Corso et al. 2020). Overall, LIPs thus played a role in almost all prominent Earth system disruptions of the Mesozoic (Clapham and Renne 2019).

LIPs can perturb the global climate system, the carbon cycle and marine and terrestrial ecosystems in many ways through the massive emission of various volatiles, including water vapor, CO₂, CH₄, SO₂ and halogens (Fig. 1.7; Self et al. 2005; 2006, Jones et al. 2016, Suarez et al. 2019, Mather and Schmidt 2021, Ernst et al. 2021, Kasbohm et al. 2021). Carbon and sulfur are released directly from the magmatic rocks and indirectly by thermogenic gas generation when magma intrudes sedimentary rocks (Fig. 1.7; Jones et al. 2016, Heimdal et al. 2020). The latter process is called contact metamorphism and is especially relevant when the intruded sediments are rich in organic carbon (shales, coal) or evaporites (Aarnes et al. 2010; 2011, Courtillot and Fluteau 2014). Explosive volcanic eruptions can inject sulfur into the stratosphere, which eventually forms aerosols that effectively scatter sunlight and thus lead to surface cooling (“volcanic winter”; Robock

2000, Robock et al. 2009, Chenet et al. 2005, Langmann 2014, Mather 2015, Jones et al. 2016). For this mechanism to become relevant during LIP emplacement, volcanic plumes must frequently reach stratospheric heights of >10 km either through explosive eruptions or by atmospheric convection over large lava flows (Self et al. 2014, Kaminski et al. 2011, Schmidt et al. 2016, Jones et al. 2016, Glaze et al. 2017, Macdonald and Wordsworth 2017, Ernst and Youbi 2017, Lindström et al. 2021). The stratospheric sulfate aerosols have relatively short atmospheric residence times that reach ~1–3 years in the stratosphere (Robock 2000, Jones et al. 2016), resulting in a variable negative radiative forcing (Schmidt et al. 2018). In contrast, $p\text{CO}_2$ can remain in the atmosphere for several millennia (Archer et al. 2009, Zeebe 2012b, Colbourn et al. 2015) and therefore yields a more continuous and longer-lasting positive radiative forcing. Through their radiative effects, volcanogenic carbon and stratospheric aerosols can thus cause both global warming and cooling on differing time scales. Considering biogeochemical cycles, the deposition of acidic fallout and the dissolution of carbon and sulfur in surface waters can cause ocean acidification and damage terrestrial ecosystems (Fig. 1.7; Hönisch et al. 2012, Greene et al. 2012, Black et al. 2014, Schmidt et al. 2016, Lindström et al. 2021). LIP volcanism can furthermore contribute to oxygen depletion in multiple ways. On the one side, ocean stratification is enhanced by warming from the surface, which reduces seawater ventilation and mixing. On the other hand, primary productivity and thus oxygen consumption by the microbial decomposition of the organic matter can be amplified by fertilization (eutrophication) directly by nutrient rich volcanic ash and by enhanced weathering in the longer term (Clapham and Renne 2019, Mather and Schmidt 2021). These mechanisms (short-term global cooling, longer-term warming, acidification and anoxia) are universally discussed for the multiple LIP episodes during the Mesozoic and the mass extinction and Ocean Anoxic Events (OAEs) that have been associated to them (Clapham and Renne 2019). The spectrum of short- and long-term environmental effects has, of course, much more facets than can be reviewed here and has been only rudimentarily reflected in Earth system modeling.

The CAMP volcanism was a precursor of the Pangea breakup and the opening of the North Atlantic ocean in the center of Pangea (Fig. 1.7; Marzoli et al. 2018, Peace et al. 2020). It represents one of the most extensive LIPs (Ernst and Jowitt 2013, Ernst and Youbi 2017, Percival et al. 2017), covering more than 10^6 km^2 in the circum-Atlantic regions of the Americas, Africa and southern Europe with extrusive and intrusive volcanic rocks (McHone 2003, Marzoli et al. 2018, Lindström et al. 2021). Absolute radiometric ages of magmatic units and ash beds range from ~201.6 to 200.9 Ma, suggesting that the CAMP was emplaced within ~700 kyr (Whiteside et al. 2007, Schoene et al. 2010, Wotzlaw et al. 2014, Blackburn et al. 2013, Davies et al. 2017, Heimdal et al. 2018, Kasbohm et al. 2021). Amounts of CAMP carbon and sulfur emissions are estimated from the original volume of magma (e.g. $2\text{--}4 \times 10^6 \text{ km}^3$; Svensen et al. 2017, Marzoli et al. 2018, Lindström et al. 2021) and its volatile content as well as potential contributions by contact metamorphism. The estimates for the total CAMP carbon emissions are on the order of 10^4 GtC (McHone 2003, Beerling and Berner 2002, Berner and Beerling 2007, Schaller et al. 2011; 2012, Heimdal et al. 2018), for example 27 000 GtC with emission rates of ~5 GtC/yr assuming four main volcanic pulses of 400 yr length (Capriolo et al. 2020; 2022, Lindström et al. 2021). However, the volume and style of LIP degassing is in general very difficult to constrain (Self et al. 2014, Black and Manga 2017) and total CAMP sulfur emission estimates range from 2 310 to 105 000 GtS (McHone 2003, Berner and Beerling 2007, van de Schootbrugge and Wignall 2015, Guex et al. 2016), e.g. 8 000–16 000 GtS based on measured sulfur concentrations (Callegaro et al. 2014, Lindström et al. 2021). The CAMP is mainly characterized by huge intrusive rock units (sills and dikes) so that thermogenic gas generation from contact metamorphism likely contributed significantly to

the end-Triassic climate perturbations (Beerling 2002, Aarnes et al. 2010, Svensen et al. 2017, Heimdal et al. 2018; 2020, Lindström et al. 2021, Capriolo et al. 2020; 2021, Kaiho et al. 2022). In contrast, preserved lava flows and pyroclastic rocks are relatively rare (Marzoli et al. 2018, Lindström et al. 2021). Also, hydrothermal vents that evidence explosive thermogenic degassing have been found for other LIPs (Svensen et al. 2007; 2009, Ganino and Arndt 2009) but still remain hypothetical for the CAMP (Heimdal et al. 2018). Nevertheless, it appears likely that also CAMP activity comprised phases of intense explosive volcanism (White et al. 2009, Self et al. 2014, Lindström et al. 2021)

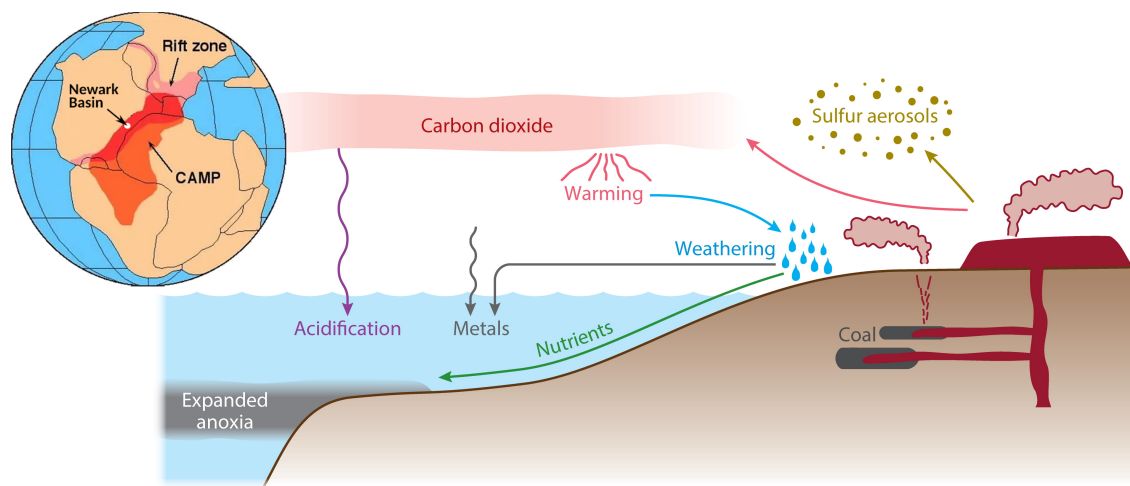


Figure 1.7: Environmental effects of Large Igneous Province Volcanism. Carbon dioxide and sulfur aerosols are sourced from both magmatic degassing and contact metamorphism of e.g. coal-bearing rocks that are intruded by magma. Volcanic degassing can result in short-term cooling from aerosols and longer-term greenhouse gas warming, ocean acidification, deposition of metals like mercury, an enhanced hydrologic cycle and weathering, as well as expanded ocean anoxia due to fertilization by weathering-derived nutrients (Clapham and Renne 2019). The inset map shows the approximate extent of the Central Atlantic Magmatic Province (CAMP) and the Newark Basin in the Late Triassic. Modified from Clapham and Renne (2019).

Besides the volcanic rock features themselves, volcanic activity and environmental change is evidenced by a variety of geochemical and paleontological proxy records. Correlation of the volcanic units with fossil records and various geochemical proxies (e.g. $\delta^{13}\text{C}$, Hg) in different sections has yielded improved chronologies of the end-Triassic events (Lindström et al. 2017b, Lindström et al. 2021). The main end-Triassic marine extinction interval is usually defined by the first and last occurrences of certain ammonoid species and lasted from ~ 201.51 Ma to up to the TJB (~ 201.36 Ma; Schoene et al. 2010, Hillebrandt et al. 2013, Wotzlaw et al. 2014, Lindström et al. 2017b, Lindström et al. 2021). The initiation of the marine extinction has been linked to the first pulse of CAMP activity indicated by a negative $\delta^{13}\text{C}$ carbon isotope excursion (the “Marshi” CIE) as well as a sharp increase of $p\text{CO}_2$ (Lindström et al. 2021). The initial CIE expresses a perturbation of the global carbon cycle (Whiteside et al. 2010, Ruhl et al. 2011, Schobben et al. 2019) and could be linked to the release of large amounts of isotopically light thermogenic gases, e.g. from sill intrusions into organic-rich sedimentary basins of Brazil (Heimdal et al. 2018; 2020, Capriolo et al. 2020, Lindström et al. 2021). Two further negative CIEs are widely recognized around the TJB and shortly after that (Lindström et al. 2017b, Lindström et al. 2021). A detailed reconstruction of atmospheric $p\text{CO}_2$ changes has been obtained from pedogenic carbonate $\delta^{13}\text{C}$ values of fossil soils from the Newark and Hartford basins (Schaller et al. 2011; 2012; 2015, Foster et al. 2017). The record exhibits multiple peaks in atmospheric CO_2 immediately after major magmatic episodes, each followed by a decline within a few 100 kyrs that is interpreted as the drawdown by weathering. This provides evidence that

CAMP activity and carbon emissions were concentrated in 4–5 shorter pulses the first of which coincided with the onset of the extinction interval (Knight et al. 2004, Schaller et al. 2011, Blackburn et al. 2013, Black and Manga 2017, Lindström et al. 2021). At the initial pulse, the reported $p\text{CO}_2$ doubles from ~ 2000 to 4000 ppm, corresponding to carbon emissions of $\sim 3000\text{--}4000$ GtC within <20 kyr (Schaller et al. 2011; 2012; 2015). The $p\text{CO}_2$ values were re-calculated by Foster et al. (2017) to ~ 1350 and 2950 ppm. Increasing $p\text{CO}_2$ and global warming during the Triassic–Jurassic transition are further corroborated by changing stomata cell density in fossil leaves (McElwain et al. 1999, Bonis, Van Konijnenburg-Van Cittert and Kürschner 2010, Bonis, Ruhl and Kürschner 2010, Steinhorsdottir et al. 2011).

There is increasing evidence of profound environmental perturbations caused by CAMP volcanism during the end-Triassic mass extinction event (ETE; Pálffy and Kocsis 2014, van de Schootbrugge and Wignall 2015, Korte et al. 2018, Lindström et al. 2021, Fox et al. 2022). This is evident, for example, through the decline or extinction of many forms of life, especially in the marine realm (Fig. 1.6). Extinction of marine genera reached $\sim 73\%$ (Raup and Sepkoski 1982, McGhee et al. 2013, Reddin et al. 2018b, Torsvik et al. 2021b) and the conodont animals are one example of a major group that went extinct (Pálffy et al. 2007, Du et al. 2020, Lindström et al. 2021). The ETE was the most severe extinction for scleractinian coral reefs that had just evolved during the Triassic and now suffered an almost complete breakdown of reef ecosystems (Flügel 2002, Kiessling et al. 2007, Lathuilière and Marchal 2009, Scotese et al. 2021). A marine calcification crisis due to ocean acidification and consequently reduced seawater carbonate saturation is evident from a generally reduced marine carbonate production during the end-Triassic extinction interval (van de Schootbrugge et al. 2007, Hautmann et al. 2008, Kiessling and Simpson 2010, Greene et al. 2012, Dunhill et al. 2018). The extinction in the marine realm is accompanied by floral changes on land (McElwain et al. 2009, Bonis and Kürschner 2012), including a decline of conifers and other trees while opportunistic ferns and other spore producing plants proliferated (van de Schootbrugge et al. 2009, Lindström 2015, Lindström et al. 2017, Gravendyck et al. 2020, Lindström et al. 2021). Sulfur emissions are also indicated by SO_2 induced damages in fossil plant leaves (Bacon et al. 2013, Elliott-Kingston et al. 2014, Steinhorsdottir et al. 2017) and they are discussed as major factor in the end-Triassic ecosystem collapse through rapid cooling trends and sulfuric acid rain (van de Schootbrugge et al. 2009, Schoene et al. 2010, Guex et al. 2016, Lindström et al. 2021). The significance and pulsed nature of CAMP volcanism during the end-Triassic extinction receive further support by spikes in sedimentary mercury concentrations that begin with the Marshi CIE in many places (Thibodeau et al. 2016, Percival et al. 2017, Lindström et al. 2019). Global warming and ocean acidification by CAMP volcanism have been frequently invoked as the primary drivers of the extinction (Greene et al. 2012, Pálffy and Kocsis 2014, Lindström et al. 2021). There is evidence for ocean deoxygenation during the end-Triassic events, but its role in the marine extinction is awaiting further clarification (van de Schootbrugge et al. 2013, van de Schootbrugge and Wignall 2015, Jost et al. 2017, Luo et al. 2018, He et al. 2022).

Environmental effects of CAMP volcanism have been investigated by a limited number of modeling studies, which either mainly relied on spatially simplified carbon cycle box models (Beerling 2002, Bachan and Payne 2015, Paris et al. 2016, Jost et al. 2017b, Heimdal et al. 2020, Capriolo et al. 2022), or equilibrium climate model simulations (Huynh and Poulsen 2005). More research targeted other LIP events (Jones et al. 2019, Heimdal et al. 2021), especially the end-Permian Siberian Traps (Winguth and Maier-Reimer 2005, Winguth et al. 2015, Cui et al. 2013, Black et al. 2018, Penn et al. 2018, Dal Corso et al. 2020b, Hülse et al. 2021) and the end-Cretaceous Deccan Traps (Schmidt et al. 2016,

Tobin et al. 2017, Hull et al. 2020). Most of this modeling focused on carbon, whereas very few studies considered potential effects of sulfate aerosols in climate models (Schmidt et al. 2016, Black et al. 2018) or spatially simplified models (Macdonald and Wordsworth 2017, Mussard et al. 2014). None of these specifically addressed the CAMP and the end-Triassic events. Paris et al. (2016) used the GEOCLIM model to test biogeochemical effect of empirically constrained CAMP carbon degassing scenarios with five brief emission pulses, each with 5300 GtC within ≤ 10 kyr. The authors show that this can explain the reconstructed $p\text{CO}_2$ changes (Schaller et al. 2011; 2012), the decrease in marine carbonate production due to ocean acidification as well as the magnitude of the initial CIE if $\delta^{13}\text{C} = -20\text{‰}$ is assumed for the volcanogenic carbon. Such a light isotopic signature is indeed expected if thermogenic methane generation provided a major part of the CAMP carbon degassing (Heimdal et al. 2018; 2020, Capriolo et al. 2020, Lindström et al. 2021). Using an atmosphere-ocean GCM, Huynh and Poulsen (2005) assessed effects of increasing $p\text{CO}_2$ on end-Triassic climate with equilibrium climate simulations at four $p\text{CO}_2$ values from 600 to 2400 ppm.

Although previous climate and carbon cycle modeling has elucidated some aspects of LIP related events in the end-Triassic and other Mesozoic periods, the timing and causal relation of volcanic activity and environmental disruptions remains only rudimentarily understood. Publication III (Landwehrs et al. 2020) is a contribution to modeling climatic and environmental effects of LIP volcanism in the context of the CAMP and the end-Triassic mass extinction event. This work specifically assesses the dynamic response of the Earth system to short pulses of carbon and sulfur emissions. To this end, coupled climate and ocean biogeochemistry model simulations with the CLIMBER-3 α +C model (see Sec. 1.1.4) are run for a Rhaetian paleogeography (Scotese 2014) and an ensemble of different emission scenarios. These consist of pulses with 1–6 kyr duration during which 2500–7500 GtC are emitted and 0–500 GtS are converted to stratospheric sulfate aerosols. Whereas the carbon emissions are continuous, the radiative aerosol forcing is composed of the effect of individual injections to reflect their dependence on explosive eruption events. The Easy Volcanic Aerosol model (EVA; Toohey et al. 2016) is used to calculate the radiative aerosol forcing, which is then implemented simply as an averaged global reduction of the solar constant. Combining these different forcings simultaneously in transient simulations with a spatially resolved Earth system model provides novel insights into the dynamic nature of environmental disruptions by the CAMP and Mesozoic LIP volcanism in general. The study analyzes the modes of global and regional cooling and warming resulting from the carbon and sulfur forcings. Furthermore, simulated sea water temperature, oxygen and pH changes are discussed with respect to Late Triassic scleractinian coral reef distributions and their potential thermal tolerance limits. Additional simulations with the carbon cycle box model LOSCAR (Zeebe 2012a) are conducted to combine the brief pulse simulations into a longer-term scenario of the period of CAMP activity as a whole. Earth system modeling, as presented in P.III, complements refined geological approaches for gaining an integrated and physically consistent understanding of the climatic and environmental mechanisms shaping this major ecologic crisis. The modeling concepts developed for this particular LIP event can be readily extended to similar events. Comparing these in a unified modeling framework could yield a more general picture of climatic effects of Mesozoic LIPs and should be the target of future research.

Within the three time scale regimes that structure this thesis, P.III deals with the most rapid and episodic mode of climate variability, characterized by irregular disruptions on annual to millennial time scales. The following section briefly describes the Earth system modeling approaches that have been established here for each of the three thematic units.

1.1.4 Modeling Paleoclimate across Time Scales

Earth system models (ESM) are useful tools to study the complex interplay of various components of the Earth system under past, present and future climate conditions and their changes. To achieve this, equations describing fundamental natural processes are represented in these models and solved numerically. General circulation models (GCMs) solve the primitive equations of mass, momentum and energy conservation on a rotating sphere to simulate the circulation of water and air masses as well as energy fluxes on Earth. In addition to the primary climate physics, ESMs include further physical, biological and chemical processes relevant in the Earth system. This thesis is based on the application of the CLIMBER-3 α and CLIMBER-X ESMs to a variety of Mesozoic paleoclimate problems. Characteristics of these models and the different modeling approaches are briefly described in the following.

Deep time paleoclimate modeling frequently faces the following challenges, among others: (I) Simulating equilibrium climate conditions for boundary conditions that characterize a certain geologic time interval, such as the continental configuration or atmospheric greenhouse gas concentrations. (II) Representing processes or events on various time scales to match geologic evidence. (III) Account for the high degree of uncertainty in the Earth system state, forcing mechanisms and model behavior associated to the incomplete knowledge about the distant past. Due to the response time of the deep ocean, (I) requires model equilibration, or “spinup”, over several thousand years for every new set of boundary conditions. Most events in Earth history that are empirically accessible took place on $>10^3$ to $>10^6$ yr time scales. To cover these periods in climate models, either long transient simulations or ensembles of equilibrium simulations for many time slices are required by (II). Large ensembles of simulations that systematically test ranges of uncertainty are also demanded by (III). All three points require that the ESM can be flexibly adapted to varying settings and that both large numbers (>10 – 100) and relatively long ($\geq 10^3$ – 10^5 yr) climate simulations can be carried out at reasonable computational cost. CMIP6 ESMs with GCMs at <100 km horizontal grid resolution achieve <40 simulated model years per day using thousands of CPU cores (Balaji et al. 2017). Several hundreds of model years can be achieved at somewhat coarser resolution of 200–300 km (Willeit et al. 2022). On current supercomputers this allows small numbers of spinup and near-future prediction runs but with much higher resource expenditure than is usually available for deep time paleoclimate research. For the latter, spatial resolution and computational demand have to be balanced with the considerable uncertainties in, e.g. paleogeography, and the need for frequent adjustments of exotic paleoclimate settings.

The CLIMBER models are Earth system models of intermediate complexity (EMICs; e.g. Eby et al. 2013) which fill this niche by being much faster due to moderate spatial resolution and partially simplified physical dynamics, while including the major Earth system components. Both CLIMBER-3 α (Montoya et al. 2005) and the newly developed CLIMBER-X (Willeit et al. 2022) are successors of the CLIMBER-2 model (Petoukhov et al. 2000, Ganopolski et al. 2001), especially in terms of its statistical-dynamical atmospheric foundations (Petoukhov et al. 2000). CLIMBER-2 has been primarily used for studying Quaternary paleoclimates with transient simulations on orbital time scales (Ganopolski and Brovkin 2017, Willeit et al. 2019, de Boer et al. 2021).

CLIMBER-X/3 α include atmosphere, ocean, sea-ice and land surface models which are coupled through fluxes of water and energy (Fig. 1.8). In CLIMBER-X these are all discretized on a regular $5^\circ \times 5^\circ$ horizontal grid (latitude \times longitude), whereas CLIMBER-3 α has a higher resolution of $3.75^\circ \times 3.75^\circ$ in the ocean but only $7.5^\circ \times 22.5^\circ$ in the atmosphere.

The model dynamics are generally computed with a time step of 0.5 or 1 days, but shorter sub-time steps are used for certain processes within individual model components and effects of the diurnal cycle are parameterized, e.g. for snow and ice melting (Willeit et al. 2022). The CLIMBER models are designed to represent mean climatological states and do not explicitly simulate synoptic weather dynamics and interannual climate variability (Willeit et al. 2022). CLIMBER-X allows integrating $\sim 10,000$ model years per day on 16 CPUs, which makes it ≈ 100 – 1000 times faster than weather-resolving climate models using comparable computational resources (Willeit et al. 2022). CLIMBER-3 α even requires only a single CPU to simulate ~ 800 model years per day, enabling many simultaneous simulations.

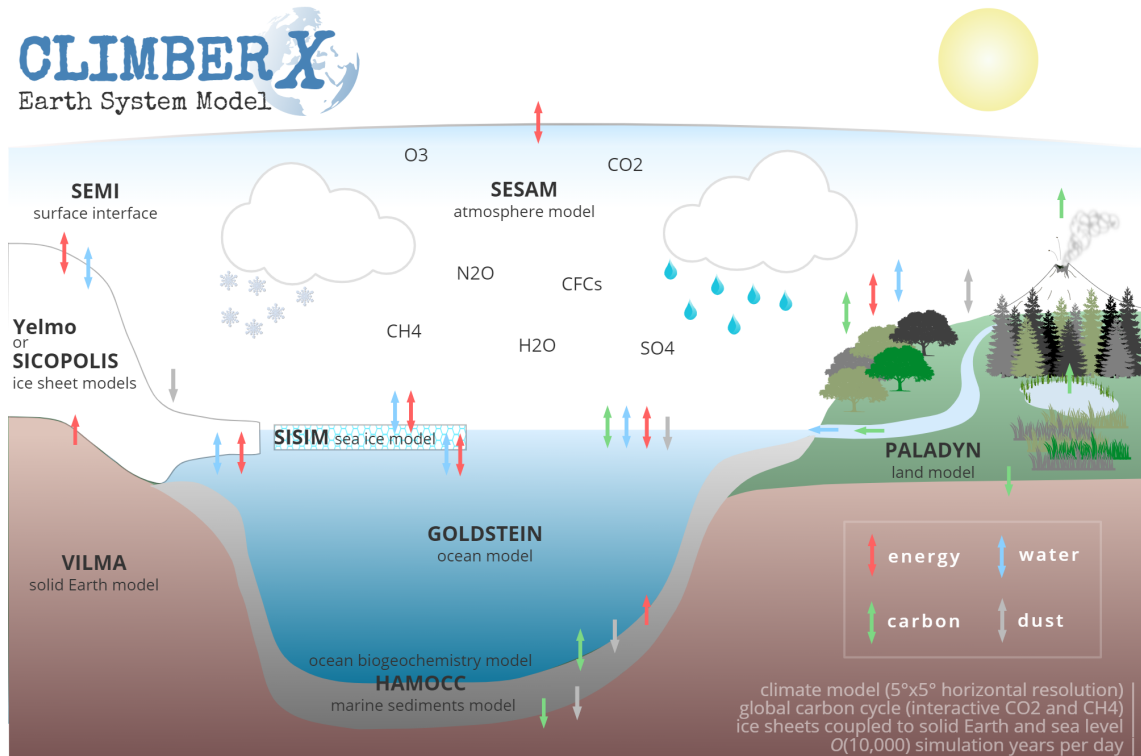


Figure 1.8: Schematic illustration of the CLIMBER-X model, including exchanges and coupling (arrows) between the different modules. From Willeit et al. (2022).

Atmosphere: In the atmospheric models of CLIMBER-X and CLIMBER-3 α (SESAM, Willeit et al. 2022, and POTSDAM2, Petoukhov et al. 2000), equations for prognostic variables like temperature and water vapor content are solved by assuming a universal vertical structure of the atmosphere on seasonal time scales. In CLIMBER-X, this is characterized by a quadratic dependence of tropospheric temperature on the altitude and an exponential decay of relative humidity, except in a layer close to the surface (Willeit et al. 2022). With these assumptions, the 3D description of the atmosphere can be reduced to a set of vertically integrated 2D prognostic equations from which the 3D distribution can be reconstructed and used for calculation of horizontal energy and water transport and vertical longwave radiation fluxes (Petoukhov et al. 2000, Willeit et al. 2022). In this sense, the atmosphere model can be considered as spatially 2.5 dimensional.

The prognostic atmospheric temperature T_a is determined from the thermodynamic energy balance equation which describes the change of the heat content $Q_T = \int_{z_s}^{H_{TOA}} \rho T dz$ of the

atmospheric column (Willeit et al. 2022):

$$\frac{\partial Q_T}{\partial t} = -\frac{1}{R_e \cos \phi} \left[\frac{\partial}{\partial \lambda} \int_{z_s}^{H_T} \rho(u\theta + \widehat{u'\theta'}) dz + \frac{\partial}{\partial \phi} \int_{z_s}^{H_T} \cos \phi \rho(v\theta + \widehat{v'\theta'}) dz \right] + c_v^{-1} (SW_a + LW_a + L_e P_w + L_s P_s + SH)$$

The bracketed terms on the right hand side represent the horizontal heat transport from the divergence of the wind field. Contributions from synoptic variability are parameterized as a macroturbulent diffusion process $\widehat{u'\theta'} = -A_T \nabla_h T$, with a diffusivity A_T (Willeit et al. 2022). The radiative balance includes the shortwave and longwave terms $SW_a + LW_a$. $L_e P_w + L_s P_s$ introduces latent heat fluxes associated to rain- and snowfall. SH is the surface latent heat flux and c_v the heat capacity of air at constant volume (Willeit et al. 2022).

The new atmospheric temperature is then numerically computed as

$$T_a(t + \Delta t) = T_a(t) + \frac{1}{c_v M_a} \frac{\partial Q_T}{\partial t} \cdot \Delta t.$$

where M_a is the average air column mass.

In a similar way, the prognostic specific humidity q_a is determined from the water balance equation for the atmospheric column water content $Q_q = \int_{z_s}^{H_{TOA}} \rho q dz$ with contributions from convection and eddy diffusion as well as evaporation and precipitation.

For the atmospheric dynamics, horizontal wind velocities are computed as the sum of geostrophic and ageostrophic components $\mathbf{u} = \mathbf{u}_g + \mathbf{u}_a$. The geostrophic wind $\mathbf{u}_g = \frac{1}{\rho f} \mathbf{k} \times \nabla_h p$ expresses the dominant balance of the Coriolis force and pressure gradient forces in the free atmosphere on synoptic and larger scales. Its vertical profile is calculated by integration of the thermal wind shear equation $\partial_z \mathbf{u}_g = \frac{g}{fT} \mathbf{k} \times \nabla_h T$ that makes use of the ideal gas law and assumes hydrostatic balance:

$$\mathbf{u}_g(z) = \frac{1}{\rho_0 f} \mathbf{k} \times \nabla_h p(0) + \int_0^z \frac{g}{fT} \mathbf{k} \times \nabla_h T$$

The sea level pressure in this equation is computed as the sum of zonally averaged and azonal components $p_{sl} = p(0) = \overline{p}_{sl} + p_{sl}^*$ (Willeit et al. 2022). \overline{p}_{sl} is parameterized through the zonal mean meridional ageostrophic wind component in the planetary boundary layer, assuming that the present mode of meridional circulation with three pairs of cells is robust for a range of climate states (Petoukhov et al. 2000, Willeit et al. 2022). The cell widths and positions of cell boundaries and the ITCZ (intertropical convergence zone) can respond to changes in the meridional temperature gradients.

Overall, SESAM and POTSDAM-2 are similar in their theoretical basis, which distinguishes them from atmosphere GCMs and makes them especially fast and useful for paleoclimate modeling. The newer SESAM model offers several improvements, including a higher resolution (Willeit et al. 2022).

Ocean: For the ocean component, CLIMBER-3 α incorporates MOM3 (Pacanowski and Griffies 2000, Hofmann and Morales Maqueda 2006), whereas CLIMBER-X relies on GOLDSTEIN (Edwards and Marsh 2005) which is also used in other existing EMICs,

e.g. GENIE (Marsh et al. 2011) and Bern3D (Müller et al. 2006). MOM3 is a three-dimensional ocean GCM and simulates ocean dynamics by solving primitive equations including the Navier-Stokes equations of motion, with contributions from pressure gradient forces, the Coriolis force and friction:

$$\partial_t \mathbf{u} + (\mathbf{u} \cdot \nabla) \mathbf{u} = -\frac{1}{\rho} \nabla p - 2\boldsymbol{\Omega} \times \mathbf{u} + \mathbf{F}$$

In GOLDSTEIN, this is simplified to a frictional geostrophic balance in which the left hand side vanishes. Both models assume hydrostatic balance $\partial_z p = -g\rho$ to diagnose pressure p and use the continuity equation for an incompressible fluid $\nabla \cdot \mathbf{u} = 0$ to derive vertical velocities from the horizontal momentum equations (Pacanowski and Griffies 2000, Willeit et al. 2022). In MOM3, the free surface height can vary due to velocity divergence and freshwater fluxes through the surface (Pacanowski and Griffies 2000). In contrast, GOLDSTEIN uses the rigid-lid approximation in which surface height is fixed (Willeit et al. 2022).

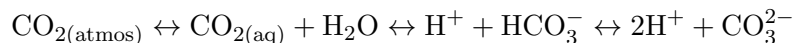
Transport of tracers like temperature and salinity is governed by a 3D advection-diffusion equation:

$$\partial_t X + \nabla \cdot (\mathbf{u}X) - \nabla \cdot (\mathbf{K}\nabla X) = Q$$

The second term represents advection and Q the sum of local sources and sinks. The third term introduces diffusion composed of iso-/diapycnal mixing as well as parameterized transport by meso-scale eddies as defined in the diffusive mixing tensor \mathbf{K} (Pacanowski and Griffies 2000, Hofmann and Morales Maqueda 2006, Müller et al. 2006, Willeit et al. 2022).

MOM3 is discretized on a regular $3.75^\circ \times 3.75^\circ$ horizontal grid in CLIMBER-3 α , whereas GOLDSTEIN has a $5^\circ \times 5^\circ$ resolution in CLIMBER-X. Both models have 24 or 23 unequally spaced vertical layers, with thicknesses increasing from 10 m at the surface to 500 m in the deep ocean. Thus, CLIMBER-3 α offers a slightly more complex and better resolved ocean GCM, while CLIMBER-X focuses on a balanced degree of complexity between the ocean and atmosphere components suitable for modeling on relatively long orbital time scales.

The global ocean biogeochemistry model HAMOCC is included both in CLIMBER-3 α (v3.1, Maier-Reimer 1993, Six and Maier-Reimer 1996) and CLIMBER-X (v5.2, Ilyina et al. 2013). Biogeochemical aspects are key in many deep time Earth system investigations but within this thesis, HAMOCC is only used in P.III to account for the ocean carbon cycle response to volcanic carbon emissions. Excess atmospheric CO_2 can dissolve in the ocean and dissociate into three forms of dissolved inorganic carbon (Zeebe 2012b, Schlesinger and Bernhardt 2020)



Dissolved inorganic carbon (DIC, or TCO_2) and total alkalinity (TA) are two of the prognostic ocean tracers to describe the marine carbon cycle in HAMOCC (Hofmann and Schellnhuber 2009).

$$\text{DIC} = \text{TCO}_2 = [\text{CO}_2] + [\text{HCO}_3^-] + [\text{CO}_3^{2-}]$$

$$\text{TA} = [\text{HCO}_3^-] + 2[\text{CO}_3^{2-}] + [\text{B}(\text{OH})_4^-] + [\text{OH}^-] - [\text{H}^+]$$

Further biogeochemical elements are O_2 , dust and tracers describing biological processes and the marine food web that include nutrients (e.g. PO_4 , Fe), phytoplankton, zooplankton, detritus, dissolved organic matter and particulate inorganic carbon (CaCO_3 shells). HAMOCC describes the cycles of these elements through a differential equation for concentration changes of each sea water tracer C^i (Ilyina et al. 2013):

$$\partial_t C^i + \mathbf{u} \nabla \cdot C^i - DC^i = \sum_k \Psi_k^i(C_k, C^i) + \Psi_{\text{air-sea}} + \Psi_{\text{sedflux}} \quad (1.1)$$

The left hand side represents tracer transport by advection and diffusion. The right hand side lists sinks and sources by biogeochemical processes (involving interactions with other tracers C_k), fluxes across the sea-air interface and interactions with the sediment. The latter are only included in the newer HAMOCC version in addition to multiple nitrogen species (Ilyina et al. 2013).

Sea Ice dynamics and thermodynamics are modeled by SISIM in CLIMBER-X (Willeit et al. 2022) and ISIS in CLIMBER-3 α (Fichefet and Maqueda 1997, Montoya et al. 2005). Both models include one ice layer and one snow layer on the respective ocean model horizontal grid resolution. The models solve sea ice energy balance equations, accounting for the surface radiation balance, sensible and latent heat fluxes to the atmosphere, conductive heat flux into the snow/ice and turbulent heat flux between ice and seawater. Sea ice can grow due to open seawater freezing, snow compaction and accretion from below.

Sea ice is advected by the simulated winds and ocean currents by solving the momentum equation for the sea ice velocity \mathbf{u}_i :

$$m \partial_t \mathbf{u}_i = \nabla \cdot \sigma + \tau_a + \tau_o - \hat{\mathbf{k}} \times m f \mathbf{u}_i - m g \nabla H_o.$$

The terms on the right hand side represent internal mechanical stress, wind and ocean stress, the Coriolis force and gravitational forces along gradients of sea surface height. In CLIMBER-X, the latter have to be diagnosed from sea water density because the rigid lid GOLDSTEIN ocean doesn't explicitly model the free surface height.

Land: In CLIMBER-3 α , land surface processes and the interaction between the atmosphere and land and sea surfaces are described by the atmosphere-surface interface (ASI) inherited from CLIMBER-2 (Montoya et al. 2005). Each model grid box consists of a mixture of the six surface types open water, sea ice, trees, grass, bare soil and ice. The state variables and surface fluxes are calculated separately for each type, considering properties like albedo, surface roughness, snow thickness and transpiration (for the two plant functional types; Petoukhov et al. 2000). Fixed global vegetation and surface cover patterns were prescribed for paleoclimate simulations in P.I and P.III, based on constraints on the approximate climate and biome zonation during the respective time periods. The hydrological balance of two soil layers is modeled and runoff is added to the freshwater flux into the ocean (Petoukhov et al. 2000, Montoya et al. 2005). For P.I, a simple method was implemented to route runoff along topographic gradients towards the coasts. Before, P.III (Landwehrs et al. 2020) used the default method for deep time paleogeographies to distribute runoff equally over all coastal cells.

The PAleo LAnd DYnAmics land model PALADYN of CLIMBER-X (Willeit and Ganopolski 2016, Willeit et al. 2022) used for P.II provides a considerably more comprehensive representation of physical and biogeochemical land surface, vegetation and carbon cycle processes. PALADYN distinguishes nine surface types, including bare soil, land ice, lakes, ocean shelf and five different vegetation types. The model solves the surface energy balance over each surface type, considering absorbed shortwave radiation, incoming and outgoing longwave radiation at the surface, the sensible and latent heat fluxes and the conductive heat exchange with the ground (Willeit and Ganopolski 2016):

$$(1 - \alpha)SW^\downarrow + \epsilon LW^\downarrow - LW^\uparrow - H - LE - G = 0$$

With the formulations of these energy fluxes, this equation is solved for the surface skin temperature.

The soil model considers prognostic equations for temperature, water and carbon in five vertical soil layers down to a depth of 3.9 m. Precipitation interception by vegetation, runoff and soil infiltration are computed at the surface. To model soil hydrology, the change of the volumetric soil water content θ_w in soil layer l is expressed by the vertical divergence of the water flux q_l and a term e_l for water extraction by evaporation (Willeit and Ganopolski 2016):

$$\rho_w \Delta z_l \frac{d\theta_{w,l}}{dt} = q_{l-1} - q_l - e_l$$

Darcy's law is used to express the fluxes q as

$$q = k \frac{\partial(\Psi - z)}{\partial z},$$

where k is the hydraulic conductivity and the soil matric potential Ψ expresses the strength of capillary forces. Both quantities are dependent on soil texture and the volumetric soil water content (Willeit and Ganopolski 2016).

Surface runoff is generated when precipitation or snow melt occur on saturated soils or when a maximum infiltration rate is exceeded. Runoff routing following the steepest slopes to the ocean or lakes is derived from the usually higher resolution topography supplied to the model before internal regridding to the coarser $5^\circ \times 5^\circ$ resolution. Topographic depressions are automatically filled by this algorithm (Willeit et al. 2022). Some paleogeographic reconstructions (e.g. Marcilly et al. 2021) may only yield land-surface masks but no further topographic information. If this is the case as in P.II, runoff routing away from the centers of the continents is still ensured.

PALADYN incorporates a dynamic vegetation model based on TRIFFID (Cox 2001) with five competing plant functional types (PFT): broadleaved trees, needleleaved trees, C3 and C4 grass and shrubs. Vegetation carbon C_v and area coverage ν_i of PFT i in each land grid cell are described with a Lotka-Volterra model for competition between species (Willeit and Ganopolski 2016):

$$\frac{dC_{v,i}}{dt} = (1 - \lambda_{NPP,i})NPP_i - \Lambda_{loc,i}$$

$$\frac{d\nu_i}{dt} = \frac{\lambda_{NPP,i} NPP_i}{C_{v,i}} \nu_{i,*} \left(1 - \sum_j c_{ij} \nu_j \right) - \gamma_{\nu,i} \nu_{i,*}$$

λ_{NPP} is a factor that determines the partitioning of NPP between the carbon stock and area spreading. Λ_{loc} is the local litterfall rate, and $\nu_{i,*} = \max(\nu_i, \nu_{seed})$ makes sure that a PFT is seeded at a small rate. The competition coefficients c_{ij} represent the impact of vegetation type j on vegetation type i (Willeit and Ganopolski 2016). In PALADYN, these coefficients also reflect bioclimatic limits like the coldest month temperature within which a PFT is competitive. Such ecological relations have to be considered with caution in deep time settings. For example, grasses have only evolved during the Cretaceous. However, the PFT classes of PALADYN are defined so broadly that they can also represent functionally similar ancient vegetation types to the degree that is relevant from a global Earth system perspective.

A further emphasis of PALADYN lies on the representation of soil carbon processes on multi-millennial orbital time scales, including carbon accumulated and stored in permafrost soils and peatlands (Willeit and Ganopolski 2016). Together with the capability of CLIMBER-X to simulate dynamic continental weathering and marine sedimentation carbon fluxes as well as dynamic ice sheets and sea levels, the possible deep time paleoclimate applications are numerous.

Model Set-Ups: For each of the three studies in this thesis, the CLIMBER-3 α and CLIMBER-X models are employed in a different mode to account for the respective processes and time scales to be studied.

Publication I investigates Mesozoic paleoclimate trends on tectonic time scales. For this purpose, a continuous series of paleogeographies for 40 equally spaced Mesozoic time slices is retrieved from a plate tectonic and paleogeographic model (Scotese and Wright 2018). For each of these paleogeographies, a set of equilibrium climate simulations is conducted with the CLIMBER-3 α model (Fig. 1.1). This means that the model is run for 5000 model years under fixed boundary conditions to approach a stable equilibrium climate state. This is done with the climate model components and deactivated marine carbon cycle (in contrast to P.III), leaving the atmospheric CO₂ concentration at fixed values. Prescribed boundary conditions like $p\text{CO}_2$ and vegetation patterns are, however, systematically varied between the individual simulations. Within the more likely ranges of e.g. $p\text{CO}_2$, the modeled climate states can be interpreted as average conditions for the 5 Myr period represented by the respective time slice. Other simulations can indicate either temporary conditions produced by natural variability, e.g. by orbital cycles or volcanic events, or possible states within the uncertainties of boundary condition reconstructions and model behavior. Although transient coupled climate model simulations on tectonic time scales are currently impossible, such a dense ensemble of equilibrium time slice experiments collectively provides a framework to represent the long-term climate evolution and study its drivers and associated uncertainties.

Part 2 introduces tectonic-scale trends through the Late Triassic to Early Jurassic by carrying out simulations for a set of 9 geologic time slices from 230 to 190 Ma (Fig. 1.1). However, the study does not assess equilibrium simulations, but transient climate simulations over 10^3 – 10^5 yr orbital time scales. The orbital parameters are changing cyclically, which results in a radiative forcing to which the modeled Earth system is responding dynamically. The longer-term mean conditions and their tectonic-scale changes across

the considered time slices can be assessed by averaging over these transient simulations. Landwehrs et al. (2022) utilize the CLIMBER-X model which allows, among other things, for a dynamic simulation of vegetation. The carbon cycle module is not used and $p\text{CO}_2$ remains fixed at one of the three considered values (750, 1500 or 3000 ppm). Including carbon cycle and continental ice sheet feedbacks in the orbital Earth system response provides opportunities for further research. Despite CLIMBER-X being an extremely fast ESM, completing the 250 000 yr simulations would normally require approximately one month on the currently available hardware. The model offers the option to speed up the climate components relative to slow processes like ice sheet dynamics, or in this case the orbital forcing. In this scheme, the climate model is only run every fifth year of the forcing, which reduces effectively the number of years to integrate to 50 000. This relative acceleration of the orbital forcing is reasonable for these experiments because the forcing acts on millennial or longer time scales that exceed the typical surface climate response times.

Publication III also uses transient simulations, but studies climatic and biogeochemical effects of LIP volcanism for a single geologic time slice at the Triassic–Jurassic boundary (Fig. 1.1). In this setting, the CLIMBER-3 α +C model is employed with its marine carbon cycle component HAMOCC. Volcanic activity is represented by pulses of carbon emissions and sulfur aerosol radiative forcing. Including HAMOCC allows to account for the partial dissolution of the excess carbon in the ocean and to quantify its acidifying effect. Changes of sea water oxygen concentrations caused by the volcanic forcings can also be assessed in this set-up. The volcanic perturbation experiments have to be started from an suitable equilibrium state of climate and biogeochemistry but constraints on the ocean carbon cycle state in deep time are usually poor. For P.III, seawater DIC and TA values were tuned manually to yield the targeted atmospheric $p\text{CO}_2$ values (1000, 1500 and 2000 ppm) at reasonably high surface ocean pH and tropical aragonite saturation. The perturbation runs with carbon and sulfur forcing were run for either 5 000 or 10 000 years. Because the use of HAMOCC slows down CLIMBER-3 α to \sim 200 model years per day this was the practically feasible limit. The new capabilities of CLIMBER-X lift this limitation and provide a more comfortable way to adjust the ocean carbon cycle state to a desired atmospheric $p\text{CO}_2$. Landwehrs et al. (2020) make additional use of the Easy Volcanic Aerosol model (EVA v1.0, Toohy et al. 2016) and the LOSCAR model (Long-term ocean-atmosphere-sediment carbon cycle reservoir model, Zeebe 2012a). EVA calculates the aerosol radiative forcing for different stratospheric sulfur injection scenarios which is then used as an input to the CLIMBER-3 α model. LOSCAR is a carbon cycle box model that allows to simulate the global carbon cycle response over the \sim 10⁵–10⁶ yr time period of CAMP activity. This added a long-term perspective to the annual to millennial scale perturbations modeled with CLIMBER-3 α +C in P.III.

To summarize the applied methodologies, ensembles of equilibrium climate simulations as well as transient climate and carbon cycle simulations with the CLIMBER-3 α and CLIMBER-X Earth system models are designed, carried out and analyzed. These are combined to characterize Mesozoic climate conditions and their changes on tectonic, orbital and millennial time scales. These ensembles are designed under consideration of various empirical or modeled evidence to constrain possible conditions at different time periods and tectonic, orbital and volcanic drivers of changes. The modeling results are then analyzed and interpreted in the context of other evidence, for example on empirically reconstructed global temperature changes through the Mesozoic, on observed orbital lake depth cyclicity in the Late Triassic, or on fossil evidence of environmental disruptions in the end-Triassic.

1.2 Synopsis of the Publications

This thesis takes a paleoclimate modeling approach to characterize environmental changes through the Mesozoic era. Major drivers of the Earth system variability on a range of time scales are assessed with numerical models. Three different time scale regimes are considered: the long-term tectonic-scale evolution ($>10^6$ yrs, [P.I](#)), periodic orbital climate pacing ($\sim 10^4$ – 10^5 yrs, [P.II](#)) and individual rapid perturbations ($\sim 10^0$ – 10^5 yrs, [P.III](#); see [Fig. 1.1](#)). Large Igneous Province (LIP) volcanic episodes have been linked to many of the major disruptions during the Mesozoic and the latter time scale is represented by one selected LIP event here. The presented approaches integrate a range of geophysical, climatic and biogeochemical interactions into a consistent framework and thereby contribute to a comprehensive perspective on the mechanisms that shaped the Earth system throughout the Mesozoic. Ultimately, Earth system modeling aims to advance the coherent interpretation of empirical geologic evidence. Available proxy information is incorporated into climate model simulations on the one hand through boundary conditions and forcing scenarios (e.g. paleogeography, $p\text{CO}_2$, vegetation patterns). On the other hand, the modeling results can then be evaluated against other empirical evidence (e.g. $\delta^{18}\text{O}$ temperatures, sedimentary cycles, geographic distributions of fossils or sedimentary climate indicators) to verify or falsify hypotheses about the mechanisms of reconstructed environmental changes. The published global model data can furthermore be used beyond the analyses conducted here to correlate and interpret other geological records and fill temporal and spatial gaps between proxy data.

This thesis is guided by the following questions:

- (I) Which long-term changes characterized the Mesozoic climate evolution on tectonic time scales and which driving factors contributed to them? Specifically, what have been the climatic effects of changing continental configuration, sea level, atmospheric CO_2 , solar luminosity and orbital configuration during supercontinent breakup and establishment of the mid-Cretaceous greenhouse climate?
- (II) Which climatic effects did orbital cycles have on Mesozoic greenhouse climates and how could this be expressed in geologic records? In particular, how can the observed cyclicity in lake sediments from the Late Triassic be linked to an astronomical climate forcing with additional trends due to continental drift and changing $p\text{CO}_2$?
- (III) In which way was the Earth system perturbed during rapid disruptive events that punctuate the Mesozoic era? Specifically, which climatic and environmental impacts could carbon and sulfur gas emissions from Large Igneous Province (LIP) volcanism have had in the context of the end-Triassic mass extinction?

These questions are addressed in three scientific articles, of which two are published and one is currently under review. The following gives an overview of the individual articles that are presented in [Chapter 2](#).

Publication I

Investigating Mesozoic Climate Trends and Sensitivities With a Large Ensemble of Climate Model Simulations

Jan Landwehrs, Georg Feulner, Stefan Petri, Benjamin Sames and Michael Wagemich

In this article, an ensemble of equilibrium climate simulations with the coupled climate model CLIMBER-3 α is analyzed to assess the Mesozoic long-term climate evolution and its drivers. For this, the period from 255 to 60 Ma is represented through a set of paleogeographic maps which evolve in 5 Myr time steps. Other important boundary conditions that are systematically varied include the atmospheric CO₂ concentration, the solar constant, the orbital configuration, the global vegetation patterns and the global sea level. The relative contribution of these drivers to regional and global climate change are then analyzed and discussed. For example, a baseline warming trend is found to result from the increasing solar luminosity and rising sea levels. Relatively high proxy p CO₂ values yield especially warm conditions during the Triassic and mid-Cretaceous. The continental fragmentation and rising sea levels contribute to weaker seasonal and zonal climate contrasts and a decrease in continental aridity that is also indicated from changing coal and evaporite abundances. Among the long-term trends of the assessed climate characteristics, the modeled effects of orbital variations are most pronounced in the seasonality of surface temperatures.

Jan Landwehrs, Georg Feulner and Michael Wagemann designed the study. Jan Landwehrs carried out and analyzed the model simulations. Jan Landwehrs wrote the article with input from all coauthors.

Published in *Paleoceanography and Paleoclimatology* (2021)

Publication II

Modes of Pangean Lake-Level Cyclicity Driven by Astronomical Pacing Modulated by Continental Position and p CO₂

Jan Landwehrs, Georg Feulner, Matteo Willeit, Stefan Petri, Benjamin Sames, Michael Wagemann, Jessica H. Whiteside and Paul E. Olsen

In this study, an ensemble of transient, orbitally-driven simulations with the coupled climate model CLIMBER-X is analyzed. This is to assess the modulation of Late Triassic climates by orbital cycles with \sim 20, 40 and 100 kyr periods and especially the implications for the interpretation of the cyclic Newark-Hartford Basin (NHB) lacustrine sediment record. The latter is one of the best evidence of astronomical climate cycles in deep Earth history, especially for the Pangean greenhouse climate, which contrasts the glacial cycles of the current ice age. The 36 simulations are carried out using two paleogeographic reconstructions for 230–190 Ma in 5 Myr steps to account for continental drift. The latter is shown to be important for the climate regime and orbital response recorded in the NHB region as it drifts from tropical wet to more seasonal and ultimately semi-arid climate zones. Eccentricity-modulated precession is found to dominate the orbital response. As this affects climate especially through the seasonality, the strongest orbital response is found for the intermediate interval from 220 to 200 Ma, in agreement with the geologic record of lake level cycles. During periods of relatively low p CO₂ the results support a dampened orbital response. An obliquity signal is not expected due to its minimal tropical radiative forcing, but it is shown that its modulation of mid- and high-latitude temperatures translates into notable shifts of the tropical rainfall belt. The article furthermore shows that differential expression of the orbital forcing in other regions with contemporaneous records can provide a more comprehensive view on the global orbital response.

Jan Landwehrs, Georg Feulner, Michael Wagemann and Matteo Willeit designed the study. Jan Landwehrs carried out and analyzed the model simulations. Jan Landwehrs wrote

the article with input from all coauthors.

Under review for *Proceedings of the National Academy of Sciences of the United States of America* (PNAS; submitted 11.03.2022)

Publication III

Climatic Fluctuations Modeled for Carbon and Sulfur Emissions from end-Triassic Volcanism

Jan Landwehrs, Georg Feulner, Matthias Hofmann and Stefan Petri

In this article, an ensemble of transient simulations with the CLIMBER-3 α +C model is analyzed to assess climatic and biogeochemical impacts of volcanogenic gas emissions and their role in the end-Triassic mass extinction. In this set-up, CLIMBER-3 α is coupled to the marine carbon cycle model HAMOCC and is exposed to pulses of volcanic carbon emission and a contemporaneous sulfur aerosol radiative forcing. The pulses have a duration of 1–6 kyr during which 2500–7500 GtC are emitted and 0–500 GtS are converted to stratospheric sulfate aerosols. The emission scenarios are designed to reflect existing constraints on the eruption of the Central Atlantic Magmatic Province (CAMP) which drove the end-Triassic events. The emission pulses lead to a sequence of transient and very variable global cooling from the aerosol forcing and subsequent sustained warming 1.8–4.4 °C from the emitted greenhouse gases. The short-lived cooling is significantly stronger at the upper end of the sulfur emission scenarios. These are especially difficult to constrain, so that the simulations serve to demonstrate implications of different scenarios. In addition to temperature changes, simulated ocean acidification as well as reduced ocean turnover and oxygenation are discussed. Fossil coral reefs are found in regions with simulated sea surface temperatures suitable to modern scleractinian corals, but the modeled alternation of cooling and warming could have further contributed to their demise. The enhanced modeling approach developed here can be extended to other LIP episodes to yield an integrated picture of rapid environmental disruptions in the Mesozoic.

Jan Landwehrs and Georg Feulner designed the study. Jan Landwehrs carried out and analyzed the model simulations. Jan Landwehrs, Georg Feulner and Matthias Hofmann discussed the results. Jan Landwehrs wrote the paper with input from all coauthors.

Published in *Earth and Planetary Science Letters* (2020)

Beyond these manuscripts, this PhD work has led to multiple ongoing research collaborations. A project led by Anna Pint and Peter Frenzel (University of Jena, Institute of Earth Sciences) addresses the climatic interpretation of sedimentary structures from the Early Permian Bromacker Lagerstätte. Jan Landwehrs carried out and analyzed CLIMBER-X climate model simulations for different 290 Ma paleogeographies and $p\text{CO}_2$ values, contributed to the paleoclimatic discussion of model and proxy results and participates in writing a manuscript entitled “Water level marks as indicators of evaporation rates in the Lower Permian continental vertebrate site Bromacker (Thuringia, Central Germany)” (in preparation). Joseph Flannery-Sutherland (University of Bristol, School of Earth Sciences) investigates the spatiotemporal patterns of Triassic reef evolution and coral diversification, including modeled seawater properties from Landwehrs et al. (2021). Jan Landwehrs provided the CLIMBER-3 α model data and contributed to a manuscript which is entitled “Evolutionary innovation and competitive replacement drove the rise of

modern coral reefs” (in preparation). A third collaboration with Carl Reddin (GeoZentrum Nordbayern, Paleontology) and Martin Aberhan (Museum für Naturkunde, Berlin) deals with Early Jurassic (Pliensbachian–Toarcian) marine invertebrates under climatic changes. Jan Landwehrs carried out and analyzed CLIMBER-X model simulations for 180 and 185 Ma paleogeographies at different $p\text{CO}_2$ values and contributed paleoclimatic discussion of model and proxy results.

2. Publications

P.I Investigating Mesozoic Climate Trends and Sensitivities with a Large Ensemble of Climate Model Simulations

Bibliographic Information

Landwehrs, J., Feulner, G., Petri, S., Sames, B. and Wagemann, M. (2021), “Investigating Mesozoic Climate Trends and Sensitivities With a Large Ensemble of Climate Model Simulations”, doi:10.1029/2020PA004134, *Paleoceanography and Paleoclimatology* 36(6), e2020PA004134.

Accompanying Data Publication:

Landwehrs, J., Feulner, G., Petri, S., Sames, B. and Wagemann, M. (2021), “Data from Climate Model Ensemble Simulations for the Mesozoic Climate Evolution”, doi:10.5880/PIK.2020.009, *GFZ Data Services*, V. 2021-02-04.

Copyright Notice

©2021 The Authors. This is the published version of this article which is open access under the Creative Commons Attribution License (CC BY 4.0).

Paleoceanography and Paleoclimatology



RESEARCH ARTICLE

10.1029/2020PA004134

Key Points:

- We assess global long-term climate trends through the Mesozoic era with an ensemble of climate model simulations
- Varying carbon dioxide levels cause anomalies around an overall warming trend due to changing paleogeography and increasing insolation
- Seasonal and zonal temperature contrasts as well as aridity decrease with time, while meridional gradients vary with paleogeography

Supporting Information:

Supporting Information may be found in the online version of this article.

Correspondence to:

J. Landwehrs,
jan.landwehrs@univie.ac.at

Citation:

Landwehrs, J., Feulner, G., Petri, S., Sames, B., & Wagreich, M. (2021). Investigating Mesozoic climate trends and sensitivities with a large ensemble of climate model simulations. *Paleoceanography and Paleoclimatology*, 36, e2020PA004134. <https://doi.org/10.1029/2020PA004134>

Received 5 OCT 2020
Accepted 13 MAY 2021

Author Contributions:

Conceptualization: Jan Landwehrs, Georg Feulner, Michael Wagreich
Data curation: Jan Landwehrs, Stefan Petri
Formal analysis: Jan Landwehrs
Investigation: Jan Landwehrs
Writing – original draft: Jan Landwehrs, Georg Feulner, Stefan Petri, Benjamin Sames, Michael Wagreich

© 2021. The Authors.

This is an open access article under the terms of the [Creative Commons Attribution License](https://creativecommons.org/licenses/by/4.0/), which permits use, distribution and reproduction in any medium, provided the original work is properly cited.

Investigating Mesozoic Climate Trends and Sensitivities With a Large Ensemble of Climate Model Simulations

Jan Landwehrs^{1,2} , Georg Feulner² , Stefan Petri² , Benjamin Sames¹ , and Michael Wagreich¹ 

¹Department of Geology, University of Vienna, Vienna, Austria, ²Earth System Analysis, Potsdam Institute for Climate Impact Research, Member of the Leibniz Association, Potsdam, Germany

Abstract The Mesozoic era (~252 to 66 million years ago) was a key interval in Earth's evolution toward its modern state, witnessing the breakup of the supercontinent Pangaea and significant biotic innovations like the early evolution of mammals. Plate tectonic dynamics drove a fundamental climatic transition from the early Mesozoic supercontinent toward the Late Cretaceous fragmented continental configuration. Here, key aspects of Mesozoic long-term environmental changes are assessed in a climate model ensemble framework. We analyze so far the most extended ensemble of equilibrium climate states simulated for evolving Mesozoic boundary conditions covering the period from 255 to 60 Ma in 5 Myr timesteps. Global mean temperatures are generally found to be elevated above the present and exhibit a baseline warming trend driven by rising sea levels and increasing solar luminosity. Warm (Triassic and mid-Cretaceous) and cool (Jurassic and end-Cretaceous) anomalies result from pCO₂ changes indicated by different reconstructions. Seasonal and zonal temperature contrasts as well as continental aridity show an overall decrease from the Late Triassic-Early Jurassic to the Late Cretaceous. Meridional temperature gradients are reduced at higher global temperatures and less land area in the high latitudes. With systematic sensitivity experiments, the influence of paleogeography, sea level, vegetation patterns, pCO₂, solar luminosity, and orbital configuration on these trends is investigated. For example, long-term seasonality trends are driven by paleogeography, but orbital cycles could have had similar-scale effects on shorter timescales. Global mean temperatures, continental humidity, and meridional temperature gradients are, however, also strongly affected by pCO₂.

1. Introduction

The Mesozoic Era, comprising the Triassic (~252–201 Ma), Jurassic (~201–145 Ma), and Cretaceous (~145–66 Ma) periods (Cohen et al., 2013), marked a transition from the last supercontinent Pangaea toward today's fragmented continental configuration and from “old” (Paleozoic) to “new” (Cenozoic) biota that are now integral parts of the modern world (e.g., mammals, birds, angiosperms, scleractinian corals, and calcareous plankton like coccolithophores) (Stanley & Luczaj, 2015). It is furthermore characterized by some of the most incisive events in Earth history, including Large Igneous Province (LIP) volcanism, Ocean Anoxic Events (OAE) and mass extinctions, bracketing, for example, the rise and fall of the dinosaurs (Clapham & Renne, 2019; Takashima et al., 2006).

Tectonic dynamics (Golonka, 2007; Müller et al., 2016; Scotese & Wright, 2018) profoundly influenced global climatic conditions throughout the Mesozoic (Donnadieu et al., 2006a, 2009), for example, by the aggregation of all continents into a contiguous Pangaeian landmass which began in the Carboniferous and culminated in the Triassic with a supercontinent almost extending from pole to pole (Parrish, 1993). This unique paleogeographic constellation shaped global climate patterns during Permian, Triassic, and Early Jurassic times, with the most prominent feature purportedly being pronounced monsoonal circulation patterns, also termed “megamonsoon” (Kutzbach & Gallimore, 1989; Parrish, 1993; Wang et al., 2014). The symmetric arrangement of huge landmasses, further enlarged by low sea levels, around the warm equatorial Tethys Sea provided optimum conditions for this phenomenon and contributed to an overall strongly seasonal climate (Parrish, 1993).

Rifting of the supercontinent began during the Triassic, but the major breakup took place in the Jurassic with the opening of the North Atlantic and continued into the Cretaceous (Holz, 2015). In the course of this

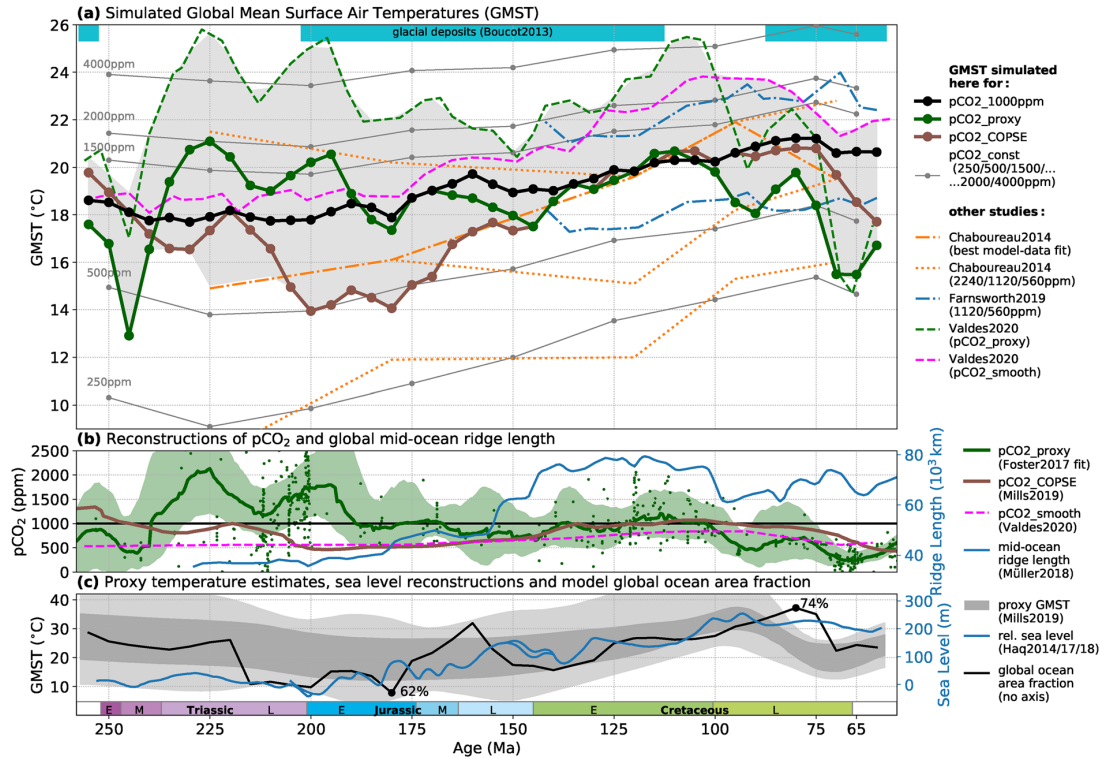


Figure 1. Simulated Mesozoic long-term global mean temperature evolution (a) for different pCO₂ pathways (b), compared with other relevant proxy and model data (a–c). (a) Each dot represents one simulated equilibrium climate state. Solid lines connect states belonging to the same pCO₂ pathway. Green and brown dots correspond to the pathways using the proxy- and model-based reconstructions pCO₂_proxy (Foster et al., 2017) and pCO₂_COPSE (Mills et al., 2019) indicated in the same colors in (b). Black and gray dots and lines correspond to the pathways with constant pCO₂ of 1,000 ppm (black) or 250–4,000 ppm (gray). The gray-shaded area indicates the envelope of temperatures simulated here (for pCO₂_proxy and pCO₂_COPSE) and in other climate modeling studies (broken lines, Chaboureaud et al., 2014; Valdes et al., 2020). Also shown are results from Farnsworth, Lunt, O'Brien, et al. (2019). Cyan-colored bars indicate the occurrence of glacial deposits (Boucot et al., 2013; Cao et al., 2018). (b) pCO₂_proxy (green) and pCO₂_COPSE (brown) reconstructions. For pCO₂_proxy, small dots indicate the raw data points while the line and the shading indicate the LOESS fit provided by Foster et al. (2017) and its 95% confidence intervals. The dashed pink line is the pCO₂_smooth reconstruction used by Valdes et al. (2020), which yields the pink dashed temperature curve in (a). Mid-ocean ridge length reconstruction (blue line, Müller & Dutkiewicz, 2018). (c) The gray shading shows GMST envelope from Mills et al. (2019) (Figure 4b) which was obtained from δ¹⁸O, TEX86, and Mg/Ca low-latitude sea-water temperature data through scaling relations (see supporting information section 6 for further discussion). The black line indicates the global ocean area fraction exhibited by the paleogeographies implemented in the simulations based on Scotese and Wright (2018). The blue line represents the long term sea-level reconstruction from Haq (2014) and Haq (2017, 2018).

fragmentation, the length of global mid-ocean ridges doubled from the Triassic into the Early Cretaceous (Müller & Dutkiewicz, 2018), which contributed to a pronounced sea-level rise (Haq, 2014, 2017, 2018; Haq et al., 1988; Miller et al., 2005; Müller et al., 2008) and high tectonic carbon degassing rates (Brune et al., 2017; Müller & Dutkiewicz, 2018; Wong et al., 2019) (see Figures 1b and 1c). The opening of new sea-ways between the fragmenting continents and flooding of almost one third of the continental area increased the marine influence in many places, leading to more temperate and humid conditions with reduced seasonality (Chaboureaud et al., 2014; Donnadieu et al., 2006a). Consequently, also the megamonsoon broke down during the Jurassic and more zonal climates were established (Parrish, 1993).

The Mesozoic is generally thought of as a prolonged greenhouse climate period between the Late Paleozoic and the current Cenozoic ice ages, characterized by an absence of major glaciations (Hallam, 1985; Frakes et al., 1992; Holz, 2015; Price, 2009). Evidence for continental ice is sparse and mainly occurs during Jurassic to Early Cretaceous times (Price, 1999), but the potential for ice sheet formation is still being investigated (e.g., Ladant & Donnadieu, 2016). Three major phases in the global temperature evolution have been traditionally proposed: A warm greenhouse climate from the Triassic into the Jurassic, slightly cooler conditions

in late Jurassic and early Cretaceous, followed by a pronounced mid to late Cretaceous warm greenhouse and cooling into the Paleogene (Frakes et al., 1992). Studying past warm climate states is not only important to improve our understanding of Earth's history, but also becomes increasingly relevant in the light of anthropogenic global warming.

The most frequently considered proxy for Mesozoic temperature trends are $\delta^{18}\text{O}$ measurements on marine fossils (Song et al., 2019; Veizer et al., 2000; Veizer & Prokoph, 2015), which yield positive temperature anomalies during the Triassic and especially the mid-Cretaceous Cenomanian to Turonian periods (~100–90 Ma) (Farnsworth, Lunt, O'Brien, et al., 2019; Friedrich et al., 2012). Trends of the atmospheric CO_2 concentration, considered a major driver of Phanerozoic climate, have been reconstructed from both proxies (Foster et al., 2017; Royer, 2014) and biogeochemistry box models (Berner, 2006; Mills et al., 2019) (see Figure 1b). Compilations of lithologic climate indicators, including coals and evaporites, have been used to infer climatic zonation at different stages of the Mesozoic (Boucot et al., 2013; Cao et al., 2018; Chumakov, 2004; Scotese et al., 2014; Ziegler et al., 2003).

A number of modeling studies provide insights into global climatic conditions during certain Triassic (e.g., Huynh & Poulsen, 2005; Winguth et al., 2015), Jurassic (e.g., Sellwood & Valdes, 2008), and especially Cretaceous (e.g., Donnadieu et al., 2006a; Fluteau et al., 2007; Laugié et al., 2020; Tabor et al., 2016; Zhou et al., 2012, and references therein) time intervals or events. However, only few climate model-based studies have been conducted that can represent long-term climatic changes during the Mesozoic in a continuous and consistent framework. These include Donnadieu et al. (2006a) and Donnadieu et al. (2009), who performed coupled climate-biogeochemistry-vegetation simulations for seven Mesozoic timeslices, and found, among other things, that the fragmentation of Pangaea induced increasingly humid conditions with higher weathering CO_2 drawdown, which alone would have caused an overall cooling through the Mesozoic. Chaboureaud et al. (2014) applied similar atmosphere-ocean and vegetation model components to five Mesozoic timeslices and assessed the match to various proxy data for three different pCO_2 values, respectively. The authors find an expansion of temperate continental areas at the expense of arid belts and argue that this potentially fostered the diversification and expansion of angiosperms in the Cretaceous. Lunt et al. (2016) and Farnsworth, Lunt, O'Brien, et al. (2019) investigate recent ensembles of comprehensive atmosphere-ocean-vegetation model simulations for each Cretaceous to Eocene geological stage (~145–34 Ma). These authors conclude that global mean temperatures within this time frame are determined by pCO_2 , increasing solar luminosity and paleogeography, mainly by the changing ocean area, as well as ocean circulation modes and feedbacks like the water vapor feedback. Based on these simulations, Farnsworth, Lunt, Robinson, et al. (2019) suggest the existence of an East Asian monsoon system since the Early Cretaceous. Very recently, a large data set of simulations with the same model for the whole Phanerozoic (Valdes et al., 2020), has become available, but a specific analysis with respect to Mesozoic climate has not yet been published. Previously, Sellwood and Valdes (2006) had discussed atmosphere-sea ice model simulations with a similar model for one Triassic, Jurassic, and Late Cretaceous timeslice, respectively, with regard to available climate proxy distributions.

Here, the CLIMBER-3 α climate model (Montoya et al., 2005) is employed to explore stepwise long-term climatic trends in the Mesozoic, using a recent set of paleogeographic reconstructions (Scotese & Wright, 2018). For this, equilibrium climate states for 40 geologic timeslices from 255 to 60 Ma were simulated. By systematically varying paleogeography, sea level, vegetation patterns, solar luminosity, the orbital configuration, and pCO_2 levels (considering different recent pCO_2 reconstructions for the Mesozoic: Foster et al., 2017; Mills et al., 2019), impacts of these respective boundary conditions are quantified. This represents the so far most extended ensemble of climate states simulated for the Mesozoic and provides the opportunity to investigate, among other things, the climatic transition from the Triassic supercontinent regime to the hot mid-Cretaceous in a continuous and consistent framework. This study investigates trends of global mean temperatures, seasonal, meridional, and zonal temperature contrasts as well as the continental aridity. Many previous concepts of Mesozoic climates are supported and can be consolidated in this framework. Other researchers are invited to use the model output data (Landwehrs et al., 2021) for further investigations.

2. Methods

2.1. Model Description

All simulations were performed with the CLIMBER-3 α Earth System Model of Intermediate Complexity (EMIC) (Montoya et al., 2005), consisting of a modified version of the ocean general circulation model MOM3 (Hofmann & Morales Maqueda, 2006; Pacanowski & Griffies, 2000), run at a horizontal resolution of $3.75^\circ \times 3.75^\circ$ with 24 vertical levels, a dynamic/thermodynamic sea-ice model (Fichefet & Maqueda, 1997), and a fast statistical-dynamical atmosphere model (Petoukhov et al., 2000) with a coarse spatial resolution of 22.5° in longitude and 7.5° in latitude. The main difference between CLIMBER-3 α and a coupled atmosphere-ocean general circulation model (AOGCM) is the simplified atmosphere model which describes the dynamics of large-scale circulation patterns, but statistically parametrizes the effects of synoptic-scale systems rather than solving the fundamental equations. This makes the model computationally efficient and allows running large ensembles of simulations. Although CLIMBER-3 α has evolved over the years, differences between simulated and observed climatic variables under present-day boundary conditions are still broadly similar to the original version described in Montoya et al. (2005). Specifically, surface air temperatures are overestimated in mountain regions like the Andes or the Tibetan plateau. Furthermore, simulated temperatures are generally too high over present-day Antarctica, in particular during Southern winter, and too low over the Northern Atlantic during Northern winter. The model has been successfully used in a number of paleoclimate studies (Brugger et al., 2017, 2019; Feulner, 2017; Landwehrs et al., 2020), and compares well with other models in model intercomparison projects (Eby et al., 2013; Zickfeld et al., 2013).

2.2. Boundary Conditions

Climate simulations were conducted for a set of 40 timeslices with a 5 Myr spacing from 255 to 60 Ma (denoted as T_{5Myr}), using paleotopographies/-bathymetries based on the reconstruction of Scotese and Wright (2018) (also see Figure S1). These were adjusted regarding model requirements, for example, by avoiding narrow ocean channels and isolated ocean cells on the model grid resolution (see supporting information section 1). Vegetation cover was prescribed for each timeslice based on the proxy-based estimates of climatic zonation by Boucot et al. (2013) and Scotese (2016) (also see Figure S1). Their five climate types were represented by certain fractions of tree, grass/shrub, and bare soil cover for tropical/boreotropical (75%, 20%, and 5%), arid (15%, 35%, and 60%), warm temperate (70%, 20%, and 10%), cold temperate (65%, 15%, and 20%), and polar (10%, 25%, and 65%) climates, using Bonan et al. (2002), Poulter et al. (2015), and Pfadenhauer and Klötzli (2015) for orientation. From these spatially heterogeneous vegetation patterns (*VegHet*), homogeneous vegetation patterns with average compositions over the entire land area were defined for sensitivity experiments: *VegHom* reflects the average composition for each respective timeslice, while *VegFix* has a constant average composition (51% trees, 25% grass/shrub, and 24% bare soil) over all timeslices (see Table S1 and Figure S3). Runoff is routed along topographic gradients, with necessary modifications, for example, where internal basins occur. The solar constant (S_0) increases approximately linearly from 1,332.7 to 1,354.7 W/m^2 ($\sim 97.9\%$ to 99.5% ; from 255 to 60 Ma) according to standard solar evolution (Bahcall et al., 2001) relative to its present-day value of 1,361 W/m^2 (Kopp & Lean, 2011).

Different pCO_2 pathways are tested here to account for the large uncertainties associated with existing pCO_2 reconstructions for the Mesozoic: The $P_{pCO_2_proxy}$ pathway corresponds to the fit to compiled proxy data provided by Foster et al. (2017) (see Figure 1b). This is contrasted with $P_{pCO_2_COPSE}$, which reflects the evolution of pCO_2 obtained with the COPSE carbon cycle model (Mills et al., 2019). This model estimate was included because it correlates reasonably with proxy-based global temperature trends (Mills et al., 2019) and helps to illustrate the spread of different proxy- and model-based pCO_2 reconstruction approaches. For the purpose of this study, the pCO_2 values of both reconstruction pathways were rounded to the nearest hundred at each timeslice. A fixed value of $pCO_2 = 1,000$ ppm ($P_{pCO_2_1000ppm}$) appears a reasonable median for most of the Mesozoic, except the Middle and Late Jurassic and the latest Cretaceous where both considered reconstructions agree on lower values (see Figure 1b). Additional simulations were performed for a subset T_{25Myr} (250, 225, 200, 175, 150, 125, 100, 75, and 65 Ma) of the timeslices, to further test the sensitivity to different boundary conditions: $P_{pCO_2_const}$ for pCO_2 fixed at (250, 500, 1,500, 2,000, 4,000) ppm, P_{S0ini} for a fixed S_0 of 1,332.7 W/m^2 as well as P_{VegHom} and P_{VegFix} for homogeneous vegetation patterns (see Table 1).

Table 1
Overview of the Ensemble of Boundary Conditions for the Climate Model Simulations

Pathway P	Timeslices	pCO ₂ (ppm)	S ₀ (W/m ²)	Vegetation pattern		
Baseline (fixed pCO ₂ ; increasing S ₀ ; changing paleogeography and heterogeneous vegetation patterns)						
<i>P</i> _{pCO₂_1000ppm}	<i>T</i> _{5Myr}	1,000	1,333–1,355	<i>VegHet</i>		
Sensitivity: pCO ₂ (two different pCO ₂ reconstructions, see Figure 1b; additional constant pCO ₂ pathways)						
<i>P</i> _{pCO₂_proxy}	<i>T</i> _{5Myr}	Foster et al. (2017) fit to proxy data	1,333–1,355	<i>VegHet</i>		
<i>P</i> _{pCO₂_COPSE}	<i>T</i> _{5Myr}	Mills et al. (2019) COPSE model	1,333–1,355	<i>VegHet</i>		
<i>P</i> _{pCO₂_const}	<i>T</i> _{25Myr}	[250, 500, 1,500, 2,000, 4,000]	1,333–1,355	<i>VegHet</i>		
Sensitivity: Solar Constant (S ₀ fixed at value at 255 Ma)						
<i>P</i> _{S0ini}	<i>T</i> _{25Myr}	1,000	1,333	<i>VegHet</i>		
Sensitivity: Homogeneous Vegetation Patterns (avg. composition of <i>VegHet</i> for individual timeslice [→ <i>VegHom</i>] or over all timeslices [→ <i>VegFix</i>])						
<i>P</i> _{VegHom}	<i>T</i> _{25Myr}	1,000	1,333–1,355	<i>VegHom</i>		
<i>P</i> _{VegFix_S0ini}	<i>T</i> _{25Myr}	1,000	1,333	<i>VegFix</i>		
Sensitivity: Orbital Configuration						
<i>P</i> _{orb}	<i>T</i> _{25Myr}	1,000	1,333–1,355	<i>VegHet</i>	[obl., ecc., prec.]	
Sensitivity: Sea Level (modified elevations and land-sea masks)						
					Sea-Level Offset (m)	
<i>P</i> _{SL}		200 Ma	1,000	1,339	<i>VegHom</i>	[+40, +200]
		150 Ma	1,000	1,344	<i>VegHom</i>	[−40, +40]
		100 Ma	1,000	1,350	<i>VegHom</i>	[−200, −40, +40]

Note. See Section 2.2 for further explanation.

To test the systematic effect of changing sea levels on global climates, further experiments were performed for raised or lowered sea levels and subsequently modified land–sea distributions for the 200 Ma (sea-level offset $\Delta SL = [+40, +200]$ m), 150 Ma $[-40, +40]$ m and 100 Ma $[-200, -40, +40]$ m timeslices. The $\Delta SL = \pm 200$ m offsets were chosen to represent potential effects of the long-term sea-level rise from the Late Triassic to the mid-Cretaceous that has been reconstructed by various methods (e.g., Wright et al., 2020, Figure 16). The $\Delta SL = \pm 40$ m offsets were tested to represent the variability of sea levels on the million-year scale captured by sedimentary regression-transgression sequences throughout the Mesozoic (Haq et al., 1988; Miller et al., 2005; Ray et al., 2019; Sames et al., 2020) and because 40 m is the vertical resolution of the elevation models from Scotese and Wright (2018). In the latter, coastlines were inferred from plate-tectonic modeling and lithofacies and should represent the average best-guess paleogeography for the covered time interval (Scotese & Wright, 2018). Independently from the determination of the coastlines, the authors assume land-ice where glacial deposits occur (Boucot et al., 2013), but for the Mesozoic only minor ice volumes at 140–120 Ma have been inferred by Scotese (2018). For the purpose of this study, continental ice-sheets were thus assumed to be absent in all simulations.

In most of the simulations, Earth's orbital parameters were fixed at a configuration representing a circular orbit (eccentricity $e = 0$, precession angle $\omega = 0^\circ$) with an intermediate obliquity ($\epsilon = 23.5^\circ$). To represent effects of lower-/upper-end obliquities and of a strongly eccentric orbit, four additional configurations with $\epsilon = 22.0^\circ$ and $\epsilon = 24.5^\circ$, $e = 0.06$, $\omega = [90, 180, 270]^\circ$ were tested for the *T*_{25Myr} subset of timeslices. All 221 simulation runs were initialized with the same idealized modern ocean temperature and salinity profile without sea ice and were integrated for 5,000 model years (see also supporting information section 2). All analyses are based on averages over the last 500 years. For the plots and analyses in Sections 3.2–3.5, atmospheric model data were interpolated on the ocean model grid to enable investigating the influence of changing land and sea areas. Table 1 provides an overview over the described ensemble of boundary conditions and an additional table with information on all individual simulation runs is included in Table S1.

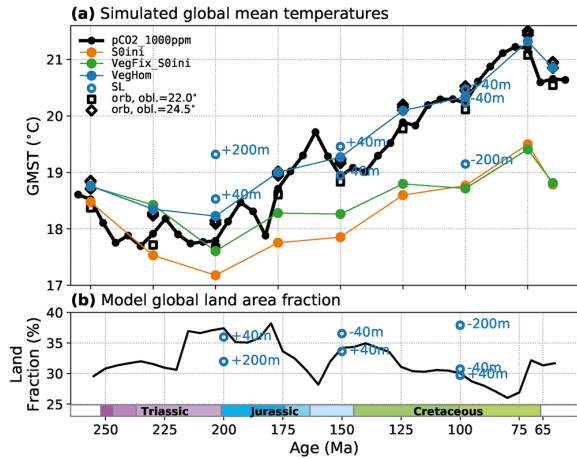


Figure 2. Simulated global mean surface air temperatures (GMST) in several sensitivity experiments at $p\text{CO}_2 = 1,000$ ppm (a), and global land area fractions in the implemented paleogeographies (b). (a) Each dot represents one equilibrium climate simulation. Black dots and lines correspond to the $P_{p\text{CO}_2,1000\text{ppm}}$ pathway and are the same as in Figure 1a. Information on the respective sensitivity experiments is given in Section 2.2 and Table 1. (a and b) Blue circles indicate the GMST (a) and global land area fraction (b) in sensitivity experiments with modified relative sea levels.

3. Results

3.1. Global Mean Temperature Evolution

The simulated global mean surface air temperatures (GMST) for all tested $p\text{CO}_2$ pathways are summarized in Figure 1a, and for all other sensitivity experiments in Figure 2a. Overall, the GMSTs at $p\text{CO}_2 = 1,000$ ppm ($P_{p\text{CO}_2,1000\text{ppm}}$, black dots and lines in Figures 1a and 2a) exhibit a slight cooling through the Triassic to a minimum of 17.7°C in the Late Triassic and then a $+3.5^\circ\text{C}$ warming to up to 21.2°C at 80 Ma in the Late Cretaceous. The two considered $p\text{CO}_2$ reconstructions ($P_{p\text{CO}_2,\text{prox}}$ and $P_{p\text{CO}_2,\text{COPSE}}$, Figure 1b) do, however, suggest deviations of up to $\sim 5^\circ\text{C}$ from this median pathway (Figure 1a). To decompose these temperature trends, we further examine the $P_{p\text{CO}_2,1000\text{ppm}}$ pathway, which reflects the effects of changing paleogeography, vegetation patterns, and the increasing solar constant S_0 . The latter elevates the GMST at 65 Ma by $+1.9^\circ\text{C}$ (difference between $P_{p\text{CO}_2,1000\text{ppm}}$ and $P_{S_0\text{ini}}$ in Figure 2a, also see Table S1), which indicates the order of warming through the Mesozoic caused by the increasing solar luminosity if everything else would have remained the same.

Despite fixed $p\text{CO}_2$ and S_0 , the $P_{S_0\text{ini}}$ temperatures exhibit variations with time (see Figure 2a) that reflect the changing distribution and extent of land masses and vegetation patterns: The GMST decreases from 18.5°C at 250 Ma to 17.2°C at 200 Ma and subsequently rises to 19.5°C at 75 Ma. These trends correlate with changes in the fraction of Earth's surface occupied by land (Figure 2b, black line), which has a higher average albedo than ocean areas and thus influences Earth's energy balance. The global land fraction in the implemented paleogeographies is highest during the

Late Triassic–Early Jurassic (up to 38%) and lowest in the Late Cretaceous (down to 26%) which is related to the change of relative sea levels (Figure 1c, blue line) that are implicitly included in the employed paleogeographic reconstructions (Scotese & Wright, 2018). The effect of raised or lowered sea levels and the resulting flooding/exposure of continental area is also demonstrated for individual timeslices (Figure 2, blue circles). For example, the global land fraction increases by +8% for a 200 m sea-level fall at 100 Ma and the GMST is reduced by -1.2°C . In contrast, a $+1.2^\circ\text{C}$ global warming is obtained for a +200 m sea-level rise at 200 Ma. These findings suggest that the lower sea level and larger continental area in the Triassic–Jurassic would have contributed to relatively low temperatures, and that the subsequent sea-level rise provided a major part of the $\approx +2^\circ\text{C}$ global warming toward the Late Cretaceous, exhibited by the $P_{S_0\text{ini}}$ pathway. To test to which extent these trends are dependent on the uncertain reconstruction of paleotopography, lapse-rate corrected global mean temperatures at sea level were calculated (see Figure S12). On the global scale, they follow the same trend although differences can be noted, especially around 100 Ma where the global mean topography height reaches a maximum. On a regional scale, differences resulting from different paleogeographic reconstructions can potentially be much more pronounced.

The described temperature rise between 200 and 75 Ma is $\sim 0.5^\circ\text{C}$ larger than for a fixed homogeneous vegetation composition ($P_{\text{VegFix},S_0\text{ini}}$, Figure 2a, green line), which yields slightly elevated temperatures in the Triassic–Jurassic. This is related to the large portion of bare land area in the Pangaea low-to mid-latitudes (for VegHet), which contributes to a higher surface albedo in these regions with high insolation and thus slightly lower GMSTs in the Triassic and Jurassic than with a homogeneous vegetation (see difference between P_{VegHom} and $P_{p\text{CO}_2,1000\text{ppm}}$, Figure 2a). In our modeling framework, the trend toward denser vegetation, especially in low-latitude land areas, thus contributes to a Late Triassic–Late Cretaceous warming, although on a slightly smaller scale than changing sea levels and solar luminosity. On the $P_{\text{VegFix},S_0\text{ini}}$ pathway, the distribution of land area is the only varying boundary condition if lapse-rate corrected air temperatures at sea level are considered. We find that global mean sea-level temperatures are indeed strongly negatively correlated with the global land fraction, but also correlate negatively with the average absolute latitude of land area which peaks around 90 Ma (see Figure S13). This indicates that paleogeographic changes contribute to the warming toward the mid-Cretaceous both by the decreasing land area and by its distribution to higher

latitudes. The simulated GMSTs also vary on the order of $\sim 0.4^{\circ}\text{C}$ – 0.6°C with the orbital configuration, with low-obliquity configurations ($\epsilon = 22.0^{\circ}$, $e = 0$) being generally cooler than those with higher obliquity and eccentricity ($\epsilon = 24.5^{\circ}$, $e = 0.06$) (see Figure 2a).

As already noted, the amplitudes of GMST variations resulting from the two considered $p\text{CO}_2$ reconstruction pathways exceed those of the other discussed boundary conditions. The $p\text{CO}_2$ proxy data and the provided fit (Foster et al., 2017) exhibit a large spread in the Triassic, yielding relatively low temperatures in the Early–Middle Triassic but very high temperatures in the Late Triassic to earliest Jurassic (up to 21.1°C at 225 Ma with 2,000 ppm). The COPSE model-derived $p\text{CO}_2$ falls to ~ 500 ppm in the Early Jurassic, yielding relatively low temperatures from the latest Triassic to the Middle Jurassic (down to 13.9°C at 200 Ma with 500 ppm). Although discrepancies between both pathways are evident, common relative trends can be identified: Elevated temperatures in the Triassic which decrease into the Jurassic, but subsequently rise again toward the mid-Cretaceous. For both reconstructions, mid-Cretaceous $p\text{CO}_2$ levels do not exceed the relatively high values around the Late Triassic, but the additional warming from the previously discussed drivers, including rising sea levels and solar luminosity, contributes to similar or higher temperatures. The $P_{p\text{CO}_2_proxy}$ pathway does not capture the prominent Cenomanian–Turonian peak (~ 100 – 90 Ma) suggested by $\delta^{18}\text{O}$ proxy data (Friedrich et al., 2012), whereas $P_{p\text{CO}_2_COPSE}$ yields sustained high temperatures above 20°C from 110 to 75 Ma and generally yields long-term trends similar to the temperature proxies (see Figure 1c), as already noted by Mills et al. (2019). Overall, the simulated GMSTs for both reconstructions are elevated above pre-industrial values of $\sim 14^{\circ}\text{C}$ for most of the Mesozoic, and for the mid-Cretaceous (around 110 Ma) both agree on temperatures $>20^{\circ}\text{C}$. For the latest Cretaceous, they consistently yield a pronounced cooling.

3.2. Seasonal Temperature Contrasts

It has been previously suggested, that the climate on the Pangaeian supercontinent was characterized by large seasonal contrasts and intense monsoons (e.g., Kutzbach & Gallimore, 1989; Parrish, 1993), but that these conditions decayed with continental breakup through the Mesozoic (e.g., Parrish, 1993). Here, we assess the systematic impact of paleogeography and other boundary conditions on the global-scale amplitude of seasonal temperature contrasts. For this, maximum surface air temperature (SAT) differences between the DJF, MAM, JJA, and SON seasonal averages were calculated. To illustrate the evolution of regional patterns through the Mesozoic, maps of the resulting temperature seasonality are shown for one Late Triassic (225 Ma) and one Late Cretaceous (75 Ma) timeslice of the $P_{p\text{CO}_2_1000\text{ppm}}$ pathway in Figures 3a and 3b. It can be seen that the vast mid- and high-latitude continents of Pangaea experience strong seasonal temperature variations in the early Mesozoic (Figure 3a), while these contrasts are reduced in the fragmented continental configuration of the Late Cretaceous (Figure 3b).

The evolution of the zonal mean continental SAT seasonality obtained from all 40 timeslices of the $P_{p\text{CO}_2_1000\text{ppm}}$ pathway is summarized in Figure 3c (contours). The gray shading indicates the changing latitudinal distribution of land area in the paleogeographies implemented for these simulations. This illustrates the correlation of the amplitude of seasonal temperature changes with the extent of land area, especially in the mid to high latitudes. These amplitudes are highest during the Early Triassic–Early Jurassic on the Southern Hemisphere and during the Late Triassic–Early Jurassic on the Northern Hemisphere and reach up to 40°C . Toward the Late Cretaceous, the mid to high latitude seasonal temperature contrasts are considerably reduced on both hemispheres and only reach $\sim 20^{\circ}\text{C}$ – 30°C . These trends are also apparent in the tropical latitudes but are strongly dampened and remain below $\sim 10^{\circ}\text{C}$.

On a global scale, the average continental SAT seasonality (Figure 3d) peaks at $\sim 22^{\circ}\text{C}$ in the Late Triassic–Early Jurassic and falls down to $\sim 15^{\circ}\text{C}$ in the Late Cretaceous. As $p\text{CO}_2$, S_0 and vegetation patterns do not significantly affect these trends, the latter are mainly driven by paleogeographic changes and closely mirror the change of the global land area fraction (see Figure 2b). The major contribution of sea-level rise to reduced seasonality in the Late Cretaceous relative to the Late Triassic–Early Jurassic is demonstrated by the experiments with elevated or lowered sea level at 200 and 100 Ma: with a sea level elevated by 200 m, at 200 Ma, the global SAT seasonality is reduced to levels comparable to those at 100 Ma, and vice versa. Although these results suggest that the long-term seasonality trends were indeed determined by sea-level changes and continental fragmentation, we also find that different orbital configurations modify SAT seasonality to a similar degree (Figure 3d). The global SAT seasonality generally varies by about 4°C – 5°C

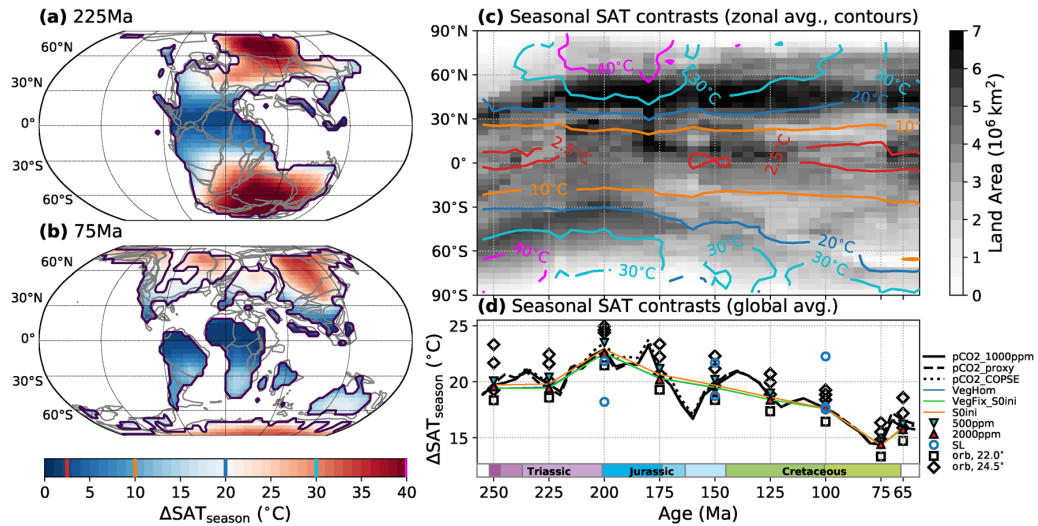


Figure 3. Simulated seasonality of surface air temperatures (SAT). (a and b) Seasonal SAT changes (max. difference between the DJF, MAM, JJA, and SON seasonal averages) for the 225 and 75 Ma timeslices of the $P_{pCO_2,1000ppm}$ pathway. Gray lines indicate the tectonic plate boundaries in the rotation model of Scotese (2008) (as published by Cao et al., 2018). (c) The gray shading shows the changing latitudinal land area distribution implemented in the simulations. Contours indicate the zonal mean SAT seasonality in the $P_{pCO_2,1000ppm}$ simulations, resolved by latitude and geologic time. For this, zonal mean data from all 5 Myr timeslices were aggregated with each timeslice represented by one grid column. The values associated the contour lines are also indicated in the colorbar of panel (b). (d) Globally averaged continental SAT seasonality for different boundary conditions.

between orbital configurations which yield a lower seasonality (lower obliquity $\epsilon = 22.0^\circ$) and higher seasonality (higher obliquity $\epsilon = 24.5^\circ$). This suggests that orbital cycles would have considerably overprinted Mesozoic long-term seasonality trends.

3.3. Meridional Temperature Contrasts

Simulated annual mean SAT for four selected timeslices at 1,000 ppm ($P_{pCO_2,1000ppm}$ pathway) are shown in Figure 4. It can be seen that for these simulations equatorial SATs mostly exceed 25°C , while temperatures below 0°C occur especially where extensive land masses exist in polar latitudes. To systematically assess the evolution of meridional temperature contrasts and their dependence on paleogeographic changes and other boundary conditions, the equator-to-pole thermal gradients were calculated for all conducted simulations. Here, these were defined as the difference between low-latitude ($<30^\circ$ lat.) and high latitude ($>60^\circ$ lat.) annual and zonal mean SATs.

Plots of zonal mean SAT and SST profiles for all timeslices are included in the accompanying data repository (also see Figure S16). The evolution of zonal mean SATs for the $P_{pCO_2,1000ppm}$ pathway is summarized in Figure 5a (contours). On the one hand, the contours reflect the previously discussed general warming trend from the Late Triassic-Early Jurassic to the Late Cretaceous. On the other hand, it can be inferred that low polar temperatures and high meridional temperature gradients (Figures 5b and 5c) correlate to first order with the amount of land in polar latitudes. From the end-Permian to the Late Triassic, Pangaea shifted northwards, which leads to a high-latitude warming and a $\sim 5^\circ\text{C}$ lower thermal gradient (Figure 5c) in the southern hemisphere, whereas the opposite is observed in the northern hemisphere (Figure 5b). The northern hemisphere thermal gradient shows a decrease from the Late Jurassic into the Late Cretaceous in line with the general decrease of land area related to sea-level rise. In contrast, the southern hemisphere meridional temperature gradient increases during this time due to the migration of Antarctica toward the South Pole. Despite the primary control of paleogeography on these trends, our experiments suggest considerable effects of other boundary conditions. For example, the northern hemisphere thermal gradients generally decrease (on the order of $\sim 5^\circ\text{C}$) in response to an increase of pCO_2 from 500 to 2,000 ppm and the associated warming. This effect can be related to the snow and sea-ice albedo feedback and is even more

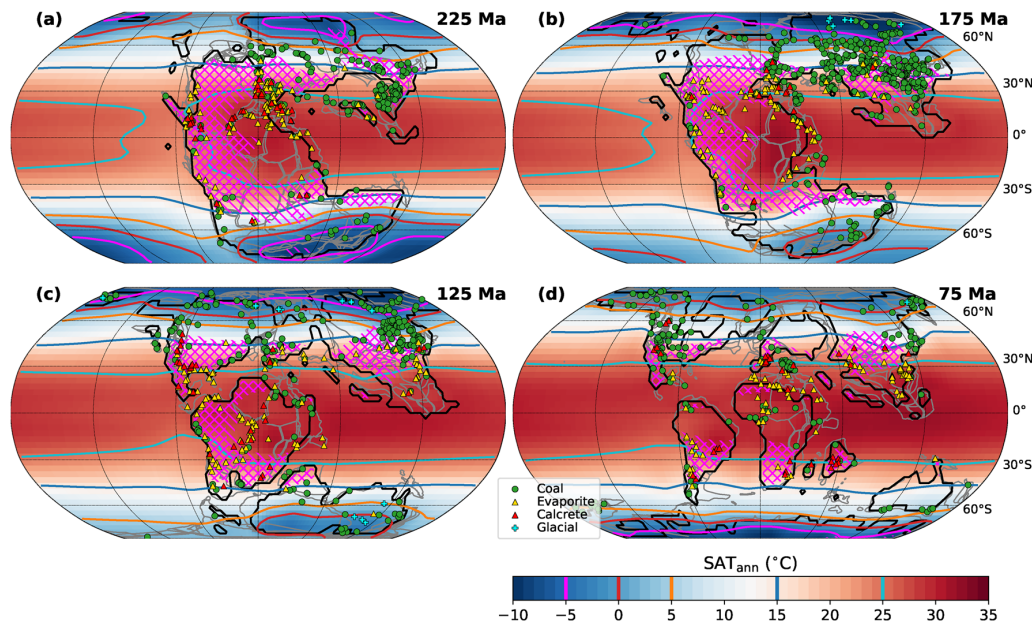


Figure 4. Simulated annual mean surface air temperatures (SAT_{ann} , colors, and contours) and arid regions (pink hatches) for four selected Mesozoic timeslices (225, 175, 125, 75 Ma) at $pCO_2 = 1,000$ ppm. Colors and contours: annual mean SAT for the $P_{pCO_2, 1000ppm}$ pathway. Pink hatches: Relatively dry regions based on an aridity index < 1.5 (see Section 3.5 for further explanation). “//” hatches are for 1,000 ppm and “\\” hatches for 500 ppm. Markers: Locations of climatic indicators from Boucot et al. (2013). Coal and evaporite/calcrete occurrences are generally viewed as indicators for humid or dry conditions, respectively, and are thus qualitatively compared with the extent of simulated hatched arid regions here (see Section 3.5). In contrast to, for example, glacial deposits, they cannot be interpreted primarily as temperature proxies. Gray lines indicate the tectonic plate boundaries in the rotation model of Scotese (2008) (as published by Cao et al., 2018).

pronounced in the southern hemisphere especially before the Middle Jurassic. Relatively low pCO_2 levels suggested by the tested reconstructions for the Jurassic and latest Cretaceous could thus have contributed to higher equator-to-pole thermal gradients relative to the mid-Cretaceous. Through the ice albedo feedback, the warming associated with the increased solar luminosity also contributes to lower thermal gradients in the Late Cretaceous on a smaller, but notable scale.

Periods with lower northern and southern temperature gradients are also found to be times with enhanced meridional heat transport by the ocean in the respective hemisphere (see supporting information section 8 and Figure S18). This also appears to be related to enhanced meridional overturning (see also Figure S19) and ocean mixing (Figures S20 and S21) and deep water formation. These are enhanced at high northern latitudes in the early Triassic as well as again in the mid- and late Cretaceous, and at high southern latitudes from the Early Triassic to the mid-Cretaceous. However, it will require further work to disentangle these phenomena and evaluate their significance. Ocean model output data are included in the accompanying data repository.

3.4. Zonal Temperature Contrasts

Our simulations suggest the existence of considerable zonal climatic contrasts prior to the breakup of Pangaea, as can be inferred from the simulated SAT patterns and the distribution of arid regions (pink hatches, see Section 3.5 for explanation) in Figures 4a and 4b: High temperatures and humid conditions are inferred for the tropical latitudes of eastern Pangaea, in contrast to its western low- to mid-latitudes, where temperatures are generally lower and arid regions are more extended. These differences are related to circulation patterns in the Panthalassa ocean where an anticyclonic subtropical gyre in each hemisphere transports warm waters along the equator into the Tethys, but colder water from higher latitudes to the western Pangean tropics and subtropics. These provide less moisture and precipitation and lower temperatures

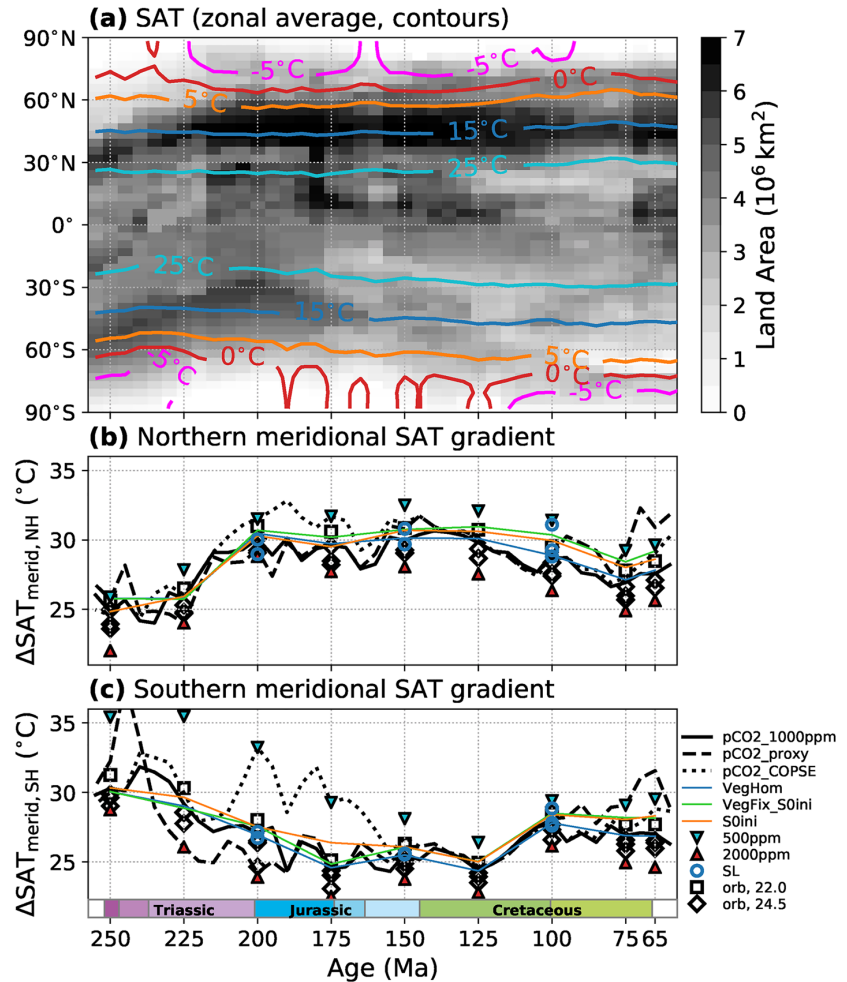


Figure 5. Evolution of simulated zonal mean surface air temperatures (SAT) (a), and the thermal contrast between low-latitude and northern (b) and southern (c) high-latitude regions. (a) Contours indicate annual zonal mean SAT for all runs of the $P_{pCO_2_{1000ppm}}$ pathway, resolved by latitude and geologic time. For this, zonal mean SAT data from all 5 Myr timeslices were aggregated with each timeslice represented by one grid column. The contour colors correspond to those in Figure 4. The gray shading indicates the changing latitudinal distribution of land area in the model paleogeographies. (b and c) Annual zonal mean SAT difference between low-latitude (<30° lat.) a northern (b) and southern (c) high-latitude regions (>60° lat.) through time for the different tested boundary conditions.

in contrast to the very warm Tethys Sea. However, the opposite effect occurs in the mid- to high latitudes where cyclonic subpolar gyres warm the western coasts compared to the eastern ones.

To systematically characterize the evolution of zonal temperature contrasts on the continents through the Mesozoic, the deviation of local annual mean SATs from their zonal mean values is calculated. For two selected timeslices of the $P_{pCO_2_{1000ppm}}$ pathway, the resulting patterns are shown in Figures 6a and 6b. As described above, the eastern tropics and the western mid- to high-latitudes of Pangaea are warmer by up to ~8°C compared to the respective western or eastern regions (Figure 6a). For the fragmented late Cretaceous continental configuration, these east-west contrasts are reduced (Figure 6b). Figure 6c summarizes the zonal mean of the absolute value of these deviations for all considered geologic timeslices of the $P_{pCO_2_{1000ppm}}$ pathway. This indicates that zonal temperature contrasts are amplified in the mid-high latitudes as well as the tropical-subtropical latitudes throughout the Triassic-Jurassic but are clearly reduced after the Middle

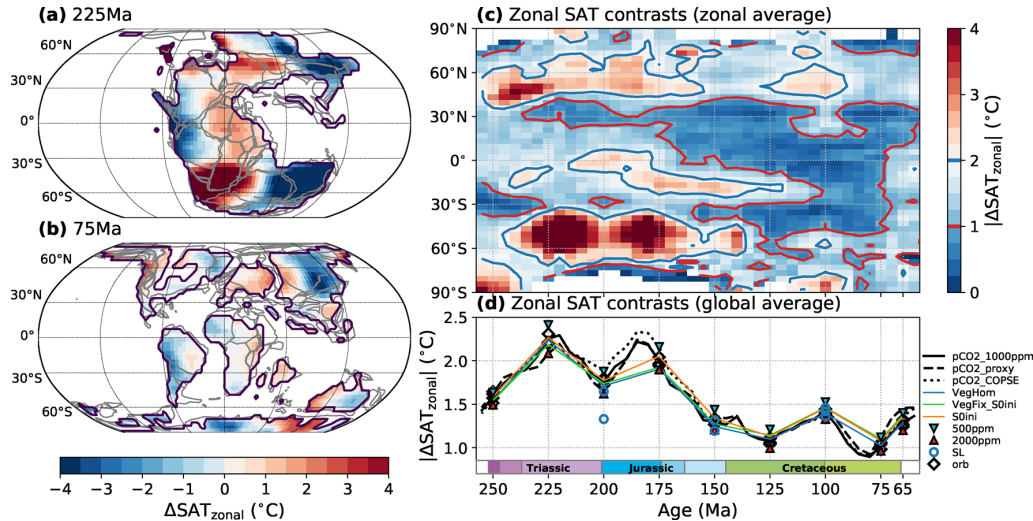


Figure 6. Zonal contrasts in simulated continental surface air temperature patterns (SAT) through the Mesozoic. (a and b) Deviation of continental annual mean SATs from their zonal mean values for two timeslices of the $P_{pCO_2,1000ppm}$ pathway. Gray lines indicate the tectonic plate boundaries in the rotation model of Scotese (2008) (as published by Cao et al., 2018). (c) Zonal mean of the absolute values of these deviations for all timeslices of the $P_{pCO_2,1000ppm}$ pathway, resolved by latitude and geologic time. For this, zonal mean data from all 5 Myr timeslices were aggregated with each timeslice represented by one grid column. The blue (red) contour lines illustrate times and periods with relatively high (low) zonal contrasts. (d) Global mean of the absolute values of these deviations for different boundary conditions.

Jurassic. More uniform zonal temperature patterns were thus established in the mid-Mesozoic while they were considerably perturbed by the supercontinent configuration before. This trend is also indicated by the global average of the absolute SAT deviations from their zonal mean (Figure 6d), which is interpreted as an indicator of global temperature “azonality”. It peaks at $\sim 2.2^\circ\text{C}$ in the Late Triassic and Early Jurassic and is halved in the Late Cretaceous. Changes in boundary conditions other than paleogeography only lead to relatively small deviations from this trend. Our simulations thus illustrate a general trend toward decreased east–west temperature contrasts through the Mesozoic, mainly driven by continental fragmentation.

3.5. Aridity

Previous modeling work (Chaboureaud et al., 2014; Donnadieu et al., 2009) suggested a reduction of the extent of arid climate conditions from the Late Triassic to the Late Cretaceous. To test this, we determine the simulated extent of relatively dry areas using the “radiative index of dryness” of Budyko (1974) which expresses the ratio of potential evaporation (RB/L) to precipitation (PRC): $AI = RB/(L \cdot PRC)$ (Stadler, 2005). Here, RB is the annual mean net surface radiation balance and L is the latent heat of water evaporation and higher values of AI indicate drier conditions. The transition from humid forest climates to dry steppe climates occurs at values around 1.5 today (Budyko, 1974; Mabbutt, 1978). The changing extent of dry land area is indicated in Figure 4 (pink hatches) for four timeslices and in Figure 7a for all timeslices of the $P_{pCO_2,1000ppm}$ pathway. It can be seen in Figure 7a that the dry regions have their largest extent in the subtropical to mid-latitudes during the Late Triassic–Early Jurassic. In the low latitudes, dry regions are extended during the Triassic–Middle Jurassic, especially in western Pangaea (see Figure 4), but successively disappear in the further course, which indicates the establishment of more continuous tropical humid conditions. The relative portion of global arid land area on the $P_{pCO_2,1000ppm}$ pathway (Figure 7b) peaks in the latest Triassic and continuously decreases into the Late Cretaceous. In agreement with Chaboureaud et al. (2014), the fraction of arid land is found to decrease with warming from elevated pCO₂. The relatively low pCO₂ suggested by the COPSE model reconstruction for the latest Triassic to Middle Jurassic would thus have significantly contributed to increased aridity during this time which would have amplified the humidification trend toward the mid-Cretaceous. Also the continuous warming from increasing solar luminosity contributes to more humid conditions through the Mesozoic (Figure 7b, difference between

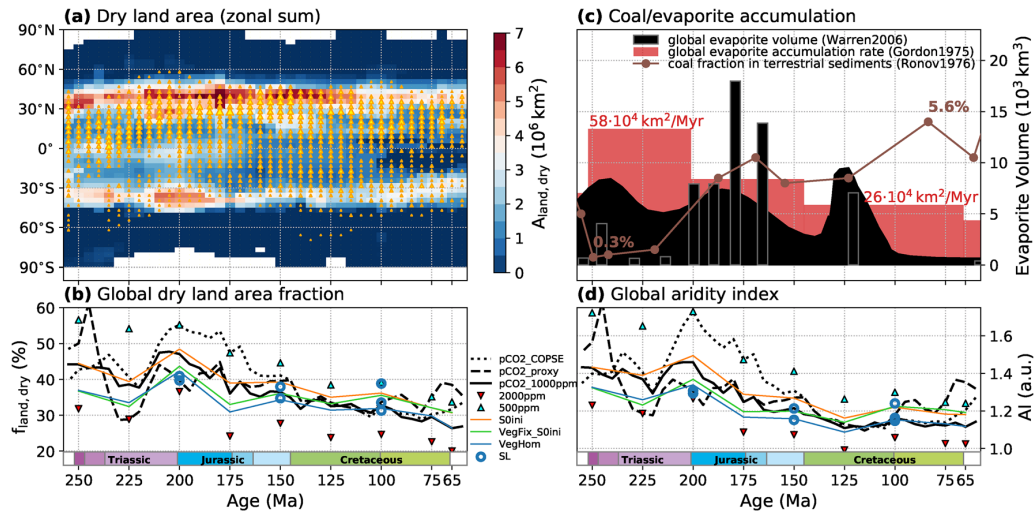


Figure 7. Extent (a and b) and intensity (d) of simulated dry continental climate conditions through the Mesozoic. (a) Zonal sum of dry land area (aridity index $AI < 1.5$, see Section 3.5) for all timeslices of the $P_{pCO_2_{1000ppm}}$ pathway (also see hatched areas in Figure 4). Triangles indicate the occurrence and frequency of evaporites in the data set of Boucot et al. (2013) at a given time and latitude. The size of the triangles scales with the number of occurrences in the respective time interval and latitudinal band (normalized with respect to its area). (b) Global fraction of land area experiencing dry climate conditions ($AI < 1.5$) for different boundary condition pathways. (d) Global aridity index based on the global mean values of precipitation and surface radiation balance on land. (c) Proxy estimates of global coal and evaporite accumulation (Gordon, 1975; Ronov et al., 1980; Warren, 2006).

$P_{pCO_2_{1000ppm}}$ and P_{S0ini}). The cooling in the latest Cretaceous resulting from decreasing pCO_2 in both considered reconstructions is found to increase aridity and to reverse the Early Jurassic to mid-Cretaceous trend toward increasingly humid climates.

Coal and evaporite occurrences are frequently used as paleoclimatic indicators of humid or arid conditions (Markwick, 2007; Ziegler et al., 2003), and a certain agreement can be observed between their distributions and the humid and dry zones simulated here for our baseline pathway $P_{pCO_2_{1000ppm}}$ (Figure 4; proxy data from Boucot et al. (2013) and Cao et al. (2018), locations reconstructed with pyGPLates, see supporting information section 1, for further explanation). For example, many of the coal deposits occur in humid mid- to high-latitude or tropical regions, while evaporites and calcretes are frequent in the relatively dry regions of the western Pangaean continents. This simple scheme can, however, not completely explain these spatial distributions (e.g., evaporites in tropical humid regions). This can be due to a variety of factors, including the range of possible local depositional environments and their variation on shorter (e.g., orbital) timescales. Considering these difficulties and the limitations of the employed climate model, a comprehensive assessment that takes into account the various boundary conditions is beyond the scope of this study. It can still be noted, that Cao et al. (2018) found a statistical Mesozoic–Cenozoic trend from a unimodal to a bimodal zonal distribution in the evaporite occurrence data of Boucot et al. (2013). Our simulations suggest that this could express the establishment of a more consistent tropical humid belt and two arid belts during the fragmentation of Pangaea (see Figure 4d), which could have displaced evaporite formation from equatorial regions especially in the eastern Panthalassa margin. The simulated overall trend toward more humid and less arid continental climates through the Mesozoic also conforms qualitatively with opposite trends of increasing coal versus decreasing evaporite deposition (Figure 7c).

4. Discussion

More than 200 equilibrium climate states for varied boundary conditions (paleogeography, sea level, vegetation patterns, pCO_2 , solar constant S_0 , and orbital configuration) were simulated and analyzed in this study, among other things, to obtain constraints on long-term global mean temperature trends through the Mesozoic. Considering a recent proxy pCO_2 reconstruction (Foster et al., 2017), the simulated global mean temperatures are elevated above pre-industrial values for most of the Mesozoic and exceed $20^\circ C$ in the Late

Triassic-Early Jurassic and mid-Cretaceous. For the same proxy $p\text{CO}_2$ reconstruction, Valdes et al. (2020) obtained similar global mean temperature trends, but up to 4°C higher absolute temperatures (Figure 1a). This expresses the higher climate sensitivity of the HadCM3 model, which is on the upper end of the likely 1.5°C–4.5°C range suggested by Stocker et al. (2014) (Farnsworth, Lunt, O'Brien, et al., 2019). The climate sensitivity exhibited by CLIMBER-3 α is more moderate in this regard, and compares reasonably with that of other Earth System Models of Intermediate Complexity (EMICs; Eby et al., 2013; Pfister & Stocker, 2017). In our simulations the GMST increase in response to a $p\text{CO}_2$ doubling from 500 to 1,000 ppm ranges from 2.8°C for the warm late Cretaceous (at 75 Ma) to 4.1°C for the cooler Late Triassic (225 Ma). At similar $p\text{CO}_2$ concentrations, Chaboureaud et al. (2014) obtained slightly less elevated Mesozoic temperatures with their model (Figure 1a) but their best-guess temperature curve agrees reasonably with that of our $P_{p\text{CO}_2_COPSE}$ pathway. Together, results from these three models illustrate the large range of uncertainty for simulated Mesozoic global mean temperatures which overall range from ~14°C to 25°C. The gray shaded area in Figure 1a indicates the temperature envelope spanned by the different models and $p\text{CO}_2$ pathways. Overall, warm temperature anomalies appear in the Late Triassic to earliest Jurassic and the late Early Cretaceous to early Late Cretaceous, while relatively lower temperatures are suggested for the Early-Middle Triassic, parts of the Early Jurassic-Early Cretaceous and the latest Cretaceous. To first order, these trends roughly conform with those inferred from proxy data (Figure 1c and Mills et al., 2019) and the occurrence of glacial deposits (Figure 1a), cyan colored bars, from Boucot et al., 2013 and Cao et al., 2018), which mainly occur in the middle Mesozoic and the latest Cretaceous and are mostly absent during the Triassic and mid-Cretaceous.

One of the major challenges in the study of warm climate periods, for example, in the Cretaceous (e.g., Laugié et al., 2020; O'Brien et al., 2017; Tabor et al., 2016) or the early Eocene (e.g., Huber & Caballero, 2011; Lunt et al., 2012; Zhu et al., 2019), is the discrepancy between more strongly elevated global temperatures with low meridional gradients inferred from proxies and the conditions simulated by climate models (e.g., Huber, 2012; Upchurch et al., 2015). Challenges lie, for example, in the correct calibration and conversion of proxy data into local and global temperature estimates. In climate models, targeted modifications, for example, of atmospheric microphysical processes, can contribute to increased climate sensitivity and high-latitude temperatures and thus an improved model-proxy agreement at reconstructed $p\text{CO}_2$ levels (Upchurch et al., 2015; Zhu et al., 2019). However, implementing and testing such modifications in CLIMBER-3 α was beyond the scope of this work. For comparison of simulated meridional temperature gradients, the same analysis as in Section 3.3 was performed with model output data from Valdes et al. (2020) and Farnsworth, Lunt, O'Brien, et al. (2019) (see supporting information section 7 with Figure S17). The zonal mean SAT profiles and the southern hemisphere high-low latitudes contrast exhibit very similar patterns in the simulations of Valdes et al. (2020), which use the same paleogeographic reconstruction (compare Figure 5 and Figure S17). In the northern hemisphere, the HadCM3 gradient is slightly higher at comparable GMSTs but also shows a similar trend, only that it decreases more strongly toward the mid-Cretaceous. This is probably mostly due to the more pronounced global warming due to increasing $p\text{CO}_2$ ($P_{p\text{CO}_2_smooth}$ pathway, see Figure 1a). The trends in the Cretaceous simulations from Farnsworth, Lunt, O'Brien, et al. (2019) are quite different, which may derive from differences in the paleogeographic reconstruction, as they also employ the HadCM3 model. This indicates the need to assess different reconstructions and models in consistent intercomparison frameworks. Lapse-rate corrected temperatures at sea level can provide a better comparability and can be obtained from the data repository for all CLIMBER-3 α simulations (also see Figure S12). Paleogeography was also identified as a major control of temperature gradients by Laugié et al. (2020), who compiled proxy and climate model estimates of zonal mean temperatures for the Cenomanian-Turonian period (~94 Ma). The gradients simulated here for this period fall within the range spanned by other models (Laugié et al., 2020), although some are closer to the lower gradients suggested by proxies (see supporting information section 7 and Figures S16a and b). At ~125 Ma, simulated SST gradients compare well with those from Steinig et al. (2020), who argue for an improved agreement with proxies when applying updated calibrations (also see Figures S16c and S16d). We conclude that this study cannot solve the issues of high climate sensitivity and flat temperature gradients in warm climate periods, but offers a new systematic perspective on the effects of different changing boundary conditions, including paleogeography, through the Mesozoic.

To compare the continental SAT seasonality simulated here (see [Section 3.2](#)) with other available climate simulations, we performed the same analysis with results from Valdes et al. (2020, for pCO_2 *smooth*) and Farnsworth, Lunt, O'Brien, et al. (2019) (see [Figure S22](#)). In both studies, the globally averaged seasonality is systematically higher, but the data from Valdes et al. (2020) yields very similar trends, both of zonally and globally averaged seasonality (compare [Figure 3](#) and [Figure S22](#)). This agreement, despite a different model set-up and a slightly different global mean temperature evolution (see [Figure 1a](#)), supports the robustness of the presented trends at least for the paleogeographic reconstruction used in both studies. For a different reconstruction, the data from Farnsworth, Lunt, O'Brien, et al. (2019) also suggests a decrease of seasonality toward a minimum in the mid-Late Cretaceous.

Our P_{SL} experiments demonstrate that long-term sea-level change could have contributed to a temperature rise on the order of 1°C from the Triassic-Jurassic to the Late Cretaceous (see [Section 3.1](#)) and that also smaller scale sea-level fluctuations can have a small, but notable effect on global climate characteristics if they significantly modify coastlines. As reconstructions of sea levels and paleo-coastlines will be constantly revised by using additional data (e.g., Cao et al., 2017; Kocsis & Scotese, 2021), it appears important to reflect their uncertainty and variability in climate model simulations. Reconstructed maximum high- and low-stand paleogeographies for each time-interval could be particularly useful.

Depending on the respective model set-up, deep-time paleoclimate simulations require information on various boundary conditions, including paleogeography, pCO_2 , vegetation patterns, solar constant S_0 , and orbital configuration. In agreement with previous work (e.g., Donnadieu et al., 2006a; Donnadieu et al., 2009; Valdes et al., 2020), we find that these critically affect Earth's climatic evolution through the Mesozoic. However, large uncertainties are associated with these boundary conditions and it is essential to systematically assess their respective effects in climate model ensembles. EMICs like the CLIMBER-3 α model are flexible and computationally less demanding tools to perform large numbers of climate simulations with varied parameters, which are often not affordable with more comprehensive atmosphere-ocean General Circulation Models. However, this comes at the cost of reduced complexity and spatial resolution. For the CLIMBER-3 α model this concerns especially its atmosphere module and its prescribed vegetation patterns. The latter do not dynamically respond to changes in other boundary conditions which can, for example, affect high-latitude temperatures (e.g., Zhou et al., 2012; Hunter et al., 2013). However, proxy-based vegetation patterns could sometimes be more realistic, despite large uncertainties, depending on the performance of the climate and vegetation models. The latter allow for a mechanistic assessment of climate-vegetation feedbacks although they might not capture important long-term evolutionary changes in terrestrial vegetation (Boyce & Lee, 2017). Here, we focus on certain large-scale aspects of the Mesozoic climate evolution and systematic sensitivity tests for various boundary conditions. Further research with more comprehensive models is clearly required.

In our attempt to model a Mesozoic long-term climate evolution, the most important factors appear to be pCO_2 and paleogeography, both of which suffer from considerable uncertainties in the reconstructions. Model-related uncertainties (e.g., in terms of climate sensitivity, the inability to model high-latitude warmth or the treatment of vegetation) add to the difficulties. The understanding of mechanisms governing the Earth System in deep time and their representation in climate models is still limited. These uncertainties are ideally addressed by developing more comprehensive proxy reconstructions and as well as improved paleoclimate models and by systematically testing them in comprehensive intercomparison projects like DeepMIP (Hollis et al., 2019; Lunt et al., 2017, 2021).

It should be noted that the kind of study presented here provides sequences of equilibrium climate states which should be representative of long-term climate trends on timescales of several million years. Here, the considered timeslices are spaced with 5 million years so that dynamics on shorter timescales cannot be represented. However, significant climatic variations occur within these timescales due to internal variability of the climate system as well as due to external factors like orbital cycles, related sea-level fluctuations, meteorite impacts, volcanism, and solar activity changes. Therefore, the obtained long-term trends can only be understood as a baseline around which Earth System states fluctuate. Individual empirical evidence may, however, often only reflect temporary conditions, for example, under a certain orbital configuration. The various sensitivity experiments, for example, with modified orbital configuration, indicate to a certain extent the degree of variation expected on these shorter time-scales.

5. Conclusions

During the Mesozoic, Earth's climate experienced a fundamental transformation from the Pangaeon supercontinent constellation into the Late Cretaceous with its fragmented continents and high sea levels. Here, we systematically assess aspects of the Mesozoic long-term climate evolution in a continuous quantitative climate modeling framework. Simulations were performed for 40 timeslices, covering the time from 255 to 60 Ma in 5 Myr steps, using a recent paleogeographic reconstruction (Scotese & Wright, 2018). For each timeslice, multiple equilibrium climate states were simulated for varied boundary conditions, including $p\text{CO}_2$, the solar constant, sea level, vegetation patterns, and orbital configuration. This ensemble was assessed here regarding global-scale trends in the simulated global mean temperatures, seasonal, meridional, and zonal temperature contrasts and the extent of arid climate conditions.

Regarding the global mean temperatures, we find that paleogeographic changes, including rising sea levels, as well as increasing solar luminosity and changing vegetation patterns provided a baseline warming trend of $\approx +3.5^\circ\text{C}$ from the Late Triassic to the Late Cretaceous. The two considered $p\text{CO}_2$ reconstructions do suggest deviations of up to 5°C from this baseline. These simulations, together with results from the few comparable climate model studies (Chaboureaud et al., 2014; Donnadieu et al., 2009; Valdes et al., 2020) and proxy estimates (e.g., Mills et al., 2019; Veizer & Prokoph, 2015), support warm anomalies in the Triassic and mid-Cretaceous. However, the spread resulting from uncertain long-term $p\text{CO}_2$ changes and the model climate sensitivity remains large, so that the different models and $p\text{CO}_2$ pathways yield Mesozoic global mean temperatures in the range of $\sim 14^\circ\text{C}$ – 25°C . The average seasonality of continental SAT is found to be highest in Late Triassic and is significantly reduced toward the Late Cretaceous, driven by the changing extent and distribution of land masses. However, we find that different orbital configurations could have modified the globally averaged SAT seasonality to a similar degree on the timescales of orbital cycles. Regarding the high- to low-latitude temperature gradients, our simulations indicate that these varied with the changing extent of land area in the high latitudes. In the baseline scenario with constant $p\text{CO}_2$, the northern hemisphere gradient thus increases through the Triassic and falls in the course of the Cretaceous, while the southern hemisphere experiences the opposite trend. However, the thermal gradients also vary on a similar scale with global mean temperature, due to the snow and sea-ice albedo feedback, with higher $p\text{CO}_2$ and solar luminosity contributing to smaller gradients. We also observe an overall reduction of east-west contrasts in the continental annual mean SATs from the Late Triassic–Early Jurassic to the Late Cretaceous related to continental fragmentation. In agreement with previous studies, continental aridity is most widespread during the Late Triassic–Early Jurassic and is reduced toward the Late Cretaceous. Our simulations do suggest, that not only continental fragmentation and rising sea levels contributed to this trend, but that higher global mean temperatures, for example, from elevated $p\text{CO}_2$ and solar luminosity generally enhance humidity on the continents. Relatively low $p\text{CO}_2$ levels suggested for parts of the Jurassic could thus have enhanced aridity and amplified the humidifying trend toward the Late Cretaceous, together with the subtle effect of warming from the rising solar luminosity.

This study aims to contribute to a consolidated picture of long-term Mesozoic climate change. The presented ensemble of simulated climate states illustrates aspects of Mesozoic climate transition from a strongly seasonal, azonal and arid Pangaeon climate toward a more balanced and humid Late Cretaceous warm climate. Existing concepts of Mesozoic long-term climate change can overall be supported in this systematic ensemble approach, using an intermediate complexity Earth System Model. The provided model data (Landwehrs et al., 2021) are expected to prove useful for further investigations.

Conflict of Interest

The authors declare that they have no conflict of interest.

Data Availability Statement

The presented data derive from simulations with the CLIMBER-3 α climate model (Montoya et al., 2005) with the boundary conditions described in Section 2. The model input and output data sets, the scripts used to generate the figures in the paper as well as additional maps for all simulation runs are available at

the institutional repository of the Potsdam Institute for Climate Impact Research (Landwehrs et al., 2021, <https://doi.org/10.5880/PIK.2020.009>).

Acknowledgments

The authors thank all researchers whose data could be incorporated in this work for their efforts to make their results accessible. Especially, C. Scotese and N. Wright are thanked for providing their paleogeographic reconstructions. The authors would like to thank A. Farnsworth, Y. Hu, one anonymous reviewer and the editor, M. Huber, for their very constructive comments that helped to improve the paper. The European Regional Development Fund (ERDF), the German Federal Ministry of Education and Research and the Land Brandenburg are gratefully acknowledged for supporting this project by providing resources on the high performance computer system at the Potsdam Institute for Climate Impact Research. BS acknowledges funding within the scope of the Earth System Science (ESS) program of the Austrian Academy of Sciences (ÖAW) (project "Late Mesozoic lacustrine systems in Tunisia and their global correlation") and project P 27687-N29 Austrian Science Fund (FWF).

References

- Bahcall, J. N., Pinsonneault, M. H., & Basu, S. (2001). Solar models: Current epoch and time dependences, neutrinos, and helioseismological properties. *Acta Pathologica Japonica*, 55(2), 990–1012. <https://doi.org/10.1086/321493>
- Berner, R. A. (2006). GEOCARBSULF: A combined model for Phanerozoic atmospheric O₂ and CO₂. *Geochimica et Cosmochimica Acta*, 70(23), 5653–5664. <https://doi.org/10.1016/j.gca.2005.11.032>
- Bonan, G. B., Levis, S., Kergoat, L., & Oleson, K. W. (2002). Landscapes as patches of plant functional types: An integrating concept for climate and ecosystem models. *Global Biogeochemical Cycles*, 16(2), 5. <https://doi.org/10.1029/2000GB001360>
- Boucot, A. J., Xu, C., Scotese, C. R., & Morley, R. J. (2013). Phanerozoic Paleoclimate. *SEPM Society for Sedimentary Geology*. <https://doi.org/10.2110/sepmcsp.11>
- Boyce, C. K., & Lee, J.-E. (2017). Plant evolution and climate over geological timescales. *Annual Review of Earth and Planetary Sciences*, 45(1), 61–87. <https://doi.org/10.1146/annurev-earth-063016-015629>
- Brugger, J., Feulner, G., & Petri, S. (2017). Baby, it's cold outside: Climate model simulations of the effects of the asteroid impact at the end of the Cretaceous. *Geophysical Research Letters*, 44(1), 419–427. <https://doi.org/10.1002/2016gl072241>
- Brugger, J., Hofmann, M., Petri, S., & Feulner, G. (2019). On the sensitivity of the Devonian climate to continental configuration, vegetation cover, orbital configuration, CO₂ concentration, and insolation. *Paleoceanography and Paleoclimatology*, 34(8), 1375–1398. <https://doi.org/10.1029/2019PA003562>
- Brune, S., Williams, S. E., & Müller, R. D. (2017). Potential links between continental rifting, CO₂ degassing and climate change through time. *Nature Geoscience*, 10(12), 941–946. <https://doi.org/10.1038/s41561-017-0003-6>
- Budyko, M. I. (1974). *Climate and life*. Academic Press, Inc.
- Cao, W., Williams, S., Flament, N., Zahirovic, S., Scotese, C., & Müller, R. D. (2018). Paleolatitudinal distribution of lithologic indicators of climate in a paleogeographic framework. *Geological Magazine*, 156(2), 331–354. <https://doi.org/10.1017/S0016756818000110>
- Cao, W., Zahirovic, S., Flament, N., Williams, S., Golonka, J., & Müller, R. D. (2017). Improving global paleogeography since the late Paleozoic using paleobiology. *Biogeosciences*, 14(23), 5425–5439. <https://doi.org/10.5194/bg-14-5425-2017>
- Chaboureaud, A.-C., Sepulchre, P., Donnadieu, Y., & Franc, A. (2014). Tectonic-driven climate change and the diversification of angiosperms. *Proceedings of the National Academy of Sciences of the United States of America*, 111(39), 14066–14070. <https://doi.org/10.1073/pnas.1324002111>
- Chumakov, N. (2004). Trends in global climate changes inferred from geological data. *Stratigraphy and Geological Correlation*, 12(2), 117–138.
- Clapham, M. E., & Renne, P. R. (2019). Flood basalts and mass extinctions. *Annual Review of Earth and Planetary Sciences*, 47(1), 275–303. <https://doi.org/10.1146/annurev-earth-053018-060136>
- Cohen, K. M., Finney, S. C., Gibbard, P. L., & Fan, J.-X. (2013). The ICS international chronostratigraphic chart. *Episodes*, 36(3), 199–204. <https://doi.org/10.18814/epiugs/2013/v36i3/002>
- Donnadieu, Y., Godd  ris, Y., & Bouttes, N. (2009). Exploring the climatic impact of the continental vegetation on the Mesozoic atmospheric CO₂ and climate history. *Climate of the Past*, 5(1), 85–96. <https://doi.org/10.5194/cp-5-85-2009>
- Donnadieu, Y., Godd  ris, Y., Pierrehumbert, R., Dromart, G., Fluteau, F., & Jacob, R. (2006a). A GEOCLIM simulation of climatic and biogeochemical consequences of Pangea breakup. *Geochemistry, Geophysics, Geosystems*, 7(11). <https://doi.org/10.1029/2006GC001278>
- Eby, M., Weaver, A. J., Alexander, K., Zickfeld, K., Abe-Ouchi, A., Cimatoribus, A. A., et al. (2013). Historical and idealized climate model experiments: An intercomparison of earth system models of intermediate complexity. *Climate of the Past*, 9(3), 1111–1140. <https://doi.org/10.5194/cp-9-1111-2013>
- Farnsworth, A., Lunt, D. J., O'Brien, C. L., Foster, G. L., Inglis, G. N., Markwick, P., et al. (2019). Climate sensitivity on geological timescales controlled by nonlinear feedbacks and ocean circulation. *Geophysical Research Letters*, 46, 9880–9889. <https://doi.org/10.1029/2019GL083574>
- Farnsworth, A., Lunt, D. J., Robinson, S. A., Valdes, P. J., Roberts, W. H. G., Clift, P. D., et al. (2019b). Past East Asian monsoon evolution controlled by paleogeography, not CO₂. *Science Advances*, 5(10), eaax1697. <https://doi.org/10.1126/sciadv.aax1697>
- Feulner, G. (2017). Formation of most of our coal brought Earth close to global glaciation. *Proceedings of the National Academy of Sciences of the United States of America*, 114(43), 11333–11337. <https://doi.org/10.1073/pnas.1712062114>
- Fichefet, T., & Maqueda, M. A. M. (1997). Sensitivity of a global sea ice model to the treatment of ice thermodynamics and dynamics. *Journal of Geophysical Research*, 102(C6), 12609–12646. <https://doi.org/10.1029/97JC00480>
- Fluteau, F., Ramstein, G., Besse, J., Guiraud, R., & Masse, J. P. (2007). Impacts of paleogeography and sea level changes on Mid-Cretaceous climate. *Paleogeography, Palaeoclimatology, Palaeoecology*, 247(3), 357–381. <https://doi.org/10.1016/j.palaeo.2006.11.016>
- Foster, G. L., Royer, D. L., & Lunt, D. J. (2017). Future climate forcing potentially without precedent in the last 420 million years. *Nature Communications*, 8(14845), 1–8. <https://doi.org/10.1038/ncomms14845>
- Frakes, L. A., Francis, J. E., & Syktus, J. I. (1992). *Climate modes of the phanerozoic*. Cambridge University Press. <https://doi.org/10.1017/CBO9780511628948>
- Friedrich, O., Norris, R. D., & Erbacher, J. (2012). Evolution of middle to Late Cretaceous oceans—A 55 m.y. record of Earth's temperature and carbon cycle. *Geology*, 40(2), 107–110. <https://doi.org/10.1130/G32701.1>
- Golonka, J. (2007). Phanerozoic paleoenvironment and paleolithofacies maps: Mesozoic. *Geologia/Akademia G  rniczno-Hutnicza im. Stanisława Staszczyka w Krakowie*, T. 33, z. 2, 211–264.
- Gordon, W. A. (1975). Distribution by latitude of phanerozoic evaporite deposits. *The Journal of Geology*, 83(6), 671–684. <https://doi.org/10.1086/628161>
- Hallam, A. (1985). A review of Mesozoic climates. *Journal of the Geological Society*, 142(3), 433–445. <https://doi.org/10.1144/gsjgs.142.3.0433>
- Haq, B. (2018). Triassic eustatic variations reexamined. *Gsa Today*, 28(12), 4–9. <https://doi.org/10.1130/GSATG381A.1>
- Haq, B. U. (2014). Cretaceous eustasy revisited. *Global and Planetary Change*, 113, 44–58. <https://doi.org/10.1016/j.gloplacha.2013.12.007>
- Haq, B. U. (2017). Jurassic sea-level variations: A reappraisal. *Gsa Today*, 28(1), 4–10. <https://doi.org/10.1130/GSATG359A.1>
- Haq, B. U., Hardenbol, J., & Vail, P. R. (1988). Mesozoic and Cenozoic chronostratigraphy and cycles of sea-level change. In C. K. Wilgus (Ed.), *Sea-level changes* (Vol. 42, pp. 71–108). SEPM Society for Sedimentary Geology. <https://doi.org/10.2110/pec.88.01.0071>

- Hofmann, M., & Morales Maqueda, M. A. (2006). Performance of a second-order moments advection scheme in an Ocean General Circulation Model. *Journal of Geophysical Research*, *111*(C5), 1–26. <https://doi.org/10.1029/2005JC003279>
- Hollis, C. J., Dunkley Jones, T., Anagnostou, E., Bijl, P. K., Cramwinckel, M. J., Cui, Y., et al. (2019). The DeepMIP contribution to PMIP4: Methodologies for selection, compilation and analysis of latest Paleocene and early Eocene climate proxy data, incorporating version 0.1 of the DeepMIP database. *Geoscientific Model Development*, *12*(7), 3149–3206. <https://doi.org/10.5194/gmd-12-3149-2019>
- Holz, M. (2015). Mesozoic paleogeography and paleoclimates - A discussion of the diverse greenhouse and hothouse conditions of an alien world. *Journal of South American Earth Sciences*, *61*, 91–107. <https://doi.org/10.1016/j.jsames.2015.01.001>
- Huber, M. (2012). Progress in greenhouse climate modeling. *Paleontological Society Papers*, *18*, 213–262. <https://doi.org/10.1017/S10893326000262X>
- Huber, M., & Caballero, R. (2011). The early Eocene equable climate problem revisited. *Climate of the Past*, *7*(2), 603–633. <https://doi.org/10.5194/cp-7-603-2011>
- Hunter, S. J., Haywood, A. M., Valdes, P. J., Francis, J. E., & Pound, M. J. (2013). Modeling equable climates of the Late Cretaceous: Can new boundary conditions resolve data-model discrepancies? *Palaogeography, Palaeoclimatology, Palaeoecology*, *392*, 41–51. <https://doi.org/10.1016/j.palaeo.2013.08.009>
- Huynh, T. T., & Poulsen, C. J. (2005). Rising atmospheric CO₂ as a possible trigger for the end-Triassic mass extinction. *Palaogeography, Palaeoclimatology, Palaeoecology*, *217*(3–4), 223–242. <https://doi.org/10.1016/j.palaeo.2004.12.004>
- Kocsis, A. T., & Scotese, C. R. (2021). Mapping paleocoastlines and continental flooding during the Phanerozoic. *Earth-Science Reviews*, *213*, 103463. <https://doi.org/10.1016/j.earscirev.2020.103463>
- Kopp, G., & Lean, J. L. (2011). A new, lower value of total solar irradiance: Evidence and climate significance. *Geophysical Research Letters*, *38*(1). <https://doi.org/10.1029/2010GL045777>
- Kutzbach, J. E., & Gallimore, R. G. (1989). Pangaeon climates: Megamonsoons of the megacontinent. *Journal of Geophysical Research*, *94*(D3), 3341–3357. <https://doi.org/10.1029/JD094iD03p03341>
- Ladant, J.-B., & Donnadieu, Y. (2016). Palaeogeographic regulation of glacial events during the Cretaceous supergreenhouse. *Nature Communications*, *7*, 12771. <https://doi.org/10.1038/ncomms12771>
- Landwehrs, J., Feulner, G., Petri, S., Sames, B., & Wagreich, M. (2021). Data from Climate Model Ensemble Simulations for the Mesozoic Climate Evolution. *GFZ Data Services*. 2021-02-04. <https://doi.org/10.5880/PIK.2020.009>
- Landwehrs, J. P., Feulner, G., Hofmann, M., & Petri, S. (2020). Climatic fluctuations modeled for carbon and sulfur emissions from end-Triassic volcanism. *Earth and Planetary Science Letters*, *537*, 116174. <https://doi.org/10.1016/j.epsl.2020.116174>
- Laugé, M., Donnadieu, Y., Ladant, J.-B., Green, J. A. M., Bopp, L., & Raison, F. (2020). Stripping back the modern to reveal the Cenomanian-Turonian climate and temperature gradient underneath. *Climate of the Past*, *16*(3), 953–971. <https://doi.org/10.5194/cp-16-953-2020>
- Lunt, D. J., Bragg, F., Chan, W.-L., Hutchinson, D. K., Ladant, J.-B., Morozova, P., et al. (2021). DeepMIP: Model intercomparison of early Eocene climatic optimum (EECO) large-scale climate features and comparison with proxy data. *Climate of the Past*, *17*(1), 203–227. <https://doi.org/10.5194/cp-17-203-2021>
- Lunt, D. J., Dunkley Jones, T., Heinemann, M., Huber, M., LeGrande, A., Winguth, A., et al. (2012). A model-data comparison for a multi-model ensemble of early Eocene atmosphere-ocean simulations: EoMIP. *Climate of the Past*, *8*(5), 1717–1736. <https://doi.org/10.5194/cp-8-1717-2012>
- Lunt, D. J., Farnsworth, A., Loftson, C., Foster, G. L., Markwick, P., O'Brien, C. L., et al. (2016). Palaeogeographic controls on climate and proxy interpretation. *Climate of the Past*, *12*(5), 1181–1198. <https://doi.org/10.5194/cp-12-1181-2016>
- Lunt, D. J., Huber, M., Anagnostou, E., Baatsen, M. L. J., Caballero, R., DeConto, R., et al. (2017). The DeepMIP contribution to PMIP4: Experimental design for model simulations of the EECO, PETM, and pre-PETM (version 1.0). *Geoscientific Model Development*, *10*(2), 889–901. <https://doi.org/10.5194/gmd-10-889-2017>
- Mabbutt, J. A. (1978). The impact of desertification as revealed by mapping. *Environmental Conservation*, *5*(1), 45–56. <https://doi.org/10.1017/S0376892900005270>
- Markwick, P. J. (2007). The palaeogeographic and paleoclimatic significance of climate proxies for data-model comparisons. In *Deep-time perspectives on climate change: Marrying the signal from computer models and biological proxies* (pp. 251–312). Geological Society of London. <https://doi.org/10.1144/TMS002.13>
- Miller, K. G., Kominz, M. A., Browning, J. V., Wright, J. D., Mountain, G. S., Katz, M. E., & Pekar, S. F. (2005). The Phanerozoic record of global sea-level change. *Science*, *310*(5752), 1293–1298. <https://doi.org/10.1126/science.1116412>
- Mills, B. J. W., Krause, A. J., Scotese, C. R., Hill, D. J., Shields, G. A., & Lenton, T. M. (2019). Modeling the long-term carbon cycle, atmospheric CO₂, and Earth surface temperature from late Neoproterozoic to present day. *Gondwana Research*, *67*, 172–186. <https://doi.org/10.1016/j.gr.2018.12.001>
- Montoya, M., Griesel, A., Levermann, A., Mignot, J., Hofmann, M., Ganopolski, A., & Rahmstorf, S. (2005). The earth system model of intermediate complexity CLIMBER-3α. Part I: Description and performance for present-day conditions. *Climate Dynamics*, *25*(2–3), 237–263. <https://doi.org/10.1007/s00382-005-0044-1>
- Müller, R. D., & Dutkiewicz, A. (2018). Oceanic crustal carbon cycle drives 26-million-year atmospheric carbon dioxide periodicities. *Science Advances*, *4*(2), eaaq0500. <https://doi.org/10.1126/sciadv.aaq0500>
- Müller, R. D., Sdrólías, M., Gaina, C., Steinberger, B., & Heine, C. (2008). Long-term sea-level fluctuations driven by ocean basin dynamics. *Science*, *319*(5868), 1357–1362. <https://doi.org/10.1126/science.1151540>
- Müller, R. D., Seton, M., Zahirovic, S., Williams, S. E., Matthews, K. J., Wright, N. M., et al. (2016). Ocean basin evolution and global-scale plate reorganization events since pangea breakup. *Annual Review of Earth and Planetary Sciences*, *44*(1), 107–138. <https://doi.org/10.1146/annurev-earth-060115-012211>
- O'Brien, C. L., Robinson, S. A., Pancost, R. D., Damsté, J. S. S., Schouten, S., Lunt, D. J., & Wrobel, N. E. (2017). Cretaceous sea-surface temperature evolution: Constraints from TEX86 and planktonic foraminiferal oxygen isotopes. *Earth-Science Reviews*, *172*, 224–247. <https://doi.org/10.1016/j.earscirev.2017.07.012>
- Pacanowski, R., & Griffies, S. (2000). *MOM 3.0 manual* (pp. 1–708). Geophysical Fluid Dynamics Laboratory.
- Parrish, J. T. (1993). Climate of the supercontinent Pangea. *The Journal of Geology*, *101*(2), 215–233. <https://doi.org/10.1086/648217>
- Petukhov, V., Ganopolski, A., Brovkin, V., Claussen, M., Eliseev, A., Kubatzki, C., & Rahmstorf, S. (2000). CLIMBER-2: A climate system model of intermediate complexity. Part I: Model description and performance for present climate. *Climate Dynamics*, *16*(1), 1–17. <https://doi.org/10.1007/PL00007919>
- Pfadenhauer, J. S., & Klötzli, F. A. (2014). *Vegetation der Erde: Grundlagen, Ökologie, Verbreitung*. Springer Spektrum. <https://doi.org/10.1007/978-3-642-41950-8>

- Pfister, P. L., & Stocker, T. F. (2017). State-dependence of the climate sensitivity in earth system models of intermediate complexity. *Geophysical Research Letters*, *44*(20), 10643–10653. <https://doi.org/10.1002/2017GL075457>
- Poulter, B., MacBean, N., Hartley, A., Khlystova, I., Arino, O., Betts, R., et al. (2015). Plant functional type classification for earth system models: Results from the European Space Agency's Land Cover Climate Change Initiative. *Geoscientific Model Development*, *8*(7), 2315–2328. <https://doi.org/10.5194/gmd-8-2315-2015>
- Price, G. (1999). The evidence and implications of polar ice during the Mesozoic. *Earth-Science Reviews*, *48*(3), 183–210. [https://doi.org/10.1016/S0012-8252\(99\)00048-3](https://doi.org/10.1016/S0012-8252(99)00048-3)
- Price, G. D. (2009). Mesozoic climates. In V. Gornitz (Ed.), *Encyclopedia of paleoclimatology and ancient environments* (pp. 554–559). Springer Netherlands. https://doi.org/10.1007/978-1-4020-4411-3_138
- Ray, D. C., van Buchem, F. S. P., Baines, G., Davies, A., Gréselle, B., Simmons, M. D., & Robson, C. (2019). The magnitude and cause of short-term eustatic Cretaceous sea-level change: A synthesis. *Earth-Science Reviews*, *197*, 102901. <https://doi.org/10.1016/j.earscirev.2019.102901>
- Ronov, A. B., Khain, V. E., Balukhovskiy, A. N., & Seslavinsky, K. B. (1980). Quantitative analysis of Phanerozoic sedimentation. *Sedimentary Geology*, *25*(4), 311–325. [https://doi.org/10.1016/0037-0738\(80\)90067-6](https://doi.org/10.1016/0037-0738(80)90067-6)
- Royer, D. L. (2014). Atmospheric CO₂ and O₂ during the phanerozoic: Tools, patterns, and impacts. In *Treatise on geochemistry* (2nd ed., Vol. 6, pp. 251–267). <https://doi.org/10.1016/B978-0-08-095975-7.01311-5>
- Sames, B., Wagreich, M., Conrad, C. P., & Iqbal, S. (2020). Aquifer-eustasy as the main driver of short-term sea-level fluctuations during Cretaceous hothouse climate phases. *Geological Society, London, Special Publications*, *498*(1), 9–38. <https://doi.org/10.1144/SP498-2019-105>
- Scotese, C. R. (2008). *The PALEOMAP project PaleoAtlas for ArcGIS, volume 2, Cretaceous paleogeographic and plate tectonic reconstructions*. PALEOMAP Project.
- Scotese, C. R. (2016). *Global climate change (modern times to 540 million years ago)*. Retrieved from https://www.researchgate.net/publication/303811641_Global_Climate_Change_Modern_Times_to_540_million_years_ago
- Scotese, C. R. (2018). *An estimate of the volume of phanerozoic ice*. Retrieved from https://www.researchgate.net/publication/325094158_An_Estimate_of_the_Volume_of_Phanerozoic_Ice
- Scotese, C. R., J., Boucot, A., & Xu, C. (2014). *Atlas of phanerozoic climatic zones*. PALEOMAP Project PaleoAtlas for ArcGIS. <https://doi.org/10.131340/2.1.2757.8567>
- Scotese, C. R., & Wright, N. (2018). *PALEOMAP paleodigital elevation models (PaleoDEMS) for the Phanerozoic*. Retrieved from <https://www.earthbyte.org/paleodem-resource-scotese-and-wright-2018>
- Sellwood, B. W., & Valdes, P. J. (2006). Mesozoic climates: General circulation models and the rock record. *Sedimentary Geology*, *190*(1), 269–287. <https://doi.org/10.1016/j.sedgeo.2006.05.013>
- Sellwood, B. W., & Valdes, P. J. (2008). Jurassic climates. *Proceedings of the Geologists' Association*, *119*(1), 5–17. [https://doi.org/10.1016/S0016-7878\(59\)80068-7](https://doi.org/10.1016/S0016-7878(59)80068-7)
- Song, H., Wignall, P. B., Song, H., Dai, X., & Chu, D. (2019). Seawater Temperature and Dissolved Oxygen over the Past 500 Million Years. *Journal of Earth Sciences*, *30*(2), 236–243. <https://doi.org/10.1007/s12583-018-1002-2>
- Stadler, S. J. (2005). Aridity indexes. In J. E. Oliver (Ed.), *Encyclopedia of world climatology* (pp. 89–94). Springer.
- Stanley, S. M., & Luczaj, J. A. (2015). *Earth system history*. Freeman/Macmillan Higher Education.
- Steinig, S., Dummann, W., Park, W., Latif, M., Kusch, S., Hofmann, P., & Flögel, S. (2020). Evidence for a regional warm bias in the Early Cretaceous TEX86 record. *Earth and Planetary Science Letters*, *539*, 116184. <https://doi.org/10.1016/j.epsl.2020.116184>
- Stocker, T., Qin, D., Plattner, G., Tignor, M., Allen, S., Boschung, J., & Midgley, P. (2014). *Climate change 2013: The Physical Science Basis. Contribution of Working Group I to the Fifth Assessment Report of IPCC the Intergovernmental panel on climate change*. Cambridge University Press. <https://doi.org/10.1017/cbo9781107415324>
- Tabor, C. R., Poulsen, C. J., Lunt, D. J., Rosenbloom, N. A., Otto-Bliesner, B. L., Markwick, P. J., et al. (2016). The cause of Late Cretaceous cooling: A multimodel-proxy comparison. *Geology*, *44*(11), 963–966. <https://doi.org/10.1130/G38363.1>
- Takashima, R., Nishi, H., Huber, B., & Leckie, R. M. (2006). Greenhouse world and the Mesozoic ocean. *Oceanography*, *19*, 82–92. <https://doi.org/10.5670/oceanog.2006.07>
- Upchurch, G. R., Kiehl, J., Shields, C., Scherer, J., & Scotese, C. (2015). Latitudinal temperature gradients and high-latitude temperatures during the latest Cretaceous: Congruence of geologic data and climate models. *Geology*, *43*(8), 683–686. <https://doi.org/10.1130/G36802.1>
- Valdes, P. J., Scotese, C. R., & Lunt, D. J. (2020). Deep ocean temperatures through time. *Climate of the Past Discussions*, 1–37. <https://doi.org/10.5194/cp-2020-83>
- Veizer, J., Goddérís, Y., & François, L. M. (2000). Evidence for decoupling of atmospheric CO₂ and global climate during the Phanerozoic eon. *Nature*, *408*(6813), 698–701. <https://doi.org/10.1038/35047044>
- Veizer, J., & Prokoph, A. (2015). Temperatures and oxygen isotopic composition of Phanerozoic oceans. *Earth-Science Reviews*, *146*, 92–104. <https://doi.org/10.1016/j.earscirev.2015.03.008>
- Wang, P. X., Wang, B., Cheng, H., Fasullo, J., Guo, Z. T., Kiefer, T., & Liu, Z. Y. (2014). The global monsoon across timescales: Coherent variability of regional monsoons. *Climate of the Past*, *10*(6), 2007–2052. <https://doi.org/10.5194/cp-10-2007-2014>
- Warren, J. K. (2006). *Evaporites: Sediments, resources and hydrocarbons*. Springer-Verlag Berlin Heidelberg. <https://doi.org/10.1007/3-540-32344-9>
- Winguth, A. M. E., Shields, C. A., & Winguth, C. (2015). Transition into a hothouse world at the permian-triassic boundary-A model study. *Palaeogeography, Palaeoclimatology, Palaeoecology*, *440*, 316–327. <https://doi.org/10.1016/j.palaeo.2015.09.008>
- Wong, K., Mason, E., Brune, S., East, M., Edmonds, M., & Zhirovic, S. (2019). Deep carbon cycling over the past 200 million years: A review of fluxes in different tectonic settings. *Frontiers in Earth Science*, *7*, 1–22. <https://doi.org/10.3389/feart.2019.00263>
- Wright, N. M., Seton, M., Williams, S. E., Whittaker, J. M., & Müller, R. D. (2020). Sea-level fluctuations driven by changes in global ocean basin volume following supercontinent break-up. *Earth-Science Reviews*, *208*, 103293. <https://doi.org/10.1016/j.earscirev.2020.103293>
- Zhou, J., Poulsen, C. J., Rosenbloom, N., Shields, C., & Briegleb, B. (2012). Vegetation-climate interactions in the warm mid-Cretaceous. *Climate of the Past*, *8*(2), 565–576. <https://doi.org/10.5194/cp-8-565-2012>
- Zhu, J., Poulsen, C. J., & Tierney, J. E. (2019). Simulation of Eocene extreme warmth and high climate sensitivity through cloud feedbacks. *Science Advances*, *5*(9), eaax1874. <https://doi.org/10.1126/sciadv.aax1874>
- Zickfeld, K., Eby, M., Weaver, A. J., Alexander, K., Crespin, E., Edwards, N. R., et al. (2013). Long-term climate change commitment and reversibility: An EMIC intercomparison. *Journal of Climate*, *26*(16), 5782–5809. <https://doi.org/10.1175/JCLI-D-12-00584.1>
- Ziegler, A., Eshel, G., Rees, P. M., Rothfus, T., Rowley, D., & Sunderlin, D. (2003). Tracing the tropics across land and sea: Permian to present. *Lethaia*, *36*(3), 227–254. <https://doi.org/10.1080/00241160310004657>

P.II Modes of Pangean Lake-Level Cyclicity Driven by Astronomical Pacing Modulated by Continental Position and $p\text{CO}_2$

Bibliographic Information

Landwehrs, J., Feulner, G., Willeit, M., Petri, S., Sames, B., Wagleich, M., Whiteside, J.H. and Olsen, P.E. (2022), “Modes of Pangean Lake-Level Cyclicity Driven by Astronomical Pacing Modulated by Continental Position and $p\text{CO}_2$ ”, (in review).

Accompanying Data Publication:

Landwehrs, J., Feulner, G., Willeit, M., Petri, S., Sames, B., Wagleich, M., Whiteside, J.H., Olsen, P.E. (2022) “Data from Climate Model Simulations for Triassic–Jurassic Orbital Climate Cycles”, doi:10.5880/PIK.2022.001, *GFZ Data Services*.

Copyright Notice

©2022 The Authors. This is the manuscript currently under review for publication in *Proceedings of the National Academy of Sciences of the United States of America (PNAS)*. Submitted 11.03.2022.

Modes of Pangean Lake-Level Cyclicity Driven by Astronomical Pacing Modulated by Continental Position and $p\text{CO}_2$

Jan Landwehrs^{a,b,*}, Georg Feulner^b, Matteo Willeit^b, Stefan Petri^b, Benjamin Sames^a, Michael Wagreich^a,
Jessica H. Whiteside^c, Paul E. Olsen^d

^a*Department of Geology, University of Vienna, Althanstraße 14, Vienna, 1090, Austria*

^b*Earth System Analysis, Potsdam Institute for Climate Impact Research, Member of the Leibniz
Association, P.O. Box 601203, Potsdam, D-14412, Germany*

^c*Ocean and Earth Science, National Oceanography Centre, University of Southampton, SO14 3ZH, Southampton, United
Kingdom*

^d*Lamont-Doherty Earth Observatory of Columbia University, Palisades, 10968, NY, United States of America*

Abstract

Orbital cyclicity is a fundamental pacemaker of Earth's climate system. The Newark-Hartford Basin (NHB) lake sediment record of eastern North America contains compelling geologic expressions of this cyclicity, reflecting variations of climatic conditions in the tropics of Pangea during the Late Triassic and earliest Jurassic (~233–199 million years ago). Climate modeling enables a deeper mechanistic understanding of Earth system modulation during this unique greenhouse and supercontinent period. We link major features of the NHB record to the combined climatic effects of orbital forcing, paleogeographic changes and atmospheric $p\text{CO}_2$ variations. An ensemble of transient, orbitally driven climate simulations is assessed for nine time-slices, three atmospheric $p\text{CO}_2$ values and two paleogeographic reconstructions. Climatic transitions from tropical humid to more seasonal and ultimately semi-arid are associated with tectonic drift of the NHB from ~5 to 20°N. The modeled orbital modulation of the precipitation–evaporation balance is most pronounced during the 220 to 200 Ma interval, whereas it is limited by weak seasonality and increasing aridity before and after this interval. Lower $p\text{CO}_2$ values at around 205 Ma contribute to drier climates and could have led to the observed damping of sediment cyclicity. Eccentricity-modulated precession dominates the orbitally driven climate response in the NHB region. High obliquity further amplifies summer precipitation through the seasonally shifting tropical rainfall belt. Regions with other proxy records are also assessed, providing guidance towards an integrated picture of global astronomical climate forcing in the Late Triassic, and ultimately of other periods in Earth history as well.

Keywords: Mesozoic, Triassic, Jurassic, Newark Basin, Orbital Cycles, Paleoclimate, Climate Model

*Corresponding author

Email address: jan.landwehrs@posteo.de (Jan Landwehrs)

Significance Statement:

The glacial cycles of the last 3 million years demonstrate the fundamental control of astronomical variations on Earth’s climate system. Sedimentary records of orbital climate cycles from much further in Earth’s past provide insights into its behavior under different conditions and potentially the factors leading into and out of extreme climatic states. We use climate model simulations to identify drivers of climatic changes recorded in lake sediments of the Newark-Hartford basins of the eastern US. During their formation from 233 to 199 million years ago, these were located in the tropics of the supercontinent Pangea. We show how the combination of astronomical forcing, the plate-tectonic drift as well as fluctuating atmospheric $p\text{CO}_2$ could have caused the reconstructed cycles and trends.

Cyclic variations in Earth’s orbit and axial orientation cause changes in insolation, and consequently in climate (e.g. [Milankovitch, 1941](#); [Hays et al., 1976](#); [Berger and Yin, 2012](#); [Hinnov, 2018](#)). Understanding this omnipresent astronomical forcing on different Earth system states (e.g. the greenhouse world of the last supercontinent Pangea and the icehouse world of the Pleistocene) provides fundamental insights into Earth’s climate dynamics throughout its history and potentially into its future. Lake sediments from the Newark and Hartford basins (eastern North America) comprise one of the most compelling records of astronomically driven climate cyclicity on ancient Earth ([Olsen and Kent, 1996](#); [Olsen et al., 2019](#)). These sediments accumulated over a period of more than 30 million years from the Late Triassic into the Early Jurassic (233–199 Ma) in rift basins that formed during the initial breakup of Pangea ([Olsen and Kent, 1996](#); [Kent et al., 2017](#)). The largely lacustrine deposits display pronounced cyclicities, interpreted as periodic variations of lake water depth linked to orbitally driven changes in the climatic precipitation–evaporation balance ([Olsen, 1986](#); [Olsen and Kent, 1996](#)). Based on cores from the Newark Basin Coring Project and Army Corps of Engineers ([Olsen et al., 1996b](#)), augmented with cores from the Hartford Basin, the composite sequence is one of the longest continuous lacustrine records available ([Olsen and Kent, 1990](#); [Kent et al., 2017](#); [Olsen et al., 2019](#)), and provides a reference for early Mesozoic orbital climate pacing in the tropics ([Olsen and Kent, 1999](#)). Cyclicities have been quantitatively assessed from facies-based depth ranks and sediment color as proxies of lake water depth and thus climate ([Olsen, 1986](#); [Olsen and Kent, 1996, 1999](#); [Kent et al., 2017](#)). A hierarchy of sedimentary successions clusters into groups expressing the ~ 20 kyr climatic precession cycle (the 1–25 m thick “Van Houten”-cycles, depending on basin position and age), modulated by ~ 100 and 405 kyr eccentricity cycles ([Olsen, 1986](#); [Olsen and Kent, 1996](#); [Kent et al., 2017](#)).

Building on these efforts, steps towards a consistent picture of astronomical pacing of Earth’s climate system can be made by clarifying effects of different orbital parameters in a greenhouse and supercontinent world and their expression at certain proxy localities. The present study contributes to this by providing a comprehensive climate model framework for the interpretation of the Newark-Hartford composite record. To identify Late Triassic climate trends and cycles and their drivers, we analyze an ensemble of orbitally-forced global climate simulations, which reflects paleogeographic changes as well as a range of cooler and warmer climate states related to atmospheric $p\text{CO}_2$ values. Orbital effects during some Mesozoic or earlier time periods have been studied with climate models before, using sets of fixed orbital parameters (e.g. [Kutzbach, 1994](#); [Valdes et al., 1995](#); [Horton et al., 2010, 2012](#); [Feulner, 2017](#); [Brugger et al., 2019](#); [Landwehrs et al., 2021](#)). Here, climate responses in the NHB to both astronomical and plate tectonic dynamics are assessed through transient climate simulations on orbital timescales for a number of Late Triassic time-slices. Because this approach is global in nature, we also use it to link contemporaneous records from different localities to form a more integrated picture of climate trends and cycles across Pangea in the Late Triassic.

1. Humid–Seasonal–Dry Climate Transition due to Continental Drift

Here, we employ the fast CLIMBER-X Earth System Model (Willeit et al., 2022), especially its coupled atmosphere, ocean, sea-ice and land-surface models, all discretized on a $5^\circ \times 5^\circ$ horizontal grid. Transient simulations are run for 250 kyr with paleogeographies for nine Late Triassic to Early Jurassic time-slices (230 to 190 Ma in 5 Myr steps) at three atmospheric $p\text{CO}_2$ values (750, 1500 and 3000 ppm). All simulations are exposed to an idealized orbital forcing that cyclically modulates eccentricity e , precession angle ω and obliquity ε with periods of 100, 40 and 20 kyr, respectively (see *Methods*).

Before analyzing dynamical orbital effects, we characterize the modeled general climatic setting of the Newark-Hartford Basin area (NHB) and effects of continental drift and $p\text{CO}_2$ across the considered time-slices. For this, averages over the last 200 kyr of each simulation are considered. The NHB was initially located within the tropical rainfall belt that broadened towards the warm Tethys sea in the east that acted as a source of moisture, in contrast to the drier western Pangea (Fig. 1f,g). At these low latitudes ($\sim 4\text{--}10^\circ\text{N}$), the area experienced warm and humid conditions with weak seasonality that correspond to *Af* climates in the Köppen classification of modern climate zones (Fig. 1a; based on simulated monthly temperatures and precipitation rates, Beck et al., 2018). This is true from 230 to 215 Ma independent of $p\text{CO}_2$ and the two considered paleogeographic reconstructions (Geo_1 and Geo_2 , see *Methods*). Around these modeled long-term average conditions (see *Methods*), orbital climate modulation and other variability can lead to dry or wet extreme periods, as discussed in following sections. With Pangea’s northward drift, the NHB moved to higher latitudes and seasonal contrasts increase with higher summer temperatures (T) and precipitation rates (PRC) and cooler, drier winters (Fig. 1b–e). This is also expressed as a transition to monsoonal (*Am*) and savanna (*Aw*) climates with pronounced wet and dry seasons (210–195 Ma, at $\sim 10\text{--}20^\circ\text{N}$), and finally to semi-arid steppe climates (*BSh*) with very hot summers and less rainfall when the NHB reached subtropical latitudes (195–190 Ma, $\sim 20\text{--}23^\circ\text{N}$).

In absolute terms, the simulated regional annual mean $T_{\text{NHB}}^{\text{ann}}$ at 230 Ma ranges from 24 to 31°C (at $p\text{CO}_2=750$ and 3000 ppm) and increases continuously by $5\text{--}6^\circ\text{C}$ until 190 Ma, while $\text{PRC}_{\text{NHB}}^{\text{ann}}$ reaches a peak of $5\text{--}6.6\text{ mm/d}$ at 220 Ma before falling to $1.8\text{--}2.8\text{ mm/d}$ at 195 Ma (also see Fig. S3). The T seasonality (monthly max.–min. difference) rises from ~ 6 to 8°C while the PRC seasonality grows from $\sim 2\text{ mm/d}$ to a peak of $5\text{--}6\text{ mm/d}$ at 200 Ma.

Because the NHB lake level cycles express changes in the hydrologic balance, the most relevant climatic parameter is the precipitation–evaporation difference (PRC–EVAP, or net precipitation). Following the modeled $\text{PRC}_{\text{NHB}}^{\text{ann}}$ and $T_{\text{NHB}}^{\text{ann}}$ trends, the most humid annual mean conditions occur around 220 Ma (Sec. 3) while potential evaporation exceeds precipitation after ~ 200 Ma ($\text{PRC-EVAP}_{\text{NHB}}^{\text{ann}} \approx 0$, Fig. S3), again showing the transition from humid to arid climate. The PRC–EVAP seasonality is highest during the intermediate 220–200 Ma period and reaches 3 mm/d , especially at high $p\text{CO}_2$. This increase under globally warmer climates is a general observation for T, PRC, PRC–EVAP and their respective seasonality in the NHB area (Fig. S3). The amplified seasonality is partly due to a strengthened late spring rainy season, as shown below, which is also relevant for the regional orbital climate response.

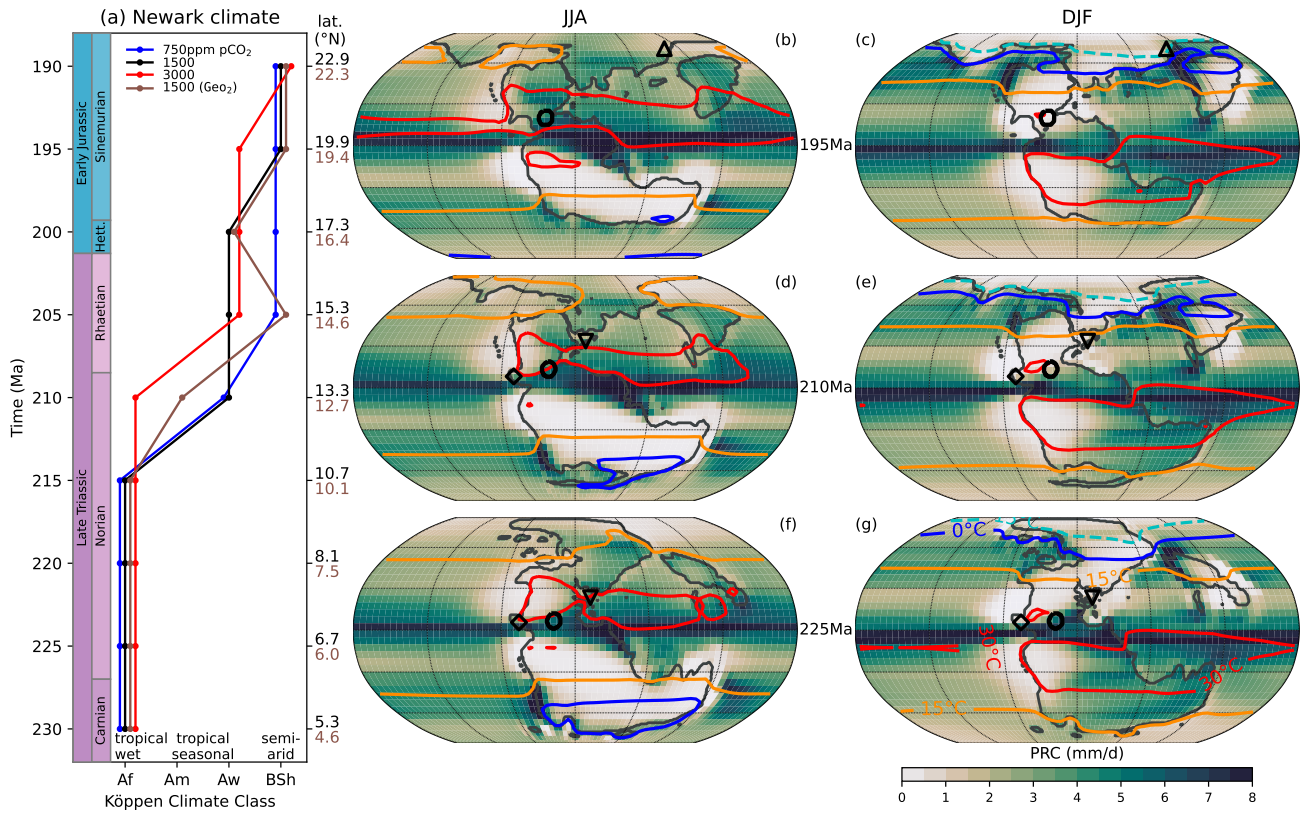


Figure 1: Long-term average climate conditions in the Newark-Hartford Basin area (a) and on the globe (b–g) through the Late Triassic and earliest Jurassic. (a): Köppen climate classes determined from the simulated long-term average monthly temperatures and precipitation rates in the NHB area marked by the black circle in the maps (b)–(g). Axis labels on the right side indicate the latitude of the NHB from the two paleogeographic reconstructions at the respective time-slice (black: Geo_1 , [Marcilly et al. 2021](#); brown: Geo_2 , [Cao et al. 2017, 2018](#); see [Methods](#)). **(b–g):** Seasonal precipitation rates (colors) and surface air temperatures (colored contours for 30, 15, 0 and -15°C) for boreal summer (JJA, left) and winter (DJF, right). Shown are long-term averages from three selected simulations for 225, 210 and 205 Ma at $p\text{CO}_2=1500$ ppm, using the Geo_1 paleogeographies. Coastlines are shown by black contours. Locations of the NHB (\circ), Germanic Basin (∇), Junggar Basin (\triangle) and Colorado Plateau (\diamond) are indicated.

2. Strong Humidity Response to Precession During 220–200 Ma at High $p\text{CO}_2$

The modeled climate response in the Newark-Hartford Basin area to the employed orbital forcing (Fig. 2a) and the resulting local insolation changes (Fig. 2b) are illustrated by changes in the maximum T, PRC and PRC–EVAP (Fig. 2c–e) and their monthly values at different phases of the orbital forcing (Fig. 2f–i). This is done for three time-slices (225, 210 and 195 Ma) which represent the changing orbital response at different stages of the latitudinal and climatic shift. Overall, the effect of eccentricity-modulated precession is most evident, and the most warm and humid conditions generally occur around local insolation maxima corresponding to minima of the precessional index (Fig. 2, left).

At 225 Ma and only $\sim 6^\circ\text{N}$, the twice yearly solar zenith passage yields two annual insolation maxima and weak wet late spring (April–May) and warm late summer (August–September) seasons (Fig. 2, right). As previously suggested (Crowley et al., 1992; Whiteside et al., 2011a), the successive amplification of these two seasons shows up as double-precession peaks, in the maximum insolation and PRC rates, but due to the weak seasonality, the precession effects are smaller than at later time-slices and higher latitudes (Fig. 2, left). Instead, the direct contribution of eccentricity to warmer and wetter conditions is more pronounced (see also Fig. S3).

At 210 Ma and $\sim 13^\circ\text{N}$, the secondary peaks remain visible due to the still broad summer and winter insolation plateaus. Nevertheless, the response to precession is much enhanced (Fig. 2, left), especially at high $p\text{CO}_2$ values. The latter contribute to increased late spring rainfall (Fig. 2g), related to enhanced moisture transport and convergence from the Tethys reaching the NHB area (Fig. S6). In contrast, maximum temperatures and therefore evaporation occur in late summer (Fig. 2g) and are thus maximized later in the precession cycle (Fig. 2c). The late spring rainfall amplification early in the precession cycle (Fig. 2d,h) is therefore not compensated by increased evaporation and leads to a strong $\text{PRC-EVAP}_{\text{NHB}}^{\text{max}}$ response to precession (Fig. 2e,i). This is also expressed by the relative lead of the $\text{PRC}_{\text{NHB}}^{\text{max}}$ and $\text{PRC-EVAP}_{\text{NHB}}^{\text{max}}$ response to the precession index (which peaks at max. June insolation), whereas the temperature response lags behind (Fig. 2, left). Similar relationships were reported by Marzocchi et al. (2015) in the north African monsoon region, which might be the closest modern analogue for this NHB climate setting. Another analogy is a feedback by which heating is limited by increased rainfall and cloud coverage, amplifying humid periods in the seasonal and orbital cycles (Fig. S5; Bosmans et al., 2015a,b; Marzocchi et al., 2015).

By 195 Ma and $\sim 20^\circ\text{N}$, more pronounced summer and winter seasons were established (Fig. 2, right), so that peaks in the response occur closer to precession minima (Fig. 2, left). The amplitudes of the $T_{\text{NHB}}^{\text{max}}$ and $\text{PRC}_{\text{NHB}}^{\text{max}}$ precession response are slightly larger than at 210 Ma due to the enhanced seasonality (Figs. 2, S3). However, the seasonality and orbital response of $\text{PRC-EVAP}_{\text{NHB}}^{\text{max}}$ is actually reduced, because the more closely coinciding temperature and rainfall seasons compensate each other to a larger degree (Fig. 2).

To summarize, substantial precession-eccentricity effects on the low-latitude Newark-Hartford Basin regional climate are observed in the model results, with maximum rainfall and temperatures around the April–June and July–September maximum insolation phases of the precession cycle, respectively. The cyclic changes can exceed 7°C , 3 mm/d and 2 mm/d for maximum T, PRC and PRC–EVAP (Fig. 2, left). For PRC–EVAP, which represents the most direct link to reconstructed lake level cycles, they are most pronounced during the transitional phase from 220 to 200 Ma at high $p\text{CO}_2$ (see also Fig. S3). In earlier and later time-slices they are limited by weak seasonality and increasing aridity, respectively.

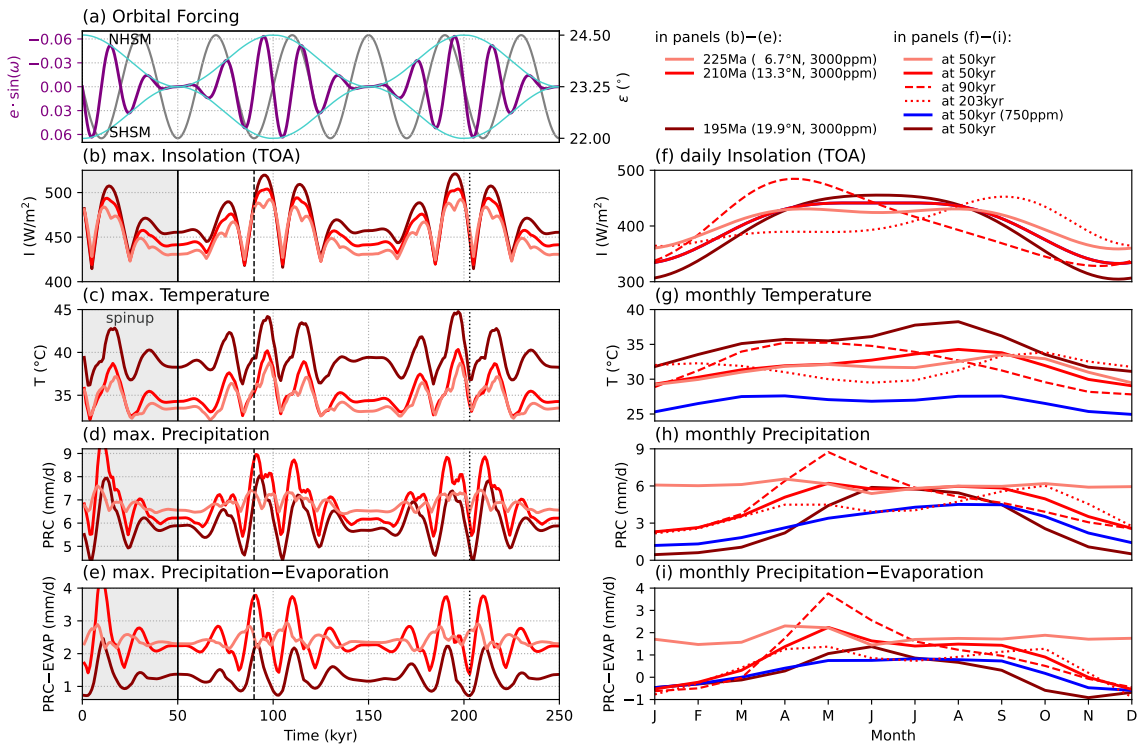


Figure 2: Effect of the imposed orbital forcing on the regional climate conditions in the Newark-Hartford Basin area. (a): Orbital forcing expressed by the precession index $e \cdot \sin(\omega)$ (e : perihelion angle, ω : eccentricity) and obliquity ϵ . The left axis is inverted so that maximum northern hemisphere summer insolation (NHSM) occurs at the top. (b–e): Maximum monthly values of regional climate quantities for three simulations at 225, 210 and 195 Ma (using $p\text{CO}_2=3000$ ppm and the Geo_1 paleogeography). Vertical lines indicate three points in time for which monthly data is shown on the right side. (f–i): Monthly values of the same quantities at minimum ω and ϵ (at 50 kyr; solid lines). Dashed/dotted lines for 210 Ma correspond to times of maximum/minimum PRC–EVAP during a precession cycle at high ω and low ϵ (90 vs. 203 kyr). Blue lines for low $p\text{CO}_2$ (750 ppm) for comparison with high $p\text{CO}_2$ (3000 ppm) at 210 Ma.

3. Net Precipitation Trends, Modulation and Threshold Explain Lake Level Changes

With the understanding of simulated long-term climate trends (Sec. 1) and orbital response (Sec. 2), physical links between the geologic record and modeled changes can be established. The left side of Fig. 3 summarizes relevant Newark-Hartford Basin proxy data, including lake depth levels derived from sediment color and facies (Olsen and Kent, 1996; Kent et al., 2017; Olsen et al., 2019), as well as amplitudes of precession- and eccentricity-scale periodicity in these timeseries (Fig. 3a–e). Proxy data for $p\text{CO}_2$ from the same strata suggest high levels until the early Rhaetian and around the Triassic-Jurassic boundary, but lower values during the Rhaetian–Hettangian and around ~ 211 Ma (Schaller et al. 2011, 2012, as reported in Foster et al. 2017).

For the comparison with climate model results (Fig. 3, right), the simulations with high/medium/low $p\text{CO}_2$ are plotted or highlighted accordingly for each time-slice (Fig. 3i–l). Together they indicate a pathway of NHB mean climate and cyclicity, driven by orbital forcing, continental drift and $p\text{CO}_2$ changes. For this, we mainly consider PRC–EVAP and especially its monthly maximum values above a certain threshold, Fig. 3i), because it has been proposed that lake sediments from the Newark-Hartford Basin and also the Quaternary north African monsoon region actually record a truncated (or clipped, rectified) orbital climate signal in the hydrological balance (e.g. Crowley et al., 1992; Ruddiman, 2008; Anderson, 2011; Hinnov, 2018; Bahr et al., 2020). The reasoning is that lacustrine sediments record orbital changes when the lakes are filled by sufficient summer maximum rainfall at times of higher humidity, whereas they lack obvious sediment facies responses when lakes dry out during other orbital phases (Ruddiman, 2008, Ch. 8). Following this concept, the clipped PRC–EVAP_{NHB}^{max} (regional monthly maximum values, Fig. 3i) and their cyclicity (Fig. 3j,k) show a remarkable consistency with the lake depth proxy record (Fig. 3b–e) when a threshold value of 1.3 mm/d is assumed (Fig. 3i). This link between orbitally paced climate and lake level changes needs to be evaluated and extended in further work, for example by an explicit representation of basin hydrology.

The simulated NHB climate during 230–225 Ma is generally tropical humid and the annual mean and maximum PRC–EVAP remain consistently above the threshold (Fig. 3i) at the high $p\text{CO}_2$ levels suggested by the proxy record (Fig. 3f). The seasonality and the orbital response are small (Fig. 3i–l). This fits to the persistent intermediate depth levels (Fig. 3b) and the low degree of cyclicity (Fig. 3d) expressed by the record in the Stockton Formation. However, all but the upper quarter of this formation is fluvial rather than lacustrine and is therefore less revealing in terms of cyclicity.

Towards 220 Ma, the mean and maximum PRC–EVAP strongly increase and reach their highest levels across all considered time-slices (Fig. 3i). The seasonality and the precession-eccentricity response also show a marked increase (Fig. 3i–k). This could partially explain the upward increase of cyclicity in lacustrine sediments in the upper Stockton Formation and the greatest prevalence of high water depths in the Lockatong Formation (Olsen and Kent, 1996). However, the main cause of this transition could have also been a relative increase of subsidence over accumulation rates. Disentangling climate and sedimentary basin dynamics remains a challenge for further work.

Proceeding to 215 Ma, the seasonality and orbital response increased further, while the mean and maximum PRC–EVAP decreased (Fig. 3i–k). This trend to somewhat drier but more variable conditions matches the lower minimum water depths and strong cyclicity found in the lower Passaic Formation (Fig. 3b–e). This trend continues at 210 Ma both in the model and the record, where Olsen and Kent (1996) noted a decreasing frequency of deep lake deposits, and more frequent red beds (indicative of aridity) through the Passaic Formation. Within the transition from tropical humid to more seasonally arid climate classes, the orbital forcing is also recognized in temporary shifts between e.g. *Af*, *Am* and *Aw* climates (Fig. S9e).

Around the Rhaetian 205 Ma time-slice, proxy $p\text{CO}_2$ values are consistently lower (Fig. 3f) and the PRC–EVAP clipping becomes important: In addition to the general aridification, PRC–EVAP_{NHB}^{max} is significantly

reduced in a cooler climate at $p\text{CO}_2=1500$ ppm so that it only exceeds the threshold occasionally and then only slightly at maximum eccentricity and minimum precession (Fig. 3i). Consequently, the precessional orbital signal in the clipped $\text{PRC-EVAP}_{\text{NHB}}^{\text{max}}$ timeseries is significantly reduced (Fig. 3i-k), despite a strong orbital climate modulation that is, however, also reduced by the lower $p\text{CO}_2$ (Sec. 2). This could explain why the upper Passaic Formation records no deep lakes and muted precessional cyclicity in general (Fig. 3b-e).

In contrast, recorded depth levels and cyclicity are significantly enhanced in the brief interval around the Triassic–Jurassic boundary (~ 201.3 Ma), associated with the emplacement of the massive Central Atlantic Magmatic Province volcanism, also tied to the end-Triassic mass extinction (Marzoli et al., 1999; Blackburn et al., 2013; Landwehrs et al., 2020). The climate simulations show that this could be partly explained by the high $p\text{CO}_2$ levels recorded at this time, because these lift $\text{PRC-EVAP}_{\text{NHB}}^{\text{max}}$ above the threshold so that a stronger cyclic climate modulation could be recorded under the more humid conditions (Fig. 3i-k; Whiteside et al., 2021).

Above the Triassic–Jurassic boundary, the PRC-EVAP seasonality and orbital modulation are reduced in the increasingly dry climate. Additionally, the humidity threshold is barely transgressed at the lower $p\text{CO}_2$ values suggested by the few $p\text{CO}_2$ data points. This trend matches the establishment of dominantly eolian sediments above the sampled part of the Portland Formation, with an absence of lacustrine and cyclic sediments (Kent et al., 2017). As already noted, both climatic and geologic processes have influenced sediment deposition in the NHB (Olsen and Kent, 1996). The replacement of lacustrine by fluvial strata in the upper Portland Formation could be more simply explained by a reduction of subsidence relative to the sediment supply rather than climate alone.

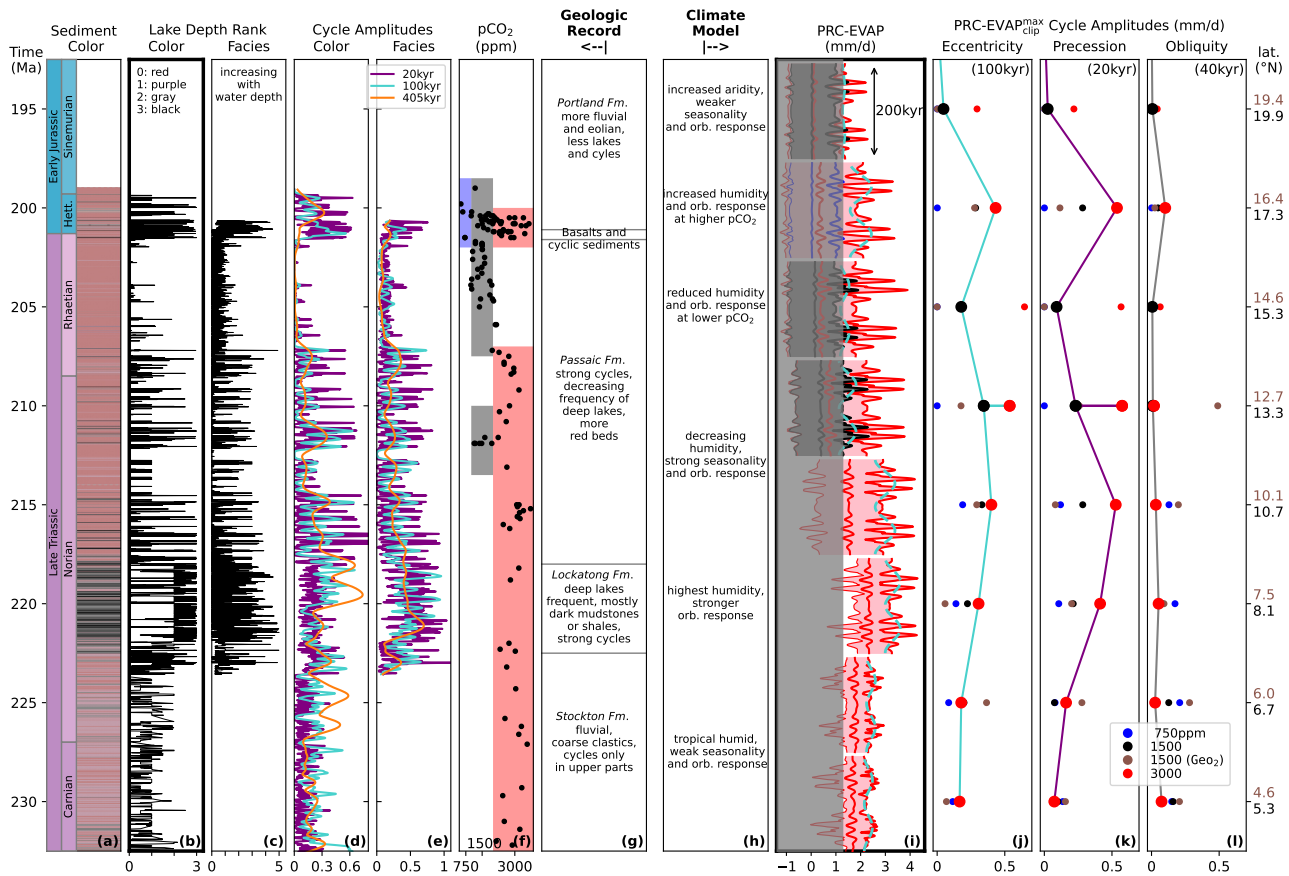


Figure 3: Comparison of the Newark-Hartford Basin geologic lake level record (left) with simulated PRC–EVAP trends and orbital cyclicity (right). (a–c): Sediment color and lake depth levels from the composite record (Kent et al., 2017; Olsen et al., 2019). (d,e): Amplitudes of precession (~20 kyr) and eccentricity cycles (~100 and ~405 kyr) in the depth levels (b,c), obtained from a continuous Morlet wavelet transform (Fig. S9). (f): Proxy $p\text{CO}_2$ from Schaller et al. (2011, 2012) as reported in Foster et al. (2017). Red/gray/blue colors indicate intervals with relatively high/medium/low values. (g,h): Notes regarding characteristics or upwards trends inferred from proxy (Olsen and Kent, 1996; Olsen et al., 1996b; Olsen and Kent, 1999; Kent et al., 2017; Olsen et al., 2019) or model data. (i): Simulated orbitally-driven PRC–EVAP in the NHB area. For each time-slice, max/mean/min values are plotted for a transient 200 kyr simulation at $p\text{CO}_2=3000$ ppm (red), and additionally 1500 or 750 ppm (black/blue) where lower $p\text{CO}_2$ values are suggested by proxy data (f). Turquoise lines indicate the eccentricity component, composed of the direct 100 kyr signal and the amplitude modulation of the 20 kyr precession cycle. The gray area indicates values below the assumed humidity threshold required for persistent lakes. The truncated/clipped PRC–EVAP_{NHB}^{max} timeseries above this threshold are the potentially closest model analogue to the depth levels in (b,c). (j,k,l): Amplitudes of orbital signals in the clipped PRC–EVAP_{NHB}^{max} timeseries in (i), obtained with a Fourier transform. Compare with (d,e). The eccentricity amplitude (j) accounts for both the 100 kyr component and the modulation of precession (turquoise lines in (i)). Each dot represents one transient simulation and bigger/connected dots indicate those which best reflect the proxy $p\text{CO}_2$ changes (f).

4. Low-Latitude Obliquity Signal from Shifting Tropical Rain Belt

Orbital climate cycles in the Newark-Hartford Basin area are generally dominated by precession and eccentricity (Sec. 2). Evidence for obliquity effects had long been scarce (Olsen et al., 2019), as expected from its minimal low-latitude radiative forcing, but was finally detected by recent work (Hinnov and Cozzi, 2021; Margulis-Ohnuma et al., 2021a; Whiteside et al., 2021). This is supported here by a small but consistent obliquity signal in the simulated PRC–EVAP_{NHB}^{max} timeseries, especially during 230–210 Ma (Fig. 3l, S3).

This phenomenon is related to a stronger thermal contrast between summer and winter hemisphere at high obliquity, which amplifies the seasonal shift of the ITCZ (Fig. S8). The stronger northward shift of tropical rainfall during boreal summer supplies additional moisture to the NHB, especially during July–August (Figs. S7, S8). This is analogous to the obliquity effects on the north African monsoon (Bosmans et al., 2015a,b), including feedbacks that actually reduce summer temperatures and increase humidity, as also discussed for the response to precession (Sec. 2).

The obliquity signal in PRC–EVAP_{NHB}^{max} is stronger at low $p\text{CO}_2$ (Fig. 3l), because at high $p\text{CO}_2$ the most humid season occurs in late spring (Sec. 2) and is thus less modulated by the late summer maximum ITCZ deflection (Fig. S7). The regional obliquity signal is also stronger for the Geo_2 paleogeographies (Fig. 3l), potentially related to the globally larger extent of landmasses (Fig. S1), and the further inland position of the NHB. However, the basic effect is consistent across all simulations (Fig. S8b). In fact, the observed obliquity signal appears nearly as strong as that of precession in the upper Passaic Formation (Margulis-Ohnuma et al., 2021b), the interval with the lowest $p\text{CO}_2$.

To conclude, all three orbital parameters can increase NHB maximum humidity through elevated northern hemisphere insolation. The Carnian–Norian low-latitude obliquity signal reflects the response of the global circulation and the low-latitude hydrological regime to a high-latitude radiative forcing. As the NHB shifts northwards, this indirect effect decays, but the direct insolation forcing appears in the regional temperatures (Figs. 3l, S3). In contrast, precession and eccentricity yield a local radiative forcing without interhemispheric asymmetry that rather enhances the land-sea thermal contrast and moisture import from the Tethys (Fig. S5).

5. Patterns of Orbital Climate Response Revealed by Other Proxy Localities

Our modeling approach can provide a global framework in which significant Late Triassic records (Olsen and Kent, 2000; Tamber, 2010; Olsen et al., 2019) mutually support the interpretation particularly of the differential climatic expression of astronomical pacing and paleogeographic shifts. Sophisticated analyses of these records are beyond the scope of this paper, but some insights suggest directions for future work.

For example, similar concepts for cyclic lake sediment deposition have been invoked for the Upper Triassic of the Germanic Basin (Vollmer et al., 2008; Bahr et al., 2020). In our model, this area receives significant summer rainfall from the Tethys (Fig. 1) and eccentricity-modulated precession dominates the T and PRC seasonality response around 225 Ma, with maxima at insolation peaks (also see Figs. S10–S13). The modeled obliquity signal is very small, but increases with the northward drift, which could explain its occurrence in younger parts of the basin (Bahr et al., 2020).

A strong obliquity-scale pacing was inferred from fluvial-lacustrine sequences in the high-latitude Junggar Basin (~ 200 Ma, $\sim 70^\circ\text{N}$; Sha et al., 2015; Olsen et al., 2019). A similarly strong response to obliquity and precession in the simulated T and PRC–EVAP supports this interpretation (see also Figs. S14–S17). In contrast to the discussed lower latitude localities, enhanced local insolation leads to drier conditions and the

PRC orbital response remains relatively small, suggesting a greater role of T and EVAP variations for the hydrological balance and cyclic lake sedimentation.

Proxy data from the Colorado Plateau (Dubiel and Hasiotis, 2011; Nordt et al., 2015) suggest an aridification through the Late Triassic (Lepre and Olsen, 2021). The simulated regional conditions do indeed shift from tropical humid to desert climate between 220 and 205 Ma, with PRC^{ann} decreasing from 1235 to 640 mm/yr while temperature averages and seasonality increase (also see Figs. S18–S21). The small northward shift ($\sim 4^\circ$) is apparently sufficient to leave the narrow tropical rain belt of western Pangea (Figs. 1, S18). While proxy cyclicity is being assessed (Lepre et al., 2021), the simulations for the relevant time-slices suggest that obliquity dominates the PRC and PRC–EVAP response through the discussed effect on ITCZ migration (Sec. 4). In contrast, the T response is dominated by eccentricity and an increasing precession component due to the northward drift, similar to the Newark Basin. This is a testable prediction for cores with climate proxy data and geochronology available for that area and time-slice.

Conclusions

The climate model results presented here show that major features of the lake level record of the Newark-Hartford Basins can be understood through the combined climatic effects of orbital forcing, paleogeographic changes (especially the northward drift of Pangea) and atmospheric $p\text{CO}_2$ variations.

Tropical humid conditions with weak seasonality and orbital response prevail in the NHB area during the 230–225 Ma time-slices ($\sim 5\text{--}7^\circ\text{N}$). Around 220 Ma ($\sim 8^\circ\text{N}$), a humidity maximum is reached and the orbital signal increases, coinciding with the deepest and consistently cyclical lake levels. From 215 to 205 Ma ($\sim 10\text{--}15^\circ\text{N}$), a shift from humid to drier and more seasonal monsoon and savanna climates matches the trend to less frequent deep-water lake deposits and more frequent aridity-related red beds. Although orbital climate modulation is high during the Rhaetian (~ 205 Ma), the record exhibits low lake levels and cyclicity. We show that this could be the result of a cooler, drier climate due to low atmospheric $p\text{CO}_2$ and a threshold characteristic of lake filling and sedimentation. Around the Triassic-Jurassic boundary (~ 200 Ma, $\sim 17^\circ\text{N}$), CAMP volcanic emissions caused temporarily elevated $p\text{CO}_2$ levels that contribute to enhanced humidity and cyclicity in the model, supporting empirical findings. After 195 Ma ($\geq 20^\circ\text{N}$), semi-arid climates with reduced seasonality and orbital response are established and intensified by lower $p\text{CO}_2$. This is mirrored by the onset of muted lake level variability and possibly replacement by fluvial and eolian environments.

Our simulations extend evidence for a strong response of tropical Pangean climates to astronomical forcings, despite or even because of a warm and ice-free greenhouse world. In spite of the primary role of precession and eccentricity, obliquity is found to affect low-latitude hydrological regimes by modulating the seasonal shift of the tropical rainfall belt.

Extending this global model framework and data to other contemporaneous records yields a more complete picture of Late Triassic climate trends and orbital forcing. For example, in both the Colorado Plateau and Junggar Basin, humidity regimes appear more prone to obliquity than in the NHB because of either ITCZ rainfall (Colorado Plateau) or high-latitude radiative forcing (Junggar Basin). Furthermore, the fast CLIMBER-X Earth System Model (Willeit et al., 2022) utilized here provides enhanced opportunities for future studies on the role of carbon cycle and ice sheet feedbacks in shaping astronomical climate dynamics in various paleoclimatic contexts.

Methods

Model Description: All simulations were conducted with CLIMBER-X (Willeit et al., 2022) which is a comprehensive Earth System Model of Intermediate Complexity (EMIC), designed to simulate the evolution of the Earth system on decadal to orbital time scales. In this study, the coupled statistical-dynamical atmosphere (SESAM, Willeit et al., 2022), 3D frictional-geostrophic ocean (GOLDSTEIN, Edwards and Marsh, 2005), dynamic-thermodynamic sea-ice (SISIM, Willeit et al., 2022), land-surface and vegetation modules (PALADYN, Willeit and Ganopolski, 2016) are used and run on a $5^\circ \times 5^\circ$ horizontal grid. Predecessors of the model have been applied to study orbital climate dynamics in the Neogene and Quaternary, for example regarding glacial cycles (Willeit et al., 2019) or the African monsoon (de Boer et al., 2021).

Boundary Conditions: An ensemble of 36 climate simulations was performed, representing a set of 9 geological time-slices from 230 to 190 Ma in 5 Myr steps with paleogeographies based on reconstructions by Marcilly et al. (2021) (Geo_1) and Cao et al. (2017) (Geo_2). Both distinguish qualitatively between exposed land, shallow marine and deep marine areas, and Cao et al. (2017) additionally represent major mountain ranges (see SI for further information). Unless otherwise indicated, we refer to the simulations with Geo_1 . Simulations were conducted for atmospheric CO_2 concentrations fixed at 750, 1500 or 3000 ppm with Geo_1 , and 1500 ppm with Geo_2 . This is to assess differences between overall warmer and cooler climate states, considering the temporal variation and uncertainty of $p\text{CO}_2$ reconstructions for that time period as compiled by Foster et al. (2017), which includes measurements on paleosol carbonates from the Newark and Hartford Basins (Schaller et al., 2015, Fig. 3f). The solar constant was set according to standard solar evolution (Bahcall et al., 2001) relative to its present-day value of 1361 W/m^2 (Kopp and Lean, 2011) and increases from 1335.4 W/m^2 at 230 Ma to 1339.8 W/m^2 at 190 Ma.

Forcings: The simulations were run for 250 000 model years and exposed to an orbital forcing that cyclically modulates the orbital parameters eccentricity (e), longitude of the perihelion (precession angle ω) and obliquity (axial tilt ε ; Fig. 2a). As the purpose of this study is to investigate general effects of these parameters rather than evaluating specific astronomical solutions, the idealized forcing contains only three periodicities (similar to Horton et al., 2012): 100 kyr, 40 kyr and 20 kyr representing the ~ 100 kyr short orbital eccentricity cycle, the 41 kyr obliquity cycle and the 19 to 23 kyr climatic precession band in today’s solar system.

Running and Analyzing the Model Simulations: The fastest external change in the simulations is the precession cycle that acts on a ~ 10 kyr time-scale. This exceeds the general response time of surface climate conditions that are analyzed here and allows a climate model iteration for updated boundary conditions to be run every 5 years, ideally resulting in a $5 \times$ model acceleration. This is similar to approaches achieving transient climate simulations on 100 kyr timescales for the Quaternary (Kutzbach et al., 2008, 2020; Tigchelaar et al., 2018). Only the final 200 kyr of the simulations were used here for analyses, while the first 50 kyr are considered as a spin-up period (effectively corresponding to 10 000 model years, considering the $5 \times$ acceleration). In the stratigraphic terminology of the Newark-Hartford Basin record, the simulated timeseries each reflect ten “Van Houten” and two “short modulating” cycles each (Olsen et al., 1996b). Although the model provides global climate information, this study focuses particularly on regional conditions relevant for the deposition of the Newark-Hartford Basin sediment record. Therefore, model output was averaged over a radius of 600 km around the reconstructed central location (Tab. S1), which is indicated by circles in all of the maps (e.g. Fig. 1). This corresponds to the approximate equatorial model grid cell size and also reflects the extent of the basins catchment area as well as uncertain paleogeographic and depositional settings which all prevent more confined local assessment.

Data Availability

Model input and output files for all simulations as well as the scripts to generate the figures are available at the institutional repository of the Potsdam Institute for Climate Impact Research (Landwehrs et al., 2022b, <https://dx.doi.org/10.5880/PIK.2022.001/>). The CLIMBER-X model is described in Willeit et al. (2022) and its source code is archived at <https://doi.org/10.5281/zenodo.6301052>.

Until acceptance of this manuscript, the data archive can be accessed through this preliminary URL:

<https://dataservices.gfz-potsdam.de/panmetaworks/review/cb1b5d9038f4d2f9d59834787e58d571a3538880781056495c03439c46ca0a40-pik/>

Acknowledgments

We would like to thank C. M. Marcilly and W. Cao and colleagues for making their paleogeographic models available. The European Regional Development Fund (ERDF), the German Federal Ministry of Education and Research and the Land Brandenburg are gratefully acknowledged for supporting this project by providing resources on the high performance computer system at the Potsdam Institute for Climate Impact Research. M.Wa. acknowledges support by the Austrian Academy of Sciences, International Programs, in the frame of UNESCO-IGCP 661.

Author Contributions

J.L., G.F., M.Wa., M.Wi., J.H.W. and P.E.O. designed research; J.L. performed research; M.Wi. provided analytic tools; J.L. analyzed data; J.L., G.F., M.Wi., S.P., B.S., M.Wa., J.H.W. and P.E.O. wrote the paper.

The authors declare that they have no conflict of interest.

References

- Anderson, R.Y., 2011. Enhanced climate variability in the tropics: a 200 000 yr annual record of monsoon variability from Pangea's equator. *Climate of the Past* 7, 757–770. doi:[10.5194/cp-7-757-2011](https://doi.org/10.5194/cp-7-757-2011).
- Bahcall, J.N., Pinsonneault, M.H., Basu, S., 2001. Solar Models: Current Epoch and Time Dependences, Neutrinos, and Helioseismological Properties. *The Astrophysical Journal* 555, 990–1012. doi:[10.1086/321493](https://doi.org/10.1086/321493).
- Bahr, A., Kolber, G., Kaboth-Bahr, S., Reinhardt, L., Friedrich, O., Pross, J., 2020. Mega-monsoon variability during the late Triassic: Re-assessing the role of orbital forcing in the deposition of playa sediments in the Germanic Basin. *Sedimentology* 67, 951–970. doi:[10.1111/sed.12668](https://doi.org/10.1111/sed.12668).
- Beck, H.E., Zimmermann, N.E., McVicar, T.R., Vergopolan, N., Berg, A., Wood, E.F., 2018. Present and future Koppen-Geiger climate classification maps at 1-km resolution. *Scientific Data* 5. doi:[10.1038/sdata.2018.214](https://doi.org/10.1038/sdata.2018.214).
- Berger, A., Yin, Q., 2012. Astronomical Theory and Orbital Forcing, in: Matthews, J. (Ed.), *The SAGE Handbook of Environmental Change*. SAGE Publications Ltd. volume 1. chapter 19, pp. 405–425. doi:[10.4135/9781446253045](https://doi.org/10.4135/9781446253045).
- Blackburn, T.J., Olsen, P.E., Bowring, S.A., McLean, N.M., Kent, D.V., Puffer, J., McHone, G., Rasbury, E.T., Et-Touhami, M., 2013. Zircon U-Pb Geochronology Links the End-Triassic Extinction with the Central Atlantic Magmatic Province. *Science* 340, 941–945. doi:[10.1126/science.1234204](https://doi.org/10.1126/science.1234204).
- de Boer, B., Peters, M., Lourens, L.J., 2021. The transient impact of the African monsoon on Plio-Pleistocene Mediterranean sediments. *Climate of the Past* 17, 331–344. doi:[10.5194/cp-17-331-2021](https://doi.org/10.5194/cp-17-331-2021).
- Bosmans, J.H.C., Drijfhout, S.S., Tuenter, E., Hilgen, F.J., Lourens, L.J., 2015a. Response of the North African summer monsoon to precession and obliquity forcings in the EC-Earth GCM. *Climate Dynamics* 44, 279–297. doi:[10.1007/s00382-014-2260-z](https://doi.org/10.1007/s00382-014-2260-z).
- Bosmans, J.H.C., Hilgen, F.J., Tuenter, E., Lourens, L.J., 2015b. Obliquity forcing of low-latitude climate. *Climate of the Past* 11, 1335–1346. doi:[10.5194/cp-11-1335-2015](https://doi.org/10.5194/cp-11-1335-2015).

- Brugger, J., Hofmann, M., Petri, S., Feulner, G., 2019. On the Sensitivity of the Devonian Climate to Continental Configuration, Vegetation Cover, Orbital Configuration, CO₂ Concentration, and Insolation. *Paleoceanography and Paleoclimatology* 34, 1375–1398. doi:[10.1029/2019PA003562](https://doi.org/10.1029/2019PA003562).
- Cao, W., Williams, S., Flament, N., Zahirovic, S., Scotese, C.R., Müller, R.D., 2018. Palaeolatitudinal distribution of lithologic indicators of climate in a palaeogeographic framework. *Geological Magazine* 156, 331–354. doi:[10.1017/S0016756818000110](https://doi.org/10.1017/S0016756818000110).
- Cao, W., Zahirovic, S., Flament, N., Williams, S., Golonka, J., Mueller, R.D., 2017. Improving global paleogeography since the late Paleozoic using paleobiology. *Biogeosciences* 14, 5425–5439. doi:[10.5194/bg-14-5425-2017](https://doi.org/10.5194/bg-14-5425-2017).
- Crowley, T.J., Kim, K.Y., Mengel, J.G., Short, D.A., 1992. Modeling 100,000-Year Climate Fluctuations in Pre-Pleistocene Time Series. *Science* 255, 705–707. doi:[10.1126/science.255.5045.705](https://doi.org/10.1126/science.255.5045.705).
- Dubiel, R.F., Hasiotis, S.T., 2011. Deposystems, Paleosols, and Climatic Variability in a Continental System: The Upper Triassic Chinle Formation, Colorado Plateau, U.S.A., in: *From River to Rock Record: The preservation of fluvial sediments and their subsequent interpretation*. SEPM Society for Sedimentary Geology. doi:[10.2110/sepmsp.097.393](https://doi.org/10.2110/sepmsp.097.393).
- Edwards, N.R., Marsh, R., 2005. Uncertainties due to transport-parameter sensitivity in an efficient 3-D ocean-climate model. *Climate Dynamics* 24, 415–433. doi:[10.1007/s00382-004-0508-8](https://doi.org/10.1007/s00382-004-0508-8).
- Feulner, G., 2017. Formation of most of our coal brought Earth close to global glaciation. *Proceedings of the National Academy of Sciences* 114, 11333–11337. doi:[10.1073/pnas.1712062114](https://doi.org/10.1073/pnas.1712062114).
- Foster, G.L., Royer, D.L., Lunt, D.J., 2017. Future climate forcing potentially without precedent in the last 420 million years. *Nature Communications* 8, 1–8. doi:[10.1038/ncomms14845](https://doi.org/10.1038/ncomms14845).
- Hays, J.D., Imbrie, J., Shackleton, N.J., 1976. Variations in the Earth's Orbit: Pacemaker of the Ice Ages. *Science* 194, 1121–1132. doi:[10.1126/science.194.4270.1121](https://doi.org/10.1126/science.194.4270.1121).
- Hinnov, L., Cozzi, A., 2021. Rhaetian (Late Triassic) Milankovitch Cycles in the Tethyan Dachstein Limestone and Laurentian Passaic Formation Linked by the g₂-g₅ Astronomical Metronome. *Boletín Geológico y Minero* 31, 269–290. doi:[10.21701/bolgeomin.131.2.004](https://doi.org/10.21701/bolgeomin.131.2.004).
- Hinnov, L.A., 2018. Cyclostratigraphy and Astrochronology in 2018, in: Montenari, M. (Ed.), *Cyclostratigraphy and Astrochronology*. Academic Press. volume 3 of *Stratigraphy & Timescales*. chapter 1, pp. 1–80. doi:[10.1016/bs.sats.2018.08.004](https://doi.org/10.1016/bs.sats.2018.08.004).
- Horton, D.E., Poulsen, C.J., Montañez, I.P., DiMichele, W.A., 2012. Eccentricity-paced late Paleozoic climate change. *Palaeogeography, Palaeoclimatology, Palaeoecology* 331–332, 150–161. doi:[10.1016/j.palaeo.2012.03.014](https://doi.org/10.1016/j.palaeo.2012.03.014).
- Horton, D.E., Poulsen, C.J., Pollard, D., 2010. Influence of high-latitude vegetation feedbacks on late Palaeozoic glacial cycles. *Nature Geoscience* 3, 572–577. doi:[10.1038/ngeo922](https://doi.org/10.1038/ngeo922).
- Kent, D.V., Olsen, P.E., Muttoni, G., 2017. Astrochronostratigraphic polarity time scale (APTS) for the Late Triassic and Early Jurassic from continental sediments and correlation with standard marine stages. *Earth-Science Reviews* 166, 153–180. doi:[10.1016/j.earscirev.2016.12.014](https://doi.org/10.1016/j.earscirev.2016.12.014).
- Kopp, G., Lean, J.L., 2011. A new, lower value of total solar irradiance: Evidence and climate significance. *Geophysical Research Letters* 38, 1–7. doi:[10.1029/2010GL045777](https://doi.org/10.1029/2010GL045777).
- Kutzbach, J.E., 1994. Idealized Pangean Climates - Sensitivity to Orbital Change, in: Klein, G.D. (Ed.), *Pangea: Paleoclimate, Tectonics, and Sedimentation during Accretion, Zenith and Breakup of a Supercontinent*, pp. 41–55. doi:[10.1130/SPE288-p41](https://doi.org/10.1130/SPE288-p41).
- Kutzbach, J.E., Guan, J., He, F., Cohen, A.S., Orland, I.J., Chen, G., 2020. African climate response to orbital and glacial forcing in 140,000-y simulation with implications for early modern human environments. *Proceedings of the National Academy of Sciences* 117, 2255–2264. doi:[10.1073/pnas.1917673117](https://doi.org/10.1073/pnas.1917673117).
- Kutzbach, J.E., Liu, X., Liu, Z., Chen, G., 2008. Simulation of the evolutionary response of global summer monsoons to orbital forcing over the past 280,000 years. *Climate Dynamics* 30, 567–579. doi:[10.1007/s00382-007-0308-z](https://doi.org/10.1007/s00382-007-0308-z).
- Landwehrs, J., Feulner, G., Hofmann, M., Petri, S., 2020. Climatic fluctuations modeled for carbon and sulfur emissions from end-Triassic volcanism. *Earth and Planetary Science Letters* 537, 116174. doi:[10.1016/j.epsl.2020.116174](https://doi.org/10.1016/j.epsl.2020.116174).
- Landwehrs, J., Feulner, G., Petri, S., Sames, B., Wagreich, M., 2021. Investigating Mesozoic Climate Trends and Sensitivities With a Large Ensemble of Climate Model Simulations. *Paleoceanography and Paleoclimatology* 36, e2020PA004134. doi:[10.1029/2020PA004134](https://doi.org/10.1029/2020PA004134).
- Landwehrs, J., Feulner, G., Willeit, M., Petri, S., Sames, B., Wagreich, M., Whiteside, J.H., Olsen, P.E., 2022b. Data from Climate Model Simulations for Triassic–Jurassic Orbital Climate Cycles doi:[10.5880/pik.2022.001](https://doi.org/10.5880/pik.2022.001).
- Lepre, C., Yazzie, O., Olsen, P., 2021. Orbital pacing of redox cycles suggested by red bed color of the Late Triassic Chinle Formation, Arizona, in: *EGU General Assembly Conference Abstracts*, pp. EGU21–3696. doi:[10.5194/egusphere-egu21-3696](https://doi.org/10.5194/egusphere-egu21-3696).
- Lepre, C.J., Olsen, P.E., 2021. Hematite reconstruction of Late Triassic hydroclimate over the Colorado Plateau. *Proceedings of the National Academy of Sciences* 118. doi:[10.1073/pnas.2004343118](https://doi.org/10.1073/pnas.2004343118).
- Marcilly, C.M., Torsvik, T.H., Domeier, M., Royer, D.L., 2021. New paleogeographic and degassing parameters for long-term carbon cycle models. *Gondwana Research* 97, 176–203. doi:[10.1016/j.gr.2021.05.016](https://doi.org/10.1016/j.gr.2021.05.016).
- Margulis-Ohnuma, M., Whiteside, J., Olsen, P., 2021a. Strong inclination pacing of climate in Late Triassic low latitudes revealed by the Earth-Saturn tilt cycle. *The Yale Undergraduate Research Journal* 2, 37. URL: <https://elischolar.library.yale.edu/yurj/vol2/iss1/37>.
- Margulis-Ohnuma, M., Whiteside, J., Olsen, P., 2021b. Strong inclination pacing of climate in Late Triassic low latitudes revealed by the Earth-Saturn tilt cycle, in: *EGU General Assembly Conference Abstracts*, pp. EGU21–6638. doi:[10.5194/egusphere-egu21-6638](https://doi.org/10.5194/egusphere-egu21-6638).
- Marzocchi, A., Lunt, D.J., Flecker, R., Bradshaw, C.D., Farnsworth, A., Hilgen, F.J., 2015. Orbital control on late Miocene climate and the North African monsoon: insight from an ensemble of sub-precessional simulations. *Climate of the Past* 11, 1271–1295. doi:[10.5194/cp-11-1271-2015](https://doi.org/10.5194/cp-11-1271-2015).

- Marzoli, A., Renne, P.R., Piccirillo, E.M., Ernesto, M., Bellieni, G., Min, A.D., 1999. Extensive 200-Million-Year-Old Continental Flood Basalts of the Central Atlantic Magmatic Province. *Science* 284, 616–618. doi:[10.1126/science.284.5414.616](https://doi.org/10.1126/science.284.5414.616).
- Milankovitch, M., 1941. Kanon der Erdbestrahlung und seine Anwendung auf das Eiszeitenproblem. Royal Serbian Academy Special Publication 133, 1–633.
- Nordt, L., Atchley, S., Dworkin, S., 2015. Collapse of the Late Triassic megamonsoon in western equatorial Pangea, present-day American Southwest. *Geological Society of America Bulletin* 127, 1798–1815. doi:[10.1130/B31186.1](https://doi.org/10.1130/B31186.1).
- Olsen, P.E., 1986. A 40-Million-Year Lake Record of Early Mesozoic Orbital Climatic Forcing. *Science* 234, 842–848. doi:[10.1126/science.234.4778.842](https://doi.org/10.1126/science.234.4778.842).
- Olsen, P.E., Kent, D.V., 1990. Continental coring of the Newark Rift. *Eos, Transactions American Geophysical Union* 71, 385–394. doi:[10.1029/E0071i015p00385-02](https://doi.org/10.1029/E0071i015p00385-02).
- Olsen, P.E., Kent, D.V., 1996. Milankovitch climate forcing in the tropics of Pangaea during the Late Triassic. *Palaeogeography, Palaeoclimatology, Palaeoecology* 122, 1–26. doi:[10.1016/0031-0182\(95\)00171-9](https://doi.org/10.1016/0031-0182(95)00171-9).
- Olsen, P.E., Kent, D.V., 1999. Long-period Milankovitch cycles from the Late Triassic and Early Jurassic of eastern North America and their implications for the calibration of the Early Mesozoic time-scale and the long-term behaviour of the planets. *Philosophical Transactions of the Royal Society of London. Series A: Mathematical, Physical and Engineering Sciences* 357, 1761–1786. doi:[10.1098/rsta.1999.0400](https://doi.org/10.1098/rsta.1999.0400).
- Olsen, P.E., Kent, D.V., 2000. High-resolution Early Mesozoic Pangean climatic transect in lacustrine environments. *Zbl. Geol. Paläontol. Teil I*, 1475–1496. doi:[10.7916/D8BC47XF](https://doi.org/10.7916/D8BC47XF).
- Olsen, P.E., Kent, D.V., Cornet, B., Witte, W.K., Schlische, R.W., 1996b. High-resolution stratigraphy of the Newark rift basin (early Mesozoic, eastern North America). *GSA Bulletin* 108, 40–77. doi:[10.1130/0016-7606\(1996\)108<0040:HRSTN>2.3.CO;2](https://doi.org/10.1130/0016-7606(1996)108<0040:HRSTN>2.3.CO;2).
- Olsen, P.E., Laskar, J., Kent, D.V., Kinney, S.T., Reynolds, D.J., Sha, J., Whiteside, J.H., 2019. Mapping Solar System chaos with the Geological Orrery. *Proceedings of the National Academy of Sciences* 116, 10664–10673. doi:[10.1073/pnas.1813901116](https://doi.org/10.1073/pnas.1813901116).
- Ruddiman, W., 2008. *Earth's Climate: Past and Future*. 2nd ed., W. H. Freeman and Company.
- Schaller, M.F., Wright, J.D., Kent, D.V., 2011. Atmospheric pCO₂ perturbations associated with the Central Atlantic Magmatic Province. *Science* 331, 1404–1409. doi:[10.1126/science.1199011](https://doi.org/10.1126/science.1199011).
- Schaller, M.F., Wright, J.D., Kent, D.V., 2015. A 30 Myr record of Late Triassic atmospheric pCO₂ variation reflects a fundamental control of the carbon cycle by changes in continental weathering. *GSA Bulletin* 127, 661–671. doi:[10.1130/B31107.1](https://doi.org/10.1130/B31107.1).
- Schaller, M.F., Wright, J.D., Kent, D.V., Olsen, P.E., 2012. Rapid emplacement of the Central Atlantic Magmatic Province as a net sink for CO₂. *Earth and Planetary Science Letters* 323–324, 27–39. doi:[10.1016/j.epsl.2011.12.028](https://doi.org/10.1016/j.epsl.2011.12.028).
- Sha, J., Olsen, P.E., Pan, Y., Xu, D., Wang, Y., Zhang, X., Yao, X., Vajda, V., 2015. Triassic–Jurassic climate in continental high-latitude Asia was dominated by obliquity-paced variations (Junggar Basin, Ürümqi, China). *Proceedings of the National Academy of Sciences* 112, 3624–3629. doi:[10.1073/pnas.1501137112](https://doi.org/10.1073/pnas.1501137112).
- Tanner, L.H., 2010. Cyclostratigraphic record of the Triassic: a critical examination. *Geological Society, London, Special Publications* 334, 119–137. doi:[10.1144/SP334.6](https://doi.org/10.1144/SP334.6).
- Tigchelaar, M., Timmermann, A., Pollard, D., Friedrich, T., Heinemann, M., 2018. Local insolation changes enhance Antarctic interglacials: Insights from an 800,000-year ice sheet simulation with transient climate forcing. *Earth and Planetary Science Letters* 495, 69–78. doi:[10.1016/j.epsl.2018.05.004](https://doi.org/10.1016/j.epsl.2018.05.004).
- Valdes, P.J., Sellwood, B.W., Price, G.D., 1995. Modelling Late Jurassic Milankovitch climate variations. *Geological Society, London, Special Publications* 85, 115–132. doi:[10.1144/GSL.SP.1995.085.01.07](https://doi.org/10.1144/GSL.SP.1995.085.01.07).
- Vollmer, T., Werner, R., Weber, M., Tougiannidis, N., Röhlhng, H.G., Hambach, U., 2008. Orbital control on Upper Triassic Playa cycles of the Steinmergel-Keuper (Norian): A new concept for ancient playa cycles. *Palaeogeography, Palaeoclimatology, Palaeoecology* 267, 1–16. doi:[10.1016/j.palaeo.2007.12.017](https://doi.org/10.1016/j.palaeo.2007.12.017).
- Whiteside, J., Schaller, M., Olsen, P., Margulis-Ohnuma, M., Yager, J., 2021. An Overture to the Anthropocene: Isotopic Evidence of Strong CO₂ Modulation of the Tropical Monsoon at the Dawn of Dinosaurs. *Conference Proceedings, 30th International Meeting on Organic Geochemistry (IMOG 2021)* 2021, 1–2. doi:[10.3997/2214-4609.202134243](https://doi.org/10.3997/2214-4609.202134243).
- Whiteside, J.H., Grogan, D.S., Olsen, P.E., Kent, D.V., 2011a. Climatically driven biogeographic provinces of Late Triassic tropical Pangea. *Proceedings of the National Academy of Sciences* 108, 8972–8977. doi:[10.1073/pnas.1102473108](https://doi.org/10.1073/pnas.1102473108).
- Willeit, M., Ganopolski, A., 2016. Paladyn v1.0, a comprehensive land surface–vegetation–carbon cycle model of intermediate complexity. *Geoscientific Model Development* 9, 3817–3857. doi:[10.5194/gmd-9-3817-2016](https://doi.org/10.5194/gmd-9-3817-2016).
- Willeit, M., Ganopolski, A., Calov, R., Brovkin, V., 2019. Mid-Pleistocene transition in glacial cycles explained by declining CO₂ and regolith removal. *Science Advances* 5. doi:[10.1126/sciadv.aav7337](https://doi.org/10.1126/sciadv.aav7337).
- Willeit, M., Ganopolski, A., Robinson, A., Edwards, N.R., 2022. The Earth system model CLIMBER-X v1.0. Part 1: climate model description and validation. *Geoscientific Model Development Discussions* 2022, 1–69. doi:[10.5194/gmd-2022-56](https://doi.org/10.5194/gmd-2022-56).

P.III Climatic Fluctuations Modeled for Carbon and Sulfur Emissions from end-Triassic Volcanism

Bibliographic Information

Landwehrs, J., Feulner, G., Hofmann, M. and Petri, S. (2020), “Climatic Fluctuations Modeled for Carbon and Sulfur Emissions from end-Triassic Volcanism”, doi:10.1016/j.epsl.2020.116174, *Earth and Planetary Science Letters* 537, 116174.

Accompanying Data Publication:

Landwehrs, J., Feulner, G., Hofmann, M., Petri, S. (2020), “Model Output for the Publication: Climatic Fluctuations Modeled for Carbon and Sulfur Emissions from end-Triassic Volcanism”, doi:10.5880/PIK.2020.002, *GFZ Data Services*.

Copyright Notice

©2020 Elsevier B.V. All rights reserved. This is the published version of the article. Authors have the permission to include their articles in a dissertation, according to the guidelines of the publisher.



Contents lists available at ScienceDirect

Earth and Planetary Science Letters

www.elsevier.com/locate/epsl



Climatic fluctuations modeled for carbon and sulfur emissions from end-Triassic volcanism

Jan Philip Landwehrs^{a,b,*}, Georg Feulner^{b,*}, Matthias Hofmann^b, Stefan Petri^b^a Department of Geodynamics and Sedimentology, University of Vienna, Althanstraße 14, 1090, Vienna, Austria^b Earth System Analysis, Potsdam Institute for Climate Impact Research, Member of the Leibniz Association, P.O. Box 601203, D-14412, Potsdam, Germany

ARTICLE INFO

Article history:

Received 23 July 2019

Received in revised form 7 February 2020

Accepted 19 February 2020

Available online 28 February 2020

Editor: T.A. Mather

Dataset link:

<http://doi.org/10.5880/PIK.2020.002>

Keywords:

Central Atlantic Magmatic Province

volcanic climate impacts

end-Triassic extinction

paleoclimate

Earth System modeling

ABSTRACT

Throughout the history of complex life, Earth's climate and biogeochemical cycles have been perturbed by Large Igneous Province (LIP) volcanism, with several LIP episodes correlating with major mass extinction events. Yet many aspects of the interplay between geological, climatic and ecological processes in the Earth System during these times of global upheaval remain poorly understood. This study focuses on the Central Atlantic Magmatic Province and the associated extinction event in the latest Triassic, about 201 million years ago. Although climate and carbon cycle models successfully reproduce aspects of the end-Triassic environmental changes, many questions regarding the causal and temporal relations behind them remain unresolved. Here, we report an effort to model and quantify the dynamic response of the Earth System to short pulses of volcanogenic volatile emissions for an ensemble of emission scenarios. For the first time in the context of the end-Triassic events, this is done with a coupled climate model and under consideration of both carbon and sulfur emissions. Tested are pulses with $\sim 1\text{--}6$ kyr duration during which 2500–7500 GtC are emitted and 0–500 GtS form stratospheric sulfate aerosols. The simultaneous emission of carbon and sulfur during one pulse of volcanic activity causes climatic fluctuations on annual to millennial timescales: A sequence of transient global cooling and subsequent sustained warming, overprinted with high interannual variability. The simulated maximum global warming ranges from +1.8 to +4.4 °C, while the amplitude of cooling is considerably higher in the upper range of the tested sulfur emission scenarios. The magnitude of temperature change varies regionally, being lowest in the Tethys realm. Changes in steric sea level ($\sim 1\text{--}3$ m) and ocean overturning strength, a surface ocean pH decrease ($\sim 0.2\text{--}0.4$) and a drop of the carbonate saturation especially in the Tethys are also obtained from the simulations during each emission pulse. By evaluating the simulated temperature changes against thermal tolerance limits of stony corals in a simplified manner, we find that these are not clearly transgressed on a global scale in the simulated warming scenarios. However, the climatic variability potentially introduced by the volcanic forcing would have represented significant stress for marine organisms. This study represents a significant step towards integrating multiple volcanic forcing mechanisms and environmental response processes in space and time to yield a more complete picture of impacts of CAMP volcanism and LIPs in general.

© 2020 Elsevier B.V. All rights reserved.

1. Introduction

During the Mesozoic era ($\sim 251.9\text{--}66$ Ma, Cohen et al. 2013), Earth moved towards a modern state, experiencing the breakup of supercontinent Pangaea and important evolutionary steps of dinosaurs, mammals, angiosperms, corals and pelagic calcifiers. Prominent extinction events punctuated this development and at

least those around the Permian-Triassic and the Triassic-Jurassic boundaries coincided with Large Igneous Province (LIP) volcanism (van de Schootbrugge and Wignall, 2015). The Central Atlantic Magmatic Province (CAMP), one of the most extensive LIPs, was emplaced in the center of Pangaea where the Atlantic would later open (Marzoli et al., 2018) and is the suspected driver of the environmental disruptions and ecological turnover that mark the end of the Triassic period ($\sim 251.9\text{--}201.3$ Ma) and the transition into the Jurassic ($\sim 201.3\text{--}145$ Ma, Pálffy and Kocsis 2014).

Blackburn et al. (2013) dated CAMP basalt units coinciding with terrestrial palynological turnover and established an age estimate

* Corresponding authors.

E-mail addresses: jan.landwehrs@univie.ac.at (J.P. Landwehrs), feulner@pik-potsdam.de (G. Feulner).<https://doi.org/10.1016/j.epsl.2020.116174>

0012-821X/© 2020 Elsevier B.V. All rights reserved.

of 201.56 Ma for the end-Triassic extinction (ETE) horizon, preceding the Triassic-Jurassic boundary (TJB) by ~ 100 – 200 kyr (Percival et al., 2017). CAMP units dated so far cover a period of ~ 700 kyr (Heimdal et al., 2018), but cluster mainly around the extinction interval between ETE horizon and TJB (Lindström et al., 2017). Volcanic activity of LIPs was likely further concentrated in shorter pulses ($\sim 10^3$ – 10^5 yr, Black and Manga, 2017). Up to five pulses of intense CAMP volcanism have been proposed (e.g. Schaller et al., 2011; Blackburn et al., 2013), of which the first could have initiated the ETE.

Pronounced contemporaneous perturbations in the marine $\delta^{13}\text{C}$ (Lindström et al., 2017) and mercury record (Percival et al., 2017) seem to attest to the pulsatory manner of CAMP outgassing. This notion is also supported by paleosol-based pCO_2 reconstructions from the Newark Basin (Schaller et al., 2011, 2012). There, pCO_2 rises from earlier values of ~ 1350 ppm to ~ 2950 ppm immediately above the lowest volcanic unit and the ETE horizon (originally higher reported values were recalculated by Foster et al. 2017). Schaller et al. (2011, 2012) argue for a volcanic emission pulse shorter than 20 kyr causing this increase which is followed by a gradual decline on a $\sim 10^5$ yr timescale.

Because the CAMP is mainly constituted by volcanic intrusions rather than outflows (Marzoli et al., 2018), the potential contribution of intrusive volcanism to volcanogenic gas emissions by triggering contact metamorphism (e.g. Aarnes et al., 2010) is increasingly considered. Both carbon (e.g. Heimdal et al., 2018) and sulfur (e.g. Callegaro et al., 2014) volatiles dissolved in magmas or stored in intruded sediments were likely degassed on the order of $\sim 10^4$ Gt by the CAMP in total.

The spectrum of volcanogenic volatiles and their environmental effects is wide, but here we restrict ourselves to impacts of carbon emissions and stratospheric sulfate aerosol formation on climate and ocean biogeochemistry. Excess atmospheric CO_2 is partly dissolved in the ocean within $\sim 10^2$ – 10^3 yr while the rest is drawn down by weathering and sedimentation on longer ($\sim 10^3$ – 10^5 yr) timescales (Zeebe, 2012b). Massive carbon emissions can therefore lead to greenhouse warming and ocean acidification for at least thousands of years (Greene et al., 2012). In contrast, volcanic sulfur gases like SO_2 only gain atmospheric residence times of ~ 1 – 3 yr if injected into the stratosphere. There, sulfate aerosols, which effectively scatter incoming solar radiation, can form and lead to a pronounced global cooling for a few years (Robock, 2000). This requires explosive eruption phases with eruption column heights clearly exceeding 10 km which could occur episodically during eruptions that form LIPs. For such eruptions and explosive phases typical timescales of decades (Self et al., 2014) and days (Glaze et al., 2017), respectively, were proposed.

Environmental and climatic changes potentially related to CAMP volcanism were also inferred from changing fossil leaf characteristics, $\delta^{18}\text{O}$ analysis, clay mineralogy and palynology. A common gap in carbonate deposition (Greene et al., 2012) and highly affected acid-sensitive biomineralizing organisms (Kießling and Simpson, 2010) could indicate ocean acidification. However, ocean anoxia and especially temperature changes may have driven the end-Triassic marine extinction which was strongest at tropical latitudes causing an almost complete loss of tropical reef ecosystems (Dunhill et al., 2018). Despite evidence for anoxia around the TJB, its role in the end-Triassic events remains unclear (van de Schootbrugge and Wignall, 2015).

Potential impacts of volcanic sulfur emissions, like global cooling episodes, are frequently invoked in the context of the end-Triassic events (e.g. Schoene et al., 2010; Guex et al., 2016) and linked to observed sea-level changes (e.g. Lindström et al., 2017) or distorted fossil leaf morphologies (Steinthorsdóttir et al., 2017). Because these climatic effects act on geologically very short

timescales, it is important to assess them with models and to clarify which signals could have been recorded by proxies.

In previous modeling, Huynh and Poulsen (2005) employed an atmosphere-ocean General Circulation Model (GCM) to simulate and analyze climate equilibrium states at different atmospheric CO_2 concentrations for Late Triassic boundary conditions. Paris et al. (2016) used temperature and runoff fields from the same GCM to simulate the carbon cycle response to CAMP carbon emission pulses with a box model. Other carbon cycle modeling studies were conducted for example by Beerling and Berner (2002) and Bachan and Payne (2015). Potential impacts of sulfur emissions were assessed in the context of other LIPs: Schmidt et al. (2016) simulated the radiative forcing and the acidifying effects for decadal flood basalt eruptions and estimated the resulting cooling with an energy budget model. Recently, Black et al. (2018) incorporated both carbon and sulfur emission estimates for the Siberian Traps at the Permian-Triassic boundary into a GCM featuring an aerosol microphysics module.

This study complements previous work on modeling aspects of the end-Triassic events by dynamically simulating effects of simultaneous pulsed emissions of both carbon and sulfur gases with an Earth System Model of Intermediate Complexity (EMIC). The simulations are constrained by current knowledge about the Late Triassic world, the CAMP volcanism and the end-Triassic events. Our simulations then provide new constraints for the environmental effects which can be expected to result from CAMP degassing. This also illuminates general aspects of the interaction of LIP volcanism, climate and ecosystems and the dynamics of a severely perturbed Earth System.

2. Modeling approach

2.1. Model description

For the simulations of the latest Triassic climate and the impacts of idealized volcanic outgassing scenarios we use the CLIMBER-3 α +C Earth System model (Montoya et al., 2005, see Supplement for further references). This model consists of the MOM3 ocean, at $3.75^\circ \times 3.75^\circ$ horizontal resolution and 24 vertical levels, the fast statistical-dynamical atmosphere POTSDAM-2 with a coarse $7.5^\circ \times 22.5^\circ$ resolution (lat. \times lon.), a sea-ice model and a marine carbon cycle module (Hofmann et al., 2019).

To calculate the radiative aerosol forcing for the emission scenarios described below, we employ the Easy Volcanic Aerosol Model (EVA v1.0, Toohey et al., 2016). For a given daily timeseries of stratospheric sulfur injections, EVA calculates the Aerosol Optical Depth (AOD) at 550 nm and how it evolves over time. The globally averaged AOD is then translated into a global radiative forcing $\Delta F_a(t)$ and introduced to CLIMBER-3 α +C as an annual mean reduction of the solar constant S_0 :

$$S(t) = S_0 + \frac{4}{1-\alpha} \cdot \Delta F_a(t) = S_0 - \frac{4}{0.7} \cdot 21 \frac{\text{W}}{\text{m}^2} \cdot \text{AOD}(t)$$

Here, $\alpha = 0.3$ is the planetary albedo. Note that the -21 W/m^2 scaling factor was obtained from recent volcanic sulfur emissions and forcings (Schmidt et al., 2018) and could be different for larger scale LIP volcanism. Because EVA is similarly tuned to historical eruptions we modified its M_{SO_4} -to-AOD scaling to better fit results of Schmidt et al. (2016) who obtained lower AODs for large injections. See Supp. Sec. 2.1 for further discussion of this simplified approach.

Metzner et al. (2012) used a similar approach and simulated reductions in global annual mean Surface Air Temperature (SAT) by up to $\sim 3^\circ\text{C}$ and a complete recovery only after 90 yr due to sulfur

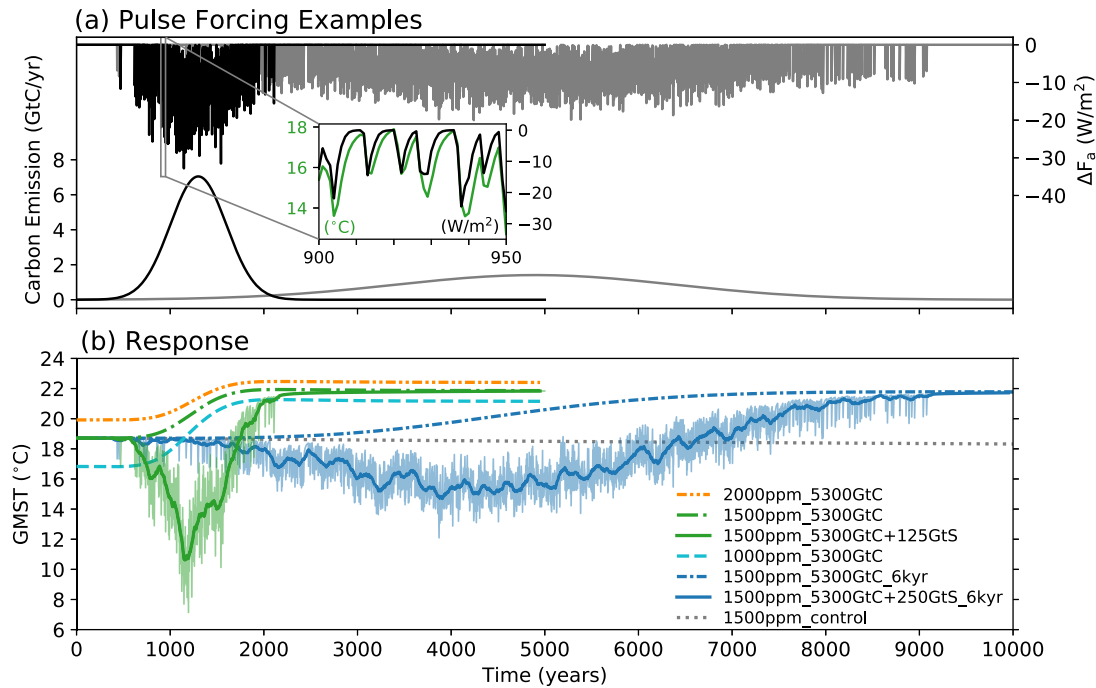


Fig. 1. Carbon and sulfur forcing scenarios (a) and resulting global mean surface temperature (GMST) responses in representative perturbation simulations (b). In (a), carbon emission rates (left scale) and sulfur aerosol radiative forcings ΔF_a (right scale) are shown for a “short” (1500ppm_5300GtC+125GtS, black lines) and “long” (1500ppm_5300GtC+250GtS_6ka, gray lines) emission pulse scenario. The simulated GMST response to these forcings is indicated in (b) by the solid green and blue lines, respectively. The thick lines represent 100 yr moving averages, while the thin lines indicate annual means. The temperature response to only carbon emissions in several scenarios with varying initial pCO_2 is indicated by dash-dotted lines in this panel. The inset in (a) illustrates the interannual variation of ΔF_a and the resulting GMST changes in the 1500ppm_5300GtC+125GtS run over an interval of 50 yr. (For interpretation of the colors in the figure(s), the reader is referred to the web version of this article.)

injections from large volcanic eruptions. This recovery time exceeds the duration of the short lived forcing because of the ocean’s thermodynamic inertia (Thompson et al., 2009).

Finally, the LOSCAR carbon cycle box model (Zeebe, 2012a) is used to simulate the long-term carbon cycle response to volcanic carbon emissions (see Supp. Sec. 2.2). Due to computational cost and the lack of sediment and weathering feedbacks, CLIMBER-3 α +C is only useful for perturbation experiments shorter than ~ 10 kyr. With LOSCAR multiple of these simulations of short- and medium-term climatic effects of volcanic pulses can be integrated into million year scenarios representing the whole CAMP emplacement period. However, studying long-term carbon cycle dynamics is not the main concern of this work and is detailed in previously mentioned studies.

2.2. Boundary conditions & equilibrium simulations

The paleogeography of the Rhaetian (~ 208.5 – 201.3 Ma), the last Triassic stage, is adopted from Scotese (2014) and slightly modified with regard to model requirements. Fig. S1 shows the established elevations and the land surface types which were synthesized from reconstructed paleobiogeographic and paleoclimatic zones. The solar constant S_0 was set to 1339 W/m², accounting for the Sun’s luminosity in the Late Triassic being $\sim 1.6\%$ lower than presently (1361 W/m², Feulner, 2012). Earth’s orbital parameters obliquity, eccentricity and precession angle were fixed at $\varepsilon = 23.5^\circ$, $e = 0$ and $\omega = 0^\circ$.

Equilibrium states of climate and marine biogeochemistry for Late Triassic boundary conditions were simulated for three different levels of atmospheric CO_2 (1000, 1500, 2000 ppm). These values roughly cover the range of pCO_2 reconstructed for the Late Triassic before CAMP activity started (Foster et al., 2017), although

the highest one appears less likely. During a spin-up and tuning period of ~ 10 kyr the ocean carbonate chemistry parameters DIC (Dissolved Inorganic Carbon) and TA (Total Alkalinity) were adjusted to yield the desired pCO_2 , an average surface ocean pH of ~ 7.6 (in line with Ridgwell and Zeebe, 2005) and a tropical aragonite saturation Ω_{Ar} of at least 2.5 (to conform with the occurrence of coral reefs, Martindale et al., 2012). All other model parameters remained unchanged from their modern default values unless otherwise mentioned.

2.3. Volcanic emission scenarios

The three simulated equilibrium states were then exposed to an ensemble of different volcanic forcing scenarios consisting of an addition of carbon to the atmosphere and/or a reduction of the solar constant, mimicking the effect of volcanic aerosols. The conducted perturbation experiments are summarized in Fig. 1 and Table 1. In each case the model is supplied with a timeseries of carbon input per year and/or an annual timeseries of the modified solar constant. The 1500 ppm initial state is considered as the baseline case, but a few perturbation experiments are conducted with the 1000 and 2000 ppm initial states to test the sensitivity of the response.

The carbon forcing scenarios consist of one Gaussian emission pulse during which a total carbon mass $M_{c,t} = [2500, 5300, 7500]$ GtC is emitted. We distinguish between “short” and “long” scenarios in which 95% of the volatiles are emitted within 1200 and 6000 yr, respectively. The peak emission rates are reached in years 1300 and 4900 of the scenarios (see Fig. 1(a)), respectively, and range from 0.7 to 10 GtC/a.

The overall temporal distribution of the sulfate aerosol forcing is similar, because a common origin of both carbon and sulfur

Table 1

Summary of the most relevant volcanic perturbation simulations. For the volcanic emission pulse experiments the peak effective stratospheric sulfur injection rate $\dot{M}_{s,max}$ and the resulting stratospheric aerosol forcing $\Delta F_{a,max}$ are 10 yr moving averages. $M_{s, single}$ is the average of the sulfur mass injected during individual events within a pulse scenario which varies randomly to a certain degree. The maximum negative and positive global mean surface temperature changes in the course of a simulation run, $\Delta T_{max,w}$ and $\Delta T_{max,c}$, represent 100 yr averages. The values of $\Delta T_{max,w}$ and $\Delta T_{max,c}$ for the various scenarios are also presented in Fig. 2.

Simulation run	$M_{s, single}$ (MtS/event)	$\dot{M}_{s,max}$ (GtS/10 yr)	$\Delta F_{a,max}$ (W/m ²)	$\Delta T_{max,w}$ (°C)	$\Delta T_{max,c}$ (°C)
Carbon only "Short" Pulse (1200 yr duration, no stratospheric sulfur injection events)					
1500ppm_2500GtC	-	-	-	+1.8	-
1500ppm_5300GtC	-	-	-	+3.2	-
1500ppm_7500GtC	-	-	-	+4.1	-
1000ppm_5300GtC	-	-	-	+4.4	-
2000ppm_5300GtC	-	-	-	+2.6	-
Carbon + Sulfur "Short" Pulse (1200 yr duration, 500 stratospheric sulfur injection events)					
1500ppm_5300GtC+50GtS	100	1.28	-12.0	+3.1	-3.6
1500ppm_5300GtC+125GtS	250	3.2	-19.4	+3.1	-8.1
1500ppm_5300GtC+250GtS	500	6.4	-28.6	+3.1	-14.8
1500ppm_5300GtC+500GtS	1000	12.8	-42.4	+3.1	-25.4
1000ppm_5300GtC+125GtS	250	3.2	-19.4	+4.3	-9.2
2000ppm_5300GtC+125GtS	250	3.2	-19.4	+2.5	-7.2
Carbon + Sulfur "Long" Pulse (6000 yr duration, 2500 stratospheric sulfur injection events)					
1500ppm_5300GtC+125GtS_6ka	50	0.65	-9.0	+3.0	-2.4
1500ppm_5300GtC+250GtS_6ka	100	1.3	-12.5	+3.0	-4.0
1500ppm_5300GtC+500GtS_6ka	200	2.6	-18.0	+3.0	-7.0
Single Sulfur Injection Event (1 day duration)			(1 yr ave.)		(1 yr ave.)
1500ppm_9MtS (Pinatubo size)	9	-	-1.9	-	-0.3
1500ppm_250MtS	250	-	-13.6	-	-2.2
1500ppm_1000MtS	1000	-	-29.9	-	-4.6

volatiles is assumed. However, as already explained, the mechanisms behind both forcings differ: While volcanogenic carbon can continuously accumulate in the troposphere over thousands of years, stratospheric aerosol formation requires explosive eruption phases and is then only sustained for few years. Therefore, the aerosol forcing is calculated as the composite effect of many day-long stratospheric injection events which obey a random normal distribution in time that is equivalent to the distribution of the carbon emissions (see Fig. 1(a)). Sulfur injections are therefore most frequent around the carbon emission peak. Injection latitudes $\leq 20^\circ$ are assumed owing to the paleolatitude of the CAMP. The total mass of injected sulfur that forms stratospheric aerosols, $M_{s,t} = [50, 125, 250, 500]$ GtS, is distributed over 500 (2500) individual injection events in the short (long) scenarios. The individual contributions $M_{s, single}$ are similar for every event within a certain scenario and range from 50 MtS to 1000 MtS. This yields a maximum of 12 eruptions and a peak sulfur flux $\dot{M}_{s,max}$ of 0.65 to 12.8 GtS/10yr. The resulting radiative forcings of these synthetic eruption histories are calculated using EVA as explained in Sec. 2.1. For $M_{s,t} = 125$ GtS, for example, the decadal mean radiative forcing $\Delta F_{a,max}$ peaks at -19.4 W/m² (see Table 1) which translates into a -8% insolation reduction.

An important reference point for these scenarios are the pCO_2 reconstructions by Schaller et al. (2011, 2012). Paris et al. (2016) demonstrated that the observed peaks as well as negative carbon isotopic excursions can be reproduced by four short emission pulses of 5300 GtC of isotopically light carbon and Bachan and Payne (2015) obtained similar results. Similar carbon emission parameters are therefore used here. The required total carbon emission of ~ 21000 GtC is in the upper range of potential outgassing from CAMP magmas, based on their volume and carbon content (Beerling and Berner, 2002). Such numbers, however, appear feasible considering new estimates of basalt magma carbon degassing (Anderson and Poland, 2017) and additional thermogenic generation of for example 24000 GtC by sills in Brazil (Heimdal et al., 2018). Similarly, CAMP could have released up to 12000 GtS from its magmas (assuming 4 MtS/km³, Callegaro et al. 2014, and 3×10^6 km³, Marzulli et al. 2018) and additional amounts by

thermal metamorphism (e.g. Guex et al., 2016). Of these volatiles, however, only a fraction is actually transported to the upper atmosphere and converted into stratospheric aerosols as modeled by Schmidt et al. (2016) and Glaze et al. (2017). Because these processes can not be simulated here, the sulfur masses used in this study reflect assumed "effective" (stratospheric aerosol forming) amounts and the resulting stratospheric aerosol radiative forcing is the only effect of sulfur emissions represented in our model. Due to the vague empirical constraints, the total effective sulfur injection during one emission pulse $M_{s,t}$ (0 to 500 GtS), was chosen to cover the range of potential effects from no impact to extreme cooling. These effective amounts represent $\leq 17\%$ of the 12 000 GtS estimate on the primary CAMP emissions when spread over four pulses.

Building on previous work, for example by Paris et al. (2016), this study explores potential impacts of CAMP volcanism in an expanded scenario range with varying $M_{c,t}$, initial pCO_2 values and an additional aerosol forcing. This scenario range reflects existing uncertainties regarding the characteristics of CAMP volcanism and the end-Triassic environmental conditions. Impacts on climate and the marine carbon cycle are, furthermore, simulated with a spatially fully resolved model.

3. Results

This work focuses on potential disruptions due to CAMP emissions. The equilibrium states simulated for Late Triassic boundary conditions are therefore only briefly characterized.

3.1. Pre-eruption equilibrium states

The simulated global annual mean SAT (GMST) at $pCO_2 = 1500$ ppm is $18.7^\circ C$ and we will refer to this climate state in the following unless otherwise noted. In the 1000 and 2000 ppm equilibrium states it is $16.8^\circ C$ and $19.9^\circ C$ instead. Doubling pCO_2 from 1500 ppm to 3000 ppm increases the GMST by $+2.86^\circ C$. In the low latitudes, annual mean temperatures exceed $25^\circ C$ and even $30^\circ C$ in eastern Pangaea and western Tethys, while the western coast

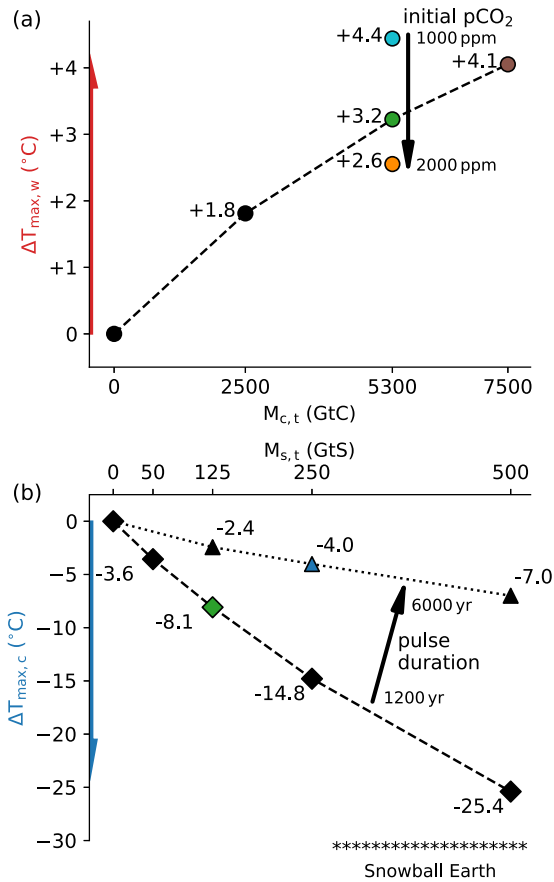


Fig. 2. Simulated maximum global warming $\Delta T_{\max,w}$ (a) and cooling $\Delta T_{\max,c}$ (b) in dependence on the total amount of carbon emission $M_{c,t}$ (a) and sulfur injection $M_{s,t}$ (b). Based on 100 yr moving average GMST timeseries of simulation runs starting from the $pCO_2 = 1500$ ppm initial state, except the cyan and orange dots in (a) which correspond to runs with initially 1000 and 2000 ppm, respectively. Colored markers belong to timeseries with the same color in Fig. 1(b). In (a), points correspond to “short” runs (1200 yr pulse) with no sulfur injection, while (b) includes “short” (diamonds, dashed line) and “long” (triangles, dotted line, 6000 yr pulse) runs with 5300 GtC carbon emission and additional sulfur injections. Information about all these runs is also presented in Table 1.

of tropical Pangaea is significantly cooler, with around 20 °C (see Fig. 3(c) or Fig. S4a).

This results from the surface ocean circulation in the Panthalassa basin which exhibits an anticyclonic subtropical gyre and a cyclonic subpolar gyre in each hemisphere. The subtropical gyres transport warm water westward along the equator into the Tethys, while bringing colder water from higher latitudes to Pangaea’s western coast. The tropical annual mean Sea Surface Temperatures (SST, herein averaged over 25 m depth) are approximately 3.7 °C higher in the Tethys (29.6 °C) than in eastern Panthalassa (25.9 °C, see Fig. S9a). Other features of the simulated ocean circulation are boundary currents at Panthalassa’s western margin, equatorial and coastal upwelling in eastern Panthalassa and a deep meridional overturning cell in southern Panthalassa driven by sinking cold water in the open ocean near the South Pole. The upwelling of nutrient rich waters in eastern Panthalassa fuels high marine biomass productivity (see Fig. S11). Below this region and in enclosed gulfs with considerable productivity, oxygen minimum zones develop (see Fig. 3(c) and Fig. S10b). Related to the high seawater temperatures, the highest carbonate saturations are predicted in the Tethys Sea (see Fig. S10a).

Significant sea ice is present north of 60°N, but only at 1000 ppm in the southern hemisphere (see Fig. S4b). The continental climate of the mid- and high latitude interiors of Gondwana and Laurasia is characterized by extreme seasonal temperature changes (see Fig. S5). There, pronounced low pressure cells develop over the heated land during the respective summer period (see Fig. S6). Air driven over the warm Tethys waters towards these continental lows brings abundant rainfall to the surrounding land while Pangaea’s western coast and parts of the hinterland receive less precipitation (see Fig. S8).

3.2. Global temperature perturbations

The GMST response in representative volcanic forcing scenarios is shown in Fig. 1(b) and listed in Table 1. The respective simulation runs can be identified by the initial pCO_2 , the total amounts of emitted carbon and sulfur, and the emission pulse duration which is 1200 yr unless otherwise noted. If only carbon is added to the atmosphere, the GMST rises smoothly in proportion to the cumulative emission, for example by 3.2 °C in the 1500ppm_5300GtC run. This results from an increase of pCO_2 which scales approximately linearly with the total carbon emission and amounts to +870 ppm (2500 GtC), +1960 ppm (5300 GtC), +2850 ppm (7500 GtC; see also Fig. S12). A slight overshoot of pCO_2 and GMST is observed in the “short” scenarios before equilibration with the deep ocean. This effect would become important if degassing was even more rapid.

In contrast to the steady carbon emissions, the idealized aerosol forcing causes irregular global temperature changes. First, the GMST drops by a few degrees after each injection event which collectively induce interannual fluctuations (see inset in Fig. 1(a)). Injections of 250 MtS, corresponding to those in the 1500ppm_5300GtC+125GtS run, cause an annual mean peak global cooling of −2.2 °C (see Table 1) which decays by 92% within 10 yr. For 1000 MtS the cooling peaks at −4.6 °C compared to a Pinatubo-sized injection (9 MtS) with a simulated annual mean peak radiative forcing of −1.9 W/m² and a maximum annual mean cooling of −0.3 °C, which is comparable to estimates for the actual Pinatubo eruption in 1991 (Thompson et al., 2009). Secondly, the cumulative effect of the many successive sulfur injection events results in a transient cold period, which lasts around 1000 yr in the “short” and 4500 yr in the “long” scenarios as shown in Fig. 1(b). This is because eruptions become so frequent towards the envisioned peak of volcanic activity that their effects overlap, accumulate and exceed that of individual ones. The maximum of this medium-term cooling is reached approximately at the time of the carbon emission peak and amounts to −8.1 °C in the 1500ppm_5300GtC+125GtS run (see also Fig. 2(b)). At this time, only half of the volcanic carbon has already entered the atmosphere, but as it further accumulates and the sulfur injections cease, the cooling cannot be sustained and greenhouse warming takes over.

Under these assumptions, the simulated combined effects of contemporaneous carbon and sulfur emissions on global temperatures are therefore a transient cold period followed by long-term warming, overprinted by interannual temperature fluctuations. The equilibrium temperature reached after the emission pulse depends almost entirely on the added amount of carbon and is only slightly affected by the addition of the aerosol forcing and the duration of the emission period (see Fig. 1(b)). The aerosol-induced cooling enhances ocean overturning and carbon solubility in seawater, so that the excess atmospheric carbon is more quickly sequestered into the ocean, which prevents the mentioned pCO_2 overshoot (Fig. S12a).

The amplitudes of global temperature change in the course of the described cooling-warming sequence depend on the emitted

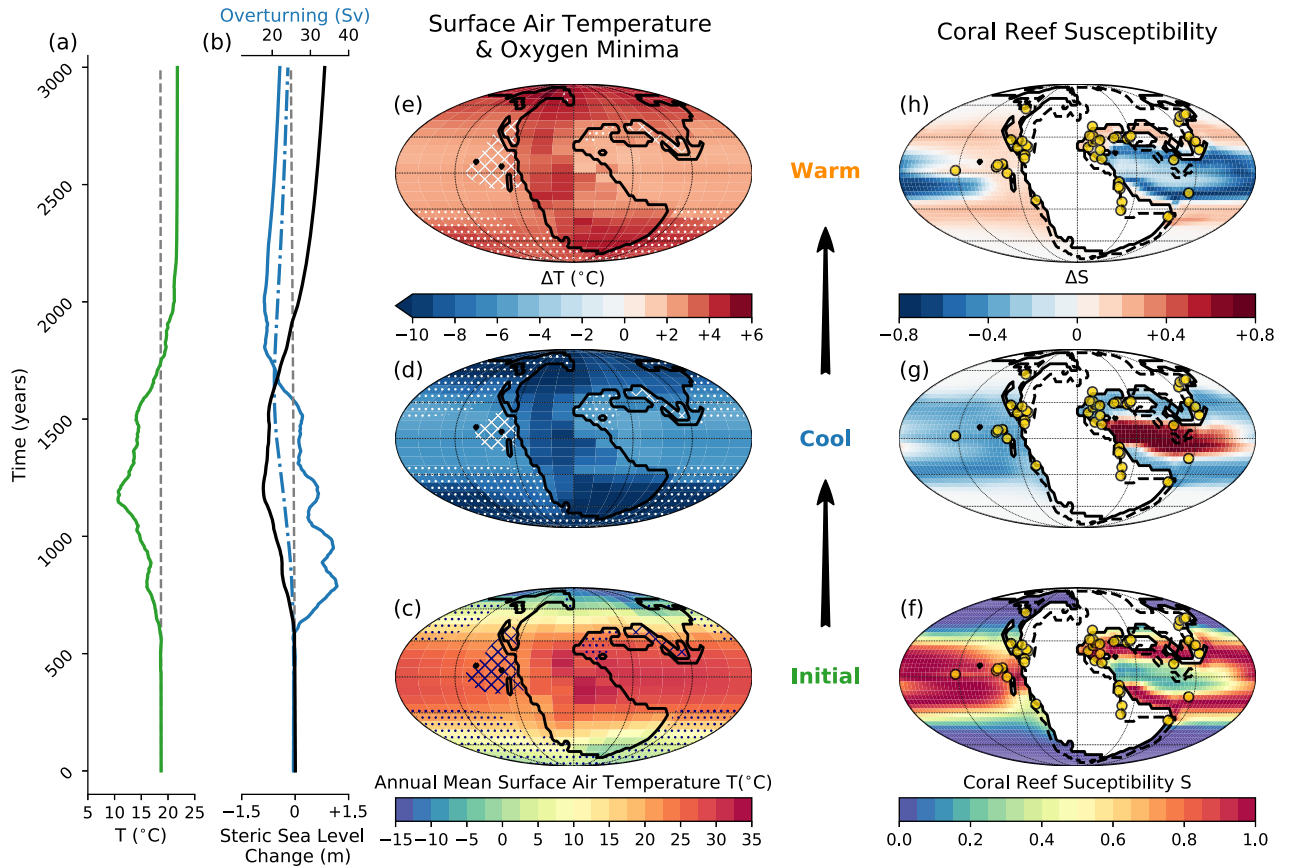


Fig. 3. Synopsis of potential effects of a volcanic carbon and sulfur emission pulse. All data was extracted from the 1500ppm_5300GtC+125GtS run, except the dash-dotted line in (b) which is from the 1500ppm_5300GtC run. Curves in (a), (b) show global 100 yr moving averages. For (b), the maximum meridional overturning streamfunction below 500 m depth in the southern hemisphere was measured. Enhanced (reduced) overturning and a steric sea-level fall (rise) occur in the cool (warm) phase. In (c), (d), (e), the minimum $[O_2]$ in the water column exceeds 200 $\mu\text{mol/l}$ in dotted regions and falls below 100 $\mu\text{mol/l}$ in hatched regions. Surface temperatures change strongest in the high latitudes and over the continents. Hypoxic zones do not expand significantly in the warm mode, but $[O_2]$ is reduced in high latitude oceans. In (f), (g), (h), yellow dots mark locations of Norian (~227–208.5 Ma, Cohen et al. 2013) and Rhaetian (~208.5–201.3 Ma) stony coral fossil reefs in the Paleobiology Database. Dashed lines in (f), (g), (h) are the coastlines reconstructed for the Norian by Scotese (2014). The coral reef susceptibility in (f), (g), (h) was calculated from the simulated SSTs according to the coral temperature characteristic shown in Fig. 4(a). Optimum seawater conditions are predicted in two subtropical Tethyan belts and in equatorial eastern Panthalassa (red color in f). A deterioration of the thermal conditions in the cool and warm phases is indicated by blue colors in (g) and (h).

carbon and sulfur amounts that were systematically varied between the emission scenarios. To illustrate this, the positive and negative maximum deviations of the 100 yr moving average time-series of the GMST from its respective initial values, $\Delta T_{\text{max,w}}$ and $\Delta T_{\text{max,c}}$, are summarized in Fig. 2(a), (b).

$\Delta T_{\text{max,w}}$ increases logarithmically with the total carbon emission when all other parameters remain equal. Tripling $M_{\text{c,t}}$ from 2500 GtC to 7500 GtC raises $\Delta T_{\text{max,w}}$ from +1.8 °C to +4.1 °C. The second important control on the global warming amplitude is the initial state because a colder climatic state with a lower $p\text{CO}_2$ reacts more sensitive to additional carbon. The $p\text{CO}_2 = 2000$ ppm initial state warms by just +2.6 °C in contrast to +4.4 °C in the 1000 ppm case (Fig. 2(a)), given the same emission of 5300 GtC.

The amplitude of peak global cooling $\Delta T_{\text{max,c}}$ increases in proportion to the total amount of injected sulfur $M_{\text{s,t}}$ (see Fig. 2(b)). When confined to roughly 1200 yr (“short” scenarios), $M_{\text{s,t}} = 125$ GtS yields $M_{\text{s,max}} = 3.2$ GtS/10 yr and a cooling by –8.1 °C in the coldest century. The coldest year lies –3.5 °C below this 100 yr average. $\Delta T_{\text{max,c}}$ reaches even –25 °C when $M_{\text{s,t}}$ and \dot{M}_{s} increase to 500 GtS and 13 GtS/10 yr, respectively. For $M_{\text{s,t}} \geq 600$ GtS, GMSTs well below –10 °C, a runaway ice-albedo feedback and the transition into a Snowball Earth state are simulated. When the $M_{\text{s,t}}$ is distributed over a five times longer emission period and

5 × more injection events (“long” scenarios), $\Delta T_{\text{max,c}}$ reduces by ~70%. An at least four times higher $M_{\text{s,t}}$ is then needed to obtain a similar cooling amplitude.

3.3. Regional and oceanic changes

Fig. 3 illustrates the envisioned three-phased perturbation and integrates further potential impacts of a carbon and sulfur emission pulse. Figs. 3(c), (d), (e) show the spatially resolved annual mean SATs in the initial pre-eruption state (c) and its changes towards the coldest century (d) and towards the warm post-eruption equilibrium state (e). The pattern of temperature change is spatially heterogeneous, but similar in the cold and the warm phase. In the 1500ppm_5300GtC+125GtS run, temperatures above the tropical oceans increase less than the global average of +3.1 °C, and in parts of the western Tethys region even by less than +2 °C. In contrast, the southern ocean, eastern Pangaea and the higher latitude continents warm by +3 to +5 °C, and the largest temperature increases are seen in the northernmost ocean regions due to sea ice loss and the subsequently lower albedo. The hottest regions in central Pangaea reach annual mean temperatures of 36 °C, compared to 32.7 °C in the initial state. In the cool phase, the temperature drop is especially pronounced around the South Pole,

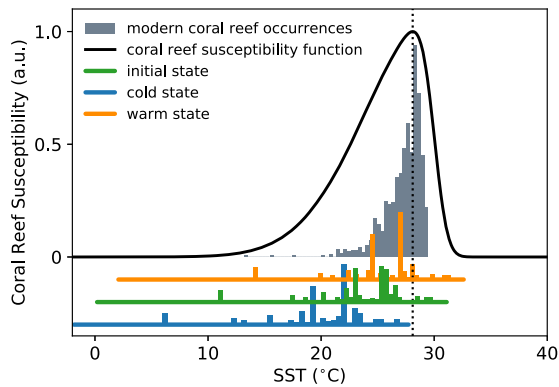


Fig. 4. Coral reef susceptibility. Grey bars indicate the frequency of modern coral reef occurrences at modern SSTs. The black line is a coral reef susceptibility function adjusted to this distribution. Horizontal green, blue and red bars show the SST range simulated in the initial, cold and warm phase of the 1500ppm_5300GtC+125GtS run. The corresponding colored vertical bars indicate at which simulated SSTs the Norian and Rhaetian fossil corals occur.

because sea ice forms and expands to latitudes down to 50°S. The low-latitude (<30°) continental interiors become more humid in the warm post-eruption state (see Fig. S14) which can be traced back to enhanced land-sea pressure gradients resulting from the stronger warming on land. Conversely, the same regions become more arid during the cold phase.

The volcanic forcing also impacts the ocean overturning circulation measured by the maximum meridional overturning streamfunction in the southern hemisphere (blue lines in Fig. 3(b)). During the first half of the transient cool phase, overturning is significantly enhanced, because cooling of the surface ocean leads to a more unstable ocean stratification. When the greenhouse warming takes over, the cooled ocean is heated from the top, leading to a more stable stratification and reduced overturning. However, also this effect is transient and the overturning largely recovers. Such a transient reduction of up to 20% is also observed when only carbon is emitted (dash-dotted line).

The changes of ocean ventilation and seawater temperatures also affect the seawater oxygen concentrations (see Fig. 3(c), (d), (e)). In the cold phase, enhanced overturning and oxygen solubility lead to generally higher oxygen concentrations, especially at high latitudes. In the following warm mode, the solubility decreases and higher temperatures allow for enhanced biomass production in the nutrient rich high latitude oceans, promoting more pronounced oxygen minimum zones especially in northern Panthalassa. In contrast, the low latitude oxygen minimum zones do not expand significantly. Bruggen et al. (2017) suggested enhanced ocean mixing and marine productivity due to aerosol induced cooling after the K-Pg asteroid impact, which is corroborated here by simulated increases of the low- to mid-latitude export biomass production during and after cooling periods (see Fig. S19). Another notable effect is the predicted steric sea-level change which parallels the global temperature perturbation (see Fig. 3(b)). The sea level drops by ~1 m in the cold phase before rising by about the same amount above its initial level, resulting in an overall change of 2–3 m, depending on the specific scenario.

3.4. Thermal limits of corals

To assess tentatively to what extent the simulated temperature changes could have threatened marine organisms, the temperature preferences of modern corals are now evaluated with respect to the simulated SSTs. A similar assessment for marine phytoplankton growth rates is included in Supp. Sec. 5.

A database of modern coral reefs was downloaded from reefbase.org (accessed April 4, 2019) and the annual mean SSTs (averaged over the upper 25 m) at the respective locations were calculated from data from Locarnini et al. (2018). Following Pohl et al. (2019), but with the SST being the only environmental parameter, a coral reef susceptibility function (a left-skewed normal distribution function peaking at 28°C) was defined based on the distribution of modern coral reefs. Furthermore, locations of Norian and Rhaetian stony coral fossil finds were retrieved via fossilworks.org (accessed March 21, 2019). Fig. 3(f), (g), (h) show these locations as well as the coral reef susceptibilities calculated from the SSTs simulated for the initial, cold and warm phase of the 1500ppm_5300GtC+125GtS run.

For the initial Late Triassic equilibrium state this method predicts ideal temperature conditions for coral reef growth in two subtropical belts in the Tethys and western Panthalassa as well as in equatorial eastern Panthalassa, while the equatorial Tethys appears too hot (see Fig. 3(f)). This pattern roughly conforms with the distribution of actual coral fossil finds, although some also occur at higher latitudes.

In the transient cold phase, the susceptibility decreases significantly at most coral locations. With the subsequent warming, the too hot equatorial belt expands, but the susceptibility increases at many reef localities in the mid-latitudes and eastern Panthalassa which previously resided at below optimum temperatures. The SSTs simulated at fossil coral reef locations in the initial state are comparable to those at modern reef locations (Fig. 4) although the Late Triassic distribution appears shifted towards lower temperatures. In the cool phase, all fossil coral locations are pushed towards below optimum temperatures, whereas only a few are pushed towards or across the upper thermal limits under a subsequent +3.1°C global warming.

3.5. Timescales of the volcanic perturbations

As outlined so far, impacts of volcanic carbon and sulfur can be simulated spatially resolved and on monthly to millennial timescales with CLIMBER-3 α +C. To integrate these results into the broader picture of the whole CAMP emplacement period, the long-term carbon cycle dynamics in response to several volcanic carbon emission pulses were simulated with LOSCAR. Fig. 5 combines results from both models. The displayed scenario of four carbon emission pulses is similar to that proposed by Paris et al. (2016) to explain the reconstructed pCO₂ changes. Both models predict a similar pCO₂ increase in response to the first volcanic pulse. In contrast to CLIMBER-3 α +C, the excess CO₂ is slowly drawn down in LOSCAR by weathering and sediment carbonate dissolution, which results in a ~300 ppm lower pCO₂ in model year 5000. The GMST for LOSCAR simply scales logarithmically with the simulated pCO₂ (Zeebe, 2012a), and shows a similar increase as in CLIMBER-3 α +C. The LOSCAR simulation suggests that the ~10⁴–10⁵ yr between the emission pulses are insufficient to remove all of the added carbon and that pCO₂ and temperature remain elevated over the whole ~700 kyr period of volcanic activity. Only after a few million years pre-eruption conditions are recovered. To this picture we can add quantitative estimates of the potential amplitudes and timescales of temperature changes caused by simultaneous sulfur emissions. The resulting pattern would be that every warming pulse was immediately preceded by a pronounced cold phase of up to a few millennia with strong interannual temperature fluctuations. In the timeline of the whole CAMP emplacement period these phases would appear as very short cold spikes with an amplitude large enough to interrupt the long-term greenhouse warming.

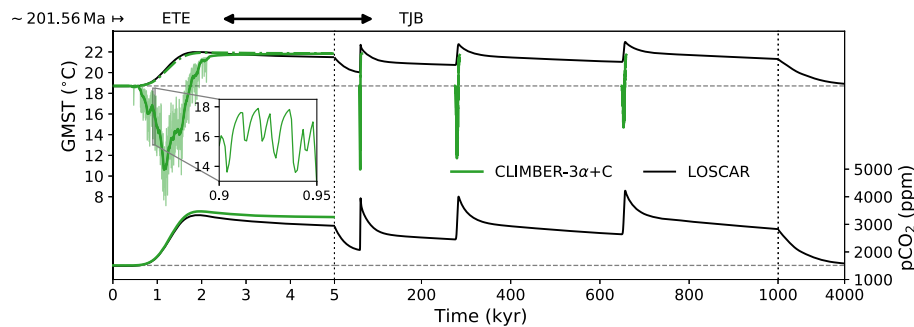


Fig. 5. Synthesis of potential global effects of pulsed volcanic carbon and sulfur emissions representative of the CAMP on timescales from 10^0 to 10^6 yr. A long-term carbon cycle simulation with the LOSCAR model (black lines) is superimposed with millennial CLIMBER-3 α +C simulations (green lines). Pulses 1 and 2: 1500ppm_5300GtC+125GtS_1200yr, Pulse 3: 1500ppm_5300GtC+500GtS_6000yr, Pulse 4: 1500ppm_5300GtC+250GtS_6000yr. The overall carbon emission scenario is similar to that of Paris et al. (2016). The specific sulfur amounts for each pulse are arbitrarily chosen to illustrate the potential effects. The simulated timeline is contextualized by approximate ages of the end-Triassic extinction horizon (ETE, \sim 201.56 Ma, Blackburn et al. 2013) and the Triassic-Jurassic boundary (TJB, \sim 201.36 Ma, Lindström et al. 2017).

4. Discussion

The general characteristics of the simulated Late Triassic climate compare well with previously published temperature, precipitation and sea-level pressure fields for more or less similar boundary conditions (Huynh and Poulsen, 2005; Donnadieu et al., 2006; Sellwood and Valdes, 2006). These conditions, notably $p\text{CO}_2$, paleogeography, vegetation patterns and the marine carbon cycle mode of operation, however, remain uncertain and need further evaluation in future work. We show that the sensitivity of the latest Triassic climate to volcanic emissions varies strongly with its initial state, exemplified by a 70% stronger global warming response when starting from a colder state with $p\text{CO}_2 \approx 1000$ ppm instead of 2000 ppm. The uncertainties related to the CAMP eruption and degassing history are similarly high. Despite growing evidence for culmination in a few pulses, further high resolution proxy records have to constrain their occurrence, duration and emission potential. Considering currently available empirical constraints, our simulations with systematically varied carbon and sulfur emission amounts and durations suggest a global warming from CAMP emission pulses of ~ 2.5 – 5 °C, but probably not more than 6 °C. The simulated temperature changes are regionally disparate, being generally larger in continental interiors and at high latitudes, despite an idealized globally homogeneous forcing. For example, under a $+3.2$ °C global warming, the temperature rise at 23°N is 2 °C larger in central Pangaea than over the Tethys. Such differences should be considered when reconstructing global temperature changes from local proxy records.

We simulated transient cooling phases for different stratospheric aerosol forcing scenarios. Approximating this forcing with a global average could have biased the simulated cooling patterns. With their more comprehensive atmospheric chemistry model, Black et al. (2018) obtained a spatially heterogeneous forcing for Siberian Trap volcanism centered at the location of this LIP in the northern hemisphere. The CAMP was, however, emplaced at low latitudes and the stratospheric circulation would have facilitated a global distribution of sulfate aerosols (Metzner et al., 2012) so that a globally averaged forcing appears a more valid approximation than it might be for other LIPs. The latitudinally resolved aerosol forcing calculated by EVA, however, exhibits a maximum around the equator and declines towards the poles (Fig. S3d). Due to the low-complexity forcing calculation, the sulfur amounts and stratospheric aerosol forcings reported herein should only be considered as rough estimates, and more comprehensive methods should be implemented in further modeling work. For the purpose of this study, namely to investigate the potential range of climatic impacts of CAMP volcanism, this simplified approach, however, allows

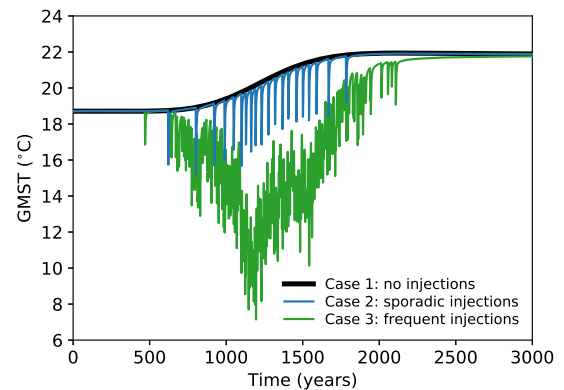


Fig. 6. Illustration of three different cases for a volcanic emission pulse with no, sporadic or frequent stratospheric sulfur injections. Three simulation runs are shown as examples: 1500ppm_5300GtC and 1500ppm_5300GtC_125GtS for Cases 1 and 3 were already presented in Fig. 1(b). For the intermediate Case 2 an example run with 10 GtS spread over 20 individual injection events was added. In all three cases 5300 GtC are emitted simultaneously.

to run many continuous multimillennial simulations with any desired aerosol forcing timeseries. This is currently hardly feasible with models like the one used by Black et al. (2018) who instead forced their climate model by repeating the aerosol forcing calculated over 10 yr during a sulfur emission period of 100–200 yr. Nevertheless, our results align with their conclusion that carbon and sulfur emissions from LIPs could have caused climatic swings on decadal to millennial timescales that would have exacerbated ecological stress.

The quantification of potential climatic effects of stratospheric sulfate aerosol formation from CAMP volcanism is an important extension of previous modeling work. From our perspective, three different cases can be distinguished in which sulfur is either never, sporadically or frequently injected into the stratosphere during phases of high volcanic activity (Fig. 6).

In Case 1, sulfur is possibly degassed but not injected into the stratosphere because no explosive eruptions with sufficiently high eruption columns occur. In Case 2, injection events are generally separated by more than a few years, but cause short-term cooling and interannual variability. In Case 3, a frequency of several injections per decade is sustained over centuries, and the deep ocean is additionally driven out of thermal equilibrium resulting in pronounced cooling phases.

Within the vague empirical constraints, most sulfur injection scenarios presented here were designed to yield the cumulative

effect of Case 3, but the ensemble of simulations also indicates under which conditions this is unlikely. Assuming a pulse duration of a few thousand years, similar to Paris et al. (2016), hundreds to a few thousand injection events need to occur if their effects should overlap for a considerable period. These numbers might conform with the high number of hydrothermal vents found in other LIPs (e.g. Svensen et al., 2007), but we are currently not aware of much evidence for or against such frequent eruptions for the CAMP.

The climatic response to such a carbon and sulfur emission pulse is a transient phase of high variability and sustained cooling, followed by long-term warming. The variability aspect is added to the picture of the end-Triassic environmental perturbations by considering the volcanic aerosol forcing as a composite of individual eruption events. Although such a succession of events cannot be empirically reconstructed for the CAMP, this concept appears more representative than a continuous sulfur injection. Earth could therefore have experienced millennia of repeated climatic perturbations with global temperature drops of up to several degrees, and even stronger sustained cooling during phases of very frequent eruptions. However, the increasingly large number of necessary eruptions makes cold phases sustained like this over several 10 kyr appear unlikely.

The simulated cooling-warming sequence causes a steric sea-level fall and subsequent rise reminiscent of the regression-transgression couplets found around the ETE and the TJB (see e.g. Lindström et al., 2017). However, these probably reflect sea-level changes on ~ 10 m and $\sim 10^4 - 10^5$ yr scales that require additional glacioeustatic mechanisms to amplify and sustain the climatically induced sea-level changes (see e.g. Miller et al., 2005; Schoene et al., 2010), which should be investigated in further research.

Global glaciations are here predicted beyond peak sulfur injection rates of ~ 13 GtS per decade. Since this did not happen in reality, our results rule out these more extreme scenarios and thus allow to restrict the emission parameter space. Macdonald and Wordsworth (2017) suggested that earlier LIP volcanism indeed caused global glaciations, but that the warm Late Triassic climate with a high tropopause made stratospheric sulfur injections from CAMP volcanism more difficult. This is another mechanism influencing Earth's sensitivity towards end-Triassic volcanic perturbations.

Our attempt to estimate the temperature stress on corals and marine phytoplankton suggests that the upper thermal limits of these groups are reached regionally, but not clearly transgressed on a large scale under a $+3$ to $+4^\circ\text{C}$ global warming. Extant corals, their photosymbionts and whole coral reef ecosystems can adjust to changing temperatures via different mechanisms, including shifts to more resistant phenotypes, as well as physiological acclimatisation or expansion to higher latitudes (Roche et al., 2018). These processes are likely outpaced by anthropogenic climate change but could have helped Late Triassic reefs to persist under warming caused by CAMP carbon emissions which were probably less rapid even for the protracted pulses considered here. However, if simultaneous sulfur emissions caused climatic fluctuations and repeatedly reversed temperature trends, the potential for adaptation appears limited. SST anomalies of $>1 - 3^\circ\text{C}$ sustained for a few weeks both above and below the regional long-term monthly temperature window cause coral bleaching and mortality events from which reefs require years to decades to recover (Roche et al., 2018; Kemp et al., 2016). In the herein studied cases, cooling caused by CAMP sulfur emissions could thus have pushed coral reefs beyond their lower thermal limits, repeatedly induced such bleaching events and overall limited coral reef growth and survival. Reef ecosystem collapse could therefore have already occurred during the hypothetical first CAMP pulse before the greenhouse warming unfolded. Reduced light availability due to aerosol shading and

blooms of cyanobacteria, sponges or algae promoted by fertilizing volcanic ash represent further potential stressors (Schils, 2012).

Pálffy and Kocsis (2014) suggested a minor role of acidification in the marine extinction because it would primarily affect the high-latitude waters. Although simulated pH reductions are larger there, Ω declines most strongly in the Tethys, where Late Triassic coral reefs were most abundant (see Figs. S15–S17). Furthermore, similar scale predictions for future changes ($+3.7^\circ\text{C}$ and $\Delta\text{pH} \approx -0.4$ until year 2100, RCP8.5 scenario) and the anticipated vulnerability of marine calcifiers (Pörtner et al., 2014), corroborate the importance of acidification in addition to thermal stress.

The higher carbonate saturation, lower nutrient levels and more uniformly high temperatures in the Tethys compared to eastern Panthalassa lend support to the notion of Martindale et al. (2015) that reefs in these two domains exhibited different characteristics because of geography and ocean circulation patterns. As mentioned before, we simulate no significant expansion of anoxia, which might therefore not have been caused immediately by warming and reduced ocean ventilation, but for example by weathering induced eutrophication in the long term.

5. Conclusions

In this study, potential climatic and environmental perturbations caused by carbon and sulfur emission pulses from end-Triassic volcanism are simulated and quantified. Including an idealized volcanic aerosol forcing and dynamically simulating volcanic emission pulses with a coupled Earth System Model featuring a marine carbon cycle module marks a progress compared to previous work in this context.

We show that under certain conditions the simultaneous emission of carbon and sulfur during a pulse of high volcanic activity of the CAMP can give rise to a transient cold phase, followed by longer-term global warming. The simulated maximum warming ranges from $+1.8$ to $+4.4^\circ\text{C}$, while the amplitude of cooling can be much higher. Because the radiative aerosol forcing is considered as the combined effect of many individual eruptions, strong inter-annual temperature fluctuations are superimposed on this cooling-warming sequence. This climatic variability on annual to millennial timescales would have enhanced the thermal stress on terrestrial and marine life. The simulated temperature changes are generally lower in the low-latitude oceans and the surrounding land areas compared to the high latitudes and the continental interiors. The climatic sensitivity of a Late Triassic equilibrium state with a pCO_2 in the lower proxy range is significantly higher compared to warmer states. No significant spread of oceanic anoxia, but a transiently reduced overturning, a steric sea-level fall and subsequent rise as well as a dropping carbonate saturation especially in the Tethys are observed.

The millennial Earth System Model simulations in combination with long-term carbon cycle simulations yield an updated overall picture of potential climatic impacts of CAMP volcanism: Each of the currently envisioned volcanic pulses, notably the first one which is associated with the onset of the end-Triassic extinction interval, could have caused a $\sim 10^2 - 10^3$ yr phase of global cooling and high climatic variability on a $\sim 10^0$ yr timescale and a subsequent global warming which decayed over $\sim 10^5$ yr. Elevated temperatures could have been sustained during the whole CAMP emplacement period, interrupted by brief cold and climatically variable phases.

Data availability

The model input and output as well as the pre-processing and post-processing scripts used to generate model input and

the figures in the paper are available at the institutional repository of the Potsdam Institute for Climate Impact Research (<http://doi.org/10.5880/PIK.2020.002>). The source code for the model used in this study is archived at the Potsdam Institute for Climate Impact Research and will be made available upon request.

Declaration of competing interest

The authors declare that they have no known competing financial interests or personal relationships that could have appeared to influence the work reported in this paper.

Author contributions

JL and GF designed the study, MH and SP contributed necessary model improvements, JL performed and analyzed the model simulations, JL, GF and MH discussed the results, JL wrote the paper with input from all coauthors.

Acknowledgements

We would like to thank Matthew Toohey and colleagues as well as Richard E. Zeebe for sharing the code of the EVA and LOSCAR models, respectively. We also thank Christopher Scotese for providing palaeocontinental reconstruction in electronic form and József Pálffy for discussions. JL thanks Prof. Michael Wagreich and the University of Vienna for the opportunity to pursue his PhD work. GF thanks the University of Vienna for support during an Ida Pfeiffer Professorship in summer 2018. The European Regional Development Fund (ERDF), the German Federal Ministry of Education and Research and the Land Brandenburg are gratefully acknowledged for supporting this project by providing resources on the high performance computer system at the Potsdam Institute for Climate Impact Research. Two anonymous reviewers are thanked for their constructive feedback.

Appendix A. Supplementary material

Supplementary material related to this article can be found online at <https://doi.org/10.1016/j.epsl.2020.116174>.

References

- Aarnes, I., Svensen, H., Connolly, J.A., Podladchikov, Y.Y., 2010. How contact metamorphism can trigger global climate changes: modeling gas generation around igneous sills in sedimentary basins. *Geochim. Cosmochim. Acta* 74, 7179–7195. <https://doi.org/10.1016/j.gca.2010.09.011>.
- Anderson, K.R., Poland, M.P., 2017. Abundant carbon in the mantle beneath Hawaii. *Nat. Geosci.* 10, 704–708. <https://doi.org/10.1038/ngeo3007>.
- Bachan, A., Payne, J.L., 2015. Modelling the impact of pulsed CAMP volcanism on pCO₂ and δ¹³C across the Triassic–Jurassic transition. *Geol. Mag.* 153, 252–270. <https://doi.org/10.1017/s0016756815000126>.
- Beerling, D.J., Berner, R.A., 2002. Biogeochemical constraints on the Triassic–Jurassic boundary carbon cycle event. *Glob. Biogeochem. Cycles* 16. <https://doi.org/10.1029/2001GB001637>. 10–1–10–13.
- Black, B.A., Manga, M., 2017. Volatiles and the tempo of flood basalt magmatism. *Earth Planet. Sci. Lett.* 458, 130–140. <https://doi.org/10.1016/j.epsl.2016.09.035>.
- Black, B.A., Neely, R.R., Lamarque, J.F., Elkins-Tanton, L.T., Kiehl, J.T., Shields, C.A., Mills, M.J., Bardeen, C., 2018. Systemic swings in end-Permian climate from Siberian Traps carbon and sulfur outgassing. *Nat. Geosci.* 11, 949–954. <https://doi.org/10.1038/s41561-018-0261-y>.
- Blackburn, T.J., Olsen, P.E., Bowring, S.A., McLean, N.M., Kent, D.V., Puffer, J., McHone, G., Rasbury, E.T., Et-Touhami, M., 2013. Zircon U–Pb geochronology links the end-Triassic extinction with the central Atlantic magmatic province. *Science* 340, 941–945. <https://doi.org/10.1126/science.1234204>.
- Brugger, J., Feulner, G., Petri, S., 2017. Baby, its cold outside: climate model simulations of the effects of the asteroid impact at the end of the Cretaceous. *Geophys. Res. Lett.* 44, 419–427. <https://doi.org/10.1002/2016gl072241>.
- Callegaro, S., Baker, D.R., De Min, A., Marzoli, A., Geraki, K., Bertrand, H., Viti, C., Nestola, F., 2014. Microanalyses link sulfur from large igneous provinces and Mesozoic mass extinctions. *Geology* 42, 895–898. <https://doi.org/10.1130/G35983.1>.
- Cohen, K., Finney, S., Gibbard, P., Fan, J.X., 2013. The ICS international chronostratigraphic chart (v2018/08). *Episodes* 36, 199–204. <https://doi.org/10.18814/epiiugs/2013/v36i3/002>.
- Donnadieu, Y., Godd eris, Y., Pierrehumbert, R., Dromart, G., Fluteau, F., Jacob, R., 2006. A GEOCLIM simulation of climatic and biogeochemical consequences of Pangea breakup. *Geochem. Geophys. Geosyst.* 7, 1–21. <https://doi.org/10.1029/2006GC001278>.
- Dunhill, A.M., Foster, W.J., Sciberras, J., Twitchett, R.J., 2018. Impact of the Late Triassic mass extinction on functional diversity and composition of marine ecosystems. *Palaeontology* 61, 133–148. <https://doi.org/10.1111/pala.12332>.
- Feulner, G., 2012. The faint young Sun problem. *Rev. Geophys.* 50, RG2006. <https://doi.org/10.1029/2011RG000375>.
- Foster, G.L., Royer, D.L., Lunt, D.J., 2017. Future climate forcing potentially without precedent in the last 420 million years. *Nat. Commun.* 8, 1–8. <https://doi.org/10.1038/ncomms14845>.
- Glaze, L.S., Self, S., Schmidt, A., Hunter, S.J., 2017. Assessing eruption column height in ancient flood basalt eruptions. *Earth Planet. Sci. Lett.* 457, 263–270. <https://doi.org/10.1016/j.epsl.2014.07.043>.
- Greene, S.E., Martindale, R.C., Ritterbush, K.A., Bottjer, D.J., Corsetti, F.A., Berelson, W.M., 2012. Recognising ocean acidification in deep time: an evaluation of the evidence for acidification across the Triassic–Jurassic boundary. *Earth-Sci. Rev.* 113, 72–93. <https://doi.org/10.1016/j.earscirev.2012.03.009>.
- Guex, J., Pilet, S., Muntener, O., Bartolini, A., Spangenberg, J., Schoene, B., Sell, B., Schaltegger, U., 2016. Thermal erosion of cratonic lithosphere as a potential trigger for mass-extinction. *Sci. Rep.* 6, 1–9. <https://doi.org/10.1038/srep23168>.
- Heimdal, T.H., Svensen, H.H., Ramezani, J., Iyer, K., Pereira, E., Rodrigues, R., Jones, M.T., Callegaro, S., 2018. Large-scale sill emplacement in Brazil as a trigger for the end-Triassic crisis. *Sci. Rep.* 8, 1–14. <https://doi.org/10.1038/s41598-017-18629-8>.
- Hofmann, M., Mathesius, S., Kriegl, E., van Vuuren, D., Schellnhuber, H., 2019. Strong time dependence of ocean acidification mitigation by atmospheric carbon dioxide removal. *Nat. Commun.* 10, 1–10. <https://doi.org/10.1038/s41467-019-13586-4>.
- Huynh, T.T., Poulsen, C.J., 2005. Rising atmospheric CO₂ as a possible trigger for the end-Triassic mass extinction. *Palaeogeogr. Palaeoclimatol. Palaeoecol.* 217, 223–242. <https://doi.org/10.1016/j.palaeo.2004.12.004>.
- Kemp, D.W., Colella, M.A., Bartlett, L.A., Ruzicka, R.R., Porter, J.W., Fitt, W.K., 2016. Life after cold death: reef coral and coral reef responses to the 2010 cold water anomaly in the Florida keys. *Ecosphere* 7, 1–17. <https://doi.org/10.1002/ecs2.1373>.
- Kiessling, W., Simpson, C., 2010. On the potential for ocean acidification to be a general cause of ancient reef crises. *Glob. Change Biol.* 17, 56–67. <https://doi.org/10.1111/j.1365-2486.2010.02204.x>.
- Lindstr m, S., van de Schootbrugge, B., Hansen, K.H., Pedersen, G.K., Alsen, P., Thibault, N., Dybkj r, K., Bjerrum, C.J., Nielsen, L.H., 2017. A new correlation of Triassic–Jurassic boundary successions in NW Europe, Nevada and Peru, and the Central Atlantic Magmatic Province: a time-line for the end-Triassic mass extinction. *Palaeogeogr. Palaeoclimatol. Palaeoecol.* 478, 80–102. <https://doi.org/10.1016/j.palaeo.2016.12.025>.
- Locarnini, R.A., Mishonov, A.V., Baranova, O.K., Boyer, T.P., Zweng, M.M., Garcia, H.E., Reagan, J.R., Seidov, D., Weathers, K., Paver, C.R., Smolyar, I., 2018. *World Ocean Atlas 2018, Volume 1: Temperature*. Mishonov, A. (Technical Ed.), NOAA Atlas NESDIS 81, 52 pp.
- Macdonald, F.A., Wordsworth, R., 2017. Initiation of Snowball Earth with volcanic sulfur aerosol emissions. *Geophys. Res. Lett.* 44, 1938–1946. <https://doi.org/10.1002/2016gl072335>.
- Martindale, R.C., Berelson, W.M., Corsetti, F.A., Bottjer, D.J., West, A.J., 2012. Constraining carbonate chemistry at a potential ocean acidification event (the Triassic–Jurassic boundary) using the presence of corals and coral reefs in the fossil record. *Palaeogeogr. Palaeoclimatol. Palaeoecol.* 350–352, 114–123. <https://doi.org/10.1016/j.palaeo.2012.06.020>.
- Martindale, R.C., Corsetti, F.A., James, N.P., Bottjer, D.J., 2015. Paleogeographic trends in Late Triassic reef ecology from northeastern Panthalassa. *Earth-Sci. Rev.* 142, 18–37. <https://doi.org/10.1016/j.earscirev.2014.12.004>.
- Marzoli, A., Callegaro, S., Dal Corso, J., Davies, J.H.F.L., Chiaradia, M., Youbi, N., Bertrand, H., Reisberg, L., Merle, R., Jourdan, F., 2018. The central Atlantic magmatic province (CAMP): a review. In: Tanner, L.H. (Ed.), *The Late Triassic World: Earth in a Time of Transition*. Springer International Publishing, pp. 91–125.
- Metzner, D., Kutterolf, S., Toohey, M., Timmreck, C., Niemeier, U., Freundt, A., Kr ger, K., 2012. Radiative forcing and climate impact resulting from SO₂ injections based on a 200,000-year record of Plinian eruptions along the Central American Volcanic Arc. *Int. J. Earth Sci.* 103, 2063–2079. <https://doi.org/10.1007/s00531-012-0814-z>.
- Miller, K.G., Kominz, M.A., Browning, J.V., Wright, J.D., Mountain, G.S., Katz, M.E., Sugarman, P.J., Cramer, B.S., Christie-Blick, N., Pekar, S.F., 2005. The Phanerozoic record of global sea-level change. *Science* 310, 1293–1298. <https://doi.org/10.1126/science.1116412>.
- Montoya, M., Griesel, A., Levermann, A., Mignot, J., Hofmann, M., Ganopolski, A., Rahmstorf, S., 2005. The Earth system model of intermediate complexity CLIMBER-3 . Part I: description and performance for present-day conditions. *Clim. Dyn.* 25, 237–263. <https://doi.org/10.1007/s00382-005-0044-1>.

- Pálffy, J., Kocsis, A., 2014. Volcanism of the Central Atlantic magmatic province as the trigger of environmental and biotic changes around the Triassic–Jurassic boundary. In: *Volcanism, Impacts, and Mass Extinctions: Causes and Effects*. In: Geological Society of America Special Papers, vol. 505, pp. 245–261.
- Paris, G., Donnadieu, Y., Beaumont, V., Fluteau, F., Godd eris, Y., 2016. Geochemical consequences of intense pulse-like degassing during the onset of the Central Atlantic Magmatic Province. *Palaeogeogr. Palaeoclimatol. Palaeoecol.* 441, 74–82. <https://doi.org/10.1016/j.palaeo.2015.04.011>.
- Percival, L.M.E., Ruhl, M., Hesselbo, S.P., Jenkyns, H.C., Mather, T.A., Whiteside, J.H., 2017. Mercury evidence for pulsed volcanism during the end-Triassic mass extinction. *Proc. Natl. Acad. Sci.* 114, 7929–7934. <https://doi.org/10.1073/pnas.1705378114>.
- Pohl, A., Laugi e, M., Borgomano, J., Michel, J., Lanteaume, C., Scotese, C.R., Frau, C., Poli, E., Donnadieu, Y., 2019. Quantifying the paleogeographic driver of Cretaceous carbonate platform development using paleoecological niche modeling. *Palaeogeogr. Palaeoclimatol. Palaeoecol.* 514, 222–232. <https://doi.org/10.1016/j.palaeo.2018.10.017>.
- P ortner, H.O., Karl, D.M., Boyd, P.W., Cheung, W., Lluch-Cota, S.E., Nojiri, Y., Schmidt, D.N., Zavalov, P.O., Alheit, J., Aristegui, J., Armstrong, C., Beaugrand, G., Belkovich, V., Bowler, C., Brewer, P., Church, M., Cooley, S.R., del Monte-Luna, P., Edwards, M., Flint, M., Follows, M.J., Fr olicher, T., Fulton, E.A., Gattuso, J.P., Hoegh-Guldberg, O., Hofmann, E.E., Knoll, A.H., Levin, L.A., Menzel, L., Moloney, C.L., Perry, R.I., Poloczanska, E.S., Roberts, J.M., Rost, B., Sarmiento, J.L., Sedlacek, J., Storch, D., Wiencke, C., Wittmann, A.C., 2014. Ocean systems. In: *Climate Change 2014: Impacts, Adaptation, and Vulnerability. Part A: Global and Sectoral Aspects. Contribution of Working Group II to the Fifth Assessment Report of the Intergovernmental Panel on Climate Change*, pp. 411–484. 10013/epic.45149.d001.
- Ridgwell, A., Zeebe, R., 2005. The role of the global carbonate cycle in the regulation and evolution of the Earth system. *Earth Planet. Sci. Lett.* 234, 299–315. <https://doi.org/10.1016/j.epsl.2005.03.006>.
- Robock, A., 2000. Volcanic eruptions and climate. *Rev. Geophys.* 38, 191–219. <https://doi.org/10.1029/1998RG000054>.
- Roche, R.C., Williams, G.J., Turner, J.R., 2018. Towards developing a mechanistic understanding of coral reef resilience to thermal stress across multiple scales. *Curr. Clim. Change Rep.* 4, 51–64. <https://doi.org/10.1007/s40641-018-0087-0>.
- Schaller, M.F., Wright, J.D., Kent, D.V., 2011. Atmospheric pCO₂ perturbations associated with the Central Atlantic Magmatic Province. *Science* 331, 1404–1409. <https://doi.org/10.1126/science.1199011>.
- Schaller, M.F., Wright, J.D., Kent, D.V., Olsen, P.E., 2012. Rapid emplacement of the Central Atlantic Magmatic Province as a net sink for CO₂. *Earth Planet. Sci. Lett.* 323–324, 27–39. <https://doi.org/10.1016/j.epsl.2011.12.028>.
- Schils, T., 2012. Episodic eruptions of volcanic ash trigger a reversible cascade of nuisance species outbreaks in pristine coral habitats. *PLoS ONE* 7, 1–7. <https://doi.org/10.1371/journal.pone.0046639>.
- Schmidt, A., Mills, M.J., Ghan, S., Gregory, J.M., Allan, R.P., Andrews, T., Bardeen, C.G., Conley, A., Forster, P.M., Gettelman, A., Portmann, R.W., Solomon, S., Toon, O.B., 2018. Volcanic radiative forcing from 1979 to 2015. *J. Geophys. Res., Atmos.* 123, 12491–12508. <https://doi.org/10.1029/2018JD028776>.
- Schmidt, A., Skeffington, R.A., Thordarson, T., Self, S., Forster, P.M., Rap, A., Ridgwell, A., Fowler, D., Wilson, M., Mann, G.W., Wignall, P.B., Carslaw, K.S., 2016. Selective environmental stress from sulphur emitted by continental flood basalt eruptions. *Nat. Geosci.* 9, 77–82. <https://doi.org/10.1038/ngeo2588>.
- Schoene, B., Guex, J., Bartolini, A., Schaltegger, U., Blackburn, T.J., 2010. Correlating the end-Triassic mass extinction and flood basalt volcanism at the 100 ka level. *Geology* 38, 387–390. <https://doi.org/10.1130/G30683.1>.
- van de Schootbrugge, B., Wignall, P.B., 2015. A tale of two extinctions: converging end-Permian and end-Triassic scenarios. *Geol. Mag.* 153, 332–354. <https://doi.org/10.1017/s0016756815000643>.
- Scotese, C.R., 2014. Atlas of Middle and Late Permian and Triassic paleogeographic maps. PALEOMAP Project PaleoAtlas for ArcGIS.
- Self, S., Schmidt, A., Mather, T., 2014. Emplacement characteristics, time scales, and volcanic gas release rates of continental flood basalt eruptions on Earth. *Spec. Pap., Geol. Soc. Am.* 505, 1–20. [https://doi.org/10.1130/2014.2505\(16\)](https://doi.org/10.1130/2014.2505(16)).
- Sellwood, B.W., Valdes, P.J., 2006. Mesozoic climates: general circulation models and the rock record. *Sediment. Geol.* 190, 269–287. <https://doi.org/10.1016/j.sedgeo.2006.05.013>.
- Steinthorsdottir, M., Elliott-Kingston, C., Bacon, K.L., 2017. Cuticle surfaces of fossil plants as a potential proxy for volcanic SO₂ emissions: observations from the Triassic–Jurassic transition of East Greenland. *Palaeobiodiv. Palaeoenviron.* 98, 49–69. <https://doi.org/10.1007/s12549-017-0297-9>.
- Svensen, H., Planke, S., Chevallier, L., Malthes-Sørensen, A., Corfu, F., Jamtveit, B., 2007. Hydrothermal venting of greenhouse gases triggering Early Jurassic global warming. *Earth Planet. Sci. Lett.* 256, 554–566. <https://doi.org/10.1016/j.epsl.2007.02.013>.
- Thompson, D.W., Wallace, J.M., Jones, P.D., Kennedy, J.J., 2009. Identifying signatures of natural climate variability in time series of global-mean surface temperature: methodology and insights. *J. Climate* 22, 6120–6141. <https://doi.org/10.1175/2009JCLI3089.1>.
- Toohy, M., Stevens, B., Schmidt, H., Timmreck, C., 2016. Easy Volcanic Aerosol (EVA v1.0): an idealized forcing generator for climate simulations. *Geosci. Model Dev.* 9, 4049–4070. <https://doi.org/10.5194/gmd-9-4049-2016>. <https://github.com/matthew2e/easy-volcanic-aerosol>.
- Zeebe, R., 2012a. LOSCAR: long-term ocean-atmosphere-sediment carbon cycle reservoir model v2.0.4. *Geosci. Model Dev.* 5, 149–166. <https://doi.org/10.5194/gmd-5-149-2012>.
- Zeebe, R.E., 2012b. History of seawater carbonate chemistry, atmospheric CO₂, and ocean acidification. *Annu. Rev. Earth Planet. Sci.* 40, 141–165. <https://doi.org/10.1146/annurev-earth-042711-105521>.

3. Concluding Discussion

The research of this thesis contributes to our understanding of Mesozoic paleoclimate conditions and the factors that shaped them. Climate dynamics are assessed here in three different regimes, driven by tectonic-scale processes (P.I), orbital cycles (P.II) and volcanic episodes (P.III), respectively. Insights into Earth’s behavior in warmer climate states and its response to greenhouse gas emission pulses and orbital climate forcing provide a wider perspective on climate changes during human history and potential extreme future climate states. However, the Mesozoic setting was characterized by the supercontinent Pangea and its breakup as well as still ancient forms of life, and thus primarily informs about the profound changes that the Earth system underwent in the course of its evolution. The presented work is essentially based on paleoclimate modeling approaches. Such modeling represents a synthesis of existing knowledge and hypotheses with simulated physical and biogeochemical consequences of tested scenarios of environmental change. Only by thorough contemplation on the model results in the context of other evidence and the characteristics of the utilized CLIMBER models, meaningful additions to an integrated picture of Mesozoic climates can be made here. Recapitulating the featured research articles, the main results and contributions to the scientific debate are now summarized together with a brief discussion of the limitations and potential continuation of this work.

P.I – Tectonic-Scale Climate Change Through the Mesozoic Era

Landwehrs et al. (2021) present the currently most extensive ensemble of climate simulations for the Mesozoic. The study identifies major long-term climate trends and their drivers through CLIMBER-3 α equilibrium climate simulations for 40 time slices from 255 to 60 Ma and systematically varied boundary conditions.

Global temperatures driven by $p\text{CO}_2$ but influenced by model climate sensitivity | The most important driver of Mesozoic global mean surface air temperature (GMST) changes is found to be the atmospheric CO_2 concentration. Using the fitted $p\text{CO}_2$ pathway of the most comprehensive available proxy reconstruction (Foster et al. 2017), the simulated GMSTs are higher than pre-industrial values for most of the Mesozoic and exceed 20°C during the Late Triassic–Early Jurassic and the mid-Cretaceous (P.I Fig. 1a). The reconstructed $p\text{CO}_2$ variations thus cause GMST differences of up to $\sim 6^\circ\text{C}$. The absolute GMST values are, however, strongly determined by the climate sensitivity exhibited by the CLIMBER-3 α model (the GMST change for a doubling of $p\text{CO}_2$; Foster and Rae 2016). For a $p\text{CO}_2$ doubling from 500 to 1000 ppm, it ranges from 2.8°C for the warm Late Cretaceous to 4.1°C in the cooler Late Triassic, and is therefore well within the $1.5\text{--}4.5^\circ\text{C}$ range suggested by the IPCC AR5 for the modern climate (Stocker et al. 2014). However, Earth’s actual climate sensitivity is quite uncertain due to the complexity of the involved feedbacks, especially in much warmer worlds than the present. Several of the most recent CMIP6 models exhibit sensitivities at the upper end of the mentioned range (Zhu et al. 2020). This seems to be at odds with paleoclimatic proxy evidence (Zhu et al.

2020) and the IPCC AR6 reconfirmed 3 °C as the best estimate with a likely range of 2.5 to 4 °C (Masson-Delmotte et al. 2021). One set of climate model simulations for a similar number of Mesozoic time slices has recently been published (Valdes et al. 2021). This uses a more sophisticated AOGCM (HadCM3) but includes less sensitivity experiments and has not yet been analyzed with respect to Mesozoic climates. HadCM3 exhibits a higher climate sensitivity and thus up to 4 °C higher Mesozoic GMSTs at comparable $p\text{CO}_2$ (P.I Fig. 1a). Nevertheless, the long-term temperature trends for the proxy $p\text{CO}_2$ pathway are similar. In comparison with Valdes et al. (2021) and also Landwehrs et al. (2021), another modeling study obtained generally less elevated temperatures at similar $p\text{CO}_2$ levels (Chaboureau et al. 2014). The significant uncertainty of the $p\text{CO}_2$ proxy record adds to the uncertainty of simulated Mesozoic global mean temperatures. P.I addresses this by systematically varying $p\text{CO}_2$ between 200 and 4000 ppm and by additionally testing a carbon cycle model-derived $p\text{CO}_2$ pathway.

Global temperature estimates are difficult but Triassic–Early Jurassic and mid-Cretaceous warm intervals are robust | Despite all uncertainties, consistent first-order trends for the Mesozoic GMST evolution emerge when the different $p\text{CO}_2$ pathways, climate models as well as $\delta^{18}\text{O}$ based proxy temperatures (Mills et al. 2019) and the occurrence of glacial deposits (Boucot et al. 2013, Cao et al. 2018) are taken into account. Together, these support warm temperature anomalies during the Late Triassic to earliest Jurassic and during the mid-Cretaceous, caused by relatively high $p\text{CO}_2$. It is worth noting, that the proxy $\delta^{18}\text{O}$ temperatures and $p\text{CO}_2$ values do not correlate perfectly in the Mesozoic, which can be due to the inaccuracies and simplifying assumptions involved in their calibration (Marcilly et al. 2021). For example, $\delta^{18}\text{O}$ paleothermometry requires assumptions about ambient seawater composition and uneven spatial sampling distorts temperature reconstructions (Song et al. 2019, Jones and Eichenseer 2021). Additionally the $\delta^{18}\text{O}$ measurements are limited to $<40^\circ$ latitude and therefore essentially represent tropical sea surface temperatures. Climate model simulations as provided by P.I can be useful to translate these tropical SSTs into global mean temperatures without making ad-hoc assumptions on meridional temperature gradients. Landwehrs et al. (2021) demonstrate that there is basically a linear correlation which varies slightly between the geologic time slices and between warmer and colder climate states (1.6 to $2.0 \Delta\text{GMST}/\Delta\text{SST}_{\text{trop}}$; A.I Fig. S14–S15).

Increasing solar luminosity and continental flooding contributed to global warming | In addition to $p\text{CO}_2$, important systematic effects of other factors on Mesozoic GMSTs are quantified by P.I. The slow increase of the sun’s luminosity translates into a warming of almost $+2^\circ\text{C}$ through the Mesozoic (P.I Fig. 2). The simulations furthermore suggest that the tectonically-driven long-term sea-level rise could have contributed a temperature increase on the order of $+1^\circ\text{C}$ from the Triassic–Jurassic to the Late Cretaceous (P.I Fig. 2). This is due to the extensive flooding of continental shelves by lower albedo seawater. However, this effect strongly relies on the paleogeographic reconstruction by Scotese and Wright (2018) that exhibits a pronounced decrease of the land surface area fraction from 38 to 26 % (P.I Fig. 2). Indeed, a robust linear negative correlation of GMST with the global land area fraction (ca. -1.6°C per 10 % increase) as well as a positive correlation with the average absolute latitude of land areas are observed (A.I Fig. S13). This indicates that a high portion of ocean area, especially at low latitudes, generally contributed to warmer temperatures in Earth history, driven by the relocation and varying flooding of continental plates. Although the global-scale trends are robust for the Mesozoic, paleogeographic reconstructions differ in their plate rotation models, topography, bathymetry and coastlines. Furthermore, cyclic variations of global sea levels (e.g. Haq et al. 1988) could have introduced changes in continental flooding and exposure that are

not reflected by the paleotopographies. It would therefore be very useful to systematically compare different paleogeographic reconstructions in further work. This does not only concern GMSTs but also patterns of climate and atmosphere/ocean circulation due to different land-sea distributions and topography/bathymetry. For example, recently updated coastlines in paleogeographic reconstructions suggest less extensive exposed land areas for the Triassic (Kocsis and Scotese 2021, Scotese 2021, Marcilly et al. 2021). This would result in a less pronounced warming from continental flooding towards the Cretaceous.

Sparse vegetation in low-latitude Pangea cooled the climate but feedbacks are not modeled | Global temperature changes due to surface albedo changes are not only rooted in continental flooding but also in the land surface cover types. It has been suggested that the area of desert land is linked to global temperatures due to its high albedo (Barron et al. 1980, Hallam 1985). P.I does indeed show that the large area of dry low-latitude land during Triassic–Jurassic times contributes to a small cooling of $\sim 0.5^\circ\text{C}$ with respect to test cases with a homogeneous distribution of vegetation. One limitation of the CLIMBER-3 α model is, however, that these vegetation patterns are not simulated interactively with climate. Landwehrs et al. (2021) therefore chose to prescribe vegetation patterns based on climate zones inferred from proxy distributions (A.I Fig. S1; Boucot et al. 2013), and homogeneous vegetation patterns were additionally tested for comparison. This introduces some empirical evidence to the model approach and avoids uncertainties of vegetation modeling, but also rules out vegetation feedbacks in the response to changing boundary conditions. Previous studies showed that vegetation feedbacks could have contributed to warmer high-latitude temperatures during the mid-Cretaceous (Zhou et al. 2012), for example. Future work should thus aim for a more sophisticated representation of vegetation dynamics, which would be possible, for example, with the CLIMBER-X model utilized in P.II.

Equator-to-pole temperature gradients depended on high-latitude land area but are potentially overestimated | Besides the described global temperature variations, P.I aimed to characterize secular Mesozoic climate trends by assessing seasonality, zonation and aridity of continental climates as well as the meridional temperature gradients. The latter range between ~ 20 and 35°C when measured as the surface air temperature difference between low and high latitudes ($<30^\circ$ and $>60^\circ$ respectively; P.I Fig. 5). They are found to depend primarily on the high latitude land area. This is manifested, for example, by a $\sim 5^\circ\text{C}$ lower (higher) equator-to-pole contrast on the southern (northern) hemisphere as Pangea drifts northwards through the Triassic. The second important effect for the meridional temperature gradient is the polar amplification of $p\text{CO}_2$ -driven global temperature changes which is partially explained by the sea ice albedo feedback. Similar to many other climate models, CLIMBER-3 α yields cooler polar temperatures and larger meridional temperature gradients than derived from marine fossil paleothermometry and high-latitude evidence of temperate flora and fauna, particularly during warming periods like the mid-Cretaceous (Hallam et al. 1993, Huber 2012, Zhang et al. 2019, Spicer et al. 2020, Klages et al. 2020, Scotese 2021, Letulle et al. 2022, Gaskell et al. 2022). Adjusting parameters of the model cloud microphysics has been proposed as one solution (Upchurch et al. 2015, Zhu et al. 2019). For example, a reduction of the cloud condensation nuclei concentration in models to levels that more closely resemble a pristine pre-industrial atmosphere leads to a less dense cover of cooling polar clouds and thus warmer polar regions (Upchurch et al. 2015). On the other hand, very recent studies revisiting the proxy temperature calibrations yield latitudinal temperature gradients more consistent with climate models (Steinig et al. 2020, Gaskell et al. 2022). Further research following-up this thesis should more thoroughly address these questions.

Climate seasonality decreased with continental flooding and fragmentation | As another consequence of the changing paleogeography, [P.I](#) demonstrates a marked decrease of seasonal temperature contrasts on the continents from the Late Triassic–Early Jurassic to the Late Cretaceous ([P.I](#) Fig. 3). The main drivers are continental fragmentation and flooding as well as the re-distribution of land area. The Triassic and Early Jurassic are characterized by large continental areas in mid- and high-latitudes which amplify the climate seasonality. This substantiates previous notions on a Mesozoic transition from strongly seasonal Pangean climates to a more equable Late Cretaceous (e.g. Hallam 1985, see Sec. 1.1.1). This can now be shown quantitatively in a coherent climate model framework that also allows to assess the relative contributions of other factors. The simulated climate seasonality is modulated to a similar degree by the orbital parameters as by the paleogeographic changes. This indicates that aspects of the Mesozoic long-term climate evolution have been significantly overprinted by shorter-term variability introduced by orbital cycles, among other things. Some proxy evidence could express temporary conditions rather than million-year average conditions, for example a particularly warm or cold North Pole at a certain orbital configuration. Further investigating such shorter-term variability is therefore also important for the interpretation of tectonic-scale trends and is indeed the focus of [P.II](#) and [P.III](#), in particular.

Continental flooding and fragmentation as well as global warming also led to more humid climates | One other previously established Mesozoic climate trend that is confirmed and further analyzed in [P.I](#) concerns the humidity of climate. It is shown in [P.I](#) that paleogeographic changes, $p\text{CO}_2$ and the increasing solar luminosity contributed to a general tendency towards weaker continental aridity through the Mesozoic ([P.I](#) Fig. 7). Continental fragmentation and sea level rise enhance the moist maritime influence in many regions. The increased solar luminosity provides a long-term warming trend leading to globally more humid conditions. The $p\text{CO}_2$ indicated by proxy records and carbon cycle modeling increases from relatively low Early Jurassic values to higher levels in the mid-Cretaceous. This contributes significantly to the global warming trend which is found to amplify the continental humidification. The tropical aridity of western Pangea during the early Mesozoic that is inferred from abundant evaporites and missing coal deposits (Boucot et al. 2013, Cao et al. 2018) is supported in our simulations by the establishment of a continuous tropical rain belt only from the Cretaceous on ([P.I](#) Figs. 4,7). Mesozoic rainfall patterns have been recently reconstructed with machine learning methods applied to the distribution of the same lithologic climate indicators (Chandra et al. 2021). However, the machine learning algorithms were trained on a limited set of Miocene and Eocene climate simulations and could potentially be improved by training on larger climate model datasets like those of Landwehrs et al. (2021) and Valdes et al. (2021). It could be worth assessing how the predictions of this statistical data-based approach compare with physical climate modeling and if combining both approaches could establish a better link between climate proxies and modeling.

Further model cross-validation and extension to the whole Phanerozoic is valuable | With a focus on the Mesozoic era, [P.I](#) yields an updated view on climate change on tectonic time scales and its drivers. Assessing a large ensemble of model simulations for a continuous set of geologic time slices and systematically varied boundary conditions provides novel possibilities to investigate and visualize these changes. A comprehensive model intercomparison for the Mesozoic like the DeepMIP (Hollis et al. 2019, Lunt et al. 2017; 2021), including systematic validation against enhanced proxy datasets, would be an important next step towards more robust insights. An extensive data set for [P.I](#) has been published for further utilization (Landwehrs et al. 2021b). The results would become even more exciting if the approach developed here would be extended to the whole Phanerozoic

and the CLIMBER-X model. This would be comparable and complementary to the work of Valdes et al. (2021), but with the possibility to test a wider range of boundary conditions (e.g. different paleogeographic reconstructions, $p\text{CO}_2$ pathways, orbital effects, sea level, vegetation, dynamic ice sheets). Of course, this represents a major challenge because a wider range of Earth system states needs to be adequately represented. For example, continental ice sheets and the evolutionary steps of land plants cannot be neglected as in our modeling for the Mesozoic. Another important development is the stronger coupling of continuous biogeochemical and plate tectonic models with climate models. Transient simulations with global 3D climate models over tectonic time scales would not necessarily be the most sensible option even if they were computationally feasible. Nevertheless, climate modeling can be increasingly incorporated into hybrid modeling approaches for long-term carbon cycle dynamics (Mills et al. 2021, Marcilly et al. 2021).

P.II – Orbital Climate Pacing in the Late Triassic

Landwehrs et al. (2022) analyze an ensemble of transient orbitally-driven CLIMBER-X simulations for the Late Triassic to Early Jurassic. These are primarily used to interpret the cycles and trends exhibited by the sedimentary Newark-Hartford Basin (NHB) lake level record. The study identifies the hydroclimatic expression of orbital forcing, continental drift and $p\text{CO}_2$ changes in this paleo-tropical region as well as a few contemporaneous proxy localities.

The Newark Basin drifted from humid to semi-arid climate zones but differences in paleogeographic reconstructions have climatic effects | The geologic time period from ~ 233 to 199 Ma that is covered by the NHB record is represented by simulations for nine time slices from 230 to 190 Ma in 5 Myr time steps. In the two tested plate-tectonic and paleogeographic reconstructions, the NHB region moves from ~ 5 to 22°N within that time frame. The simulations suggest that this northward drift from tropical to sub-tropical latitudes results in a transition from tropical humid to more seasonal and ultimately semi-arid climates (P.II Fig. 1). This general trend holds for the three tested $p\text{CO}_2$ levels (750, 1500 and 3000 ppm) and both paleogeographic reconstructions. For the latter, the reconstructions of Marcilly et al. (2021) and Cao et al. (2017; 2018) were selected (termed Geo_1 and Geo_2), because a paleomagnetic reference frame can be used for their plate rotation models in GPlates. In contrast to the reconstructions by Scotese and Wright (2018) that have been used in P.I, the NHB paleolatitudes in these models therefore agree better with local paleomagnetic constraints (Kent and Tauxe 2005). While the coastlines may also be more reliable, Geo_1 and Geo_2 only distinguish qualitatively between exposed land, shallow marine and deep marine areas and thus provide much less topographic detail than Scotese and Wright (2018). Geo_2 additionally represents major mountain ranges but in Geo_1 the continents and sea floor are entirely flat. On the one hand, paleotopography is climatically very important as it affects the atmospheric circulation, causes rain shadow effects and can affect monsoon strength as the Tibetan Plateau does in today’s climate (Ruddiman 2014). On the other hand, very detailed paleotopographies might not reflect the actual degree of uncertainty, compared to more conservative, less detailed approaches. As attempted in P.II, paleoclimate modeling approaches should ideally incorporate multiple available paleogeographic reconstructions to constrain effects of their global and regional differences. This implies a significantly larger modeling effort, of course. In the case of the Newark-Hartford Basins, further research could more comprehensively assess the role of paleogeography in the regional tectonic and orbital climate modulation. Particularly relevant are the Central Pangean Mountains, a mountain belt which crossed tropical Pangea (encompassing the Appalachians) and significantly affected

its climate (Otto-Bliesner 1993; 1998, Heavens et al. 2015).

Orbital variability peaked under humid but strongly seasonal climates at high $p\text{CO}_2$ | A significant orbital climate modulation is simulated for the NHB region, dominated by climatic (eccentricity-modulated) precession (P.II Fig. 2). The NHB lake level cyclicity is thought to represent primarily the hydrological balance of the basin catchment area and especially the orbital modulation of the maximum rainfall and humidity season. Therefore, the analyses of P.II focus on the balance of simulated precipitation and evaporation (PRC–EVAP) and its monthly maximum values. At the lowest latitudes ($\sim 5\text{--}7^\circ\text{N}$) during 230–225 Ma, tropical humid conditions with a weak seasonality and orbital climate response prevail in the NHB region (P.II Fig. 2i–k). The record still consists mainly of lacustrine sediments at this time and reveals little cyclicity. This changes around the 220 Ma time slice ($\sim 8^\circ\text{N}$), when the highest humidity as well as amplified seasonality and orbital signal coincide with the deepest and consistently cyclical lake levels. During the following 215–200 Ma time slices ($\sim 10\text{--}15^\circ\text{N}$), humidity overall decreases again but seasonality and orbital modulation of PRC–EVAP are very high. This might explain the strongly cyclic lake sediments with less frequent deep water deposits and more common aridity-related red beds. The orbital climate modulation remains high during the Rhaetian (~ 205 Ma) but low lake levels and weak cyclicity are recorded. Landwehrs et al. (2022) show that this could be the result of a cooler and drier climate due to the low atmospheric $p\text{CO}_2$ indicated by the proxy record for this time. If lake filling and sedimentation indeed exhibited the proposed threshold characteristic (see Sec. 1.1.2), only humidity peaks related to pronounced climatic precession minima would be recorded as a weak, clipped orbital signal. In contrast, CAMP volcanic emissions caused temporarily elevated $p\text{CO}_2$ levels around the Triassic–Jurassic boundary (~ 200 Ma, $\sim 17^\circ\text{N}$; see Sec. 1.1.3, P.II and P.III). These contribute to enhanced humidity and orbital cyclicity in the model, in agreement with reinvigorated cyclicity in the lake level record. Increasingly dry climates with reduced seasonality and orbital response are established and intensified by lower $p\text{CO}_2$ during the following 195–190 Ma interval ($\geq 20^\circ\text{N}$). This trend matches the onset of muted lake level variability and the replacement of lacustrine by fluvial and eolian sedimentary environments in the NHB.

Low-latitude obliquity signals from effects on the tropical rain belt | The discussed findings demonstrate that the orbital signal recorded in very long sedimentary archives is influenced by continental drift and long-term $p\text{CO}_2$ changes. To unravel the nature of the global orbital climate pacing from such records, these factors therefore have to be accounted for in spatially explicit models. To our knowledge, P.II represents the first study of this kind, at least for the Mesozoic era. Dynamic climate modeling is furthermore necessary because the orbital climate response is not exclusively determined by the local insolation that can be calculated analytically. Although the latter can approximate temperature changes, the regional climate is additionally determined by the response of rainfall and humidity, linked to the atmospheric circulation as well as cloud and vegetation feedbacks. For example, a contribution of obliquity to the NHB lake level cycles has long been neglected due to its minimal direct radiative forcing in the tropical paleolatitudes of this locality (see Sec. 1.1.2). However, signals of obliquity and its modulation by the orbital inclination have been recently detected (Margulis-Ohnuma et al. 2021, Whiteside et al. 2021). The simulated NHB PRC–EVAP balance does indeed exhibit systematic effects of obliquity that can potentially explain these empirical findings. As expected, the obliquity signal in the local temperate seasonality is quite small but increases steadily as the NHB drifts to higher latitudes (A.II Fig. S3). In contrast, the PRC and PRC–EVAP obliquity is most pronounced at the lowest latitudes during the earlier time slices and decays with time (P.II Fig. 3l, A.II Fig. S3). High obliquity leads to an enhanced thermal

contrast between the northern and the southern hemisphere during boreal summer, which amplifies the northward shift of the Intertropical Convergence Zone (ITCZ; [A.II Fig. S8](#)). In combination with enhanced cloud cover and the slightly lower insolation at the equator ([Fig. 1.3c](#)), this results in higher humidity in the NHB. This is similar to effects on the more recent African monsoon system ([Bosmans et al. 2015a;b](#)). It can be concluded that enhanced northern hemisphere insolation due to both climatic precession and obliquity could have amplified wet seasons in the NHB but with different underlying mechanisms. The climatic precession generally represents the dominant component of the orbital signal, however.

The orbital climate modulation varies between proxy localities | It has become clear that the local expression of an orbital forcing bears a complex relation to paleogeographic and climatic patterns. A global perspective on the Late Triassic orbital climate pacing can therefore not rely on only one excellent record like the NHB but has to include other, spatially distributed archives. Paleoclimate modeling could provide a unifying framework to interpret and correlate the differently expressed orbital climate signals of multiple contemporaneous records. As a very first step into this direction, [P.II](#) briefly evaluates the presented climate simulations for the paleolocations of the Germanic Basin, the Junggar Basin and Colorado Plateau. Similar to the NHB, the Germanic Basin was situated in eastern Pangea, although at middle latitudes, and similar concepts have been developed for its cyclic lake sediments ([Vollmer et al. 2008](#), [Bahr et al. 2020](#)). Strongly seasonal summer rainfall is simulated in this region and climatic precession dominates the T and PRC seasonality response, with maxima at insolation peaks ([A.II Figs. S10–13](#)). Obliquity effects are relatively small but also increase with the northward drift. In the Junggar Basin, at even higher northern latitudes ($\sim 70^\circ\text{N}$ at 200 Ma), the strength of obliquity signals in T and PRC–EVAP is comparably strong as that of precession, in agreement with geological evidence ([Sha et al. 2015](#), [Olsen et al. 2019](#)). For the Colorado Plateau in the western tropics of Pangea, the T response is dominated by eccentricity and precession but PRC and PRC–EVAP are strongly modulated by obliquity. Similar to the NHB this is related to shifts in the tropical rainfall. A more sophisticated integration and correlation could be attempted in future research. The approach developed here could furthermore be applied to other astronomically paced Mesozoic records like the Cretaceous Songliao Basin ([Liu et al. 2020](#)) for which hydroclimate changes have been reconstructed as well.

Astronomical dynamics are complex but can be simplified for climate modeling purposes | The orbital forcing that drives the simulations in [P.II](#) is composed of the typical main periodicities of precession (~ 20 kyr), obliquity (~ 40 kyr) and short eccentricity modulation (~ 100 kyr) in an idealized way. It does not correspond to a specific full astronomical solution as these can currently not be accurately calculated back into the Triassic. However, it is clear that the periods of obliquity and precession as well as the diurnal cycle have been shorter in the Mesozoic than today because Earth’s rotation slows down due to tidal dissipation in the Earth–Moon system ([Berger and Loutre 1994](#), [Laskar et al. 2004](#), [Olsen and Whiteside 2009](#), [Hinnov 2018](#), [Huang 2018](#)). For 225 Ma, [Waltham \(2015\)](#) obtained periods of 36.7 kyr, 18.1–22.1 kyr and 23.1 hours for obliquity, climatic precession and length-of-day. Additionally, longer periods are not represented in the transient climate model simulations, although the 405 kyr eccentricity cycle provides the most important astrochronostratigraphic metronome, for example. This is because computational speed limits the length of climate simulations and furthermore because [P.II](#) aims to study the primary climatic effects of the three orbital parameters. For this purpose, it is sufficient to consider only the fastest modes and to approximate their frequencies.

Orbital-scale climate modeling requires reasonable model acceleration | Continued work could, however, attempt to test specific astronomical solutions (Laskar et al. 2004; 2011, Zeebe 2017) in climate models and cyclostratigraphic records. For example deep time archives like the NHB record could eventually serve as anchors to extend astronomical solutions beyond their current ~ 60 Ma prediction limit (Olsen et al. 2019, Ikeda and Tada 2020). For this, CLIMBER-X simulations on the million-year scale would need to be carried out. In P.II, durations of 250 kyr are comfortably achieved by applying an acceleration factor of $\times 5$. This essentially implies that the orbital forcing is accelerated relative to the annual cycle of the climate model. A precession cycle of 20 kyr in the time scale of the forcing is thus compressed to 4 kyr in the climate model. In other words, the forcing is advanced by five years at every model year. Similar acceleration procedures have been widely used and evaluated to speed up transient orbital climate simulations (Lorenz and Lohmann 2004, Lunt et al. 2006, Timm and Timmermann 2007, Timmermann et al. 2007, Tigchelaar et al. 2018, Lu et al. 2019, Kutzbach et al. 2008; 2020). They rely on the assumption that the astronomical forcing operates on much longer time scales (millennia) than the atmosphere and the mixed-layer ocean (months to a few years; Lorenz and Lohmann 2004). These studies use acceleration factors of $5\times$, $10\times$ and even $100\times$, with only moderate effects on surface climate conditions. However, the deep ocean has millennial equilibration time scales and thus exhibits a dampened orbital response that can affect the ocean circulation, especially at acceleration greater than $5\times$. For the NHB climate conditions analyzed in P.II, effects of the $5\times$ acceleration are found to be negligible. An acceleration factor of $100\times$ would promote CLIMBER-X simulations over a 5 Myr orbital forcing, instead of 250 kyr. With a small set of such model runs, the Late Triassic surface climate response to a specific astronomical solution could be simulated quasi-continuously and linked to records from the NHB, for example. However, the orbital response to ≤ 100 kyr cycles in this approach is limited to atmosphere, land, sea ice and surface ocean.

Quaternary perspectives on African orbital climate change are useful | While our understanding of the orbital climate pacing in the Newark rift basins remains limited, studies on the Quaternary astronomical effects on North and East African lake systems (e.g. Kutzbach and Street-Perrott 1985, Trauth et al. 2010; 2021, Maslin et al. 2014) and the African monsoon (e.g. Tuenter et al. 2003, Braconnot et al. 2008, Kutzbach and Liu 1997, Kutzbach et al. 2008; 2020, Verschuren et al. 2009, Bosmans et al. 2015a;b, Marzocchi et al. 2015, Claussen et al. 2017, Skonieczny et al. 2019) could provide useful analogies. These show, for example, that the most humid conditions and the deepest lakes are related to maximum insolation phases of the climatic precession cycles (Sec. 1.1.2; Trauth et al. 2001; 2003; 2010; 2015, Maslin et al. 2014, Ruddiman 2014). Some of these studies also pick up the concept of a threshold response of the lake levels (see Sec. 1.1.2; Trauth et al. 2010, Maslin et al. 2014, Ivory et al. 2016). Such threshold effects (also clipping or rectification) have been invoked for cyclostratigraphic records in general (Ziegler et al. 2010a, Hinnov 2018) and in the Mesozoic context (Laurin et al. 2019, Chu et al. 2020). Transferring more of these insights and methods to ancient basin lakes could foster important progress. So far, the link between orbital climate pacing and reconstructed lake level changes established in P.II remains conceptual and should be complemented by a physically consistent representation of basin hydrology in future work. This could be achieved with an idealized but explicit lake balance modeling approach (e.g. Kutzbach and Street-Perrott 1985, Morrill et al. 2001, Sepulchre et al. 2008, Fraedrich 2013, Fischer et al. 2020).

Ice sheet and carbon cycle feedbacks will add new dimensions | Despite the discussed limitations, P.II represents a significant contribution to the research on the orbital

spacing of paleoclimates. The novel modeling approach is enabled by the computational efficiency of the CLIMBER-X model which allows for orbital-scale transient model runs as well as ensembles of such simulations for changing paleogeographies and $p\text{CO}_2$ values. So far, the simulations have been performed with the coupled dynamic atmosphere, ocean, sea ice, vegetation and land surface modules of CLIMBER-X. Feedbacks of continental ice sheets and the global carbon cycle are therefore not yet represented in this approach. Their importance for the orbital climate response is, however, evident for the Quaternary glacial–interglacial cycles (e.g. Ganopolski and Brovkin 2017). Ice sheets likely played a smaller role in the much warmer Mesozoic climates and there is little evidence for major glaciations during the Late Triassic. However, ephemeral ice sheets could have still been growing during colder phases at favorable orbital configurations. Glacial–interglacial $p\text{CO}_2$ changes in the Quaternary are on the order of ~ 100 ppm and thus much smaller than the $p\text{CO}_2$ differences covered in P.II. Nevertheless, it would be an exciting target for further research to explore these additional factors especially during particularly warm and cold periods of the Mesozoic. Building on P.II, this would provide important insights into the astronomical pacing of Earth’s climate in greenhouse and supercontinent states beyond the much better studied Quaternary glacial cycles. The CLIMBER-X model will provide excellent opportunities to study these effects with its dynamic ice-sheet and carbon cycle modules.

P.III – Climatic Disruptions by end-Triassic Volcanism

Landwehrs et al. (2020) assess climatic and environmental effects of volcanogenic gas emissions of the Central Atlantic Magmatic Province (CAMP) which likely caused the end-Triassic extinction event. For this, an ensemble of transient climate-biogeochemistry simulations was conducted with the CLIMBER-3 α +C model. These are driven by brief pulses of carbon emissions and a radiative forcing representing the effect of stratospheric sulfate aerosols. The study mainly analyzes the resulting warming and cooling for different emission scenarios, but also considers ocean acidification and deoxygenation. Many of these aspects are represented for the first time in a transient coupled climate model framework for the end-Triassic events.

Volcanic carbon emissions cause long-term global warming which is amplified in cooler background climate states | One of the major challenges of P.III is the development of forcing scenarios that, on the one hand, incorporate current constraints on the CAMP emission history and general characteristics of LIP volcanism and, on the other hand, can be implemented in the CLIMBER-3 α +C. Given the still large uncertainties regarding the CAMP emissions, one of the virtues of the study is that a wide range of scenarios can be tested. The study overall follows previous work that assumed 4–5 major brief emission pulses (≤ 10 kyr) within ~ 600 kyr, of which the first coincided with the onset of the marine extinction interval at ~ 201.56 – 201.51 Ma (Sec. 1.1.3; Paris et al. 2016). For the carbon emission pulses, an intermediate total emission of 5300 GtC is adopted from Paris et al. (2016) and 2500 and 7500 GtC are tested to account for lower and higher estimates. These carbon emission pulses are found to increase the atmospheric $p\text{CO}_2$ by ~ 900 – 2800 ppm and result in a global warming of $+1.8$ – 4.4 °C (P.III Fig. 2a, A.III Fig. S12). The warming amplitude grows quasi-logarithmically with the total emission but importantly also depends on the initial climate state. Three initial states with $p\text{CO}_2$ levels of 1000, 1500 and 2000 ppm have been considered to account for the uncertainty in the Late Triassic pre-eruption $p\text{CO}_2$. While the coolest 1000 ppm state warms by 4.4 °C, the 2000 ppm state only experiences a 2.6 °C warming. This indicates that already warmer climate states at later stages of the CAMP or before other LIP episodes could have

been less sensitive to volcanic greenhouse gas emissions. As discussed above for P.I, this temperature response is, however, strongly determined by the characteristic (moderate) climate sensitivity exhibited by the CLIMBER-3 α model.

Carbon emissions furthermore result in ocean stratification, acidification and deoxygenation | The CLIMBER-3 α +C model includes a comprehensive marine carbon cycle module (HAMOCC), so that parts of the emitted carbon are dissolved in the model's ocean. This leads to ocean acidification and a surface ocean pH reduction of ~ 0.4 (A.III Fig. S15), which is on the same order as expected for the SSP3-7.0 emission scenario for a 3.6 °C warming until the end of the 21st century (Masson-Delmotte et al. 2021). Warming the ocean from the top leads to a reduction of ocean overturning, mixing and sea water oxygen concentrations (P.III Fig. 3b, A.III Fig. S13). Besides thermal perturbations, ocean acidification and anoxia are discussed as possible drivers of the end-Triassic marine extinction and comparable events (e.g. Kiessling and Simpson 2010). Although signs of both processes are observed in P.III, extended research will be necessary to evaluate their ecologic importance. The modeling approach presented here can only cover a few of the relevant biogeochemical processes. For example, only the acidifying effects of carbon are captured, without contributions of other volatile species, especially SO₂. In any case, the initial pH and carbonate saturation state of the ocean are very difficult to constrain. For ocean anoxia, contributions by eutrophication due to excess nutrients from enhanced continental weathering or ash deposition could be more important than that of ocean warming and ventilation. CLIMBER-3 α +C only includes the marine carbon cycle and thus misses the dynamics of the land carbon cycle and the slow weathering and sedimentation feedbacks. Due to this fact, the excess carbon is not slowly drawn down after an emission pulse, which limits the applicability of the model to events shorter than ~ 10 kyr. For this reason, and to put the CLIMBER-3 α +C simulations into a longer-term perspective, P.III includes a few simulations with the LOSCAR carbon cycle model. These suggest that the extreme levels of $p\text{CO}_2$ and global warming would have decayed within $\sim 10^4$ – 10^5 yrs between the emission pulses but could have remained elevated for the whole CAMP emplacement period (P.III Fig. 5). A more comprehensive integration of the climate and carbon cycle responses to volcanic emissions could be achieved with the CLIMBER-X model, as outlined in the outlook section below.

Volcanogenic sulfur aerosols drive significant short-term cooling but different scenarios need to be considered | Most research on climatic disruptions by LIPs revolves around carbon emissions, also because these can be linked relatively clearly to geologic evidence like carbon isotope excursions (CIEs), reconstructed $p\text{CO}_2$ peaks and indicators of warming. Although volcanological considerations suggest that equally large quantities of sulfur were emitted by the CAMP (e.g. Heimdal et al. 2018, see Sec. 1.1.3), their effects would have been much more short-lived and are therefore not resolvable by sulfur isotopic records, for example (Lindström et al. 2021). The characteristics of CAMP sulfur emissions and potentially associated cooling events are thus very difficult to constrain empirically. P.III therefore tests a range of sulfur emission scenarios and describes the simulated climatic consequences to clarify their potential amplitudes and temporal characteristics. Three cases are considered (P.III Fig. 6), of which Case 1 assumes that sulfur is degassed alongside with carbon but is not injected into the stratosphere by explosive eruptions. The climate response would then be dominated by the long-term greenhouse warming. Single eruptions with an effective stratospheric sulfur injection of 9, 250 or 1000 MtS lead to a peak global cooling of 0.3, 2.2 and 4.6 °C which largely decays within less than 10 years (P.III Tab. 1). If such events were separated by more than a few years during a CAMP pulse (Case 2), they would therefore have caused annual-scale cooling episodes within the overall warming trend. If they were more frequent and their negative

radiative forcing is sustained over centuries (Case 3), this could have resulted in a much more pronounced cooling for the $\sim 10^2$ – 10^3 yr duration of the emission pulse. This is because the intermediate and deep ocean is driven out of thermal equilibrium, and feedbacks, for example related to albedo changes from sea ice, amplify the temperature decline. The peak cooling strongly depends on the frequency and magnitude of the injection events and reaches -25°C in the tested scenarios (P.III Fig. 2b). However, the scenario with 125 GtS over 500 eruptions within ~ 1 kyr and a resulting -8°C cooling is considered as a more moderate Case 3 scenario. For the duration of the volcanic activity pulse, this cooling offsets the slowly accumulating greenhouse warming which then takes over as the emission pulse ceases. The post-eruption climate state is therefore only determined by the cumulative carbon emissions and not the emitted sulfur.

Simultaneous carbon and sulfur emissions can cause cooling–warming sequences and spatially heterogeneous changes | Publication III describes different scenarios for the combined effects of LIP carbon and sulfur emission pulses, of which Case 3 is the most intriguing one. For these scenarios, the simultaneous release of carbon and sulfur volatiles causes a sequence of millennial-scale cooling and amplified inter-annual climate variability, followed by a steady long-term global warming. A corresponding sequence of enhanced and subsequently reduced ocean mixing, overturning and oxygen concentrations is also simulated (P.III Fig. 3, A.III Fig. S13). The enhanced ocean ventilation associated with the sulfur cooling pulse promotes tropical marine biomass productivity through nutrient upwelling, whereas the productivity in the light- and temperature-limited higher latitudes is reduced (A.III Fig. S18–19). The modeling provides further indication of regionally differentiated changes that could ultimately help to integrate signals from globally distributed records. For example, temperature variations over the continents and high-latitude oceans are more pronounced than in the tropics and especially the already hot Tethys realm. In the baseline scenario (1500ppm_5300GtC + 125GtS), the latter warms by not more than 2°C , compared to 3 – 5°C over the higher latitude continents and 3°C globally. Ocean acidification, measured by the pH reduction, is also stronger at high latitudes where the uptake of CO_2 by the ocean is generally larger (A.III Fig. S17). However, these patterns result from simplifying assumptions, especially concerning the effects of sulfur emissions. While CO_2 is a well-mixed greenhouse gas, more complex and spatially variable effects of LIP-derived sulfur in the atmosphere are expected to result from atmospheric chemistry, microphysics and transport processes. These have been only addressed in a very few climate modeling studies (Schmidt et al. 2016, Black et al. 2018) and are not represented in the CLIMBER-3 α +C model. Instead, only a stratospheric aerosol radiative forcing is implemented in the simplest possible way by modulating the top-of-the-atmosphere solar irradiation globally, similar to Metzner et al. (2012). The radiative forcing is obtained from the averaged aerosol optical depth calculated by the Easy Volcanic Aerosol model (EVA; Toohey et al. 2016). EVA has been calibrated to smaller scale historical volcanic eruptions, and the global averaging obscures the spatial variation of the aerosol forcing that is linked to the latitudinal position of the eruptions in particular. The latter effect could have been less important for the CAMP due to its equatorial position, but for other LIPs at higher latitudes the aerosol forcing was probably more confined to their respective hemispheres (Black et al. 2018). The fixed basic structure of the atmospheric circulation in CLIMBER-3 α might additionally not fully reflect the profound and rapid disruptions presented by volcanic winters produced by LIPs.

The simulated climatic variations represent thermal stress on ancient coral reefs | The presented results of P.III clearly show how empirically constrained carbon and sulfur emission scenarios for the CAMP volcanism lead to profound climate perturbations. Their ecological severity cannot be comprehensively estimated here. Nevertheless, P.III

tentatively evaluates the simulated sea surface temperatures (SST) and their variations against the distribution of Late Triassic scleractinian fossil coral reefs. Many of them roughly occur in regions with SSTs close to the optimum temperature $\sim 28^\circ\text{C}$ of their modern relatives (P.III Figs. 3–4). For the 1500 ppm initial state these prevail particularly in two subtropical belts in the Tethys and the tropical-subtropical eastern Panthalassa. A global warming of $+3.1^\circ\text{C}$ (in the 1500ppm_5300GtC + 125GtS scenario) pushes the low-latitude habitats in the Tethys to the upper thermal limits but these are not clearly transgressed at the fossil reef localities globally. This extremely simplified approach provides no clear evidence that CAMP greenhouse warming pulses must have eradicated coral reef ecosystems globally simply by overheating. However, the space within the coral thermal niche is contracted to the equatorial Tethys during the intervening -8°C cool phase (P.III Fig. 3g). The simulated alternation of cooling and warming as well as the annual-scale variability introduced by volcanic eruptions could therefore have amplified the overall thermal stress on coral reefs and other ecosystems significantly. Another interesting finding is the $\sim 1\text{ m}$ thermosteric sea level drop and subsequent rise induced by the cooling-warming sequence (A.III Fig. S13a). The end-Triassic disappearance of reefs has also been linked to sea level changes, particularly to a Late Triassic regression leading to the emergence of platform reefs, followed by an Early Jurassic transgression (Flügel 2002, Lindström et al. 2021). In the Austrian Alps, an emergence of 5–15 m for a brief interval of 10–50 kyr has been inferred in this context (Flügel 2002). Regional tectonic processes linked to the CAMP might well have been the cause for this. Another hypothesis is a LIP-induced cold episode with a temporary sea level fall from the thermosteric effect and minor glaciations. Ice sheets would be required to amplify and sustain the sea level drop because the simulated thermosteric effect alone is clearly too small.

The potential of Mesozoic LIPs to cause minor glaciations is worth further investigation | Recent geologic findings on the SO_2 and CO_2 generation by CAMP volcanism corroborate again the possibility of a brief sulfur-induced cooling during the end-Triassic extinction that precedes longer-term warming by CO_2 (Kaiho et al. 2022). With their capability to drive global cooling, LIPs are even discussed as causes of some of the major global glaciations in Earth history (Macdonald and Wordsworth 2017, Youbi et al. 2021). For the Mesozoic there is currently no robust link between LIP episodes and the known cool phases of the Jurassic and Cretaceous. Further modeling work could explore which factors would have promoted or prevented minor glaciations during different Mesozoic LIP episodes and how they influence the possible degree of glaciation and sea level change. The presence or absence of glacial indicators could thereby serve as a constraint on sulfur-driven cooling scenarios. The CLIMBER-X model with its capability to simulate dynamic ice sheets and sea levels over $\sim 10^4$ yr time scales provides the necessary means to test such scenarios in further research. The model experiments could consider both the characteristics of the respective LIPs (latitude, emission rates, eruption style) as well as the background Earth system state (determined by the $p\text{CO}_2$, solar constant, continental configuration, among other things).

Outstanding Questions and Further Ideas

One challenge of the presented work that is inherent to all model-based research was to figure out, which scientific questions can be appropriately addressed with the available modeling tools and empirical data constraints. Materials like fossils or sediments hold some ground truth that needs to be deciphered and interpreted by the adept geologist. In contrast, generating knowledge from models relies on the sensible design of experiments suitable to elucidate certain relations. In the case of paleoclimate modeling, an

understanding of conditions and dominant processes in the ancient Earth system has to be implemented into an available model, anticipating their potential consequences in this particular framework. For a useful paleoclimate application, this model needs to be able to represent the relevant natural mechanisms that govern the phenomenon of interest. It also has to be computationally feasible to run a certain number of simulations over the relevant time scales and with a suitable spatial resolution. Furthermore, geologic evidence of sufficient spatial and temporal coverage is required to design boundary conditions and forcings for Earth system model simulations. If this is the case, model and proxy data have to be robustly linked to common environmental quantities, given the limitations and complications of both approaches. The following final paragraphs briefly reflect on a few more ideas that remained uncompleted or arose newly during this work.

Linking proxy and fossil distributions and simulated climatic patterns is revealing for both sides | A robust evaluation of simulated Mesozoic climate patterns against global distributions of geologic and paleontologic climate indicators can be extremely useful. On the one hand, this helps to validate the capability of models to represent features of ancient climate and to compare the performance of different models. On the other hand, the proxy–model fit for ensembles of simulations reflecting varying boundary conditions can indicate the environmental drivers of changes in their distribution by determining which scenarios can best explain the latter. Compilations of lithologic climate indicators and fossil occurrences for the Mesozoic are available, for example from Boucot et al. (2013) and the Paleobiology Database (paleobiodb.org). During the preparation of P.I, attempts were made to systematically correlate continental climate patterns simulated by CLIMBER-3 α (Landwehrs et al. 2021) to the distributions of these lithologic indicators (Fig. S1). One approach was to convert the modeled monthly surface temperatures and precipitation rates into Köppen-Geiger climate classes and to quantify to which degree the occurrences of coal, evaporite and glacial deposits (Boucot et al. 2013) coincide with potentially suitable humid, dry and cold climate classes, respectively. Using the simulations at various $p\text{CO}_2$ levels, this could provide constraints on the Mesozoic $p\text{CO}_2$ and global temperature evolution, for example. Similarly, the scleractinian coral reef occurrences recorded in the Paleobiology Database were compared to the simulated sea surface temperatures for each Mesozoic time slice (Fig. S2). If the reefs simply tracked a certain thermal niche then this could again constrain the global temperature and climate evolution. However, these analyzes did not yield conclusive results yet. One challenge is that systematic assessments beyond visual inspection require sophisticated statistical methods to correlate simulated environmental conditions with presence/absence data, also accounting for an incomplete and inhomogeneous spatial and temporal sampling (Close et al. 2020). Another major difficulty is the paleoclimatic interpretation of the mentioned proxies as it is not clear to which degree occurrences of coal, evaporite, glacial deposits and corals can simply be predicted from temperature and precipitation, even under ideal circumstances. Furthermore, the proxy–model match is certainly obscured to some degree by biases in the simulated climate patterns. Considering these challenges, a clear hypothesis that could have been robustly tested within the given framework did not offer itself immediately. Nevertheless, it is worth to further investigate potential climatic drivers of geographical and ecological shifts exhibited Mesozoic marine biota, for example (e.g. Kiessling 2001; 2009b, Reddin et al. 2018). This is actually part of the ongoing collaborations mentioned in Sec. 1.2 which address the evolution of corals in the Triassic and the role of cooling and warming events in marine invertebrate fossil assemblages of the Pliensbachian–Toarcian.

Global monsoon patterns were reshaped during the Mesozoic | The investigations on the long-term evolution of Mesozoic climate characteristics (P.I) have also resulted in

an assessment of simulated monsoonal climate patterns. For this, the simulated monthly precipitation rates were used to estimate the areal extent of strongly seasonal rainfall conditions that classify as monsoonal (Figs. S1, S3). According to Wang et al. (2014), a monsoonal climate is characterized by a precipitation difference between the wet summer and dry winter season of ≥ 2 mm/d, as well as more than 55 % of annual rainfall during the five consecutive wettest months. The changing global monsoon patterns yielded quite interesting results, indicating a transition from the Pangean megamonsoon to the precursors of the Asian monsoon. However, the coarse resolution and simplified structure of the atmosphere module of CLIMBER-3 α necessitate thorough validation of these findings. There is currently no sophisticated proxy record that would outline monsoon-like climates through the Mesozoic. The database of lithologic climate indicators of Boucot et al. (2013) could potentially be useful, assuming that a strong seasonal alternation of humid and arid conditions prevailed where evaporites/kaolinite and coal/bauxite/kaolinite deposition occur closely together (M. Wagnreich, pers. comm.). Data from a recently presented modeling study on the monsoon evolution over the last 250 Myr (Hu et al. 2021, unpublished) could eventually be used for cross-validation and could be complemented by the modeling of P.I. With the improved and better resolved atmosphere of the CLIMBER-X model, this topic could be addressed again with slightly greater confidence, building on the approach developed for P.I. However, the unique strengths of this model would be especially useful in assessing not only monsoon patterns and generally climate seasonality but especially how these were modulated by orbital forcing through the Mesozoic. First results already show a significant response of the global monsoon patterns, with characteristic differences between the stages of the Mesozoic (Fig. S3). This would provide fundamental new insights in the light of current research on the orbital forcing of the modern global monsoon system (e.g. Ding et al. 2021).

Modeling orbital effects on groundwater storage can provide constraints on aquifer eustasy | The dynamical modeling approaches to orbital climate pacing developed here represent an innovation for the Mesozoic and many deep time paleoclimate modeling applications in general. The concept of aquifer eustasy as the cause of ancient sea level cycles (Sames et al. 2020) is one important issue for which these methods could foster significant progress. The starting point of this hypothesis is the observation of significant sea level cycles during particularly warm greenhouse phases like the Cretaceous. Because continental glaciations and therefore glacio-eustatic sea level changes have probably been limited during these times, alternative explanations are required. It has been proposed that orbital cycles modulated the water transfer between the continents in a way that led to global changes of the continental groundwater storage equivalent to 10–40 m global sea level changes (Wagnreich et al. 2014, Wendler et al. 2016, Li et al. 2018, Sames et al. 2016; 2020). Global climate variations, for example linked to the ENSO, do indeed have measurable effects on global land water storage and sea level today (Boening et al. 2012, Eicker et al. 2016, Gregory et al. 2019, Kuo et al. 2021, Wu et al. 2021). In some of these studies, the terrestrial water storage anomaly (TWSA) is simply obtained from the difference of the precipitation, evapotranspiration and runoff on the land surface (P–ET–R). More explicit hydrological groundwater modules in global Earth system models are only now becoming available (Gleeson et al. 2021, Condon et al. 2021) and have not been applied in deep time paleoclimate research. On the other hand, comprehensive spatially resolved models are required to represent the complex spatial and temporal patterns of orbital hydroclimate change that are paced by the different components of the astronomical insolation forcing (Sec. 1.1.2, P.II). These patterns have to be considered even for a first order estimate of the aquifer eustasy sea level potential because there seems to be no obvious and direct way in which certain astronomical configurations would drive a net water transfer between ocean and land synchronously across the globe. Furthermore, such

an orbitally-paced transfer mechanism must be able to act on the long time scales of the reconstructed sea level fluctuations (~ 405 kyr to 2.4 Myr; Sames et al. 2016; 2020), considering the basic astronomical time scales of 10^4 – 10^5 yrs and the characteristic response time scales of aquifer groundwater storages. In some preliminary work, transient orbital climate simulations with the CLIMBER-X model for Mesozoic time slices have been assessed here with respect to continental water storage and sea level changes (Fig. S4). Naively assuming that the TWS anomalies obtained from the simulated P–ET–R can be entirely accumulated by aquifers, the water volumes added to or released from the terrestrial water storage exceed ± 10 m sea-level equivalent (Fig. S4). Extending this work could provide important constraints on the volumes and preconditions of aquifer eustasy and should aim to establish robust links to relevant cyclostratigraphic records. The idea to study orbitally-driven hydroclimatic changes in the context of the Late Triassic Newark-Hartford Basin in P.II partly resulted from these considerations. This first case study appeared especially useful and feasible because it made use of a well-studied, long-term and high-resolution record with a relatively clear climatic interpretation. Aquifer eustasy has also been discussed in the context of the Newark basin orbital signals (Li et al. 2016; 2018, Hinnov and Cozzi 2021, Wang et al. 2022).

Outline of an imaginary project proposal | As a possible promising continuation of this thesis and the discussed ideas, one could propose a project entitled “Modeling Mesozoic Orbital Climate Cycles in Monsoons, Sedimentary Archives and Sea Level”. This could build on the approaches developed here and make full use of the strengths of the CLIMBER-X model to simulate climate, ice sheets and biogeochemical cycles on orbital time scales. (I) The project could investigate long-term trends in the orbital forcing of climate seasonality and monsoons from the Pangean megamonsoon to the predecessors of today’s East Asian monsoon in the Late Cretaceous. (II) The potential contributions of groundwater storage and possible ice sheets to sea level fluctuations at different warmer and cooler stages of the Mesozoic could be addressed. And (III), the framework for climatic interpretation and correlation of specific cyclostratigraphic archives could be extended to other terrestrial records, potentially linking them to marine ones through sea level changes.

An unified climate modeling framework for Mesozoic LIP disruptions could elucidate their varying severity | As already concluded above, this work opens up many opportunities for an extended and enhanced investigation of climatic and environmental effects of LIP volcanism. It could be particularly revealing to represent different Mesozoic LIP episodes in a consistent model framework to identify commonalities and differences of the factors determining associated environmental changes. Mesozoic and Cenozoic mass extinctions, OAEs and hyperthermal events in general can be conceptually differentiated by the volume and rapidity of LIP emissions (Rothman 2017, Clapham and Renne 2019, Song et al. 2021). The end-Permian and end-Triassic extinction events, the Pliensbachian–Toarcian boundary event and the PETM are closely associated to rapid carbon emission events (Clapham and Renne 2019, Kasbohm et al. 2021). They are often linked to sharp negative CIEs and environmental changes dominated by warming and perhaps acidification and deoxygenation, but without major black shale deposition (Clapham and Renne 2019). In contrast, the OAEs were probably characterized by a more gradual, longer-term carbon release which promoted widespread anoxia and black shale deposition through weathering feedbacks (Clapham and Renne 2019). Temperature and pH perturbations would have been muted during these events due to mitigating feedbacks. The five major Phanerozoic extinction events were possibly characterized by temperature changes of ≥ 5 °C with rates of ≥ 10 °C/Myr (Song et al. 2021). It has been hypothesized that the lesser severity of extinction during the Cretaceous OAEs and the PETM compared to the end-Permian and end-Triassic events resulted from a shift to a more stabilized ocean car-

bon cycle that may have reduced the likelihood of catastrophic environmental disruptions (Ridgwell 2005, Clapham and Renne 2019). This could be explained by the rise of calcifying phytoplankton organism like the coccolithophores and dinoflagellates which shifted the marine carbonate factory into the open ocean (the “Mesozoic marine revolution”; Ridgwell 2005, Payne and Van de Schootbrugge 2007, Knoll and Follows 2016). The establishment of this pelagic carbonate reservoir during the Mesozoic could have enhanced the buffering of the marine and global carbon cycles against perturbations (Zeebe and Westbroek 2003, Ridgwell and Zeebe 2005, Clapham and Renne 2019). Some of these additional factors determining Earth’s sensitivity to Mesozoic LIPs could be addressed with the CLIMBER-X model making use of its dynamic vegetation, terrestrial carbon cycle and eventually weathering and sedimentation feedbacks. Due to the representation of the latter mechanisms and its computational speed, this model enables simulations of longer-term effects of volcanic episodes ($\sim 10^4$ – 10^5 yr). Preliminary test simulation have applied carbon and sulfur emission pulses to different Mesozoic time slices, including a suppression of pelagic carbonate production. An envisaged improvement is the implementation of a latitudinally resolved volcanic aerosol forcing to represent the position of different LIPs (Torsvik et al. 2021b). In contrast to the equatorial CAMP, the aerosol forcing of the end-Permian Siberian Traps was predominantly restricted to the northern hemisphere (Black et al. 2018). It would be exciting to explore how the response to characteristic LIP forcings is modulated by the evolving Earth system state, determined especially by the paleogeography and the background $p\text{CO}_2$.

Conclusions

This thesis contributes to our understanding of the Earth system by researching the paleoclimates of the Mesozoic era (~ 252 –66 million years ago). It integrates numerical Earth system modeling and geological evidence to characterize Mesozoic climate change and its drivers on tectonic, orbital and millennial time scales. The first part of this work (P.I) provides a new perspective on the long-term climate evolution through the whole Mesozoic. The supercontinent Pangea and its disintegration are the dominant factors of the Mesozoic transition from the ancient Paleozoic towards the current Cenozoic era. This work demonstrates that the rifting of Pangea leads to enhanced continental flooding which, together with the slowly increasing solar luminosity, caused a baseline warming trend from the Triassic into the Late Cretaceous. The interplay of tectonic carbon degassing and continental weathering led to elevated $p\text{CO}_2$ levels in the Triassic and the mid-Cretaceous which caused particularly hot climate phases in the overall warm Mesozoic climate, as shown here. The continental fragmentation and rising sea levels are found to be the major drivers of a trend from strongly seasonal and dry continental climates to more equable and humid conditions. This work supports and substantiates many previous findings on Mesozoic climates in a consistent climate model framework. The latter made use of the fast CLIMBER-3 α Earth system model (ESM) which enabled a large ensemble of climate simulations with systematically varied boundary conditions to identify the contributions of different driving factors of climatic change. The established modeling workflows provide a basis for extended work on specific aspects or other geologic time periods.

Within the long-term evolution of the Earth system, astronomical cycles are responsible for a major mode of climate variability. Although cyclostratigraphic records provide compelling evidence for this cyclicity in the Mesozoic, global perspectives on the orbital climate pacing during greenhouse climate periods of Earth history are still less well researched than for the late Cenozoic ice age. The second part of this thesis (P.II) studies the orbital response of the Late Triassic climate with a strong link to the cyclic lake

sediment record from the Newark-Hartford Basins. A significant climate pacing by the insolation forcing of eccentricity-modulated precession is found for this tropical region. A smaller indirect effect of obliquity on the latitudinal shift of the tropical rainfall belt also modulates the low-latitude hydroclimate. A plate-tectonic shift from a tropical humid regime to subtropical semi-arid latitudes as well as reconstructed variations of the $p\text{CO}_2$ are proposed as possible explanations for the varying expression of orbital cyclicity in the NHB lake level record. The most pronounced orbital signal is modeled for relatively humid but strongly seasonal climate at high $p\text{CO}_2$ during the intermediate interval from ~ 220 to 200 Ma. This work is enabled by the possibility to perform transient climate simulations over orbital time scales with the newly developed CLIMBER-X ESM. That novel modeling approach can be readily extended to other time periods and records to achieve an integrated but differentiated picture of the Mesozoic orbital climate pacing. Ice sheet and sea level effects could possibly also be included.

Finally, this thesis deals with the prominent and irregular geologic events that punctuated the Mesozoic. As discussed above, these include mass extinction and ocean anoxic events of which many are associated to episodes of Large Igneous Province (LIP) volcanism. Focusing on the Central Atlantic Magmatic Province (CAMP) and the end-Triassic extinction event (~ 201.5 Ma) the third part of the thesis (P.III) assesses potential effects of brief carbon and sulfur emission pulses from LIP volcanism. The carbon emissions cause long-term global warming and, to a certain extent, ocean acidification and deoxygenation. In contrast, the sulfur emissions can cause episodic global cooling, due to the negative radiative forcing associated to stratospheric sulfur aerosol from explosive eruptions. Various emission scenarios are tested in this work to illustrate their range of possible effects within the relatively loose constraints on the actual characteristics of CAMP emissions. The study shows that the simultaneous pulsed emission of sulfur and carbon could have caused sequences of millennial-scale global cooling and high climatic variability, followed by longer-term global warming. The simulated temperature changes push fossil stony coral reef habitats towards the thermal limits of their modern relatives. However, it could have been especially the rapid alternation of cold and warm anomalies that caused the worst extinction in the history of scleractinian corals. Amplified temperature changes over the continents and high-latitudes compared to the tropical Tethys sea indicate that it is important to study LIP effects in spatially resolved models like CLIMBER-3 α +C in this case. Important further progress can be made by extending the modeling approaches developed here to a unified framework of Mesozoic LIP episodes. Assessing additional long-term carbon cycle, ice sheet and sea level effects in the CLIMBER-X model would be especially revealing.

Altogether, this work illustrates the intriguing richness of paleoclimatic trends and events that characterize the Mesozoic. Researching the drivers of these profound changes by integrating Earth system modeling and geological evidence provides a broad perspective on the mechanisms governing the Earth system. Although this thesis presents an important contribution towards a more comprehensive understanding of Mesozoic climate change across various time scales, only some of the interesting aspects could be covered here. A focus has been the Late Triassic to Early Jurassic interval, leaving many opportunities for further investigations of important periods like the mid-Cretaceous. The latter is actively being studied as one of the warmest, prolonged and most recent greenhouse phases which makes it particularly relevant in the light of current and future climate change. Therefore, the endeavor of Mesozoic paleoclimate research goes on and bringing together geology and Earth system modeling will be a crucial part of that.

Bibliography

- Aarnes, I., Fristad, K., Planke, S. and Svensen, H. (2011), ‘The impact of host-rock composition on devolatilization of sedimentary rocks during contact metamorphism around mafic sheet intrusions’, doi:10.1029/2011GC003636 *Geochemistry, Geophysics, Geosystems* **12**(10).
- Aarnes, I., Svensen, H., Connolly, J. A. and Podladchikov, Y. Y. (2010), ‘How contact metamorphism can trigger global climate changes: Modeling gas generation around igneous sills in sedimentary basins’, doi:10.1016/j.gca.2010.09.011 *Geochimica et Cosmochimica Acta* **74**(24), 7179–7195.
- Alley, N. F., Hore, S. B. and Frakes, L. A. (2020), ‘Glaciations at high-latitude Southern Australia during the Early Cretaceous’, doi:10.1080/08120099.2019.1590457 *Australian Journal of Earth Sciences* **67**(8), 1045–1095.
- Aloisi, G. (2018), ‘A pronounced fall in the CaCO₃ saturation state and the total alkalinity of the surface ocean during the Mid Mesozoic’, doi:10.1016/j.chemgeo.2018.04.014 *Chemical Geology* **487**, 39–53.
- Archer, D., Eby, M., Brovkin, V., Ridgwell, A., Cao, L., Mikolajewicz, U., Caldeira, K., Matsumoto, K., Munhoven, G., Montenegro, A. and Tokos, K. (2009), ‘Atmospheric lifetime of fossil fuel carbon dioxide’, doi:10.1146/annurev.earth.031208.100206 *Annual Review of Earth and Planetary Sciences* **37**(1), 117–134.
- Ashkenazy, Y. and Gildor, H. (2008), ‘Timing and significance of maximum and minimum equatorial insolation’, doi:10.1029/2007PA001436 *Paleoceanography* **23**(1).
- Bachan, A. and Payne, J. L. (2015), ‘Modelling the impact of pulsed CAMP volcanism on pCO₂ and $\delta^{13}\text{C}$ across the Triassic–Jurassic transition’, doi:10.1017/s0016756815000126 *Geological Magazine* **153**(02), 252–270.
- Bacon, K. L., Belcher, C. M., Haworth, M. and McElwain, J. C. (2013), ‘Increased atmospheric SO₂ detected from changes in leaf physiognomy across the Triassic–Jurassic boundary interval of east greenland’, doi:10.1371/journal.pone.0060614 *PLoS ONE* **8**(4), e60614.
- Bahr, A., Kolber, G., Kaboth-Bahr, S., Reinhardt, L., Friedrich, O. and Pross, J. (2020), ‘Mega-monsoon variability during the late Triassic: Re-assessing the role of orbital forcing in the deposition of playa sediments in the Germanic Basin’, doi:10.1111/sed.12668 *Sedimentology* **67**(2), 951–970.
- Balaji, V., Maisonnave, E., Zadeh, N., Lawrence, B. N., Biercamp, J., Fladrich, U., Aloisio, G., Benson, R., Caubel, A., Durachta, J., Foujols, M.-A., Lister, G., Mocavero, S., Underwood, S. and Wright, G. (2017), ‘CPMIP: measurements of real computational performance of Earth system models in CMIP6’, doi:10.5194/gmd-10-19-2017 *Geoscientific Model Development* **10**(1), 19–34.
- Bambach, R. K. (2006), ‘Phanerozoic Biodiversity and Mass Extinctions’, doi:10.1146/annurev.earth.33.092203.122654 *The Annual Review of Earth and Planetary Sciences* **34**.
- Barron, E., Sloan, J. and Harrison, C. (1980), ‘Potential significance of land—sea distribution and surface albedo variations as a climatic forcing factor; 180 m.y. to the present’, doi:10.1016/0031-0182(80)90047-4 *Palaeogeography, Palaeoclimatology, Palaeoecology* **30**, 17–40.
- Batenburg, S. J., De Vleeschouwer, D., Sprovieri, M., Hilgen, F. J., Gale, A. S., Singer, B. S., Koeberl, C., Coccioni, R., Claeys, P. and Montanari, A. (2016), ‘Orbital control on the timing of oceanic anoxia in the late cretaceous’, doi:10.5194/cp-12-1995-2016 *Climate of the Past* **12**(10), 1995–2009.
- Beerling, D. (2002), ‘CO₂ and the end-Triassic mass extinction’, doi:10.1038/415386a *Nature* **415**(6870), 386–387.
- Beerling, D. J. and Berner, R. A. (2002), ‘Biogeochemical constraints on the Triassic–Jurassic boundary carbon cycle event’, doi:10.1029/2001GB001637 *Global Biogeochemical Cycles* **16**(3), 10–1–10–13.
- Benson, R. B. (2018), ‘Dinosaur Macroevolution and Macroecology’, doi:10.1146/annurev-ecolsys-110617-062231 *Annual Review of Ecology, Evolution, and Systematics* **49**(1), 379–408.

- Berger, A. and Loutre, M. F. (1994), *Astronomical Forcing through Geological Time*, John Wiley & Sons, Ltd, doi:10.1002/9781444304039.ch2 chapter 2, pp. 15–24.
- Berger, A. and Loutre, M. F. (1997), ‘Intertropical Latitudes and Precessional and Half-Precessional Cycles’, doi:10.1126/science.278.5342.1476 *Science* **278**(5342), 1476–1478.
- Berger, A., Loutre, M. F. and Mélice, J. L. (2006), ‘Equatorial insolation: from precession harmonics to eccentricity frequencies’, doi:10.5194/cp-2-131-2006 *Climate of the Past* **2**(2), 131–136.
- Berger, A. and Yin, Q. (2012), Astronomical Theory and Orbital Forcing, in J. Matthews, ed., ‘The SAGE Handbook of Environmental Change’, Vol. 1, SAGE Publications Ltd, doi:10.4135/9781446253045 chapter 19, pp. 405–425.
- Berner, R. A. (2006), ‘GEOCARBSULF: A combined model for Phanerozoic atmospheric O₂ and CO₂’, doi:10.1016/j.gca.2005.11.032 *Geochimica et Cosmochimica Acta* **70**(23), 5653 – 5664.
- Berner, R. A. and Beerling, D. J. (2007), ‘Volcanic degassing necessary to produce a CaCO₃ undersaturated ocean at the Triassic-Jurassic boundary’, doi:10.1016/j.palaeo.2006.06.039 *Palaeogeography, Palaeoclimatology, Palaeoecology* **244**(1-4), 368–373.
- Berner, R. and Kothavala, Z. (2001), ‘GEOCARB III: A revised model of atmospheric CO₂ over phanerozoic time’, doi:10.2475/ajs.301.2.182 *American Journal of Science* **301**(2), 182–204.
- Black, B. A., Karlstroim, L. and Mather, T. A. (2021), ‘The life cycle of large igneous provinces’, doi:10.1038/s43017-021-00221-4 *Nature Reviews Earth & Environment* **2**(12), 840–857.
- Black, B. A., Lamarque, J.-F., Shields, C. A., Elkins-Tanton, L. T. and Kiehl, J. T. (2014), ‘Acid rain and ozone depletion from pulsed Siberian Traps magmatism’, doi:10.1130/g34875.1 *Geology* **42**(1), 67–70.
- Black, B. A. and Manga, M. (2017), ‘Volatiles and the tempo of flood basalt magmatism’, doi:10.1016/j.epsl.2016.09.035 *Earth and Planetary Science Letters* **458**, 130–140.
- Black, B. A., Neely, R. R., Lamarque, J.-F., Elkins-Tanton, L. T., Kiehl, J. T., Shields, C. A., Mills, M. J. and Bardeen, C. (2018), ‘Systemic swings in end-Permian climate from Siberian Traps carbon and sulfur outgassing’, doi:10.1038/s41561-018-0261-y *Nature Geoscience* **11**(12), 949–954.
- Blackburn, T. J., Olsen, P. E., Bowring, S. A., McLean, N. M., Kent, D. V., Puffer, J., McHone, G., Rasbury, E. T. and Et-Touhami, M. (2013), ‘Zircon U-Pb Geochronology Links the End-Triassic Extinction with the Central Atlantic Magmatic Province’, doi:10.1126/science.1234204 *Science* **340**(6135), 941–945.
- Boening, C., Willis, J. K., Landerer, F. W., Nerem, R. S. and Fasullo, J. (2012), ‘The 2011 La Niña: So strong, the oceans fell’, doi:10.1029/2012GL053055 *Geophysical Research Letters* **39**(19), L19602.
- Bond, D. P. and Grasby, S. E. (2017), ‘On the causes of mass extinctions’, doi:10.1016/j.palaeo.2016.11.005 *Palaeogeography, Palaeoclimatology, Palaeoecology* **478**, 3–29.
- Bond, D. P. and Wignall, P. B. (2014), Large igneous provinces and mass extinctions: An update, in ‘Volcanism, Impacts, and Mass Extinctions: Causes and Effects’, doi:10.1130/2014.2505(02) Geological Society of America.
- Bonis, N. R. and Kürschner, W. M. (2012), ‘Vegetation history, diversity patterns, and climate change across the Triassic/Jurassic boundary’, doi:10.1666/09071.1 *Paleobiology* **38**(02), 240–264.
- Bonis, N., Ruhl, M. and Kürschner, W. (2010), ‘Climate change driven black shale deposition during the end-triassic in the western tethys’, doi:10.1016/j.palaeo.2009.06.016 *Palaeogeography, Palaeoclimatology, Palaeoecology* **290**(1-4), 151–159.
- Bonis, N., Van Konijnenburg-Van Cittert, J. and Kürschner, W. (2010), ‘Changing CO₂ conditions during the end-Triassic inferred from stomatal frequency analysis on *Lepidopteris ottonis* (Goepfert) Schimper and *Ginkgoites taeniatus* (Braun) Harris’, doi:10.1016/j.palaeo.2010.05.034 *Palaeogeography, Palaeoclimatology, Palaeoecology* **295**(1), 146–161.
- Bosmans, J. H. C., Drijfhout, S. S., Tuenter, E., Hilgen, F. J. and Lourens, L. J. (2015a), ‘Response of the North African summer monsoon to precession and obliquity forcings in the EC-Earth GCM’, doi:10.1007/s00382-014-2260-z *Climate Dynamics* **44**(1-2), 279–297.
- Bosmans, J. H. C., Drijfhout, S. S., Tuenter, E., Lourens, L. J., Hilgen, F. J. and Weber, S. L. (2012), ‘Monsoonal response to mid-holocene orbital forcing in a high resolution GCM’, doi:10.5194/cp-8-723-2012 *Climate of the Past* **8**(2), 723–740.
- Bosmans, J. H. C., Hilgen, F. J., Tuenter, E. and Lourens, L. J. (2015b), ‘Obliquity forcing of low-latitude climate’, doi:10.5194/cp-11-1335-2015 *Climate of the Past* **11**(10), 1335–1346.
- Boucot, A. J., Xu, C., Scotese, C. R. and Morley, R. J. (2013), *Phanerozoic Paleoclimate: An Atlas of Lithologic Indicators of Climate*, doi:10.2110/sepmsp.11 SEPM Society for Sedimentary Geology.
- Boulila, S., Galbrun, B., Gardin, S. and Pellenard, P. (2022), ‘A Jurassic record encodes an analogous Dansgaard-Oeschger climate periodicity’, doi:10.1038/s41598-022-05716-8 *Scientific Reports* **12**(1).

- Boyce, C. K. and Lee, J.-E. (2017), ‘Plant Evolution and Climate Over Geological Timescales’, doi:10.1146/annurev-earth-063016-015629 *Annual Review of Earth and Planetary Sciences* **45**(1), 61–87.
- Braconnot, P., Marzin, C., Grégoire, L., Mosquet, E. and Marti, O. (2008), ‘Monsoon response to changes in Earth’s orbital parameters: comparisons between simulations of the Eemian and of the Holocene’, doi:10.5194/cp-4-281-2008 *Climate of the Past* **4**(4), 281–294.
- Brugger, J., Feulner, G., Hofmann, M. and Petri, S. (2021), ‘A Pronounced Spike in Ocean Productivity Triggered by the Chicxulub Impact’, doi:10.1029/2020GL092260 *Geophysical Research Letters* **48**(12), e2020GL092260.
- Brugger, J., Feulner, G. and Petri, S. (2017), ‘Baby, its cold outside: Climate model simulations of the effects of the asteroid impact at the end of the Cretaceous’, doi:10.1002/2016gl072241 *Geophysical Research Letters* **44**(1), 419–427.
- Brugger, J., Hofmann, M., Petri, S. and Feulner, G. (2019), ‘On the Sensitivity of the Devonian Climate to Continental Configuration, Vegetation Cover, Orbital Configuration, CO₂ Concentration, and Insolation’, doi:10.1029/2019PA003562 *Paleoceanography and Paleoclimatology* **34**(8), 1375–1398.
- Brune, S., Williams, S. E. and Mueller, R. D. (2017), ‘Potential links between continental rifting, CO₂ degassing and climate change through time’, doi:10.1038/s41561-017-0003-6 *Nature Geoscience* **10**(12), 941–946.
- Brusatte, S. L., Nesbitt, S. J., Irmis, R. B., Butler, R. J., Benton, M. J. and Norell, M. A. (2010), ‘The origin and early radiation of dinosaurs’, doi:10.1016/j.earscirev.2010.04.001 *Earth-Science Reviews* **101**(1), 68–100.
- Bush, A. M. and Bambach, R. K. (2011), ‘Paleoecologic Megatrends in Marine Metazoa’, doi:10.1146/annurev-earth-040809-152556 *Annual Review of Earth and Planetary Sciences* **39**(1), 241–269.
- Bush, A. M. and Payne, J. L. (2021), ‘Biotic and Abiotic Controls on the Phanerozoic History of Marine Animal Biodiversity’, doi:10.1146/annurev-ecolsys-012021-035131 *Annual Review of Ecology, Evolution, and Systematics* **52**(1), 269–289.
- Callegaro, S., Baker, D. R., De Min, A., Marzoli, A., Geraki, K., Bertrand, H., Viti, C. and Nestola, F. (2014), ‘Microanalyses link sulfur from large igneous provinces and Mesozoic mass extinctions’, doi:10.1130/G35983.1 *Geology* **42**(10), 895–898.
- Cao, W., Williams, S., Flament, N., Zahirovic, S., Scotese, C. R. and Müller, R. D. (2018), ‘Palaeolatitudinal distribution of lithologic indicators of climate in a palaeogeographic framework’, doi:10.1017/S0016756818000110 *Geological Magazine* **156**(2), 331–354.
- Cao, W., Zahirovic, S., Flament, N., Williams, S., Golonka, J. and Mueller, R. D. (2017), ‘Improving global paleogeography since the late Paleozoic using paleobiology’, doi:10.5194/bg-14-5425-2017 *Biogeosciences* **14**(23), 5425–5439.
- Capriolo, M., Marzoli, A., Aradi, L. E., Ackerson, M. R., Bartoli, O., Callegaro, S., Dal Corso, J., Ernesto, M., Vasconcellos, E. M. G., De Min, A., Newton, R. J. and Szabo, C. (2021), ‘Massive methane fluxing from magma-sediment interaction in the end-Triassic Central Atlantic Magmatic Province’, doi:10.1038/s41467-021-25510-w *Nature Communications* **12**(1).
- Capriolo, M., Marzoli, A., Aradi, L. E., Callegaro, S., Dal Corso, J., Newton, R. J., Mills, B. J. W., Wignall, P. B., Bartoli, O., Baker, D. R., Youbi, N., Remusat, L., Spiess, R. and Szab, C. (2020), ‘Deep CO₂ in the end-Triassic Central Atlantic Magmatic Province’, doi:10.1038/s41467-020-15325-6 *Nature Communications* **11**(1).
- Capriolo, M., Mills, B. J. W., Newton, R. J., Corso, J. D., Dunhill, A. M., Wignall, P. B. and Marzoli, A. (2022), ‘Anthropogenic-scale CO₂ degassing from the Central Atlantic Magmatic Province as a driver of the end-Triassic mass extinction’, doi:10.1016/j.gloplacha.2021.103731 *Global and Planetary Change* **209**, 103731.
- Cather, S. M., Dunbar, N. W., McDowell, F. W., McIntosh, W. C. and Scholle, P. A. (2009), ‘Climate forcing by iron fertilization from repeated ignimbrite eruptions: The icehouse–silicic large igneous province (SLIP) hypothesis’, doi:10.1130/GES00188.1 *Geosphere* **5**(3), 315–324.
- Catling, D. C. and Zahnle, K. J. (2020), ‘The Archean atmosphere’, doi:10.1126/sciadv.aax1420 *Science Advances* **6**(9), eaax1420.
- Chaboureaud, A.-C., Sepulchre, P., Donnadieu, Y. and Franc, A. (2014), ‘Tectonic-driven climate change and the diversification of angiosperms’, doi:10.1073/pnas.1324002111 *Proceedings of the National Academy of Sciences* **111**(39), 14066–14070.
- Chandler, M. A., Rind, D. and Ruedy, R. (1992), ‘Pangaeon climate during the Early Jurassic: GCM simulations and the sedimentary record of paleoclimate’, doi:10.1130/0016-7606(1992)104<0543:PCDTEJ>2.3.CO;2 *GSA Bulletin* **104**(5), 543–559.

- Chandra, R., Cripps, S., Butterworth, N. and Muller, R. D. (2021), ‘Precipitation reconstruction from climate-sensitive lithologies using Bayesian machine learning’, doi:10.1016/j.envsoft.2021.105002 *Environmental Modelling & Software* **139**, 105002.
- Charbonnier, G., Boulila, S., Spangenberg, J. E., Adatte, T., Föllmi, K. B. and Laskar, J. (2018), ‘Obliquity pacing of the hydrological cycle during the Oceanic Anoxic Event 2’, doi:10.1016/j.epsl.2018.07.029 *Earth and Planetary Science Letters* **499**, 266–277.
- Chenet, A.-L., Fluteau, F. and Courtillot, V. (2005), ‘Modelling massive sulphate aerosol pollution, following the large 1783 Laki basaltic eruption’, doi:10.1016/j.epsl.2005.04.046 *Earth and Planetary Science Letters* **236**(3), 721–731.
- Chiarenza, A. A., Mannion, P. D., Farnsworth, A., Carrano, M. T. and Varela, S. (2022), ‘Climatic constraints on the biogeographic history of Mesozoic dinosaurs’, doi:10.1016/j.cub.2021.11.061 *Current Biology* **32**(3), 570–585.e3.
- Chu, R., Wu, H., Zhu, R., Fang, Q., Deng, S., Cui, J., Yang, T., Li, H., Cao, L. and Zhang, S. (2020), ‘Orbital forcing of Triassic megamonsoon activity documented in lacustrine sediments from Ordos Basin, China’, doi:10.1016/j.palaeo.2019.109542 *Palaeogeography, Palaeoclimatology, Palaeoecology* **541**, 109542.
- Clapham, M. E. and Renne, P. R. (2019), ‘Flood Basalts and Mass Extinctions’, doi:10.1146/annurev-earth-053018-060136 *Annual Review of Earth and Planetary Sciences* **47**(1), 275–303.
- Claussen, M., Dallmeyer, A. and Bader, J. (2017), doi:10.1093/acrefore/9780190228620.013.532 ‘Theory and Modeling of the African Humid Period and the Green Sahara’.
- Close, R. A., Benson, R. B. J., Saupe, E. E., Clapham, M. E. and Butler, R. J. (2020), ‘The spatial structure of Phanerozoic marine animal diversity’, doi:10.1126/science.aay8309 *Science* **368**(6489), 420–424.
- Cohen, K. M., Finney, S. C., Gibbard, P. L. and Fan, J. X. (2013, updated), ‘The ICS International Chronostratigraphic Chart’, doi:10.18814/epiiugs/2013/v36i3/002 *Episodes* **36**(3), 199–204.
- Colbourn, G., Ridgwell, A. and Lenton, T. M. (2015), ‘The time scale of the silicate weathering negative feedback on atmospheric CO₂’, doi:10.1002/2014gb005054 *Global Biogeochemical Cycles* **29**(5), 583–596.
- Condamine, F. L., Silvestro, D., Koppellus, E. B. and Antonelli, A. (2020), ‘The rise of angiosperms pushed conifers to decline during global cooling’, doi:10.1073/pnas.2005571117 *Proceedings of the National Academy of Sciences* **117**(46), 28867–28875.
- Condon, L. E., Kollet, S., Bierkens, M. F. P., Fogg, G. E., Maxwell, R. M., Hill, M. C., Fransen, H.-J. H., Verhoef, A., Van Loon, A. F., Sulis, M. and Abesser, C. (2021), ‘Global Groundwater Modeling and Monitoring: Opportunities and Challenges’, doi:10.1029/2020WR029500 *Water Resources Research* **57**(12), e2020WR029500.
- Conrad, C. P. (2013), ‘The solid Earth’s influence on sea level’, doi:10.1130/B30764.1 *GSA Bulletin* **125**(7-8), 1027–1052.
- Courtillot, V. and Fluteau, F. (2014), A review of the embedded time scales of flood basalt volcanism with special emphasis on dramatically short magmatic pulses, in ‘Volcanism, Impacts, and Mass Extinctions: Causes and Effects’, doi:10.1130/2014.2505(15) Geological Society of America.
- Cox, P. M. (2001), Description of the “TRIFFID” dynamic global vegetation model, Hadley Centre Technical Note 24, Technical report, Hadley Centre, Met Office, Bracknell, UK.
- Craggs, H. J., Valdes, P. J. and Widdowson, M. (2012), ‘Climate model predictions for the latest Cretaceous: An evaluation using climatically sensitive sediments as proxy indicators’, doi:10.1016/j.palaeo.2011.11.004 *Palaeogeography, Palaeoclimatology, Palaeoecology* **315–316**, 12–23.
- Crowley, T. (1998), ‘Significance of tectonic boundary conditions for paleoclimate simulations’, *Oxford Monographs on Geology and Geophysics* **39**(1), 3–20.
- Crowley, T. J. (2000), Carbon dioxide and Phanerozoic climate, in ‘Warm Climates in Earth History’, Cambridge University Press, chapter 14, pp. 425–444.
- Crowley, T. J., Baum, S. K. and Hyde, W. T. (1992b), ‘Milankovitch fluctuations on supercontinents’, doi:10.1029/92GL00561 *Geophysical Research Letters* **19**(8), 793–796.
- Crowley, T. J., Kim, K.-Y., Mengel, J. G. and Short, D. A. (1992), ‘Modeling 100,000-Year Climate Fluctuations in Pre-Pleistocene Time Series’, doi:10.1126/science.255.5045.705 *Science* **255**(5045), 705–707.
- Crucifix, M., Loutre, M. F. and Berger, A. (2007), *The Climate Response to the Astronomical Forcing*, Springer New York, New York, NY, doi:10.1007/978-0-387-48341-2_17 pp. 213–226.
- Cui, Y., Kump, L. R. and Ridgwell, A. (2013), ‘Initial assessment of the carbon emission rate and climatic consequences during the end-Permian mass extinction’, doi:10.1016/j.palaeo.2013.09.001 *Palaeogeography, Palaeoclimatology, Palaeoecology* **389**, 128–136.

- Dal Corso, J., Bernardi, M., Sun, Y., Song, H., Seyfullah, L. J., Preto, N., Gianolla, P., Ruffell, A., Kustatscher, E., Roghi, G., Merico, A., Hohn, S., Schmidt, A. R., Marzoli, A., Newton, R. J., Wignall, P. B. and Benton, M. J. (2020), ‘Extinction and dawn of the modern world in the Carnian (Late Triassic)’, doi:10.1126/sciadv.aba0099 *Science Advances* **6**(38), eaba0099.
- Dal Corso, J., Mills, B. J. W., Chu, D., Newton, R. J., Mather, T. A., Shu, W., Wu, Y., Tong, J. and Wignall, P. B. (2020b), ‘Permo-Triassic boundary carbon and mercury cycling linked to terrestrial ecosystem collapse’, doi:10.1038/s41467-020-16725-4 *Nature Communications* **11**(1).
- Dal Corso, J., Song, H., Callegaro, S., Chu, D., Sun, Y., Hilton, J., Grasby, S. E., Joachimski, M. M. and Wignall, P. B. (2022), ‘Environmental crises at the Permian–Triassic mass extinction’, doi:10.1038/s43017-021-00259-4 *Nature Reviews Earth & Environment* .
- Davies, J., Marzoli, A., Bertrand, H., Youbi, N., Ernesto, M. and Schaltegger, U. (2017), ‘End-Triassic mass extinction started by intrusive CAMP activity’, doi:10.1038/ncomms15596 *Nature Communications* **8**(15596), 1–8.
- de Boer, B., Peters, M. and Lourens, L. J. (2021), ‘The transient impact of the African monsoon on Pliocene–Pleistocene Mediterranean sediments’, doi:10.5194/cp-17-331-2021 *Climate of the Past* **17**(1), 331–344.
- Ding, Z., Huang, G., Liu, F., Wu, R. and Wang, P. (2021), ‘Responses of global monsoon and seasonal cycle of precipitation to precession and obliquity forcing’, doi:10.1007/s00382-021-05663-6 *Climate Dynamics* **56**(11–12), 3733–3747.
- Donnadieu, Y., Godd eris, Y. and Bouttes, N. (2009), ‘Exploring the climatic impact of the continental vegetation on the Mesozoic atmospheric CO₂ and climate history’, doi:10.5194/cp-5-85-2009 *Climate of the Past* **5**(1), 85–96.
- Donnadieu, Y., Godd eris, Y., Pierrehumbert, R., Dromart, G., Fluteau, F. and Jacob, R. (2006a), ‘A GEOCLIM simulation of climatic and biogeochemical consequences of Pangea breakup’, doi:10.1029/2006GC001278 *Geochemistry, Geophysics, Geosystems* **7**(11), 1–21.
- Donnadieu, Y., Pierrehumbert, R., Jacob, R. and Fluteau, F. (2006b), ‘Modelling the primary control of paleogeography on Cretaceous climate’, doi:10.1016/j.epsl.2006.06.007 *Earth and Planetary Science Letters* **248**(1), 426 – 437.
- Donnadieu, Y., Puc eat, E., Moiroud, M., Guillocheau, F. and Deconinck, J.-F. (2016), ‘A better-ventilated ocean triggered by Late Cretaceous changes in continental configuration’, doi:10.1038/ncomms10316 *Nature Communications* **7**.
- Du, Y., Chiari, M., Kar adi, V., Nicora, A., Onoue, T., P alfy, J., Roghi, G., Tomimatsu, Y. and Rigo, M. (2020), ‘The asynchronous disappearance of conodonts: New constraints from Triassic–Jurassic boundary sections in the Tethys and Panthalassa’, doi:10.1016/j.earscirev.2020.103176 *Earth-Science Reviews* **203**, 103176.
- Dunhill, A. M., Foster, W. J., Sciberras, J. and Twitchett, R. J. (2018), ‘Impact of the Late Triassic mass extinction on functional diversity and composition of marine ecosystems’, doi:10.1111/pala.12332 *Palaeontology* **61**(1), 133–148.
- Dunne, E. M., Farnsworth, A., Greene, S. E., Lunt, D. J. and Butler, R. J. (2021), ‘Climatic drivers of latitudinal variation in Late Triassic tetrapod diversity’, doi:10.1111/pala.12514 *Palaeontology* **64**(1), 101–117.
- Eby, M., Weaver, A. J., Alexander, K., Zickfeld, K., Abe-Ouchi, A., Cimatoribus, A. A., Crespin, E., Drijfhout, S. S., Edwards, N. R., Eliseev, A. V., Feulner, G., Fichfet, T., Forest, C. E., Goosse, H., Holden, P. B., Joos, F., Kawamiya, M., Kicklighter, D., Kienert, H., Matsumoto, K., Mokhov, I. I., Monier, E., Olsen, S. M., Pedersen, J. O. P., Perrette, M., Philippon-Berthier, G., Ridgwell, A., Schlosser, A., Schneider von Deimling, T., Shaffer, G., Smith, R. S., Spahni, R., Sokolov, A. P., Steinacher, M., Tachiiri, K., Tokos, K., Yoshimori, M., Zeng, N. and Zhao, F. (2013), ‘Historical and idealized climate model experiments: an intercomparison of Earth system models of intermediate complexity’, doi:10.5194/cp-9-1111-2013 *Climate of the Past* **9**(3), 1111–1140.
- Edwards, N. R. and Marsh, R. (2005), ‘Uncertainties due to transport-parameter sensitivity in an efficient 3-D ocean-climate model’, doi:10.1007/s00382-004-0508-8 *Climate Dynamics* **24**(4), 415–433.
- Eicker, A., Forootan, E., Springer, A., Longuevergne, L. and Kusche, J. (2016), ‘Does GRACE see the terrestrial water cycle “intensifying”?’’, doi:10.1002/2015JD023808 *Journal of Geophysical Research: Atmospheres* **121**(2), 733–745.
- Elliott-Kingston, C., Haworth, M. and McElwain, J. (2014), ‘Damage structures in leaf epidermis and cuticle as an indicator of elevated atmospheric sulphur dioxide in early Mesozoic floras’, doi:10.1016/j.revpalbo.2014.05.001 *Review of Palaeobotany and Palynology* **208**, 25–42.
- Erba, E., Duncan, R. A., Bottini, C., Tiraboschi, D., Weissert, H., Jenkyns, H. C. and Malinverno, A. (2015), Environmental consequences of Ontong Java Plateau and Kerguelen Plateau volcanism, *in* Neal,

- CR and Sager, WW and Sano, T and Erba, E, ed., ‘Origin, Evolution, Environmental Impact of Oceanic LIPs’, Vol. 511 of *Geological Society of America Special Papers*, doi:10.1130/2015.2511(15) pp. 271–303.
- Ernst, R. E., Dickson, A. and Bekker, A. (2021), *Large igneous provinces: A driver of global environmental and biotic changes*, Vol. 255, doi:10.1002/9781119507444 American Geophysical Union (AGU).
- Ernst, R. E. and Jowitt, S. M. (2013), Large Igneous Provinces (LIPs) and Metallogeny, in ‘Tectonics, Metallogeny, and Discovery: The North American Cordillera and Similar Accretionary Settings’, Vol. 17, Society of Economic Geologists, doi:10.5382/SP.17.02 pp. 17–51.
- Ernst, R. E. and Youbi, N. (2017), ‘How Large Igneous Provinces affect global climate, sometimes cause mass extinctions, and represent natural markers in the geological record’, doi:10.1016/j.palaeo.2017.03.014 *Palaeogeography, Palaeoclimatology, Palaeoecology* **478**, 30–52.
- Farnsworth, A., Lunt, D. J., O’Brien, C. L., Foster, G. L., Inglis, G. N., Markwick, P., Pancost, R. D. and Robinson, S. A. (2019a), ‘Climate Sensitivity on Geological Timescales Controlled by Nonlinear Feedbacks and Ocean Circulation’, doi:10.1029/2019GL083574 *Geophysical Research Letters* **46**.
- Feulner, G. (2012), ‘The faint young Sun problem’, doi:10.1029/2011RG000375 *Reviews of Geophysics* **50**, RG2006.
- Feulner, G. (2017), ‘Formation of most of our coal brought Earth close to global glaciation’, doi:10.1073/pnas.1712062114 *Proceedings of the National Academy of Sciences* **114**(43), 11333–11337.
- Fichefet, T. and Maqueda, M. A. M. (1997), ‘Sensitivity of a global sea ice model to the treatment of ice thermodynamics and dynamics’, doi:10.1029/97JC00480 *Journal of Geophysical Research: Oceans* **102**(C6), 12609–12646.
- Fischer, M. L., Markowska, M., Bachofer, F., Foerster, V. E., Asrat, A., Zielhofer, C., Trauth, M. H. and Junginger, A. (2020), ‘Determining the Pace and Magnitude of Lake Level Changes in Southern Ethiopia Over the Last 20,000 Years Using Lake Balance Modeling and SEBAL’, doi:10.3389/feart.2020.00197 *Frontiers in Earth Science* **8**.
- Fluteau, F., Ramstein, G., Besse, J., Guiraud, R. and Masse, J. (2007), ‘Impacts of palaeogeography and sea level changes on Mid-Cretaceous climate’, doi:10.1016/j.palaeo.2006.11.016 *Palaeogeography, Palaeoclimatology, Palaeoecology* **247**(3), 357 – 381.
- Flögel, S., Beckmann, B., Hofmann, P., Bornemann, A., Westerhold, T., Norris, R., Dullo, C. and Wagner, T. (2008), ‘Evolution of tropical watersheds and continental hydrology during the Late Cretaceous greenhouse; impact on marine carbon burial and possible implications for the future’, doi:10.1016/j.epsl.2008.06.011 *Earth and Planetary Science Letters* **274**(1), 1–13.
- Flögel, S., Hay, W. W., DeConto, R. M. and Balukhovskiy, A. N. (2005), ‘Formation of sedimentary bedding couplets in the Western Interior Seaway of North America—implications from climate system modeling’, doi:10.1016/j.palaeo.2004.12.011 *Palaeogeography, Palaeoclimatology, Palaeoecology* **218**(1), 125–143.
- Flögel, S. and Wagner, T. (2006), ‘Insolation-control on the Late Cretaceous hydrological cycle and tropical African climate—global climate modelling linked to marine climate records’, doi:10.1016/j.palaeo.2005.09.034 *Palaeogeography, Palaeoclimatology, Palaeoecology* **235**(1), 288–304.
- Flögel, S., Wallmann, K. and Kuhnt, W. (2011), ‘Cool episodes in the Cretaceous — Exploring the effects of physical forcings on Antarctic snow accumulation’, doi:10.1016/j.epsl.2011.04.024 *Earth and Planetary Science Letters* **307**(3), 279–288.
- Flügel, E. (2002), Triassic Reef Patterns, in J. Golonka, W. Kiessling and E. Flügel, eds, ‘Phanerozoic Reef Patterns’, SEPM Society for Sedimentary Geology, doi:10.2110/pec.02.72.0391 pp. 391–463.
- Foster, G. L. and Rae, J. W. (2016), ‘Reconstructing ocean pH with boron isotopes in foraminifera’, doi:10.1146/annurev-earth-060115-012226 *Annual Review of Earth and Planetary Sciences* **44**(1), 207–237.
- Foster, G. L., Royer, D. L. and Lunt, D. J. (2017), ‘Future climate forcing potentially without precedent in the last 420 million years’, doi:10.1038/ncomms14845 *Nature Communications* **8**(14845), 1–8.
- Fox, C. P., Whiteside, J. H., Olsen, P. E., Cui, X., Summons, R. E., Idiz, E. and Grice, K. (2022), ‘Two-pronged kill mechanism at the end-Triassic mass extinction’, doi:10.1130/G49560.1 *Geology* .
- Fraedrich, K. (2013), ‘A minimalist model of terminal lakes: Qinghai Lake (China) and Lake Chad (N Africa)’, doi:10.2166/nh.2013.015 *Hydrology Research* **46**(2), 222–231.
- Frakes, L. A. and Francis, J. E. (1988), ‘A guide to Phanerozoic cold polar climates from high-latitude ice-rafting in the Cretaceous’, doi:10.1038/333547a0 *Nature* **333**(6173), 547–549.
- Frakes, L. A., Francis, J. E. and Syktus, J. I. (1992), *Climate Modes of the Phanerozoic*, doi:10.1017/CBO9780511628948 Cambridge University Press.
- Ganino, C. and Arndt, N. T. (2009), ‘Climate changes caused by degassing of sediments during the emplacement of large igneous provinces’, doi:10.1130/G25325A.1 *Geology* **37**(4), 323–326.

- Ganopolski, A. and Brovkin, V. (2017), ‘Simulation of climate, ice sheets and CO₂ evolution during the last four glacial cycles with an Earth system model of intermediate complexity’, doi:10.5194/cp-13-1695-2017 *Climate of the Past* **13**(12), 1695–1716.
- Ganopolski, A., Petoukhov, V., Rahmstorf, S., Brovkin, V., Claussen, M., Eliseev, A. and Kubatzki, C. (2001), ‘CLIMBER-2: a climate system model of intermediate complexity. Part II: model sensitivity’, doi:10.1007/s003820000144 *Climate Dynamics* **17**(10), 735–751.
- Gaskell, D. E., Huber, M., O’Brien, C. L., Inglis, G. N., Acosta, R. P., Poulsen, C. J. and Hull, P. M. (2022), ‘The latitudinal temperature gradient and its climate dependence as inferred from foraminiferal $\delta^{18}\text{O}$ over the past 95 million years’, doi:10.1073/pnas.2111332119 *Proceedings of the National Academy of Sciences* **119**(11), e2111332119.
- Gernon, T. M., Hincks, T. K., Merdith, A. S., Rohling, E. J., Palmer, M. R., Foster, G. L., Bataille, C. P. and Mueller, R. D. (2021), ‘Global chemical weathering dominated by continental arcs since the mid-Palaeozoic’, doi:10.1038/s41561-021-00806-0 *Nature Geoscience* **14**(9), 690+.
- Glaze, L. S., Self, S., Schmidt, A. and Hunter, S. J. (2017), ‘Assessing eruption column height in ancient flood basalt eruptions’, doi:10.1016/j.epsl.2014.07.043 *Earth and Planetary Science Letters* **457**, 263–270.
- Gleeson, T., Wagener, T., Döll, P., Zipper, S. C., West, C., Wada, Y., Taylor, R., Scanlon, B., Rosolem, R., Rahman, S., Oshinlaja, N., Maxwell, R., Lo, M.-H., Kim, H., Hill, M., Hartmann, A., Fogg, G., Famiglietti, J. S., Ducharne, A., de Graaf, I., Cuthbert, M., Condon, L., Bresciani, E. and Bierkens, M. F. P. (2021), ‘GMD perspective: The quest to improve the evaluation of groundwater representation in continental to global-scale models’, doi:10.5194/gmd-14-7545-2021 *Geoscientific Model Development* **14**(12), 7545–7571.
- Goddéris, Y., Donnadiéu, Y., Hir, G. L., Lefebvre, V. and Nardin, E. (2014), ‘The role of palaeogeography in the Phanerozoic history of atmospheric CO₂ and climate’, doi:10.1016/j.earscirev.2013.11.004 *Earth-Science Reviews* **128**, 122–138.
- Goddéris, Y. and Donnadiéu, Y. (2019), ‘A sink- or a source-driven carbon cycle at the geological timescale? Relative importance of palaeogeography versus solid Earth degassing rate in the Phanerozoic climatic evolution’, doi:10.1017/S0016756817001054 *Geological Magazine* **156**(2), 355–365.
- Goddéris, Y., Donnadiéu, Y., de Vargas, C., Pierrehumbert, R. T., Dromart, G. and van de Schootbrugge, B. (2008), ‘Causal or casual link between the rise of nannoplankton calcification and a tectonically-driven massive decrease in Late Triassic atmospheric CO₂?’, doi:10.1016/j.epsl.2007.11.051 *Earth and Planetary Science Letters* **267**(1), 247–255.
- Gough, D. O. (1981), ‘Solar interior structure and luminosity variations’, doi:10.1007/BF00151270 *Solar Physics* **74**(1), 21–34.
- Gravendyck, J., Schobben, M., Bachelier, J. B. and Kürschner, W. M. (2020), ‘Macroecological patterns of the terrestrial vegetation history during the end-Triassic biotic crisis in the central European Basin: A palynological study of the Bonenburg section (NW-Germany) and its supra-regional implications’, doi:10.1016/j.gloplacha.2020.103286 *Global and Planetary Change* **194**, 103286.
- Greene, S. E., Martindale, R. C., Ritterbush, K. A., Bottjer, D. J., Corsetti, F. A. and Berelson, W. M. (2012), ‘Recognising ocean acidification in deep time: An evaluation of the evidence for acidification across the Triassic-Jurassic boundary’, doi:10.1016/j.earscirev.2012.03.009 *Earth-Science Reviews* **113**(1-2), 72–93.
- Gregory, J. M., Griffies, S. M., Hughes, C. W., Lowe, J. A., Church, J. A., Fukumori, I., Gomez, N., Kopp, R. E., Landerer, F., Le Cozannet, G., Ponte, R. M., Stammer, D., Tamisiea, M. E. and van de Wal, R. S. W. (2019), ‘Concepts and Terminology for Sea Level: Mean, Variability and Change, Both Local and Global’, doi:10.1007/s10712-019-09525-z *Surveys in Geophysics* **40**(6, SI), 1251–1289.
- Guex, J., Pilet, S., Müntener, O., Bartolini, A., Spangenberg, J., Schoene, B., Sell, B. and Schaltegger, U. (2016), ‘Thermal erosion of cratonic lithosphere as a potential trigger for mass-extinction’, doi:10.1038/srep23168 *Scientific Reports* **6**(23168), 1–9.
- Hallam, A. (1984), ‘Continental humid and arid zones during the Jurassic and Cretaceous’, doi:10.1016/0031-0182(84)90094-4 *Palaeogeography, Palaeoclimatology, Palaeoecology* **47**(3), 195–223.
- Hallam, A. (1985), ‘A review of Mesozoic climates’, doi:10.1144/gsjgs.142.3.0433 *Journal of the Geological Society* **142**(3), 433–445.
- Hallam, A., Crame, J. A., Manceñido, M. O., Francis, J., Parrish, J. T., Allen, J. R. L., Hoskins, B. J., Sellwood, B. W., Spicer, R. A. and Valdes, P. J. (1993), ‘Jurassic climates as inferred from the sedimentary and fossil record’, doi:10.1098/rstb.1993.0114 *Philosophical Transactions of the Royal Society of London. Series B: Biological Sciences* **341**(1297), 287–296.
- Haq, B. U., Hardenbol, J. and Vail, P. R. (1987), ‘Chronology of Fluctuating Sea Levels Since the Triassic’, doi:10.1126/science.235.4793.1156 *Science* **235**(4793), 1156–1167.

- Haq, B. U., Hardenbol, J. and Vail, P. R. (1988), Mesozoic and Cenozoic chronostratigraphy and cycles of sea-level change, in C. K. Wilgus, ed., 'Sea-Level Changes', Vol. 42 of *SEPM Special Publications*, SEPM Society for Sedimentary Geology, doi:10.2110/pec.88.01.0071 pp. 71–108.
- Hautmann, M., Benton, M. J. and Tomašových, A. (2008), 'Catastrophic ocean acidification at the Triassic-Jurassic boundary', doi:10.1127/0077-7749/2008/0249-0119 *Neues Jahrbuch für Geologie und Paläontologie - Abhandlungen* **249**(1), 119–127.
- Hay, W. W. and Flögel, S. (2012), 'New thoughts about the Cretaceous climate and oceans', doi:10.1016/j.earscirev.2012.09.008 *Earth-Science Reviews* **115**(4), 262 – 272.
- Hays, J. D., Imbrie, J. and Shackleton, N. J. (1976), 'Variations in the Earth's Orbit: Pacemaker of the Ice Ages', doi:10.1126/science.194.4270.1121 *Science* **194**(4270), 1121–1132.
- He, T., Newton, R. J., Wignall, P. B., Reid, S., Dal Corso, J., Takahashi, S., Wu, H., Todaro, S., Di Stefano, P., Randazzo, V., Rigo, M. and Dunhill, A. M. (2022), 'Shallow ocean oxygen decline during the end-Triassic mass extinction', doi:10.1016/j.gloplacha.2022.103770 *Global and Planetary Change* **210**, 103770.
- Heavens, N. G., Mahowald, N. M., Soreghan, G. S., Soreghan, M. J. and Shields, C. A. (2015), 'A model-based evaluation of tropical climate in Pangaea during the late Palaeozoic icehouse', doi:10.1016/j.j.palaeo.2015.02.024 *Palaeogeography, Palaeoclimatology, Palaeoecology* **425**, 109–127.
- Heimdal, T. H., Goddérís, Y., Jones, M. T. and Svensen, H. H. (2021), 'Assessing the importance of thermogenic degassing from the Karoo Large Igneous Province (LIP) in driving Toarcian carbon cycle perturbations', doi:10.1038/s41467-021-26467-6 *Nature Communications* **12**(1).
- Heimdal, T. H., Jones, M. T. and Svensen, H. H. (2020), 'Thermogenic carbon release from the Central Atlantic magmatic province caused major end-Triassic carbon cycle perturbations', doi:10.1073/pnas.2000095117 *Proceedings of the National Academy of Sciences* **117**(22), 11968–11974.
- Heimdal, T. H., Svensen, H. H., Ramezani, J., Iyer, K., Pereira, E., Rodrigues, R., Jones, M. T. and Callegaro, S. (2018), 'Large-scale sill emplacement in Brazil as a trigger for the end-Triassic crisis', doi:10.1038/s41598-017-18629-8 *Scientific Reports* **8**(141), 1–14.
- Hilgen, F. J., Hinnov, L. A., Abdul Aziz, H., Abels, H. A., Batenburg, S., Bosmans, J. H. C., de Boer, B., Hüsing, S. K., Kuiper, K. F., Lourens, L. J., Rivera, T., Tuenter, E., Van de Wal, R. S. W., Wotzlaw, J.-F. and Zeeden, C. (2015), 'Stratigraphic continuity and fragmentary sedimentation: the success of cyclostratigraphy as part of integrated stratigraphy', doi:10.1144/SP404.12 *Geological Society, London, Special Publications* **404**(1), 157–197.
- Hillebrandt, A., Krystyn, L., Kürschner, W., Bonis, N., Ruhl, M., Richoz, S., Schobben, M. A. N., Urlichs, M., Bown, P., Kment, K., McRoberts, C., Simms, M. and Tomášových, A. (2013), 'The Global Stratotype Sections and Point (GSSP) for the base of the Jurassic system at Kuhjoch (Karwendel Mountains, Northern Calcareous Alps, Tyrol, Austria)', *Episodes* **36**(3), 162–198.
- Hinnov, L. A. (2013), 'Cyclostratigraphy and its revolutionizing applications in the earth and planetary sciences', doi:10.1130/B30934.1 *GSA Bulletin* **125**(11-12), 1703–1734.
- Hinnov, L. A. (2018), Cyclostratigraphy and Astrochronology in 2018, in M. Montenari, ed., 'Cyclostratigraphy and Astrochronology', Vol. 3 of *Stratigraphy & Timescales*, Academic Press, doi:10.1016/bs.sats.2018.08.004 chapter 1, pp. 1–80.
- Hinnov, L. and Cozzi, A. (2021), 'Rhaetian (Late Triassic) Milankovitch Cycles in the Tethyan Dachstein Limestone and Laurentian Passaic Formation Linked by the g2-g5 Astronomical Metronome', doi:10.21701/bolgeomin.131.2.004 *Boletín Geológico y Minero* **31**, 269–290.
- Hofmann, M. and Morales Maqueda, M. A. (2006), 'Performance of a second-order moments advection scheme in an Ocean General Circulation Model', doi:10.1029/2005JC003279 *Journal of Geophysical Research: Oceans* **111**(C5), 1–26.
- Hofmann, M. and Schellnhuber, H.-J. (2009), 'Oceanic acidification affects marine carbon pump and triggers extended marine oxygen holes', doi:10.1073/pnas.0813384106 *Proceedings of the National Academy of Sciences* **106**(9), 3017–3022.
- Hollis, C. J., Dunkley Jones, T., Anagnostou, E., Bijl, P. K., Cramwinckel, M. J., Cui, Y., Dickens, G. R., Edgar, K. M., Eley, Y., Evans, D., Foster, G. L., Frieling, J., Inglis, G. N., Kennedy, E. M., Kozdon, R., Lauretano, V., Lear, C. H., Littler, K., Lourens, L., Meckler, A. N., Naafs, B. D. A., Pälike, H., Pancost, R. D., Pearson, P. N., Röhl, U., Royer, D. L., Salzmann, U., Schubert, B. A., Seebeck, H., Sluijs, A., Speijer, R. P., Stassen, P., Tierney, J., Tripathi, A., Wade, B., Westerhold, T., Witkowski, C., Zachos, J. C., Zhang, Y. G., Huber, M. and Lunt, D. J. (2019), 'The DeepMIP contribution to PMIP4: methodologies for selection, compilation and analysis of latest Paleocene and early Eocene climate proxy data, incorporating version 0.1 of the DeepMIP database', doi:10.5194/gmd-12-3149-2019 *Geoscientific Model Development* **12**(7), 3149–3206.

- Horton, D. E., Poulsen, C. J., Montañez, I. P. and DiMichele, W. A. (2012), ‘Eccentricity-paced late Palaeozoic climate change’, doi:10.1016/j.palaeo.2012.03.014 *Palaeogeography, Palaeoclimatology, Palaeoecology* **331–332**, 150–161.
- Horton, D. E., Poulsen, C. J. and Pollard, D. (2010), ‘Influence of high-latitude vegetation feedbacks on late Palaeozoic glacial cycles’, doi:10.1038/ngeo922 *Nature Geoscience* **3**(8), 572–577.
- Hu, Y., Guo, J., Li, X., Lan, J., Lin, Q., Han, J., Zhang, J., Liu, Y. and Yang, J. (2021), Evolution of the monsoon system over the past 250 million years, in ‘EGU General Assembly Conference Abstracts’, doi:10.5194/egusphere-egu21-1459 pp. EGU21–1459.
- Huang, C. (2018), Astronomical time scale for the mesozoic, in M. Montenari, ed., ‘Cyclostratigraphy and Astrochronology’, Vol. 3 of *Stratigraphy & Timescales*, Academic Press, doi:10.1016/bs.sats.2018.08.005 chapter 2, pp. 81–150.
- Huang, H., Gao, Y., Ma, C., Jones, M. M., Zeeden, C., Ibarra, D. E., Wu, H. and Wang, C. (2021), ‘Organic carbon burial is paced by a 173-ka obliquity cycle in the middle to high latitudes’, doi:10.1126/sciadv.abf9489 *Science Advances* **7**(28), eabf9489.
- Huber, M. (2012), ‘Progress in Greenhouse Climate Modeling’, doi:10.1017/S108933260000262X *The Paleontological Society Papers* **18**, 213–262.
- Hull, P. M., Bornemann, A., Penman, D. E., Henehan, M. J., Norris, R. D., Wilson, P. A., Blum, P., Alegret, L., Batenburg, S. J., Bown, P. R., Bralower, T. J., Cournede, C., Deutsch, A., Donner, B., Friedrich, O., Jehle, S., Kim, H., Kroon, D., Lippert, P. C., Loroch, D., Moebius, I., Moriya, K., Peppe, D. J., Ravizza, G. E., Röhl, U., Schueth, J. D., Sepúlveda, J., Sexton, P. F., Sibert, E. C., Śliwińska, K. K., Summons, R. E., Thomas, E., Westerhold, T., Whiteside, J. H., Yamaguchi, T. and Zachos, J. C. (2020), ‘On impact and volcanism across the Cretaceous–Paleogene boundary’, doi:10.1126/science.aay5055 *Science* **367**(6475), 266–272.
- Hunter, S., Haywood, A., Valdes, P., Francis, J. and Pound, M. (2013), ‘Modelling equable climates of the Late Cretaceous: Can new boundary conditions resolve data-model discrepancies?’, doi:10.1016/j.palaeo.2013.08.009 *Palaeogeography, Palaeoclimatology, Palaeoecology* **392**, 41 – 51.
- Huynh, T. T. and Poulsen, C. J. (2005), ‘Rising atmospheric CO₂ as a possible trigger for the end-Triassic mass extinction’, doi:10.1016/j.palaeo.2004.12.004 *Palaeogeography, Palaeoclimatology, Palaeoecology* **217**(3–4), 223–242.
- Hönisch, B., Ridgwell, A., Schmidt, D. N., Thomas, E., Gibbs, S. J., Sluijs, A., Zeebe, R., Kump, L., Martindale, R. C., Greene, S. E., Kiessling, W., Ries, J., Zachos, J. C., Royer, D. L., Barker, S., Marchitto, T. M., Moyer, R., Pelejero, C., Ziveri, P., Foster, G. L. and Williams, B. (2012), ‘The Geological Record of Ocean Acidification’, doi:10.1126/science.1208277 *Science* **335**(6072), 1058–1063.
- Hülse, D., Lau, V. K., van de Velde, S. J., Arndt, S., Meyer, K. M. and Ridgwell, A. (2021), ‘End-permian marine extinction due to temperature-driven nutrient recycling and euxinia’, doi:10.1038/s41561-021-00829-7 *Nature Geoscience* **14**(11), 862+.
- Hüneke, H. and Henrich, R. (2011), Pelagic Sedimentation in Modern and Ancient Oceans, in ‘Deep-Sea Sediments’, Vol. 63 of *Developments in Sedimentology*, Elsevier, doi:10.1016/B978-0-444-53000-4.00004-4 chapter 4, pp. 215–351.
- Ikeda, M., Ozaki, K. and Legrand, J. (2020), ‘Impact of 10-Myr scale monsoon dynamics on Mesozoic climate and ecosystems’, doi:10.1038/s41598-020-68542-w *Scientific Reports* **10**(1).
- Ikeda, M. and Tada, R. (2014), ‘A 70 million year astronomical time scale for the deep-sea bedded chert sequence (Inuyama, Japan): Implications for Triassic–Jurassic geochronology’, doi:10.1016/j.epsl.2014.04.031 *Earth and Planetary Science Letters* **399**, 30–43.
- Ikeda, M. and Tada, R. (2020), ‘Reconstruction of the chaotic behavior of the Solar System from geologic records’, doi:10.1016/j.epsl.2020.116168 *Earth and Planetary Science Letters* **537**, 116168.
- Ilyina, T., Six, K. D., Segschneider, J., Maier-Reimer, E., Li, H. and Núñez-Riboni, I. (2013), ‘Global ocean biogeochemistry model HAMOCC: Model architecture and performance as component of the MPI-Earth system model in different CMIP5 experimental realizations’, doi:10.1029/2012MS000178 *Journal of Advances in Modeling Earth Systems* **5**(2), 287–315.
- Ivory, S. J., Blome, M. W., King, J. W., McGlue, M. M., Cole, J. E. and Cohen, A. S. (2016), ‘Environmental change explains cichlid adaptive radiation at Lake Malawi over the past 1.2 million years’, doi:10.1073/pnas.1611028113 *Proceedings of the National Academy of Sciences* **113**(42), 11895–11900.
- Jenkyns, H. C. (2010), ‘Geochemistry of oceanic anoxic events’, doi:10.1029/2009GC002788 *Geochemistry, Geophysics, Geosystems* **11**(3).
- Jones, L. A. and Eichenseer, K. (2021), ‘Uneven spatial sampling distorts reconstructions of Phanerozoic seawater temperature’, doi:10.1130/G49132.1 *Geology* **50**(2), 238–242.

- Jones, M. T., Jerram, D. A., Svensen, H. H. and Grove, C. (2016), ‘The effects of large igneous provinces on the global carbon and sulphur cycles’, doi:10.1016/j.palaeo.2015.06.042 *Palaeogeography, Palaeoclimatology, Palaeoecology* **441**, 4–21.
- Jones, S. M., Hoggett, M., Greene, S. E. and Jones, T. D. (2019), ‘Large Igneous Province thermogenic greenhouse gas flux could have initiated Paleocene-Eocene Thermal Maximum climate change’, doi:10.1038/s41467-019-12957-1 *Nature Communications* **10**.
- Joo, Y. J., Sageman, B. B. and Hurtgen, M. T. (2020), ‘Data-model comparison reveals key environmental changes leading to Cenomanian-Turonian Oceanic Anoxic Event 2’, doi:10.1016/j.earscirev.2020.103123 *Earth-Science Reviews* **203**, 103123.
- Jost, A. B., Bachan, A., van de Schootbrugge, B., Brown, S. T., DePaolo, D. J. and Payne, J. L. (2017b), ‘Additive effects of acidification and mineralogy on calcium isotopes in Triassic/Jurassic boundary limestones’, doi:10.1002/2016gc006724 *Geochemistry, Geophysics, Geosystems* **18**(1), 113–124.
- Jost, A. B., Bachan, A., van de Schootbrugge, B., Lau, K. V., Weaver, K. L., Maher, K. and Payne, J. L. (2017), ‘Uranium isotope evidence for an expansion of marine anoxia during the end-Triassic extinction’, doi:10.1002/2017gc006941 *Geochemistry, Geophysics, Geosystems* **18**(8), 3093–3108.
- Kaiho, K., Tanaka, D., Richoz, S., Jones, D. S., Saito, R., Kameyama, D., Ikeda, M., Takahashi, S., Aftabuzzaman, M. and Fujibayashi, M. (2022), ‘Volcanic temperature changes modulated volatile release and climate fluctuations at the end-Triassic mass extinction’, doi:10.1016/j.epsl.2021.117364 *Earth and Planetary Science Letters* **579**, 117364.
- Kaminski, E., Chenet, A.-L., Jaupart, C. and Courtillot, V. (2011), ‘Rise of volcanic plumes to the stratosphere aided by penetrative convection above large lava flows’, doi:10.1016/j.epsl.2010.10.037 *Earth and Planetary Science Letters* **301**(1-2), 171–178.
- Karlsen, K. S., Conrad, C. P. and Magni, V. (2019), ‘Deep Water Cycling and Sea Level Change Since the Breakup of Pangea’, doi:10.1029/2019GC008232 *Geochemistry, Geophysics, Geosystems* **20**(6), 2919–2935.
- Karlsen, K. S., Domeier, M., Gaina, C. and Conrad, C. P. (2020), ‘A tracer-based algorithm for automatic generation of seafloor age grids from plate tectonic reconstructions’, doi:10.1016/j.cageo.2020.104508 *Computers & Geosciences* **140**, 104508.
- Kasbohm, J., Schoene, B. and Burgess, S. (2021), *Radiometric Constraints on the Timing, Tempo, and Effects of Large Igneous Province Emplacement*, American Geophysical Union (AGU), doi:10.1002/9781119507444.ch2 chapter 2, pp. 27–82.
- Kasting, J. F. (1993), ‘Earth’s Early Atmosphere’, doi:10.1126/science.11536547 *Science* **259**(5097), 920–926.
- Kent, D. V. and Olsen, P. E. (1999), ‘Astronomically tuned geomagnetic polarity timescale for the Late Triassic’, doi:10.1029/1999JB900076 *Journal of Geophysical Research: Solid Earth* **104**(B6), 12831–12841.
- Kent, D. V., Olsen, P. E. and Muttoni, G. (2017), ‘Astrochronostratigraphic polarity time scale (APTS) for the Late Triassic and Early Jurassic from continental sediments and correlation with standard marine stages’, doi:10.1016/j.earscirev.2016.12.014 *Earth-Science Reviews* **166**, 153–180.
- Kent, D. V. and Tauxe, L. (2005), ‘Corrected Late Triassic Latitudes for Continents Adjacent to the North Atlantic’, doi:10.1126/science.1105826 *Science* **307**(5707), 240–244.
- Kidder, D. L. and Worsley, T. R. (2010), ‘Phanerozoic large igneous provinces (LIPs), HEATT (haline euxinic acidic thermal transgression) episodes, and mass extinctions’, doi:10.1016/j.palaeo.2010.05.036 *Palaeogeography, Palaeoclimatology, Palaeoecology* **295**(1-2), 162–191.
- Kiessling, W. (2001), ‘Paleoclimatic significance of Phanerozoic reefs’, doi:10.1130/0091-7613(2001)029<0751:PSOPR>2.0.CO;2 *Geology* **29**(8), 751–754.
- Kiessling, W. (2009b), ‘Geologic and biologic controls on the evolution of reefs’, doi:10.1146/annurev.ecolsys.110308.120251 *Annual Review of Ecology, Evolution, and Systematics* **40**(1), 173–192.
- Kiessling, W., Aberhan, M., Brenneis, B. and Wagner, P. J. (2007), ‘Extinction trajectories of benthic organisms across the Triassic–Jurassic boundary’, doi:10.1016/j.palaeo.2006.06.029 *Palaeogeography, Palaeoclimatology, Palaeoecology* **244**(1-4), 201–222.
- Kiessling, W., Flügel, E. and Golonka, J. (2002), *Phanerozoic Reef Patterns*, doi:10.2110/pec.02.72 SEPM Society for Sedimentary Geology.
- Kiessling, W. and Simpson, C. (2010), ‘On the potential for ocean acidification to be a general cause of ancient reef crises’, doi:10.1111/j.1365-2486.2010.02204.x *Global Change Biology* **17**(1), 56–67.
- Klages, J. P., Salzmann, U., Bickert, T., Hillenbrand, C., Gohl, K., Kuhn, G., Bohaty, S. M., Titschack, J., Müller, J., Frederichs, T., Bauersachs, T., Ehrmann, W., van de Flierdt, T., Pereira, P. S., Larter, R. D.,

- Lohmann, G., Niezgodzki, I., Uenzelmann-Neben, G., Zundel, M., Spiegel, C., Mark, C., Chew, D. M., Francis, J. E., Nehrke, G., Schwarz, F., Smith, J. A., Freudenthal, T., Esper, O., Pälike, H., Ronge, T. A., Dziadek, R. and the Science Team of Expedition PS104 (2020), ‘Temperate rainforests near the South Pole during peak Cretaceous warmth’, doi:10.1038/s41586-020-2148-5 *Nature* **580**, 81–86.
- Knight, K., Nomade, S., Renne, P., Marzoli, A., Bertrand, H. and Youbi, N. (2004), ‘The Central Atlantic Magmatic Province at the Triassic–Jurassic boundary: paleomagnetic and $^{40}\text{Ar}/^{39}\text{Ar}$ evidence from Morocco for brief, episodic volcanism’, doi:10.1016/j.epsl.2004.09.022 *Earth and Planetary Science Letters* **228**(1), 143–160.
- Knoll, A. H. and Follows, M. J. (2016), ‘A bottom-up perspective on ecosystem change in Mesozoic oceans’, doi:10.1098/rspb.2016.1755 *Proceedings of the Royal Society B: Biological Sciences* **283**(1841), 20161755.
- Kocsis, Á. T. and Scotese, C. R. (2021), ‘Mapping paleocoastlines and continental flooding during the Phanerozoic’, doi:10.1016/j.earscirev.2020.103463 *Earth-Science Reviews* **213**, 103463.
- Korte, C., Ruhl, M., Pálffy, J., Ullmann, C. V. and Hesselbo, S. P. (2018), *Chemostratigraphy Across the Triassic–Jurassic Boundary*, American Geophysical Union (AGU), doi:10.1002/9781119382508.ch10 chapter 10, pp. 183–210.
- Kuo, Y.-N., Lo, M.-H., Liang, Y.-C., Tseng, Y.-H. and Hsu, C.-W. (2021), ‘Terrestrial Water Storage Anomalies Emphasize Interannual Variations in Global Mean Sea Level During 1997–1998 and 2015–2016 El Niño Events’, doi:10.1029/2021GL094104 *Geophysical Research Letters* **48**(18), e2021GL094104.
- Kutzbach, J., Bonan, G., Foley, J. and Harrison, S. (1996), ‘Vegetation and soil feedbacks on the response of the African monsoon to orbital forcing in the early to middle Holocene’, doi:10.1038/384623a0 *Nature* **384**(6610), 623–626.
- Kutzbach, J. E. (1981), ‘Monsoon Climate of the Early Holocene: Climate Experiment with the Earth’s Orbital Parameters for 9000 Years Ago’, doi:10.1126/science.214.4516.59 *Science* **214**(4516), 59–61.
- Kutzbach, J. E. (1994), Idealized Pangean Climates - Sensitivity to Orbital Change, in Klein, G.D., ed., ‘Pangea: Paleoclimate, Tectonics, and Sedimentation during Accretion, Zenith and Breakup of a Supercontinent’, number 288 in ‘Geological Society of America Special Papers’, doi:10.1130/SPE288-p41 pp. 41–55.
- Kutzbach, J. E. and Gallimore, R. G. (1989), ‘Pangaeian climates: Megamonsoons of the megacontinent’, doi:10.1029/JD094iD03p03341 *Journal of Geophysical Research: Atmospheres* **94**(D3), 3341–3357.
- Kutzbach, J. E., Guan, J., He, F., Cohen, A. S., Orland, I. J. and Chen, G. (2020), ‘African climate response to orbital and glacial forcing in 140,000-y simulation with implications for early modern human environments’, doi:10.1073/pnas.1917673117 *Proceedings of the National Academy of Sciences* **117**(5), 2255–2264.
- Kutzbach, J. E., Liu, X., Liu, Z. and Chen, G. (2008), ‘Simulation of the evolutionary response of global summer monsoons to orbital forcing over the past 280,000 years’, doi:10.1007/s00382-007-0308-z *Climate Dynamics* **30**(6), 567–579.
- Kutzbach, J. E. and Liu, Z. (1997), ‘Response of the African Monsoon to Orbital Forcing and Ocean Feedbacks in the Middle Holocene’, doi:10.1126/science.278.5337.440 *Science* **278**(5337), 440–443.
- Kutzbach, J. E. and Otto-Bliesner, B. L. (1982), ‘The Sensitivity of the African-Asian Monsoonal Climate to Orbital Parameter Changes for 9000 Years B.P. in a Low-Resolution General Circulation Model’, doi:10.1175/1520-0469(1982)039<1177:TSOTAA>2.0.CO;2 *Journal of Atmospheric Sciences* **39**(6), 1177 – 1188.
- Kutzbach, J. E. and Street-Perrott, F. A. (1985), ‘Milankovitch forcing of fluctuations in the level of tropical lakes from 18 to 0 kyr BP’, doi:10.1038/317130a0 *Nature* **317**(6033), 130–134.
- Kutzbach, J. E. and Webb III, T. (1991), ‘Late Quaternary climatic and vegetational change in eastern North America: concepts, models, and data’, *Quaternary Landscapes* pp. 175–217.
- Ladant, J.-B. and Donnadieu, Y. (2016), ‘Palaeogeographic regulation of glacial events during the Cretaceous supergreenhouse’, doi:10.1038/ncomms12771 *Nature Communications* **7**, 12771.
- Ladant, J.-B., Poulsen, C. J., Fluteau, F., Tabor, C. R., MacLeod, K. G., Martin, E. E., Haynes, S. J. and Rostami, M. A. (2020), ‘Paleogeographic controls on the evolution of Late Cretaceous ocean circulation’, doi:10.5194/cp-16-973-2020 *Climate of the Past* **16**(3), 973–1006.
- Landwehrs, J., Feulner, G., Hofmann, M. and Petri, S. (2020), ‘Climatic fluctuations modeled for carbon and sulfur emissions from end-Triassic volcanism’, doi:10.1016/j.epsl.2020.116174 *Earth and Planetary Science Letters* **537**, 116174.
- Landwehrs, J., Feulner, G., Petri, S., Sames, B. and Wagerich, M. (2021), ‘Investigating Mesozoic Climate Trends and Sensitivities With a Large Ensemble of Climate Model Simulations’, doi:10.1029/2020PA004134 *Paleoceanography and Paleoclimatology* **36**(6), e2020PA004134.

- Landwehrs, J., Feulner, G., Petri, S., Sames, B. and Wagemann, M. (2021b), doi:10.5880/PIK.2020.009 'Data from Climate Model Ensemble Simulations for the Mesozoic Climate Evolution'.
- Landwehrs, J., Feulner, G., Willeit, M., Petri, S., Sames, B., Wagemann, M., Whiteside, J. H. and Olsen, P. E. (2022), 'Modes of Pangean Lake-Level Cyclicity Driven by Astronomical Pacing Modulated by Continental Position and $p\text{CO}_2$ '. (submitted).
- Landwehrs, J., Feulner, G., Willeit, M., Sames, B. and Wagemann, M. (2021c), Transient Climate Simulations of Orbital Effects on Mesozoic Climates, in 'EGU General Assembly Conference Abstracts', EGU General Assembly Conference Abstracts, doi:10.5194/egusphere-egu21-4093 pp. EGU21-4093.
- Langmann, B. (2014), 'On the Role of Climate Forcing by Volcanic Sulphate and Volcanic Ash', doi:10.1155/2014/340123 *Advances in Meteorology* **2014**, 1–17.
- Laskar, J., Fienga, A., Gastineau, M. and Manche, H. (2011), 'La2010: a new orbital solution for the long-term motion of the Earth', doi:10.1051/0004-6361/201116836 *Astronomy & Astrophysics* **532**, A89.
- Laskar, J., Joutel, F. and Boudin, F. (1993), 'Orbital, precessional, and insolation quantities for the Earth from -20 Myr to +10 Myr', *Astronomy & Astrophysics* **270**(1-2), 522–533.
- Laskar, J., Robutel, P., Joutel, F., Gastineau, M., Correia, A. C. M. and Levrard, B. (2004), 'A long-term numerical solution for the insolation quantities of the Earth', doi:10.1051/0004-6361:20041335 *A&A* **428**(1), 261–285.
- Lathuilière, B. and Marchal, D. (2009), 'Extinction, survival and recovery of corals from the Triassic to Middle Jurassic time', doi:10.1111/j.1365-3121.2008.00856.x *Terra Nova* **21**(1), 57–66.
- Laugié, M., Donnadieu, Y., Ladant, J.-B., Green, J. A. M., Bopp, L. and Raison, F. (2020), 'Stripping back the modern to reveal the Cenomanian–Turonian climate and temperature gradient underneath', doi:10.5194/cp-16-953-2020 *Climate of the Past* **16**(3), 953–971.
- Laurin, J., Barclay, R. S., Sageman, B. B., Dawson, R. R., Pagani, M., Schmitz, M., Eaton, J., McInerney, F. A. and McElwain, J. C. (2019), 'Terrestrial and marginal-marine record of the mid-Cretaceous Oceanic Anoxic Event 2 (OAE 2): High-resolution framework, carbon isotopes, CO_2 and sea-level change', doi:10.1016/j.palaeo.2019.03.019 *Palaeogeography, Palaeoclimatology, Palaeoecology* **524**, 118–136.
- Laurin, J., Uličný, D., Čech, S., Trubač, J., Zachariáš, J. and Svobodová, A. (2021), 'Chronology and eccentricity phasing for the early turonian greenhouse (93–94 ma): Constraints on astronomical control of the carbon cycle', doi:https://doi.org/10.1029/2020PA004188 *Paleoceanography and Paleoclimatology* **36**(4), e2020PA004188. <https://agupubs.onlinelibrary.wiley.com/doi/abs/10.1029/2020PA004188>
- Lenton, T. M., Daines, S. J. and Mills, B. J. (2018), 'COPSE reloaded: An improved model of biogeochemical cycling over Phanerozoic time', doi:10.1016/j.earscirev.2017.12.004 *Earth-Science Reviews* **178**, 1–28.
- Lepre, C. J. and Olsen, P. E. (2021), 'Hematite reconstruction of Late Triassic hydroclimate over the Colorado Plateau', doi:10.1073/pnas.2004343118 *Proceedings of the National Academy of Sciences* **118**(7).
- Lepre, C., Yazzie, O. and Olsen, P. (2021), Orbital pacing of redox cycles suggested by red bed color of the Late Triassic Chinle Formation, Arizona, in 'EGU General Assembly Conference Abstracts', doi:10.5194/egusphere-egu21-3696 pp. EGU21-3696.
- Letulle, T., Suan, G., Daëron, M., Rogov, M., Lécuyer, C., Vinçon-Laugier, A., Reynard, B., Montagnac, G., Lutikov, O. and Schlögl, J. (2022), 'Clumped isotope evidence for early jurassic extreme polar warmth and high climate sensitivity', doi:10.5194/cp-18-435-2022 *Climate of the Past* **18**(3), 435–448. <https://cp.copernicus.org/articles/18/435/2022/>
- Li, H.-T., Yi, T.-S., Gao, L.-M., Ma, P.-F., Zhang, T., Yang, J.-B., Gitzendanner, M. A., Fritsch, P. W., Cai, J., Luo, Y., Wang, H., van der Bank, M., Zhang, S.-D., Wang, Q.-F., Wang, J., Zhang, Z.-R., Fu, C.-N., Yang, J., Hollingsworth, P. M., Chase, M. W., Soltis, D. E., Soltis, P. S. and Li, D.-Z. (2019b), 'Origin of angiosperms and the puzzle of the Jurassic gap', doi:10.1038/s41477-019-0421-0 *Nature Plants* **5**(5), 461–470.
- Li, M., Hinnov, L. A., Huang, C. and Ogg, J. G. (2018), 'Sedimentary noise and sea levels linked to land-ocean water exchange and obliquity forcing', doi:10.1038/s41467-018-03454-y *Nature Communications* **9**.
- Li, M., Huang, C., Hinnov, L., Ogg, J., Chen, Z.-Q. and Zhang, Y. (2016), 'Obliquity-forced climate during the Early Triassic hothouse in China', doi:10.1130/G37970.1 *Geology* **44**(8), 623–626.
- Li, M., Huang, C., Ogg, J., Zhang, Y., Hinnov, L., Wu, H., Chen, Z.-Q. and Zou, Z. (2019), 'Paleoclimate proxies for cyclostratigraphy: Comparative analysis using a Lower Triassic marine section in South China', doi:10.1016/j.earscirev.2019.01.011 *Earth-Science Reviews* **189**, 125–146.
- Lindström, S. (2015), 'Palynofloral patterns of terrestrial ecosystem change during the end-Triassic event – a review', doi:10.1017/s0016756815000552 *Geological Magazine* **153**(02), 223–251.

- Lindström, S., Erlström, M., Piasecki, S., Nielsen, L. H. and Mathiesen, A. (2017), ‘Palynology and terrestrial ecosystem change of the Middle Triassic to lowermost Jurassic succession of the eastern Danish Basin’, doi:10.1016/j.revpalbo.2017.04.007 *Review of Palaeobotany and Palynology* **244**, 65–95.
- Lindström, S., van de Schootbrugge, B., Hansen, K. H., Pedersen, G. K., Alsen, P., Thibault, N., Dybkjær, K., Bjerrum, C. J. and Nielsen, L. H. (2017b), ‘A new correlation of Triassic–Jurassic boundary successions in NW Europe, Nevada and Peru, and the Central Atlantic Magmatic Province: A time-line for the end-Triassic mass extinction’, doi:10.1016/j.palaeo.2016.12.025 *Palaeogeography, Palaeoclimatology, Palaeoecology* **478**, 80–102.
- Lindström, S., Callegaro, S., Davies, J., Tegner, C., van de Schootbrugge, B., Pedersen, G. K., Youbi, N., Sanei, H. and Marzoli, A. (2021), ‘Tracing volcanic emissions from the Central Atlantic Magmatic Province in the sedimentary record’, doi:10.1016/j.earscirev.2020.103444 *Earth-Science Reviews* **212**, 103444.
- Lindström, S., Sanei, H., van de Schootbrugge, B., Pedersen, G. K., Leshner, C. E., Tegner, C., Heunisch, C., Dybkjær, K. and Outridge, P. M. (2019), ‘Volcanic mercury and mutagenesis in land plants during the end-Triassic mass extinction’, doi:10.1126/sciadv.aaw4018 *Science Advances* **5**(10), eaaw4018.
- Liu, D., Huang, C., Kemp, D. B., Li, M., Ogg, J. G., Yu, M. and Foster, W. J. (2021), ‘Paleoclimate and sea level response to orbital forcing in the Middle Triassic of the eastern Tethys’, doi:10.1016/j.gloplacha.2021.103454 *Global and Planetary Change* **199**, 103454.
- Liu, W., Wu, H., Hinnov, L. A., Baddouh, M., Wang, P., Gao, Y., Zhang, S., Yang, T., Li, H. and Wang, C. (2020), ‘An 11 million-year-long record of astronomically forced fluvial-alluvial deposition and paleoclimate change in the Early Cretaceous Songliao synrift basin, China’, doi:https://doi.org/10.1016/j.palaeo.2019.109555 *Palaeogeography, Palaeoclimatology, Palaeoecology* **541**, 109555.
- Lorenz, S. J. and Lohmann, G. (2004), ‘Acceleration technique for Milankovitch type forcing in a coupled atmosphere-ocean circulation model: method and application for the Holocene’, doi:10.1007/s00382-004-0469-y *Climate Dynamics* **23**, 727–743.
- Lourens, L. J. (2016), The variation of the earth’s movements (orbital, tilt and precession), in T. M. Letcher, ed., ‘Climate Change’, 2 edn, Elsevier, Boston, doi:10.1016/B978-0-444-63524-2.00025-7 chapter 25, pp. 399–418.
- Loutre, M. (2003), Ice age (Milankovitch Theory), in J. R. Holton, ed., ‘Encyclopedia of Atmospheric Sciences’, Academic Press, Oxford, doi:10.1016/B0-12-227090-8/00173-1 pp. 995–1003.
- Loutre, M.-F. (2009a), Obliquity, in V. Gornitz, ed., ‘Encyclopedia of Paleoclimatology and Ancient Environments’, Springer Netherlands, Dordrecht, doi:10.1007/978-1-4020-4411-3_154 pp. 625–626.
- Loutre, M.-F. (2009b), *Precession, Climatic*, Springer Netherlands, Dordrecht, doi:10.1007/978-1-4020-4411-3_194 pp. 825–826.
- Loutre, M.-F., Paillard, D., Vimeux, F. and Cortijo, E. (2004), Does mean annual insolation have the potential to change the climate?, Vol. 221, doi:10.1016/S0012-821X(04)00108-6 pp. 1–14.
- Lowery, C. M., Bown, P. R., Fraass, A. J. and Hull, P. M. (2020), ‘Ecological Response of Plankton to Environmental Change: Thresholds for Extinction’, doi:10.1146/annurev-earth-081619-052818 *Annual Review of Earth and Planetary Sciences* **48**(1), 403–429.
- Lu, Z., Liu, Z., Chen, G. and Guan, J. (2019), ‘Prominent Precession Band Variance in ENSO Intensity Over the Last 300,000 Years’, doi:10.1029/2019GL083410 *Geophysical Research Letters* **46**(16), 9786–9795.
- Lunt, D. J., Bragg, F., Chan, W.-L., Hutchinson, D. K., Ladant, J.-B., Morozova, P., Niezgodzki, I., Steinig, S., Zhang, Z., Zhu, J., Abe-Ouchi, A., Anagnostou, E., de Boer, A. M., Coxall, H. K., Donnadiou, Y., Foster, G., Inglis, G. N., Knorr, G., Langebroek, P. M., Lear, C. H., Lohmann, G., Poulsen, C. J., Sepulchre, P., Tierney, J. E., Valdes, P. J., Volodin, E. M., Dunkley Jones, T., Hollis, C. J., Huber, M. and Otto-Bliesner, B. L. (2021), ‘DeepMIP: model intercomparison of early Eocene climatic optimum (EECO) large-scale climate features and comparison with proxy data’, doi:10.5194/cp-17-203-2021 *Climate of the Past* **17**(1), 203–227.
- Lunt, D. J., Farnsworth, A., Loptson, C., Foster, G. L., Markwick, P., O’Brien, C. L., Pancost, R. D., Robinson, S. A. and Wrobel, N. (2016), ‘Palaeogeographic controls on climate and proxy interpretation’, doi:10.5194/cp-12-1181-2016 *Climate of the Past* **12**(5), 1181–1198.
- Lunt, D. J., Huber, M., Anagnostou, E., Baatsen, M. L. J., Caballero, R., DeConto, R., Dijkstra, H. A., Donnadiou, Y., Evans, D., Feng, R., Foster, G. L., Gasson, E., von der Heydt, A. S., Hollis, C. J., Inglis, G. N., Jones, S. M., Kiehl, J., Kirtland Turner, S., Korty, R. L., Kozdon, R., Krishnan, S., Ladant, J.-B., Langebroek, P., Lear, C. H., LeGrande, A. N., Littler, K., Markwick, P., Otto-Bliesner, B., Pearson, P., Poulsen, C. J., Salzmann, U., Shields, C., Snell, K., Stärrz, M., Super, J., Tabor, C., Tierney, J. E., Tourte, G. J. L., Tripathi, A., Upchurch, G. R., Wade, B. S., Wing, S. L., Winguth, A. M. E., Wright,

- N. M., Zachos, J. C. and Zeebe, R. E. (2017), ‘The DeepMIP contribution to PMIP4: experimental design for model simulations of the EECO, PETM, and pre-PETM (version 1.0)’, doi:10.5194/gmd-10-889-2017 *Geoscientific Model Development* **10**(2), 889–901.
- Lunt, D. J., Williamson, M. S., Valdes, P. J., Lenton, T. M. and Marsh, R. (2006), ‘Comparing transient, accelerated, and equilibrium simulations of the last 30 000 years with the GENIE-1 model’, doi:10.5194/cp-2-221-2006 *Climate of the Past* **2**(2), 221–235.
- Luo, G., Richoz, S., van de Schootbrugge, B., Algeo, T. J., Xie, S., Ono, S. and Summons, R. E. (2018), ‘Multiple sulfur-isotopic evidence for a shallowly stratified ocean following the Triassic–Jurassic boundary mass extinction’, doi:10.1016/j.gca.2018.04.015 *Geochimica et Cosmochimica Acta* **231**, 73–87.
- Läpple, T. and Lohmann, G. (2009), ‘Seasonal cycle as template for climate variability on astronomical timescales’, doi:10.1029/2008PA001674 *Paleoceanography* **24**(4).
- Macdonald, F. A. and Wordsworth, R. (2017), ‘Initiation of Snowball Earth with volcanic sulfur aerosol emissions’, doi:10.1002/2016gl072335 *Geophysical Research Letters* **44**(4), 1938–1946.
- Maier-Reimer, E. (1993), ‘Geochemical cycles in an ocean general circulation model. Preindustrial tracer distributions’, doi:10.1029/93GB01355 *Global Biogeochemical Cycles* **7**(3), 645–677.
- Marcilly, C. M., Torsvik, T. H., Domeier, M. and Royer, D. L. (2021), ‘New paleogeographic and degassing parameters for long-term carbon cycle models’, doi:10.1016/j.gr.2021.05.016 *Gondwana Research* **97**, 176–203.
- Margulis-Ohnuma, M., Whiteside, J. and Olsen, P. (2021), ‘Strong inclination pacing of climate in Late Triassic low latitudes revealed by the Earth–Saturn tilt cycle’, *The Yale Undergraduate Research Journal* **2**(1), 37. <https://elischolar.library.yale.edu/yurj/vol2/iss1/37>
- Markwick, P. J. (2007), The palaeogeographic and palaeoclimatic significance of climate proxies for data-model comparisons, in ‘Deep-Time Perspectives on Climate Change: Marrying the Signal from Computer Models and Biological Proxies’, doi:10.1144/TMS002.13 Geological Society of London.
- Marsh, R., Müller, S. A., Yool, A. and Edwards, N. R. (2011), ‘Incorporation of the C-GOLDSTEIN efficient climate model into the GENIE framework: “eb_go_gs” configurations of GENIE’, doi:10.5194/gmd-4-957-2011 *Geoscientific Model Development* **4**(4), 957–992.
- Martindale, R. C., Foster, W. J. and Velledits, F. (2019), ‘The survival, recovery, and diversification of metazoan reef ecosystems following the end-Permian mass extinction event’, doi:10.1016/j.palaeo.2017.08.014 *Palaeogeography, Palaeoclimatology, Palaeoecology* **513**, 100–115.
- Martinez, M. and Dera, G. (2015), ‘Orbital pacing of carbon fluxes by a ~9-My eccentricity cycle during the Mesozoic’, doi:10.1073/pnas.1419946112 *Proceedings of the National Academy of Sciences* **112**(41), 12604–12609.
- Martinez, M., Guillois, L., Boulvais, P. and Deconinck, J.-F. (2020), ‘Inverted Responses of the Carbon Cycle to Orbital Forcing in Mesozoic Periplatform Marginal Basins: Implications for Astrochronology’, doi:10.1029/2019PA003705 *Paleoceanography and Paleoclimatology* **35**(6), e2019PA003705.
- Marzocchi, A., Lunt, D. J., Flecker, R., Bradshaw, C. D., Farnsworth, A. and Hilgen, F. J. (2015), ‘Orbital control on late Miocene climate and the North African monsoon: insight from an ensemble of sub-precessional simulations’, doi:10.5194/cp-11-1271-2015 *Climate of the Past* **11**(10), 1271–1295.
- Marzoli, A., Callegaro, S., Dal Corso, J., Davies, J. H. F. L., Chiaradia, M., Youbi, N., Bertrand, H., Reisberg, L., Merle, R. and Jourdan, F. (2018), The Central Atlantic Magmatic Province (CAMP): A Review, in L. H. Tanner, ed., ‘The Late Triassic World: Earth in a Time of Transition’, Springer International Publishing, doi:10.1007/978-3-319-68009-5_4 pp. 91–125.
- Maslin, M. A., Brierley, C. M., Milner, A. M., Shultz, S., Trauth, M. H. and Wilson, K. E. (2014), ‘East African climate pulses and early human evolution’, doi:10.1016/j.quascirev.2014.06.012 *Quaternary Science Reviews* **101**, 1–17.
- Masson-Delmotte, V., P., Zhai, A., Pirani, S., Connors, C., Péan, S., Berger, N., Caud, Y., Chen, L., Goldfarb, M., Gomis, M., Huang, K., Leitzell, E., Lonnoy, J., Matthews, T., Maycock, T., Waterfield, O., Yelekçi, R., Yu and Zhou, B. (2021), ‘IPCC, 2021: Climate Change 2021: The Physical Science Basis. Contribution of Working Group I to the Sixth Assessment Report of the Intergovernmental Panel on Climate Change’. <https://www.ipcc.ch/report/ar6/wg1/>
- Mather, T. A. (2015), ‘Volcanoes and the environment: Lessons for understanding Earth's past and future from studies of present-day volcanic emissions’, doi:10.1016/j.jvolgeores.2015.08.016 *Journal of Volcanology and Geothermal Research* **304**, 160–179.
- Mather, T. A. and Schmidt, A. (2021), *Environmental Effects of Volcanic Volatile Fluxes From Subaerial Large Igneous Provinces*, American Geophysical Union (AGU), doi:10.1002/9781119507444.ch4 chapter 4, pp. 103–116.

- Matthews, K. J., Maloney, K. T., Zahirovic, S., Williams, S. E., Seton, M. and Mueller, R. D. (2016), ‘Global plate boundary evolution and kinematics since the late Paleozoic’, doi:10.1016/j.gloplacha.2016.10.002 *Global and Planetary Change* **146**, 226–250.
- McElwain, J. C., Beerling, D. J. and Woodward, F. I. (1999), ‘Fossil Plants and Global Warming at the Triassic-Jurassic Boundary’, doi:10.1126/science.285.5432.1386 *Science* **285**(5432), 1386–1390.
- McElwain, J. C., Wagner, P. J. and Hesselbo, S. P. (2009), ‘Fossil Plant Relative Abundances Indicate Sudden Loss of Late Triassic Biodiversity in East Greenland’, doi:10.1126/science.1171706 *Science* **324**(5934), 1554–1556.
- McGhee, G. R., Clapham, M. E., Sheehan, P. M., Bottjer, D. J. and Droser, M. L. (2013), ‘A new ecological-severity ranking of major Phanerozoic biodiversity crises’, doi:10.1016/j.palaeo.2012.12.019 *Palaeogeography, Palaeoclimatology, Palaeoecology* **370**, 260–270.
- McHone, J. G. (2003), Volatile Emissions from Central Atlantic Magmatic Province Basalts: Mass Assumptions and Environmental Consequences, in ‘The Central Atlantic Magmatic Province: Insights from Fragments of Pangea’, American Geophysical Union (AGU), doi:10.1029/136GM013 pp. 241–254.
- Metzner, D., Kutterolf, S., Toohey, M., Timmreck, C., Niemeier, U., Freundt, A. and Krüger, K. (2012), ‘Radiative forcing and climate impact resulting from SO₂ injections based on a 200,000-year record of Plinian eruptions along the Central American Volcanic Arc’, doi:10.1007/s00531-012-0814-z *International Journal of Earth Sciences* **103**(7), 2063–2079.
- Milankovitch, M. (1941), ‘Kanon der Erdbestrahlung und seine Anwendung auf das Eiszeitenproblem’, *Royal Serbian Academy Special Publication* **133**, 1–633.
- Mills, B. J., Donnadiou, Y. and Godd eris, Y. (2021), ‘Spatial continuous integration of Phanerozoic global biogeochemistry and climate’, doi:10.1016/j.gr.2021.02.011 *Gondwana Research* **100**, 73–86.
- Mills, B. J., Krause, A. J., Scotese, C. R., Hill, D. J., Shields, G. A. and Lenton, T. M. (2019), ‘Modelling the long-term carbon cycle, atmospheric CO₂, and Earth surface temperature from late Neoproterozoic to present day’, doi:10.1016/j.gr.2018.12.001 *Gondwana Research* **67**, 172 – 186.
- Monta nez, I. P. and Poulsen, C. J. (2013), ‘The Late Paleozoic Ice Age: An Evolving Paradigm’, doi:10.1146/annurev.earth.031208.100118 *Annual Review of Earth and Planetary Sciences* **41**(1), 629–656.
- Monteiro, F. M., Pancost, R. D., Ridgwell, A. and Donnadiou, Y. (2012), ‘Nutrients as the dominant control on the spread of anoxia and euxinia across the Cenomanian-Turonian oceanic anoxic event (OAE2): Model-data comparison’, doi:10.1029/2012PA002351 *Paleoceanography* **27**(4).
- Montoya, M., Griesel, A., Levermann, A., Mignot, J., Hofmann, M., Ganopolski, A. and Rahmstorf, S. (2005), ‘The earth system model of intermediate complexity CLIMBER-3 . Part I: description and performance for present-day conditions’, doi:10.1007/s00382-005-0044-1 *Climate Dynamics* **25**(2-3), 237–263.
- Morrill, C., Small, E. E. and Sloan, L. C. (2001), ‘Modeling orbital forcing of lake level change: Lake Gosiute (Eocene), North America’, doi:10.1016/S0921-8181(00)00084-9 *Global and Planetary Change* **29**(1), 57–76.
- Mussard, M., Le Hir, G., Fluteau, F., Lefebvre, V. and Godd eris, Y. (2014), ‘Modeling the carbon-sulfate interplays in climate changes related to the emplacement of continental flood basalts’, doi:10.1130/2014.2505(17) *Special Paper of the Geological Society of America* **505**, 339–352.
- M uller, S. A., Joos, F., Edwards, N. R. and Stocker, T. F. (2006), ‘Water mass distribution and ventilation time scales in a cost-efficient, three-dimensional ocean model’, doi:10.1175/JCLI3911.1 *Journal of Climate* **19**(21), 5479 – 5499.
- Niezgodzki, I., Knorr, G., Lohmann, G., Tyszka, J. and Markwick, P. J. (2017), ‘Late Cretaceous climate simulations with different CO₂ levels and subarctic gateway configurations: A model-data comparison’, doi:10.1002/2016PA003055 *Paleoceanography* **32**(9), 980–998.
- Nordt, L., Breecker, D. and White, J. (2022), ‘Jurassic greenhouse ice-sheet fluctuations sensitive to atmospheric CO₂ dynamics’, doi:10.1038/s41561-021-00858-2 *Nature Geoscience* **15**(1), 54+.
- O’Brien, C. L., Robinson, S. A., Pancost, R. D., Damst e, J. S. S., Schouten, S., Lunt, D. J., Alsenz, H., Bornemann, A., Bottini, C., Brassell, S. C., Farnsworth, A., Forster, A., Huber, B. T., Inglis, G. N., Jenkyns, H. C., Linnert, C., Littler, K., Markwick, P., McAnena, A., Mutterlose, J., Naafs, B. D. A., P uttmann, W., Sluijs, A., van Helmond, N. A., Vellekoop, J., Wagner, T. and Wrobel, N. E. (2017), ‘Cretaceous sea-surface temperature evolution: Constraints from TEX86 and planktonic foraminiferal oxygen isotopes’, doi:10.1016/j.earscirev.2017.07.012 *Earth-Science Reviews* **172**, 224 – 247.
- Olsen, P. E. (1986), ‘A 40-Million-Year Lake Record of Early Mesozoic Orbital Climatic Forcing’, doi:10.1126/science.234.4778.842 *Science* **234**(4778), 842–848.

- Olsen, P. E. (1997), ‘Stratigraphic record of the early Mesozoic breakup of Pangea in the Laurasia-Gondwana rift system’, doi:10.1146/annurev.earth.25.1.337 *Annual Review of Earth and Planetary Sciences* **25**(1), 337–401.
- Olsen, P. E. (2010), ‘Fossil great lakes of the Newark Supergroup - 30 years later’, *New York State Geological Association 82nd annual meeting; field trip guidebook* **82**, 101.
- Olsen, P. E. and Kent, D. V. (1990), ‘Continental coring of the Newark Rift’, doi:10.1029/EO071i015p00385-02 *Eos, Transactions American Geophysical Union* **71**(15), 385–394.
- Olsen, P. E. and Kent, D. V. (1996), ‘Milankovitch climate forcing in the tropics of Pangaea during the Late Triassic’, doi:10.1016/0031-0182(95)00171-9 *Palaeogeography, Palaeoclimatology, Palaeoecology* **122**(1), 1–26.
- Olsen, P. E., Kent, D. V., Cornet, B., Witte, W. K. and Schlische, R. W. (1996b), ‘High-resolution stratigraphy of the Newark rift basin (early Mesozoic, eastern North America)’, doi:10.1130/0016-7606(1996)108<0040:HRSTN>2.3.CO;2 *GSA Bulletin* **108**(1), 40–77.
- Olsen, P. E., Laskar, J., Kent, D. V., Kinney, S. T., Reynolds, D. J., Sha, J. and Whiteside, J. H. (2019), ‘Mapping Solar System chaos with the Geological Orrery’, doi:10.1073/pnas.1813901116 *Proceedings of the National Academy of Sciences* **116**(22), 10664–10673.
- Olsen, P. E. and Whiteside, J. H. (2009), Pre-Quaternary Milankovitch Cycles and Climate Variability, in V. Gornitz, ed., ‘Encyclopedia of Paleoclimatology and Ancient Environments’, Springer Netherlands, Dordrecht, doi:10.1007/978-1-4020-4411-3_195 pp. 826–835.
- Olsen, P., Schlische, R. and Fedosh, M. (1996), ‘580 ky duration of the Early Jurassic flood basalt event in eastern North America estimated using Milankovitch cyclostratigraphy’, *Bulletin of the Museum of Northern Arizona* **60**, 11–22.
- Otto-Bliesner, B. L. (1993), ‘Tropical mountains and coal formation: A climate model study of the Westphalian (306 Ma)’, doi:10.1029/93GL02235 *Geophysical Research Letters* **20**(18), 1947–1950.
- Otto-Bliesner, B. L. (1998), Effects of tropical mountain elevations on the climate of the Late Carboniferous: Climate model simulations, in T. J. Crowley and K. Burke, eds, ‘Tectonic Boundary Conditions for Climate Reconstructions’, Oxford University Press, chapter 5, pp. 100–115.
- Pacanowski, R. and Griffies, S. (2000), ‘MOM 3.0 Manual’, *Geophysical Fluid Dynamics Laboratory* pp. 1–708.
- Pálfy, J., Demény, A., Haas, J., Carter, E. S., Görög, Á., Halász, D., Oravecz-Scheffer, A., Hetényi, M., Márton, E., Orchard, M. J., Ozsvárt, P., Vető, I. and Zajzon, N. (2007), ‘Triassic–Jurassic boundary events inferred from integrated stratigraphy of the Csóvár section, Hungary’, doi:10.1016/j.palaeo.2006.06.021 *Palaeogeography, Palaeoclimatology, Palaeoecology* **244**(1–4), 11–33.
- Pálfy, J. and Kocsis, A. (2014), Volcanism of the Central Atlantic magmatic province as the trigger of environmental and biotic changes around the Triassic–Jurassic boundary, in ‘Volcanism, Impacts, and Mass Extinctions: Causes and Effects’, Vol. 505, Geological Society of America, doi:10.1130/2014.2505(12) pp. 245–261.
- Paris, G., Donnadiou, Y., Beaumont, V., Fluteau, F. and Goddérés, Y. (2016), ‘Geochemical consequences of intense pulse-like degassing during the onset of the Central Atlantic Magmatic Province’, doi:10.1016/j.palaeo.2015.04.011 *Palaeogeography, Palaeoclimatology, Palaeoecology* **441**, 74–82.
- Park, J. and Oglesby, R. J. (1991), ‘Milankovitch rhythms in the Cretaceous: A GCM modelling study’, doi:10.1016/0921-8181(91)90001-D *Global and Planetary Change* **4**(4), 329–355.
- Parrish, J. T. (1993), ‘Climate of the Supercontinent Pangea’, doi:10.1086/648217 *The Journal of Geology* **101**(2), 215–233.
- Payne, J. L. and Van de Schootbrugge, B. (2007), Life in Triassic Oceans: Links Between Planktonic and Benthic Recovery and Radiation, in P. G. Falkowski and A. H. Knoll, eds, ‘Evolution of Primary Producers in the Sea’, Academic Press, Burlington, doi:10.1016/B978-012370518-1/50010-2 chapter 9, pp. 165–189.
- Peace, A. L., Phethean, J., Franke, D., Foulger, G., Schiffer, C., Welford, J., McHone, G., Rocchi, S., Schnabel, M. and Doré, A. (2020), ‘A review of Pangaea dispersal and Large Igneous Provinces – In search of a causative mechanism’, doi:10.1016/j.earscirev.2019.102902 *Earth-Science Reviews* **206**, 102902.
- Penn, J. L., Deutsch, C., Payne, J. L. and Sperling, E. A. (2018), ‘Temperature-dependent hypoxia explains biogeography and severity of end-Permian marine mass extinction’, doi:10.1126/science.aat1327 *Science* **362**(6419), eaat1327.
- Percival, L. M. E., Ruhl, M., Hesselbo, S. P., Jenkyns, H. C., Mather, T. A. and Whiteside, J. H. (2017), ‘Mercury evidence for pulsed volcanism during the end-Triassic mass extinction’, doi:10.1073/pnas.1705378114 *Proceedings of the National Academy of Sciences* **114**(30), 7929–7934.

- Percival, L. M. E., van Helmond, N. A. G. M., Selby, D., Goderis, S. and Claeys, P. (2020), ‘Complex Interactions Between Large Igneous Province Emplacement and Global-Temperature Changes During the Cenomanian-Turonian Oceanic Anoxic Event (OAE 2)’, doi:10.1029/2020PA004016 *Paleoceanography and Paleoclimatology* **35**(10), e2020PA004016.
- Percival, L. M., Jenkyns, H. C., Mather, T. A., Dickson, A. J., Batenburg, S. J., Ruhl, M., Hesselbo, S. P., Barclay, R., Jarvis, I., Robinson, S. A. and Woelders, L. (2018), ‘Does large igneous province volcanism always perturb the mercury cycle? comparing the records of oceanic anoxic event 2 and the end-cretaceous to other mesozoic events’, doi:10.2475/08.2018.01 *American Journal of Science* **318**(8), 799–860.
- Percival, L., Tedeschi, L., Creaser, R., Bottini, C., Erba, E., Giraud, F., Svensen, H., Savian, J., Trindade, R., Coccioni, R., Frontalini, F., Jovane, L., Mather, T. and Jenkyns, H. (2021), ‘Determining the style and provenance of magmatic activity during the Early Aptian Oceanic Anoxic Event (OAE 1a)’, doi:10.1016/j.gloplacha.2021.103461 *Global and Planetary Change* **200**, 103461.
- Percival, L., Witt, M., Mather, T., Hermoso, M., Jenkyns, H., Hesselbo, S., Al-Suwaidi, A., Storm, M., Xu, W. and Ruhl, M. (2015), ‘Globally enhanced mercury deposition during the end-Pliensbachian extinction and Toarcian OAE: A link to the Karoo–Ferrar Large Igneous Province’, doi:10.1016/j.epsl.2015.06.064 *Earth and Planetary Science Letters* **428**, 267–280.
- Petoukhov, V., Ganopolski, A., Brovkin, V., Claussen, M., Eliseev, A., Kubatzki, C. and Rahmstorf, S. (2000), ‘CLIMBER-2: a climate system model of intermediate complexity. Part I: model description and performance for present climate’, doi:10.1007/PL00007919 *Climate Dynamics* **16**(1), 1–17.
- Poulsen, C. J., Pollard, D. and White, T. S. (2007), ‘General circulation model simulation of the $\delta^{18}\text{O}$ content of continental precipitation in the middle Cretaceous: A model-proxy comparison’, doi:10.1130/G23343A.1 *Geology* **35**(3), 199–202.
- Poulsen, C. J. and Zhou, J. (2013), ‘Sensitivity of Arctic Climate Variability to Mean State: Insights from the Cretaceous’, doi:10.1175/JCLI-D-12-00825.1 *Journal of Climate* **26**(18), 7003 – 7022.
- Price, G. D. (1999), ‘The evidence and implications of polar ice during the Mesozoic’, doi:10.1016/S0012-8252(99)00048-3 *Earth-Science Reviews* **48**(3), 183 – 210.
- Price, G. D. (2009), Mesozoic climates, in V. Gornitz, ed., ‘Encyclopedia of Paleoclimatology and Ancient Environments’, Springer Netherlands, doi:10.1007/978-1-4020-4411-3_138 pp. 554–559.
- Rampino, M. R. and Self, S. (2015), Large Igneous Provinces and Biotic Extinctions, in H. Sigurdsson, ed., ‘The Encyclopedia of Volcanoes’, second edn, Academic Press, Amsterdam, doi:10.1016/B978-0-12-385938-9.00061-4 chapter 61, pp. 1049–1058.
- Raup, D. M. and Sepkoski, J. J. (1982), ‘Mass Extinctions in the Marine Fossil Record’, doi:10.1126/science.215.4539.1501 *Science* **215**(4539), 1501–1503.
- Reddin, C. J., Kocsis, Á. T. and Kiessling, W. (2018), ‘Marine invertebrate migrations trace climate change over 450 million years’, doi:10.1111/geb.12732 *Global Ecology and Biogeography* **27**(6), 704–713.
- Reddin, C. J., Kocsis, Á. T. and Kiessling, W. (2018b), ‘Climate change and the latitudinal selectivity of ancient marine extinctions’, doi:10.1017/pab.2018.34 *Paleobiology* **45**(1), 70–84.
- Rees, P. M., Noto, C. R., Parrish, J. M. and Parrish, J. T. (2004), ‘Late Jurassic Climates, Vegetation, and Dinosaur Distributions’, doi:10.1086/424577 *The Journal of Geology* **112**(6), 643–653.
- Ridgwell, A. (2005), ‘A Mid Mesozoic Revolution in the regulation of ocean chemistry’, doi:10.1016/j.margeo.2004.10.036 *Marine Geology* **217**(3), 339–357.
- Ridgwell, A. and Zeebe, R. (2005), ‘The role of the global carbonate cycle in the regulation and evolution of the Earth system’, doi:10.1016/j.epsl.2005.03.006 *Earth and Planetary Science Letters* **234**(3-4), 299–315.
- Robinson, S. A., Ruhl, M., Astley, D. L., Naafs, B. D. A., Farnsworth, A. J., Bown, P. R., Jenkyns, H. C., Lunt, D. J., O’Brien, C., Pancost, R. D. and Markwick, P. J. (2017), ‘Early Jurassic North Atlantic sea-surface temperatures from TEX86 palaeothermometry’, doi:10.1111/sed.12321 *Sedimentology* **64**(1), 215–230.
- Robock, A. (2000), ‘Volcanic eruptions and climate’, doi:10.1029/1998RG000054 *Reviews of Geophysics* **38**(2), 191–219.
- Robock, A., Ammann, C. M., Oman, L., Shindell, D., Levis, S. and Stenchikov, G. (2009), ‘Did the toba volcanic eruption of ~74 ka b.p. produce widespread glaciation?’, doi:10.1029/2008JD011652 *Journal of Geophysical Research: Atmospheres* **114**(D10).
- Rossignol-Strick, M. (1985), ‘Mediterranean Quaternary sapropels, an immediate response of the African monsoon to variation of insolation’, doi:10.1016/0031-0182(85)90056-2 *Palaeogeography, Palaeoclimatology, Palaeoecology* **49**(3), 237–263.

- Rothman, D. H. (2017), ‘Thresholds of catastrophe in the Earth system’, doi:10.1126/sciadv.1700906 *Science Advances* **3**(9), e1700906.
- Royer, Berner, R., Montañez, I., Tabor, N. and Beerling, D. (2004), ‘CO₂ as a primary driver of Phanerozoic climate’, doi:10.1130/1052-5173(2004)014<0004:CAAPDO>2.0.CO;2. *GSA Today* **14**, 3–7.
- Royer, D. L., Donnadieu, Y., Park, J., Kowalczyk, J. and Godd eris, Y. (2014), ‘Error analysis of CO₂ and O₂ estimates from the long-term geochemical model GEOCARBSULF’, doi:10.2475/09.2014.01 *American Journal of Science* **314**(9), 1259–1283.
- Ruddiman, W. R. (2014), *Earth’s Climate: Past and Future*, 3rd edn, W. H. Freeman and Company.
- Ruebsam, W. and Schwark, L. (2021), ‘Impact of a northern-hemispherical cryosphere on late Pliensbachian–early Toarcian climate and environment evolution’, doi:10.1144/SP514-2021-11 *Geological Society, London, Special Publications* **514**(1), 359–385.
- Ruhl, M., Bonis, N. R., Reichart, G.-J., Damste, J. S. S. and K urschner, W. M. (2011), ‘Atmospheric Carbon Injection Linked to End-Triassic Mass Extinction’, doi:10.1126/science.1204255 *Science* **333**(6041), 430–434.
- Ruhl, M., Deenen, M., Abels, H., Bonis, N., Krijgsman, W. and K urschner, W. (2010), ‘Astronomical constraints on the duration of the early Jurassic Hettangian stage and recovery rates following the end-Triassic mass extinction (St Audrie’s Bay/East Quantoxhead, UK)’, doi:10.1016/j.epsl.2010.04.008 *Earth and Planetary Science Letters* **295**(1-2), 262–276.
- Ruhl, M., Hesselbo, S. P., Hinnov, L., Jenkyns, H. C., Xu, W., Riding, J. B., Storm, M., Minisini, D., Ullmann, C. V. and Leng, M. J. (2016), ‘Astronomical constraints on the duration of the Early Jurassic Pliensbachian Stage and global climatic fluctuations’, doi:10.1016/j.epsl.2016.08.038 *Earth and Planetary Science Letters* **455**, 149–165.
- Sageman, B. (2009), Ocean Anoxic Events, in V. Gornitz, ed., ‘Encyclopedia of Paleoclimatology and Ancient Environments’, Springer Netherlands, Dordrecht, doi:10.1007/978-1-4020-4411-3_155 pp. 626–629.
- Sames, B., Wagemreich, M., Conrad, C. P. and Iqbal, S. (2020), ‘Aquifer-eustasy as the main driver of short-term sea-level fluctuations during Cretaceous hothouse climate phases’, doi:10.1144/SP498-2019-105 *Geological Society, London, Special Publications* **498**(1), 9–38.
- Sames, B., Wagemreich, M., Wendler, J., Haq, B., Conrad, C., Melinte-Dobrinescu, M., Hu, X., Wendler, I., Wolfgring, E., Yilmaz, I. and Zorina, S. (2016), ‘Review: Short-term sea-level changes in a greenhouse world — A view from the Cretaceous’, doi:10.1016/j.palaeo.2015.10.045 *Palaeogeography, Palaeoclimatology, Palaeoecology* **441**, 393 – 411.
- Schaller, M. F., Wright, J. D. and Kent, D. V. (2011), ‘Atmospheric pCO₂ perturbations associated with the Central Atlantic Magmatic Province’, doi:10.1126/science.1199011 *Science* **331**(6023), 1404–1409.
- Schaller, M. F., Wright, J. D. and Kent, D. V. (2015), ‘A 30 Myr record of Late Triassic atmospheric pCO₂ variation reflects a fundamental control of the carbon cycle by changes in continental weathering’, doi:10.1130/B31107.1 *GSA Bulletin* **127**(5-6), 661–671.
- Schaller, M. F., Wright, J. D., Kent, D. V. and Olsen, P. E. (2012), ‘Rapid emplacement of the Central Atlantic Magmatic Province as a net sink for CO₂’, doi:10.1016/j.epsl.2011.12.028 *Earth and Planetary Science Letters* **323-324**, 27–39.
- Schlesinger, W. H. and Bernhardt, E. S. (2020), *Biogeochemistry*, 4th edn, doi:10.1016/B978-0-12-814608-8.09992-8 Academic Press.
- Schmidt, A., Mills, M. J., Ghan, S., Gregory, J. M., Allan, R. P., Andrews, T., Bardeen, C. G., Conley, A., Forster, P. M., Gettelman, A., Portmann, R. W., Solomon, S. and Toon, O. B. (2018), ‘Volcanic radiative forcing from 1979 to 2015’, doi:10.1029/2018JD028776 *Journal of Geophysical Research: Atmospheres* **123**(22), 12491–12508.
- Schmidt, A., Skeffington, R. A., Thordarson, T., Self, S., Forster, P. M., Rap, A., Ridgwell, A., Fowler, D., Wilson, M., Mann, G. W., Wignall, P. B. and Carslaw, K. S. (2016), ‘Selective environmental stress from sulphur emitted by continental flood basalt eruptions’, doi:10.1038/ngeo2588 *Nature Geoscience* **9**(1), 77–82.
- Schobben, M., Gravendyck, J., Mangels, F., Struck, U., Bussert, R., K urschner, W. M., Korn, D., Sander, P. M. and Aberhan, M. (2019), ‘A comparative study of total organic carbon- $\delta^{13}\text{C}$ signatures in the Triassic-Jurassic transitional beds of the Central European Basin and western Tethys shelf seas’, doi:10.1127/nos/2019/0499 *Newsletters on Stratigraphy* **52**(4), 461–486.
- Schoene, B., Guex, J., Bartolini, A., Schaltegger, U. and Blackburn, T. J. (2010), ‘Correlating the end-Triassic mass extinction and flood basalt volcanism at the 100 ka level’, doi:10.1130/G30683.1 *Geology* **38**(5), 387–390.

- Schulte, P., Alegret, L., Arenillas, I., Arz, J. A., Barton, P. J., Bown, P. R., Bralower, T. J., Christeson, G. L., Claeys, P., Cockell, C. S., Collins, G. S., Deutsch, A., Goldin, T. J., Goto, K., Grajales-Nishimura, J. M., Grieve, R. A. F., Gulick, S. P. S., Johnson, K. R., Kiessling, W., Koeberl, C., Kring, D. A., MacLeod, K. G., Matsui, T., Melosh, J., Montanari, A., Morgan, J. V., Neal, C. R., Nichols, D. J., Norris, R. D., Pierazzo, E., Ravizza, G., Rebolledo-Vieyra, M., Reimold, W. U., Robin, E., Salge, T., Speijer, R. P., Sweet, A. R., Urrutia-Fucugauchi, J., Vajda, V., Whalen, M. T. and Willumsen, P. S. (2010), ‘The Chicxulub Asteroid Impact and Mass Extinction at the Cretaceous-Paleogene Boundary’, doi:10.1126/science.1177265 *Science* **327**(5970), 1214–1218.
- Scotese, C. R. (2014), ‘Atlas of Middle and Late Permian and Triassic Paleogeographic Maps’, doi:10.13140/2.1.2609.9209 PALEOMAP Project PaleoAtlas for ArcGIS.
- Scotese, C. R. (2021), ‘An Atlas of Phanerozoic Paleogeographic Maps: The Seas Come In and the Seas Go Out’, doi:10.1146/annurev-earth-081320-064052 *Annual Review of Earth and Planetary Sciences* **49**(1), 679–728.
- Scotese, C. R., Song, H., Mills, B. J. and van der Meer, D. G. (2021), ‘Phanerozoic paleotemperatures: The earth’s changing climate during the last 540 million years’, doi:10.1016/j.earscirev.2021.103503 *Earth-Science Reviews* **215**, 103503.
- Scotese, C. R. and Wright, N. (2018), ‘PALEOMAP paleodigital elevation models (PaleoDEMS) for the Phanerozoic’. <https://www.earthbyte.org/paleodem-resource-scotese-and-wright-2018>
- Self, S., Schmidt, A. and Mather, T. (2014), ‘Emplacement characteristics, time scales, and volcanic gas release rates of continental flood basalt eruptions on Earth’, doi:10.1130/2014.2505(16) *Geological Society of America Special Papers* **505**, 1–20.
- Self, S., Thordarson, T. and Widdowson, M. (2005), ‘Gas Fluxes from Flood Basalt Eruptions’, doi:10.2113/gselements.1.5.283 *Elements* **1**(5), 283–287.
- Self, S., Widdowson, M., Thordarson, T. and Jay, A. E. (2006), ‘Volatile fluxes during flood basalt eruptions and potential effects on the global environment: A deccan perspective’, doi:10.1016/j.epsl.2006.05.041 *Earth and Planetary Science Letters* **248**(1-2), 518–532.
- Sellwood, B. W., Price, G. D., Shackleton, N. J., Francis, J., Allen, J. R. L., Hoskins, B. J., Sellwood, B. W., Spicer, R. A. and Valdes, P. J. (1993), ‘Sedimentary facies as indicators of Mesozoic palaeoclimate’, doi:10.1098/rstb.1993.0107 *Philosophical Transactions of the Royal Society of London. Series B: Biological Sciences* **341**(1297), 225–233.
- Sellwood, B. W. and Valdes, P. J. (2006), ‘Mesozoic climates: General circulation models and the rock record’, doi:10.1016/j.sedgeo.2006.05.013 *Sedimentary Geology* **190**(1), 269 – 287.
- Sellwood, B. W. and Valdes, P. J. (2008), ‘Jurassic climates’, doi:10.1016/S0016-7878(59)80068-7 *Proceedings of the Geologists’ Association* **119**(1), 5 – 17.
- Sellwood, B. W., Valdes, P. J. and Price, G. D. (2000), ‘Geological evaluation of multiple general circulation model simulations of Late Jurassic palaeoclimate’, doi:10.1016/S0031-0182(99)00138-8 *Palaeogeography, Palaeoclimatology, Palaeoecology* **156**(1), 147–160.
- Sepkoski, J. J. (1981), ‘A factor analytic description of the Phanerozoic marine fossil record’, doi:10.1017/S0094837300003778 *Paleobiology* **7**(1), 36–53.
- Sepkoski, J. J. (1984), ‘A kinetic model of Phanerozoic taxonomic diversity. III. Post-Paleozoic families and mass extinctions’, doi:10.1017/S0094837300008186 *Paleobiology* **10**(2), 246–267.
- Sepulchre, P., Schuster, M., Ramstein, G., Krinnezr, G., Girard, J.-F., Vignaud, P. and Brunet, M. (2008), ‘Evolution of Lake Chad Basin hydrology during the mid-Holocene: A preliminary approach from lake to climate modelling’, doi:10.1016/j.gloplacha.2007.08.010 *Global and Planetary Change* **61**(1), 41–48.
- Seton, M., Gaina, C., Müller, R. and Heine, C. (2009), ‘Mid-Cretaceous seafloor spreading pulse: Fact or fiction?’, doi:10.1130/G25624A.1 *Geology* **37**(8), 687–690.
- Sha, J., Olsen, P. E., Pan, Y., Xu, D., Wang, Y., Zhang, X., Yao, X. and Vajda, V. (2015), ‘Triassic–Jurassic climate in continental high-latitude Asia was dominated by obliquity-paced variations (Junggar Basin, Ürümqi, China)’, doi:10.1073/pnas.1501137112 *Proceedings of the National Academy of Sciences* **112**(12), 3624–3629.
- Six, K. D. and Maier-Reimer, E. (1996), ‘Effects of plankton dynamics on seasonal carbon fluxes in an ocean general circulation model’, doi:10.1029/96GB02561 *Global Biogeochemical Cycles* **10**(4), 559–583.
- Skonieczny, C., McGee, D., Winckler, G., Bory, A., Bradtmiller, L. I., Kinsley, C. W., Polissar, P. J., Pol-Holz, R. D., Rossignol, L. and Malaizé, B. (2019), ‘Monsoon-driven Saharan dust variability over the past 240,000 years’, doi:10.1126/sciadv.aav1887 *Science Advances* **5**(1), eaav1887.
- Smoot, J. P. (1991), ‘Sedimentary facies and depositional environments of early Mesozoic Newark Super-group basins, eastern North America’, doi:10.1016/0031-0182(91)90055-V *Palaeogeography, Palaeoclimatology, Palaeoecology* **84**(1), 369–423.

- Smoot, J. P. and Olsen, P. E. (1994), Climatic Cycles as Sedimentary Controls of Rift-Basin Lacustrine Deposits in the Early Mesozoic Newark Basin Based on Continuous Core, *in* 'Lacustrine Reservoirs and Depositional Systems', doi:10.2110/cor.94.01.0201 SEPM Society for Sedimentary Geology.
- Song, H., Kemp, D. B., Tian, L., Chu, D., Song, H. and Dai, X. (2021), 'Thresholds of temperature change for mass extinctions', doi:10.1038/s41467-021-25019-2 *Nature Communications* **12**(1).
- Song, H., Wignall, P. B., Song, H., Dai, X. and Chu, D. (2019), 'Seawater Temperature and Dissolved Oxygen over the Past 500 Million Years', doi:10.1007/s12583-018-1002-2 *Journal of Earth Science* **30**(2), 236–243.
- Spicer, R., Valdes, P., Hughes, A., Yang, J., Spicer, T., Herman, A. and Farnsworth, A. (2020), 'New insights into the thermal regime and hydrodynamics of the early Late Cretaceous Arctic', doi:10.1017/S0016756819000463 *Geological Magazine* **157**(10), 1729–1746.
- Stanley, S. M. and Luczaj, J. A. (2015), *Earth System History*, 4th edn, Freeman/Macmillan Higher Education, New York, NY.
- Steinig, S., Dummann, W., Park, W., Latif, M., Kusch, S., Hofmann, P. and Flögel, S. (2020), 'Evidence for a regional warm bias in the Early Cretaceous TEX86 record', doi:10.1016/j.epsl.2020.116184 *Earth and Planetary Science Letters* **539**, 116184.
- Steinthorsdottir, M., Elliott-Kingston, C. and Bacon, K. L. (2017), 'Cuticle surfaces of fossil plants as a potential proxy for volcanic SO₂ emissions: observations from the Triassic–Jurassic transition of East Greenland', doi:10.1007/s12549-017-0297-9 *Palaeobiodiversity and Palaeoenvironments* **98**(1), 49–69.
- Steinthorsdottir, M., Jeram, A. J. and McElwain, J. C. (2011), 'Extremely elevated CO₂ concentrations at the Triassic/Jurassic boundary', doi:10.1016/j.palaeo.2011.05.050 *Palaeogeography, Palaeoclimatology, Palaeoecology* **308**(3-4), 418–432.
- Stocker, T., Qin, D., Plattner, G., Tignor, M., Allen, S., Boschung, J., Nauels, A., Xia, Y., Bex, V. and Midgley, P. (2014), doi:10.1017/cbo9781107415324 'Climate Change 2013: The Physical Science Basis. Contribution of Working Group I to the Fifth Assessment Report of IPCC the Intergovernmental Panel on Climate Change.'
- Suarez, C. A., Edmonds, M. and Jones, A. P. (2019), 'Earth Catastrophes and their Impact on the Carbon Cycle', doi:10.2138/gselements.15.5.301 *Elements* **15**(5), 301–306.
- Suchéras-Marx, B., Mattioli, E., Allemand, P., Giraud, F., Pittet, B., Plancq, J. and Escarguel, G. (2019), 'The colonization of the oceans by calcifying pelagic algae', doi:10.5194/bg-16-2501-2019 *Biogeosciences* **16**(12), 2501–2510.
- Sun, Y., Joachimski, M. M., Wignall, P. B., Yan, C., Chen, Y., Jiang, H., Wang, L. and Lai, X. (2012), 'Lethally Hot Temperatures During the Early Triassic Greenhouse', doi:10.1126/science.1224126 *Science* **338**(6105), 366–370.
- Svensen, H. H., Torsvik, T. H., Callegaro, S., Augland, L., Heimdal, T. H., Jerram, D. A., Planke, S. and Pereira, E. (2017), 'Gondwana Large Igneous Provinces: plate reconstructions, volcanic basins and sill volumes', doi:10.1144/sp463.7 *Geological Society, London, Special Publications* p. SP463.7.
- Svensen, H., Planke, S., Chevallier, L., Malthes-Sørenssen, A., Corfu, F. and Jamtveit, B. (2007), 'Hydrothermal venting of greenhouse gases triggering Early Jurassic global warming', doi:10.1016/j.epsl.2007.02.013 *Earth and Planetary Science Letters* **256**(3-4), 554–566.
- Svensen, H., Planke, S., Polozov, A. G., Schmidbauer, N., Corfu, F., Podladchikov, Y. Y. and Jamtveit, B. (2009), 'Siberian gas venting and the end-Permian environmental crisis', doi:10.1016/j.epsl.2008.11.015 *Earth and Planetary Science Letters* **277**(3-4), 490–500.
- Tabor, C. R., Bardeen, C. G., Otto-Bliesner, B. L., Garcia, R. R. and Toon, O. B. (2020), 'Causes and Climatic Consequences of the Impact Winter at the Cretaceous-Paleogene Boundary', doi:https://doi.org/10.1029/2019GL085572 *Geophysical Research Letters* **47**(3), e60121.
- Tabor, C. R., Poulsen, C. J., Lunt, D. J., Rosenbloom, N. A., Otto-Bliesner, B. L., Markwick, P. J., Brady, E. C., Farnsworth, A. and Feng, R. (2016), 'The cause of Late Cretaceous cooling: A multimodel-proxy comparison', doi:10.1130/G38363.1 *Geology* **44**(11), 963–966.
- Takashima, R., Nishi, H., Huber, B. and Leckie, R. (2006), 'Greenhouse world and the Mesozoic ocean', doi:10.5670/oceanog.2006.07 *Oceanography* **19**(SPL.ISS. 4), 82–92.
- Tang, C. M. (2022), 'Mesozoic era', Encyclopaedia Britannica. Accessed February 10, 2022. <https://www.britannica.com/science/Mesozoic-Era>
- Thibault, N. and Husson, D. (2016), 'Climatic fluctuations and sea-surface water circulation patterns at the end of the Cretaceous era: Calcareous nannofossil evidence', *Palaeogeography, Palaeoclimatology, Palaeoecology* **441**, 152–164. doi:10.1016/j.palaeo.2015.07.049 Impact, Volcanism, Global changes and Mass Extinctions.

- Thibodeau, A. M., Ritterbush, K., Yager, J. A., West, A. J., Ibarra, Y., Bottjer, D. J., Berelson, W. M., Bergquist, B. A. and Corsetti, F. A. (2016), ‘Mercury anomalies and the timing of biotic recovery following the end-Triassic mass extinction’, doi:10.1038/ncomms11147 *Nature Communications* **7**, 11147.
- Tierney, J. E., Poulsen, C. J., Montañez, I. P., Bhattacharya, T., Feng, R., Ford, H. L., Hönisch, B., Inglis, G. N., Petersen, S. V., Sahoo, N., Tabor, C. R., Thirumalai, K., Zhu, J., Burls, N. J., Foster, G. L., Goddérís, Y., Huber, B. T., Ivany, L. C., Turner, S. K., Lunt, D. J., McElwain, J. C., Mills, B. J. W., Otto-Bliesner, B. L., Ridgwell, A. and Zhang, Y. G. (2020), ‘Past climates inform our future’, doi:10.1126/science.aay3701 *Science* **370**(6517), eaay3701.
- Tigchelaar, M., Timmermann, A., Friedrich, T., Heinemann, M. and Pollard, D. (2019), ‘Nonlinear response of the Antarctic Ice Sheet to late Quaternary sea level and climate forcing’, doi:10.5194/tc-13-2615-2019 *The Cryosphere* **13**(10), 2615–2631.
- Tigchelaar, M., Timmermann, A., Pollard, D., Friedrich, T. and Heinemann, M. (2018), ‘Local insolation changes enhance Antarctic interglacials: Insights from an 800,000-year ice sheet simulation with transient climate forcing’, doi:10.1016/j.epsl.2018.05.004 *Earth and Planetary Science Letters* **495**, 69–78.
- Timm, O. and Timmermann, A. (2007), ‘Simulation of the Last 21 000 Years Using Accelerated Transient Boundary Conditions’, doi:10.1175/JCLI4237.1 *Journal of Climate* **20**(17), 4377 – 4401.
- Timmermann, A., Lorenz, S. J., An, S.-I., Clement, A. and Xie, S.-P. (2007), ‘The Effect of Orbital Forcing on the Mean Climate and Variability of the Tropical Pacific’, doi:10.1175/JCLI4240.1 *Journal of Climate* **20**(16), 4147 – 4159.
- Tobin, T. S., Bitz, C. M. and Archer, D. (2017), ‘Modeling climatic effects of carbon dioxide emissions from Deccan Traps volcanic eruptions around the Cretaceous–Paleogene boundary’, doi:10.1016/j.palaeo.2016.05.028 *Palaeogeography, Palaeoclimatology, Palaeoecology* **478**, 139–148.
- Toohey, M., Stevens, B., Schmidt, H. and Timmreck, C. (2016), ‘Easy Volcanic Aerosol (EVA v1.0): an idealized forcing generator for climate simulations’, doi:10.5194/gmd-9-4049-2016 *Geoscientific Model Development* **9**(11), 4049–4070.
- Torsvik, T. H. and Cocks, L. R. M. (2016), *Earth History and Palaeogeography*, doi:10.1017/9781316225523 Cambridge University Press.
- Torsvik, T. H. and Cocks, L. R. M. (2017), ‘The integration of palaeomagnetism, the geological record and mantle tomography in the location of ancient continents’, doi:10.1017/S001675681700098X *Geological Magazine* **156**(2), 242–260.
- Torsvik, T. H., Domeier, M. and Cocks, L. R. M. (2021), Phanerozoic paleogeography and Pangea, in L. J. Pesonen, J. Salminen, S. Åke Elming, D. A. Evans and T. Veikkolainen, eds, ‘Ancient Supercontinents and the Paleogeography of Earth’, Elsevier, doi:10.1016/B978-0-12-818533-9.00003-5 chapter 18, pp. 577–603.
- Torsvik, T. H., Svensen, H. H., Steinberger, B., Royer, D. L., Jerram, D. A., Jones, M. T. and Domeier, M. (2021b), *Connecting the Deep Earth and the Atmosphere*, American Geophysical Union (AGU), doi:10.1002/9781119528609.ch16 chapter 16, pp. 413–453.
- Trauth, M. H., Asrat, A., Cohen, A. S., Duesing, W., Foerster, V., Kaboth-Bahr, S., Kraemer, K. H., Lamb, H. F., Marwan, N., Maslin, M. A. and Schäbitz, F. (2021), ‘Recurring types of variability and transitions in the ~620 kyr record of climate change from the Chew Bahir basin, southern Ethiopia’, doi:10.1016/j.quascirev.2020.106777 *Quaternary Science Reviews* **266**, 106777.
- Trauth, M. H., Bergner, A. G., Foerster, V., Junginger, A., Maslin, M. A. and Schaebitz, F. (2015), ‘Episodes of environmental stability versus instability in Late Cenozoic lake records of Eastern Africa’, doi:10.1016/j.jhevol.2015.03.011 *Journal of Human Evolution* **87**, 21–31.
- Trauth, M. H., Deino, A. L., Bergner, A. G. and Strecker, M. R. (2003), ‘East African climate change and orbital forcing during the last 175 kyr BP’, doi:10.1016/S0012-821X(02)01105-6 *Earth and Planetary Science Letters* **206**(3), 297–313.
- Trauth, M. H., Deino, A. and Strecker, M. R. (2001), ‘Response of the East African climate to orbital forcing during the last interglacial (130–117 ka) and the early last glacial (117–60 ka)’, doi:10.1130/0091-7613(2001)029<0499:ROTEAC>2.0.CO;2 *Geology* **29**(6), 499–502.
- Trauth, M. H., Maslin, M. A., Deino, A. L., Junginger, A., Lesoloyia, M., Odada, E. O., Olago, D. O., Olaka, L. A., Strecker, M. R. and Tiedemann, R. (2010), ‘Human evolution in a variable environment: the amplifier lakes of Eastern Africa’, doi:10.1016/j.quascirev.2010.07.007 *Quaternary Science Reviews* **29**(23), 2981–2988.
- Trotter, J. A., Williams, I. S., Nicora, A., Mazza, M. and Rigo, M. (2015), ‘Long-term cycles of Triassic climate change: a new $\delta^{18}\text{O}$ record from conodont apatite’, doi:10.1016/j.epsl.2015.01.038 *Earth and Planetary Science Letters* **415**, 165–174.

- Tuenter, E., Weber, S., Hilgen, F. and Lourens, L. (2003), ‘The response of the African summer monsoon to remote and local forcing due to precession and obliquity’, doi:10.1016/S0921-8181(02)00196-0 *Global and Planetary Change* **36**(4), 219–235.
- Upchurch, G. R., Kiehl, J., Shields, C., Scherer, J. and Scotese, C. R. (2015), ‘Latitudinal temperature gradients and high-latitude temperatures during the latest Cretaceous: Congruence of geologic data and climate models’, doi:10.1130/G36802.1 *Geology* **43**(8), 683–686.
- Valdes, P. J. and Glover, R. W. (1999), ‘Modelling the climate response to orbital forcing’, doi:10.1098/rsta.1999.0405 *Philosophical Transactions of the Royal Society of London. Series A: Mathematical, Physical and Engineering Sciences* **357**(1757), 1873–1890.
- Valdes, P. J., Scotese, C. R. and Lunt, D. J. (2021), ‘Deep ocean temperatures through time’, doi:10.5194/cp-17-1483-2021 *Climate of the Past* **17**(4), 1483–1506.
- Valdes, P. J. and Sellwood, B. W. (1992), ‘A palaeoclimate model for the Kimmeridgian’, doi:10.1016/0031-0182(92)90165-2 *Palaeogeography, Palaeoclimatology, Palaeoecology* **95**(1), 47 – 72.
- Valdes, P. J., Sellwood, B. W. and Price, G. D. (1995), ‘Modelling Late Jurassic Milankovitch climate variations’, doi:10.1144/GSL.SP.1995.085.01.07 *Geological Society, London, Special Publications* **85**(1), 115–132.
- van de Schootbrugge, B., Bachan, A., Suan, G., Richoz, S. and Payne, J. L. (2013), ‘Microbes, mud and methane: cause and consequence of recurrent Early Jurassic anoxia following the end-Triassic mass extinction’, doi:10.1111/pala.12034 *Palaeontology* **56**(4), 685–709.
- van de Schootbrugge, B., Quan, T. M., Lindström, S., Püttmann, W., Heunisch, C., Pross, J., Fiebig, J., Petschick, R., Röhling, H.-G., Richoz, S., Rosenthal, Y. and Falkowski, P. G. (2009), ‘Floral changes across the Triassic/Jurassic boundary linked to flood basalt volcanism’, doi:10.1038/ngeo577 *Nature Geoscience* **2**(8), 589–594.
- van de Schootbrugge, B., Tremolada, F., Rosenthal, Y., Bailey, T., Feist-Burkhardt, S., Brinkhuis, H., Pross, J., Kent, D. and Falkowski, P. (2007), ‘End-Triassic calcification crisis and blooms of organic-walled ‘disaster species’’, doi:10.1016/j.palaeo.2006.06.026 *Palaeogeography, Palaeoclimatology, Palaeoecology* **244**(1-4), 126–141.
- van de Schootbrugge, B. and Wignall, P. B. (2015), ‘A tale of two extinctions: converging end-Permian and end-Triassic scenarios’, doi:10.1017/s0016756815000643 *Geological Magazine* **153**(02), 332–354.
- van der Kooi, C. J. and Ollerton, J. (2020), ‘The origins of flowering plants and pollinators’, doi:10.1126/science.aay3662 *Science* **368**(6497), 1306–1308.
- Veizer, J. and Prokoph, A. (2015), ‘Temperatures and oxygen isotopic composition of Phanerozoic oceans’, doi:10.1016/j.earscirev.2015.03.008 *Earth-Science Reviews* **146**, 92–104.
- Verschuren, D., Damste, J. S. S., Moernaut, J., Kristen, I., Blaauw, M., Fagot, M., Haug, G. H. and Members, C. P. (2009), ‘Half-precessional dynamics of monsoon rainfall near the East African Equator’, doi:10.1038/nature08520 *Nature* **462**(7273), 637–641.
- Vickers, M. L., Price, G. D., Jerrett, R. M., Sutton, P., Watkinson, M. P. and FitzPatrick, M. (2019), ‘The duration and magnitude of Cretaceous cool events: Evidence from the northern high latitudes’, doi:10.1130/B35074.1 *GSA Bulletin* **131**(11-12), 1979–1994.
- Vinós, J. (2019), doi:10.6084/m9.figshare.7836935.v1 ‘Phanerozoic temperature-CO₂’. [https://figshare.com/articles/figure/Phanerozoic_temperature-CO₂_pdf/7836935](https://figshare.com/articles/figure/Phanerozoic_temperature-CO2_pdf/7836935)
- Vollmer, T., Werner, R., Weber, M., Tougiannidis, N., Röhling, H.-G. and Hambach, U. (2008), ‘Orbital control on Upper Triassic Playa cycles of the Steinmergel-Keuper (Norian): A new concept for ancient playa cycles’, doi:10.1016/j.palaeo.2007.12.017 *Palaeogeography, Palaeoclimatology, Palaeoecology* **267**(1), 1–16.
- Wagreich, M., Lein, R. and Sames, B. (2014), ‘Eustasy, its controlling factors, and the limno-eustatic hypothesis—concepts inspired by eduard suess’, *Austrian Journal of Earth Sciences* **107**, 115–131. https://www.ajes.at/images/AJES/archive/Band%20107_1/wagreich_et_al_ajes_107_1.pdf
- Waltham, D. (2015), ‘Milankovitch Period Uncertainties and Their Impact On Cyclostratigraphy’, doi:10.2110/jsr.2015.66 *Journal of Sedimentary Research* **85**(8), 990–998.
- Wang, M., Li, M., Kemp, D. B., Boulila, S. and Ogg, J. G. (2022), ‘Sedimentary noise modeling of lake-level change in the late triassic newark basin of north america’, doi:10.1016/j.gloplacha.2021.103706 *Global and Planetary Change* **208**, 103706.
- Wang, P. X., Wang, B., Cheng, H., Fasullo, J., Guo, Z. T., Kiefer, T. and Liu, Z. Y. (2014), ‘The global monsoon across timescales: coherent variability of regional monsoons’, doi:10.5194/cp-10-2007-2014 *Climate of the Past* **10**(6), 2007–2052.

- Weber, S. and Tuenter, E. (2011), ‘The impact of varying ice sheets and greenhouse gases on the intensity and timing of boreal summer monsoons’, doi:10.1016/j.quascirev.2010.12.009 *Quaternary Science Reviews* **30**(3), 469–479.
- Wendler, J. E., Wendler, I., Vogt, C. and Kuss, J. (2016), ‘Link between cyclic eustatic sea-level change and continental weathering: Evidence for aquifer-eustasy in the Cretaceous’, *Palaeogeography, Palaeoclimatology, Palaeoecology* **441**, 430 – 437.
- White, J. D. L., Bryan, S. E., Ross, P.-S., Self, S. and Thordarson, T. (2009), Physical volcanology of continental large igneous provinces: update and review, in ‘Studies in Volcanology: The Legacy of George Walker’, doi:10.1144/IAVCEI002.15 Geological Society of London.
- Whiteside, J. H., Grogan, D. S., Olsen, P. E. and Kent, D. V. (2011a), ‘Climatically driven biogeographic provinces of Late Triassic tropical Pangea’, doi:10.1073/pnas.1102473108 *Proceedings of the National Academy of Sciences* **108**(22), 8972–8977.
- Whiteside, J. H., Olsen, P. E., Eglinton, T., Brookfield, M. E. and Sambrotto, R. N. (2010), ‘Compound-specific carbon isotopes from Earth’s largest flood basalt eruptions directly linked to the end-Triassic mass extinction’, doi:10.1073/pnas.1001706107 *Proceedings of the National Academy of Sciences* **107**(15), 6721–6725.
- Whiteside, J. H., Olsen, P. E., Eglinton, T. I., Cornet, B., McDonald, N. G. and Huber, P. (2011b), ‘Pangean great lake paleoecology on the cusp of the end-Triassic extinction’, doi:10.1016/j.palaeo.2010.11.025 *Palaeogeography, Palaeoclimatology, Palaeoecology* **301**(1), 1–17.
- Whiteside, J. H., Olsen, P. E., Kent, D. V., Fowell, S. J. and Et-Touhami, M. (2007), ‘Synchrony between the Central Atlantic magmatic province and the Triassic-Jurassic mass-extinction event?’, doi:10.1016/j.palaeo.2006.06.035 *Palaeogeography, Palaeoclimatology, Palaeoecology* **244**(1-4), 345–367.
- Whiteside, J., Schaller, M., Olsen, P., Margulis-Ohnuma, M. and Yager, J. (2021), ‘An Overture to the Anthropocene: Isotopic Evidence of Strong CO₂ Modulation of the Tropical Monsoon at the Dawn of Dinosaurs’, doi:10.3997/2214-4609.202134243 *Conference Proceedings, 30th International Meeting on Organic Geochemistry (IMOG 2021)* **2021**(1), 1–2.
- Wicander, R. and Monore, J. (2010), *Historical Geology - Evolution of Earth and Life Through Time*.
- Willeit, M. and Ganopolski, A. (2016), ‘Paladyn v1.0, a comprehensive land surface–vegetation–carbon cycle model of intermediate complexity’, doi:10.5194/gmd-9-3817-2016 *Geoscientific Model Development* **9**(10), 3817–3857.
- Willeit, M., Ganopolski, A., Calov, R. and Brovkin, V. (2019), ‘Mid-Pleistocene transition in glacial cycles explained by declining CO₂ and regolith removal’, doi:10.1126/sciadv.aav7337 *Science Advances* **5**(4).
- Willeit, M., Ganopolski, A., Robinson, A. and Edwards, N. R. (2022), ‘The Earth system model CLIMBER-X v1.0. Part 1: climate model description and validation’, doi:10.5194/gmd-2022-56 *Geoscientific Model Development Discussions* **2022**, 1–69.
- Winguth, A. M. and Maier-Reimer, E. (2005), ‘Causes of the marine productivity and oxygen changes associated with the Permian–Triassic boundary: A reevaluation with ocean general circulation models’, *Marine Geology* **217**(3), 283 – 304. Ocean Chemistry over the Phanerozoic and its links to Geological Processes.
- Winguth, A. M., Shields, C. A. and Winguth, C. (2015), ‘Transition into a Hothouse World at the Permian-Triassic boundary – A model study’, doi:10.1016/j.palaeo.2015.09.008 *Palaeogeography, Palaeoclimatology, Palaeoecology* **440**, 316–327.
- Winguth, A. and Winguth, C. (2013), ‘Precession-driven monsoon variability at the Permian–Triassic boundary - Implications for anoxia and the mass extinction’, *Global and Planetary Change* **105**, 160–170. doi:10.1016/j.gloplacha.2012.06.006 New developments in Permian-Triassic paleoceanographic and global climate system research.
- Wotzlaw, J.-F., Guex, J., Bartolini, A., Gallet, Y., Krystyn, L., McRoberts, C. A., Taylor, D., Schoene, B. and Schaltegger, U. (2014), ‘Towards accurate numerical calibration of the Late Triassic: High-precision U-Pb geochronology constraints on the duration of the Rhaetian’, doi:10.1130/g35612.1 *Geology* **42**(7), 571–574.
- Wright, N. M., Seton, M., Williams, S. E., Whittaker, J. M. and Müller, R. D. (2020), ‘Sea-level fluctuations driven by changes in global ocean basin volume following supercontinent break-up’, doi:10.1016/j.earscirev.2020.103293 *Earth-Science Reviews* **208**, 103293.
- Wu, R.-J., Lo, M.-H. and Scanlon, B. R. (2021), ‘The Annual Cycle of Terrestrial Water Storage Anomalies in CMIP6 Models Evaluated against GRACE Data’, doi:10.1175/JCLI-D-21-0021.1 *Journal of Climate* **34**(20), 8205 – 8217.
- Youbi, N., Ernst, R. E., Mitchell, R. N., Boumehdi, M. A., El Moume, W., Lahna, A. A., Bensalah, M. K., Söderlund, U., Doblas, M. and Tassinari, C. C. G. (2021), *Preliminary Appraisal of a Correlation Be-*

- tween Glaciations and Large Igneous Provinces Over the Past 720 Million Years*, American Geophysical Union (AGU), doi:10.1002/9781119507444.ch8 chapter 8, pp. 169–190.
- Young, A., Flament, N., Williams, S. E., Merdith, A., Cao, X. and Dietmar Müller, R. (2022), ‘Long-term Phanerozoic sea level change from solid Earth processes’, doi:10.1016/j.epsl.2022.117451 *Earth and Planetary Science Letters* **584**, 117451.
- Zahirovic, S., Eleish, A., Doss, S., Pall, J., Cannon, J., Pistone, M., Tetley, M. G., Young, A. and Fox, P. (2022), ‘Subduction and carbonate platform interactions’, doi:10.1002/gdj3.146 *Geoscience Data Journal* **0**(0), 1–13.
- Zeebe, R. (2012a), ‘LOSCAR: Long-term Ocean-atmosphere-Sediment Carbon cycle Reservoir model v2.0.4’, doi:10.5194/gmd-5-149-2012 *Geoscientific Model Development* **5**(1), 149–166.
- Zeebe, R. E. (2012b), ‘History of Seawater Carbonate Chemistry, Atmospheric CO₂, and Ocean Acidification’, doi:10.1146/annurev-earth-042711-105521 *Annual Review of Earth and Planetary Sciences* **40**(1), 141–165.
- Zeebe, R. E. (2017), ‘Numerical Solutions for the Orbital Motion of the Solar System over the Past 100 Myr: Limits and New Results’, doi:10.3847/1538-3881/aa8cce *The Astronomical Journal* **154**(5), 193.
- Zeebe, R. E. and Westbroek, P. (2003), ‘A simple model for the CaCO₃ saturation state of the ocean: The “Strangelove,” the “Neritan,” and the “Cretan” Ocean’, doi:10.1029/2003GC000538 *Geochemistry, Geophysics, Geosystems* **4**(12).
- Zhang, H. and Torsvik, T. H. (2022), ‘Circum-Tethyan magmatic provinces, shifting continents and Permian climate change’, doi:10.1016/j.epsl.2022.117453 *Earth and Planetary Science Letters* **584**, 117453.
- Zhang, J., Liu, Y., Fang, X., Wang, C. and Yang, Y. (2019), ‘Large dry-humid fluctuations in Asia during the Late Cretaceous due to orbital forcing: A modeling study’, doi:10.1016/j.palaeo.2019.06.003 *Palaeogeography, Palaeoclimatology, Palaeoecology* **533**, 109230.
- Zhou, J., Poulsen, C. J., Rosenbloom, N., Shields, C. and Briegleb, B. (2012), ‘Vegetation-climate interactions in the warm mid-Cretaceous’, doi:10.5194/cp-8-565-2012 *Climate of the Past* **8**(2), 565–576.
- Zhu, J., Poulsen, C. J. and Otto-Bliesner, B. L. (2020), ‘High climate sensitivity in cmip6 model not supported by paleoclimate’, *Nature Climate Change* **10**, 378 – 379.
- Zhu, J., Poulsen, C. J. and Tierney, J. E. (2019), ‘Simulation of Eocene extreme warmth and high climate sensitivity through cloud feedbacks’, doi:10.1126/sciadv.aax1874 *Science Advances* **5**(9).
- Ziegler, A., Eshel, G., Rees, P. M., Rothfus, T., David, R. and Sunderlin, D. (2003), ‘Tracing the tropics across land and sea: Permian to present’, doi:10.1080/00241160310004657 *Lethaia* **36**(3), 227–254.
- Ziegler, M., Tuenter, E. and Lourens, L. (2010a), ‘The precession phase of the boreal summer monsoon as viewed from the eastern Mediterranean (ODP Site 968)’, doi:10.1016/j.quascirev.2010.03.011 *Quaternary Science Reviews* **29**(11), 1481–1490.

Appendix

A.I Supplementary Information to [P.I](#)

Supporting Information for “Investigating Mesozoic Climate Trends and Sensitivities with a Large Ensemble of Climate Model Simulations”

Jan Landwehrs^{1,2}, Georg Feulner², Stefan Petri², Benjamin Sames¹ and
Michael Wagreich¹

¹Department of Geology, University of Vienna, Althanstraße 14, 1090 Vienna, Austria

²Earth System Analysis, Potsdam Institute for Climate Impact Research, Member of the Leibniz Association, P.O. Box 601203,
D-14412 Potsdam, Germany

Contents of this file

1. Sections 1–10
2. Table S1
3. Figures S1–S22

Additional Supporting Information (Files uploaded separately):

See data repository at

<https://doi.org/10.5880/PIK.2020.009>

Corresponding author: J. Landwehrs, jan.landwehrs@univie.ac.at

February 5, 2021, 7:43pm

1. Boundary Conditions: Orography, Bathymetry and Vegetation (Figs. S1–S3)

The topography (see Fig. S1) and bathymetry (see Fig. S2) implemented in the model simulations are based on the paleogeographic reconstructions of Scotese and Wright (2018). After interpolating onto the ocean model grid, the following necessary adjustments were made: Narrow straits with less than two grid cell widths were closed or widened. Isolated ocean cells needed to be removed or connected to the global ocean. To improve model stability, the minimum ocean depth was increased to 461 m and the upper-/lowermost grid row were set to a uniform median depth. Also, random variations of the deepest sea floor were introduced where it was completely flat in the original elevation model. The adjustments were kept as small and consistent as possible. As this study assesses global scale surface climates over a long geological time span, it was beyond the scope of this work to review specific features like ocean gateway configurations with regard to proxy evidence. Given the uncertainties in the paleogeographic reconstructions itself, such a review would certainly be warranted when focusing on the connection between tectonic changes, ocean circulation and climate for specific time periods and geographical regions.

For Fig. 4 and Fig. 7b, locations at the respective timeslice were reconstructed with pyGPlates using the data and the (Scotese, 2008) paleorotation model provided by (Cao et al., 2018). For Fig. 7b, the occurrences were sampled on the $3.75 \times 3.75^\circ$ grid and the size of the triangles scales with the frequency of the occurrences on this grid. Because the paleogeography changes within the relatively broad time-bins of the proxy data, the locations show a certain drift for timeslices within these time-bins.

2. Spin-Up (Figs. S4–S6)

Fig. S4 shows GMST timeseries (Fig. S4 during the 5000 yr spin-up for all simulations.

For a subset of runs ($P_{pCO2_1000ppm}$ for T_{25Myr}), Fig. S6 shows global mean ocean seawater temperature and salinity at different depths over time.

For the same subset, Fig. S5 shows the relation of global mean top-of-the-atmosphere radiation balance (RBTP) and GMST during spin-up.

Fig. S6 shows global mean seawater temperature and salinity at three depth levels during spinup.

Similar plots for each individual run are included in the accompanying data repository (AllRuns_Spinup.pdf).

3. Atmosphere Fields (Figs. S7–S11)

Figures S7 to S10 illustrate the simulated surface air temperatures, precipitation and surface radiation balance for the four exemplary timeslices 75, 125, 175 and 225 Ma presented in the main article figures (similar maps for all simulation runs are included in the data repository). Figure S11 indicates the simulated change of precipitation and the surface radiation balance on land through time.

4. Global Mean Sea-Level Temperatures (Fig. S12)

Fig. S12 shows simulated global mean surface air temperatures compared to lapse-rate corrected global mean temperatures at sea-level for the $P_{\text{pCO}_2,1000\text{ppm}}$ and the $P_{\text{VegFix}_S0\text{ini}}$ pathways.

5. Correlation of Global Mean Temperatures with the Total Area and Distribution of Land (Fig. S13)

Fig. S13 shows the correlation of lapse-rate corrected global mean air temperatures at sea level (GMT_{SL}) with the global land area fraction (a) and the average absolute latitude of land area (b). For the simulations of the $P_{\text{VegFix}_S0\text{ini}}$ pathway.

6. Proxy and Model Temperature Estimates (Figs. S14–S15)

Climate models inherently yield self-constrained global temperature fields, but might miss important processes that shaped these in reality. Proxy approaches often aim to compile consistent and globally distributed datasets to generate meridional or global SST or SAT distributions to obtain GMST estimates. Retrieving and calibrating such datasets is challenging and converting them into GMSTs is non-trivial. For example, the GMST estimates from (Mills et al., 2019, Fig 4b) (also see Fig. 1c of the present article) were mainly obtained from reconstructed tropical SST anomalies via a scaling factor of 1.5 (Mills et al., 2019):

$$\Delta\text{GMST} = \text{GMST}_{\text{ref}} + 1.5 \cdot \Delta\text{SST}_{\text{trop}} \quad (1)$$

Where $\text{GMST}_{\text{ref}} = 15^\circ\text{C}$ and $\Delta\text{SST}_{\text{trop}} = -4.55 \cdot \delta^{18}\text{O}_{\text{trop}}$ (Mills et al., 2019).

We tested the correlation of SST_{trop} and GMST (see Fig. S14a) in our model ensemble and indeed found an overall solid linear relationship (see Fig. S15a). However, we obtain a scaling factor of ~ 1.79 , indicating a stronger amplification of temperature changes at higher latitudes. Our results also suggest that the scaling is slightly higher for cooler climate states (see Fig. S15b), which could to some extent explain its variation through geologic time (Fig. S15c). For the latter panel, the correlation was calculated separately for the 9 $T_{25\text{Myr}}$ timeslices and their climate states at $\text{pCO}_2 =$

February 5, 2021, 7:43pm

[250, 500, 1000, 1500, 2000, 4000] ppm. The 75 Ma timeslice, which is warm-biased by other boundary conditions (e.g. S_0 , paleogeography), exhibits a slightly smaller scaling factor compared to the cold-biased 200 Ma timeslice (Fig. S15c, see inset).

Using the mean scaling factor of 1.79 and a reference GMST of 15 °C (as in Mills et al., 2019), we can calculate tropical SST anomalies for our simulations (Fig. S14b). These can be compared with the results from (Mills et al., 2019). (For this, we had to scale their GMST envelope back to $\Delta\text{SST}_{\text{trop}}$ via Eq. 1, as the authors did not report the underlying low-latitude SST anomalies in the same form.) As described in Sec. 3.1 of the paper, there appears to be a qualitative agreement on a slight cooling towards the end-Triassic to Early Jurassic, a warming towards the mid-Cretaceous, and a cooling at the end of the Cretaceous. However, the proxy estimates of $\Delta\text{SST}_{\text{trop}}$ are amplified by a factor of 2 or 3 compared to those in our model (note the different y-axis scales in Fig. S14b). As discussed, this can have several reasons, including a too low model climate sensitivity or uncertainties in the proxy temperature calibration. In future work, we aim at more comprehensive proxy–model comparisons than could be achieved within the framework of this study.

7. Meridional Temperature Gradients (Figs. S16–S17)

Simulated zonal mean SAT and SST profiles for the 95 and 125 Ma timeslices are shown in Fig. S16 for comparison with Laugié et al. (2020) and Steinig et al. (2020) as discussed in the main text (Sec. 4). Similar plots for all timeslices are included in the accompanying data repository. The figures also indicate numerical values of the global, low latitude ($<30^\circ$), high latitude ($>60^\circ$) averages and the difference between the latter two (upper left corner). As in Laugié et al. (2020) the meridional temperature gradient was also determined as the average change in °C per °lat. via a linear regression between 30 and 80° latitude (upper right corner). The figures also include zonal mean temperatures calculated from model output from Valdes, Scotese, and Lunt (2020) and Farnsworth et al. (2019a).

For comparison with Fig. 5, zonal mean SAT and low–high latitude SAT differences are shown for data from Valdes et al. (2020) and Farnsworth et al. (2019a) in Fig. S17.

8. Meridional Heat Transport (Fig. S18)

Fig. S18 shows the change of the zonal and global mean meridional atmospheric/ocean/total heat transport through time. On a global average, the MHT varies less than ± 0.2 PW around ~ 2.6 PW between all simulations. It tends to be increased in cooler states, for low-obliquity orbital configurations (which are also cooler) and for homogeneous vegetation patterns. Three phases with relative strengthening ocean MHT in the northern (until ~ 220 Ma), southern (~ 220 –110 Ma) and again northern (~ 110 –60 Ma)

hemisphere can be identified. To some degree, these periods also appear to coincide to with enhanced overturning (see Fig. S19 and AllRuns_OceanCrosssections.pdf) and mixing in the respective hemisphere (see Fig. S21).

9. Ocean Fields (Figs. S19–S21)

Fig. S19 include meridional ocean cross-sections showing the annual mean ocean temperatures as a zonal mean, at 180°W and 60°E. They also show the global mean meridional overturning streamfunction. Similar plots for every simulation of the whole ensemble are included in the data repository (AllRuns_OceanCrosssections.pdf).

Fig. S20 show annual mean sea surface temperatures, surface salinity and mixed layer depth for simulations of the $P_{\text{pCO}_2.1000\text{ppm}}$ pathway. Similar plots for every simulation of the whole ensemble are included in the data repository (AllRuns_Maps.pdf).

Fig. S21 shows the zonal and annual mean mixed layer depth through time, aggregated for the $P_{\text{pCO}_2.1000\text{ppm}}$ pathway.

10. Seasonality (Fig. S22)

The same analysis of continental SAT seasonality as presented in Sec. 3.2 of the main paper was performed with modeling results from Valdes et al. (2020) and Farnsworth et al. (2019a) (see Fig. S22).

11. Table of runs

Table S1: List of all equilibrium climate simulations included in the analyses.

Run	Age (Ma)	pCO ₂ (ppm)	pCO ₂ pathway	S ₀ (W/m ²)	Land fraction (%)	T _{ann} (°C)	PRC _{ann} (mm/a)	T _{ann,trend} (°C/500yrs)	Radiation imbalance (W/m ²)
0	060Ma_400ppm	60	400 proxy	1354.7	31.7	16.7	1022	0.015	0.042
1	060Ma_500ppm	60	500 COPSE	1354.7	31.7	17.7	1059	-0.044	0.065
2	060Ma_1000ppm	60	1000	1354.7	31.7	20.6	1178	0.002	0.022
3	065Ma_250ppm	65	250	1354.1	31.3	14.7	954	0.003	0.033
4	065Ma_300ppm	65	300 proxy	1354.1	31.3	15.5	984	-0.003	0.028
5	065Ma_500ppm	65	500	1354.1	31.3	17.7	1070	0.000	0.035
6	065Ma_600ppm	65	600 COPSE	1354.1	31.3	18.5	1101	0.003	0.022
7	065Ma_1000ppm	65	1000	1354.1	31.3	20.7	1188	-0.004	0.04
8	065Ma_1000ppm_S0ini	65	1000	1332.7	31.3	18.8	1101	-0.057	0.027
9	065Ma_1000ppm_S0ini_VegFix	65	1000	1332.7	31.3	18.8	1092	0.006	0.013
10	065Ma_1000ppm_VegHom	65	1000	1354.1	31.3	20.9	1195	0.004	0.048
11	065Ma_1000ppm_orb_22p0-0p00-000	65	1000	1354.1	31.3	20.5	1191	0.007	0.039
12	065Ma_1000ppm_orb_24p5-0p06-090	65	1000	1354.1	31.3	20.9	1195	0.015	0.094
13	065Ma_1000ppm_orb_24p5-0p06-180	65	1000	1354.1	31.3	21.0	1198	0.006	0.025
14	065Ma_1000ppm_orb_24p5-0p06-270	65	1000	1354.1	31.3	20.9	1197	0.012	0.029
15	065Ma_1500ppm	65	1500	1354.1	31.3	22.2	1256	0.009	0.039
16	065Ma_2000ppm	65	2000	1354.1	31.3	23.3	1302	0.012	0.023
17	065Ma_4000ppm	65	4000	1354.1	31.3	25.6	1405	0.016	0.133
18	070Ma_300ppm	70	300 proxy	1353.5	32.2	15.5	983	0.004	-0.001
19	070Ma_800ppm	70	800 COPSE	1353.5	32.2	19.7	1142	0.004	0.036
20	070Ma_1000ppm	70	1000	1353.5	32.2	20.6	1180	0.006	0.037
21	075Ma_250ppm	75	250	1352.9	26.9	15.4	985	0.027	0.003
22	075Ma_500ppm	75	500 proxy	1352.9	26.9	18.4	1096	0.001	0.032
23	075Ma_900ppm	75	900 COPSE	1352.9	26.9	20.8	1193	0.006	0.04
24	075Ma_1000ppm	75	1000	1352.9	26.9	21.2	1211	-0.015	0.054
25	075Ma_1000ppm_S0ini	75	1000	1332.7	26.9	19.5	1130	0.000	0.025
26	075Ma_1000ppm_S0ini_VegFix	75	1000	1332.7	26.9	19.4	1111	-0.010	0.036
27	075Ma_1000ppm_VegHom	75	1000	1352.9	26.9	21.3	1209	0.008	0.055
28	075Ma_1000ppm_orb_22p0-0p00-000	75	1000	1352.9	26.9	21.1	1214	-0.000	0.038
29	075Ma_1000ppm_orb_24p5-0p06-090	75	1000	1352.9	26.9	21.5	1217	0.010	0.064
30	075Ma_1000ppm_orb_24p5-0p06-180	75	1000	1352.9	26.9	21.5	1221	0.001	0.025
31	075Ma_1000ppm_orb_24p5-0p06-270	75	1000	1352.9	26.9	21.4	1221	0.016	0.027
32	075Ma_1500ppm	75	1500	1352.9	26.9	22.7	1276	0.009	0.081
33	075Ma_2000ppm	75	2000	1352.9	26.9	23.7	1321	0.025	0.107
34	075Ma_4000ppm	75	4000	1352.9	26.9	26.0	1422	0.012	0.169
35	080Ma_700ppm	80	700 proxy	1352.4	26.0	19.8	1149	-0.009	0.075
36	080Ma_900ppm	80	900 COPSE	1352.4	26.0	20.8	1192	-0.005	0.036
37	080Ma_1000ppm	80	1000	1352.4	26.0	21.2	1209	0.018	0.02
38	085Ma_600ppm	85	600 proxy	1351.8	27.1	19.1	1122	-0.038	0.019
39	085Ma_900ppm	85	900 COPSE	1351.8	27.1	20.7	1190	0.001	0.036
40	085Ma_1000ppm	85	1000	1351.8	27.1	21.1	1208	0.005	0.041
41	090Ma_500ppm	90	500 proxy	1351.2	28.0	18.1	1086	0.147	0.087
42	090Ma_900ppm	90	900 COPSE	1351.2	28.0	20.5	1185	0.007	0.049
43	090Ma_1000ppm	90	1000	1351.2	28.0	20.9	1203	0.016	0.044
44	095Ma_600ppm	95	600 proxy	1350.6	28.7	18.5	1099	0.004	0.045
45	095Ma_1000ppm	95	1000 COPSE	1350.6	28.7	20.6	1185	-0.001	0.036
46	100Ma_250ppm	100	250	1350.0	30.0	14.4	949	-0.009	0.016
47	100Ma_500ppm	100	500	1350.0	30.0	17.4	1060	-0.016	0.016
48	100Ma_900ppm	100	900 proxy	1350.0	30.0	19.8	1158	0.003	0.072
49	100Ma_1000ppm	100	1000 COPSE	1350.0	30.0	20.2	1176	0.002	0.068
50	100Ma_1000ppm_S0ini	100	1000	1332.7	30.0	18.8	1106	0.000	0.026
51	100Ma_1000ppm_S0ini_VegFix	100	1000	1332.7	30.0	18.7	1098	-0.005	-0.06
52	100Ma_1000ppm_SL+40	100	1000	1350.0	29.7	20.4	1180	0.142	0.031
53	100Ma_1000ppm_SL-200	100	1000	1350.0	37.9	19.1	1120	0.014	0.015
54	100Ma_1000ppm_SL-40	100	1000	1350.0	30.7	20.1	1172	0.005	0.034
55	100Ma_1000ppm_VegHom	100	1000	1350.0	30.0	20.3	1184	0.005	0.068
56	100Ma_1000ppm_VegHom_SL+40	100	1000	1350.0	29.7	20.5	1188	0.074	0.046
57	100Ma_1000ppm_VegHom_SL-200	100	1000	1350.0	37.9	19.1	1124	-0.013	0.059
58	100Ma_1000ppm_VegHom_SL-40	100	1000	1350.0	30.7	20.2	1180	0.000	0.01
59	100Ma_1000ppm_orb_22p0-0p00-000	100	1000	1350.0	30.0	20.1	1178	0.005	0.067
60	100Ma_1000ppm_orb_24p5-0p06-090	100	1000	1350.0	30.0	20.5	1187	0.007	0.043
61	100Ma_1000ppm_orb_24p5-0p06-180	100	1000	1350.0	30.0	20.5	1185	0.011	0.051
62	100Ma_1000ppm_orb_24p5-0p06-270	100	1000	1350.0	30.0	20.5	1183	0.007	0.045
63	100Ma_1500ppm	100	1500	1350.0	30.0	21.8	1243	0.025	0.081
64	100Ma_2000ppm	100	2000	1350.0	30.0	22.8	1289	0.017	0.114
65	100Ma_4000ppm	100	4000	1350.0	30.0	25.1	1394	0.011	0.158
66	105Ma_1000ppm	105	1000 proxy	1349.5	30.5	20.3	1178	0.005	0.081
67	105Ma_1100ppm	105	1100 COPSE	1349.5	30.5	20.7	1195	-0.001	0.077
68	110Ma_1000ppm	110	1000	1348.9	30.6	20.3	1161	0.001	0.035
69	110Ma_1100ppm	110	1100 proxyCOPSE	1348.9	30.6	20.7	1177	0.002	0.027
70	115Ma_1000ppm	115	1000 COPSE	1348.3	30.3	20.2	1152	0.002	0.052
71	115Ma_1100ppm	115	1100 proxy	1348.3	30.3	20.6	1169	0.003	0.053
72	120Ma_1000ppm	120	1000 proxyCOPSE	1347.7	30.4	19.8	1128	-0.000	0.058
73	125Ma_250ppm	125	250	1347.2	31.1	13.5	900	-0.003	0.033
74	125Ma_500ppm	125	500	1347.2	31.1	16.9	1014	-0.000	0.027
75	125Ma_900ppm	125	900 proxy	1347.2	31.1	19.5	1116	0.001	0.034
76	125Ma_1000ppm	125	1000 COPSE	1347.2	31.1	19.9	1135	0.003	0.039
77	125Ma_1000ppm_S0ini	125	1000	1332.7	31.1	18.6	1074	0.000	0.032
78	125Ma_1000ppm_S0ini_VegFix	125	1000	1332.7	31.1	18.8	1090	0.001	0.042
79	125Ma_1000ppm_VegHom	125	1000	1347.2	31.1	20.1	1152	0.003	0.048
80	125Ma_1000ppm_orb_22p0-0p00-000	125	1000	1347.2	31.1	19.8	1135	0.002	0.035
81	125Ma_1000ppm_orb_24p5-0p06-090	125	1000	1347.2	31.1	20.2	1146	0.003	0.008
82	125Ma_1000ppm_orb_24p5-0p06-180	125	1000	1347.2	31.1	20.2	1149	0.003	0.026
83	125Ma_1000ppm_orb_24p5-0p06-270	125	1000	1347.2	31.1	20.1	1147	0.003	0.015
84	125Ma_1500ppm	125	1500	1347.2	31.1	21.5	1206	0.006	0.062
85	125Ma_2000ppm	125	2000	1347.2	31.1	22.6	1255	0.009	0.083
86	125Ma_4000ppm	125	4000	1347.2	31.1	24.9	1367	0.021	0.136
87	130Ma_900ppm	130	900 proxyCOPSE	1346.6	33.5	19.1	1092	-0.015	0.023
88	130Ma_1000ppm	130	1000	1346.6	33.5	19.5	1111	-0.004	0.022
89	135Ma_1000ppm	135	1000 proxyCOPSE	1346.0	34.2	19.3	1103	0.002	0.017
90	140Ma_900ppm	140	900 proxyCOPSE	1345.4	34.9	18.6	1077	-0.001	0.01

91	140Ma_1000ppm	140	1000		1345.4	34.9	19.0	1096	-0.001	0.023
92	145Ma_700ppm	145	700	proxyCOPSE	1344.8	34.3	17.5	1027	-0.013	0.022
93	145Ma_1000ppm	145	1000		1344.8	34.3	19.1	1093	-0.000	0.02
94	150Ma_250ppm	150	250		1344.3	34.2	12.0	825	-0.003	0.004
95	150Ma_500ppm	150	500		1344.3	34.2	15.7	946	-0.005	-0.01
96	150Ma_700ppm	150	700	COPSE	1344.3	34.2	17.3	1007	-0.035	0.027
97	150Ma_800ppm	150	800	proxy	1344.3	34.2	18.0	1032	-0.009	0.023
98	150Ma_1000ppm	150	1000		1344.3	34.2	18.9	1072	-0.004	0.034
99	150Ma_1000ppm_S0ini	150	1000		1332.7	34.2	17.9	1023	-0.023	0.038
100	150Ma_1000ppm_SL+40	150	1000		1332.7	34.2	18.3	1066	0.005	0.012
101	150Ma_1000ppm_VegFix	150	1000		1344.3	33.6	19.1	1074	-0.001	0.025
102	150Ma_1000ppm_SL+40	150	1000		1344.3	36.5	18.6	1050	0.005	0.029
103	150Ma_1000ppm_VegHom	150	1000		1344.3	34.2	19.3	1110	0.001	0.016
104	150Ma_1000ppm_VegHom_SL+40	150	1000		1344.3	33.6	19.5	1114	-0.000	0.015
105	150Ma_1000ppm_VegHom_SL+40	150	1000		1344.3	36.5	18.9	1087	-0.007	0.022
106	150Ma_1000ppm_orb_22p0-0p00-000	150	1000		1344.3	34.2	18.8	1071	-0.003	0.031
107	150Ma_1000ppm_orb_24p5-0p06-090	150	1000		1344.3	34.2	19.2	1084	0.001	0.024
108	150Ma_1000ppm_orb_24p5-0p06-180	150	1000		1344.3	34.2	19.2	1086	0.001	0.007
109	150Ma_1000ppm_orb_24p5-0p06-270	150	1000		1344.3	34.2	19.2	1084	0.004	0.016
110	150Ma_1500ppm	150	1500		1344.3	34.2	20.6	1143	0.002	0.046
111	150Ma_2000ppm	150	2000		1344.3	34.2	21.7	1193	0.010	0.074
112	150Ma_4000ppm	150	4000		1344.3	34.2	24.2	1309	0.016	0.093
113	155Ma_700ppm	155	700	COPSE	1343.7	31.9	17.7	1018	0.057	0.043
114	155Ma_800ppm	155	800	proxy	1343.7	31.9	18.3	1043	0.153	0.007
115	155Ma_1000ppm	155	1000		1343.7	31.9	19.3	1083	-0.002	0.02
116	160Ma_600ppm	160	600	COPSE	1343.1	28.2	17.3	1005	0.000	0.025
117	160Ma_800ppm	160	800	proxy	1343.1	28.2	18.7	1059	0.001	0.032
118	160Ma_1000ppm	160	1000		1343.1	28.2	19.7	1101	0.000	0.034
119	165Ma_600ppm	165	600	COPSE	1342.5	30.5	16.8	978	0.007	0.027
120	165Ma_900ppm	165	900	proxy	1342.5	30.5	18.8	1059	0.157	-0.029
121	165Ma_1000ppm	165	1000		1342.5	30.5	19.3	1078	0.000	0.007
122	170Ma_500ppm	170	500	COPSE	1341.9	32.5	15.4	919	-0.005	0.021
123	170Ma_1000ppm	170	1000	proxy	1341.9	32.5	19.0	1053	-0.000	0.023
124	175Ma_250ppm	175	250		1341.4	33.6	10.9	785	0.000	0.042
125	175Ma_500ppm	175	500	COPSE	1341.4	33.6	15.0	914	0.001	0.024
126	175Ma_1000ppm	175	1000	proxy	1341.4	33.6	18.7	1051	-0.001	0.027
127	175Ma_1000ppm_S0ini	175	1000		1332.7	33.6	17.8	1012	0.027	0.035
128	175Ma_1000ppm_S0ini_VegFix	175	1000		1332.7	33.6	18.3	1065	0.001	0.012
129	175Ma_1000ppm_VegHom	175	1000		1341.4	33.6	19.0	1097	0.000	0.016
130	175Ma_1000ppm_orb_22p0-0p00-000	175	1000		1341.4	33.6	18.6	1050	0.004	0.009
131	175Ma_1000ppm_orb_24p5-0p06-090	175	1000		1341.4	33.6	18.9	1060	-0.000	0.015
132	175Ma_1000ppm_orb_24p5-0p06-180	175	1000		1341.4	33.6	19.0	1067	-0.001	0.02
133	175Ma_1000ppm_orb_24p5-0p06-270	175	1000		1341.4	33.6	19.0	1070	-0.000	-0.008
134	175Ma_1500ppm	175	1500		1341.4	33.6	20.4	1127	0.002	0.014
135	175Ma_2000ppm	175	2000		1341.4	33.6	21.6	1180	-0.005	0.006
136	175Ma_4000ppm	175	4000		1341.4	33.6	24.1	1305	-0.000	0.018
137	180Ma_500ppm	180	500	COPSE	1340.9	38.2	14.1	865	-0.009	0.017
138	180Ma_900ppm	180	900	proxy	1340.9	38.2	17.4	980	-0.007	0.001
139	180Ma_1000ppm	180	1000		1340.9	38.2	17.9	1000	0.005	0.015
140	185Ma_500ppm	185	500	COPSE	1340.3	35.8	14.5	887	0.091	-0.005
141	185Ma_900ppm	185	900	proxy	1340.3	35.8	17.8	1005	-0.002	0.006
142	185Ma_1000ppm	185	1000		1340.3	35.8	18.3	1026	0.018	0.005
143	190Ma_500ppm	190	500	COPSE	1339.8	35.1	14.8	886	0.001	0.023
144	190Ma_1000ppm	190	1000		1339.8	35.1	18.5	1016	-0.000	0.038
145	190Ma_1100ppm	190	1100	proxy	1339.8	35.1	18.9	1033	-0.000	0.033
146	195Ma_500ppm	195	500	COPSE	1339.2	35.1	14.2	864	0.000	0.029
147	195Ma_1000ppm	195	1000		1339.2	35.1	18.1	1001	-0.016	0.005
148	195Ma_1700ppm	195	1700	proxy	1339.2	35.1	20.5	1098	-0.114	0.059
149	200Ma_250ppm	200	250		1338.7	37.4	9.9	731	0.002	0.031
150	200Ma_500ppm	200	500	COPSE	1338.7	37.4	13.9	847	-0.010	0.028
151	200Ma_1000ppm	200	1000		1338.7	37.4	17.8	978	0.006	0.027
152	200Ma_1000ppm_S0ini	200	1000		1332.7	37.4	17.2	952	0.001	0.02
153	200Ma_1000ppm_S0ini_VegFix	200	1000		1332.7	37.4	17.6	1003	-0.009	0.016
154	200Ma_1000ppm_SL+200	200	1000		1338.7	32.0	19.0	1011	-0.009	0.013
155	200Ma_1000ppm_SL+40	200	1000		1338.7	36.0	18.1	990	-0.017	0.016
156	200Ma_1000ppm_VegHom	200	1000		1338.7	37.4	18.2	1030	0.006	0.014
157	200Ma_1000ppm_VegHom_SL+200	200	1000		1338.7	32.0	19.3	1060	-0.043	0.078
158	200Ma_1000ppm_VegHom_SL+40	200	1000		1338.7	36.0	18.5	1042	-0.147	0.009
159	200Ma_1000ppm_orb_22p0-0p00-000	200	1000		1338.7	37.4	17.7	972	0.007	0.038
160	200Ma_1000ppm_orb_24p5-0p06-090	200	1000		1338.7	37.4	18.1	997	0.021	0.001
161	200Ma_1000ppm_orb_24p5-0p06-180	200	1000		1338.7	37.4	18.1	996	0.002	-0.009
162	200Ma_1000ppm_orb_24p5-0p06-270	200	1000		1338.7	37.4	18.1	995	0.033	-0.013
163	200Ma_1500ppm	200	1500		1338.7	37.4	19.7	1052	-0.006	0.015
164	200Ma_1700ppm	200	1700	proxy	1338.7	37.4	20.2	1074	0.019	0.023
165	200Ma_2000ppm	200	2000		1338.7	37.4	20.9	1102	0.005	0.024
166	200Ma_4000ppm	200	4000		1338.7	37.4	23.4	1223	-0.017	0.044
167	205Ma_600ppm	205	600	COPSE	1338.1	37.1	15.0	873	0.001	0.034
168	205Ma_1000ppm	205	1000		1338.1	37.1	17.8	971	0.005	0.016
169	205Ma_1500ppm	205	1500	proxy	1338.1	37.1	19.6	1045	0.008	0.035
170	210Ma_800ppm	210	800	COPSE	1337.6	36.6	16.6	925	0.043	0.051
171	210Ma_1000ppm	210	1000		1337.6	36.6	17.7	967	-0.005	0.019
172	210Ma_1300ppm	210	1300	proxy	1337.6	36.6	19.0	1017	-0.034	0.004
173	215Ma_900ppm	215	900	COPSE	1337.0	36.9	17.4	962	0.001	0.032
174	215Ma_1000ppm	215	1000		1337.0	36.9	17.9	982	0.000	0.018
175	215Ma_1300ppm	215	1300	proxy	1337.0	36.9	19.2	1032	0.000	0.011
176	220Ma_1000ppm	220	1000	COPSE	1336.5	30.6	18.2	1011	0.009	0.004
177	220Ma_1600ppm	220	1600	proxy	1336.5	30.6	20.4	1101	-0.005	0.013
178	225Ma_250ppm	225	250		1336.0	30.9	9.1	719	0.001	0.047
179	225Ma_500ppm	225	500		1336.0	30.9	13.8	844	-0.000	0.06
180	225Ma_900ppm	225	900	COPSE	1336.0	30.9	17.3	962	0.000	-0.005
181	225Ma_1000ppm	225	1000		1336.0	30.9	17.9	983	0.001	0.003
182	225Ma_1000ppm_S0ini	225	1000		1332.7	30.9	17.5	968	0.000	0
183	225Ma_1000ppm_S0ini_VegFix	225	1000		1332.7	30.9	18.4	1052	0.000	-0.021
184	225Ma_1000ppm_VegHom	225	1000		1336.0	30.9	18.3	1032	0.000	-0.013
185	225Ma_1000ppm_orb_22p0-0p00-000	225	1000		1336.0	30.9	17.7	981	0.000	0.005
186	225Ma_1000ppm_orb_24p5-0p06-090	225	1000		1336.0	30.9	18.3	1003	-0.000	0.005
187	225Ma_1000ppm_orb_24p5-0p06-180	225	1000		1336.0	30.9	18.2	997	0.002	0.004
188	225Ma_1000ppm_orb_24p5-0p06-270	225	1000		1336.0	30.9	18.3	993	-0.004	-0.025
189	225Ma_1500ppm	225	1500		1336.0	30.9	19.9	1059	-0.006	0.002
190	225Ma_2000ppm	225	2000	proxy	1336.0	30.9	21.1	1111	-0.022	0.008
191	225Ma_4000ppm	225	4000		1336.0	30.9	23.6	1227	0.001	0.016
192	230Ma_800ppm	230	800	COPSE	1335.4	31.6	16.5	936	0.001	0.008
193	230Ma_1000ppm	230	1000		1335.4	31.6	17.7	979	0.009	-0.004

February 5, 2021, 7:43pm

194	230Ma_1900ppm	230	1900	proxy	1335.4	31.6	20.7	1099	-0.000	0.001
195	235Ma_800ppm	235	800	COPSE	1334.9	32.0	16.6	934	0.010	0.038
196	235Ma_1000ppm	235	1000		1334.9	32.0	17.9	979	0.003	-0.004
197	235Ma_1400ppm	235	1400	proxy	1334.9	32.0	19.4	1040	-0.003	-0
198	240Ma_800ppm	240	800	proxy	1334.3	31.7	16.5	942	0.026	0.008
199	240Ma_900ppm	240	900	COPSE	1334.3	31.7	17.2	964	0.041	0.022
200	240Ma_1000ppm	240	1000		1334.3	31.7	17.8	984	0.004	0.016
201	245Ma_400ppm	245	400	proxy	1333.8	31.3	12.9	818	-0.001	0.049
202	245Ma_1000ppm	245	1000	COPSE	1333.8	31.3	18.1	992	0.001	-0.015
203	250Ma_250ppm	250	250		1333.2	30.8	10.3	740	0.001	0.016
204	250Ma_500ppm	250	500		1333.2	30.8	14.9	869	-0.001	0.022
205	250Ma_700ppm	250	700	proxy	1333.2	30.8	16.8	933	0.000	0.005
206	250Ma_1000ppm	250	1000		1333.2	30.8	18.5	998	0.001	-0.009
207	250Ma_1000ppm_S0ini	250	1000		1332.7	30.8	18.5	996	-0.011	-0.01
208	250Ma_1000ppm_S0ini_VegFix	250	1000		1332.7	30.8	18.8	1040	-0.003	-0.009
209	250Ma_1000ppm_VegHom	250	1000		1333.2	30.8	18.8	1039	-0.003	-0.005
210	250Ma_1000ppm_orb_22p0-0p00-000	250	1000		1333.2	30.8	18.4	995	-0.005	-0.005
211	250Ma_1000ppm_orb_24p5-0p06-090	250	1000		1333.2	30.8	18.7	1023	-0.048	0.021
212	250Ma_1000ppm_orb_24p5-0p06-180	250	1000		1333.2	30.8	18.8	1016	-0.012	0.008
213	250Ma_1000ppm_orb_24p5-0p06-270	250	1000		1333.2	30.8	18.9	1008	0.014	0.005
214	250Ma_1100ppm	250	1100	COPSE	1333.2	30.8	18.9	1015	0.003	-0.011
215	250Ma_1500ppm	250	1500		1333.2	30.8	20.3	1070	-0.001	-0.02
216	250Ma_2000ppm	250	2000		1333.2	30.8	21.4	1120	0.009	-0.011
217	250Ma_4000ppm	250	4000		1333.2	30.8	23.9	1238	0.002	-0.011
218	255Ma_800ppm	255	800	proxy	1332.7	29.6	17.6	967	-0.001	-0.004
219	255Ma_1000ppm	255	1000		1332.7	29.6	18.6	1007	0.002	-0
220	255Ma_1300ppm	255	1300	COPSE	1332.7	29.6	19.8	1054	0.002	0.016

February 5, 2021, 7:43pm

References

- Boucot, A. J., Xu, C., Scotese, C. R., & Morley, R. J. (2013). *Phanerozoic Paleoclimate: An Atlas of Lithologic Indicators of Climate*. SEPM Society for Sedimentary Geology. doi: 10.2110/sepmcsp.11
- Cao, W., Williams, S., Flament, N., Zahirovic, S., Scotese, C. R., & Müller, R. D. (2018). Palaeolatitudinal distribution of lithologic indicators of climate in a palaeogeographic framework. *Geological Magazine*, *156*(2), 331-354. doi: 10.1017/S0016756818000110
- Farnsworth, A., Lunt, D. J., O'Brien, C. L., Foster, G. L., Inglis, G. N., Markwick, P., . . . Robinson, S. A. (2019a). Climate Sensitivity on Geological Timescales Controlled by Nonlinear Feedbacks and Ocean Circulation. *Geophysical Research Letters*, *46*. doi: 10.1029/2019GL083574
- Laugié, M., Donnadiou, Y., Ladant, J.-B., Green, J. A. M., Bopp, L., & Raisson, F. (2020). Stripping back the modern to reveal the Cenomanian–Turonian climate and temperature gradient underneath. *Climate of the Past*, *16*(3), 953–971. doi: 10.5194/cp-16-953-2020
- Mills, B. J., Krause, A. J., Scotese, C. R., Hill, D. J., Shields, G. A., & Lenton, T. M. (2019). Modelling the long-term carbon cycle, atmospheric CO₂, and Earth surface temperature from late Neoproterozoic to present day. *Gondwana Research*, *67*, 172 - 186. doi: 10.1016/j.gr.2018.12.001
- Scotese, C. R. (2008). The PALEOMAP Project PaleoAtlas for ArcGIS, Volume 2, Cretaceous paleogeographic and plate tectonic reconstructions. *PALEOMAP Project, Arlington, Texas*.

February 5, 2021, 7:43pm

Scotese, C. R. (2016). *Global Climate Change (Modern Times to 540 million years ago)*.

Retrieved from https://www.researchgate.net/publication/303811641_Global_Climate_Change_Modern_Times_to_540_million_years_ago

Scotese, C. R., & Wright, N. (2018). PALEOMAP paleodigital elevation models

(PaleoDEMS) for the Phanerozoic. Retrieved from <https://www.earthbyte.org/paleodem-resource-scotese-and-wright-2018>

Steinig, S., Dumann, W., Park, W., Latif, M., Kusch, S., Hofmann, P., & Flögel, S.

(2020). Evidence for a regional warm bias in the Early Cretaceous TEX86 record.

Earth and Planetary Science Letters, 539, 116184. doi: 10.1016/j.epsl.2020.116184

Valdes, P. J., Scotese, C. R., & Lunt, D. J. (2020). Deep Ocean Temperatures through

Time. *Climate of the Past Discussions*, 1–37. doi: 10.5194/cp-2020-83

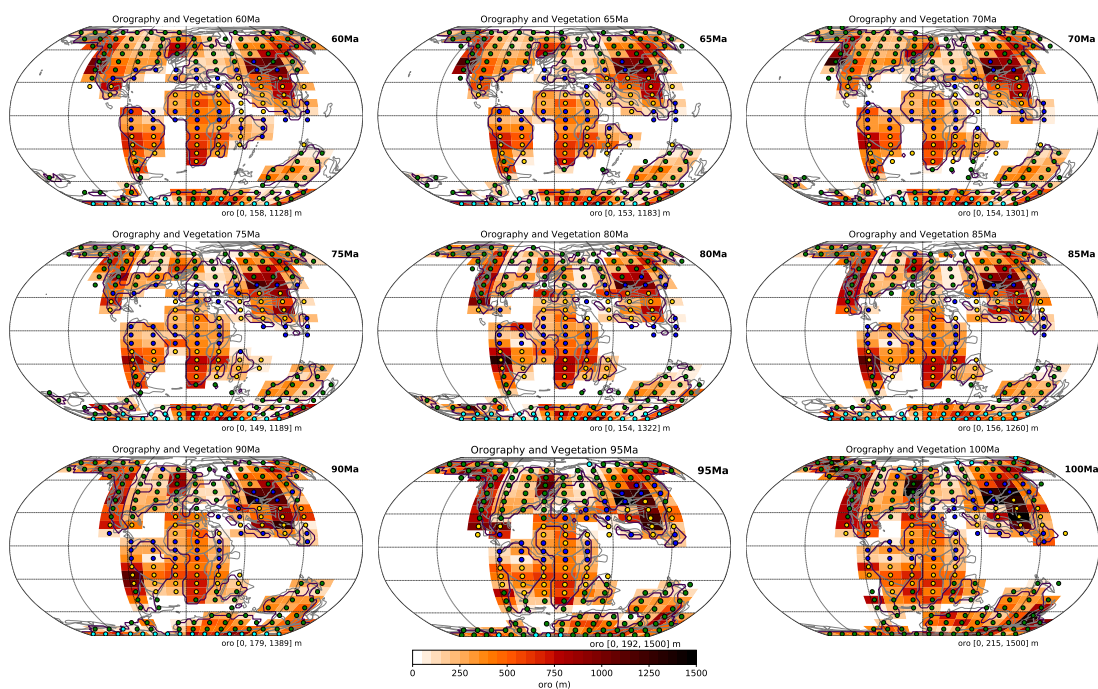
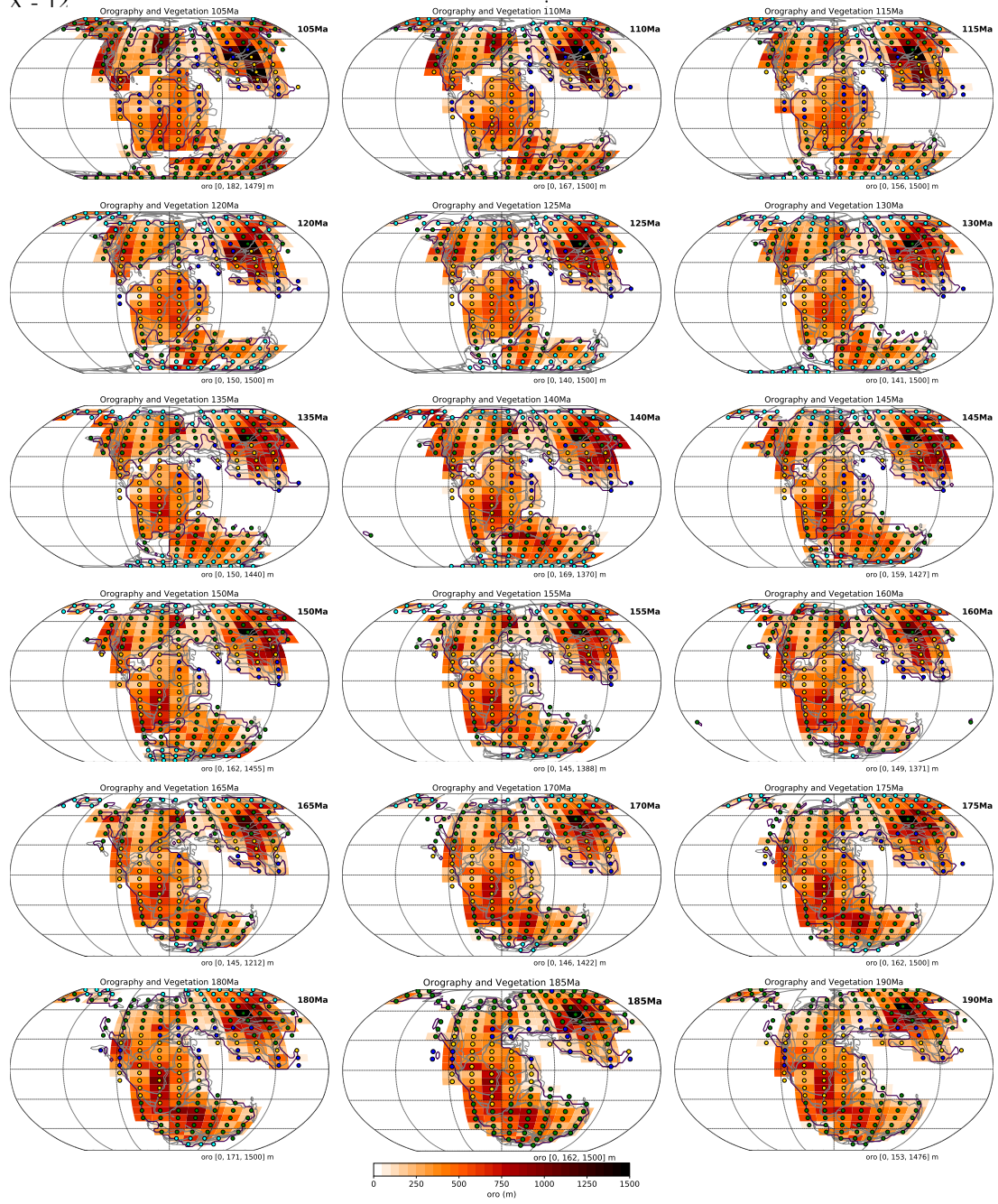


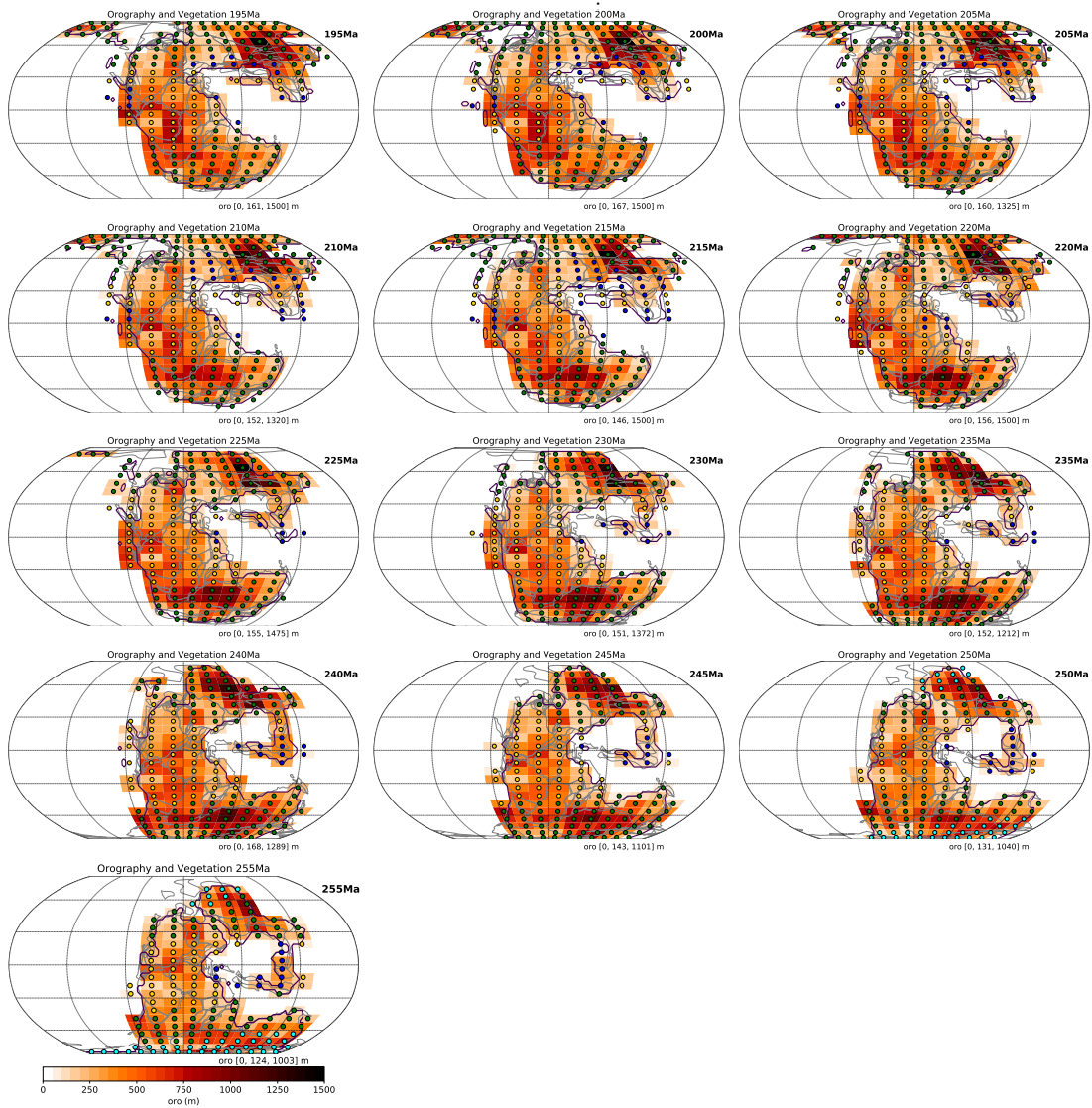
Figure S1. Orography (colors, based on Scotese and Wright (2018)) and Vegetation cover (dots) on the atmosphere model grid for all timeslices. The black lines indicate the land-sea mask on the ocean model grid resolution. Dots indicate the vegetation patterns (VegHet) approximated from the proxy-inferred climate zones from (Boucot et al., 2013; Scotese, 2016). Blue: tropical/boreotropical (75 % tree, 20 % grass/shrub, 5 % bare soil), yellow: arid (15 %, 35 %, 60 %), green: warm temperate (70 %, 20 %, 10 %), cyan: cold temperate (65 %, 15 %, 20 %), grey: polar (10 %, 25 %, 65 %)

February 5, 2021, 7:43pm



... Fig.S1 continued

February 5, 2021, 7:43pm



... Fig. S1 continued

February 5, 2021, 7:43pm

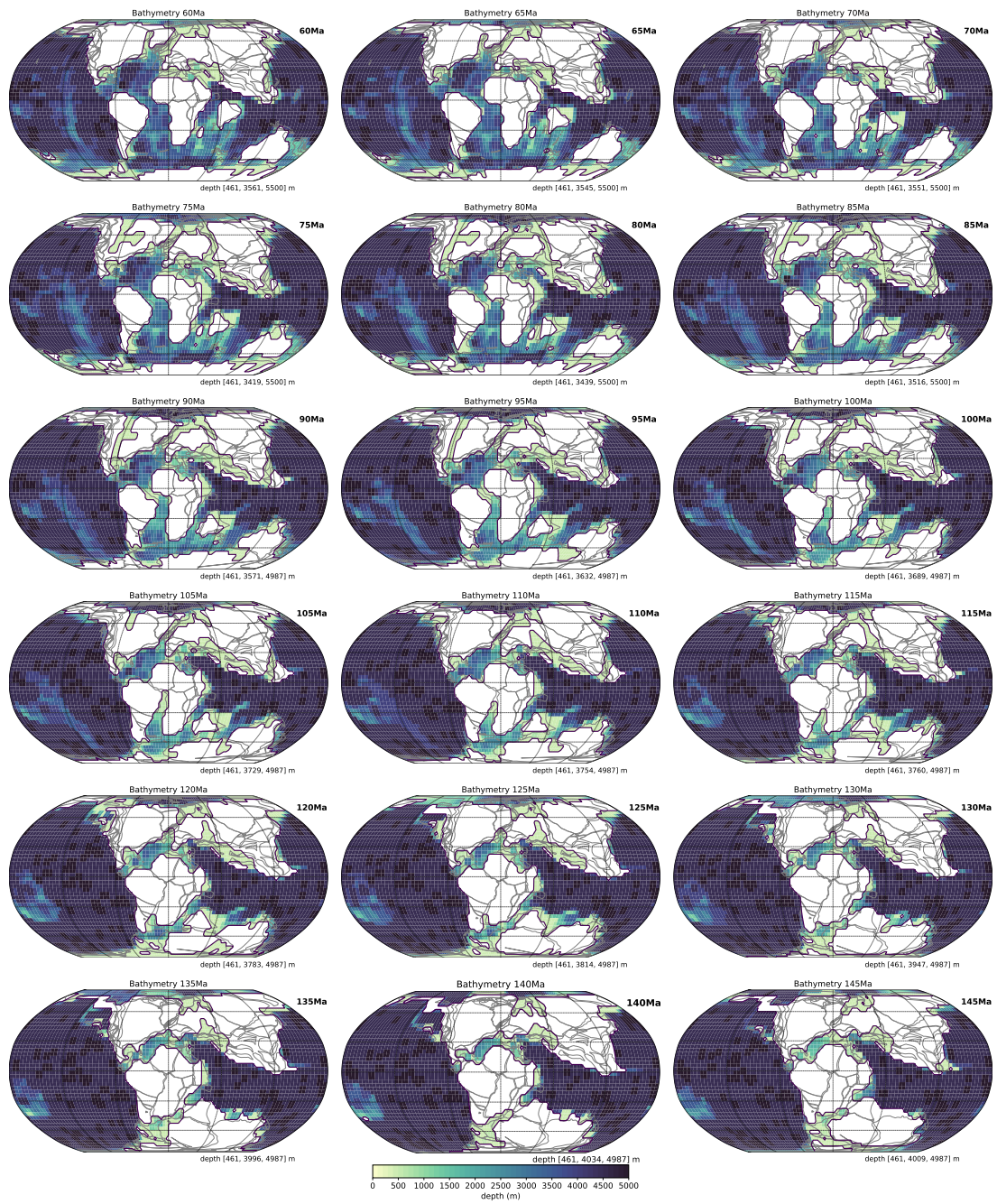
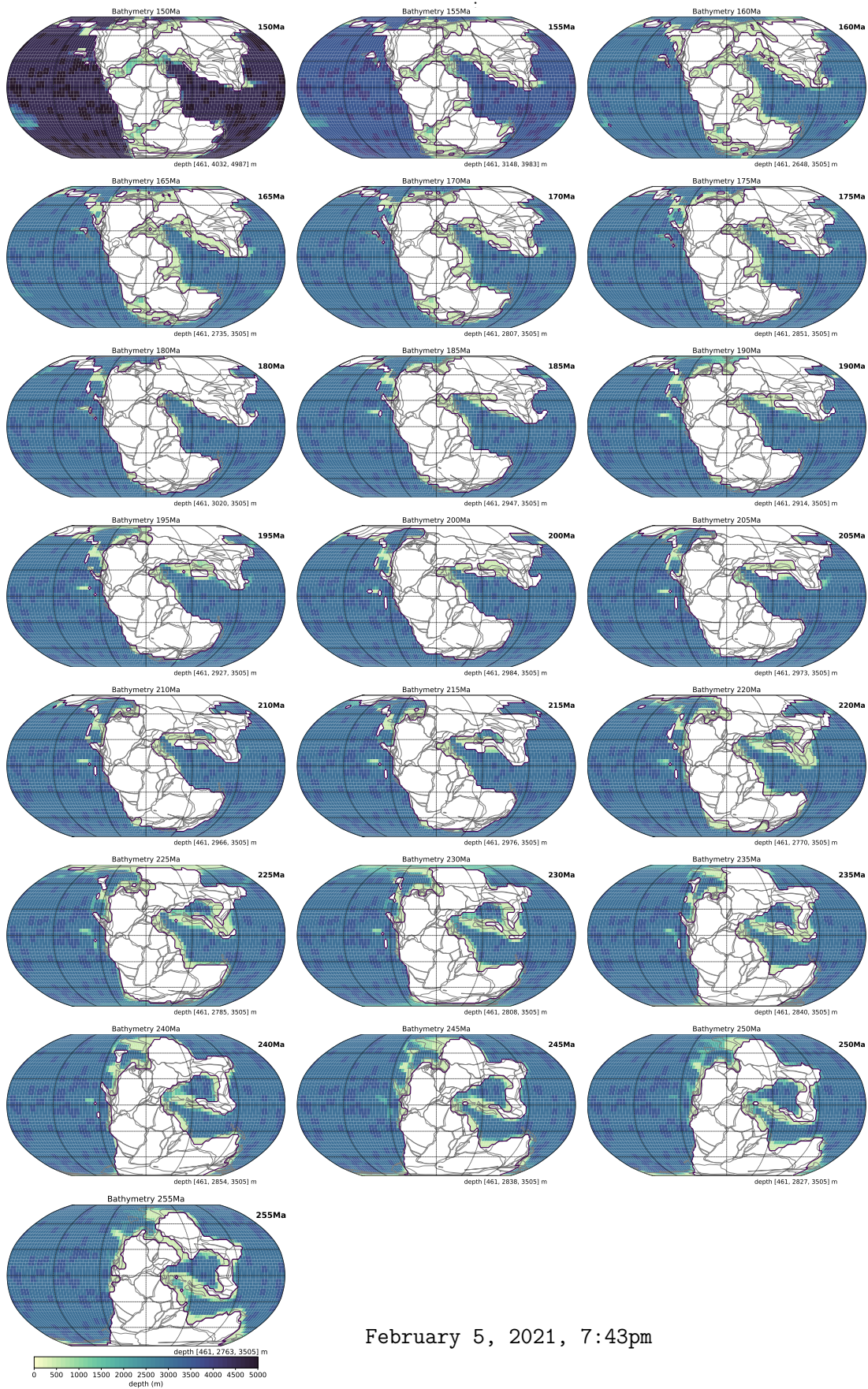


Figure S2. Bathymetry for all timeslices as implemented in the simulations based on Scotese and Wright (2018). Adjustments were made due to model requirements (see Supp. Sec. 1 for further explanation).

February 5, 2021, 7:43pm



February 5, 2021, 7:43pm

... Fig. S2 continued

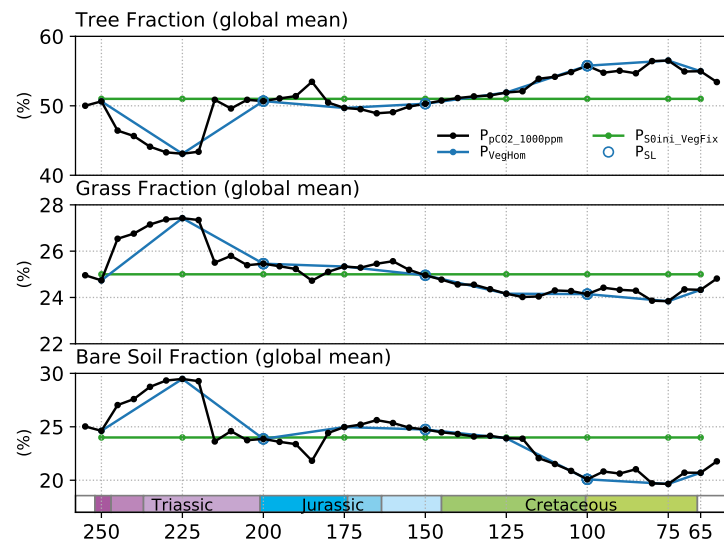


Figure S3. Global mean fractions of tree, grass/shrub and bare soil land cover fraction in different boundary condition pathways.

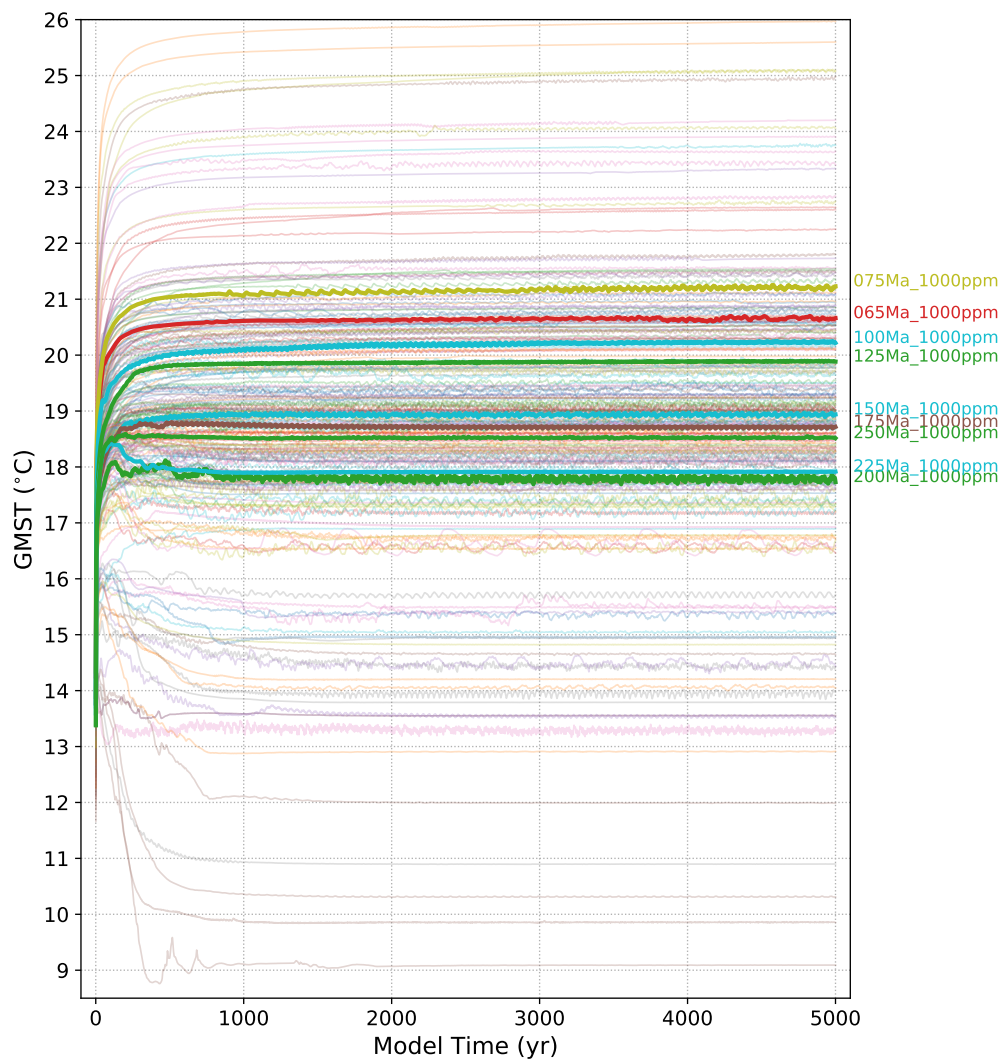


Figure S4. Global mean surface air temperature (GMST) during spin-up for all simulation runs. For the highlighted representative subset of runs ($P_{\text{pCO}_2, 1000\text{ppm}}$ for $T_{25\text{Myr}}$), mean ocean temperatures and salinity timeseries are shown in Fig. S21.

February 5, 2021, 7:43pm

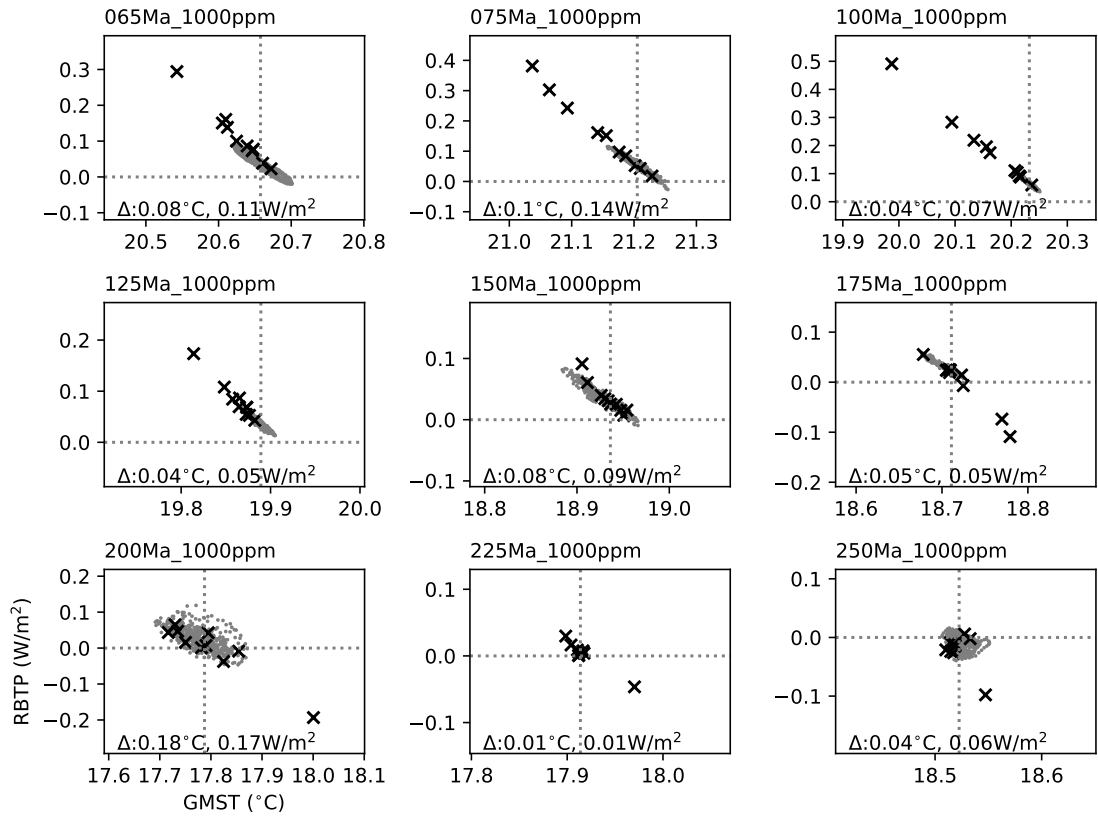


Figure S5. Global mean top-of-the-atmosphere radiation balance (RBTP) over the global mean surface air temperature (GMST) during spinup (Gregory Plot), for the $T_{25\text{Myr}}$ timeslices of the $P_{\text{pCO}_2, 1000\text{ppm}}$ pathway. Crosses represent 500 yr timesteps from model year 500 to 5000, while grey dots represent annual data over the last 500 years of the simulations (years 4500–5000). The maximum variation of GMST and RBTP over the last 500 years is also given in each panel. The vertical dashed line indicates the average GMST over the last 500 years.

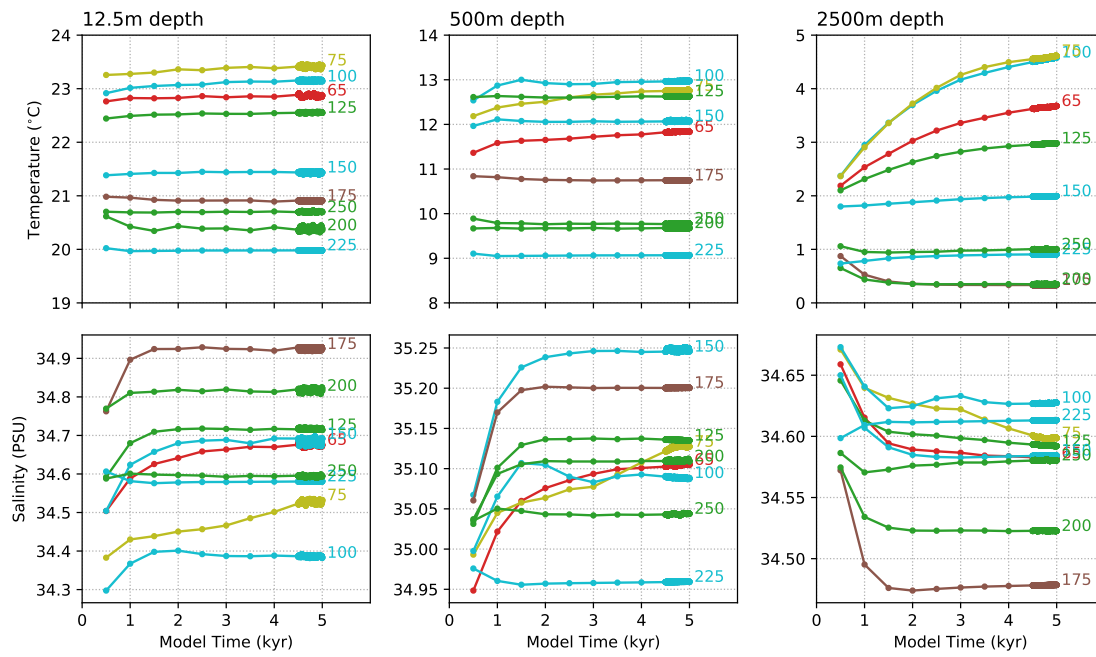


Figure S6. Global mean seawater temperature and salinity at three depth levels during spinup for a subset of the simulation runs ($P_{\text{pCO}_2.1000\text{ppm}}$ for $T_{25\text{Myr}}$, also see Figs. S4,S5).

February 5, 2021, 7:43pm

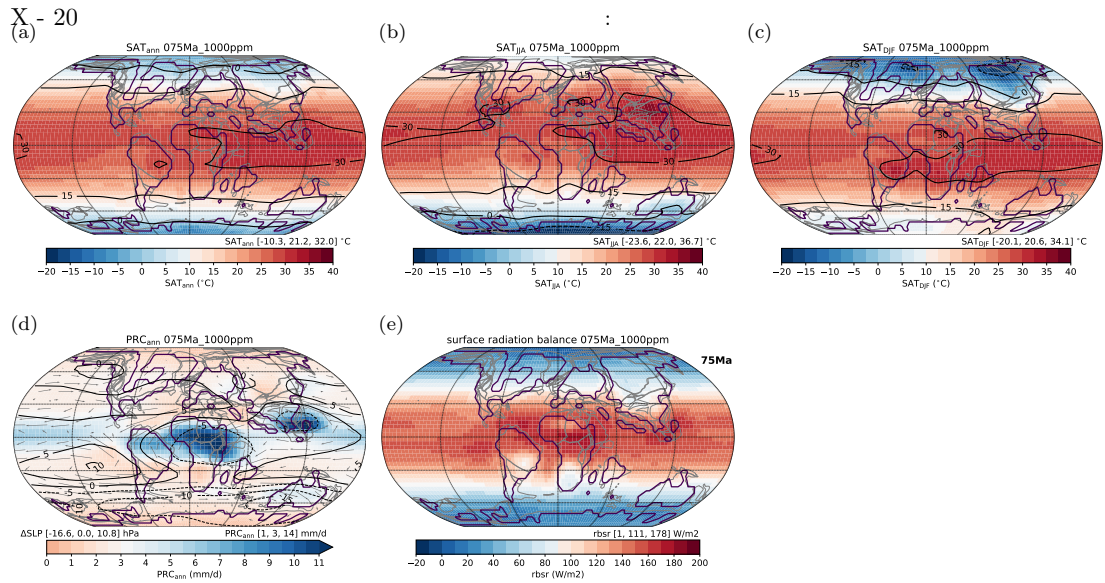


Figure S7. Annual mean surface air temperatures (a), precipitation rates (d) and surface radiation balance (e) for the P_{pc02_1000ppm} pathway at 75 Ma. Seasonal JJA and DJF surface air temperatures (b,c) for the same simulation. Similar plots are included in the accompanying data repository for all runs (AllRuns_Maps.pdf)

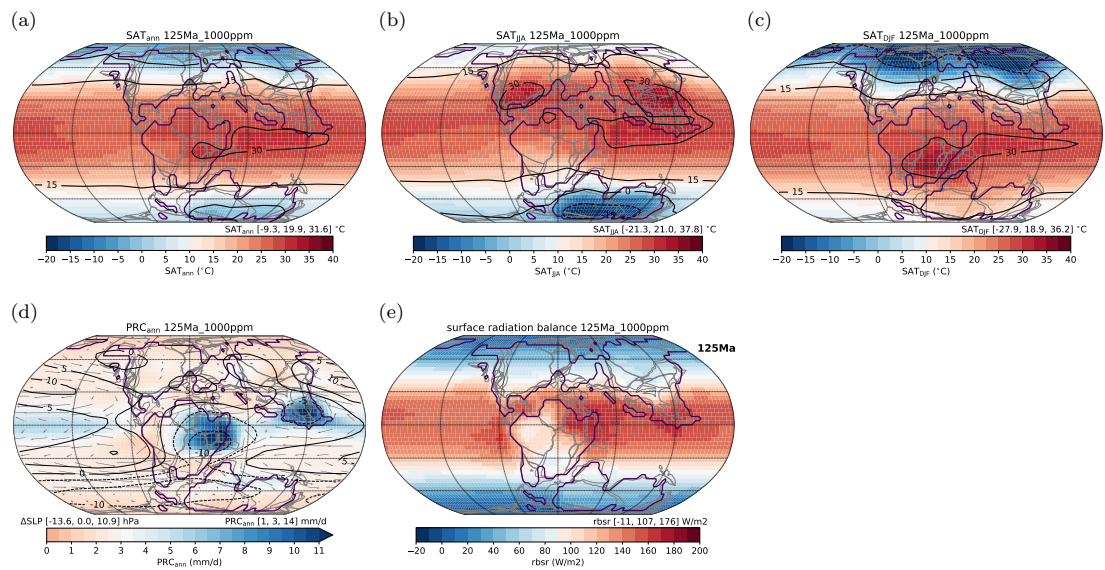


Figure S8. Same as Fig.S7 but at 125 Ma

February 5, 2021, 7:43pm

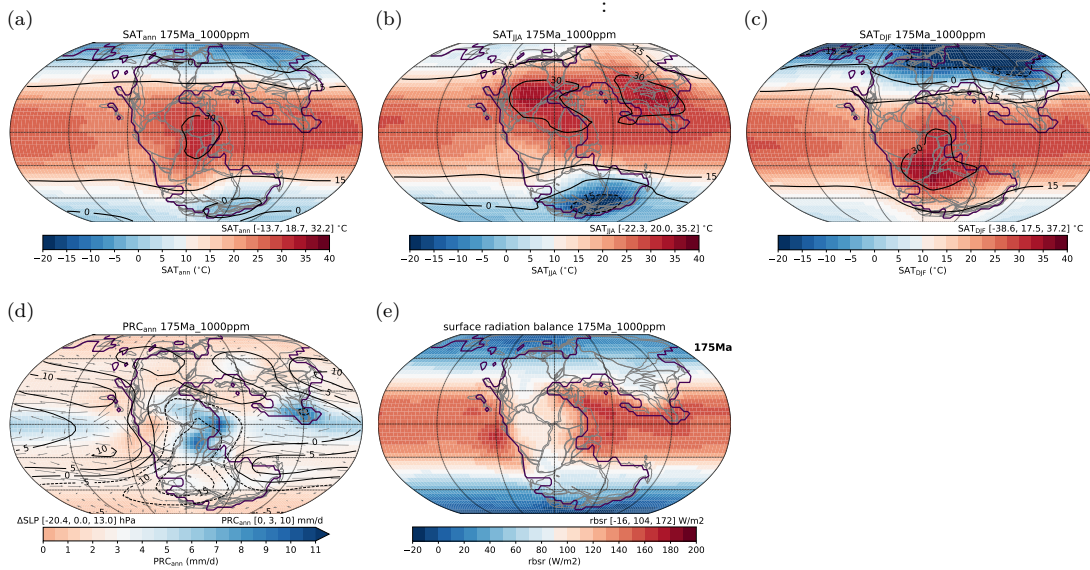


Figure S9. Same as Fig. S7 but at 175 Ma

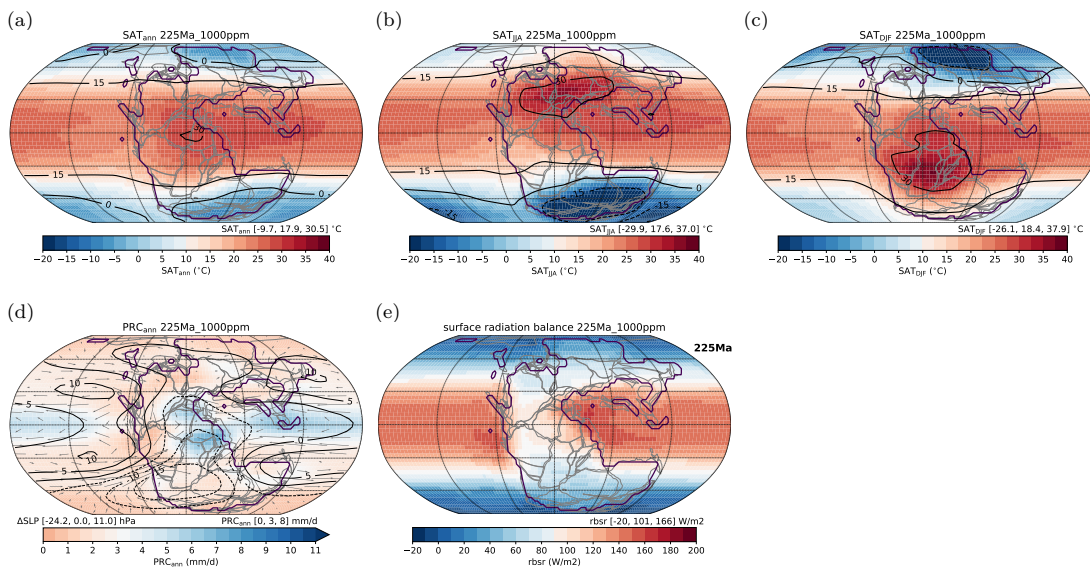


Figure S10. Same as Fig. S7 but at 225 Ma

February 5, 2021, 7:43pm

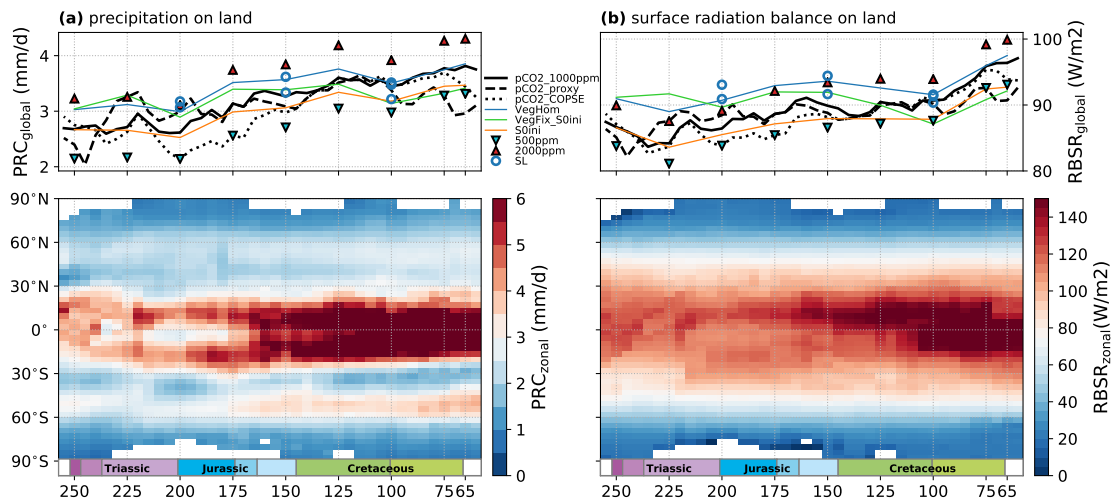


Figure S11. Zonal and global mean precipitation (a) and surface radiation balance (b) on land. Zonal mean values in the bottom panels are from the $P_{pCO_2,1000ppm}$ baseline pathway, while the top panels also include results from the other pathways.

February 5, 2021, 7:43pm

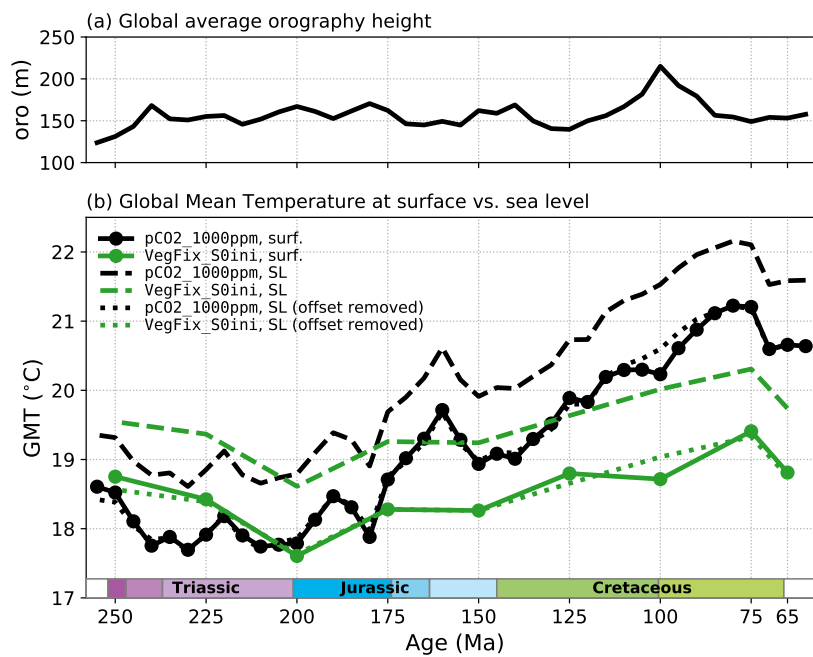


Figure S12. (a): Globally averaged height of the orography (Scotese & Wright, 2018) as implemented in the CLIMBER-3 α model simulations. (b): Global mean surface air temperatures (GMST, solid lines) compared to lapse-rate corrected global mean temperatures at sea-level (dashed lines), for $P_{pCO_2_1000ppm}$ (black) and P_{VegFix_S0ini} (green). Dotted lines are also sea-level temperatures, but the offset to GMST at 150 Ma was removed to illustrate differences in the evolution through time.

February 5, 2021, 7:43pm

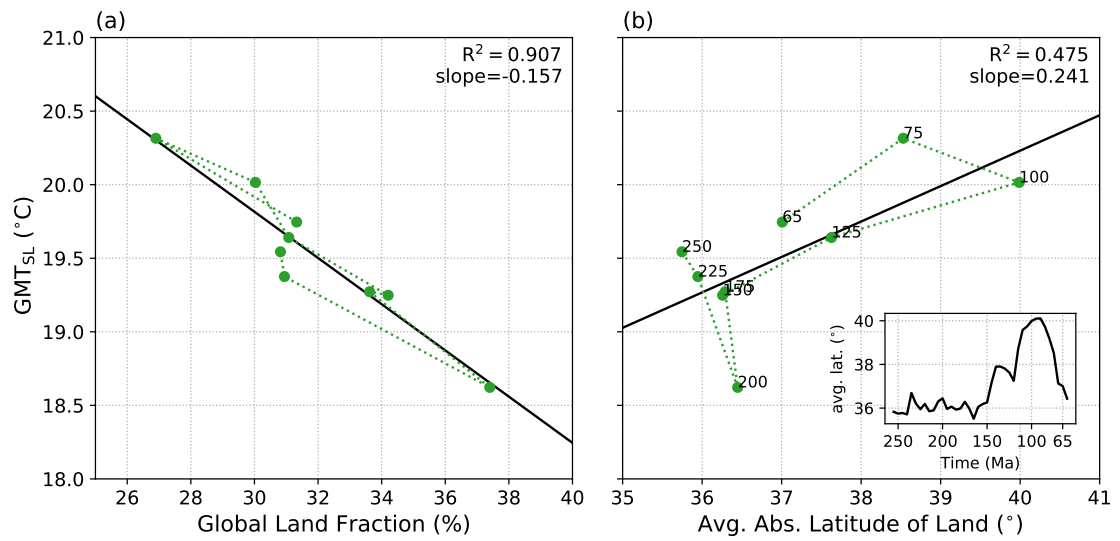


Figure S13. Correlation of lapse-rate corrected global mean air temperatures at sea level (GMT_{SL}) with (a) the global land area fraction and (b) the average absolute latitude of land area the time evolution of which is also shown in the inset. For the simulations of the P_{VegFix_S0ini} pathway.

February 5, 2021, 7:43pm

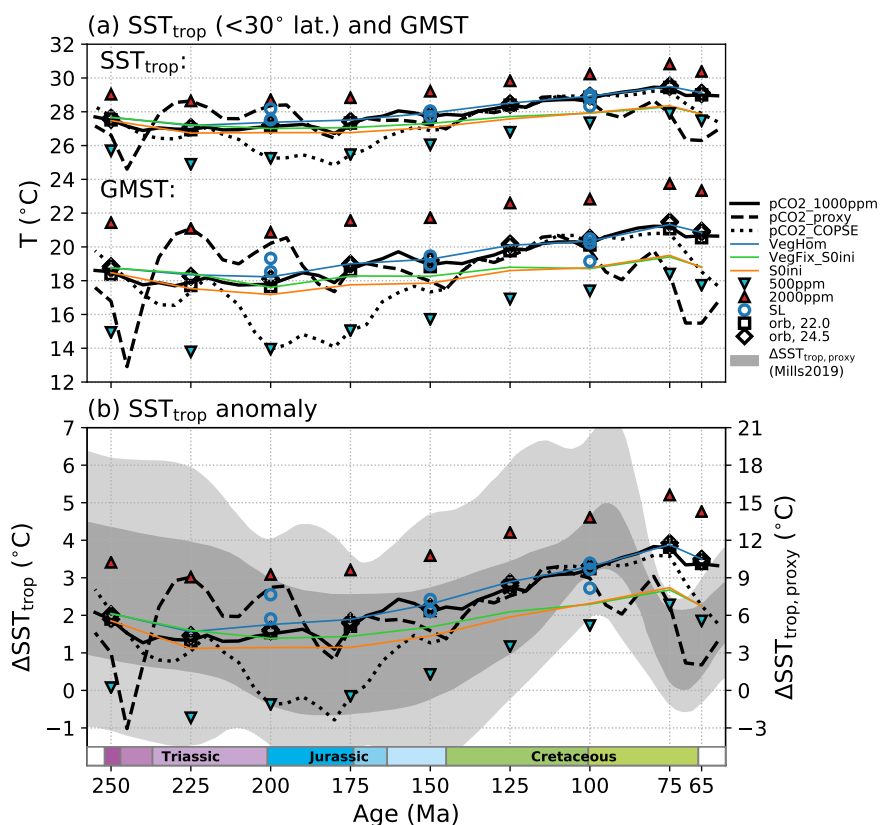


Figure S14. (a): Simulated global mean surface air temperatures and tropical sea surface temperatures (latitudes < 30°). (b): The gray shading indicates proxy-based tropical SST anomalies ($\Delta\text{SST}_{\text{trop}}$, relative to the present) from (Mills et al., 2019). For this the GMST envelope from Mills et al. (2019, Fig. 4a) was scaled back to ($\Delta\text{SST}_{\text{trop}}$) using Eq. 1 from the supplement to (Mills et al., 2019). Lines and markers indicate $\Delta\text{SST}_{\text{trop}}$ obtained for the CLIMBER-3 α simulations, using the the scaling factor of 1.79 (as determined in Fig. S15). See Supp. Sec. 6 for further explanation.

February 5, 2021, 7:43pm

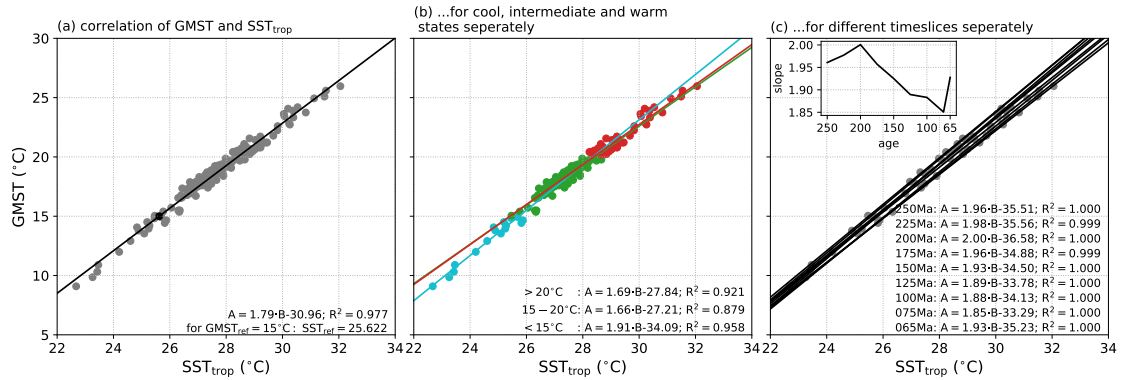


Figure S15. Correlation of simulated global mean surface air temperatures and tropical sea surface temperatures (latitudes $< 30^{\circ}$). (a): For all simulations of the $P_{pCO_2,1000ppm}$ pathway and all pCO_2 sensitivity experiments (each represented by one gray dot). (b): For cool ($GMST < 15^{\circ}C$, cyan), intermediate ($15^{\circ}C < GMST < 20^{\circ}C$, green) and warm ($GMST > 20^{\circ}C$, red) states separately. (c): Separately for the T_{25Myr} timeslices including their climate states at $pCO_2 = [250, 500, 1000, 1500, 2000, 4000]$ ppm. The inset indicates the obtained scaling factor for these timeslices. See Supp. Sec. 6 for further explanation.

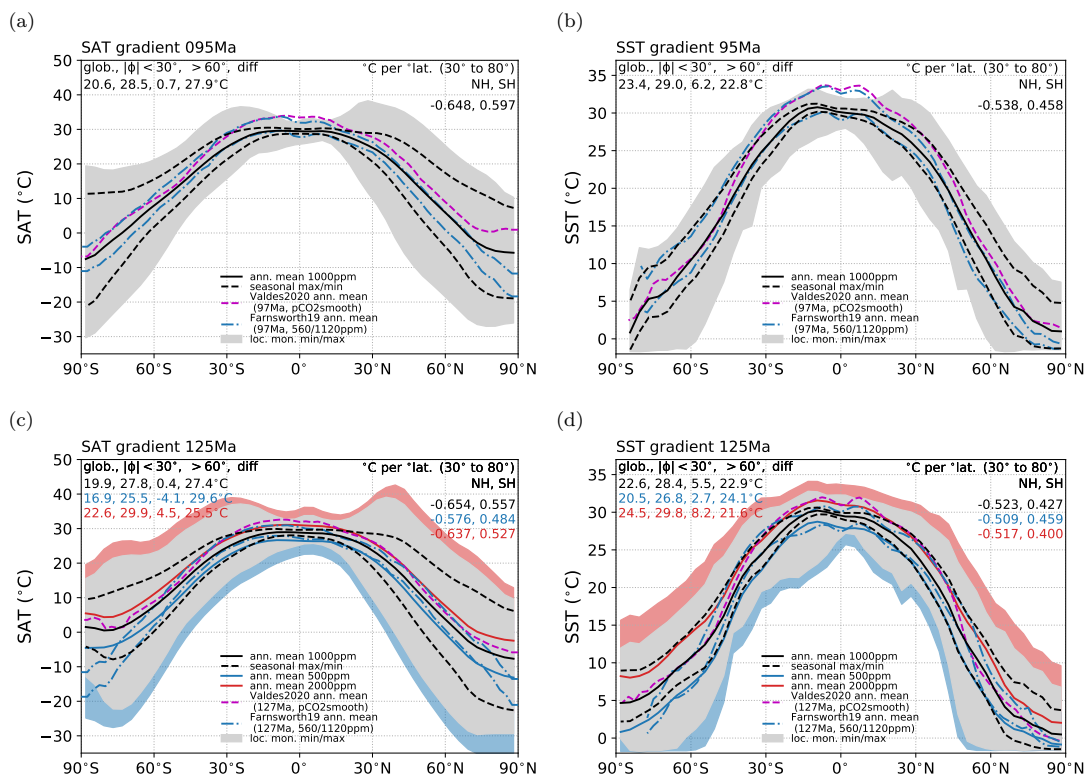


Figure S16. Simulated zonal mean SAT (left) and SST (right) profiles for the 95 and 125 Ma timeslices. For 1000ppm: annual mean (solid black line), seasonal min./max. (dashed black lines). For 500/1000/2000 ppm: monthly min./max. (blue/grey/red shading). Additionally annual mean for 500 ppm (solid blue line), 2000 ppm (solid red line), Valdes et al. (2020) data (dashed magenta line, `pCO2_smooth`), Farnsworth et al. (2019a) data (dashed blue line). Upper left corners: Numerical values of the global, low latitude ($<30^\circ$), high latitude ($>60^\circ$) averages and the difference between the latter two. Upper right corners: average meridional temperature gradient in °C per °lat. between 30 and 80° latitude. Similar plots for all 40 Mesozoic timeslices are included in the accompanying data repository (`AllTimeslices_MeridionalGradient_SST.pdf` and `AllTimeslices_MeridionalGradient_SST.pdf`).

February 5, 2021, 7:43pm

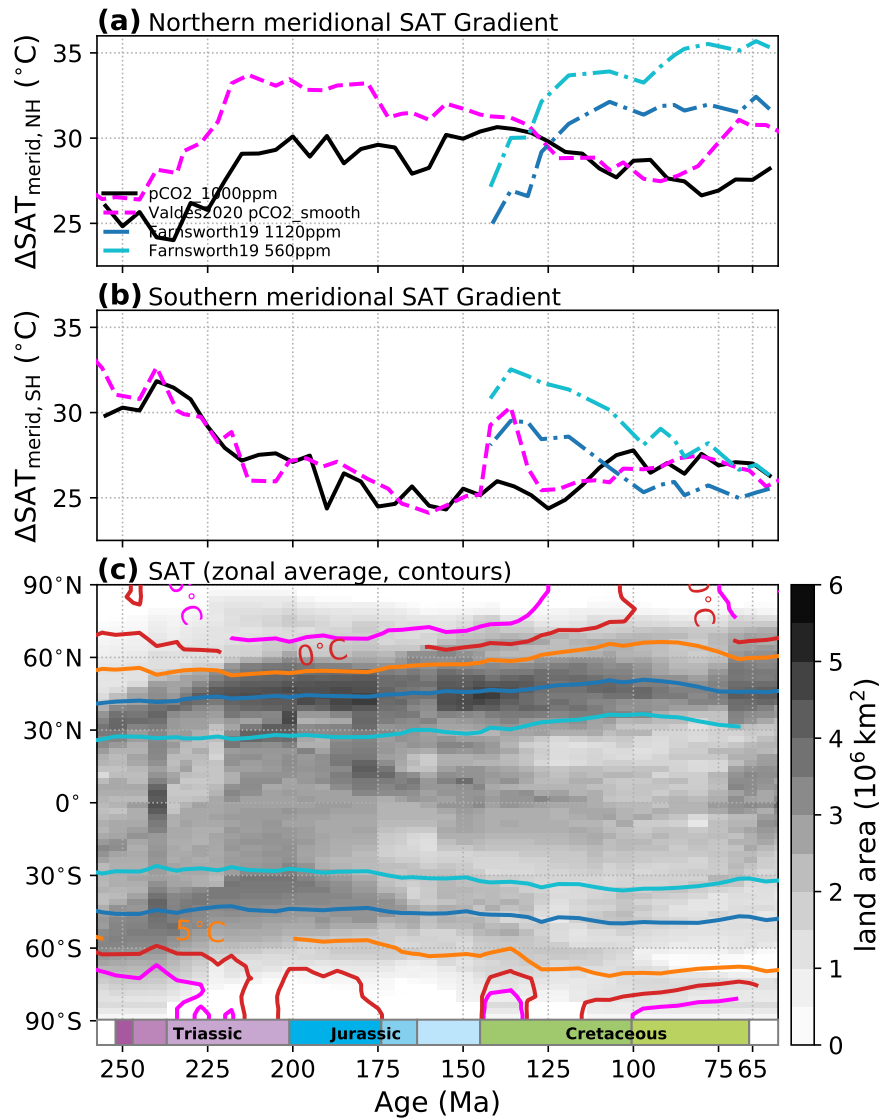


Figure S17. Evolution of simulated zonal mean Surface Air Temperatures (SAT, c) and the thermal contrast between low-latitude and northern (a) and southern (c) high-latitude regions for data from Valdes et al. (2020) and Farnsworth et al. (2019a). (For comparison with Fig. 5.) (c): Contours indicate annual zonal mean SAT for all runs of the pCO₂ smooth pathway from Valdes et al. (2020). The grey shading indicates the changing latitudinal distribution of land area in the model paleogeographies. (a,b): Annual zonal mean SAT difference between low-latitude (<30° lat.) and northern (a) and southern (b) high-latitude regions (>60° lat.) through time.

February 5, 2021, 7:43pm

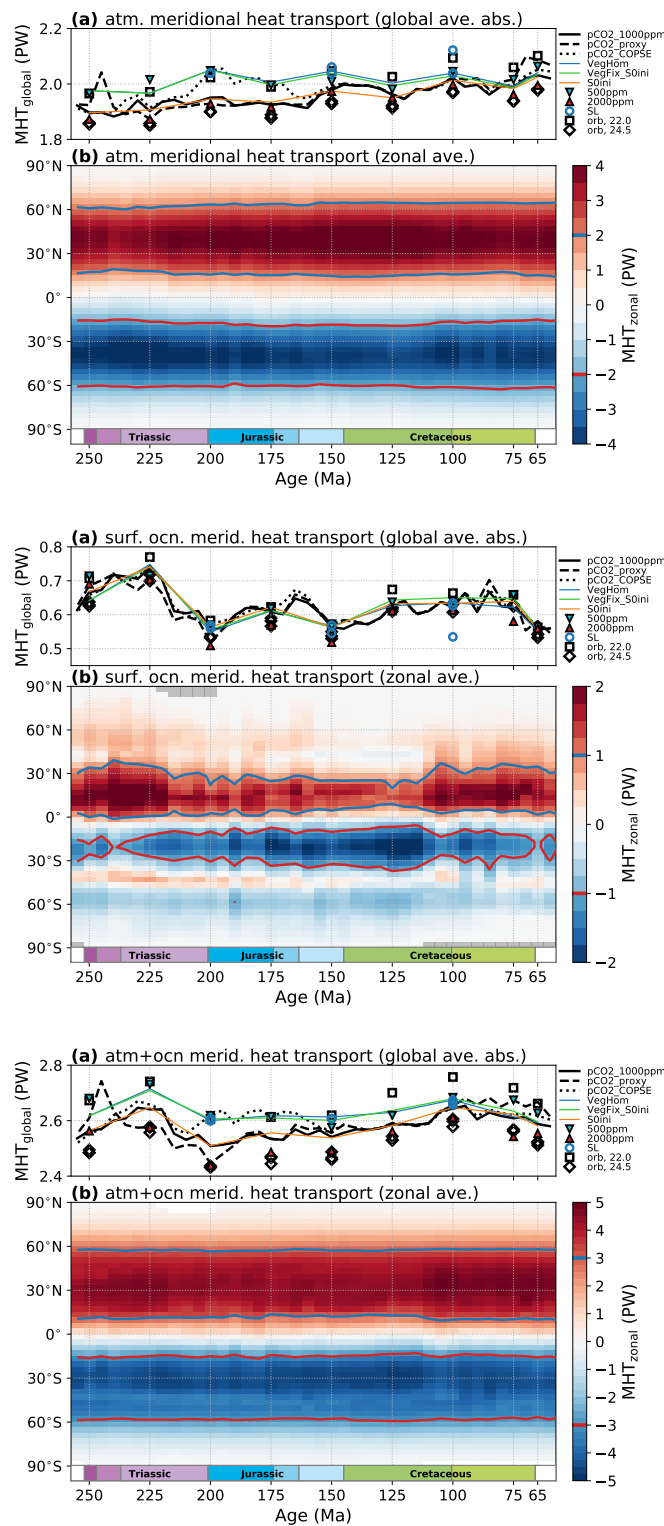


Figure S18. Meridional heat transport (MHT) by the atmosphere (top), ocean (middle) and in total (bottom). For the respective bottom panels, zonal mean values from all timeslices of the $P_{pCO2.1000ppm}$ pathway have been aggregated. The upper panels indicate global mean values of the absolute MHT values.

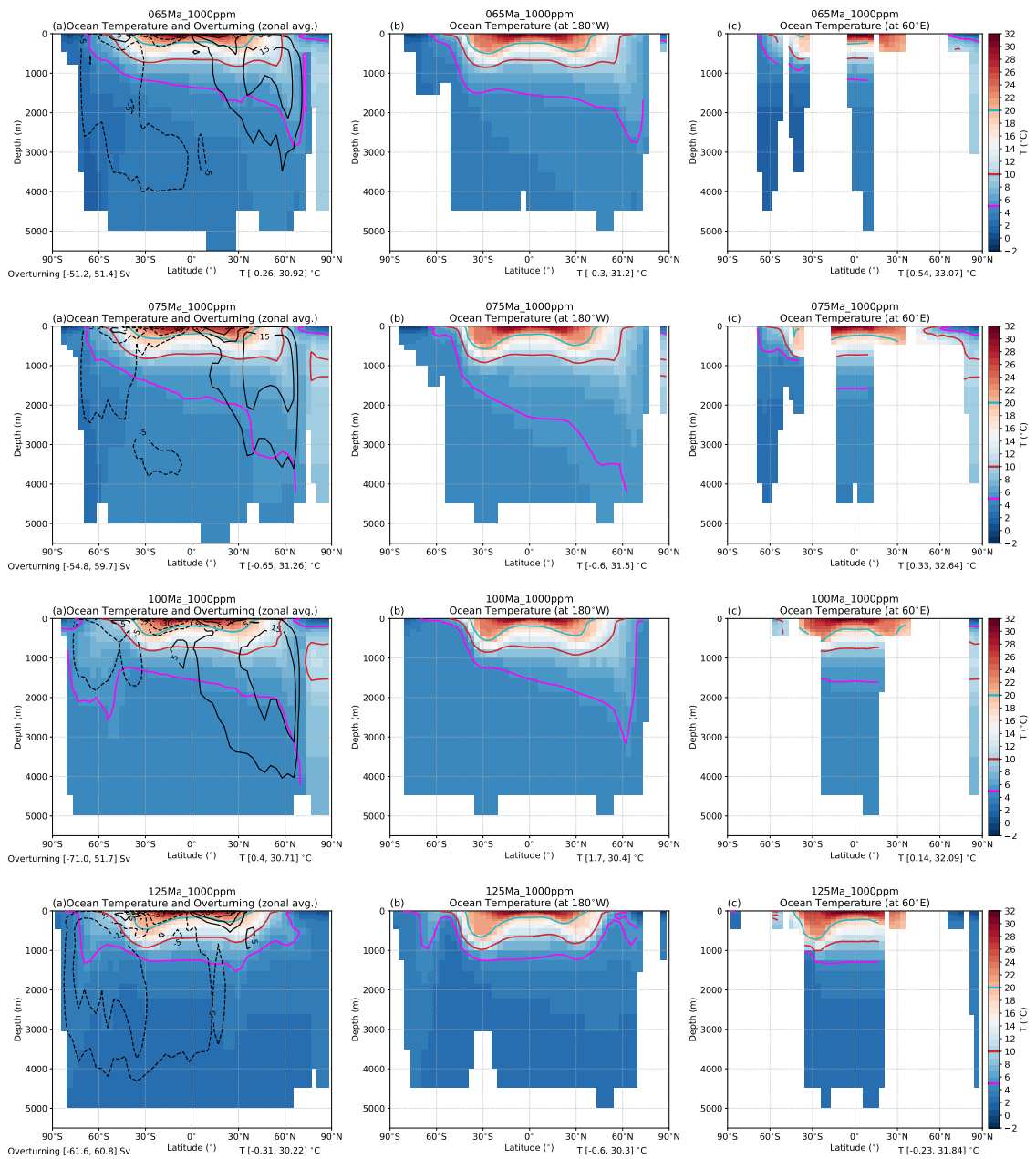
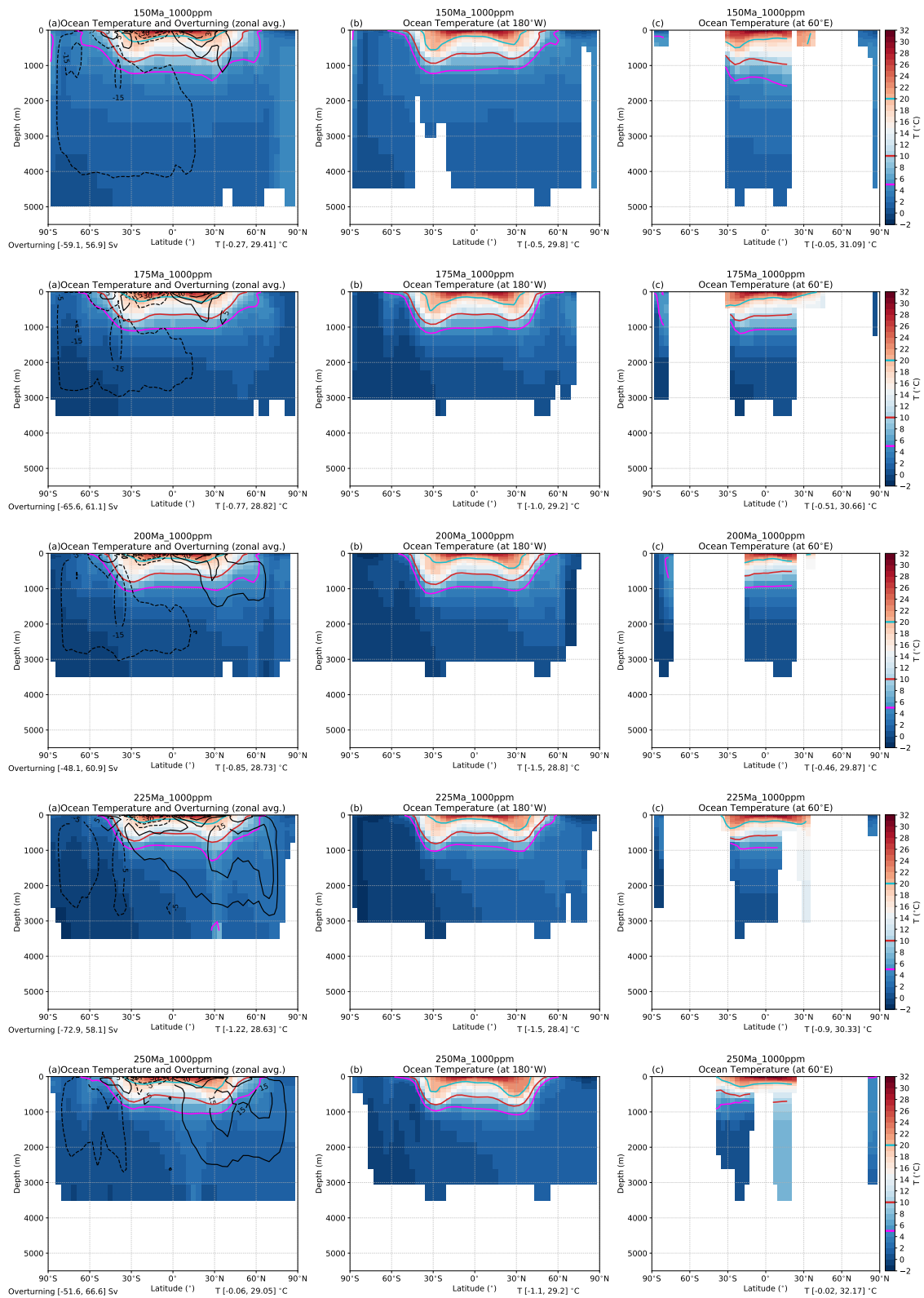


Figure S19. Meridional cross-sections showing the annual mean ocean temperatures as a zonal mean (a), at 180°W (b) and 60°E (c). In (a), the black contours indicate the global mean meridional overturning streamfunction.

February 5, 2021, 7:43pm



... Fig. S19 continued
February 5, 2021, 7:43pm

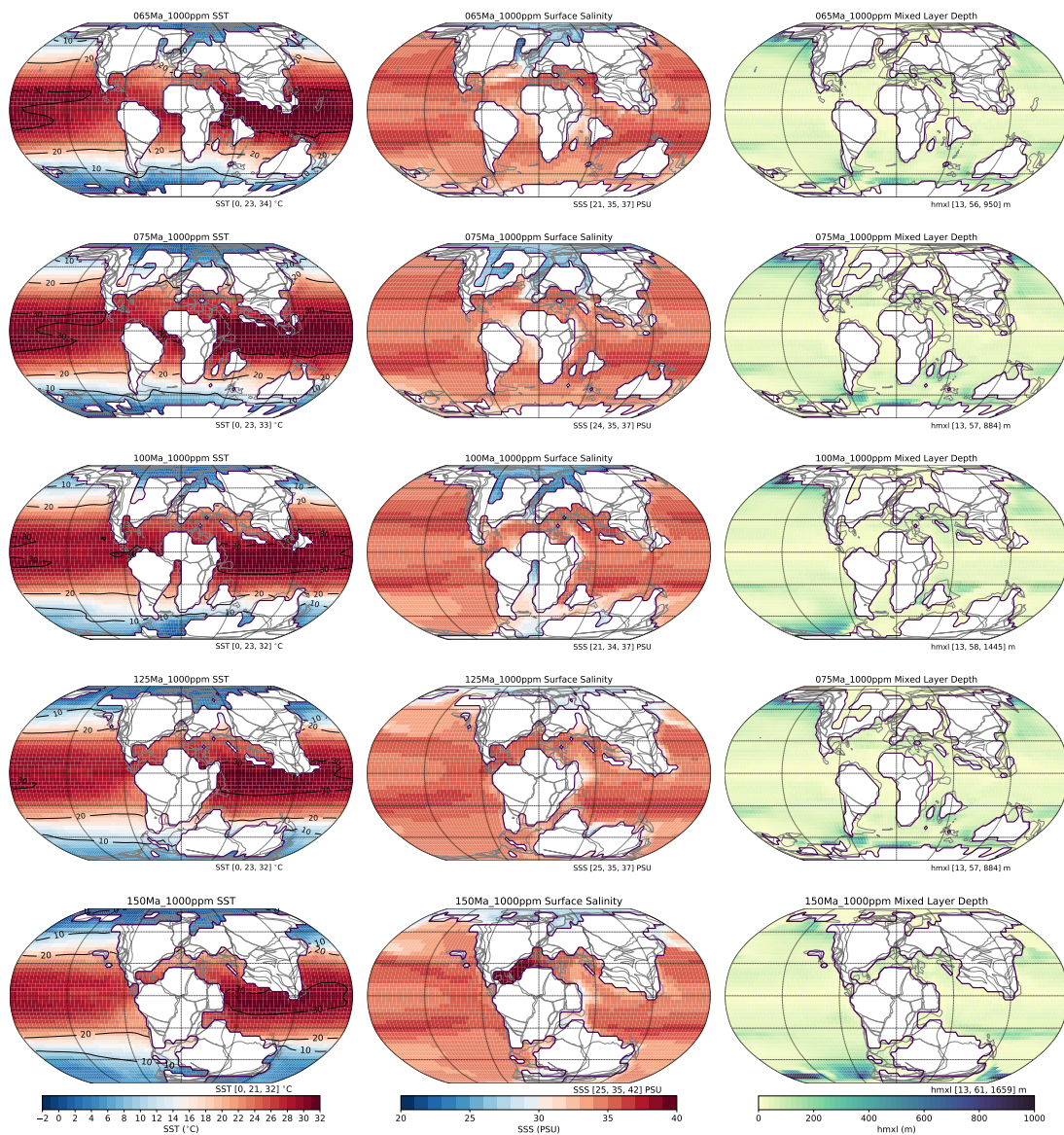
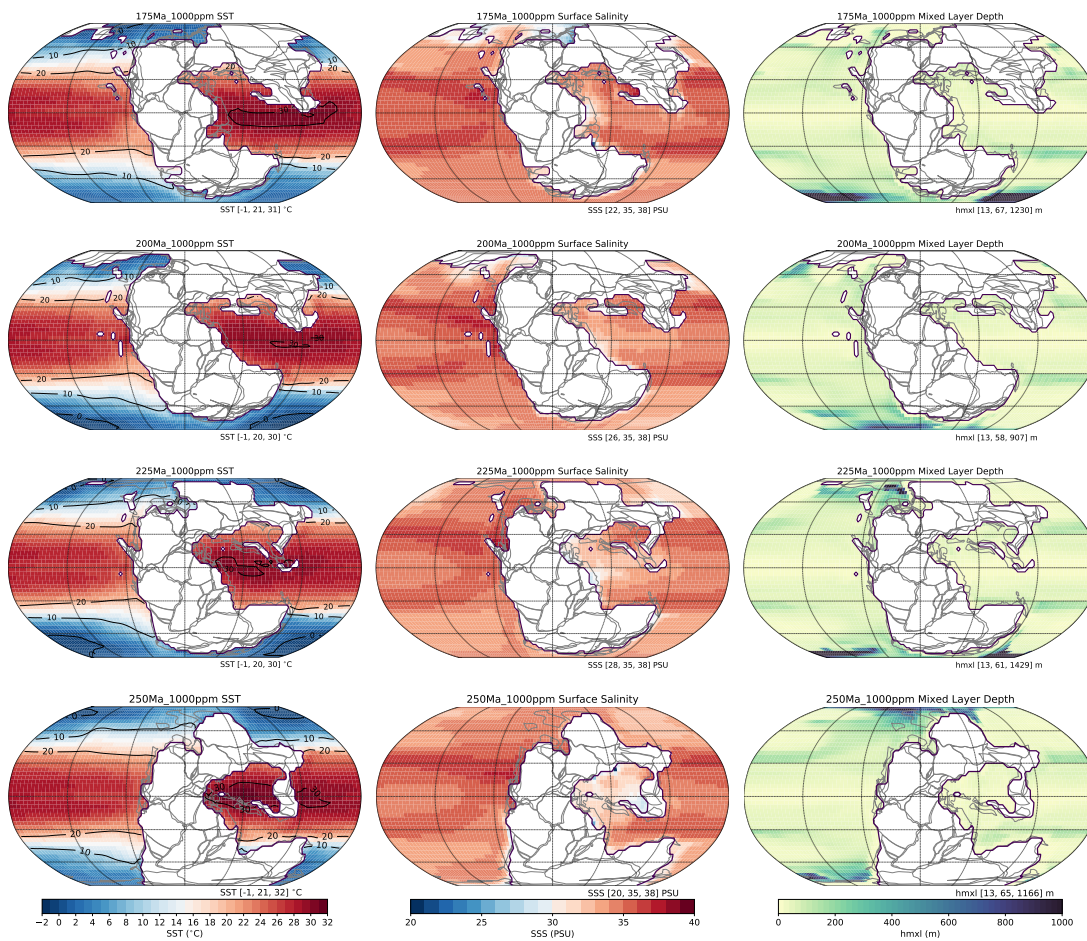


Figure S20. Annual mean Sea Surface Temperatures (left), Surface Salinity (middle) and Mixed Layer Depth (right). For the P_{pc02_1000ppm} pathway.

February 5, 2021, 7:43pm



... Fig. S20 continued

February 5, 2021, 7:43pm

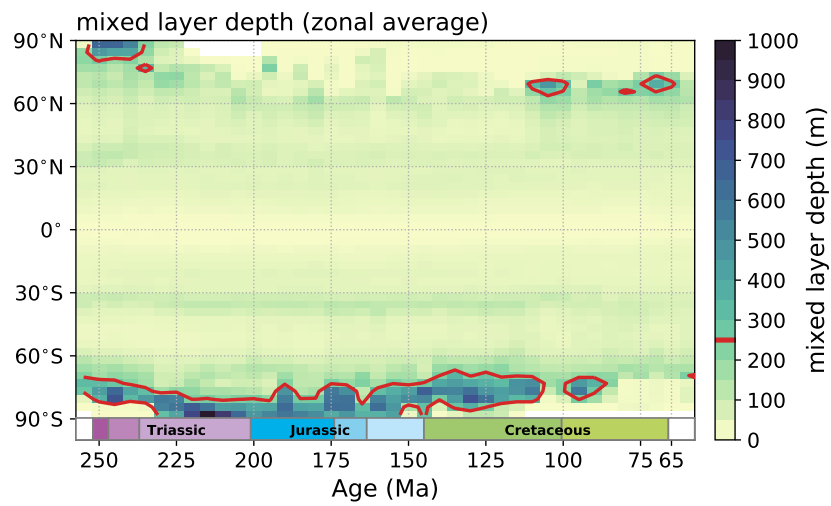


Figure S21. Zonal and annual mean mixed layer depth, aggregated for the simulations of the $P_{pc02_1000ppm}$ pathway.

February 5, 2021, 7:43pm

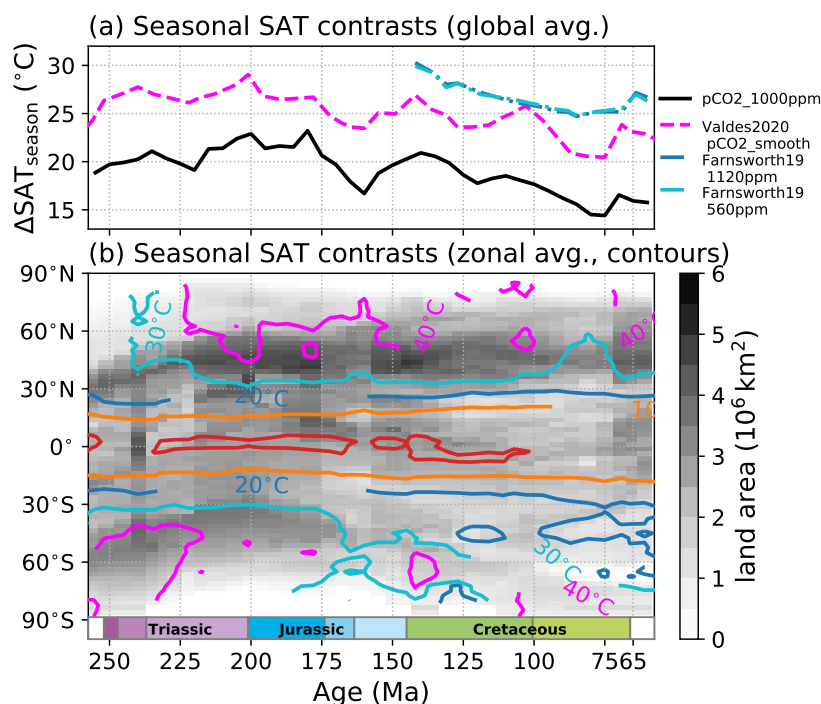


Figure S22. Simulated seasonality of surface air temperatures (SAT). With data from Valdes et al. (2020, $\text{P}_{\text{pCO}_2_{\text{smooth}}}$ pathway) and Farnsworth et al. (2019a) for comparison with the results from CLIMBER-3 α presented in Fig. 3. (b): Zonal averages of the seasonal differences (max. difference between the DJF, MAM, JJA and SON seasonal averages) for all timeslices of the (Valdes et al., 2020) simulations (contours). The grey shading shows the changing latitudinal land area distribution implemented in the simulations. (a): Globally averaged continental SAT seasonality.

February 5, 2021, 7:43pm

A.II Supplementary Information to P.II

SUPPLEMENTARY INFORMATION for

“Modes of Pangean Lake-Level Cyclicality Driven by Astronomical Pacing
Modulated by Continental Position and $p\text{CO}_2$ ”

Landwehrs, Feulner, Willeit, Petri, Sames, Wagreich, Whiteside and Olsen
([2022](#))

1. Paleogeographies

Paleogeographies and paleo-locations (Figs. S1–S2, Tab. S1) were generated with pyGPlates and GPlates using the data provided by Marcilly et al. (2021) and Cao et al. (2017, 2018). A paleomagnetic reference frame was used (instead of a mantle/hotspot frame) to better constrain the climatically important paleolatitudinal positioning (as suggested by Marcilly et al. 2021 SI and Cao et al. 2018). In the case of the Cao et al. (2017) data, the plate rotation model was replaced with the modified one from Cao et al. (2018) (both based on Matthews et al. 2016). The present day location of the Somerset core (40.50576°N, 74.565386°W, Kent et al. 2017 Tab. 1) was used to track the approximate paleo-location of the Newark Basin. Similar to the approach of Chandra et al. (2021), paleo-elevations were set to 200 m for exposed lowland, 1700 m for mountain ranges, and furthermore to –200 m and –3200 m for shallow and deep marine regions, respectively. To remove the influence of uncertain local topography changes and enable comparability, the Newark-Hartford Basin neighbourhood was always set to the lowland elevation. The generated paleogeographies were provided to CLIMBER-X in 1°×1° resolution and regridded internally to the model resolution.

Table S1: Paleolocations ([lat,lon]) of the Newark Basin and other discussed localities in the two employed paleogeographic reconstructions.

Age (Ma)	Newark B. (Marcilly2021)	. (Cao201718)	Colorado P. (Marcilly2021)	. (Cao201718)	Junggar B. (Marcilly2021)	. (Cao201718)	Germanic B. (Marcilly2021)	. (Cao201718)
190	[22.92, -23.31]	[22.31, -11.7]	[17.3, -52.76]	[15.02, -40.47]	[68.48, 107.28]	[70.59, 126.66]	[42.86, 14.13]	[44.9, 24.98]
195	[19.94, -24.34]	[19.37, -11.84]	[13.39, -52.98]	[12.0, -40.13]	[71.79, 102.83]	[73.3, 122.24]	[41.49, 10.07]	[42.97, 22.71]
200	[17.33, -25.33]	[16.43, -11.96]	[10.31, -53.46]	[8.98, -39.84]	[73.88, 95.35]	[75.88, 116.19]	[39.64, 6.76]	[40.98, 20.63]
205	[15.33, -23.52]	[14.58, -11.67]	[9.28, -51.7]	[8.09, -39.65]	[72.45, 85.95]	[75.55, 106.51]	[36.56, 7.9]	[38.56, 20.77]
210	[13.32, -21.78]	[12.73, -11.44]	[8.23, -50.0]	[7.2, -39.51]	[70.52, 78.4]	[74.83, 97.5]	[33.5, 9.0]	[36.14, 20.88]
215	[10.7, -20.31]	[10.09, -11.3]	[6.96, -48.58]	[5.86, -39.43]	[67.53, 70.72]	[73.4, 86.49]	[29.57, 9.9]	[32.79, 20.85]
220	[8.08, -18.95]	[7.45, -11.27]	[5.69, -47.23]	[4.51, -39.44]	[64.13, 65.27]	[71.47, 77.49]	[25.66, 10.77]	[29.45, 20.78]
225	[6.68, -17.33]	[6.01, -10.98]	[5.55, -45.64]	[4.29, -39.22]	[61.67, 64.43]	[69.19, 73.85]	[23.31, 12.68]	[27.06, 21.39]
230	[5.27, -15.77]	[4.56, -10.76]	[5.4, -44.07]	[4.05, -39.01]	[59.18, 63.95]	[66.84, 70.94]	[20.94, 14.52]	[24.66, 21.93]

Table S2: Overview of the ensemble of simulations.

Name	Timeslices (Ma)	$p\text{CO}_2$ (ppm)	Paleogeography	Orbital Forcing	Duration (kyr)
Baseline Experiments					
S_{Geo_1} (27 runs)	230:5:190	750, 1500, 3000	Geo_1 : Marcilly et al. (2021)	e, ε, ω (ecc+obl+per)	250
Alternative Paleogeography					
S_{Geo_2} (9 runs)	230:5:190	1500	Geo_2 : Cao et al. (2017, 2018)	e, ε, ω	250

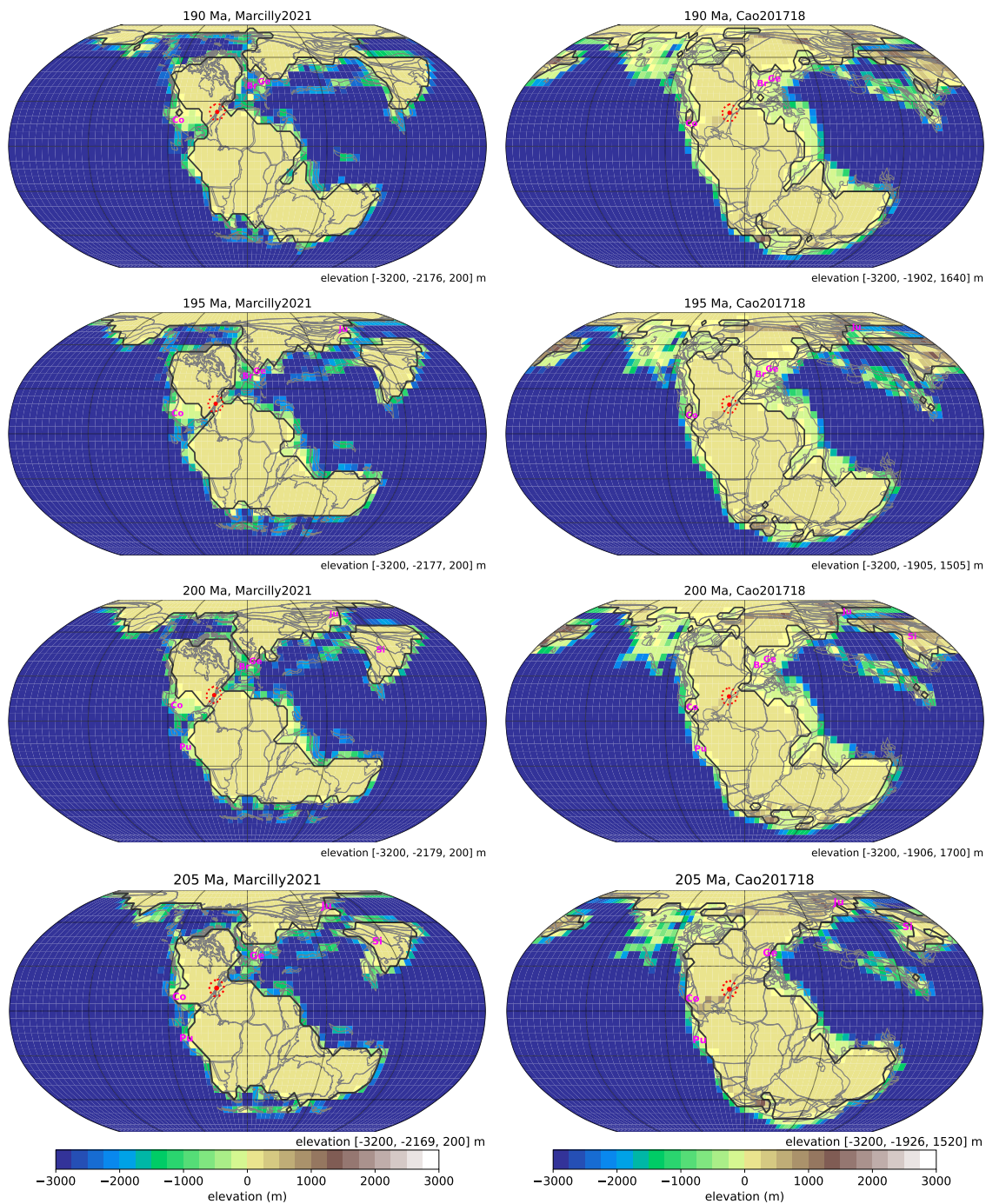


Figure S1: Bedrock elevation as implemented in the CLIMBER-X simulations. Based on paleogeographic reconstructions of Marcilly et al. (2021) (left) and Cao et al. (2017, 2018) (right). Black outlines are coastlines (elevation > 0), and grey lines indicate tectonic plates. Red dots and circles indicate the reconstructed location of the Newark Basin and the area considered for the regional analyses of model output. Locations of contemporaneous proxy localities discussed in Landwehrs et al. (2022) and Olsen et al. (2019) are added (Ge = Germanic Basin, Co = Colorado B., Ju = Junggar B., Br = Bristol Channel B., Si = Sichuan B., Pu = Pucara B.). Numbers in brackets indicate minimum, mean and maximum elevations.

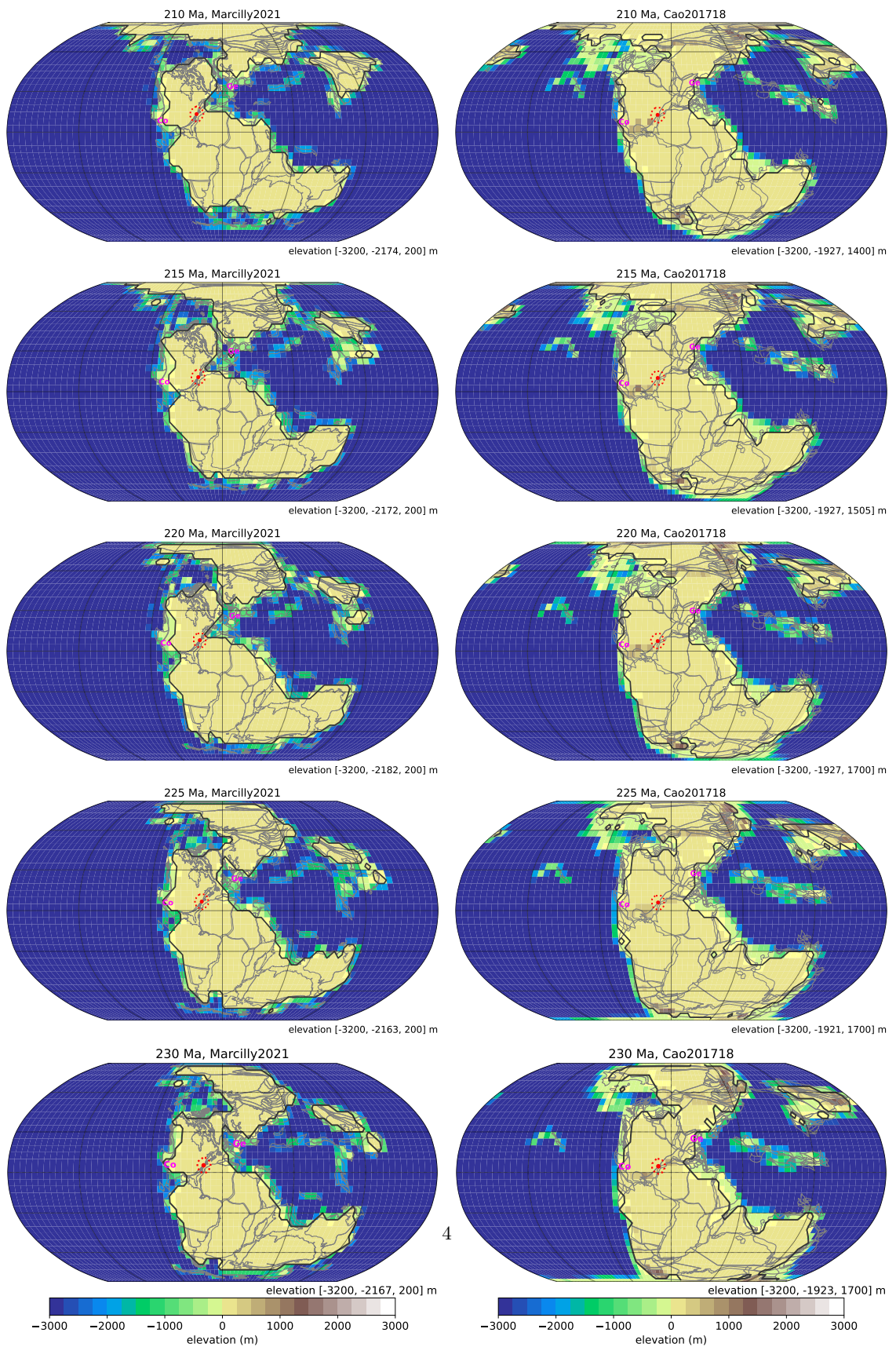


Figure S2: Continuation of Fig. S1.

14 **2. Supplementary Model Output Figures**

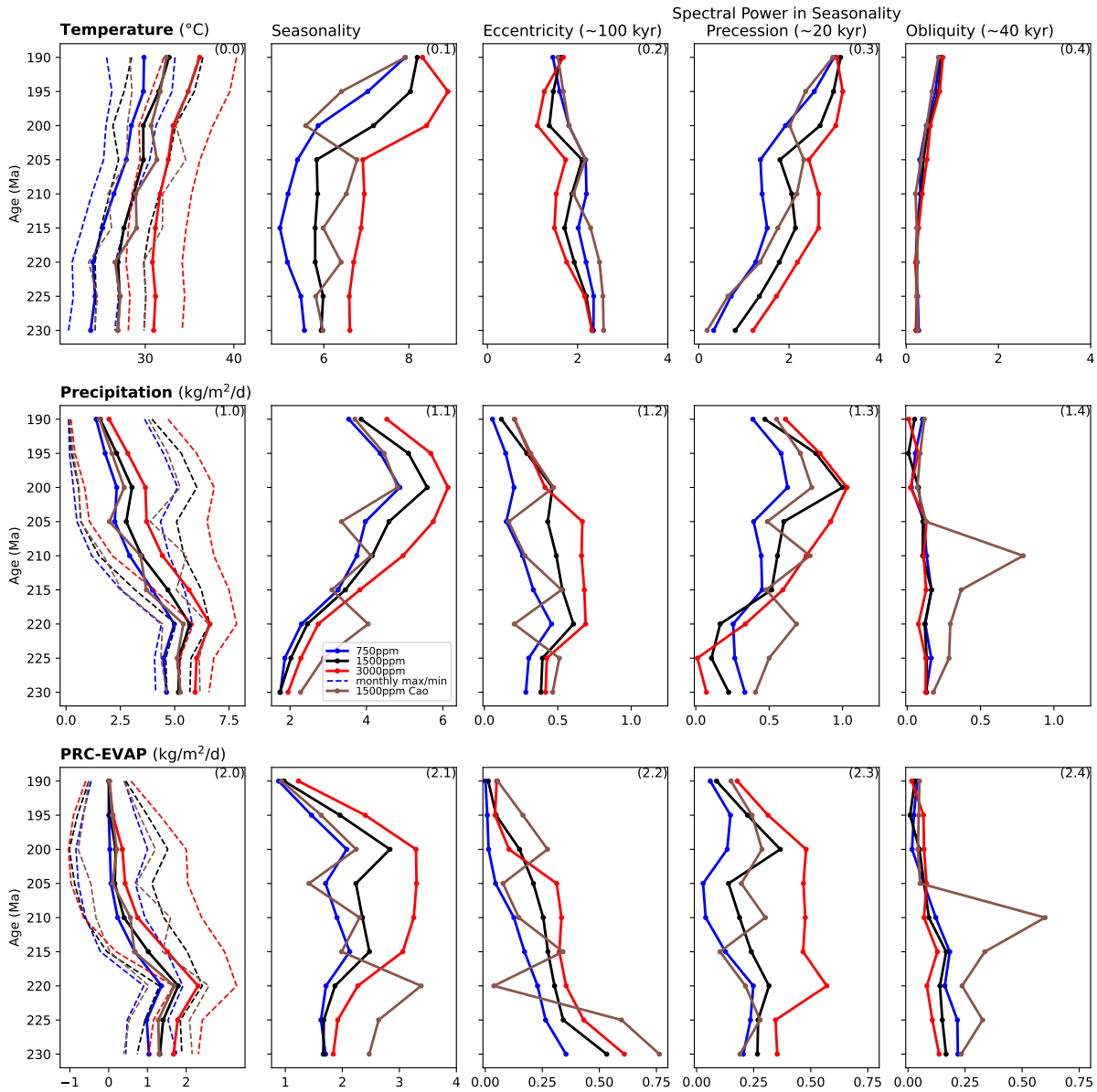


Figure S3: Summary of long-term trends in simulated average T, PRC and PRC-EVAP (first column) and their seasonality (second column) in the Newark-Hartford Basin area. The three rightmost columns show the amplitudes of the eccentricity (100 kyr), precession (40 kyr) and obliquity (20 kyr) signals in the seasonality timeseries. The data are aggregated from the ensemble of transient simulations (see e.g. Fig. S4). The regional values were obtained by averaging over the circular areas indicated in Fig. S1. The leftmost column shows annual mean values (solid lines) and maximum/minimum monthly mean values (dashed lines), e.g. the temperatures during the hottest and the coldest month. The amplitudes of the orbital response are determined from maxima in the seasonality timeseries Fourier spectra as indicated in Fig. S4.

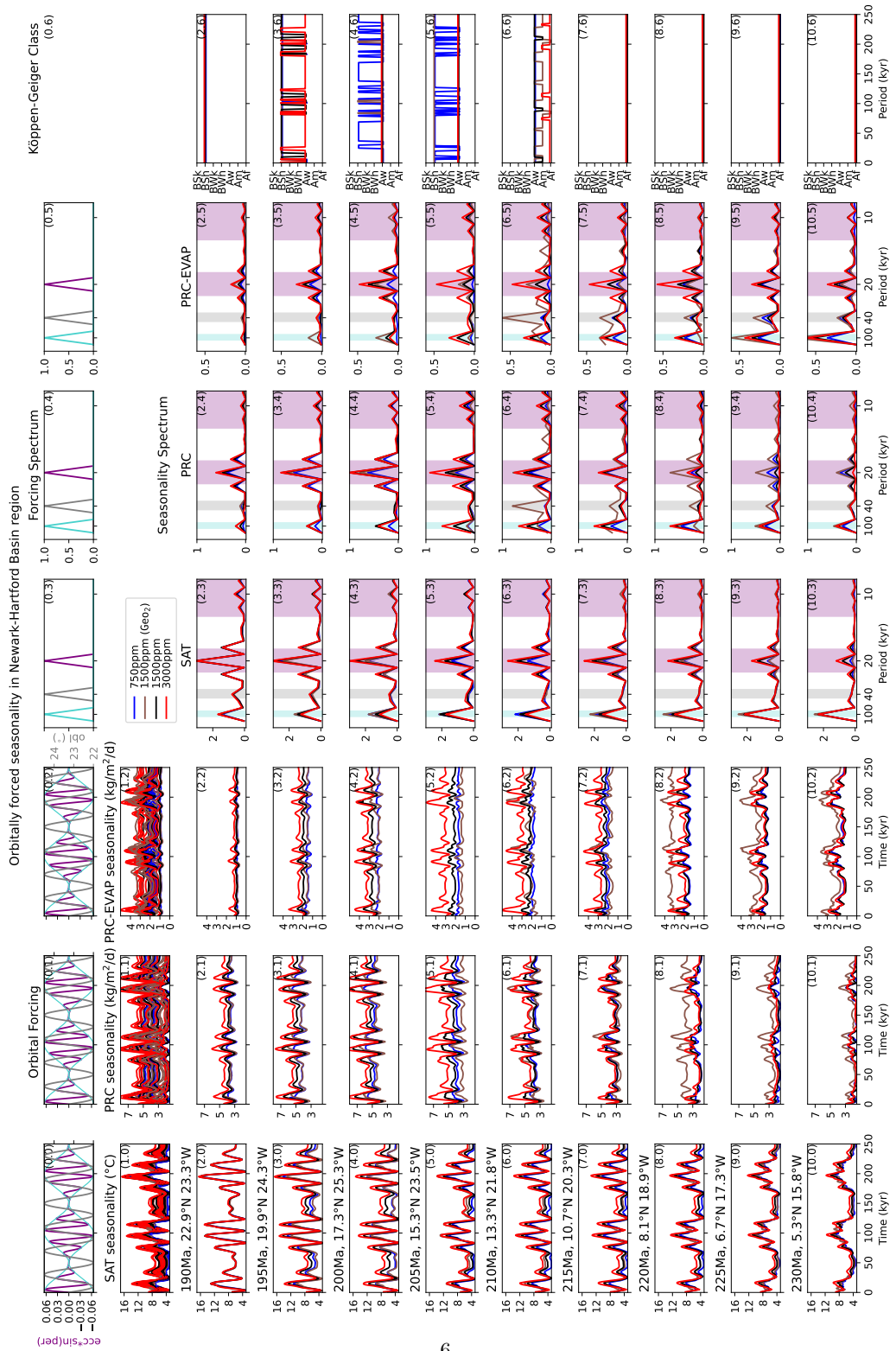


Figure S4: Seasonality timeseries and their fourier spectra in the Newark-Hartford basin area for all simulations of the ensemble. Each row represents one timeslice. The three leftmost columns show the regional seasonality timeseries for T, PRC and PRC-EVAP. The next three columns show the Fourier spectra of the last 200 kyr of these timeseries. The last column shows the Köppen climate class obtained from the regional climate conditions at each output time step.

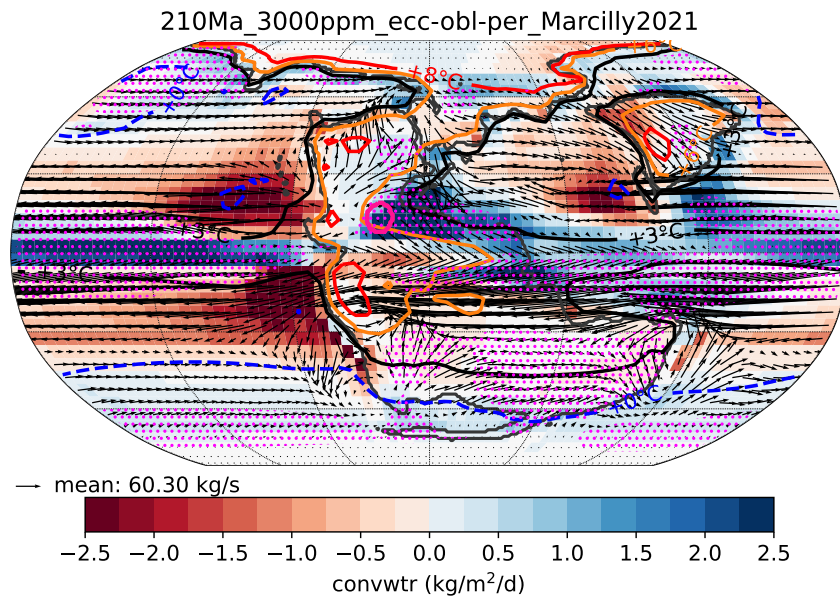


Figure S5: Effects of precession on temperature and moisture cycling. Differences in moisture convergence (convwtr, colors) during the month of May between maximum (90 kyr, near min. precession / max. summer insolation) and minimum (203 kyr, near max. precession / min. summer insolation) PRC-EVAP precession phases in the Newark-Hartford Basin area are shown for one simulation at 210 Ma (see Fig. 2 in the main article). Arrows indicate difference in the whole column moisture transport. Contours indicate differences in surface air temperatures. Pink Dots indicate an increase of the cloud fraction (>1%).

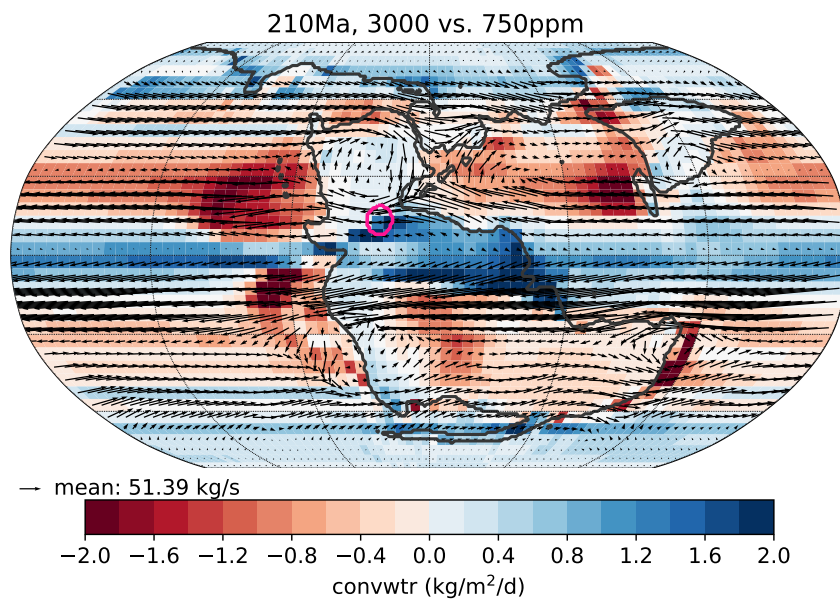


Figure S6: Effects of elevated $p\text{CO}_2$ on moisture cycling. Differences in moisture convergence (convwtr, colors) during the month of May between $p\text{CO}_2=3000$ and 750 ppm are shown for 210 Ma (at 50 kyr, when obliquity and eccentricity are minimal). Arrows indicate difference in the whole column moisture transport.

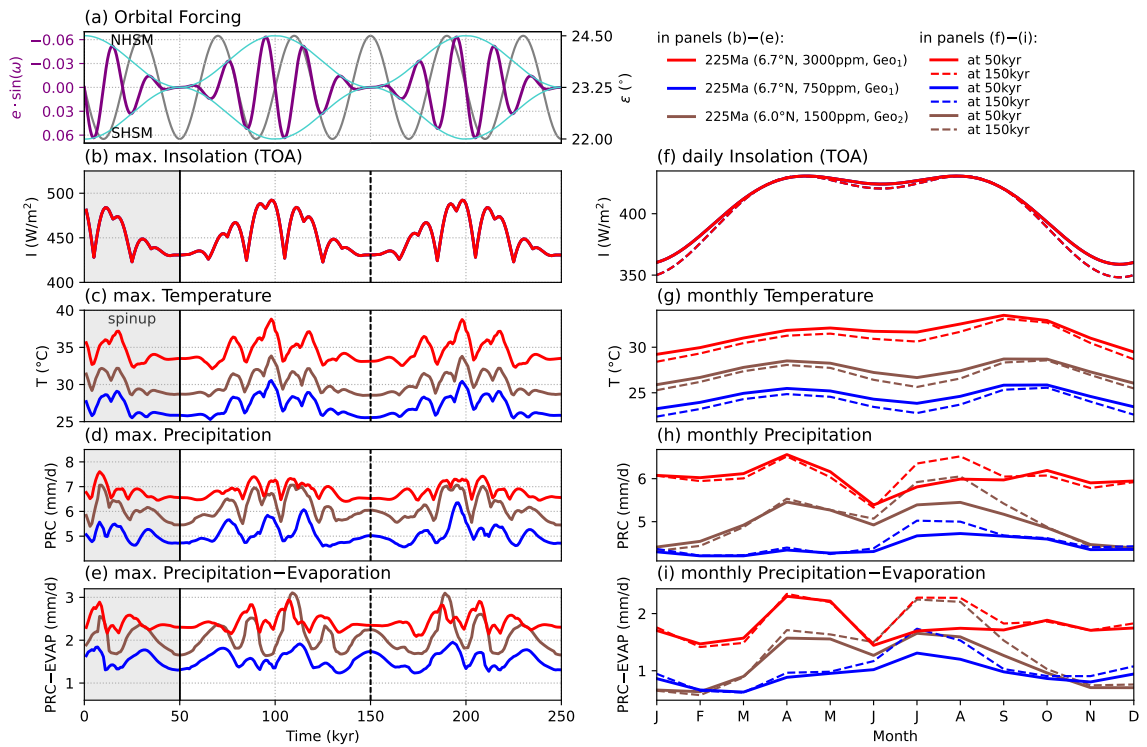


Figure S7: Effect of obliquity on the regional climate conditions in the Newark-Hartford basin area. (a): Orbital forcing expressed by the precession index $e \cdot \sin(\omega)$ (e : perihelion angle, ω : eccentricity) and obliquity ϵ . The left axis is inverted so that maximum northern hemisphere summer insolation (NHSM) occurs at the top. (b–e): Maximum monthly values of regional climate quantities for three simulations at 225 Ma, using $p\text{CO}_2=3000$ and 750 ppm for the Geo_1 paleogeography (red/blue) and 1500 ppm for Geo_2 (brown). Vertical lines indicate two points in time for which monthly data is shown on the right side. (f–i): Monthly values of the same quantities at minimum (at 50 kyr; solid lines) and maximum (at 150 kyr; dashed lines) obliquity ω (at minimum ϵ).

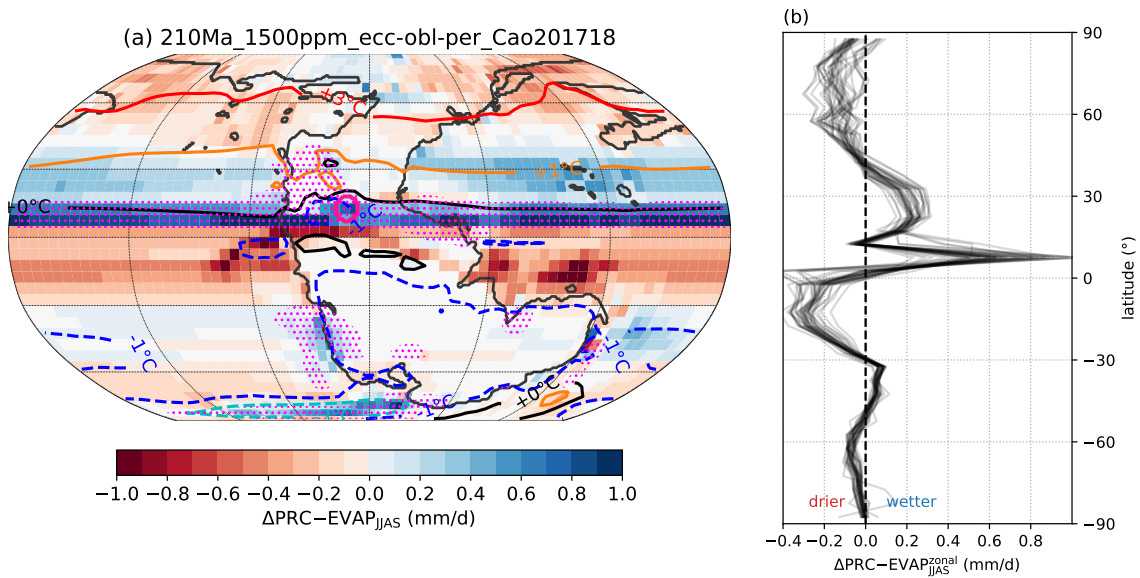


Figure S8: Effects of obliquity on temperature and humidity. (a): PRC-EVAP (colors) and T (contours) difference between max. and min. obliquity (150 vs. 50 kyr, see Fig. S7) during June-September. This is shown for one simulation (210 Ma, $p\text{CO}_2=1500$ ppm GeO_2 paleogeography). Dots indicate an increase of the cloud fraction (>1%). **(b):** Zonal mean of the PRC-EVAP^{JJAS} difference for all simulations of the ensemble.

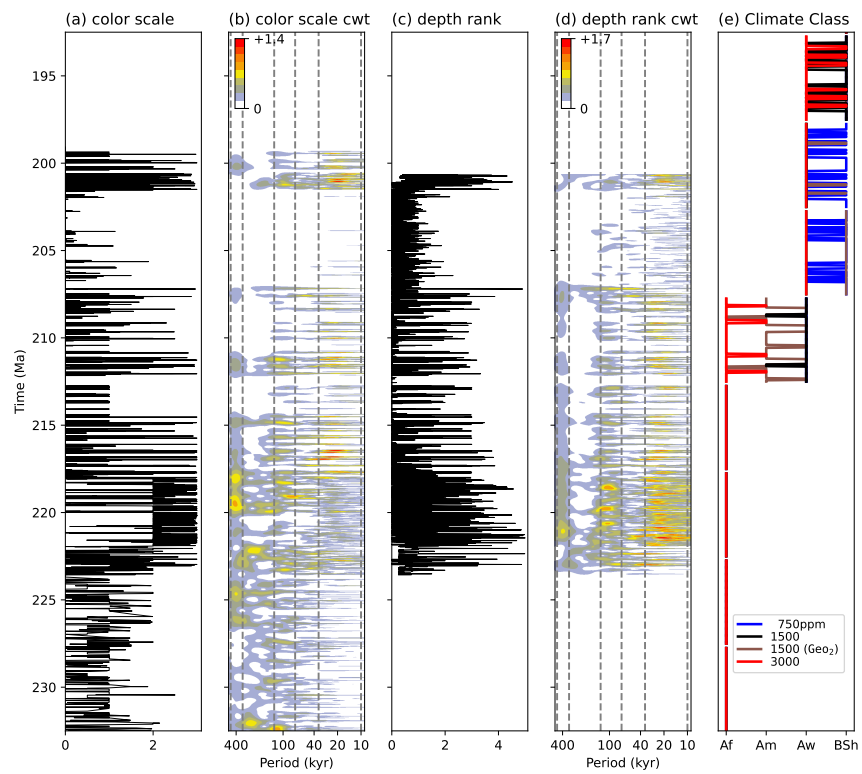


Figure S9: Proxy lake depth levels (a,c) from Olsen et al. (2019) and periodicities therein (b,d). (b,d): Continuous wavelet transform (CWT) amplitudes of data in (a,c), using a Morlet wavelet. From the values between the dashed vertical lines, average amplitudes in the ~ 405 kyr, ~ 100 kyr and ~ 20 kyr bands have been determined (see Fig. 3d,e of the main article). **(e):** Köppen climate class during the transient simulations, determined from monthly rainfall and temperatures in the Newark-Hartford Basin Area (see Figs. 1a and 3i of the main article).

15 **3. Other Localities**

16 *3.1. Germanic Basin*

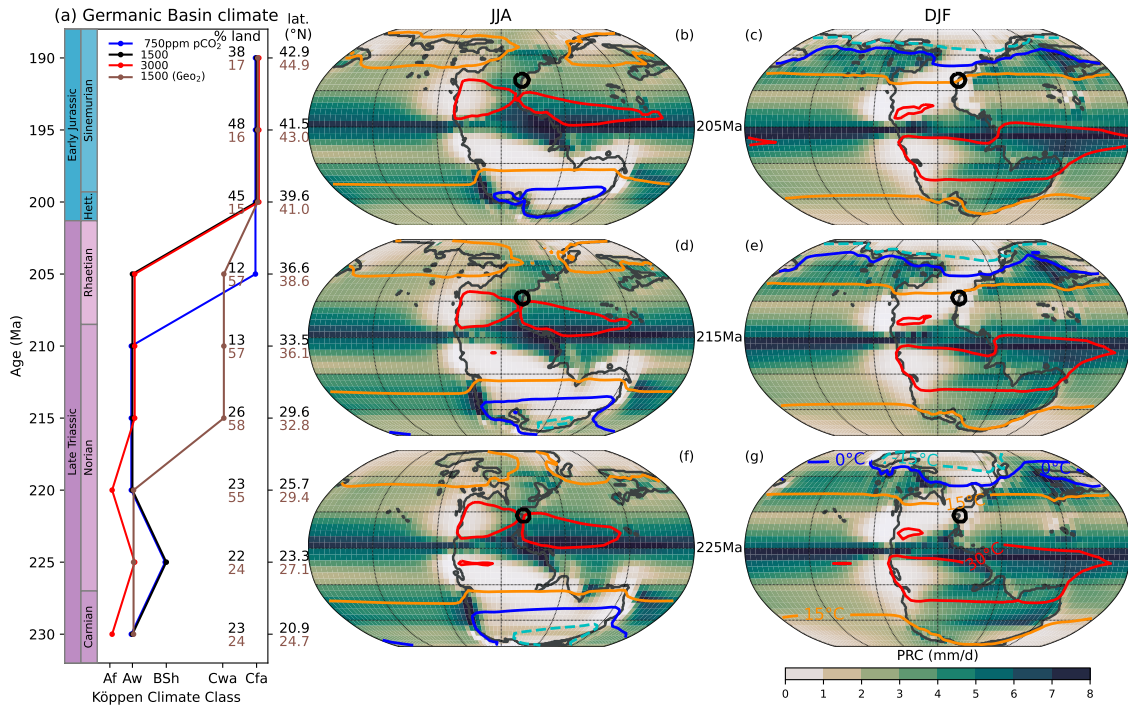


Figure S10: Long-term average climate condition in the Germanic basin area. Similar to Fig. 1 in the main article. The percentage of land area in the neighborhood indicated by the black circle in (b–g) is given on the y-axis of (a). Only this fraction has been used for the regional climate analyses in (a) and Figs. S11–S13. (b–g): Results are shown for simulations with Geo₂ paleogeography and pCO₂ = 1500 ppm.

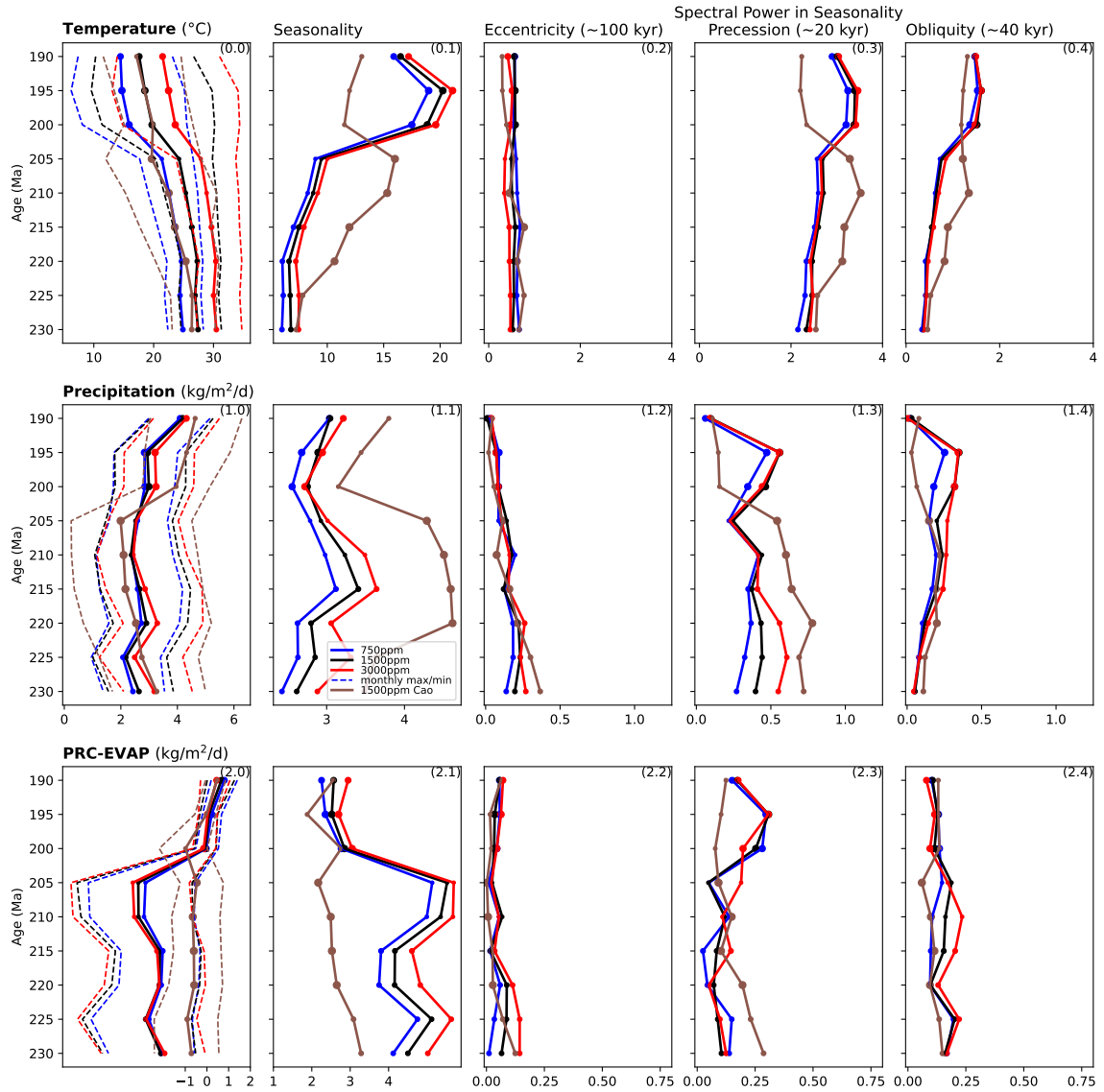


Figure S11: Summary of long-term trends in simulated average T , PRC and PRC-EVAP (first column) and their seasonality (second column) in the Germanic basin area. The three columns on the right show the amplitudes of the eccentricity (100 kyr), precession (40 kyr) and obliquity (20 kyr) signals in the seasonality timeseries. Similar to Fig. S3. The size of the dots additionally scales with the fraction of land in the considered neighborhood (Fig. S10).

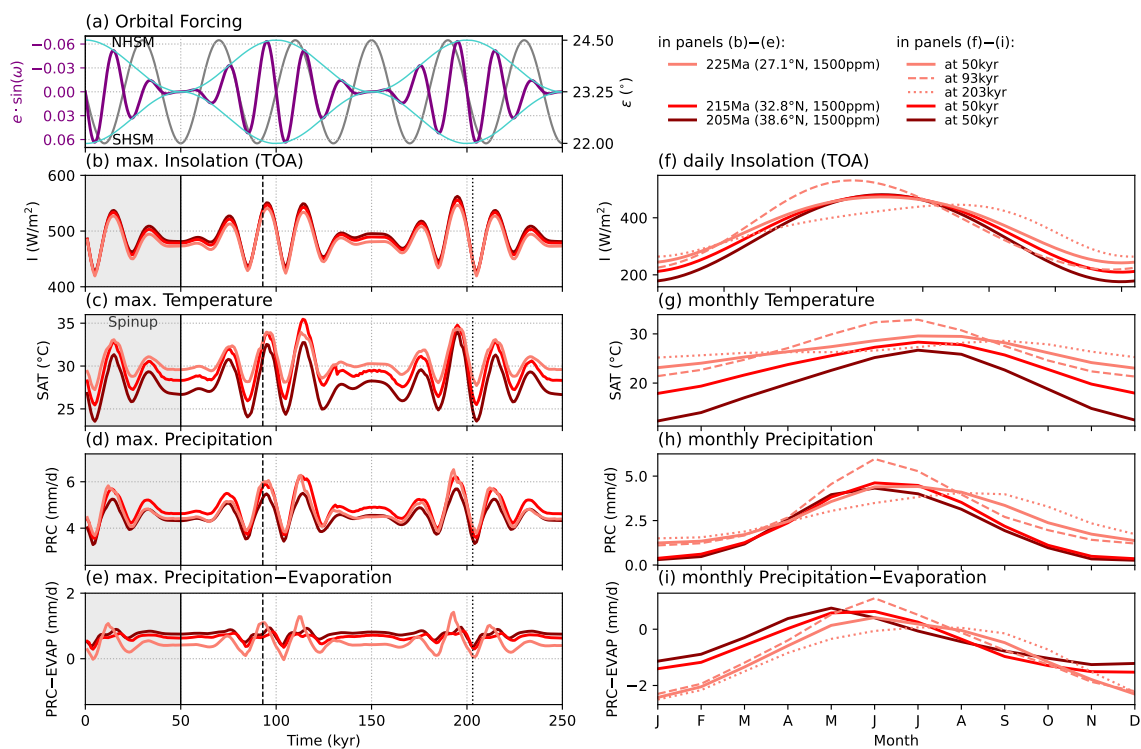


Figure S12: Effect of the imposed orbital forcing on the regional climate conditions in the Germanic basin area. Similar to Fig. 2 in the main article. Results are shown for simulations using the Geo_2 paleogeographies.

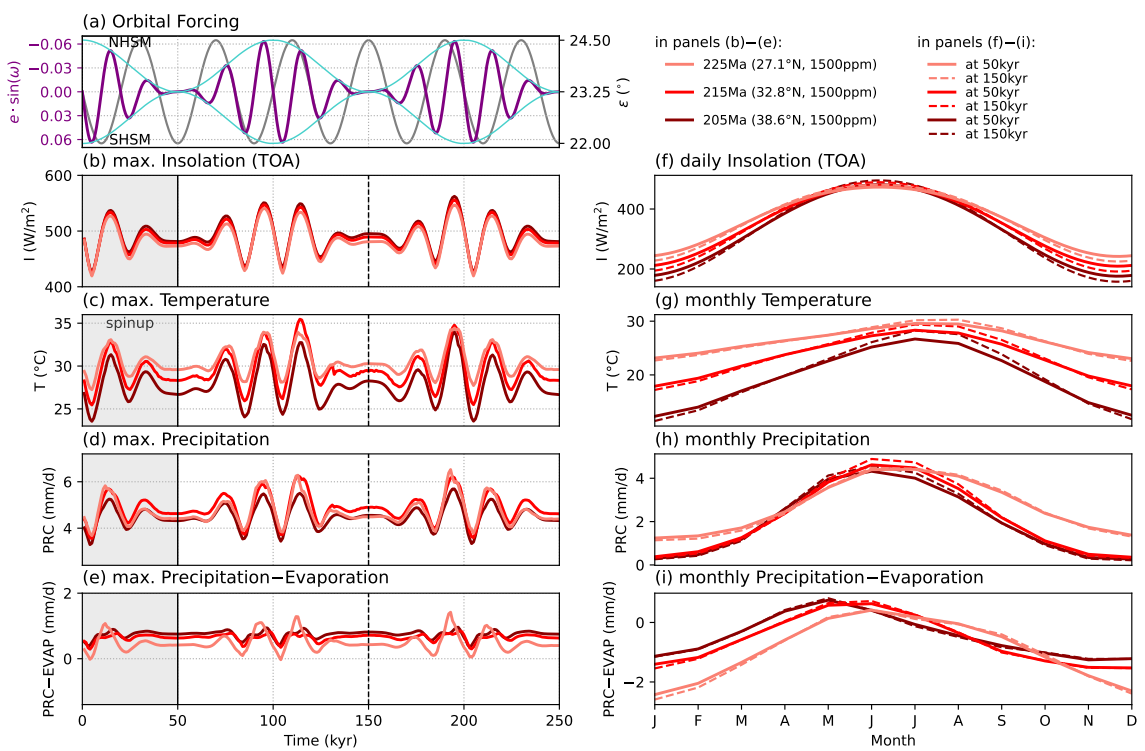


Figure S13: Effect of obliquity on the regional climate conditions in the Germanic basin area. Similar to Fig. S7. Results are shown for simulations using the GeO_2 paleogeographies.

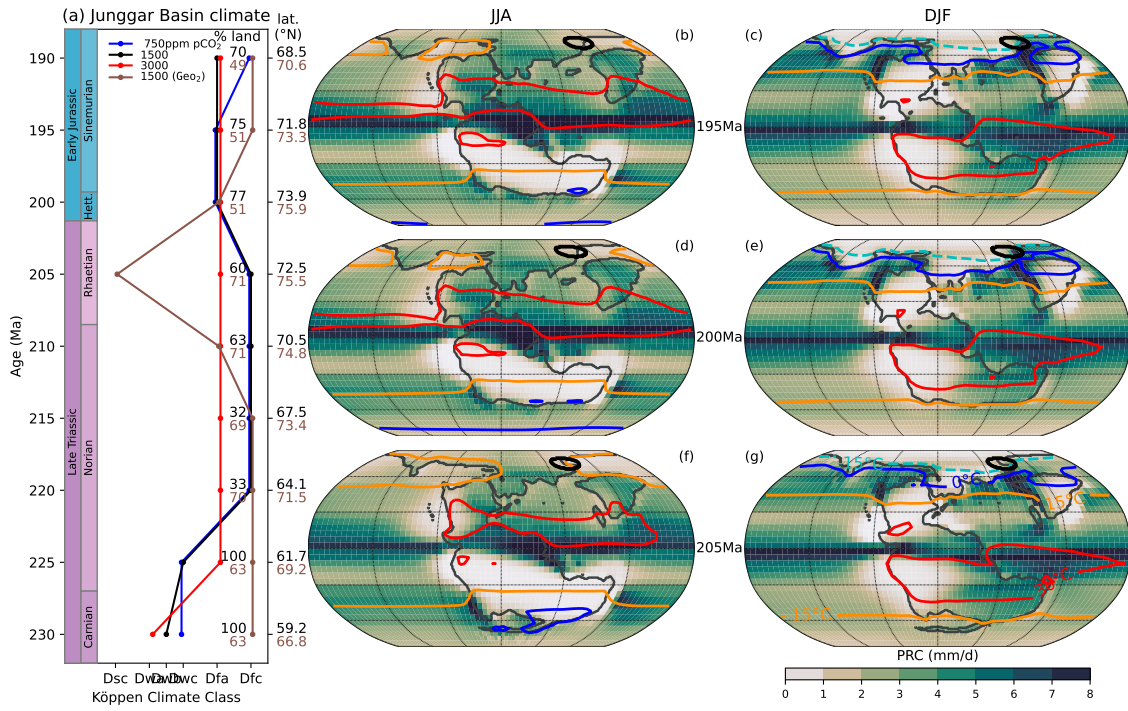


Figure S14: Long-term average climate condition in the Junggar basin area. Similar to Fig. 1 in the main article. The percentage of land area in the neighborhood indicated by the black circle in (b–g) is given on the y-axis of (a). Only this fraction has been used for the regional climate analyses in (a) and Figs. S15–S17. (b–g): Results are shown for simulations with Geo₁ paleogeography and pCO₂ = 1500 ppm.

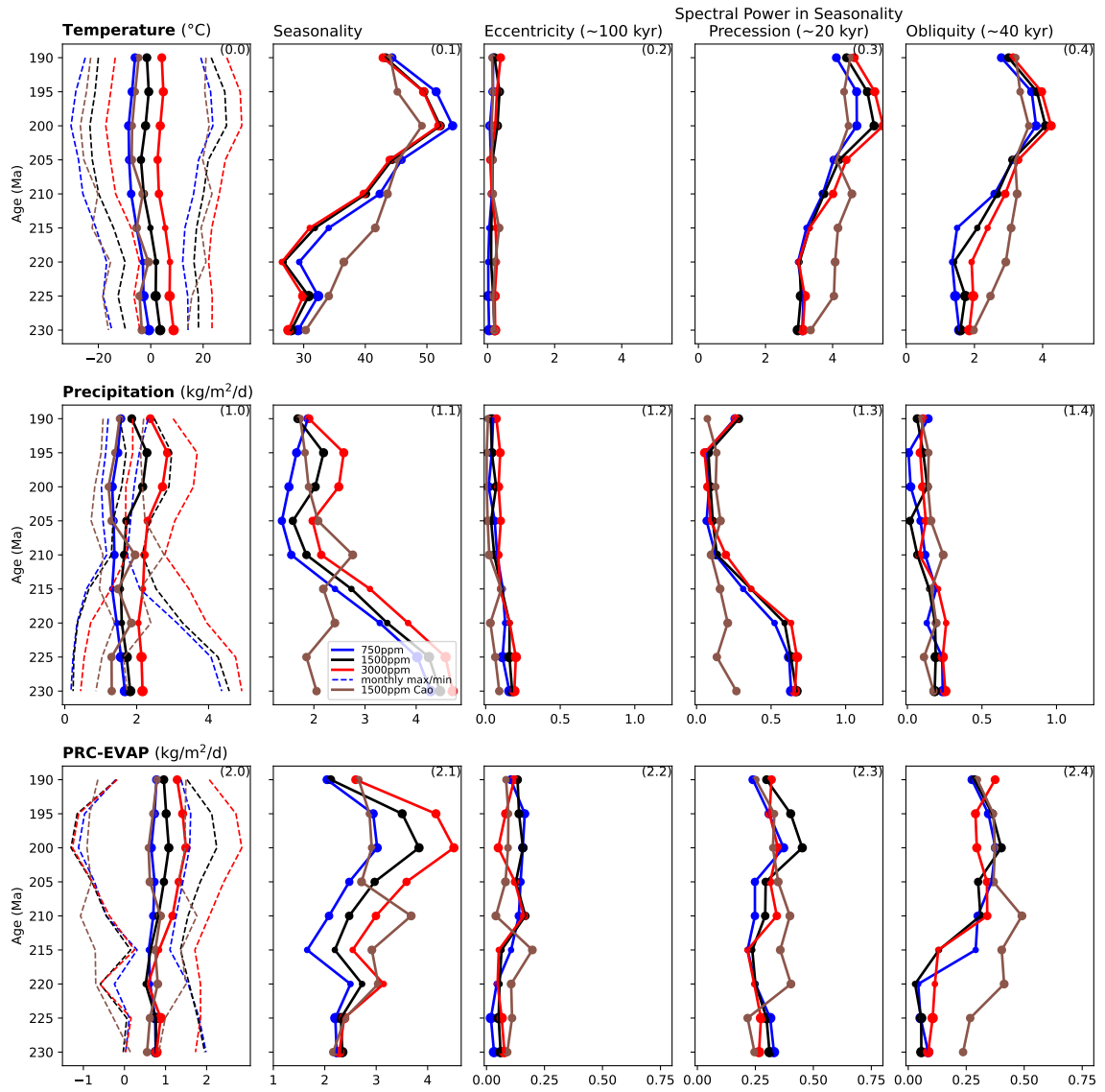


Figure S15: Summary of long-term trends in simulated average T, PRC and PRC-EVAP (first column) and their seasonality (second column) in the Junggar basin area. The three columns on the right show the amplitudes of the eccentricity (100 kyr), precession (40 kyr) and obliquity (20 kyr) signals in the seasonality timeseries. Similar to Fig. S3. The size of the dots additionally scales with the fraction of land in the considered neighborhood (Fig. S14).

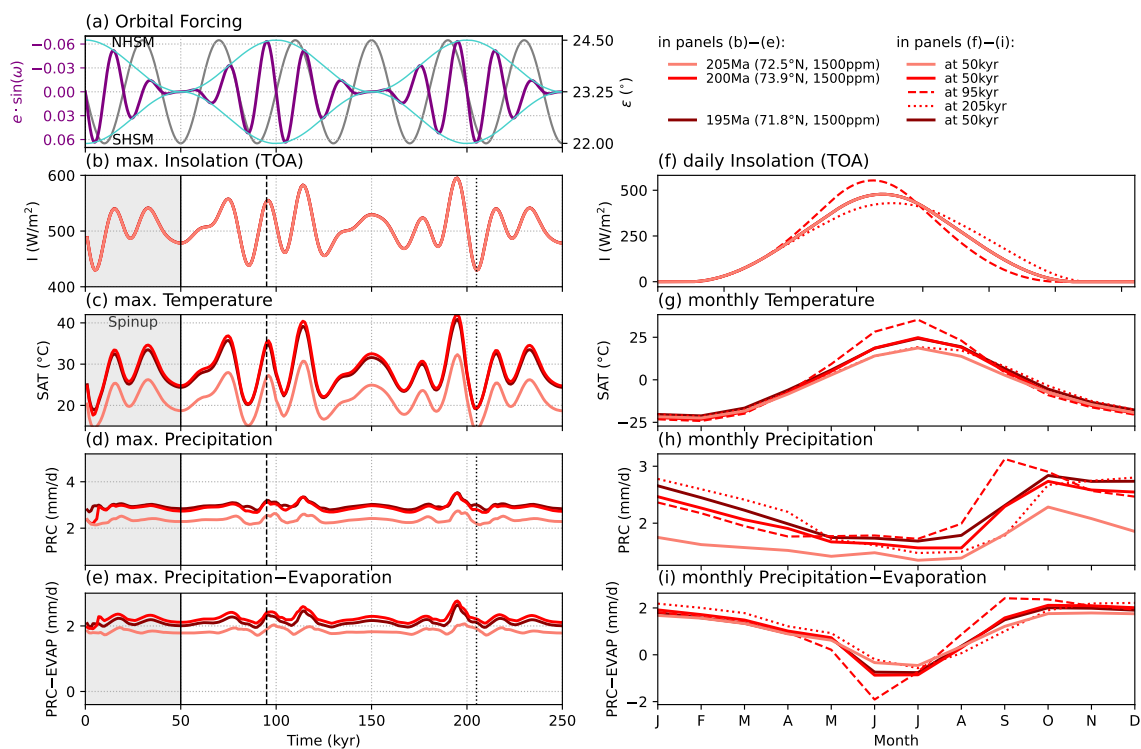


Figure S16: Effect of the imposed orbital forcing on the regional climate conditions in the Junggar basin area. Similar to Fig. 2 in the main article. Results are shown for simulations using the Geo₁ paleogeographies.

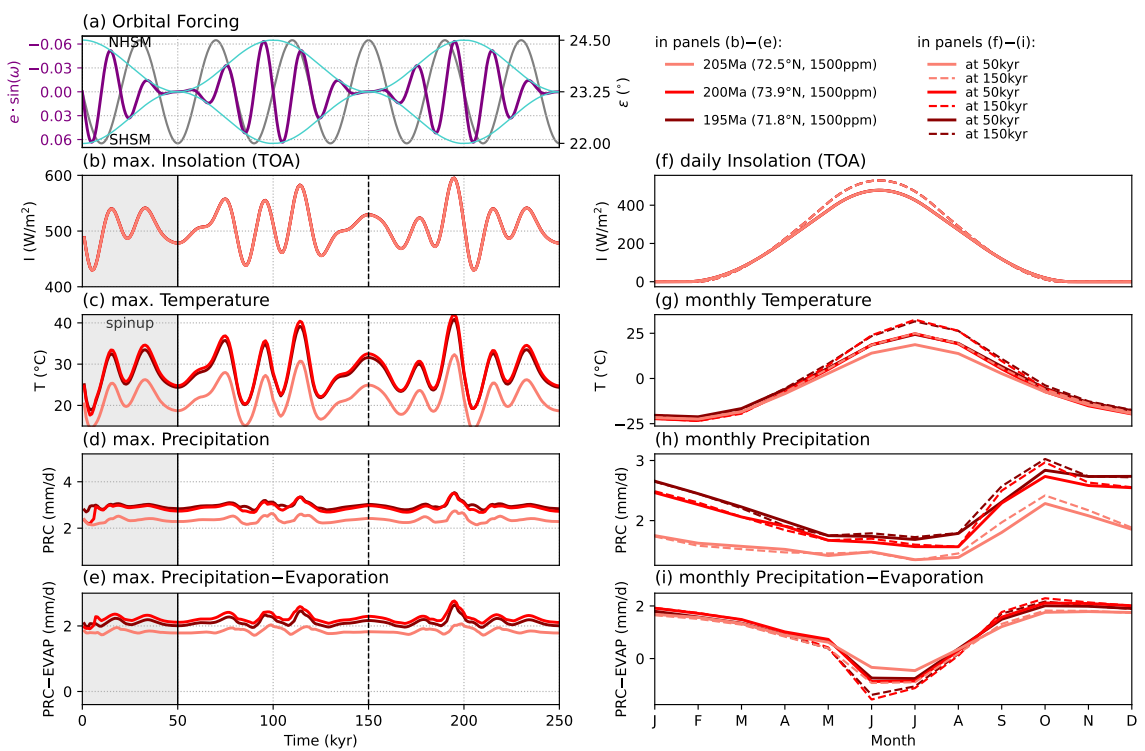


Figure S17: Effect of obliquity on the regional climate conditions in the Junggar basin area. Similar to Fig. S7. Results are shown for simulations using the Geo_1 paleogeographies.

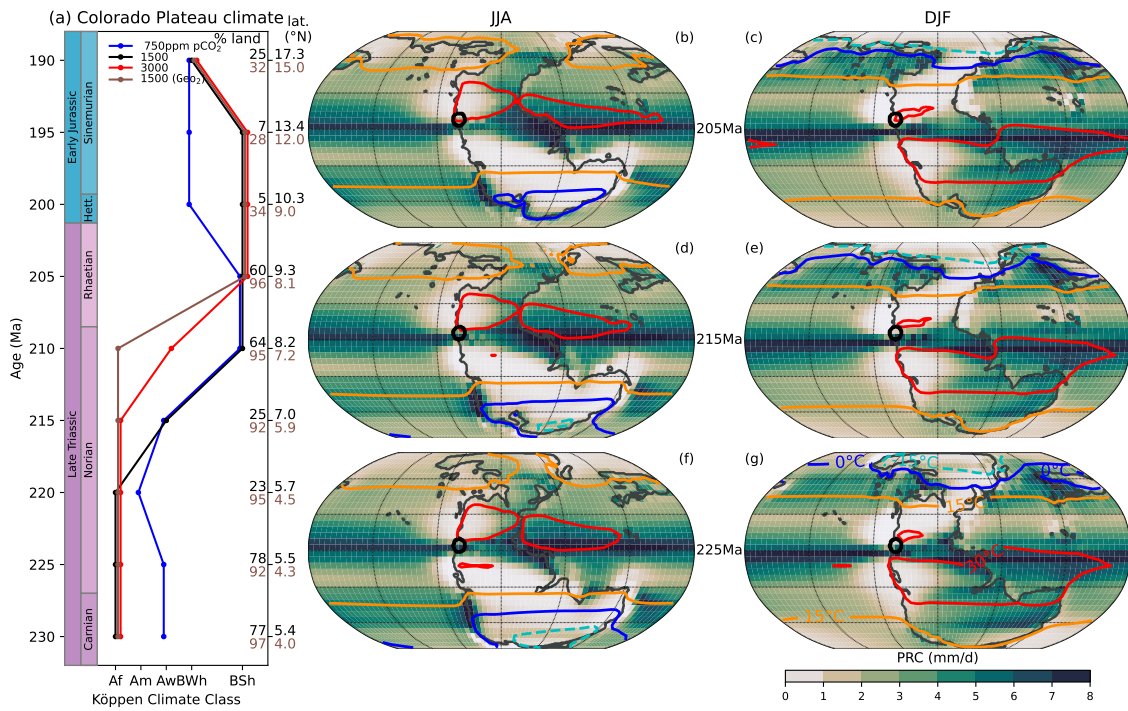


Figure S18: Long-term average climate condition in the Colorado Plateau area. Similar to Fig. 1 in the main article. The percentage of land area in the neighborhood indicated by the black circle in (b–g) is given on the y-axis of (a). Only this fraction has been used for the regional climate analyses in (a) and Figs. S19–S21. (b–g): Results are shown for simulations with Geo₂ paleogeography and pCO₂ = 1500 ppm.

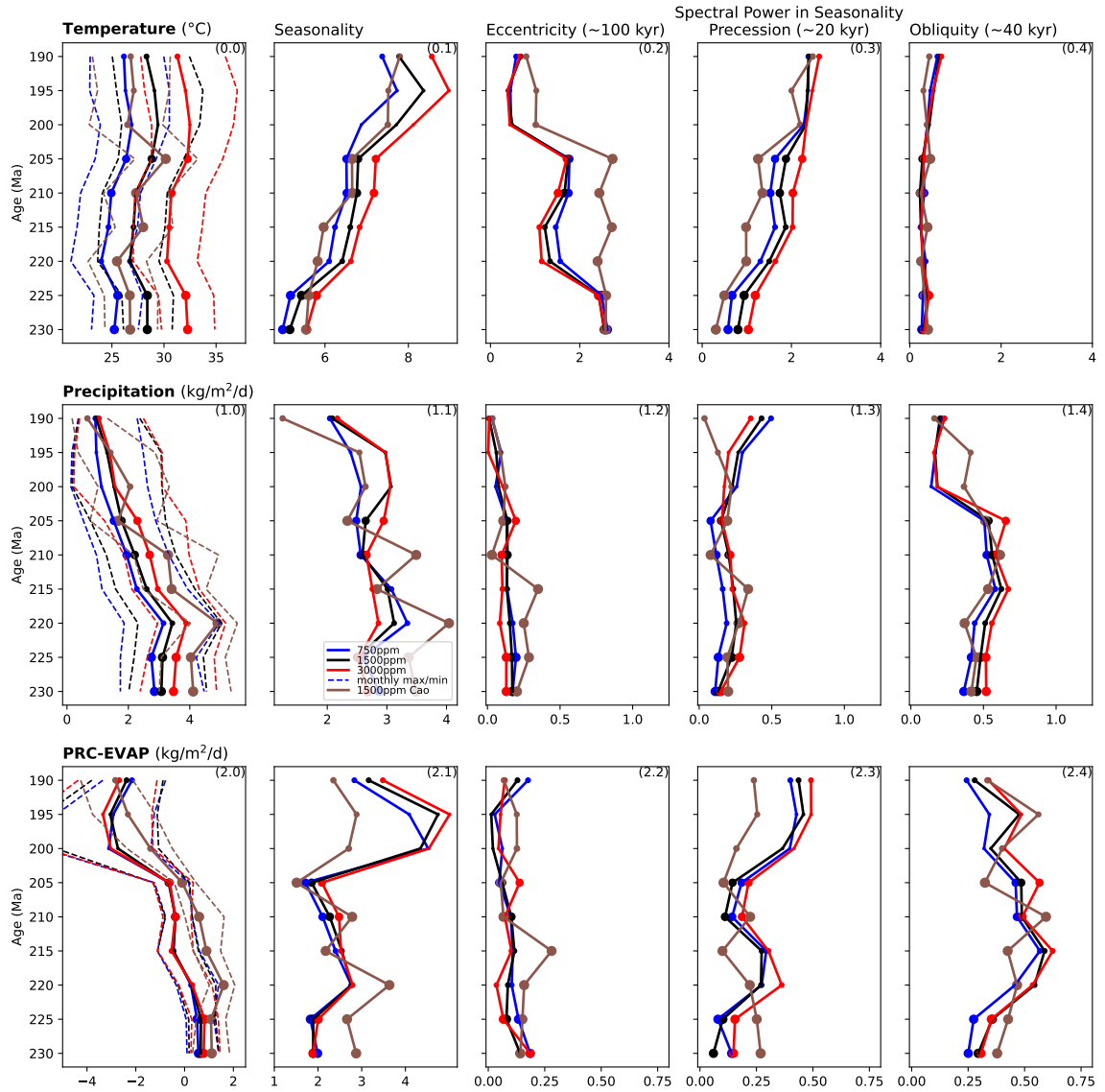


Figure S19: Summary of long-term trends in simulated average T, PRC and PRC-EVAP (first column) and their seasonality (second column) in the Colorado plateau area. The three columns on the right show the amplitudes of the eccentricity (100 kyr), precession (40 kyr) and obliquity (20 kyr) signals in the seasonality timeseries. Similar to Fig. S3. The size of the dots additionally scales with the fraction of land in the considered neighborhood (Fig. S18).

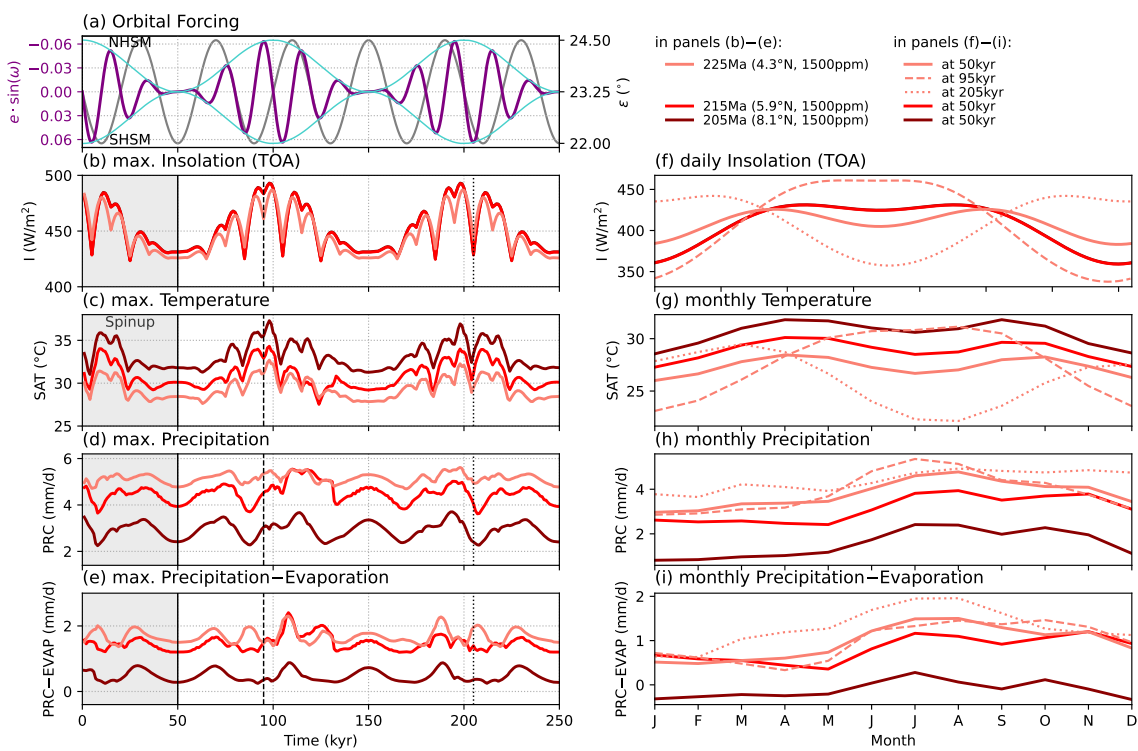


Figure S20: Effect of the imposed orbital forcing on the regional climate conditions in the Colorado Plateau area. Similar to Fig. 2 in the main article. Results are shown for simulations using the Geo_2 paleogeographies.

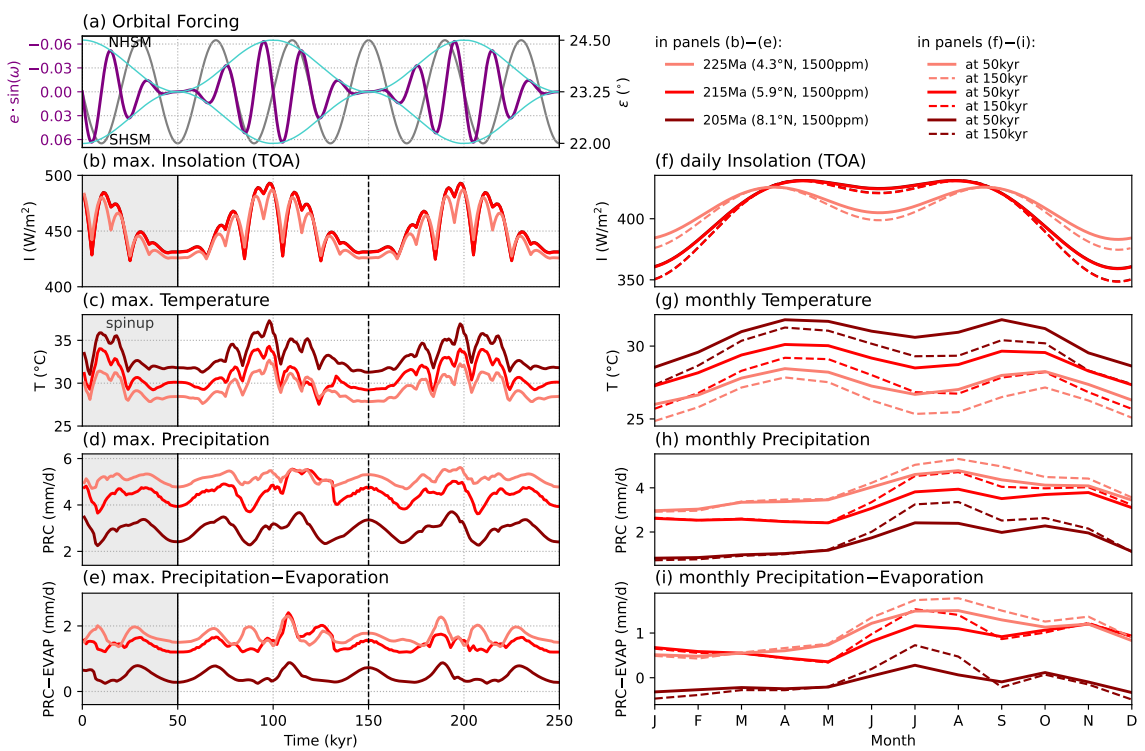


Figure S21: Effect of obliquity on the regional climate conditions in the Germanic basin area. Similar to Fig. S7. Results are shown for simulations using the GeO_2 paleogeographies.

19 **References**

- 20 Cao, W., Williams, S., Flament, N., Zahirovic, S., Scotese, C.R., Müller, R.D., 2018. Palaeolatitudinal distribution of lithologic
21 indicators of climate in a palaeogeographic framework. *Geological Magazine* 156, 331–354. doi:[10.1017/S0016756818000110](https://doi.org/10.1017/S0016756818000110).
- 22 Cao, W., Zahirovic, S., Flament, N., Williams, S., Golonka, J., Mueller, R.D., 2017. Improving global paleogeography since
23 the late Paleozoic using paleobiology. *Biogeosciences* 14, 5425–5439. doi:[10.5194/bg-14-5425-2017](https://doi.org/10.5194/bg-14-5425-2017).
- 24 Chandra, R., Cripps, S., Butterworth, N., Muller, R.D., 2021. Precipitation reconstruction from climate-sensitive lithologies
25 using Bayesian machine learning. *Environmental Modelling & Software* 139, 105002. doi:[10.1016/j.envsoft.2021.105002](https://doi.org/10.1016/j.envsoft.2021.105002).
- 26 Kent, D.V., Olsen, P.E., Muttoni, G., 2017. Astrochronostratigraphic polarity time scale (APTS) for the Late Triassic and
27 Early Jurassic from continental sediments and correlation with standard marine stages. *Earth-Science Reviews* 166, 153–180.
28 doi:[10.1016/j.earscirev.2016.12.014](https://doi.org/10.1016/j.earscirev.2016.12.014).
- 29 Landwehrs, J., Feulner, G., Willeit, M., Petri, S., Sames, B., Wagnreich, M., Whiteside, J.H., Olsen, P.E., 2022. Modes of
30 Pangean Lake-Level Cyclicity Driven by Astronomical Pacing Modulated by Continental Position and $p\text{CO}_2$ (subm.).
- 31 Marcilly, C.M., Torsvik, T.H., Domeier, M., Royer, D.L., 2021. New paleogeographic and degassing parameters for long-term
32 carbon cycle models. *Gondwana Research* 97, 176–203. doi:[10.1016/j.gr.2021.05.016](https://doi.org/10.1016/j.gr.2021.05.016).
- 33 Matthews, K.J., Maloney, K.T., Zahirovic, S., Williams, S.E., Seton, M., Mueller, R.D., 2016. Global plate boundary evolution
34 and kinematics since the late Paleozoic. *Global and Planetary Change* 146, 226–250. doi:[10.1016/j.gloplacha.2016.10.002](https://doi.org/10.1016/j.gloplacha.2016.10.002).
- 35 Olsen, P.E., Laskar, J., Kent, D.V., Kinney, S.T., Reynolds, D.J., Sha, J., Whiteside, J.H., 2019. Mapping Solar System
36 chaos with the Geological Orrery. *Proceedings of the National Academy of Sciences* 116, 10664–10673. doi:[10.1073/pnas.
37 1813901116](https://doi.org/10.1073/pnas.1813901116).

A.III Supplementary Information to P.III

SUPPLEMENTARY INFORMATION for
“Climatic fluctuations modeled for carbon and sulfur emissions
from end-Triassic volcanism”
Landwehrs, Feulner, Hofmann & Petri (2020)

1 **1. Further References**

- 2 • modeling Mesozoic climates: Totmann-Parrish & Curtis (1982)
3 • modeling sulfur effects: Mussard et al. (2014)
4 • modeling carbon cycle: Berner & Beerling (2007), Heimdal & Svensen (2019)
5 • age of the Triassic-Jurassic boundary: Wotzlaw et al. (2014)
6 • CAMP: McHone (2003)
7 • dating of CAMP units: Knight et al. (2004), Davies et al. (2017)
8 • $\delta^{13}\text{C}$ records and their correlation: Zaffani et al. (2018)
9 • pCO_2 reconstruction: Schaller et al. (2014)
10 • impacts of volcanism, especially LIP volcanism: Mather (2015), Jones et al. (2016), Bond & Wignall
11 (2014), Bond & Grasby (2017), Ernst & Youbi (2017), Clapham & Renne (2019)
12 • LIP carbon emission and cycling: Black & Gibson (2019)
13 • climatic forcing of volcanic aerosols: Langmann (2014)
14 • fossil leaf studies: e.g. McElwain et al. (1999, 2007, 2009), Mander et al. (2010), Steinhorsdottir et al.
15 (2011), Soh et al. (2017), Haworth et al. (2014)
16 • temperature estimates from $\delta^{18}\text{O}$ measurements: e.g. Korte et al. (2009), Trotter et al. (2015)
17 • clay mineralogy studies: e.g. Pálffy & Zajzon (2012), Zajzon et al. (2012)
18 • palynology studies: e.g. Lindström (2015)
19 • evidence for anoxia: Ciarapica (2007), Wignall & Bond (2008), Richo et al. (2012), Jaraula et al.
20 (2013), Kasprak et al. (2015), Luo et al. (2018)
21 • sea level changes: Hallam (1997), Hallam & Wignall (1999), Schneebeli-Hermann et al. (2017), Barth
22 et al. (2018)
23 • coral temperature tolerance limits: Kleypas et al. (2015), Guan et al. (2015)

24 **2. Modeling Approach**

25 Further references regarding the respective model components:

- 26 • Ocean MOM3: Pacanowski & Griffies (2000), Hofmann & Morales Maqueda (2006)
- 27 • Atmosphere POTSDAM-2: Petoukhov et al. (2000)
- 28 • Sea-ice model: Fichefet & Maqueda (1997)
- 29 • Marine biogeochemistry HAMOCC: Maier-Reimer (1993), Six & Maier-Reimer (1996), Hofmann &
- 30 Schellnhuber (2009), Mathesius et al. (2015), Hofmann et al. (2019)

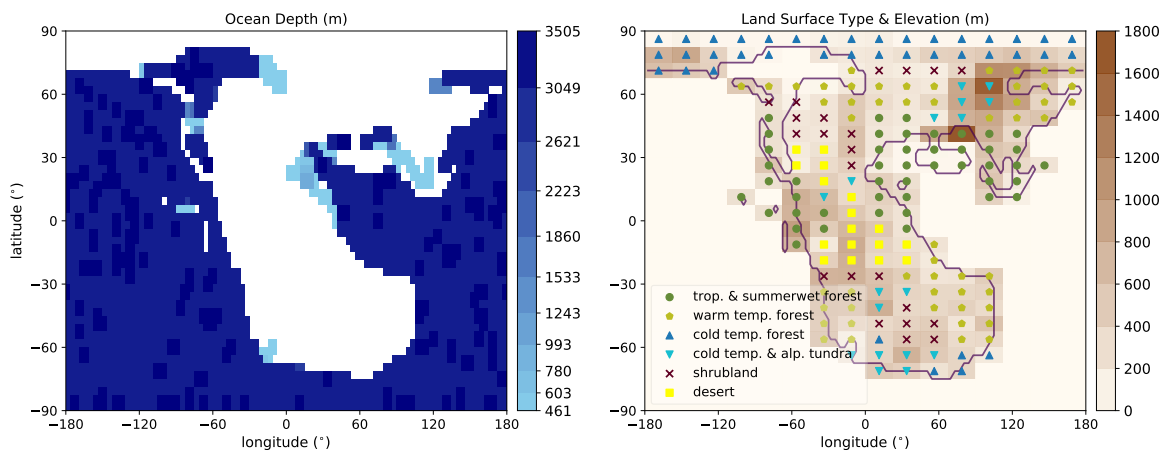


Figure S1: Left: Seafloor topography in the MOM3 ocean grid. Right: Land surface type and elevation on the POTSDAM-2 atmosphere grid. The six surface and vegetation types are expressed as combinations of the three types available in CLIMBER-3 α : trees, grass and bare soil (following Bonan et al. 2002). Tropical and summerwet forest (95 % trees, 0 % grass, 5 % bare land), warm temperate forest (75 %, 0 %, 25 %), cold temperate forest (50 %, 0 %, 50 %), cold temperate and alpine tundra (25 %, 25 %, 50 %), shrubland (0 %, 80 %, 20 %) and desert (0 %, 0 %, 100 %). The land surface types which were synthesized from reconstructions of paleobiogeographic (Retallack 2009, Willis & McElwain 2002) and paleoclimatic zones (Scotese et al. 2014).

31 *2.1. Volcanic Aerosol Forcing*

32 As outlined in the main text, the calculation of the aerosol radiative forcing for a given stratospheric sulfur
 33 injection history is partly adopted from Metzner et al. (2012) and Toohy et al. (2016). The aerosol optical
 34 depth (defined as $AOD = -\ln(I/I_0)$, where I/I_0 is the attenuation of incoming solar radiation at wavelength
 35 550 nm, Jones et al. 2005) is calculated by the EVA model (Toohy et al. 2016) and scaled linearly into a
 36 radiative forcing. Because this simplified approach cannot capture all chemical and microphysical feedbacks
 37 that govern the impacts of the large sulfur amounts potentially emitted by LIPs, simulations with more
 38 comprehensive atmospheric chemistry models are an important reference point. Therefore, the “Deccan

39 scale” scenario by Schmidt et al. (2016), where 1200 GtS/yr are emitted over a decade at 21 °S, is reproduced
40 here and the outcomes and their implications are briefly discussed in the following.

41 First of all, Schmidt et al. (2016) demonstrated that only a fraction of the sulfur injected into the stratosphere
42 actually forms aerosols due to the depletion of atmospheric oxidants. In their “Deccan Scale” case this
43 fraction is 44 %. As the EVA model does not capture this effect, the sulfur masses used in the present
44 study should be interpreted as only the amount that is effectively converted to stratospheric aerosols. When
45 the EVA model is fed with the effective stratospheric sulfur injection of 528 MtS/yr (44 % of 1200 MtS/yr),
46 corresponding to the “Deccan scale” scenario, a global mean AOD of about 2.1 is obtained compared to a
47 value of 1.2 reported by Schmidt et al. (2016) (see Fig. S2a). This suggests, that the AOD in EVA might
48 still grow too much at high sulfur injection rates despite the built-in non-linear scaling $\text{AOD} \sim M^{2/3}$ for
49 large sulfur injections. The simulation by Schmidt et al. (2016) is therefore used here to calibrate the AOD
50 scaling in EVA. An AOD close to 1.2 in the described scenario is obtained when the scaling is changed to
51 $\text{AOD} \sim M^{2/3-0.1}$ (see Fig. S2a). This does not alter the EVA results for Pinatubo sized eruptions because
52 for this lower injection range a different, linear, scaling is implemented.

53 Subsequently, the AOD is converted into a global mean radiative forcing ΔF_a via the scaling factor of
54 -21 W/m^2 , as suggested by Schmidt et al. (2018), instead of -24 W/m^2 as used by Metzner et al. (2012).
55 However, it needs to be stressed that this scaling relation was obtained by examining recent volcanic sulfur
56 emissions and forcings and could be different for larger scale LIP volcanism. The result is a radiative forcing
57 of -26.8 W/m^2 (see Fig. S2b) which is still somewhat larger than the net forcing of -16.25 W/m^2 reported
58 by Schmidt et al. (2016) that also incorporates e.g. positive forcing contributions from portions of the SO_2
59 that are not oxidized to sulphuric acid aerosols. However, the peak annual mean global cooling of -8.6°C
60 that we simulate for this emission scenario is not too different from the -6.6°C obtained by Schmidt et al.
61 (2016) (see Fig. S2c). Without the described modification of the two scaling relations, the simulated cooling
62 for this emission scenario would be -15.8°C . Keeping in mind the very different models used in both
63 approaches and the large uncertainties involved, we consider the results more comparable after the AOD
64 scaling of EVA is reduced for these large sulfur injections.

65 It should be stressed that also the models used to calculate the temperature response are quite different.
66 Whereas in this study a coupled climate model and a simplified the volcanic forcing generation are used,
67 Schmidt et al. (2016) simplify at the climate part of the modeling approach by using a comprehensive
68 atmospheric chemistry model in combination with a zero-dimensional energy budget model, which does not
69 allow them to represent features of an ancient world (e.g. the end-Cretaceous) and the spatially resolved
70 climatic response to volcanic perturbations in their approach. Differences in the global temperature response
71 are therefore expected. For example, it is demonstrated here, that the global response also varies between
72 different background climate states with different initial pCO_2 values. Also the response of the three-
73 dimensional ocean model on timescales from years to millennia is an important factor. For example, given a

74 prolonged emission of 50 years the mean cooling obtained by Schmidt et al. (2016) increases to only $\sim -9^\circ\text{C}$
 75 while the cooling here grows less asymptotically to -16.7°C (see Fig. S2c). This indicates that not only the
 76 amplitude but also the duration of the forcing determines the climatic response due to the thermal inertia
 77 of the deep ocean and the ice-albedo feedback. These processes are more mechanistically represented in
 78 the modeling approach employed in the present study. During the emission pulses described in the main
 79 text an fluctuating aerosol forcing that represents the effect of multiple eruptions is sustained for several
 80 centuries. Due to the slow thermal response of the ocean larger temperature changes than for a 10 yr forcing
 81 can therefore arise even if the peak forcing is similar.

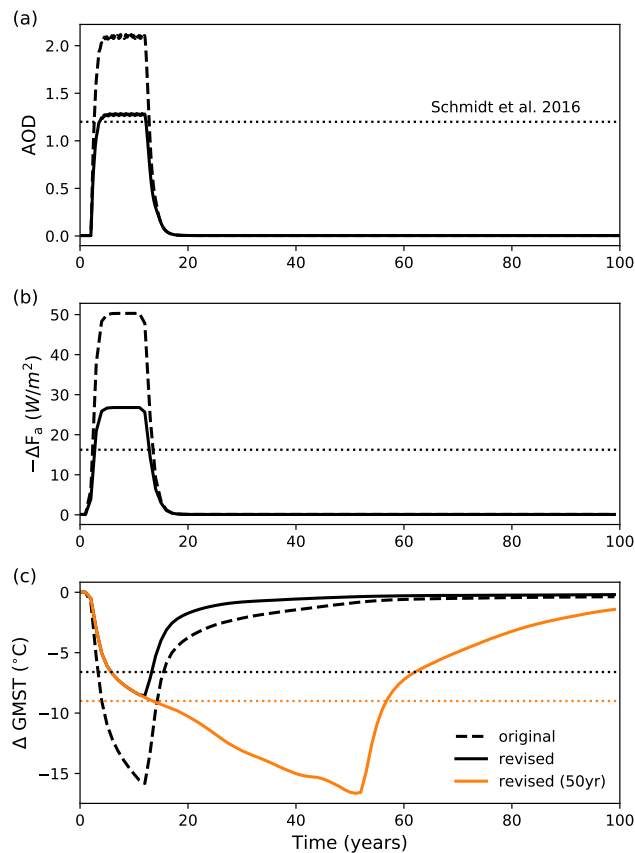


Figure S2: Comparison of the results obtained for the “Deccan scale” emission scenario by Schmidt et al. (2016). 1200 GtS/yr are emitted at 21°S for 10 years of which 44% actually form stratospheric aerosols. Solid black lines represent results obtained with the EVA+CLIMBER-3 α approach after modifying the AOD scaling of EVA to $\text{AOD} \sim M^{2/3-0.1}$ and using a scaling factor of 21 W/m^2 between AOD and radiative forcing. Dashed black lines represent results without these modifications. With them, the results are more comparable with those reported by Schmidt et al. (2016) which are indicated by the horizontal dotted lines.

82 The following Fig. S3 illustrates the generation of the aerosol forcing for the CAMP emission pulse scenarios

83 and their characteristics.

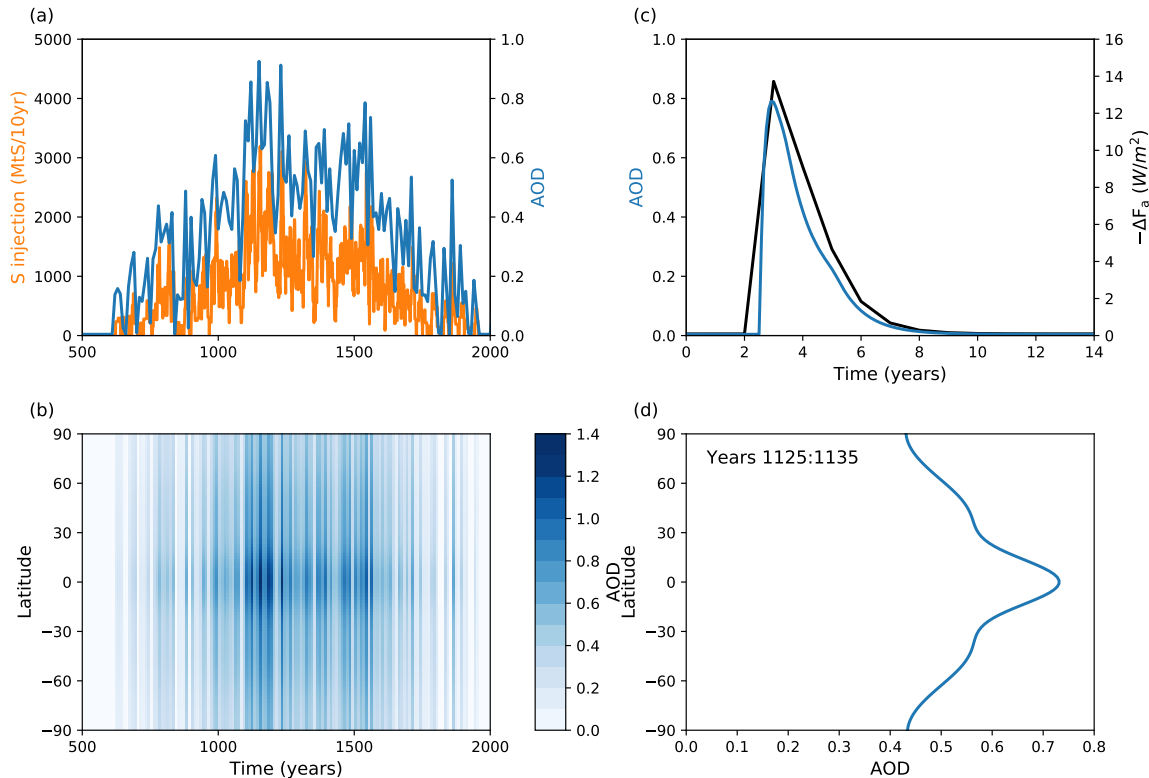


Figure S3:

textbfllustration of the aerosol forcing calculation for a volcanic emission pulse scenario. The 1500ppm_5300GtC_125 GtS run is used as an example. First, a stratospheric sulfur injection history, consisting of 500 low-latitude stratospheric sulfur injections is generated (orange line in (a)). This is fed into the EVA model which calculates a latitudinally resolved monthly AOD timeseries (plotted in (b) as a 10 yr average; see also (d) for the latitudinal AOD distribution for a 10 yr period near the emission peak). The AOD is then averaged annually and globally (see blue line in (a), again plotted as a 10yr average) and converted into a radiative forcing via a scaling factor of -21 W/m^2 . This conversion is also illustrated in (c) which shows the calculated monthly global mean AOD and the resulting annual and global mean radiative forcing for a single 250 MtS injection, of which the 1500ppm_5300GtC_125 GtS injection history is composed.

84 *2.2. LOSCAR Carbon Cycle Model Configuration*

85 Basically, the Paleocene-Eocene configuration of LOSCAR (v2.0.4.2), as described in Zeebe (2012a), was
 86 used to derive the long-term response of the atmospheric CO_2 concentration to multiple CAMP carbon
 87 emission pulses. Several parameters were changed with respect to the end-Triassic boundary conditions and
 88 the performed CLIMBER-3 α climate simulations: The equilibrium pCO_2 was set to 1500 ppm, the climate
 89 sensitivity to the value of 2.86°C from CLIMBER-3 α (for doubling pCO_2 from 1500 to 3000 ppm), the

90 initial temperatures in the ocean boxes to the average seawater temperature simulated by CLIMBER-3 α
91 for $p\text{CO}_2 = 1500$ ppm in the equivalent ocean regions (low latitude surface/intermediate/deep oceans and
92 high latitude surface oceans), and the ratio between calcification on the shelves and in the open ocean was
93 set to its maximum value, because pelagic calcifiers had not yet proliferated in the Late Triassic (Hüneke &
94 Henrich 2011). The ocean box configuration that reflects the paleogeography 55 Ma ago to some degree was
95 not modified. Because the goal was only to obtain an estimate of the long-term global response of $p\text{CO}_2$
96 to CAMP carbon emission pulses, this simplification can be expected to have only minor influence on the
97 results.

98 The global mean surface temperature in response to changing atmospheric CO_2 concentrations was calculated
99 through the following equation (see Zeebe 2012b, Royer et al. 2012):

$$T(p\text{CO}_2) = 18.7^\circ\text{C} + 2.86^\circ\text{C} \cdot \ln\left(\frac{p\text{CO}_2}{1500 \text{ ppm}}\right)$$

100 Here, 18.7°C is the simulated Late Triassic equilibrium temperature at 1500 ppm.

101 **3. Results: Pre-Eruption Equilibrium Climates**

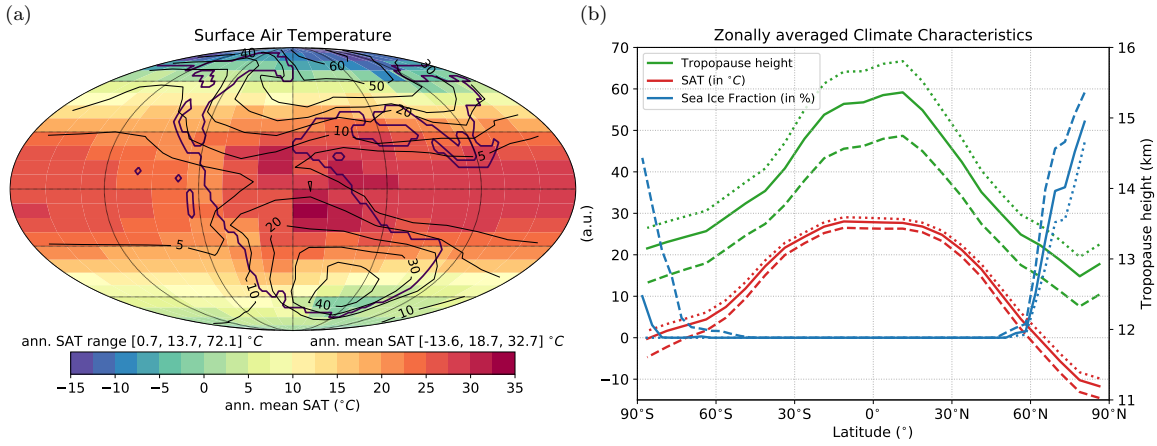


Figure S4: Annual mean SAT (a) and zonally averages of SAT, sea ice fraction and tropopause height (b) at $p\text{CO}_2 = 1500 \text{ ppm}$. (a) Contours indicate the annual temperature range on a monthly basis. (b) Solid lines correspond to the $p\text{CO}_2 = 1500 \text{ ppm}$ equilibrium state, while dashed and dotted lines correspond to 1000 ppm and 2000 ppm, respectively.

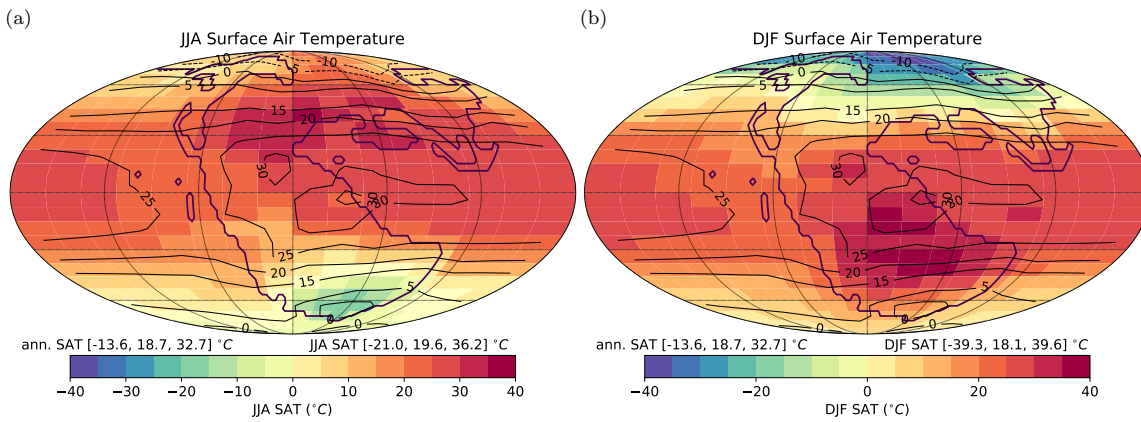


Figure S5: Seasonal surface air temperatures at $p\text{CO}_2 = 1500 \text{ ppm}$. Colours indicate JJA (a) and DJF (b) seasonal averages, while contour lines indicate the annual means.

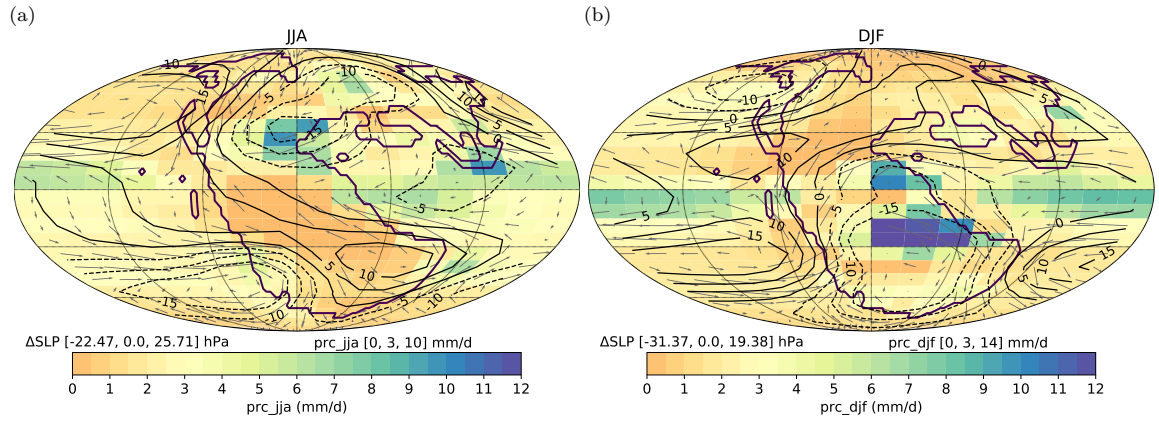


Figure S6: Boreal summer (a) and winter (b) precipitation (colours), sea level pressure anomalies (contours) and surface wind velocities (vectors) at $p\text{CO}_2 = 1500\text{ppm}$. Solid (dashed) contours indicate positive (negative) SLP anomalies with respect to the annual mean values.

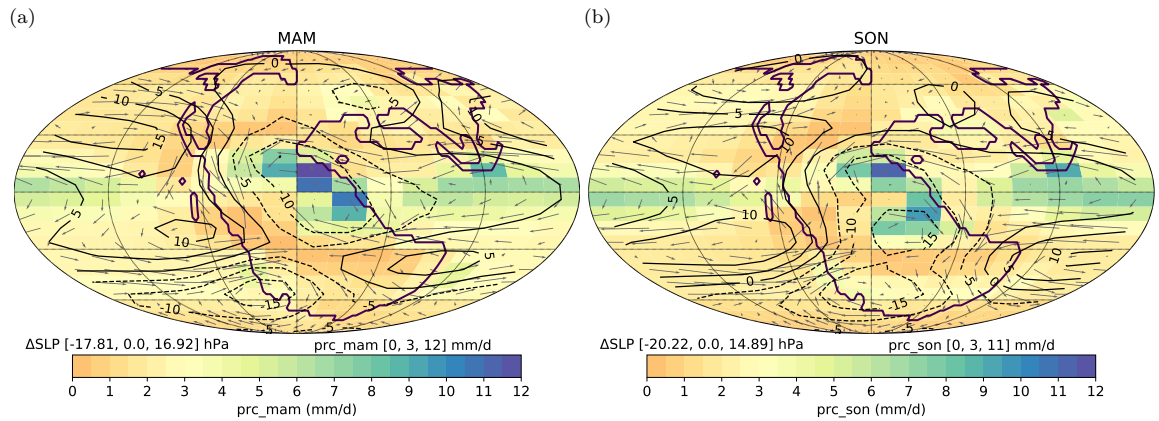


Figure S7: March-April-May (a) and September-October-November (b) precipitation (colours), sea level pressure anomalies (contours) and surface wind velocities (vectors) at $p\text{CO}_2 = 1500\text{ppm}$. Solid (dashed) contours indicate positive (negative) SLP anomalies with respect to the annual mean values.

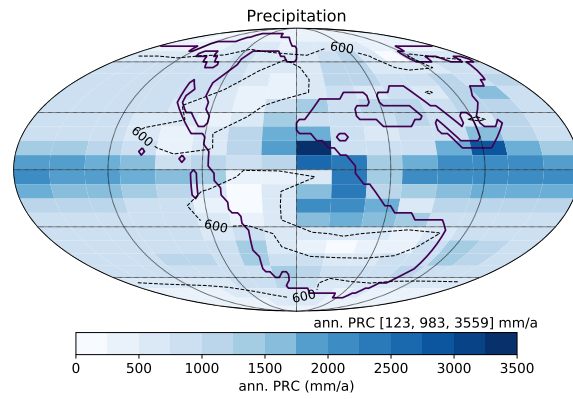


Figure S8: Annual precipitation at $p\text{CO}_2 = 1500 \text{ ppm}$. Contours indicate regions with $\leq 600 \text{ mm/a}$.

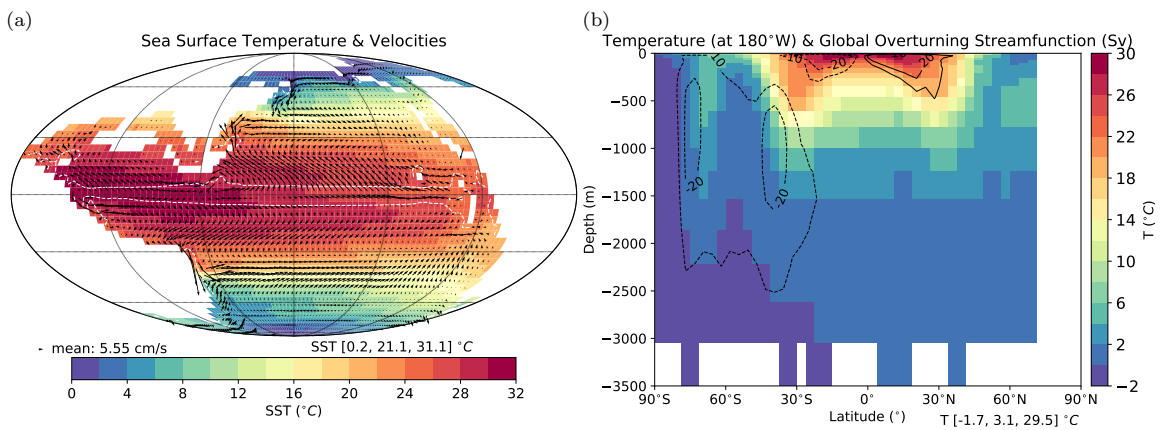


Figure S9: Ocean circulation and temperature at $p\text{CO}_2 = 1500 \text{ ppm}$. (a) Annual mean SST and horizontal velocities in a view centered on the Panthalassa Ocean. White contour lines encircle upwelling regions. (b) Ann. mean seawater temperature at 180°W (colours) and zonal mean overturning streamfunction (contours). Negative values (dashed contour lines) indicate counter-clockwise circulation.

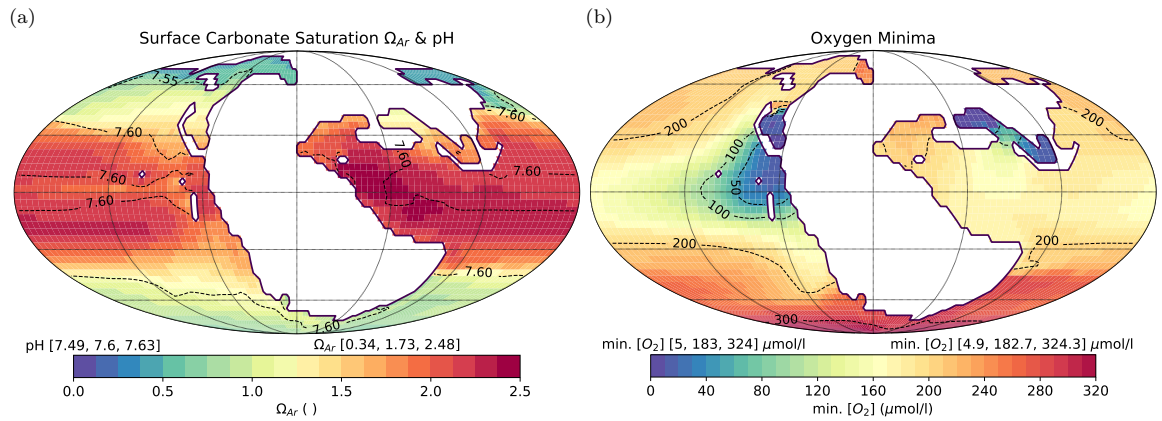


Figure S10: Annual mean surface carbonate saturation and pH (a) and oxygen minima in the water column (b) at $p\text{CO}_2 = 1500\text{ppm}$. In (a), contours indicate annual mean surface pH.

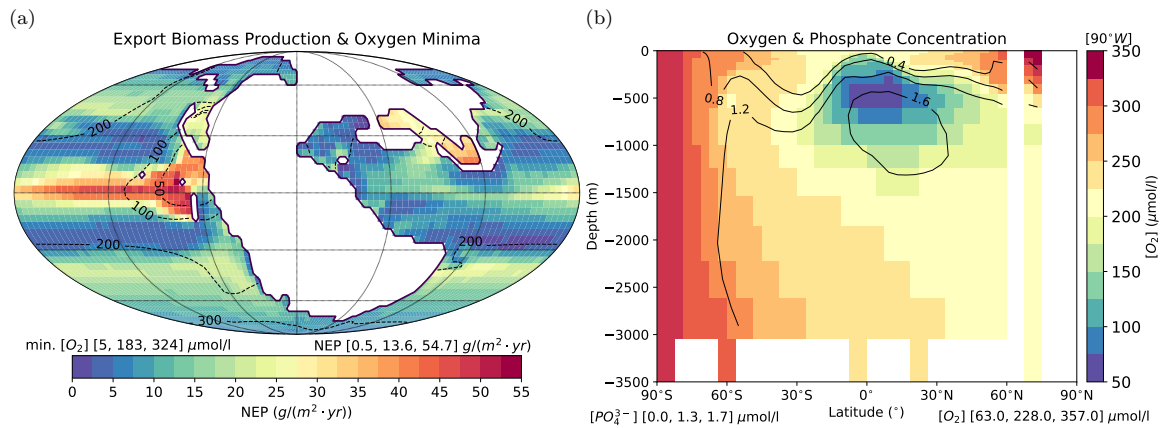


Figure S11: Marine biomass production and oxygen concentration at $p\text{CO}_2 = 1500\text{ppm}$. Contours indicate minimal oxygen concentrations in the water column in (a) and phosphate concentration in the 90°W cross-section in (b).

102 4. Results: Perturbation Experiments

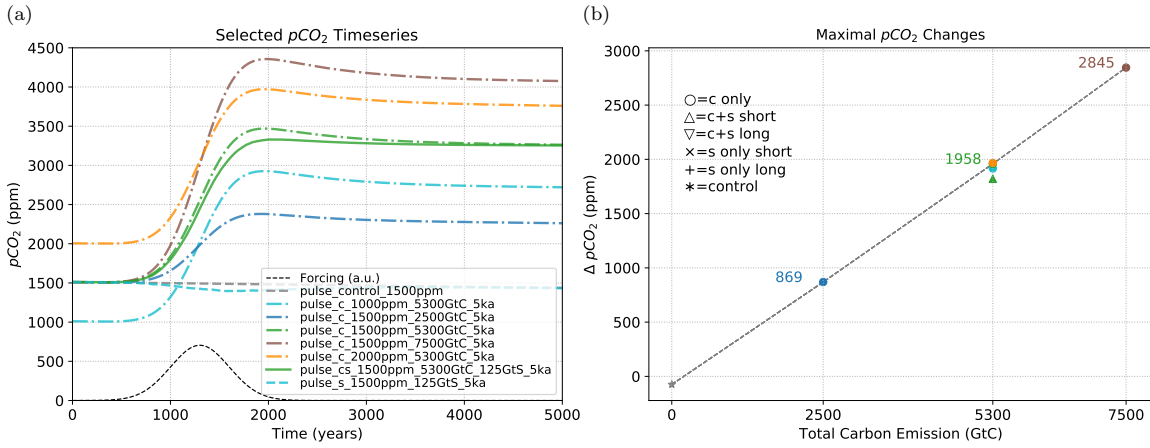


Figure S12: Atmospheric pCO_2 timeseries (a) and maximum changes depending on the emitted amount of carbon (b). (b) Displays maximal positive and negative deviations from the initial pCO_2 . The dashed line again connects short scenario runs with initially $pCO_2=1500$ ppm and zero sulfur emission.

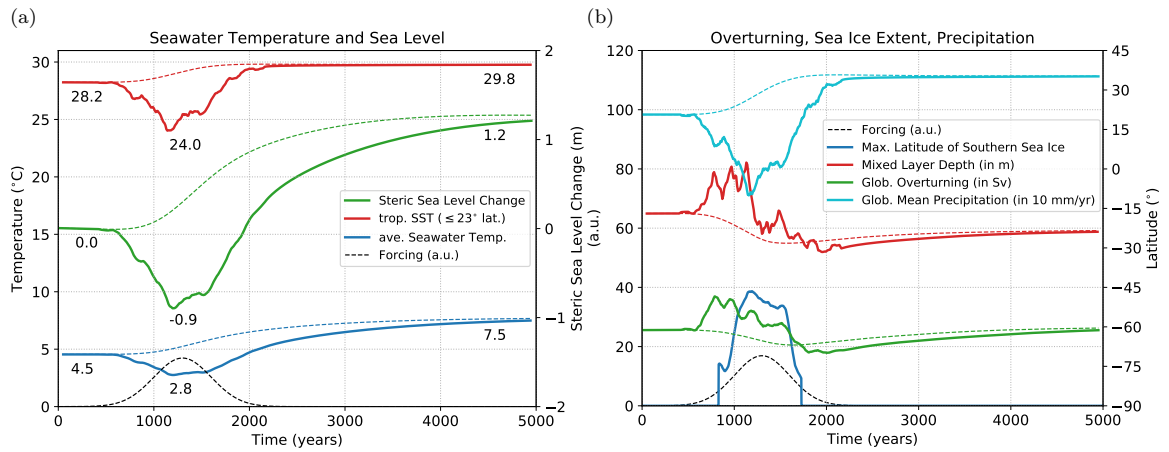


Figure S13: Change of several ocean and climate characteristics in the course of the 1500ppm_5300GtC+125GtS (solid lines) and 1500ppm_5300GtC (dashed lines) runs. The differences between dashed and solid lines are caused by the addition of sulfur emission. All quantities are 100yr moving averages. (b) Sea ice extent around the South Pole was quantified by the lowest latitude where an annual sea ice fraction $>10\%$ occurs. The green lines display the maximum meridional overturning streamfunction below 500 m depth in the southern hemisphere. Respective scaling factors for the left y axis are noted in the legend.

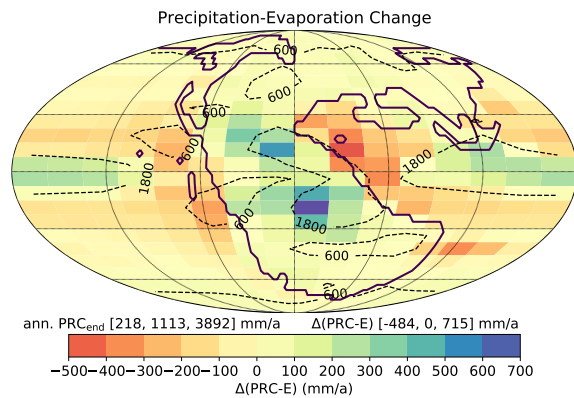


Figure S14: Change of the precipitation-evaporation difference. Between start and end of the 1500ppm_5300GtC+125GtS run. Blue colours indicate more humid conditions. Annual precipitation at the end of the run is indicated by contour lines.

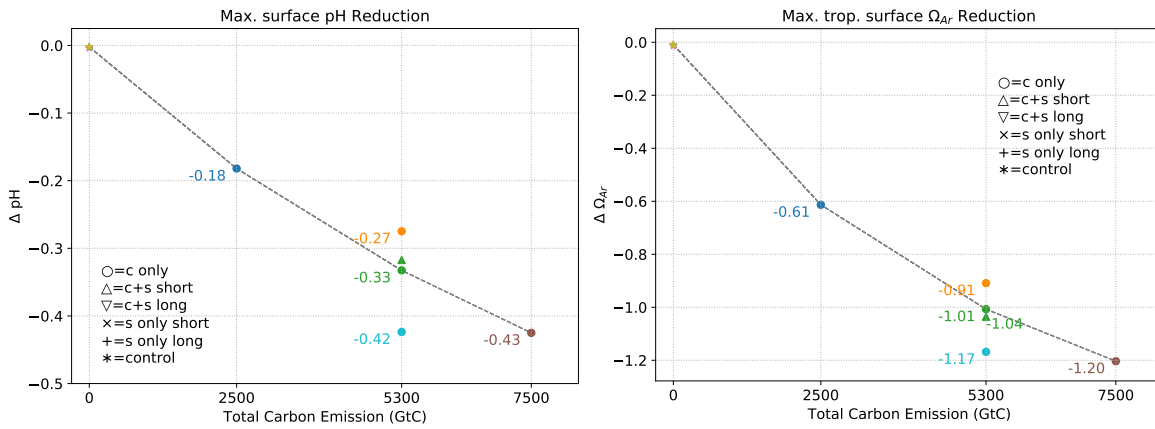


Figure S15: Maximum reduction of global mean surface pH (a) and tropical ($< 30^\circ$) surface carbonate saturation Ω_{Ar} (b) as a function of the total carbon emission. The displayed values are the maximum deviations of the 100yr moving average from an non-negligible positive drift in the control runs. The dashed lines again connect short scenario runs with initially $pCO_2 = 1500$ ppm and zero sulfur emission.

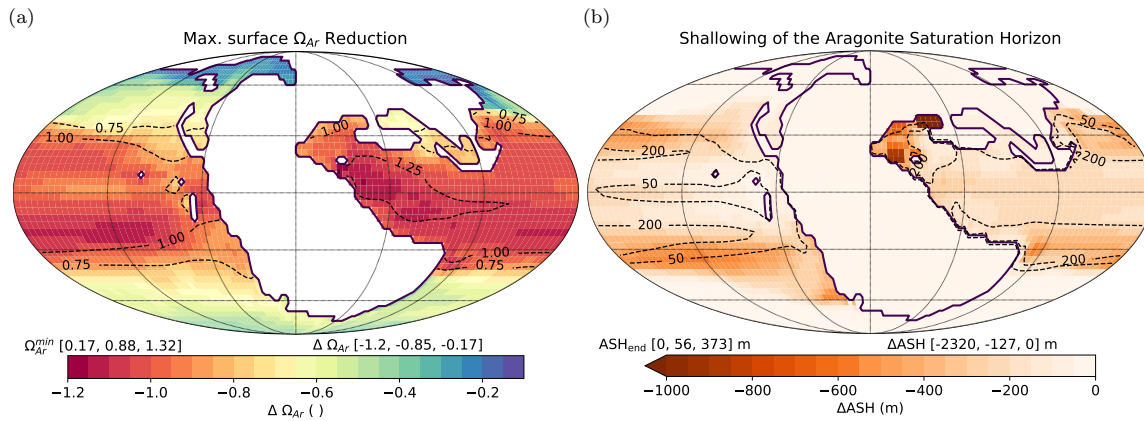


Figure S16: Maximum reduction of surface carbonate saturation Ω_{Ar} (a) and shallowing of the aragonite saturation horizon (ASH) depth (b) during the 1500ppm_5300GtC+125GtS run. (a) $\Delta\Omega_{Ar}$ (colours) is the deviation of the 100yr moving average from the initial values at the time of maximal global surface acidification. Contours indicate Ω_{Ar} at this time. (b) Displays the difference between the depths at which $\Omega_{Ar} = 1$ occurs at the beginning and the end of the simulation run. The initial ASH was set to equal the seafloor depth where no undersaturation occurs in the water column (shallow regions in NW Tethys).

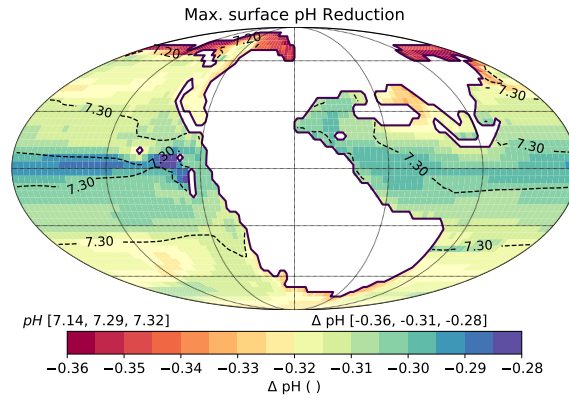


Figure S17: Maximum reduction of surface pH during the 1500ppm_5300GtC+125GtS run. (a) ΔpH (colours) is the deviation of the 100yr moving average from the initial values at the time of maximum global surface acidification. Contours indicate the pH at this time.

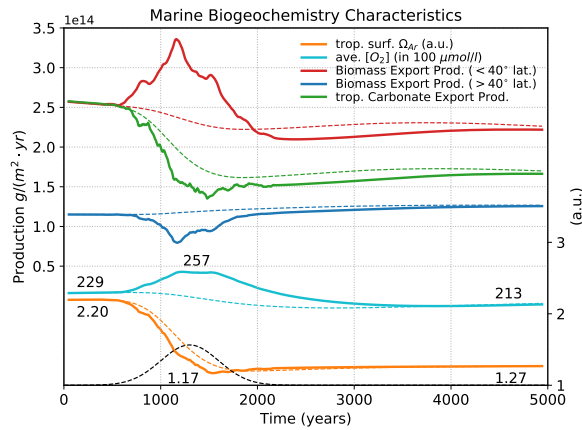


Figure S18: Change of several marine biogeochemistry characteristics in the course of the 1500ppm_5300GtC+125GtS (solid lines) and 1500ppm_5300GtC.5ka (dashed lines) runs. The differences between dashed and solid lines are caused by the addition of sulfur emission. All quantities are 100yr moving averages. The right y axis scales with a factor of 100 for the oxygen concentration.

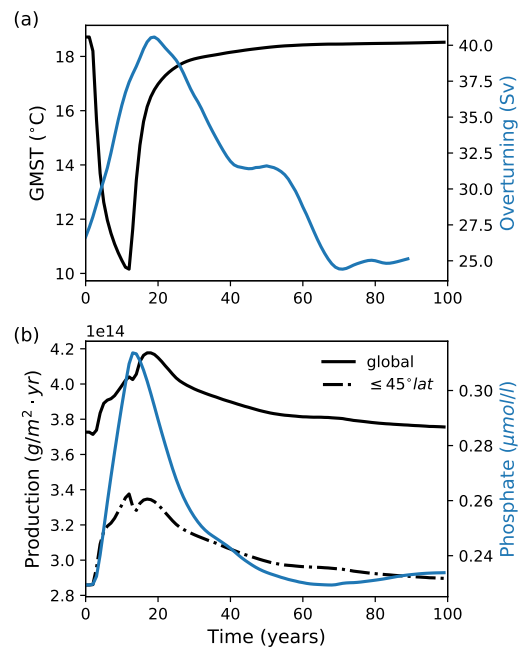


Figure S19: Increase of the marine export production in response to aerosol induced cooling and ocean mixing.

The forcing scenario consists of a constant injection of 528 MtS/yr for 10 years (corresponding to that in Fig. S2) which leads to a peak global cooling of -8.6 °C (black line in (a)). In response, the ocean overturning (defined as described in the main text) and the global mean surface phosphate nutrient concentration (averaged over the upper 100m ocean layer, blue line in (b)) increase. A corresponding increase of the global marine biomass export production can be observed (black line in (b)). This trend derives mainly from the mid- to low latitudes, whereas the productivity in the high latitudes is reduced for the duration of the cooling.

103 **5. Thermal Limits of Phytoplankton**

104 In analogy to the assessment of thermal limits of coral reef growth presented in the main paper, a similar
 105 assessment for marine phytoplankton growth rates based on the work of Thomas et al. (2012, 2015, 2017),
 106 is briefly outlined here. Those authors found optimal growth temperatures of around 27 °C for modern
 107 tropical phytoplankton groups. They also suggested an exponential decrease of growth rates and a maximum
 108 persistence limit at about 6 °C above that optimum. Such a temperature characteristic is shown in Fig. S20
 109 in conjunction with the simulated distribution of net biomass export production (NEP) over the simulated
 110 SSTs. In the initial Late Triassic equilibrium state, the simulated SSTs and NEPs fit well to the modern
 111 maximum growth rate function. The SSTs in the highly productive equatorial eastern Panthalassa are
 112 close to the optimum temperature, although slightly lower, while temperature in the warmest waters in the
 113 equatorial Tethys surpass the optimum. Apart from the low nutrient availability, marine biomass production
 114 in this region could therefore have been limited by temperature. However, one could argue, that Late Triassic
 115 phytoplankton groups were adapted to the higher maximum SSTs simulated for the Late Triassic, which
 116 exceed the modern ones by $\approx 1.6^\circ\text{C}$ (compared to data from Locarnini et al. 2018). The dashed line
 117 in Fig. S20 illustrates such a shift towards higher optimum and maximum persistence temperatures. In
 118 both cases, the upper thermal limits are not transgressed under global warming in this considered emission
 119 scenario (1500ppm_5300GtC+125GtS), although the temperature limitations to phytoplankton growth are
 120 exacerbated in the hottest regions. At the same time, phytoplankton growth in the nutrient rich high
 121 latitude oceans is promoted by the warming. In the cold phase, the opposite trend is observed in these
 122 regions.

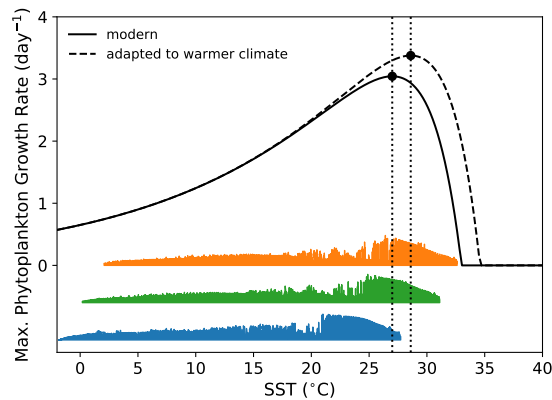


Figure S20: Phytoplankton growth rate temperature characteristic. Horizontal green, blue and red bars show on the one hand the SST range simulated in the initial, cold and warm phase of the 1500ppm_5300GtC+125GtS run and indicates the simulated NEP (Net Biomass Export Production) at every SST level on the other hand. The temperature limitation functions are proposed based on Thomas et al. (2012, 2015, 2017).

123 References

- 124 Barth, G., Franz, M., Heunisch, C., Ernst, W., Zimmermann, J. & Wolfgramm, M. (2018), 'Marine and terrestrial sedimentation
125 across the T–J transition in the north German basin', *Palaeogeography, Palaeoclimatology, Palaeoecology* **489**, 74–94.
- 126 Berner, R. A. & Beerling, D. J. (2007), 'Volcanic degassing necessary to produce a CaCO₃ undersaturated ocean at the
127 Triassic–Jurassic boundary', *Palaeogeography, Palaeoclimatology, Palaeoecology* **244**(1–4), 368–373.
- 128 Black, B. A. & Gibson, S. A. (2019), 'Deep Carbon and the Life Cycle of Large Igneous Provinces', *Elements* **15**(5), 319–324.
- 129 Bonan, G. B., Levis, S., Kergoat, L. & Oleson, K. W. (2002), 'Landscapes as patches of plant functional types: An integrating
130 concept for climate and ecosystem models', *Global Biogeochemical Cycles* **16**(2), 5 1–18.
- 131 Bond, D. P. & Grasby, S. E. (2017), 'On the causes of mass extinctions', *Palaeogeography, Palaeoclimatology, Palaeoecology*
132 **478**, 3–29.
- 133 Bond, D. P. & Wignall, P. B. (2014), 'Large igneous provinces and mass extinctions: an update', *Volcanism, impacts, and*
134 *mass extinctions: causes and effects* **505**, 29–55.
- 135 Ciarapica, G. (2007), 'Regional and global changes around the Triassic–Jurassic boundary reflected in the late No-
136 rian–Hettangian history of the Apennine basins', *Palaeogeography, Palaeoclimatology, Palaeoecology* **244**(1–4), 34–51.
- 137 Clapham, M. E. & Renne, P. R. (2019), 'Flood basalts and mass extinctions', *Annual Review of Earth and Planetary Sciences*
138 **47**(1), 275–303.
- 139 Davies, J., Marzoli, A., Bertrand, H., Youbi, N., Ernesto, M. & Schaltegger, U. (2017), 'End-Triassic mass extinction started
140 by intrusive CAMP activity', *Nature Communications* **8**(15596), 1–8.
- 141 Ernst, R. E. & Youbi, N. (2017), 'How large igneous provinces affect global climate, sometimes cause mass extinctions, and
142 represent natural markers in the geological record', *Palaeogeography, Palaeoclimatology, Palaeoecology* **478**, 30–52.
- 143 Fichefet, T. & Maqueda, M. M. (1997), 'Sensitivity of a global sea ice model to the treatment of ice thermodynamics and
144 dynamics', *Journal of Geophysical Research: Oceans* **102**(C6), 12609–12646.
- 145 Guan, Y., Hohn, S. & Merico, A. (2015), 'Suitable environmental ranges for potential coral reef habitats in the tropical ocean',
146 *PLoS one* **10**(6), 1–17.
- 147 Hallam, A. (1997), 'Estimates of the amount and rate of sea-level change across the Rhaetian–Hettangian and Pliensbachian-
148 Toarcian boundaries (latest Triassic to early Jurassic)', *Journal of the Geological Society* **154**(5), 773–779.
- 149 Hallam, A. & Wignall, P. (1999), 'Mass extinctions and sea-level changes', *Earth-Science Reviews* **48**(4), 217–250.
- 150 Haworth, M., Gallagher, A., Sum, E., Hill-Donnelly, M., Steinhorsdottir, M. & McElwain, J. (2014), 'On the reconstruction
151 of plant photosynthetic and stress physiology across the Triassic–Jurassic boundary', *Turkish Journal of Earth Sciences*
152 **23**(3), 321–329.
- 153 Heimdal, T. H. & Svensen, H. H. (2019), 'Modeling the effects of carbon release from the Central Atlantic Magmatic Province on
154 atmospheric pCO₂ and oceanic δ¹³C at the Triassic–Jurassic boundary', *Geophysical Research Abstracts* **21**, EGU2019–7542.
155 EGU General Assembly 2019.
- 156 Hofmann, M., Mathesius, S., Kriegler, E., van Vuuren, D. & Schellnhuber, H. (2019), 'Strong time dependence of ocean
157 acidification mitigation by atmospheric carbon dioxide removal', *Nature Communications* **10**(1), 1–10.
- 158 Hofmann, M. & Morales Maqueda, M. (2006), 'Performance of a second-order moments advection scheme in an ocean general
159 circulation model', *Journal of Geophysical Research: Oceans* **111**(C5), 1–26.
- 160 Hofmann, M. & Schellnhuber, H.-J. (2009), 'Oceanic acidification affects marine carbon pump and triggers extended marine
161 oxygen holes', *PNAS* **106**(9), 3017–3022.
- 162 Hüneke, H. & Henrich, R. (2011), Chapter 4 - Pelagic Sedimentation in Modern and Ancient Oceans, in H. Hüneke & T. Mulder,
163 eds, 'Deep-Sea Sediments', Vol. 63 of *Developments in Sedimentology*, Elsevier, pp. 215 – 351.
- 164 Jaraula, C. M., Grice, K., Twitchett, R. J., Böttcher, M. E., LeMetayer, P., Dastidar, A. G. & Opazo, L. F. (2013), 'Elevated
165 pCO₂ leading to Late Triassic extinction, persistent photic zone euxinia, and rising sea levels', *Geology* **41**(9), 955–958.

- 166 Jones, G. S., Gregory, J. M., Stott, P. A., Tett, S. F. B. & Thorpe, R. B. (2005), 'An AOGCM simulation of the climate
167 response to a volcanic super-eruption', *Climate Dynamics* **25**(7-8), 725–738.
- 168 Jones, M. T., Jerram, D. A., Svensen, H. H. & Grove, C. (2016), 'The effects of large igneous provinces on the global carbon
169 and sulphur cycles', *Palaeogeography, Palaeoclimatology, Palaeoecology* **441**, 4–21.
- 170 Kasprak, A. H., Sepúlveda, J., Price-Waldman, R., Williford, K. H., Schoepfer, S. D., Haggart, J. W., Ward, P. D., Summons,
171 R. E. & Whiteside, J. H. (2015), 'Episodic photic zone euxinia in the northeastern Panthalassic Ocean during the end-Triassic
172 extinction', *Geology* **43**(4), 307–310.
- 173 Kleypas, J. A., McManus, J. W. & Meñez, L. A. (2015), 'Environmental Limits to Coral Reef Development: Where Do We
174 Draw the Line?', *Integrative and Comparative Biology* **39**(1), 146–159.
- 175 Knight, K., Nomade, S., Renne, P., Marzoli, A., Bertrand, H. & Youbi, N. (2004), 'The Central Atlantic Magmatic Province at
176 the Triassic-Jurassic boundary - paleomagnetic and $^{40}\text{Ar}/^{39}\text{Ar}$ evidence from Morocco for brief, episodic volcanism', *Earth
177 and Planetary Science Letters* **228**, 143–160.
- 178 Korte, C., Hesselbo, S. P., Jenkyns, H. C., Rickaby, R. E. & Spötl, C. (2009), 'Palaeoenvironmental significance of carbon- and
179 oxygen-isotope stratigraphy of marine Triassic-Jurassic boundary sections in SW Britain', *Journal of the Geological Society*
180 **166**, 431–445.
- 181 Landwehrs, J. P., Feulner, G., Hofmann, M. & Petri, S. (2020), 'Climatic fluctuations modeled for carbon and sulfur emissions
182 from end-Triassic volcanism', *Earth and Planetary Science Letters* .
- 183 Langmann, B. (2014), 'On the role of climate forcing by volcanic sulphate and volcanic ash', *Advances in Meteorology* **2014**, 1–
184 17.
- 185 Lindström, S. (2015), 'Palynofloral patterns of terrestrial ecosystem change during the end-Triassic event – a review', *Geological
186 Magazine* **153**(02), 223–251.
- 187 Locarnini, R. A., Mishonov, A. V., Baranova, O. K., Boyer, T. P., Zweng, M. M., Garcia, H. E., Reagan, J. R., Seidov, D.,
188 Weathers, K., Paver, C. R. & Smolyar, I. (2018), 'World Ocean Atlas 2018, Volume 1: Temperature', *A. Mishonov, Technical
189 Ed.* pp. 1–52. NOAA Atlas NESDIS 81.
- 190 Luo, G., Richoz, S., Van De Schootbrugge, B., Algeo, T. J., Xie, S., Ono, S. & Summons, R. E. (2018), 'Multiple sulfur-
191 isotopic evidence for a shallowly stratified ocean following the Triassic-Jurassic boundary mass extinction', *Geochimica et
192 Cosmochimica Acta* **231**, 73–87.
- 193 Maier-Reimer, E. (1993), 'Geochemical cycles in an ocean general circulation model. Preindustrial tracer distributions', *Global
194 Biogeochemical Cycles* **7**(3), 645–677.
- 195 Mander, L., Kürschner, W. M. & McElwain, J. C. (2010), 'An explanation for conflicting records of Triassic–Jurassic plant
196 diversity', *Proceedings of the National Academy of Sciences* **107**(35), 15351–15356.
- 197 Mather, T. A. (2015), 'Volcanoes and the environment: Lessons for understanding earth's past and future from studies of
198 present-day volcanic emissions', *Journal of Volcanology and Geothermal Research* **304**, 160–179.
- 199 Mathesius, S., Hofmann, M., Caldeira, K. & Schellnhuber, H. J. (2015), 'Long-term response of oceans to CO₂ removal from
200 the atmosphere', *Nature Climate Change* **5**(12), 1107–1113.
- 201 McElwain, J. C., Beerling, D. J. & Woodward, F. I. (1999), 'Fossil plants and global warming at the Triassic-Jurassic boundary',
202 *Science* **285**(5432), 1386–1390.
- 203 McElwain, J. C., Popa, M. E., Hesselbo, S. P., Haworth, M. & Surlyk, F. (2007), 'Macroecological responses of terrestrial
204 vegetation to climatic and atmospheric change across the Triassic/Jurassic boundary in East Greenland', *Paleobiology*
205 **33**(4), 547–573.
- 206 McElwain, J. C., Wagner, P. J. & Hesselbo, S. P. (2009), 'Fossil plant relative abundances indicate sudden loss of Late Triassic
207 biodiversity in East Greenland', *Science* **324**(5934), 1554–1556.
- 208 McHone, J. G. (2003), *Volatile Emissions from Central Atlantic Magmatic Province Basalts: Mass Assumptions and Envi-*

209 *ronmental Consequences*, American Geophysical Union (AGU), pp. 241–254.

210 Metzner, D., Kutterolf, S., Toohey, M., Timmreck, C., Niemeier, U., Freundt, A. & Krüger, K. (2012), ‘Radiative forcing and
211 climate impact resulting from SO₂ injections based on a 200,000-year record of Plinian eruptions along the Central American
212 Volcanic Arc’, *International Journal of Earth Sciences* **103**(7), 2063–2079.

213 Mussard, M., Le Hir, G., Fluteau, F., Lefebvre, V. & Godd eris, Y. (2014), ‘Modeling the carbon-sulfate interplays in climate
214 changes related to the emplacement of continental flood basalts’, *Special Paper of the Geological Society of America* **505**, 339–
215 352.

216 Pacanowski, R. & Griffies, S. (2000), ‘MOM 3.0 Manual’, *Geophys. Fluid Dyn. Lab., Natl. Atmos. Admin., Princeton* pp. 1–708.

217 P alfy, J. & Zajzon, N. (2012), ‘Environmental changes across the Triassic–Jurassic boundary and coeval volcanism inferred
218 from elemental geochemistry and mineralogy in the kendlbachgraben section (Northern Calcareous Alps, Austria)’, *Earth
219 and Planetary Science Letters* **335–336**, 121–134.

220 Petoukhov, V., Ganopolski, A., Brovkin, V., Claussen, M., Eliseev, A., Kubatzki, C. & Rahmstorf, S. (2000), ‘CLIMBER-2: a
221 climate system model of intermediate complexity. Part I: model description and performance for present climate’, *Climate
222 Dynamics* **16**, 1–17.

223 Retallack, G. J. (2009), Triassic-Jurassic climates, in ‘Encyclopedia of Paleoclimatology and Ancient Environments’, Springer,
224 pp. 962–968.

225 Richoz, S., van de Schootbrugge, B., Pross, J., P uttmann, W., Quan, T. M., Lindstr om, S., Heunisch, C., Fiebig, J., Maquil,
226 R., Schouten, S., Hauzenberger, C. A. & Wignall, P. B. (2012), ‘Hydrogen sulphide poisoning of shallow seas following the
227 end-Triassic extinction’, *Nature Geoscience* **5**(9), 662–667.

228 Royer, D., Pagani, M. & Beerling, D. (2012), ‘Geobiological constraints on Earth system sensitivity to CO₂ during the Creta-
229 ceous and Cenozoic’, *Geobiology* **10**(4), 298–310.

230 Schaller, M. F., Wright, J. D. & Kent, D. V. (2014), ‘A 30 Myr record of late triassic atmospheric pCO₂ variation reflects
231 a fundamental control of the carbon cycle by changes in continental weathering’, *Geological Society of America Bulletin*
232 **127**(5/6), 661–671.

233 Schmidt, A., Mills, M. J., Ghan, S., Gregory, J. M., Allan, R. P., Andrews, T., Bardeen, C. G., Conley, A., Forster, P. M.,
234 Gettelman, A., Portmann, R. W., Solomon, S. & Toon, O. B. (2018), ‘Volcanic radiative forcing from 1979 to 2015’, *Journal
235 of Geophysical Research: Atmospheres* **123**(22), 12491–12508.

236 Schmidt, A., Skeffington, R. A., Thordarson, T., Self, S., Forster, P. M., Rap, A., Ridgwell, A., Fowler, D., Wilson, M., Mann,
237 G. W., Wignall, P. B. & Carslaw, K. S. (2016), ‘Selective environmental stress from sulphur emitted by continental flood
238 basalt eruptions’, *Nature Geoscience* **9**(1), 77–82.

239 Schneebeli-Hermann, E., Looser, N., Hochuli, P. A., Furrer, H., Reisdorf, A. G., Wetzler, A. & Bernasconi, S. M. (2017),
240 ‘Palynology of Triassic–Jurassic boundary sections in northern Switzerland’, *Swiss Journal of Geosciences* **111**(1), 99–115.

241 Scotese, C., J. Boucot, A. & Xu, C. (2014), ‘Atlas of Phanerozoic climatic zones’, PALEOMAP Project PaleoAtlas for ArcGIS.

242 Six, K. D. & Maier-Reimer, E. (1996), ‘Effects of plankton dynamics on seasonal carbon fluxes in an ocean general circulation
243 model’, *Global Biogeochemical Cycles* **10**(4), 559–583.

244 Soh, W. K., Wright, I. J., Bacon, K. L., Lenz, T. I., Steinhorsdottir, M., Parnell, A. C. & McElwain, J. C. (2017), ‘Palaeo
245 leaf economics reveal a shift in ecosystem function associated with the end-Triassic mass extinction event’, *Nature Plants*
246 **3**(17104), 1–8.

247 Steinhorsdottir, M., Jeram, A. J. & McElwain, J. C. (2011), ‘Extremely elevated CO₂ concentrations at the triassic/jurassic
248 boundary’, *Palaeogeography, Palaeoclimatology, Palaeoecology* **308**(3-4), 418–432.

249 Thomas, M. K., Aranguren-Gassis, M., Kremer, C. T., Gould, M. R., Anderson, K., Klausmeier, C. A. & Litchman, E. (2017),
250 ‘Temperature-nutrient interactions exacerbate sensitivity to warming in phytoplankton’, *Global Change Biology* **23**(8), 3269–
251 3280.

- 252 Thomas, M. K., Kremer, C. T., Klausmeier, C. A. & Litchman, E. (2012), ‘A global pattern of thermal adaptation in marine
253 phytoplankton’, *Science* **338**(6110), 1085–1088.
- 254 Thomas, M. K., Kremer, C. T. & Litchman, E. (2015), ‘Environment and evolutionary history determine the global biogeog-
255 raphy of phytoplankton temperature traits’, *Global Ecology and Biogeography* **25**(1), 75–86.
- 256 Toohey, M., Stevens, B., Schmidt, H. & Timmreck, C. (2016), ‘Easy Volcanic Aerosol (EVA v1.0): an idealized forcing generator
257 for climate simulations’, *Geoscientific Model Development* **9**(11), 4049–4070. [https://github.com/matthew2e/easy-volcanic-](https://github.com/matthew2e/easy-volcanic-aerosol)
258 [aerosol](https://github.com/matthew2e/easy-volcanic-aerosol).
- 259 Totmann-Parrish, J. & Curtis, R. L. (1982), ‘Atmospheric circulation, upwelling, and organic-rich rocks in the Mesozoic and
260 Cenozoic eras’, *Palaeogeography, Palaeoclimatology, Palaeoecology* **40**, 31–66.
- 261 Trotter, J. A., Williams, I. S., Nicora, A., Mazza, M. & Rigo, M. (2015), ‘Long-term cycles of Triassic climate change: a new
262 $\delta^{18}\text{O}$ record from conodont apatite’, *Earth and Planetary Science Letters* **415**, 165–174.
- 263 Wignall, P. B. & Bond, D. P. G. (2008), ‘The end-Triassic and Early Jurassic mass extinction records in the British Isles’,
264 *Proceedings of the Geologists’ Association* **119**, 73–84.
- 265 Willis, K. & McElwain, J. (2002), *The Evolution of Plants*, New York, Oxford University Press.
- 266 Wotzlaw, J.-F., Guex, J., Bartolini, A., Gallet, Y., Krystyn, L., McRoberts, C. A., Taylor, D., Schoene, B. & Schaltegger, U.
267 (2014), ‘Towards accurate numerical calibration of the Late Triassic: High-precision U-Pb geochronology constraints on the
268 duration of the Rhaetian’, *Geology* **42**(7), 571–574.
- 269 Zaffani, M., Jadoul, F. & Rigo, M. (2018), ‘A new Rhaetian $\delta^{13}\text{C}_{org}$ record: Carbon cycle disturbances, volcanism, end-Triassic
270 mass extinction (ETE)’, *Earth-Science Reviews* **178**, 92–104.
- 271 Zajzon, N., Kristály, F., Pálffy, J. & Németh, T. (2012), ‘Detailed clay mineralogy of the Triassic-Jurassic boundary section at
272 Kendlbachgraben (Northern Calcareous Alps, Austria)’, *Clay Minerals* **47**(2), 177–189.
- 273 Zeebe, R. (2012a), ‘LOSCAR: Long-term Ocean-atmosphere-Sediment CARbon cycle Reservoir model v2.0.4’, *Geoscientific*
274 *Model Development* **5**(1), 149–166.
- 275 Zeebe, R. E. (2012b), ‘History of Seawater Carbonate Chemistry, Atmospheric CO_2 , and Ocean Acidification’, *Annual Review*
276 *of Earth and Planetary Sciences* **40**(1), 141–165.

A.IV Supplementary Figures

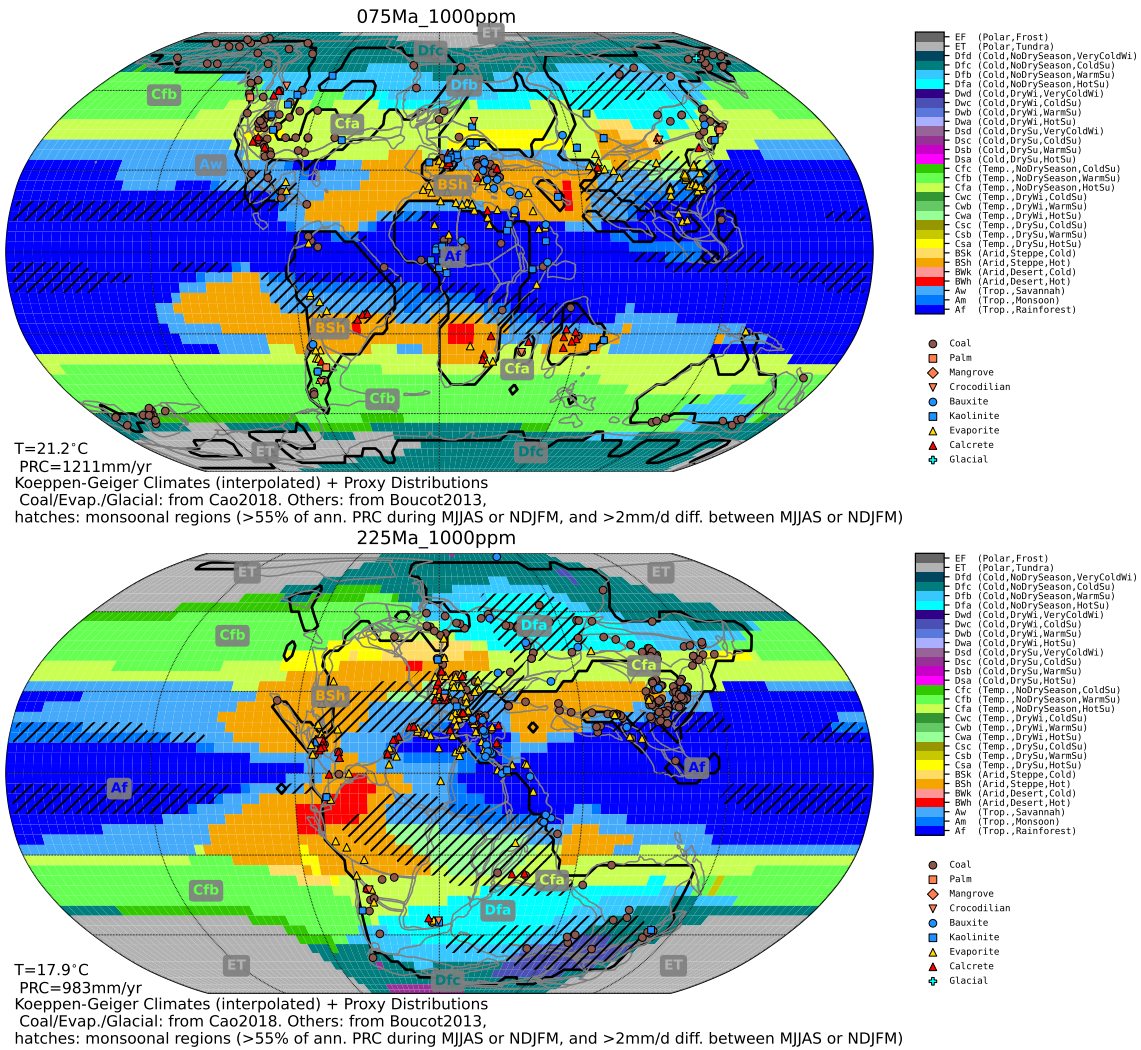


Figure S1: Simulated climate zones (colored areas) and monsoonal conditions (black hatches) as well as lithologic climate indicators (markers) for the 75 and 225 Ma time slices. Colored areas indicate Köppen climate zones determined from monthly surface temperatures and precipitation rates simulated by CLIMBER-3 α (P.I). Black hatches indicate monsoonal climate conditions determined from the simulated monthly precipitation rates using the monsoon definition of Wang et al. 2014 ($|\text{PRC}_{\text{MJJAS}} - \text{NDJFM}| \geq 2 \text{ mm/d}$ and $\text{PRC}_{\text{MMJAS}}/\text{PRC}_{\text{ann}} \geq 0.5$). Markers indicate occurrences of lithologic climate indicators from Boucot et al. 2013.

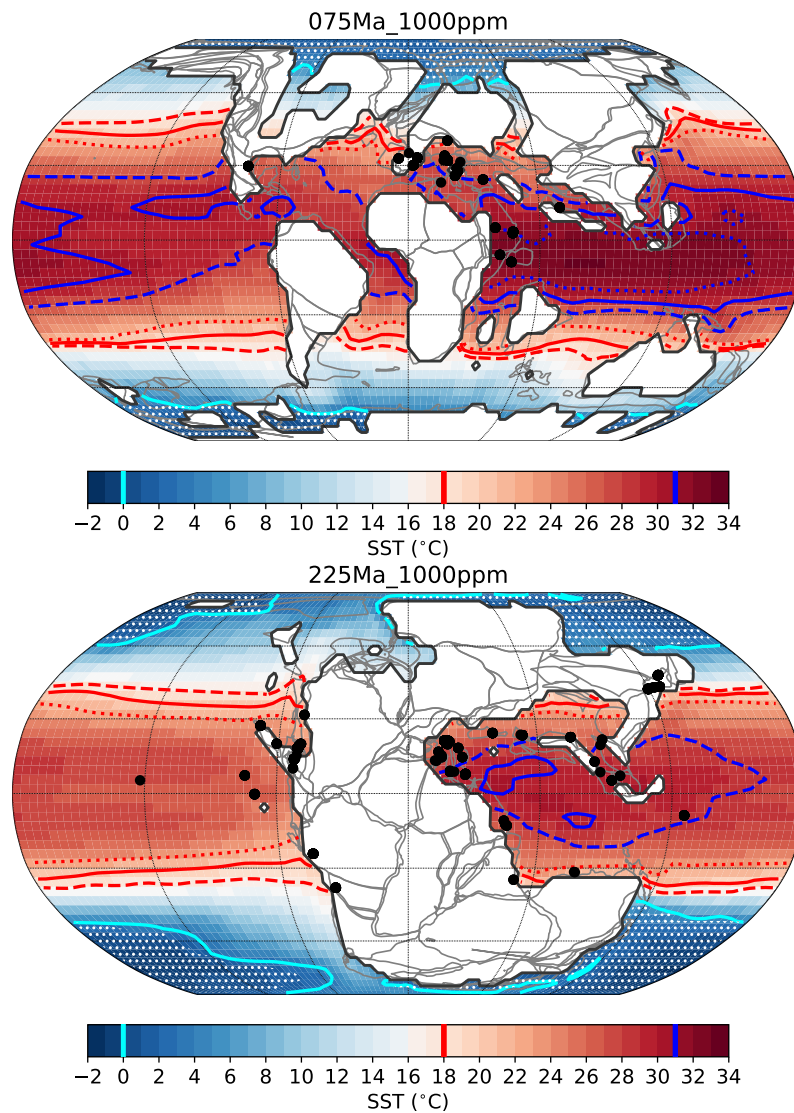


Figure S2: Simulated sea surface temperatures (SST, colors) and coral reef occurrences (dots) for the 75 and 225 Ma time slices. The color shading indicates annual mean SSTs simulated by CLIMBER-3 α (P.I). The blue and red colored contours indicate the monthly maximum 31 °C and monthly minimum 18 °C isotherms that approximate the thermal niche of modern scleractinian coral reefs. The solid contours are for $p\text{CO}_2 = 1000$ ppm, whereas the dashed and dotted contours are for 2000 and 500 ppm, respectively. The black dots indicate fossil scleractinian coral reef occurrences from the Paleobiology Database for the respective time period. The white dots indicate the simulated annual mean extent of sea ice.

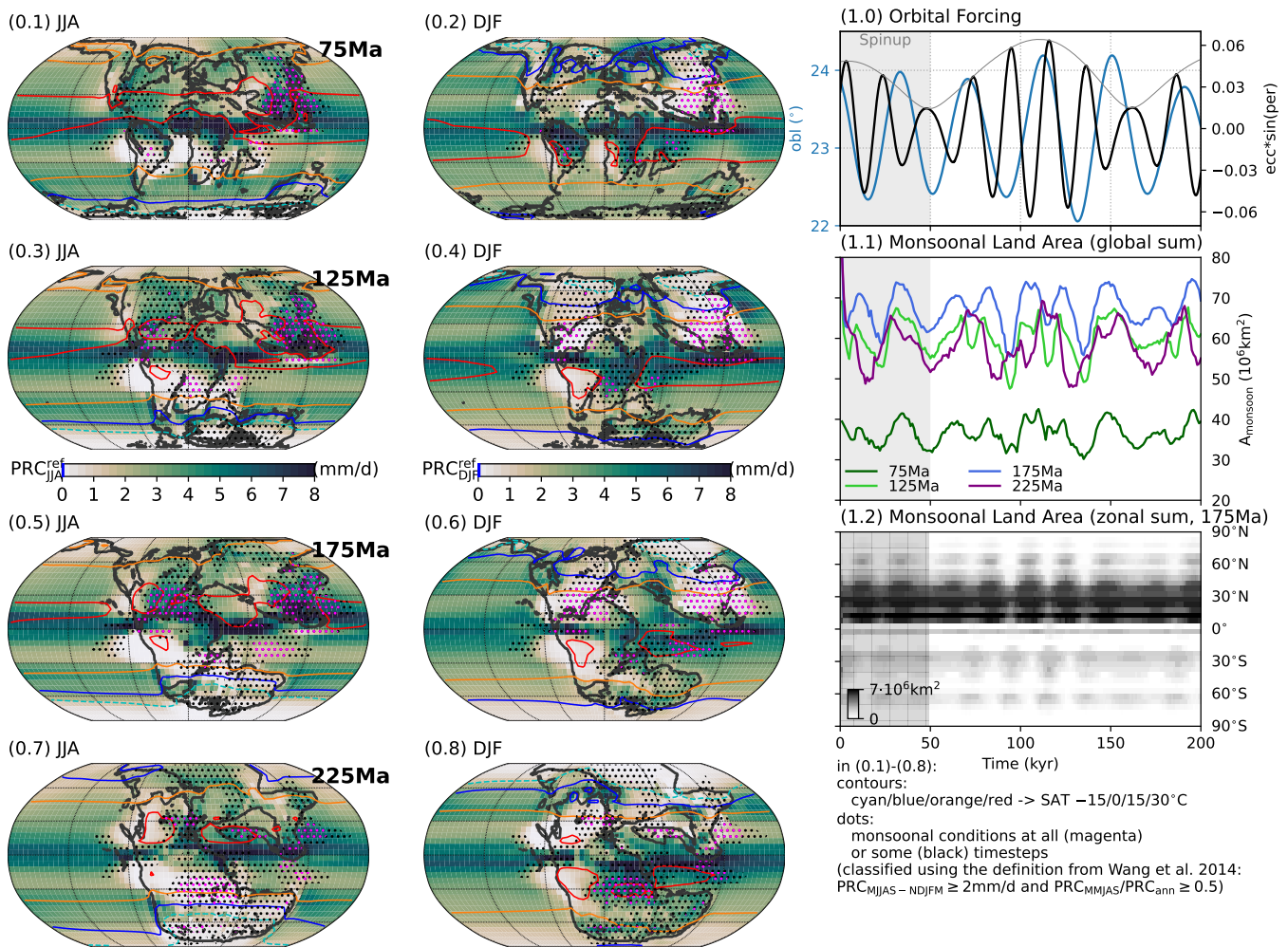


Figure S3: Simulated precipitation and monsoonal areas as well as their orbital modulation for the 75, 125, 175 and 225 Ma time slices. Maps on the left side show the seasonal (JJA and DJF) precipitation (colors) and surface temperatures (colored contours) simulated by CLIMBER-X for the four time slices. These are long-term averages over the orbitally-driven simulations. The dots indicate areas where monsoonal conditions are simulated for at least one (black dots) or all (pink dots) time steps of the simulation. Monsoonal conditions are determined from the monthly rainfall rates using the definition of Wang et al. (2014). Panel (1.0) indicates the applied orbital forcing. Panel (1.2) shows the zonal sum of monsoonal areas for the 175 Ma time slice and how this changes in response to the orbital forcing. Similarly, panel (1.1) shows the changing global extent of monsoonal areas for all four time slices. Modified from Landwehrs et al. (2021c).

Orbitally driven changes of the Terrestrial Water Storage Anomaly (TWSA) and Sea Level Equivalent diagnosed from the balance of Precipitation–Evapotranspiration–Runoff (P-ET-R)

run: 125Ma_orb_1000ppm_ecc-obl-per

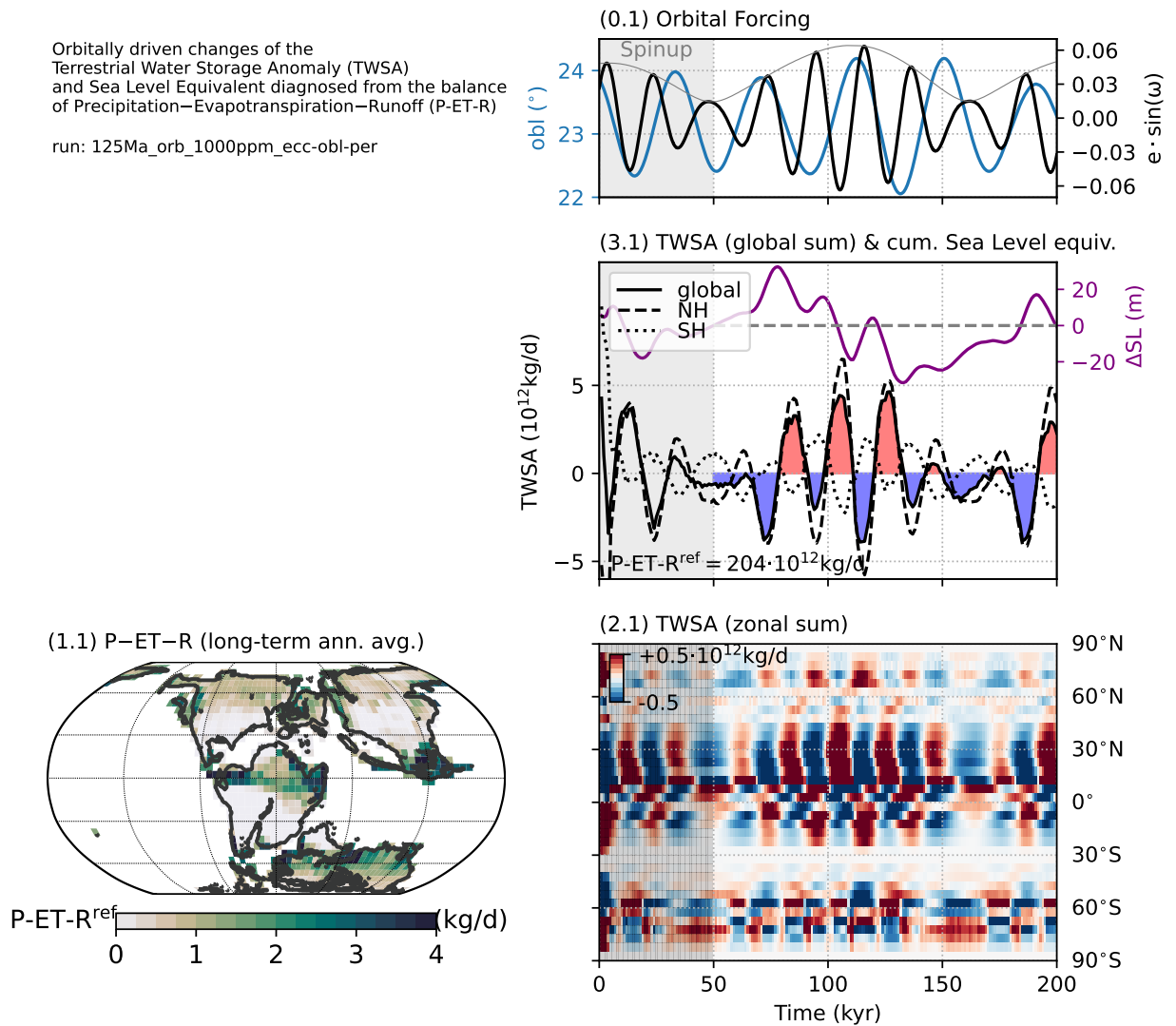


Figure S4: Simulated orbital modulation of the hydrological balance and Terrestrial Water Storage Anomaly (TWSA) at 125 Ma. Panel (0.1) shows the applied orbital forcing. Panel (1.1) shows the long-term annual average Precipitation–Evapotranspiration–Runoff balance. Panel (2.1) zonal average TWSA, which is the deviation from the long-term P–ET–R. Panel (3.1) shows the orbital response of the TWSA averaged over the whole globe (solid black line) or over the northern or southern hemisphere (dashed and dotted black lines). In the upper part of this panel, the cumulative global TWSA has been converted into an equivalent sea level change (purple line). The simulation was carried out with the CLIMBER-X model. Modified from Landwehrs et al. (2021c).